

Important Notice

This copy may be used only for the purposes of research and private study, and any use of the copy for a purpose other than research or private study may require the authorization of the copyright owner of the work in question. Responsibility regarding questions of copyright that may arise in the use of this copy is assumed by the recipient.

UNIVERSITY OF CALGARY

Orientation Azimuth Calibration of Borehole Geophones

by

Pietro Giuseppe Gagliardi

A THESIS

SUBMITTED TO THE FACULTY OF GRADUATE STUDIES
IN PARTIAL FULFILMENT OF THE REQUIREMENTS FOR THE
DEGREE OF MASTER OF SCIENCE

DEPARTMENT OF GEOSCIENCE

CALGARY, ALBERTA

SEPTEMBER, 2012

© Pietro Giuseppe Gagliardi 2012

Abstract

Using results from field experiments and forward modelling, factors affecting the orientation calibration of borehole geophones were investigated. Well deviation, lateral raybending and anisotropy were all found to produce systematic deviations in orientation analysis. A method was developed to compensate for effects due to a deviated well, and successfully applied to a field dataset. The effects due to lateral raybending and anisotropy were characterised using analytic and finite-difference models; these produced one-cycle and two-cycle sinusoidal trends when orientation was plotted against source-well azimuth. Significant evidence of these trends was found in field examples, in that the magnitude of the trends was greater than the standard deviations in orientation azimuth.

Analytic and hodogram methods of orientation analysis were compared, and it was found that the analytic method produced more consistent results. The optimal size of the analysis window was related to the wavelength of the direct P-wave arrival, but should generally be determined experimentally. Finally, it was shown that the optimal source-well offset range for calibration surveys was between 1 and 2 times the receiver depth.

Acknowledgements

First, I would like to thank my supervisor, Dr. Don Lawton, for guidance, support, encouragement and advice over the last three years, starting with my final year as an undergraduate student. The (not so subtle) attempts at coercing me to do an M. Sc. with CREWES provided a unique and advantageous beginning to my graduate studies. How many undergrads are lucky enough to get an office and computer to work on their Honours Thesis? Don truly understood how I worked, and truly cares for his students; I could not have had a better supervisor for my Master's degree.

Thank you to the faculty and associated faculty of CREWES, who have all been very supportive of my endeavours over the course of my degree. Thank you to Dr. Gary Margrave who, between a short MATLAB summer course and the signal processing course, gave me a great starting point to learn MATLAB, which ended up being integral to my thesis. I am very grateful to Dr. Larry Lines for giving me the opportunity to deliver a lecture in Petrophysics – it's an experience I will never forget. Thank you to Dr. Kris Innanen for encouragement and support through my research, as well as my TA duties for GOPH 355. And of course, for so readily agreeing to sit on my defense committee! Thanks to Dr. Rob Ferguson for giving me an opportunity to be a TA while I was an undergrad, which led to a fulfilling three semesters as TA Coordinator of GOPH 355. Heartfelt thanks to Dr. Brian Russell for taking the time to have an important discussion with me about career paths. Finally, I would like to thank Dr. Mike Wieser from the Department of Physics and Astronomy for agreeing to be my external examiner, and taking such a great interest in my work.

I would also like to thank all of the staff of CREWES. Thanks to Kevin Bertram for getting all of my (and the rest of CREWES!) posters printed over the last couple of years. It takes a great deal of time and effort, and the posters have always turned out great! Another big thanks goes to Kevin Hall for providing tireless tech support. It's not often that someone drops what they are doing for 2 hours to fix your computer, at lunchtime, without an appointment, without a hint of complaint, while maintaining their awesome sarcastic sense of humour. But that's just another day for Kevin! Of course,

thank you to Laura Baird for being the glue that holds CREWES together. Thank you for the constant encouragement and optimism, and for making sure I stayed on the ball with deadlines. I will miss working with all three of you.

The students of CREWES have been a huge part of my journey in the last two years. Thank you to Faranak Mahmoudian for constantly giving me advice, and for extremely helpful discussions surrounding seismic anisotropy. I am grateful to Steve Kim for patiently putting up with my ramblings and joining me for many coffee runs. To my neighbours across the hall: Byron Kelly, Andrew Nicol and Jessie Arthur; to the two Shahins: Shahin One (Jabbari) and Shahin Two (Moradi); and to Patricia Gavotti, David Cho and Hormoz Izadi; thank you for all the support, and for reminding me to have a little bit of fun once in a while!

I am grateful to CREWES sponsors and NSERC for financial support. I would also like to thank Henry Bland of Pinnacle Technologies (a brand of Halliburton) for providing some insight into the topic of geophone orientation calibration, along with an insightful post-presentation comment that eventually sparked the idea for spider plots.

I have been blessed to have some very knowledgeable and personable office mates – in particular, Dr. Rob Taerum and Melissa Newton. Rob gave me essential advice throughout my graduate studies, particularly while writing my thesis. Melissa was always willing to listen to the roadblocks I would encounter in my research, and provide me with a unique angle. I certainly chose the right office to work in! Additionally, the students and staff working in the Microseismic Industry Consortium, particularly Jubran Akram and Neda Boroumand, were a great help in providing me with context for my research.

Dr. Ed Krebs, Tracy Quinton, Cathy Hubbell and the rest of the Geoscience staff played essential roles through my undergraduate and graduate studies. The staff of the Gallagher Library were a great help while looking up papers, books and theses. The department is lucky to have such dedicated and hardworking staff! I would also like to

thank the students I've had over the years, especially those of GOPH 355, for all of the uplifting comments that could quickly turn a stressful day of teaching into a very rewarding one.

There are three fellow grad students that have been a crucial part of this stage of my life, and will continue to be a part of my life as good friends. Chris Bird was someone I constantly looked up to, and his work ethic and accomplishments were a benchmark that I strived towards. His enthusiasm was contagious, and he was a constant inspiration to me throughout my graduate studies. Heather Lloyd was a staunch supporter of mine throughout this experience; she was willing to sit through most of the talks I gave in the last two years, and was always able to give me useful comments and criticisms. She was someone I could bounce ideas off of, share my accomplishments with, and talk to about my problems (both academic and personal). And of course, I would like to thank Keith D'Arcy, who has been my friend since day one of my undergraduate degree. Who would have guessed that we both would have ended up switching majors from physics into geoscience, and both gone on to do our Master's degrees? Keith was instrumental in helping me to get through the transition to geophysics, and provided me with ample opportunities to learn more about geology.

There are several members of my family that have been great supporters of my endeavours as a Master's student. First of all, thank you to Zia and Uncle Vince for helping me get my foot in the door as a geophysicist, and for constant encouragement through my studies. Thank you to Nonna, Grandma and Grandpa for unconditional love and support; and to Nonno, you might not be here in person anymore, but I know you have been with me in spirit. Thank you to Antonella Fulginiti, my future sister in law (aka Sis-Ta-Be), and thank you to the Hough family (Paula, Les, Sheridan and Gavin). Even though they have only been in my life a few years, they are all family to me, and have been a big source of support through this thesis.

Thank you to my brother, Anthony, for your support throughout this degree. It is not always the case that siblings get along well, but Anth has always been my best friend.

He supported me throughout this thesis, and made sure that I kept myself grounded. To Mom and Dad; I don't think it's possible to convey how thankful I am for you being in my life. You have always been my greatest supporters, teachers, role models and heroes. You are what I aspire to every day, and I am proud to be your son.

An immense thank you to my girlfriend, Rachael Hough; you have been with me every step of this journey. Your love has helped me get through the more difficult times in this degree; you shared in all of my accomplishments with enthusiasm that was often greater than my own. Every day I am reminded of how lucky I am to have found you; and in that vein, (in a somewhat unorthodox manner) I would like to thank this thesis for providing the right circumstances for our relationship to blossom. Rachael, I love you all ways...

Finally, I would like to thank God for all the blessings He has given me in my life and throughout this experience.

To Mom and Dad, my role models in everything; to Nonno, Pietro Gagliardi.

Table of Contents

| | |
|--|--------|
| Abstract | ii |
| Acknowledgements | iii |
| Dedication | vii |
| Table of Contents | viii |
| List of Tables | xii |
| List of Figures and Illustrations | xiv |
| List of Symbols, Abbreviations and Nomenclature | xxxiii |
| | |
| CHAPTER ONE: INTRODUCTION | 1 |
| 1.1 Borehole Geophone Orientation | 1 |
| 1.1.1 Vertical Seismic Profile (VSP) Surveys | 1 |
| 1.1.2 Importance and Application to Microseismic Studies | 2 |
| 1.1.3 Calibration Surveys | 3 |
| 1.2 Seismic Repeatability | 7 |
| 1.2.1 Time-Lapse Seismology | 7 |
| 1.2.2 NRMS Repeatability (NRMS) | 8 |
| 1.2.3 Predictability (PRED) | 8 |
| 1.2.4 Signal to Distortion Ratio (SDR) | 9 |
| 1.3 Rotation Methods | 9 |
| 1.3.1 Analytic | 9 |
| 1.3.2 Hodograms | 10 |
| 1.3.3 Common Reference Frame | 11 |
| 1.3.4 Spider Plots | 12 |
| 1.4 Field Study Site: Pembina CO ₂ Project | 13 |
| 1.5 Objectives and Outline of Thesis | 14 |
| 1.5.1 Objectives | 14 |
| 1.5.2 Outline | 14 |
| 1.6 Software | 16 |
| 1.6.1 MATLAB | 16 |
| 1.6.2 TIGER | 16 |
| 1.6.3 GEDCO Vista | 16 |
| | |
| CHAPTER TWO: PEMBINA TIME-LAPSE FIELD EXAMPLE | 17 |
| 2.1 Introduction | 17 |
| 2.2 Survey Parameters | 17 |
| 2.3 Field Experiment | 21 |
| 2.3.1 Seismic Repeatability | 21 |
| 2.3.2 Orientation Azimuth | 26 |
| 2.3.2.1 Repeatability between Surveys and Window Tests | 26 |
| 2.3.2.2 Consistency within Surveys | 32 |
| 2.4 Controlled Experiment | 42 |
| 2.4.1 Experiment Parameters | 42 |
| 2.4.2 Time-Shift Tests | 43 |
| 2.4.3 Amplitude Tests | 45 |
| 2.4.4 Noise Tests | 46 |

| | |
|--|-----|
| 2.5 Discussion..... | 49 |
| 2.5.1 Repeatability..... | 49 |
| 2.5.2 Orientation Azimuths | 50 |
| 2.6 Summary..... | 51 |
| | |
| CHAPTER THREE: EFFECTS OF RANDOM NOISE ON ORIENTATION | |
| ANALYSIS..... | 54 |
| 3.1 Introduction..... | 54 |
| 3.2 Finite Difference Modelling | 54 |
| 3.3 Additive Noise | 57 |
| 3.3.1 Noise Generation | 57 |
| 3.3.2 Noise Addition..... | 59 |
| 3.4 Results..... | 60 |
| 3.4.1 Noise Pattern 1 | 60 |
| 3.4.2 Noise Pattern 2 | 66 |
| 3.5 Discussion..... | 70 |
| 3.6 Summary..... | 70 |
| | |
| CHAPTER FOUR: PEMBINA DEVIATED WELL EXAMPLE | 72 |
| 4.1 Introduction..... | 72 |
| 4.2 Survey parameters..... | 72 |
| 4.3 Orientation in a Deviated Well | 76 |
| 4.4 Results..... | 78 |
| 4.5 Modelling Deviation Error..... | 97 |
| 4.6 Discussion..... | 103 |
| 4.7 Summary..... | 104 |
| | |
| CHAPTER FIVE: DIPPING BEDS | 106 |
| 5.1 Introduction..... | 106 |
| 5.2 Raytracing..... | 106 |
| 5.2.1 Algorithm | 106 |
| 5.2.1.1 Overview..... | 106 |
| 5.2.1.2 Definitions of Interface Plane and Initial Ray | 108 |
| 5.2.1.3 Vector Form of Snell's Law | 109 |
| 5.2.1.4 Raypath Distances and Source-Well Azimuth..... | 110 |
| 5.2.2 Tests Using Constant Dip and Constant Velocity | 111 |
| 5.3 Finite Difference Modelling | 115 |
| 5.3.1 Model Parameters..... | 115 |
| 5.3.2 Results | 117 |
| 5.3.3 Comparison to Raytracing Method | 123 |
| 5.4 Discussion..... | 123 |
| 5.5 Summary..... | 124 |
| | |
| CHAPTER SIX: HTI MEDIUM | 126 |
| 6.1 Introduction..... | 126 |
| 6.2 Background..... | 126 |
| 6.2.1 Weak Anisotropy..... | 126 |

| | |
|--|-----|
| 6.2.2 Group and Phase Angle | 126 |
| 6.2.3 Measurement at Receiver | 127 |
| 6.3 Analytic Modelling | 128 |
| 6.3.1 Maximum Angle Difference Dependent on δ and ε | 128 |
| 6.3.2 Modelled Calibration Survey | 130 |
| 6.4 Finite Difference Modelling | 135 |
| 6.4.1 Model Parameters | 135 |
| 6.4.2 Results | 138 |
| 6.4.3 Comparison to Analytic Method | 143 |
| 6.5 Discussion..... | 144 |
| 6.6 Summary..... | 145 |
| | |
| CHAPTER SEVEN: LOUSANA 3D FIELD EXAMPLE | 147 |
| 7.1 Introduction..... | 147 |
| 7.2 Survey Geometry | 147 |
| 7.3 2D walkaway results | 150 |
| 7.4 3D walkaway Results..... | 155 |
| 7.4.1 Sector analysis | 155 |
| 7.4.2 Geophone orientation statistics..... | 159 |
| 7.4.3 Offset analysis | 162 |
| 7.5 Discussion..... | 167 |
| 7.6 Summary..... | 168 |
| | |
| CHAPTER EIGHT: DISCUSSION, CONCLUSIONS AND RECOMMENDATIONS | 170 |
| 8.1 Discussion..... | 170 |
| 8.2 Conclusions..... | 174 |
| 8.2.1 Objective 1: Effects of Noise, Deviation, Raybending and Anisotropy..... | 174 |
| 8.2.2 Objective 2: Analysis Method and Survey Design..... | 175 |
| 8.2.3 Objective 3: Analysis of Field Data | 176 |
| 8.2.4 Other Conclusions | 177 |
| 8.3 Recommendations..... | 178 |
| | |
| REFERENCES | 180 |
| | |
| APPENDIX A: MATHEMATICAL PROOFS | 183 |
| A.1. Orthonormal Vector Basis of Pseudo-Coordinates..... | 183 |
| A.2. Snell's Law in Vector Form..... | 185 |
| | |
| APPENDIX B: EXPANDED RESULTS FOR PEMBINA TIME-LAPSE STUDY..... | 189 |
| | |
| APPENDIX C: EXPANDED RESULTS FOR RANDOM NOISE MODELLING | 214 |
| | |
| APPENDIX D: EXPANDED RESULTS FOR DEVIATED WELL STUDY | 228 |
| | |
| APPENDIX E: EXPANDED RESULTS FOR FINITE-DIFFERENCE MODELS | 242 |
| E.1. Dipping Interface..... | 242 |

| | |
|--|-----|
| E.2. HTI Medium..... | 242 |
| APPENDIX F: EXPANDED RESULTS FOR LOUSANA STUDY | 258 |

List of Tables

| | |
|--|-----|
| Table 2.1: Receiver depths used in field study. | 18 |
| Table 2.2: Summary of repeatability metrics of Violet Grove z-component data. Receiver 2 has been omitted. | 25 |
| Table 2.3: Summary of repeatability metrics of Violet Grove x-component data. Receiver 4 has been omitted. | 25 |
| Table 2.4: Summary of repeatability metrics of Violet Grove y-component data. Receiver 6 has been omitted. | 26 |
| Table 2.5: Percentage of orientation azimuth differences falling within 1, 2, 5 and 10 degrees, using different window sizes for angle calculations. | 31 |
| Table 2.6: Percentage of orientation azimuth differences falling within 1, 2, 5 and 10 degrees, using different window sizes for angle calculations. Receivers 4 and 6 were not included. | 31 |
| Table 2.7: Percentage of angle differences falling within 1, 2, and 5 degrees, for all 3 lines, calculated using a 100 ms window. Receivers 4 and 6 have been omitted. | 31 |
| Table 2.8: Means and standard deviations of geophone orientation azimuths for Phase I and Phase III, using all data and offsets only greater than 500 m. | 33 |
| Table 3.1: Numerical parameters used for acquisition. | 55 |
| Table 3.2: Numerical parameters used to create the geological model. | 55 |
| Table 3.3: Geophone orientation statistics of angles calculated analytically using Noise Pattern 1. | 65 |
| Table 3.4: Geophone orientation statistics of angles calculated analytically using Noise Pattern 2. | 67 |
| Table 4.1: Receiver numbering of different tool levels. | 74 |
| Table 4.2: Geophone orientation statistics for shallow-level receivers. | 94 |
| Table 4.3: Geophone orientation statistics for mid-level receivers. | 94 |
| Table 4.4: Geophone orientation statistics for deep-level receivers. | 95 |
| Table 4.5: Average standard deviations for each tool position, excluding the receiver at shuttle position 14. | 95 |
| Table 4.6: Geophone orientation statistics for modelled deviation surveys. Averages are calculated using all receivers. | 102 |

| | |
|--|-----|
| Table 5.1: Parameters used for raytracing tests. | 112 |
| Table 5.2: Numerical parameters used for acquisition. | 116 |
| Table 5.3: Standard deviation of receiver orientation azimuth. | 122 |
| Table 6.1: Numerical parameters used for acquisition. | 136 |
| Table 6.2: Standard deviation of receiver orientation azimuth. | 142 |
| Table 7.1: Geophone orientation statistics for a subset of the 2D dataset made using the analytic method, for different outlier conditions. Means and standard deviations are in degrees. | 151 |
| Table 7.2: Comparison of geophone orientation statistics for a subset of the 2D dataset for different analysis methods. Means and standard deviations are in degrees. | 152 |
| Table 7.3: Geophone orientation statistics for 3D dataset made using the analytic method. Means and standard deviations are in degrees. | 161 |
| Table 7.4: Geophone orientation statistics for binned 3D dataset made using the analytic method. Means and standard deviations are in degrees. | 161 |

List of Figures and Illustrations

| | |
|---|----|
| Figure 1.1: Schematic illustrations of (a) a zero-offset VSP and (b) a walkaway VSP, shown in cross-sectional view..... | 1 |
| Figure 1.2: Plan view illustration of the source-well offset and source-well azimuth for two possible source locations..... | 2 |
| Figure 1.3: Plan view of mapped microseismic events for three injection wells, from a study done by Refunjol et al. (2012)..... | 2 |
| Figure 1.4: Schematic diagram showing the raypaths of a shot to a geophone at 1800 m depth in (a, c, e) a vertical well and (b, d, f) a deviated well. H1 and H2 components of the geophones are shown in blue..... | 5 |
| Figure 1.5: (a) Perspective and (b) plan view diagrams showing the lateral raybending which occurs when a dipping interface is present. Rays are coloured by arrival azimuth at geophone as a visual aid..... | 6 |
| Figure 1.6: Simple illustration showing the difference between group (ray) angle ϕ and phase (wavefront) angle θ . Adapted from Thomsen (1986). | 7 |
| Figure 1.7: Example of a hodogram plot used in this thesis. (a) shows hodogram corresponding to the trace shown in (b); the colour scale used to plot (a) represents trace time, shown as a colour bar in (b). | 10 |
| Figure 1.8: Illustration of the relationship between θ (green), ϕ_s (red) and ϕ_r (blue)... | 11 |
| Figure 1.9: Annotated example of the spider plots used throughout this thesis. | 12 |
| Figure 1.10: Location of study area, in the Pembina oilfield. Figure from Dashtgard et al. (2006). | 13 |
| Figure 2.1: Shotpoint geometry for Violet Grove walkaway VSP used in this study. Coordinates are measured from the wellhead. | 18 |
| Figure 2.2: Common shot gather for shot 2145, from Line 2, at X=886.5 m, Y=207.3 m, for Phase I (a) and Phase III (b). H1 component is shown in blue, H2 component is shown in red, and vertical component is shown in green. | 19 |
| Figure 2.3: Common receiver gather from Line 2 for Receiver 3 at 1538 m MD, for Phase I (a) and Phase III (b). H1 component is shown in blue, H2 component is shown in red, and vertical component is shown in green. For display purposes, gathers have been decimated to half of their original traces. | 20 |
| Figure 2.4: Comparison of NRMS repeatability (a), predictability (b) and \log_{10} SDR (c) of Receiver 3 for Line 1, vs. source offset. The z-component is shown in black, x-component is shown in cyan, and y-component is shown in magenta. The dashed line in the NRMS plot indicates the theoretical noise line. | 22 |

| | |
|--|----|
| Figure 2.5: Comparison of NRMS repeatability (a), predictability (b) and \log_{10} SDR (c) of Receiver 3 for Line 2, vs. source offset. The z-component is shown in black, x-component is shown in cyan, and y-component is shown in magenta. The dashed line in the NRMS plot indicates the theoretical noise line. | 23 |
| Figure 2.6: Comparison of NRMS repeatability (a), predictability (b) and \log_{10} SDR (c) of Receiver 3 for Line 3, vs. source offset. The z-component is shown in black, x-component is shown in cyan, and y-component is shown in magenta. The dashed line in the NRMS plot indicates the theoretical noise line. | 24 |
| Figure 2.7: Orientation azimuth differences, calculated using a window of 50 ms, for individual geophones for (a) Line 2 and (b) Line 3. | 27 |
| Figure 2.8: Orientation azimuth differences, calculated using a window of 100 ms, for individual geophones for (a) Line 2 and (b) Line 3. | 28 |
| Figure 2.9: Orientation azimuth differences, calculated using a window of 200 ms, for individual geophones for (a) Line 2 and (b) Line 3. | 29 |
| Figure 2.10: Orientation azimuth differences, calculated using hodograms with a window size of 100 ms, for individual geophones for (a) Line 2 and (b) Line 3. | 30 |
| Figure 2.11: Histograms of the calculated geophone azimuths; results include both lines. Phase I is shown in blue and Phase III is shown in red. Bin sizes were based on Phase I calculations. Dashed lines indicate means; Phase I is green and Phase III is gray. Note that the Phase III means for receivers 4 and 6 are significantly different due to the high-amplitude noise on these geophones. | 34 |
| Figure 2.12: Histograms of the calculated geophone azimuths, including only the far offsets (greater than 500 m); results include both lines. Phase I is shown in blue, Phase III is shown in red. Bin sizes were based on Phase I calculations using all offsets. Dashed lines indicate means; Phase I is green and Phase III is gray. | 35 |
| Figure 2.13: Deviation from mean geophone azimuth vs. source-receiver offset for Phase I. Line 1 is in green, Line 2 is in blue and Line 3 is in red. All plots show a window of $\pm 8^\circ$ centered on the mean. | 36 |
| Figure 2.14: Deviation from mean geophone azimuth vs. source-receiver offset for Phase III. Line 1 is in green, Line 2 is in blue and Line 3 is in red. All plots show a window of $\pm 8^\circ$ centered on the mean. | 37 |
| Figure 2.15: Phase III average frequency spectra for raw Line 1 (green) Line 2 (blue) and Line 3 (red) traces, measured in dB down from the maximum amplitude of Line 1. | 38 |
| Figure 2.16: Deviation from mean geophone azimuth vs. source-receiver azimuth for Phase I. Line 1 is in green, Line 2 is in blue and Line 3 is in red. All plots show a window of $\pm 8^\circ$ centered on the mean. | 39 |

| | |
|---|----|
| Figure 2.17: Deviation from mean geophone azimuth vs. source-receiver azimuth for Phase III. Line 1 is in green, Line 2 is in blue and Line 3 is in red. All plots show a window of +/- 8° centered on the mean. | 40 |
| Figure 2.18: Spider plots for (a) Phase I and (b) Phase III orientation angles, using statistics calculated using far offsets. Angular grid spacing is 5° and radial grid spacing is 250 m. Receivers 4 and 6 have been omitted..... | 41 |
| Figure 2.19: Traces used for controlled repeatability experiment; baseline is shown in blue and monitor is shown in red. | 42 |
| Figure 2.20: Noise used for controlled repeatability experiment; Noise A (from baseline) is shown in blue and Noise B (from monitor) is shown in red. | 43 |
| Figure 2.21: SDR (a), log ₁₀ SDR (b), NRMS repeatability (c) and predictability (d) for time-shift experiment, showing traces left at the original sample rate (black) and traces resampled to 0.1 ms (red). Bottommost panel (e) is a wiggle display of the time-shifted traces (red) overlapping the original trace (blue). | 44 |
| Figure 2.22: SDR (a), log ₁₀ SDR (b), NRMS repeatability (c) and predictability (d) for amplitude experiment. Bottommost panel (e) is a wiggle display of the amplitude modified traces (red) overlapping the original trace (blue). | 47 |
| Figure 2.23: SDR (a), log ₁₀ SDR (b), NRMS repeatability (c) and predictability (d) for additive noise experiment, showing addition of Noise A (black) and Noise B (red). Two bottommost panels are wiggle displays of Noise A (e) and Noise B (f), showing noisy traces (red) overlapping the original trace (blue)..... | 48 |
| Figure 2.24: log ₁₀ SDR (a), NRMS repeatability (b) and predictability (c) for additive noise experiment, detailing the interval between 0 and 0.15. | 49 |
| Figure 3.1: 2-D slice of the geological model used in this study. Density is shown on the left, P-velocity is shown in the middle, and S-velocity is shown on the right. | 56 |
| Figure 3.2: Plan view of acquisition geometry used in this experiment. Shots are numbered from left to right..... | 56 |
| Figure 3.3: Raw x-component data from Shot 3, prior to addition of noise, overlain in red by the P-wave velocity model..... | 57 |
| Figure 3.4: Generated random noise; noise added to the x-component is shown in blue, and noise added to the y-component is shown in red. S/N is given at the top of each panel. Note the differences in scale..... | 58 |
| Figure 3.5: Amplitude histograms (left side) and amplitude spectra (right side) of generated noise; noise added to the x-component is shown in blue, and noise added to the y-component is shown in red. S/N is given at the top of each panel.... | 58 |

| | |
|--|----|
| Figure 3.6: X-component traces from Shot 3, after the addition of noise, for the first 10 receivers; S/N increases to the right. Red arrows indicate traces with S/N values of 0.05, 1, 20 and infinity..... | 59 |
| Figure 3.7: Error in orientation azimuth vs. x-coordinate offset for the first and second sets of receivers with S/N of 0.05, 1, 20 and infinity. Analytic results are shown in blue and hodogram results are shown in green. | 61 |
| Figure 3.8: Error in orientation azimuth vs. x-coordinate offset for the third and fourth sets of receivers with S/N of 0.05, 1, 20 and infinity. Analytic results are shown in blue and hodogram results are shown in green. | 62 |
| Figure 3.9: Error in orientation azimuth vs. horizontal offset for receivers with signal to noise ratios of 0.05 (top) and 1 (bottom), calculated using analytic (a) and hodogram (b) methods. Hotter colours correspond to larger depths..... | 63 |
| Figure 3.10: Error in orientation azimuth vs. horizontal offset for receivers with signal to noise ratio of 20, calculated using analytic (a) and hodogram (c) methods. Hotter colours correspond to larger depths. | 64 |
| Figure 3.11: Error in mean orientation azimuth (a) and standard deviation (b) vs. receiver depth. Analytic results are shown in blue and hodogram results shown in green..... | 64 |
| Figure 3.12: Mean orientation azimuth error vs. receiver depth for Noise Pattern 2. Cooler colours correspond to lower S/N ratios..... | 68 |
| Figure 3.13: Standard deviation of orientation azimuth vs. receiver depth for Noise Pattern 2. Cooler colours correspond to lower S/N ratios..... | 68 |
| Figure 3.14: Error in mean orientation azimuth vs. natural log of S/N ratio for Noise Pattern 2. Warmer colours correspond to larger depths..... | 69 |
| Figure 3.15: Natural log of orientation azimuth standard deviation vs. natural log of S/N ratio for Noise Pattern 2. Warmer colours correspond to larger depths. | 69 |
| Figure 4.1: Deviation survey of the well used in this study, where the wellhead is the origin of the coordinate system. The dashed lines are projections of the well onto the x-z and x-y planes. | 73 |
| Figure 4.2: Survey geometry of shots used in 16-level VSP experiment. Line 1 is shown in green, Line 2 is shown in blue, and Line 6 is shown in magenta; different markers represent the different tool levels. The wellhead is shown in black, and represents the origin of the coordinate system. | 74 |
| Figure 4.3: (a) Common shot gather for mid tool position, with shot coordinates X=-555 m and Y=-38 m, and (b) common receiver gather of Receiver 17 (1038 m | |

| | |
|---|----|
| MD), for Line 6. The x component is shown in blue, and the y component is shown in red. | 75 |
| Figure 4.4: Illustration of pseudo-coordinates defined for a deviated well. | 77 |
| Figure 4.5: Survey geometry of shots used in 16-level VSP experiment, after being projected using Equations 4.5 and 4.6. Shots are shown relative to the geophone location, displayed as a red square at the origin. Line 1 is shown in green, Line 2 is shown in blue and Line 6 is shown in magenta. | 79 |
| Figure 4.6: Deviation from mean orientation azimuth vs. pseudo offset for Receivers 1-8 (shallow-level). Line 1 is shown in green, Line 2 in blue, and Line 6 in magenta. | 80 |
| Figure 4.7: Deviation from mean orientation azimuth vs. pseudo offset for Receivers 17-24 (mid-level). Line 1 is shown in green, Line 2 in blue, and Line 6 in magenta. | 81 |
| Figure 4.8: Deviation from mean orientation azimuth vs. pseudo offset for Receivers 33-40 (deep-level). Line 1 is shown in green, Line 2 in blue, and Line 6 in magenta. | 82 |
| Figure 4.9: Deviation from mean orientation azimuth vs. pseudo azimuth for Receivers 1-8 (shallow-level). Line 1 is shown in green, Line 2 in blue, and Line 6 in magenta. | 83 |
| Figure 4.10: Deviation from mean orientation azimuth vs. pseudo azimuth for Receivers 17-24 (mid-level). Line 1 is shown in green, Line 2 in blue, and Line 6 in magenta. | 84 |
| Figure 4.11: Deviation from mean orientation azimuth vs. pseudo azimuth for Receivers 33-40 (deep-level). Line 1 is shown in green, Line 2 in blue, and Line 6 in magenta. | 85 |
| Figure 4.12: Deviation from mean orientation azimuth vs. pseudo azimuth for shuttle positions 1-8, combining data from all tool levels. Line 1 is shown in green, Line 2 in blue, and Line 6 in magenta. | 86 |
| Figure 4.13: Deviation from mean orientation azimuth vs. offset for Receivers 1-8 (shallow-level), calculated under a vertical well assumption. Line 1 is shown in green, Line 2 in blue, and Line 6 in magenta. | 87 |
| Figure 4.14: Deviation from mean orientation azimuth vs. offset for Receivers 17-24 (mid-level), calculated under a vertical well assumption. Line 1 is shown in green, Line 2 in blue, and Line 6 in magenta. | 88 |

| | |
|---|-----|
| Figure 4.15: Deviation from mean orientation azimuth vs. offset for Receivers 33-40 (deep-level), calculated under a vertical well assumption. Line 1 is shown in green, Line 2 in blue, and Line 6 in magenta..... | 89 |
| Figure 4.16: Orientation azimuth histograms for Receivers 1-8 (shallow-level). Line 1 is shown in green, Line 2 in blue, and Line 6 in magenta. | 90 |
| Figure 4.17: Orientation azimuth histograms for Receivers 17-24 (mid-level). Line 1 is shown in green, Line 2 in blue, and Line 6 in magenta. | 91 |
| Figure 4.18: Orientation azimuth histograms for Receivers 30-40 (deep-level). Line 1 is shown in green, Line 2 in blue, and Line 6 in magenta. | 92 |
| Figure 4.19: Differences in mean orientation azimuth for each geophone depth. Differences between Line 1 and 2 are shown in black; differences between Line 1 and 6 are shown in red; and differences between Line 6 and 2 are shown in blue..... | 93 |
| Figure 4.20: Spider plot showing the first and third receivers at each level; angular grid spacing is 5° and radial grid spacing is 250 m. | 96 |
| Figure 4.21: Difference of mean orientation azimuth for each shuttle position; differences from shallow-mid tool level are shown in black, shallow-deep tool level in red and mid-deep tool level in blue..... | 96 |
| Figure 4.22: Randomly generated error in deviation azimuth angle (green) and inclination angle (blue). | 97 |
| Figure 4.23: Cumulative geophone positioning error resulting from modelled deviation survey error. Isolated effects of azimuth and inclination are shown in green and blue respectively, and overall effects are shown in red..... | 98 |
| Figure 4.24: Modelled errors in orientation angle for Receiver 1 (798 m), resulting from (a) correct deviation survey, (b) errors in azimuth angle, (c) inclination angle, and (d) errors in both angles..... | 99 |
| Figure 4.25: Modelled errors in orientation angle for Receiver 25 (1159 m), resulting from (a) correct deviation survey, (b) errors in azimuth angle, (c) inclination angle, and (d) errors in both angles..... | 100 |
| Figure 4.26: Modelled errors in orientation angle for Receiver 48 (1505 m), resulting from (a) correct deviation survey, (b) errors in azimuth angle, (c) inclination angle, and (d) errors in both angles..... | 101 |
| Figure 5.1: Flowchart of the algorithm used for raytracing..... | 107 |
| Figure 5.2: Schematic diagram of the general setup of raytracing experiment. V_I and V_T are the velocities of the lower and upper layer, z_c is the vertical distance from | |

| | |
|---|-----|
| the receiver to the interface, z_s is the depth of the receiver, and γ is the dip of the interface..... | 108 |
| Figure 5.3: Snell's Law, with $V_I > V_T$ | 109 |
| Figure 5.4: Deviation in azimuth resulting from constant dip test, plotted against ray launching azimuth and inclination. Hotter colours represent positive deviation, cooler colours represent negative deviation. Red and blue triangles represent largest negative and positive deviation for constant inclination angles..... | 113 |
| Figure 5.5: Deviation in azimuth resulting from constant velocity test, plotted against ray launching azimuth and inclination. Hotter colours represent positive deviation, cooler colours represent negative deviation. Red and blue triangles represent largest negative and positive deviation for constant inclination angles.. | 114 |
| Figure 5.6: Plan view of surface geometry used in TIGER. Line 1 is shown in blue, Line 2 is shown in black and Line 3 is shown in red. Additionally, the strike and dip of the layer interface are indicated, and the orientations of the H1 and H2 components are shown..... | 116 |
| Figure 5.7: Example of raw TIGER output from the shot at $x = 130$ m and $y = 100$ m. H1-component output is shown in blue and H2-component output is shown in red. | 117 |
| Figure 5.8: Example of raw TIGER output from Receiver 5 at 50 m. H1-component output is shown in blue and H2-component output is shown in red..... | 117 |
| Figure 5.9: Deviation of orientation angle for Receiver 5 (50 m depth) plotted as a function of source-well azimuth (a) and source-well offset (b). Line 1 is shown in blue, Line 2 in black and Line 3 in red. | 119 |
| Figure 5.10: Deviation of orientation angle for Receiver 15 (150 m depth) plotted as a function of source-well azimuth (a) and source-well offset (b). Line 1 is shown in blue, Line 2 in black and Line 3 in red. | 119 |
| Figure 5.11: Deviation of orientation angle for Receiver 20 (200 m depth) plotted as a function of source-well azimuth (a) and source-well offset (b). Line 1 is shown in blue, Line 2 in black and Line 3 in red. | 120 |
| Figure 5.12: Deviation of orientation angle for Receiver 30 (300 m depth) plotted as a function of source-well azimuth (a) and source-well offset (b). Line 1 is shown in blue, Line 2 in black and Line 3 in red. | 120 |
| Figure 5.13: Deviation of orientation angle for Receiver 20 (200 m depth), using a 50 ms analysis window, plotted as a function of source-well azimuth (a) and source-well offset (b). Line 1 is shown in blue, Line 2 in black and Line 3 in red. | 121 |

| | |
|--|-----|
| Figure 5.14: Deviation of orientation angle for Receiver 30 (300 m depth), using a 50 ms analysis window, plotted as a function of source-well azimuth (a) and source-well offset (b). Line 1 is shown in blue, Line 2 in black and Line 3 in red. | 121 |
| Figure 5.15: Standard deviation of orientation azimuth found using 100 ms window (a) and 50 ms window (b). The depth of the velocity interface at the well is indicated with a black line. | 122 |
| Figure 5.16: Comparison of deviation in geophone orientation angle using TIGER (blue) and raytracing (red) methods. The difference between the two methods is shown in black. | 123 |
| Figure 6.1: Maximum difference between group and phase angle, in degrees, as a function of epsilon and delta; the line $\delta = \epsilon$ is drawn in for convenience. Hotter colours represent larger values. | 128 |
| Figure 6.2: Maximum difference between group and phase angle, in degrees, using a constant epsilon of 0.15. | 129 |
| Figure 6.3: Maximum difference between group and phase angle, in degrees, using a constant delta of 0.05. | 129 |
| Figure 6.4: Anisotropic wavefront as a function of group angle (a) and phase angle (b), using parameters $v_0 = 3000$ m/s, $\delta = 0.025$ and $\epsilon = 0.1$. | 132 |
| Figure 6.5: Difference between group and phase angle, in degrees, using parameters $v_0 = 3000$ m/s, $\delta = 0.025$ and $\epsilon = 0.1$. | 133 |
| Figure 6.6: Surface geometry used in modelled calibration survey. Coordinates are relative to the well location. | 133 |
| Figure 6.7: Calculated deviation in orientation angle due to anisotropy vs. source-well offset (a) and azimuth (b). Deviation for Line 1 is shown in red, deviation for Line 2 is shown in green, and deviation for Line 3 is shown in magenta. Azimuths where zero deviation is expected are shown as vertical lines. | 134 |
| Figure 6.8: Plan view of surface geometry used in TIGER. Line 1 is shown in blue, Line 2 is shown in black and Line 3 is shown in red. | 136 |
| Figure 6.9: Example of raw TIGER output from the shot at $x = 130$ m and $y = 100$ m. H1-component output is shown in blue and H2-component output is shown in red. | 137 |
| Figure 6.10: Example of raw TIGER output from the receiver at 50 m depth. H1-component output is shown in blue and H2-component output is shown in red. | 137 |

| | |
|--|-----|
| Figure 6.11: Deviation in orientation angle for Receiver 5 (50 m depth) plotted as a function of source-well azimuth (a) and source-well offset (b). Line 1 is shown in blue, Line 2 in black and Line 3 in red. | 139 |
| Figure 6.12: Deviation in orientation angle for Receiver 15 (150 m depth) plotted as a function of source-well azimuth (a) and source-well offset (b). Line 1 is shown in blue, Line 2 in black and Line 3 in red. | 139 |
| Figure 6.13: Deviation in orientation angle for Receiver 20 (200 m depth) plotted as a function of source-well azimuth (a) and source-well offset (b). Line 1 is shown in blue, Line 2 in black and Line 3 in red. | 140 |
| Figure 6.14: Deviation in orientation angle for Receiver 30 (300 m depth) plotted as a function of source-well azimuth (a) and source-well offset (b). Line 1 is shown in blue, Line 2 in black and Line 3 in red. | 140 |
| Figure 6.15: Deviation in orientation angle for Receiver 5 (50 m depth), using a 50 ms analysis window, plotted as a function of source-well azimuth (a) and source-well offset (b). Line 1 is shown in blue, Line 2 in black and Line 3 in red. | 141 |
| Figure 6.16: Deviation in orientation angle for Receiver 30 (300 m depth), using a 50 ms analysis window, plotted as a function of source-well azimuth (a) and source-well offset (b). Line 1 is shown in blue, Line 2 in black and Line 3 in red. | 141 |
| Figure 6.17: Standard deviation of orientation azimuth found using 100 ms window (a) and 50 ms window (b). The depth of the layer interface is indicated with a black line. | 143 |
| Figure 6.18: Comparison of deviation in geophone orientation angle using TIGER (blue) and analytic (red) methods. The difference between the two methods is shown in black. Azimuths with an expected error of zero are labelled with vertical lines. | 144 |
| Figure 7.1: Surface geometry for the 2D walkaway VSP surveys. Coordinate origin is at the well. Lines are identified as E, SE and S. | 148 |
| Figure 7.2: Surface geometry for the 3D VSP survey, showing an outline of the 2D walkaway VSP area. Coordinate origin is at the well. | 148 |
| Figure 7.3: Raw shot gather from a near offset shot of the East line of the 2D walkaway VSP survey; coordinates are 33 m north and 386 m east of the well. H1-component is shown in blue and H2-component is shown in red. No gain has been applied. | 149 |
| Figure 7.4: Raw shot gather from a near offset shot of the 3D VSP survey; coordinates are 81 m south and 33 m east of the well. H1-component is shown in blue and H2-component is shown in red. No gain has been applied. | 149 |

| | |
|---|-----|
| Figure 7.5: Examples of hodograms from the East line of the 2D walkaway VSP data. | 150 |
| Figure 7.6: Variation in geophone orientation azimuths for several receiver positions, calculated using the analytic method, for the 2D walkaway dataset coloured by line; E is shown in blue, SE is shown in magenta and S is shown in green. | 152 |
| Figure 7.7: (a) Standard deviations for each receiver using the analytic (blue) and hodogram (red) methods. (b) Differences in mean orientation for each receiver; value is calculated by subtracting the hodogram mean from the analytic mean. Vertical lines are represent the top of each tool level. | 153 |
| Figure 7.8: Orientation standard deviations for each receiver calculated using the (a) analytic and (b) hodogram methods. Red is calculated using all data points, cyan after removal of outliers and black after removal of outliers and near offsets less than 500 m. | 154 |
| Figure 7.9: Azimuthal sectoring for the 3D walkaway VSP survey. | 155 |
| Figure 7.10: Deviation in geophone orientation azimuths, versus source-well offset, for several receivers in the 3D dataset calculated using analytic method, coloured by bin; 0°-180° is shown in blue, 45°-225° is shown in cyan, 90°-270° is shown in yellow and 135°-315° is shown in red. | 156 |
| Figure 7.11: Deviation in geophone orientation azimuths, versus source-well azimuth, for several receivers in the 3D dataset calculated using analytic method, for 3D walkaway coloured by offset. Hotter colours represent far offsets, cooler colours represent near offsets. | 157 |
| Figure 7.12: Histograms of orientation azimuth for several receivers in the 3D dataset calculated using analytic method. | 158 |
| Figure 7.13: Histograms of orientation azimuth for several receivers in the 3D dataset calculated using analytic method, after rejection of near offset shots (less than 500 m). | 158 |
| Figure 7.14: Radial plot of geophone orientation azimuths for a subset of receivers. All shots are shown, but statistics are found from far offset data only. Envelope lines represent one standard deviation. Radial spacing is 500m, angular spacing is 5°. | 159 |
| Figure 7.15: Orientation azimuth standard deviations for each receiver calculated using the analytic method, using azimuthal sectoring. Red is calculated using all data points, cyan after removal of outliers and black after removal of outliers and near offsets less than 500 m. | 160 |
| Figure 7.16: Standard deviation of geophone orientation azimuth versus geophone depth and sectored offset range. | 162 |

| | |
|---|-----|
| Figure 7.17: Constant offset slices from Figure 7.16, showing 600-950 m bin in green, 950-1300 m bin in cyan, and 1300-1650 m bin in black. | 163 |
| Figure 7.18: Average standard deviation for all receivers (except receiver 2) at each offset bin. | 163 |
| Figure 7.19: Diagram illustrating geometry of a surface source and a borehole geophone embedded in a homogeneous, isotropic medium. | 165 |
| Figure 7.20: Modelled relative amplitude change of the horizontal components of a borehole geophone, as a function of the source-well offset/receiver depth ratio. Horizontal line is drawn in at -2 dB, which intersects the curve at offset/depth ratios of approximately 0.5 and 2..... | 165 |
| Figure 7.21: Estimated signal to noise of first break window, versus offset, for the H_{\max} component of a subset of receivers in the 3D dataset. Data were rotated using angle estimates from the analytic method. | 166 |
| Figure 7.22: Illustration of raybending that would occur due to a linear velocity gradient where velocity increases downwards..... | 166 |
| Figure 8.1: Comparison of Violet Grove time-lapse dataset deviations (Chapter 2) as a function of source-well azimuth (left) with modelled deviations due to a dipping interface (upper right) and anisotropy (lower right). | 172 |
| Figure 8.2: Comparison of Lousana 3D dataset (Chapter 7) deviations as a function of source-well azimuth (left) with modelled deviations due to a dipping interface (upper right) and anisotropy (lower right). | 172 |
| Figure 8.3: Comparison of Violet Grove deviated well dataset (Chapter 4) deviations as a function of source-well azimuth (left) with modelled deviations due to a dipping interface (upper right) and anisotropy (lower right). | 173 |
| Figure B.1: Comparison of NRMS repeatability (a), predictability (b) and \log_{10} SDR (c) of Receiver 1 for Line 1, vs. source offset. The z-component is shown in black, x-component is shown in cyan, and y-component is shown in magenta. The dashed line in the NRMS plot indicates the theoretical noise line. | 190 |
| Figure B.2: Comparison of NRMS repeatability (a), predictability (b) and \log_{10} SDR (c) of Receiver 1 for Line 2, vs. source offset. The z-component is shown in black, x-component is shown in cyan, and y-component is shown in magenta. The dashed line in the NRMS plot indicates the theoretical noise line. | 191 |
| Figure B.3: Comparison of NRMS repeatability (a), predictability (b) and \log_{10} SDR (c) of Receiver 1 for Line 3, vs. source offset. The z-component is shown in black, x-component is shown in cyan, and y-component is shown in magenta. The dashed line in the NRMS plot indicates the theoretical noise line. | 192 |

Figure B.4: Comparison of NRMS repeatability (a), predictability (b) and \log_{10} SDR (c) of Receiver 2 for Line 1, vs. source offset. The z-component is shown in black, x-component is shown in cyan, and y-component is shown in magenta. The dashed line in the NRMS plot indicates the theoretical noise line. 193

Figure B.5: Comparison of NRMS repeatability (a), predictability (b) and \log_{10} SDR (c) of Receiver 2 for Line 2, vs. source offset. The z-component is shown in black, x-component is shown in cyan, and y-component is shown in magenta. The dashed line in the NRMS plot indicates the theoretical noise line. 194

Figure B.6: Comparison of NRMS repeatability (a), predictability (b) and \log_{10} SDR (c) of Receiver 2 for Line 3, vs. source offset. The z-component is shown in black, x-component is shown in cyan, and y-component is shown in magenta. The dashed line in the NRMS plot indicates the theoretical noise line. 195

Figure B.7: Comparison of NRMS repeatability (a), predictability (b) and \log_{10} SDR (c) of Receiver 3 for Line 1, vs. source offset. The z-component is shown in black, x-component is shown in cyan, and y-component is shown in magenta. The dashed line in the NRMS plot indicates the theoretical noise line. 196

Figure B.8: Comparison of NRMS repeatability (a), predictability (b) and \log_{10} SDR (c) of Receiver 3 for Line 2, vs. source offset. The z-component is shown in black, x-component is shown in cyan, and y-component is shown in magenta. The dashed line in the NRMS plot indicates the theoretical noise line. 197

Figure B.9: Comparison of NRMS repeatability (a), predictability (b) and \log_{10} SDR (c) of Receiver 3 for Line 3, vs. source offset. The z-component is shown in black, x-component is shown in cyan, and y-component is shown in magenta. The dashed line in the NRMS plot indicates the theoretical noise line. 198

Figure B.10: Comparison of NRMS repeatability (a), predictability (b) and \log_{10} SDR (c) of Receiver 4 for Line 1, vs. source offset. The z-component is shown in black, x-component is shown in cyan, and y-component is shown in magenta. The dashed line in the NRMS plot indicates the theoretical noise line. 199

Figure B.11: Comparison of NRMS repeatability (a), predictability (b) and \log_{10} SDR (c) of Receiver 4 for Line 2, vs. source offset. The z-component is shown in black, x-component is shown in cyan, and y-component is shown in magenta. The dashed line in the NRMS plot indicates the theoretical noise line. 200

Figure B.12: Comparison of NRMS repeatability (a), predictability (b) and \log_{10} SDR (c) of Receiver 4 for Line 3, vs. source offset. The z-component is shown in black, x-component is shown in cyan, and y-component is shown in magenta. The dashed line in the NRMS plot indicates the theoretical noise line. 201

Figure B.13: Comparison of NRMS repeatability (a), predictability (b) and \log_{10} SDR (c) of Receiver 5 for Line 1, vs. source offset. The z-component is shown in

| | |
|---|-----|
| black, x-component is shown in cyan, and y-component is shown in magenta. The dashed line in the NRMS plot indicates the theoretical noise line. | 202 |
| Figure B.14: Comparison of NRMS repeatability (a), predictability (b) and \log_{10} SDR (c) of Receiver 5 for Line 2, vs. source offset. The z-component is shown in black, x-component is shown in cyan, and y-component is shown in magenta. The dashed line in the NRMS plot indicates the theoretical noise line. | 203 |
| Figure B.15: Comparison of NRMS repeatability (a), predictability (b) and \log_{10} SDR (c) of Receiver 5 for Line 3, vs. source offset. The z-component is shown in black, x-component is shown in cyan, and y-component is shown in magenta. The dashed line in the NRMS plot indicates the theoretical noise line. | 204 |
| Figure B.16: Comparison of NRMS repeatability (a), predictability (b) and \log_{10} SDR (c) of Receiver 6 for Line 1, vs. source offset. The z-component is shown in black, x-component is shown in cyan, and y-component is shown in magenta. The dashed line in the NRMS plot indicates the theoretical noise line. | 205 |
| Figure B.17: Comparison of NRMS repeatability (a), predictability (b) and \log_{10} SDR (c) of Receiver 6 for Line 2, vs. source offset. The z-component is shown in black, x-component is shown in cyan, and y-component is shown in magenta. The dashed line in the NRMS plot indicates the theoretical noise line. | 206 |
| Figure B.18: Comparison of NRMS repeatability (a), predictability (b) and \log_{10} SDR (c) of Receiver 6 for Line 3, vs. source offset. The z-component is shown in black, x-component is shown in cyan, and y-component is shown in magenta. The dashed line in the NRMS plot indicates the theoretical noise line. | 207 |
| Figure B.19: Comparison of NRMS repeatability (a), predictability (b) and \log_{10} SDR (c) of Receiver 7 for Line 1, vs. source offset. The z-component is shown in black, x-component is shown in cyan, and y-component is shown in magenta. The dashed line in the NRMS plot indicates the theoretical noise line. | 208 |
| Figure B.20: Comparison of NRMS repeatability (a), predictability (b) and \log_{10} SDR (c) of Receiver 7 for Line 2, vs. source offset. The z-component is shown in black, x-component is shown in cyan, and y-component is shown in magenta. The dashed line in the NRMS plot indicates the theoretical noise line. | 209 |
| Figure B.21: Comparison of NRMS repeatability (a), predictability (b) and \log_{10} SDR (c) of Receiver 7 for Line 3, vs. source offset. The z-component is shown in black, x-component is shown in cyan, and y-component is shown in magenta. The dashed line in the NRMS plot indicates the theoretical noise line. | 210 |
| Figure B.22: Comparison of NRMS repeatability (a), predictability (b) and \log_{10} SDR (c) of Receiver 8 for Line 1, vs. source offset. The z-component is shown in black, x-component is shown in cyan, and y-component is shown in magenta. The dashed line in the NRMS plot indicates the theoretical noise line. | 211 |

| | |
|--|-----|
| Figure B.23: Comparison of NRMS repeatability (a), predictability (b) and \log_{10} SDR (c) of Receiver 8 for Line 2, vs. source offset. The z-component is shown in black, x-component is shown in cyan, and y-component is shown in magenta. The dashed line in the NRMS plot indicates the theoretical noise line. | 212 |
| Figure B.24: Comparison of NRMS repeatability (a), predictability (b) and \log_{10} SDR (c) of Receiver 8 for Line 3, vs. source offset. The z-component is shown in black, x-component is shown in cyan, and y-component is shown in magenta. The dashed line in the NRMS plot indicates the theoretical noise line. | 213 |
| Figure C.1: Error in orientation azimuth vs. x-coordinate offset for Receivers 1 to 8. Analytic results are shown in blue and hodogram results are shown in green. | 215 |
| Figure C.2: Error in orientation azimuth vs. x-coordinate offset for Receivers 1 to 8. Analytic results are shown in blue and hodogram results are shown in green. | 216 |
| Figure C.3: Error in orientation azimuth vs. x-coordinate offset for Receivers 1 to 8. Analytic results are shown in blue and hodogram results are shown in green. | 217 |
| Figure C.4: Error in orientation azimuth vs. x-coordinate offset for Receivers 1 to 8. Analytic results are shown in blue and hodogram results are shown in green. | 218 |
| Figure C.5: Error in orientation azimuth vs. x-coordinate offset for Receivers 1 to 8. Analytic results are shown in blue and hodogram results are shown in green. | 219 |
| Figure C.6: Error in orientation azimuth vs. x-coordinate offset for Receivers 1 to 8. Analytic results are shown in blue and hodogram results are shown in green. | 220 |
| Figure C.7: Error in orientation azimuth vs. x-coordinate offset for Receivers 1 to 8. Analytic results are shown in blue and hodogram results are shown in green. | 221 |
| Figure C.8: Error in orientation azimuth vs. x-coordinate offset for Receivers 1 to 8. Analytic results are shown in blue and hodogram results are shown in green. | 222 |
| Figure C.9: Error in orientation azimuth vs. horizontal offset for receivers with signal to noise ratios of 0.05 (top) and 0.1 (bottom), calculated using analytic (a) and hodogram (b) methods. Hotter colours correspond to larger depths..... | 223 |
| Figure C.10: Error in orientation azimuth vs. horizontal offset for receivers with signal to noise ratios of 0.05 (top) and 0.1 (bottom), calculated using analytic (a) and hodogram (b) methods. Hotter colours correspond to larger depths..... | 224 |
| Figure C.11: Error in orientation azimuth vs. horizontal offset for receivers with signal to noise ratios of 0.05 (top) and 0.1 (bottom), calculated using analytic (a) and hodogram (b) methods. Hotter colours correspond to larger depths..... | 225 |

| | |
|---|-----|
| Figure C.12: Error in orientation azimuth vs. horizontal offset for receivers with signal to noise ratios of 0.05 (top) and 0.1 (bottom), calculated using analytic (a) and hodogram (b) methods. Hotter colours correspond to larger depths..... | 226 |
| Figure C.13: Error in orientation azimuth vs. horizontal offset for receivers with signal to noise ratios of 0.05 (top) and 0.1 (bottom), calculated using analytic (a) and hodogram (b) methods. Hotter colours correspond to larger depths..... | 227 |
| Figure D.1: Deviation from mean orientation azimuth vs. pseudo offset for Receivers 9-16 (shallow-level). Line 1 is shown in green, Line 2 in blue, and Line 6 in magenta. | 229 |
| Figure D.2: Deviation from mean orientation azimuth vs. pseudo offset for Receivers 25-32 (mid-level). Line 1 is shown in green, Line 2 in blue, and Line 6 in magenta. | 230 |
| Figure D.3: Deviation from mean orientation azimuth vs. pseudo offset for Receivers 41-48 (deep-level). Line 1 is shown in green, Line 2 in blue, and Line 6 in magenta. | 231 |
| Figure D.4: Deviation from mean orientation azimuth vs. pseudo azimuth for Receivers 9-16 (shallow-level). Line 1 is shown in green, Line 2 in blue, and Line 6 in magenta..... | 232 |
| Figure D.5: Deviation from mean orientation azimuth vs. pseudo azimuth for Receivers 25-32 (mid-level). Line 1 is shown in green, Line 2 in blue, and Line 6 in magenta. | 233 |
| Figure D.6: Deviation from mean orientation azimuth vs. pseudo azimuth for Receivers 41-48 (deep-level). Line 1 is shown in green, Line 2 in blue, and Line 6 in magenta..... | 234 |
| Figure D.7: Deviation from mean orientation azimuth vs. pseudo azimuth for shuttle positions 9-16, combining data from all tool levels. Line 1 is shown in green, Line 2 in blue, and Line 6 in magenta. | 235 |
| Figure D.8: Deviation from mean orientation azimuth vs. offset for Receivers 9-16 (shallow-level), calculated under a vertical well assumption. Line 1 is shown in green, Line 2 in blue, and Line 6 in magenta..... | 236 |
| Figure D.9: Deviation from mean orientation azimuth vs. offset for Receivers 25-32 (mid-level), calculated under a vertical well assumption. Line 1 is shown in green, Line 2 in blue, and Line 6 in magenta..... | 237 |
| Figure D.10: Deviation from mean orientation azimuth vs. offset for Receivers 41-48 (deep-level), calculated under a vertical well assumption. Line 1 is shown in green, Line 2 in blue, and Line 6 in magenta..... | 238 |

| | |
|---|-----|
| Figure D.11: Orientation azimuth histograms for Receivers 9-16 (shallow-level). Line 1 is shown in green, Line 2 in blue, and Line 6 in magenta. | 239 |
| Figure D.12: Orientation azimuth histograms for Receivers 25-32 (mid-level). Line 1 is shown in green, Line 2 in blue, and Line 6 in magenta. | 240 |
| Figure D.13: Orientation azimuth histograms for Receivers 41-48 (deep-level). Line 1 is shown in green, Line 2 in blue, and Line 6 in magenta. | 241 |
| Figure E.1: Deviation of orientation angle for Receiver 12 (120 m depth) plotted as a function of source-well azimuth (a) and source-well offset (b), using a dipping interface model..... | 243 |
| Figure E.2: Deviation of orientation angle for Receiver 13 (130 m depth) plotted as a function of source-well azimuth (a) and source-well offset (b), using a dipping interface model..... | 243 |
| Figure E.3: Deviation of orientation angle for Receiver 14 (140 m depth) plotted as a function of source-well azimuth (a) and source-well offset (b), using a dipping interface model..... | 244 |
| Figure E.4: Deviation of orientation angle for Receiver 15 (150 m depth) plotted as a function of source-well azimuth (a) and source-well offset (b), using a dipping interface model..... | 244 |
| Figure E.5: Deviation of orientation angle for Receiver 16 (160 m depth) plotted as a function of source-well azimuth (a) and source-well offset (b), using a dipping interface model..... | 245 |
| Figure E.6: Deviation of orientation angle for Receiver 17 (170 m depth) plotted as a function of source-well azimuth (a) and source-well offset (b), using a dipping interface model..... | 245 |
| Figure E.7: Deviation of orientation angle for Receiver 18 (180 m depth) plotted as a function of source-well azimuth (a) and source-well offset (b), using a dipping interface model..... | 246 |
| Figure E.8: Deviation of orientation angle for Receiver 19 (190 m depth) plotted as a function of source-well azimuth (a) and source-well offset (b), using a dipping interface model..... | 246 |
| Figure E.9: Deviation of orientation angle for Receiver 20 (200 m depth) plotted as a function of source-well azimuth (a) and source-well offset (b), using a dipping interface model..... | 247 |
| Figure E.10: Deviation of orientation angle for Receiver 21 (210 m depth) plotted as a function of source-well azimuth (a) and source-well offset (b), using a dipping interface model..... | 247 |

| | |
|---|-----|
| Figure E.11: Deviation of orientation angle for Receiver 22 (220 m depth) plotted as a function of source-well azimuth (a) and source-well offset (b), using a dipping interface model..... | 248 |
| Figure E.12: Deviation of orientation angle for Receiver 23 (230 m depth) plotted as a function of source-well azimuth (a) and source-well offset (b), using a dipping interface model..... | 248 |
| Figure E.13: Deviation of orientation angle for Receiver 24 (240 m depth) plotted as a function of source-well azimuth (a) and source-well offset (b), using a dipping interface model..... | 249 |
| Figure E.14: Deviation of orientation angle for Receiver 25 (250 m depth) plotted as a function of source-well azimuth (a) and source-well offset (b), using a dipping interface model..... | 249 |
| Figure E.15: Deviation of orientation angle for Receiver 8 (80 m depth) plotted as a function of source-well azimuth (a) and source-well offset (b), using a model of an HTI medium. | 250 |
| Figure E.16: Deviation of orientation angle for Receiver 9 (90 m depth) plotted as a function of source-well azimuth (a) and source-well offset (b), using a model of an HTI medium. | 250 |
| Figure E.17: Deviation of orientation angle for Receiver 10 (100 m depth) plotted as a function of source-well azimuth (a) and source-well offset (b), using a model of an HTI medium. | 251 |
| Figure E.18: Deviation of orientation angle for Receiver 11 (110 m depth) plotted as a function of source-well azimuth (a) and source-well offset (b), using a model of an HTI medium. | 251 |
| Figure E.19: Deviation of orientation angle for Receiver 12 (120 m depth) plotted as a function of source-well azimuth (a) and source-well offset (b), using a model of an HTI medium. | 252 |
| Figure E.20: Deviation of orientation angle for Receiver 13 (130 m depth) plotted as a function of source-well azimuth (a) and source-well offset (b), using a model of an HTI medium. | 252 |
| Figure E.21: Deviation of orientation angle for Receiver 14 (140 m depth) plotted as a function of source-well azimuth (a) and source-well offset (b), using a model of an HTI medium. | 253 |
| Figure E.22: Deviation of orientation angle for Receiver 15 (150 m depth) plotted as a function of source-well azimuth (a) and source-well offset (b), using a model of an HTI medium. | 253 |

| | |
|---|-----|
| Figure E.23: Deviation of orientation angle for Receiver 16 (160 m depth) plotted as a function of source-well azimuth (a) and source-well offset (b), using a model of an HTI medium. | 254 |
| Figure E.24: Deviation of orientation angle for Receiver 17 (170 m depth) plotted as a function of source-well azimuth (a) and source-well offset (b), using a model of an HTI medium. | 254 |
| Figure E.25: Deviation of orientation angle for Receiver 18 (180 m depth) plotted as a function of source-well azimuth (a) and source-well offset (b), using a model of an HTI medium. | 255 |
| Figure E.26: Deviation of orientation angle for Receiver 19 (190 m depth) plotted as a function of source-well azimuth (a) and source-well offset (b), using a model of an HTI medium. | 255 |
| Figure E.27: Deviation of orientation angle for Receiver 20 (200 m depth) plotted as a function of source-well azimuth (a) and source-well offset (b), using a model of an HTI medium. | 256 |
| Figure E.28: Deviation of orientation angle for Receiver 21 (210 m depth) plotted as a function of source-well azimuth (a) and source-well offset (b), using a model of an HTI medium. | 256 |
| Figure E.29: Deviation of orientation angle for Receiver 22 (220 m depth) plotted as a function of source-well azimuth (a) and source-well offset (b), using a model of an HTI medium. | 257 |
| Figure E.30: Deviation of orientation angle for Receiver 23 (230 m depth) plotted as a function of source-well azimuth (a) and source-well offset (b), using a model of an HTI medium. | 257 |
| Figure F.1: Deviation in geophone orientation azimuths, versus source-well offset, for Receivers 1-8 in the 2D dataset calculated using analytic method, coloured by line; E is shown in blue, SE is shown in magenta and S is shown in green. | 259 |
| Figure F.2: Deviation in geophone orientation azimuths, versus source-well offset, for Receivers 9-16 in the 2D dataset calculated using analytic method, coloured by line; E is shown in blue, SE is shown in magenta and S is shown in green. | 260 |
| Figure F.3: Deviation in geophone orientation azimuths, versus source-well offset, for Receivers 17-24 in the 2D dataset calculated using analytic method, coloured by line; E is shown in blue, SE is shown in magenta and S is shown in green. | 261 |
| Figure F.4: Deviation in geophone orientation azimuths, versus source-well offset, for Receivers 25-32 in the 2D dataset calculated using analytic method, coloured by line; E is shown in blue, SE is shown in magenta and S is shown in green. | 262 |

| | |
|--|-----|
| Figure F.5: Deviation in geophone orientation azimuths, versus source-well offset, for Receivers 33-40 in the 2D dataset calculated using analytic method, coloured by line; E is shown in blue, SE is shown in magenta and S is shown in green. | 263 |
| Figure F.6: Deviation in geophone orientation azimuths, versus source-well offset, for Receivers 41-48 in the 2D dataset calculated using analytic method, coloured by line; E is shown in blue, SE is shown in magenta and S is shown in green. | 264 |
| Figure F.7: Deviation in geophone orientation azimuths, versus source-well offset, for Receivers 49-56 in the 2D dataset calculated using analytic method, coloured by line; E is shown in blue, SE is shown in magenta and S is shown in green. | 265 |
| Figure F.8: Deviation in geophone orientation azimuths, versus source-well offset, for Receivers 57-64 in the 2D dataset calculated using analytic method, coloured by line; E is shown in blue, SE is shown in magenta and S is shown in green. | 266 |
| Figure F.9: Deviation in geophone orientation azimuths, versus source-well offset, for Receivers 1-8 in the 3D dataset calculated using analytic method, coloured by bin; 0°-180° is shown in blue, 45°-225° is shown in cyan, 90°-270° is shown in yellow and 135°-315° is shown in red. | 267 |
| Figure F.10: Deviation in geophone orientation azimuths, versus source-well offset, for Receivers 9-16 in the 3D dataset calculated using analytic method, coloured by bin; 0°-180° is shown in blue, 45°-225° is shown in cyan, 90°-270° is shown in yellow and 135°-315° is shown in red. | 268 |
| Figure F.11: Deviation in geophone orientation azimuths, versus source-well azimuth, for Receivers 1-8 in the 3D dataset calculated using analytic method, for 3D walkaway coloured by offset. Hotter colours represent far offsets, cooler colours represent near offsets. | 269 |
| Figure F.12: Deviation in geophone orientation azimuths, versus source-well azimuth, for Receivers 9-16 in the 3D dataset calculated using analytic method, for 3D walkaway coloured by offset. Hotter colours represent far offsets, cooler colours represent near offsets. | 270 |
| Figure F.13: Histograms of orientation azimuth for Receivers 1-8 in the 3D dataset calculated using analytic method. | 271 |
| Figure F.14: Histograms of orientation azimuth for Receivers 9-16 in the 3D dataset calculated using analytic method. | 272 |
| Figure F.15: Histograms of orientation azimuth for Receivers 1-8 in the 3D dataset calculated using analytic method, after rejection of near offset shots. | 273 |
| Figure F.16: Histograms of orientation azimuth for Receivers 9-16 in the 3D dataset calculated using analytic method, after rejection of near offset shots. | 274 |

List of Symbols, Abbreviations and Nomenclature

| | |
|---------------|--|
| b | Baseline trace |
| m | Monitor trace |
| δ | Thomsen parameter Delta |
| ε | Thomsen parameter Epsilon |
| θ | Phase (wavefront) angle |
| | Measured angle between H1-component and source |
| θ_I | Angle between incident ray and interface normal |
| θ_T | Angle between transmitted ray and interface normal |
| ρ | Density |
| ϕ | Group (ray) angle |
| ϕ_r | H1-component orientation azimuth |
| ϕ_s | Source-receiver azimuth |
| V_I | Velocity of medium of incident ray |
| V_T | Velocity of medium of transmitted ray |
| V_P | P-wave velocity |
| V_S | S-wave velocity |
| σ | Standard deviation |
| 2D | Two-dimensional |
| 3D | Three-dimensional |
| 4D | Four-dimensional |
| NRMS | Normalised root mean square |
| PRED | Predictability |
| SDR | Signal to distortion ratio |
| S/N | Signal to noise |
| VSP | Vertical seismic profile |

Chapter One: Introduction

1.1 Borehole Geophone Orientation

1.1.1 Vertical Seismic Profile (VSP) Surveys

A vertical seismic profile (VSP) is a measurement of seismic signal emanating from a surface source, recorded by borehole receivers (Hinds et al., 1996). Performing a seismic experiment in this way is beneficial in that it generally results in lower ambient noise levels than when using receivers on the surface, and has the ability to record both downgoing and upgoing wavefields (Hinds et al., 1996). The low noise levels recorded by borehole geophones are particularly useful for passive seismic monitoring, where they are able to record microseismic events with small magnitudes (Maxwell et al., 2010). There are several different types of VSP surveys: the zero-offset VSP, where the source is almost directly above the receivers (Cassell, 1984); the offset VSP, where the source has a lateral offset from the receivers (Cassell, 1984); and the walkaway VSP, where several source offsets are recorded (Lines and Newrick, 2004). Figure 1.1 illustrates the basic designs of a zero-offset VSP and a walkaway VSP. In the case of an offset or walkaway VSP, it is useful to know the source-well offset and the source-well azimuth. The source-well offset is defined as the lateral distance from the wellhead to the source, and the source-well azimuth is defined as the angle between the source-well offset vector and North (Figure 1.2).

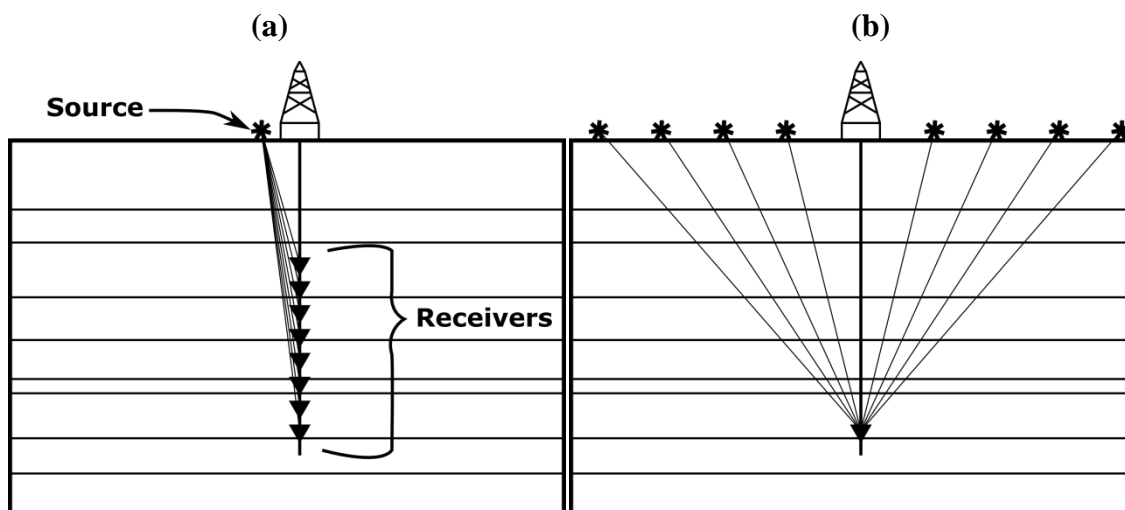


Figure 1.1: Schematic illustrations of (a) a zero-offset VSP and (b) a walkaway VSP, shown in cross-sectional view.

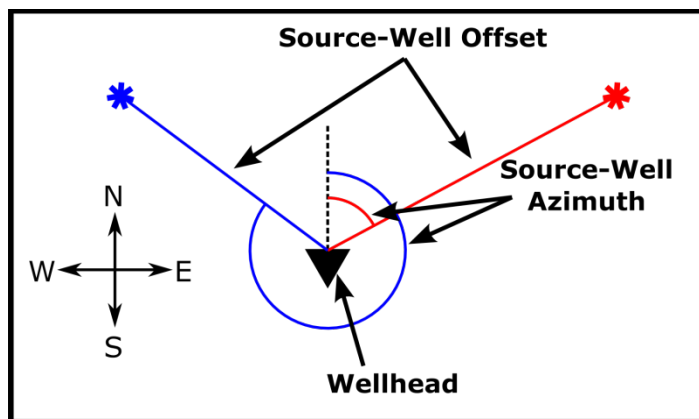


Figure 1.2: Plan view illustration of the source-well offset and source-well azimuth for two possible source locations.

1.1.2 Importance and Application to Microseismic Studies

Multi-component borehole geophones are increasingly being used for microseismic monitoring, in which data recorded by these geophones are used to determine the hypocentres and characteristics of microseismic events associated with hydraulic fracturing (Maxwell et al., 2010). Microseismic studies are important for imaging and characterisation of developing fracture networks, stimulated for the purpose of extracting hydrocarbons (Maxwell et al., 2010). Figure 1.3 shows an example of microseismic event locations from a case study done by Refunjol et al. (2012).

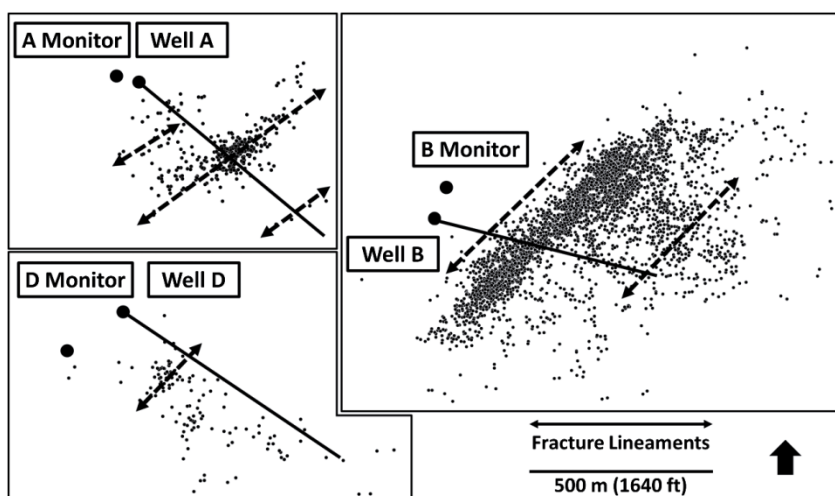


Figure 1.3: Plan view of mapped microseismic events for three injection wells, from a study done by Refunjol et al. (2012).

Unfortunately, when deploying a string of borehole geophones into a well they tend to rotate, resulting in an unknown orientation of their horizontal components once installed. In order to deduce the location of a microseismic event, the orientation of these receivers must first be determined (Le Calvez et al., 2005). Uncertainty in the orientation of borehole geophones can contribute to uncertainty in microseismic event location (Le Calvez et al., 2005; Refunjol et al., 2012); thus, it is important to develop experiments which can aid in the calibration of borehole geophone orientation.

1.1.3 Calibration Surveys

In order to determine the orientation of borehole geophones, calibration surveys are required; often calibration is performed using perforation shots (Le Calvez et al., 2005; Eisner et al., 2009) but other seismic sources, such as surface seismic sources, can also be used. The fidelity of these calibrations will affect the accuracy in locating microseismic events (Eisner et al., 2009) as well as for optimum VSP imaging and analysis, particularly for converted (PS) waves (Müller et al., 2010). Geophone orientation analysis also has applications to ocean bottom seismic experiments and earthquake monitoring; Li and Yuan (1999) performed such an analysis on seismic data acquired with 3-C ocean bottom nodes in the North Sea, and Oye and Ellsworth (2005) performed orientation analysis of borehole geophones near the San Andreas Fault.

When calibrating geophone orientation angles, there are four assumptions typically made that simplify the orientation analysis:

- 1) Signal to noise (S/N) of the P-wave first arrivals is high.

- 2) The well is vertical, ensuring that the horizontal components of the geophone lie in the X-Y plane. For example, Figures 1.4a, c and e show a raypath from a seismic source recording into a vertical well; there will be no P-wave first arrival energy on the H1 horizontal component. Compare this to the scenario shown in Figures 1.4b, d and f, which has a source at the same source-H1 azimuth, but involves a deviated well. There will now be extra P-wave first arrival energy on

the H1 component, resulting in a skewed orientation analysis. Additionally, errors in the deviation survey of the well, whether the well is deviated or assumed vertical, will contribute to error in the geophone positioning and orientation (Bulant et al., 2007).

- 3) Strata are laterally homogeneous (i.e., horizontal), ensuring that there is no lateral raybending (Bulant et al., 2007; Eisner et al., 2009). Figure 1.5 shows an example where there is a dipping interface; from plan view (Figure 1.5b), it is evident that the source-well azimuth is different than the azimuth of the ray as it reaches the geophone at depth. This will have an effect on orientation analysis if source-well azimuths are not aligned in the dip direction.
- 4) All layers are isotropic (Bulant et al., 2007; Eisner et al., 2009), ensuring that the angle measured at the geophone is equal to the energy transport direction (group or ray angle). A simple schematic illustration of an anisotropic wavefront is shown in Figure 1.6.

All four of these have the potential to skew results of a calibration, and thus introduce errors in the locations of microseismic events that are being monitored. The main focus of this thesis will be to separately examine these effects on geophone orientation calibration; however, it must be noted that these effects could be present simultaneously in field studies. Finally, there are other effects that could skew orientation analysis, such as converted S-wave arrivals and reflected arrivals, which are noted in this thesis.

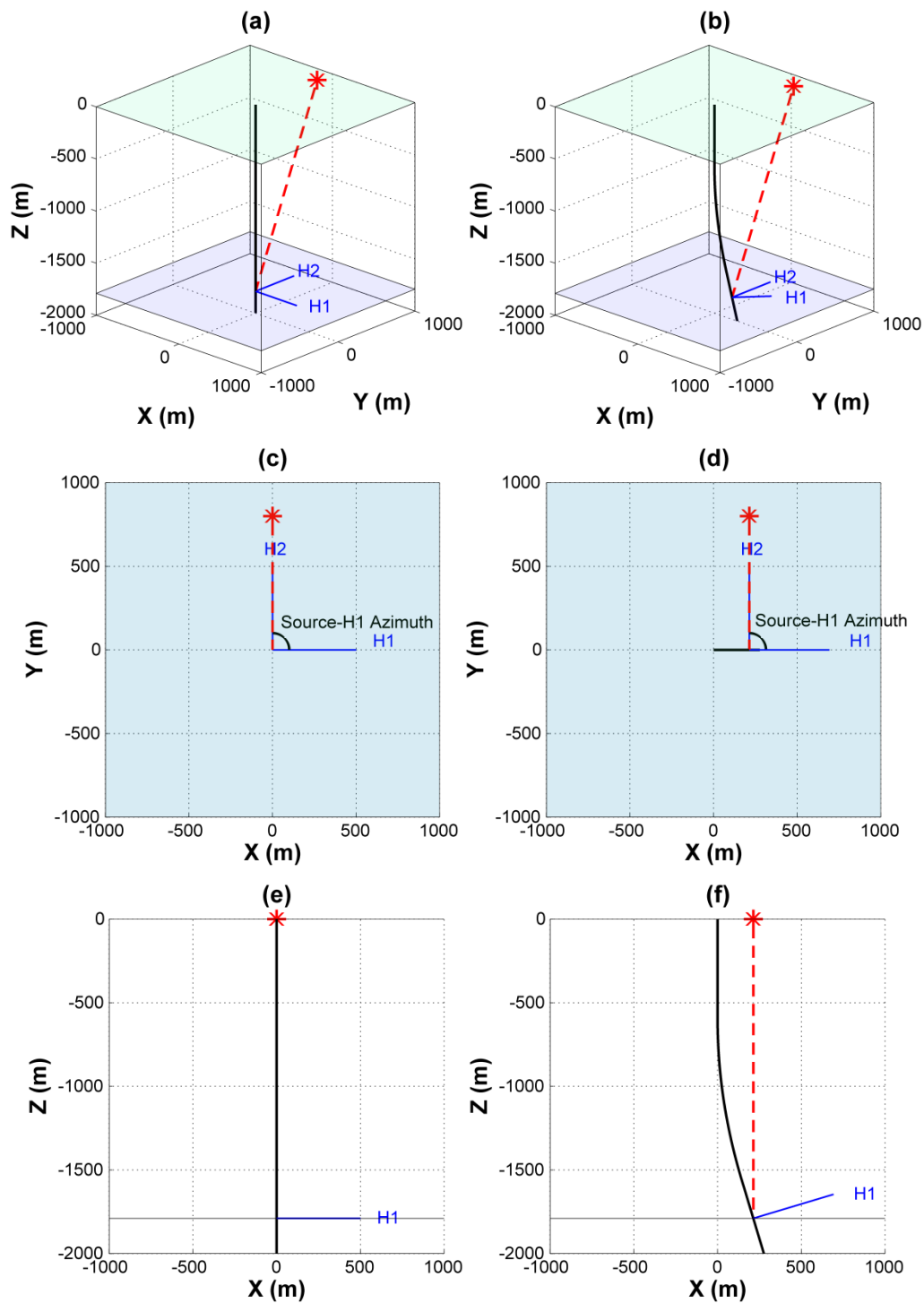


Figure 1.4: Schematic diagram showing the raypaths of a shot to a geophone at 1800 m depth in (a, c, e) a vertical well and (b, d, f) a deviated well. H1 and H2 components of the geophones are shown in blue.

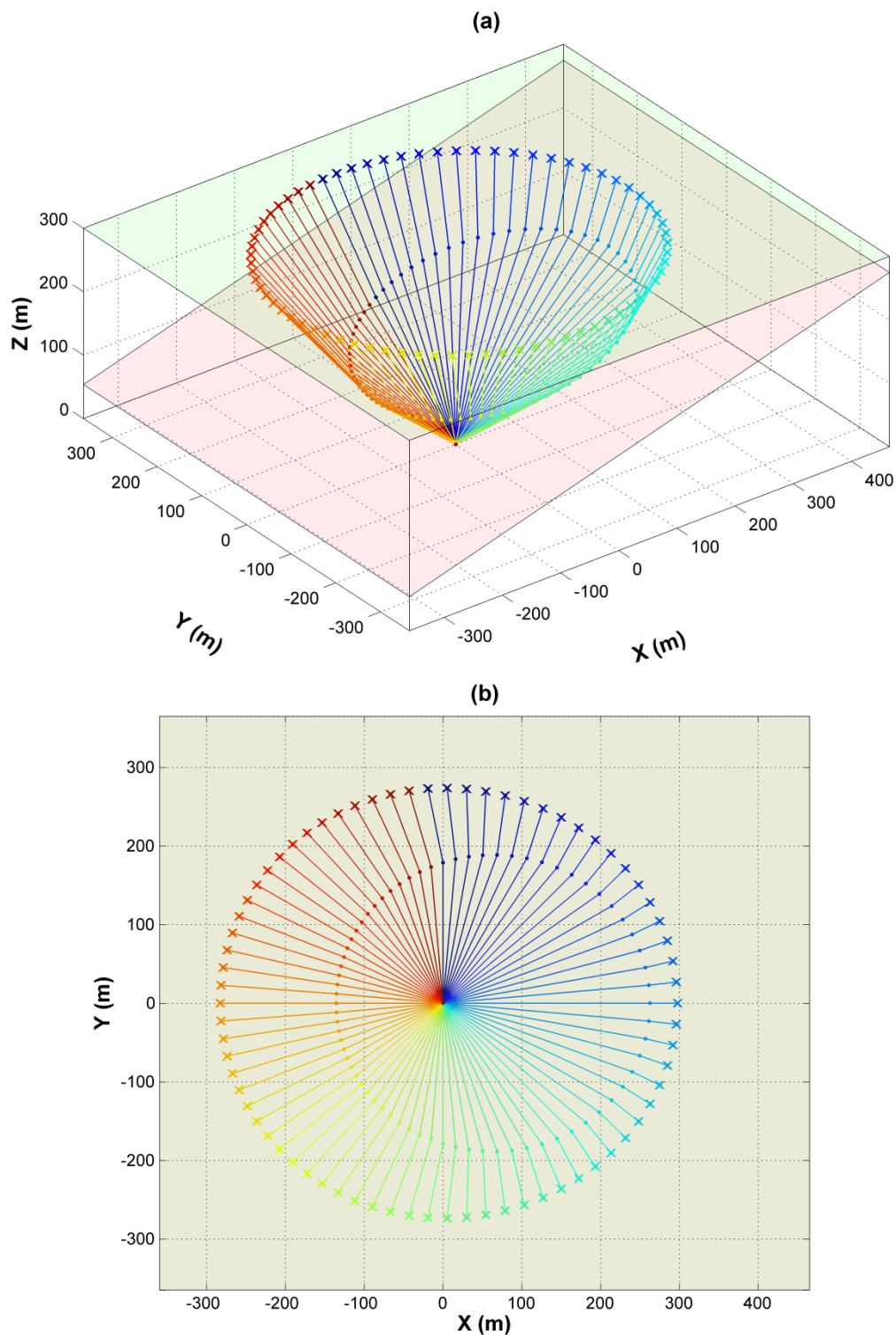


Figure 1.5: (a) Perspective and (b) plan view diagrams showing the lateral raybending which occurs when a dipping interface is present. Rays are coloured by arrival azimuth at geophone as a visual aid.

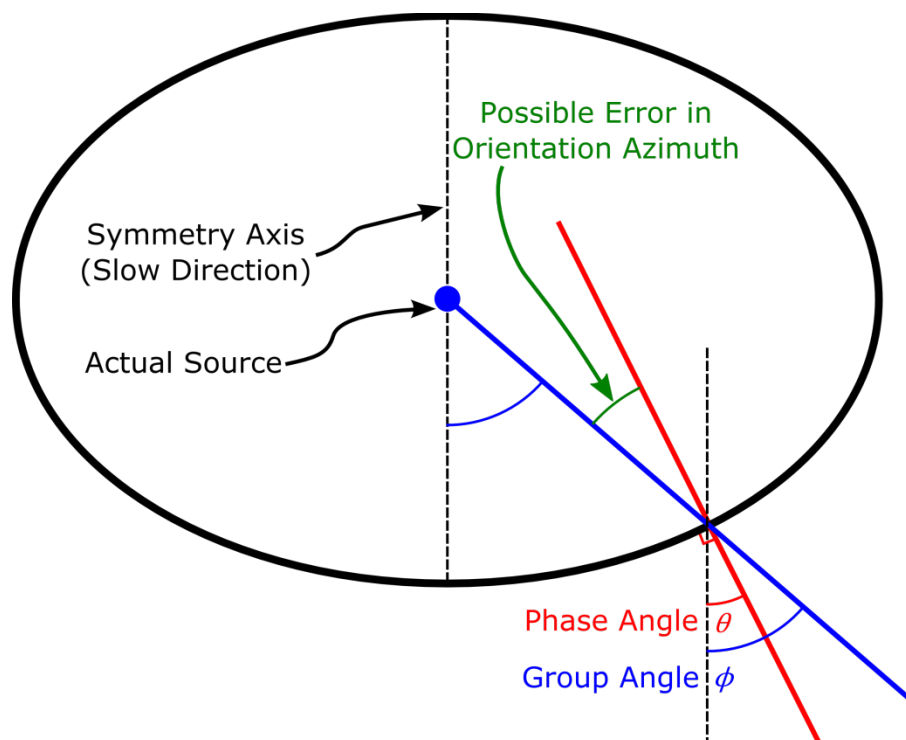


Figure 1.6: Simple illustration showing the difference between group (ray) angle ϕ and phase (wavefront) angle θ . Adapted from Thomsen (1986).

1.2 Seismic Repeatability

1.2.1 Time-Lapse Seismology

Time-lapse seismology has become a widely used tool for applications such as reservoir monitoring (Lumley, 2001; Calvert, 2005) and CO₂ sequestration studies (Lumley, 2010); the goal is to detect changes in the subsurface, and therefore must include at least two separate seismic experiments. In this thesis, the first is referred to as a “baseline” survey, while subsequent experiments are called “monitor” surveys. The ideal end result of a time-lapse experiment is to have a reliable measure of changes in the subsurface, while minimising or eliminating changes due to other factors, which can be grouped together as “4D noise” (Cantillo, 2012). Some sources of 4D noise include source and receiver mispositioning, changes in the near-surface (weathering) layer and changes in the ambient noise (Lumley, 2001).

In order to determine the amount of change between a baseline and monitor survey, it is useful to define some quantitative metrics. Two commonly used metrics are called the normalised root mean square (NRMS) repeatability and predictability (Kragh and Christie, 2002). These provide a measure of the trace-by-trace “repeatability”; that is, the overall similarity of a monitor trace to a baseline trace. However, these do not necessarily distinguish between 4D noise and meaningful changes in the subsurface, leading to some ambiguity in their interpretation. Cantillo (2011) provides a new metric, called signal to distortion ratio, which he suggests is more meaningful than either of the metrics provided by Kragh and Christie (2002). This thesis will include a study done to further understand the best use of these three metrics.

1.2.2 NRMS Repeatability (NRMS)

NRMS repeatability is defined (Kragh and Christie, 2002) as:

$$NRMS = \frac{2\sqrt{\sum_{t_1}^{t_2}(b_t - m_t)^2/N}}{\sqrt{\sum_{t_1}^{t_2}(b_t)^2/N + \sum_{t_1}^{t_2}(m_t)^2/N}}, \quad (1.1)$$

where b and m are the baseline and monitor traces, t_1 and t_2 are the start and end times of the desired window, and N represents the total number of samples per trace within the window. The values for NRMS repeatability are generally given in percent, and range from 0 % to 200 %, where lower values represent more repeatable traces; it is also interesting to note that uncorrelated noise will have a value of $\sqrt{2}$ (roughly 141 %) (Kragh and Christie, 2002).

1.2.3 Predictability (PRED)

Predictability is defined (Kragh and Christie, 2002) as:

$$PRED = \frac{(\sum_{-n}^{+n} b \otimes m)^2}{(\sum_{-n}^{+n} b \otimes b)(\sum_{-n}^{+n} m \otimes m)}, \quad (1.2)$$

where b and m are the baseline and monitor traces windowed from t_1 to t_2 , \otimes is the crosscorrelation operator, and the sum is performed over lags $-n$ to $+n$. For this thesis, only the zero lag values are considered (i.e. $n=0$). Cantillo (2011) notes that the number of lags used in the summation can have an important effect on the predictability value; thus, it is difficult to gain a good understanding of this metric without consistency in the number of lags used. The values for predictability range from 0 to 1, where higher values represent more repeatable traces (Kragh and Christie, 2002).

1.2.4 Signal to Distortion Ratio (SDR)

The signal to distortion ratio is defined as (Cantillo, 2011):

$$SDR = \frac{\sum_{t_1}^{t_2} b_t^2}{\sum_{t_1}^{t_2} d_t^2} = \frac{\max(b \otimes m)^2}{1 - \max(b \otimes m)^2}, \quad (1.3)$$

given the model

$$m = \delta_t * b + d. \quad (1.4)$$

Here, b , m and \otimes are defined as above, δ_t is a delta function representing time lag, and d (the “distortion”) encompasses all changes between the baseline and monitor traces, once time-shifts have been removed. Cantillo (2011) suggests that this metric, along with time-shift measurements, would be more suitable for repeatability studies than the currently used NRMS and PRED methods. Throughout this thesis, the \log_{10} of SDR was favoured, as it allowed for more useful trace by trace comparisons; a logarithmic scale was also favoured by Cantillo (2012).

1.3 Rotation Methods

1.3.1 Analytic

A simple analytic method for determining geophone orientation is given by DiSiena et al. (1984):

$$\tan 2\theta = \frac{2H_1 \otimes H_2}{H_1 \otimes H_1 + H_2 \otimes H_2}, \quad (1.5)$$

where \otimes is a zero-lag crosscorrelation operator, H_1 and H_2 are the windowed horizontal component data and θ is the angle between the H1-component and source.

1.3.2 Hodograms

In addition to the analytic solution described above, geophone orientation analysis was also undertaken using hodograms. A hodogram is a cross-plot of amplitudes for two receiver components, typically windowed over the first arrivals; in this case, the two horizontal components. An example of a hodogram is shown in Figure 1.7. The source-receiver angle is found by taking the inverse tangent of the slope of the line of best fit.

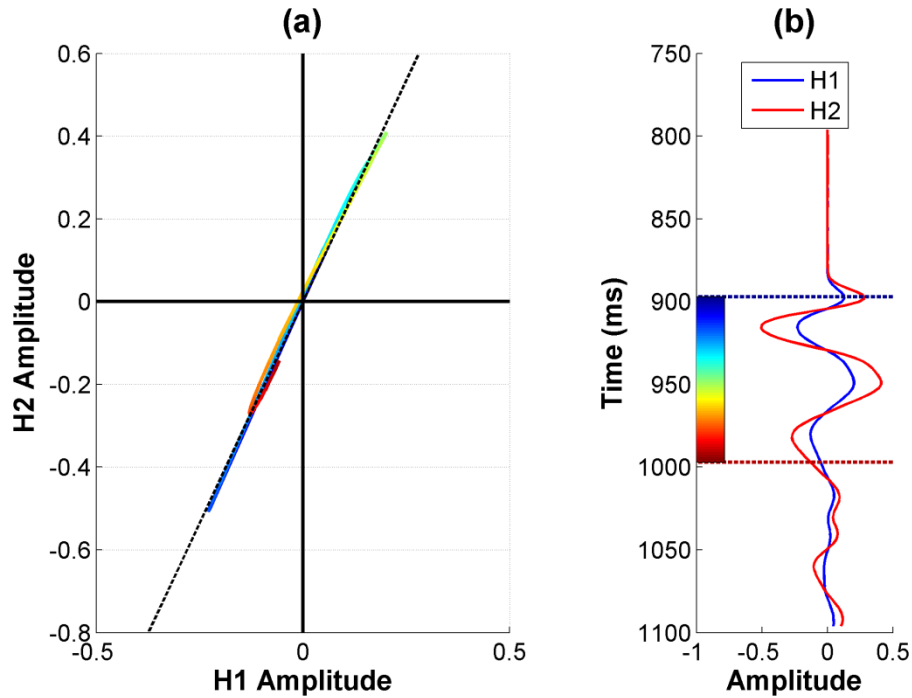


Figure 1.7: Example of a hodogram plot used in this thesis. (a) shows hodogram corresponding to the trace shown in (b); the colour scale used to plot (a) represents trace time, shown as a colour bar in (b).

1.3.3 Common Reference Frame

Once θ is found, it can be converted into an azimuth relative to geographic north using

$$\phi_r = \phi_s + \theta, \quad (1.6)$$

where ϕ_s is the source-receiver azimuth, relative to North, and ϕ_r is the H1 component orientation azimuth. Conversion to the receiver orientation azimuth provides a standard reference frame for all potential source locations (Figure 1.8). If the well is vertical, we can assume that the horizontal components of the borehole geophones will be oriented on a plane parallel to the surface x-y plane; thus, when examining the source-receiver azimuth, it is sufficient to precisely use the x and y coordinates of the source location; that is,

$$\phi_s = \arctan(x_s/y_s). \quad (1.7)$$

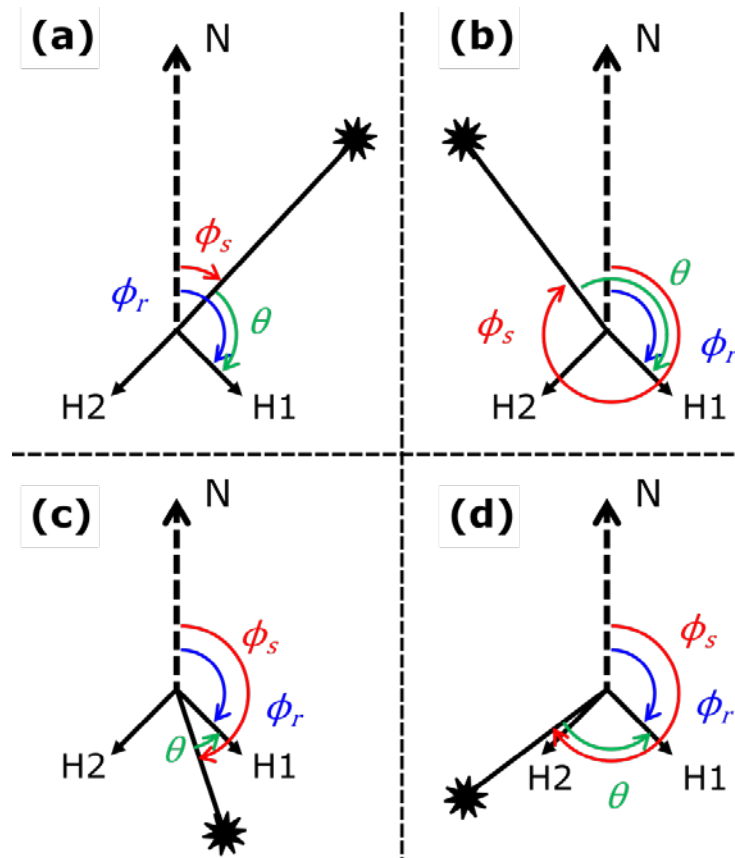


Figure 1.8: Illustration of the relationship between θ (green), ϕ_s (red) and ϕ_r (blue).

1.3.4 Spider Plots

In order to effectively present the orientation angle results of the case studies examined in this thesis, for multi-source surveys, a polar type of plot, called a “spider” plot, was developed. The process for generating these plots was as follows:

- 1) Plot a straight line beginning at the origin and extending to the maximum source-well offset, in the direction of the receiver’s mean orientation azimuth.
- 2) Draw two envelope lines in a similar manner, representing one standard deviation to either side of the mean.
- 3) Plot individual data points at a distance from the origin equal to their absolute source-well offset, using their individual orientation azimuths as the direction.

Figure 1.9 shows an annotated example of one of these plots, using a fictitious dataset consisting of one receiver and 6 source locations.

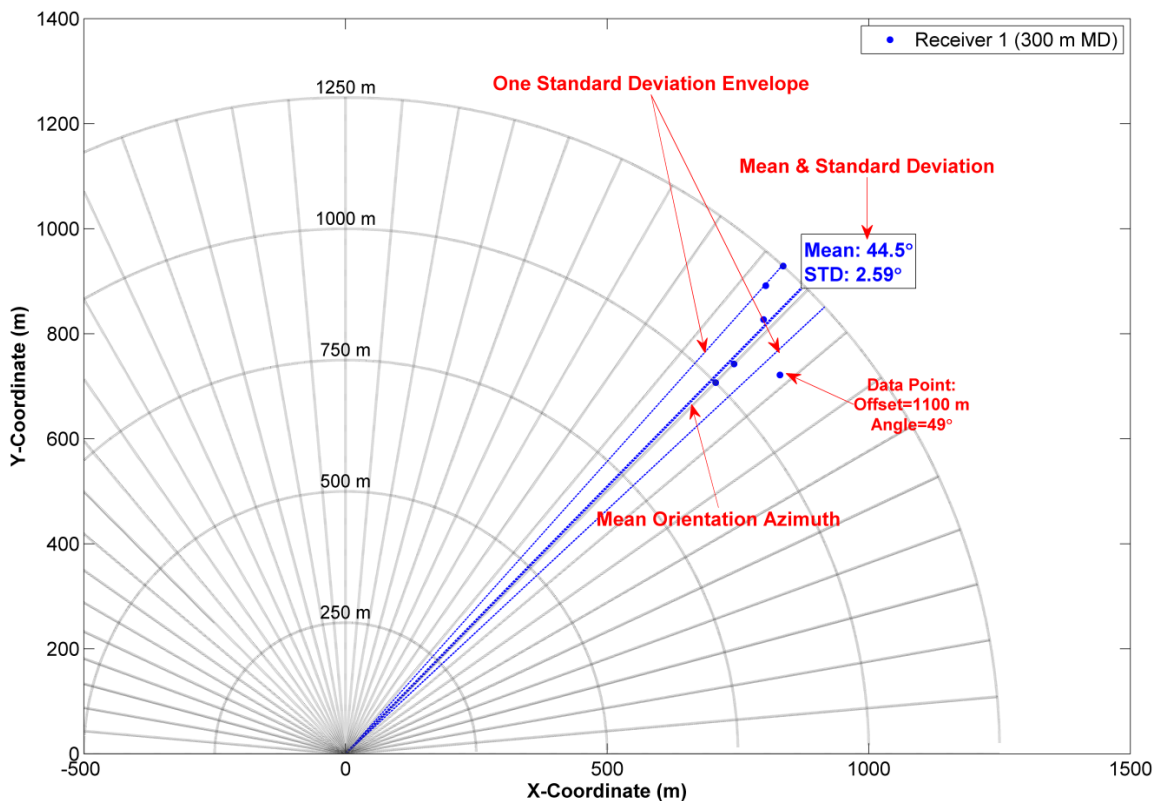


Figure 1.9: Annotated example of the spider plots used throughout this thesis.

1.4 Field Study Site: Pembina CO₂ Project

The Pembina oilfield (Figure 1.10) is just over 100 km southwest of Edmonton and its major pool, in the Cardium, is the largest conventional oil pool that has been discovered in Western Canada (Hitchon, 2009). This oilfield was chosen out of several potential sites for a CO₂ monitoring pilot. Through the partnership of the Canadian and Alberta governments, the University of Calgary, the University of Alberta, Penn West and Schlumberger, a wealth of interesting information regarding many geophysical and geological concepts, including CO₂ sequestration time-lapse geophysics, have been studied (Hitchon, 2009). Over the course of this project, CO₂ was injected into the Cardium Formation near Violet Grove, Alberta. In addition to surface seismic surveys, a vertical seismic profile was recorded in an observation well 1650 m deep (Hitchon, 2009).

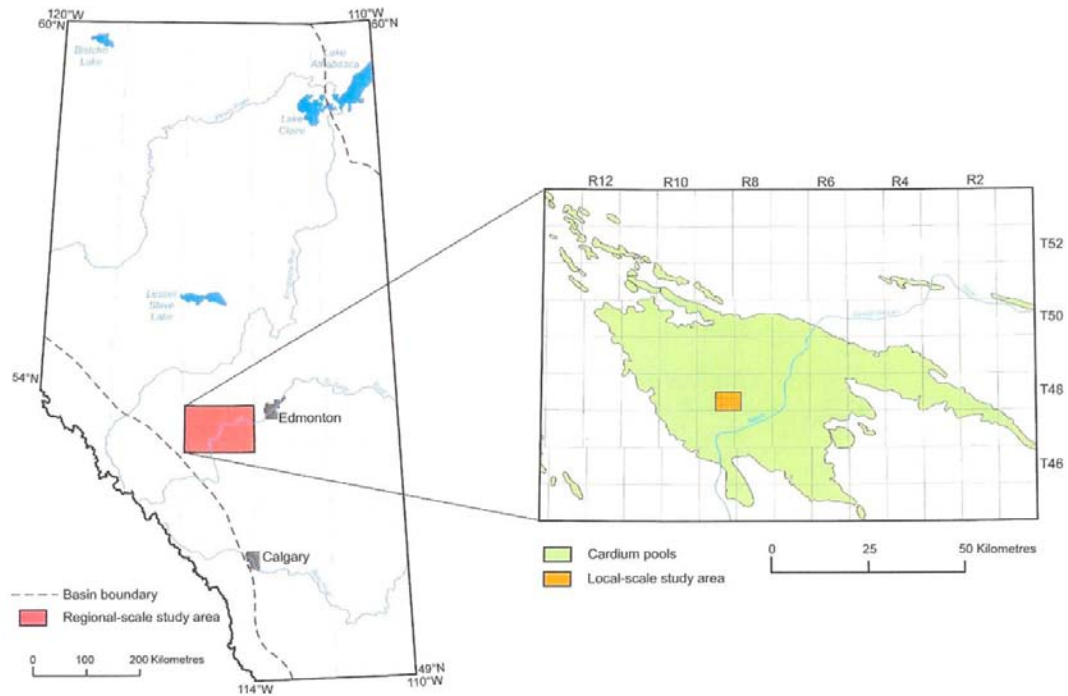


Figure 1.10: Location of study area, in the Pembina oilfield. Figure from Dashtgard et al. (2006).

1.5 Objectives and Outline of Thesis

1.5.1 Objectives

The main objectives of this thesis are as follows:

- 1) To characterise and quantify the effects of noise, well deviation, lateral raybending and seismic anisotropy on geophone orientation azimuth calibration surveys, and to develop a method to determine geophone orientation in a deviated well.
- 2) To determine the optimal method and survey design for geophone orientation calibration surveys and understand their repeatability.
- 3) To perform analysis of geophone orientation using case studies, and to look for signatures of well deviation, lateral raybending and seismic anisotropy where their effects are initially assumed to be minimal.

1.5.2 Outline

This thesis is broken up into seven additional chapters:

Chapter 2 is made up of two parts: first, repeatability and orientation azimuth analyses are performed on a field dataset from Violet Grove, Alberta, including the repeatability of the orientation azimuth analysis. Second, an experiment is performed to investigate the sensitivity of repeatability metrics to several controlled trace perturbations.

Chapter 3 consists of an orientation analysis on a dataset modelled using TIGER, consisting of horizontal, isotropic layers and a vertical well. Random noise is added to the output of this model, and each of the three geophone orientation calculation methods (analytic, hodogram and inversion) is tested.

Chapter 4 begins with another case study from Violet Grove, where geophones were deployed into a deviated well. A method is developed to compensate for the effects of the deviation, and the data are analysed for geophone orientation. Additionally, a simple model is created to test the effects of deviation survey error on the final outcome of geophone orientation analysis.

Chapter 5 characterises the effect of a dipping velocity interface on geophone orientation analysis. A simple two-layer raytracing algorithm is developed and tested using MATLAB, to examine the effects of various velocity contrasts and interface dip angles. Finite difference modelling is then done in TIGER, and the results directly compared to the raytracing; the effects of transmitted converted waves are also noted.

Chapter 6 is a characterisation of the effect of HTI on geophone orientation analysis. Investigation is first done analytically, using code developed in MATLAB to find the differences in phase and group angle for a variety of values of ε and δ . TIGER is again used to undertake finite difference modelling, using a two layer example where the upper layer is an HTI medium and the lower layer is isotropic.

Chapter 7 is a field example from Lousana, Alberta, consisting of a 3D walkaway VSP dataset. The data are binned based on azimuth in order to look for any azimuthal trends in the calculated geophone orientation, and results are compared to the analyses done in Chapters 4-6. Additionally, the data are binned based on offset in order to determine the optimal offset range for geophone orientation analysis.

Finally, Chapter 8 discusses and summarises the conclusions of Chapters 2-7, and provides suggestions for future work.

1.6 Software

1.6.1 MATLAB

MATLAB is a high-level computing language developed by MathWorks, optimised for matrix algebra. It was used extensively throughout this thesis, performing all calculations and analyses and generating almost all of the figures found within. Significant code developed during this project is included in Appendix F and the Digital Appendix.

1.6.2 TIGER

TIGER is a 3D anisotropic elastic finite difference modelling software package developed by SINTEF Petroleum Research, which is able to run in a parallel computing environment. Users may specify density, P-wave and S-wave velocity, Thomsen parameters for weak anisotropy (ϵ , δ and γ), orientation of anisotropic symmetry axis (direction and dip) and Q values (Q_P , Q_S , Q_{11} , Q_{13} and Q_{66}) for a geologic model, giving it a wide variety of applications. Additionally, it is very flexible in terms of source and receiver geometry. This software was used to generate the finite difference models examined in chapters 2, 5 and 6.

1.6.3 GEDCO Vista

Vista is a seismic processing software package that can handle both 2D and 3D seismic data. For the purposes of this thesis, it was used mainly for quality control, first break picking, conversion of seismic file formats and organisation of headers.

Chapter Two: Pembina Time-Lapse Field Example

2.1 Introduction

The main objective of this chapter was to understand seismic repeatability metrics and investigate the repeatability of orientation angle calculations for a field study. Three seismic repeatability metrics will be studied using a controlled experiment as well as a field example, and recommendations will be made about their use. Repeatability of geophone orientation analysis was studied using various window sizes, and a recommendation is made about the optimum window size for general studies. This chapter also serves as an introduction to the types of plots and analyses used through the remainder of this thesis.

2.2 Survey Parameters

The VSP data used in this field example was from the Pembina CO₂ enhanced oil recovery project. The VSP consisted of eight 3-component geophones placed every 20 m, starting at 1498 m depth, in the observation well 07-11-048-09W5 near Violet Grove, Alberta (Hitchon, 2009). Table 2.1 provides a listing of all the receiver depths. Three surface seismic lines were common between the baseline and monitor: Line 1, which was north-south, and Lines 2 and 3, which were oriented east-west (Figure 2.1). An example of a Phase I (baseline, acquired in March 2005) raw shot gather is shown in Figure 2.2a, and the corresponding raw shot gather from Phase III (monitor, acquired in March 2007) is shown in Figure 2.2b; finally, an example of a Phase I common receiver gather is shown in Figure 2.3a, and the corresponding common receiver gather is shown in Figure 2.3b. Note that certain components suffered from extremely poor signal quality due to cable degradation between Phase I and Phase III; these were: vertical component of Receiver 2, H1 component of Receiver 4 and H2 component of Receiver 6. Finally, Receiver 5 suffered a large increase in noise between surveys, again due to cable degradation.

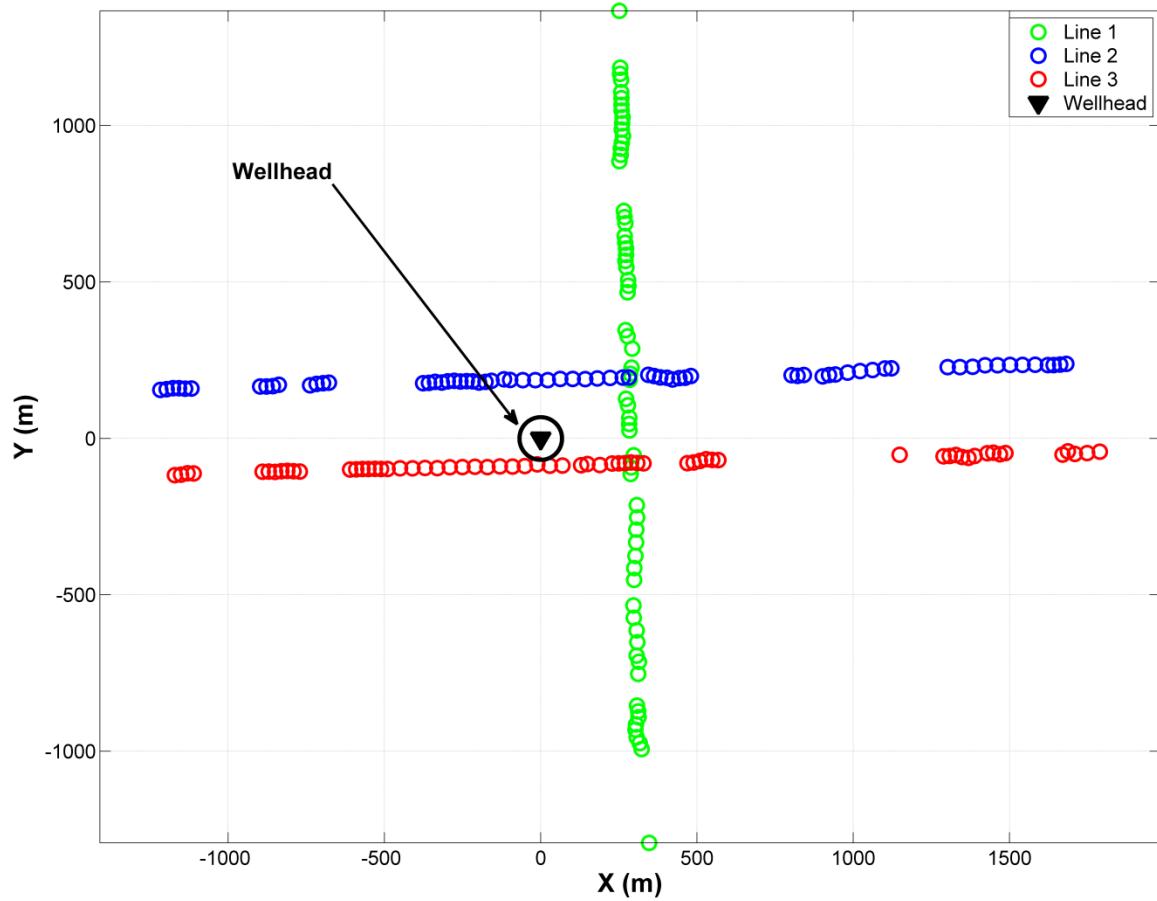


Figure 2.1: Shotpoint geometry for Violet Grove walkaway VSP used in this study. Coordinates are measured from the wellhead.

Table 2.1: Receiver depths used in field study.

| Receiver Number | Receiver Measured Depth (m) |
|-----------------|-----------------------------|
| 1 | 1498.0 |
| 2 | 1518.1 |
| 3 | 1538.9 |
| 4 | 1558.7 |
| 5 | 1579.7 |
| 6 | 1599.7 |
| 7 | 1620.5 |
| 8 | 1640.5 |

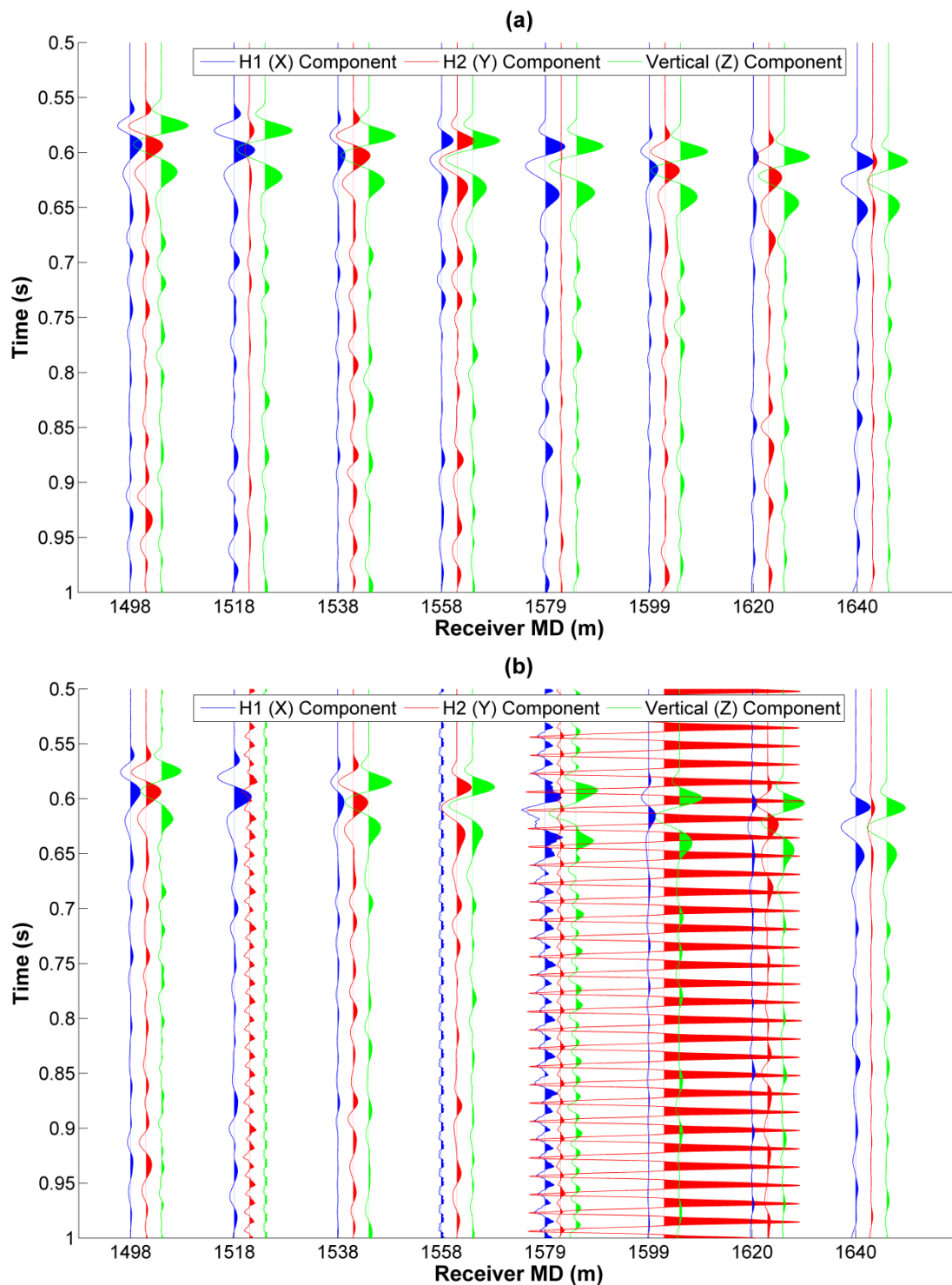


Figure 2.2: Common shot gather for shot 2145, from Line 2, at X=886.5 m, Y=207.3 m, for Phase I (a) and Phase III (b). H1 component is shown in blue, H2 component is shown in red, and vertical component is shown in green.

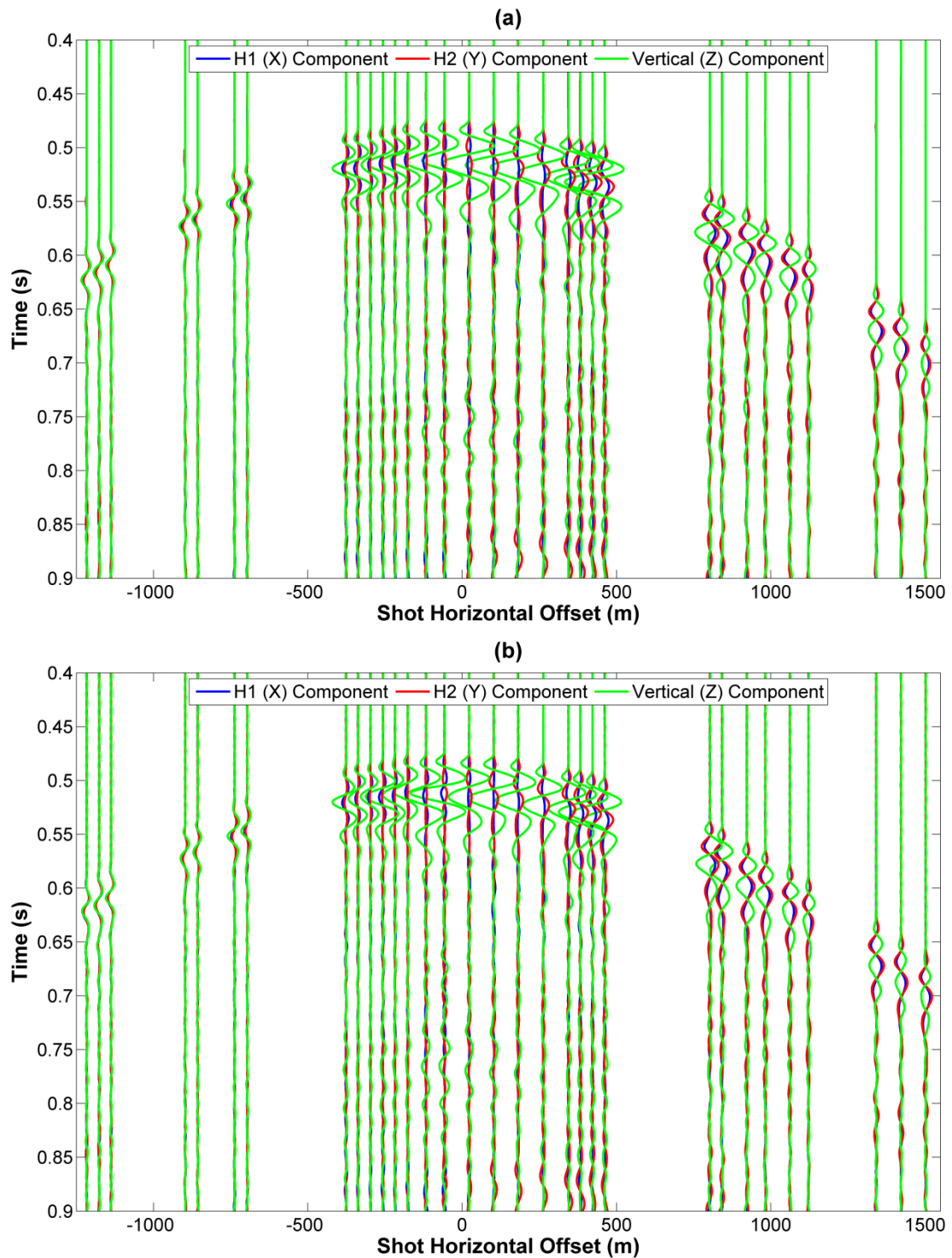


Figure 2.3: Common receiver gather from Line 2 for Receiver 3 at 1538 m MD, for Phase I (a) and Phase III (b). H1 component is shown in blue, H2 component is shown in red, and vertical component is shown in green. For display purposes, gathers have been decimated to half of their original traces.

2.3 Field Experiment

2.3.1 Seismic Repeatability

Results of seismic repeatability analysis for Receiver 3 (1538 m depth) are shown in Figures 2.4 – 2.6, separated by source line. This receiver was chosen arbitrarily for results shown in this chapter; all receivers are shown in Appendix B. Note that repeatability analysis was done for the full trace lengths. These plots reveal that \log_{10} SDR produces trends that closely mirror NRMS. It also appears very similar to PRED, though differences are more noticeable than with NRMS. Tables 2.2 – 2.4 summarise the results of the entire dataset numerically, on a receiver by receiver basis. Values calculated in these tables do not include components that were problematic in Phase III. When examining \log_{10} SDR values, recall that a value of 0 represents a signal to distortion ratio of 1; positive values indicate a higher proportion of signal, whereas negative values indicate a higher proportion of noise. Further, a study by Cantillo (2012) indicates that there is almost no visible difference between traces with a value of approximately 2.5 for \log_{10} SDR. The results seen here indicate that there are some differences between Phase I and Phase III seismic traces; thus, the comparison of orientation azimuths is also expected to show some differences.

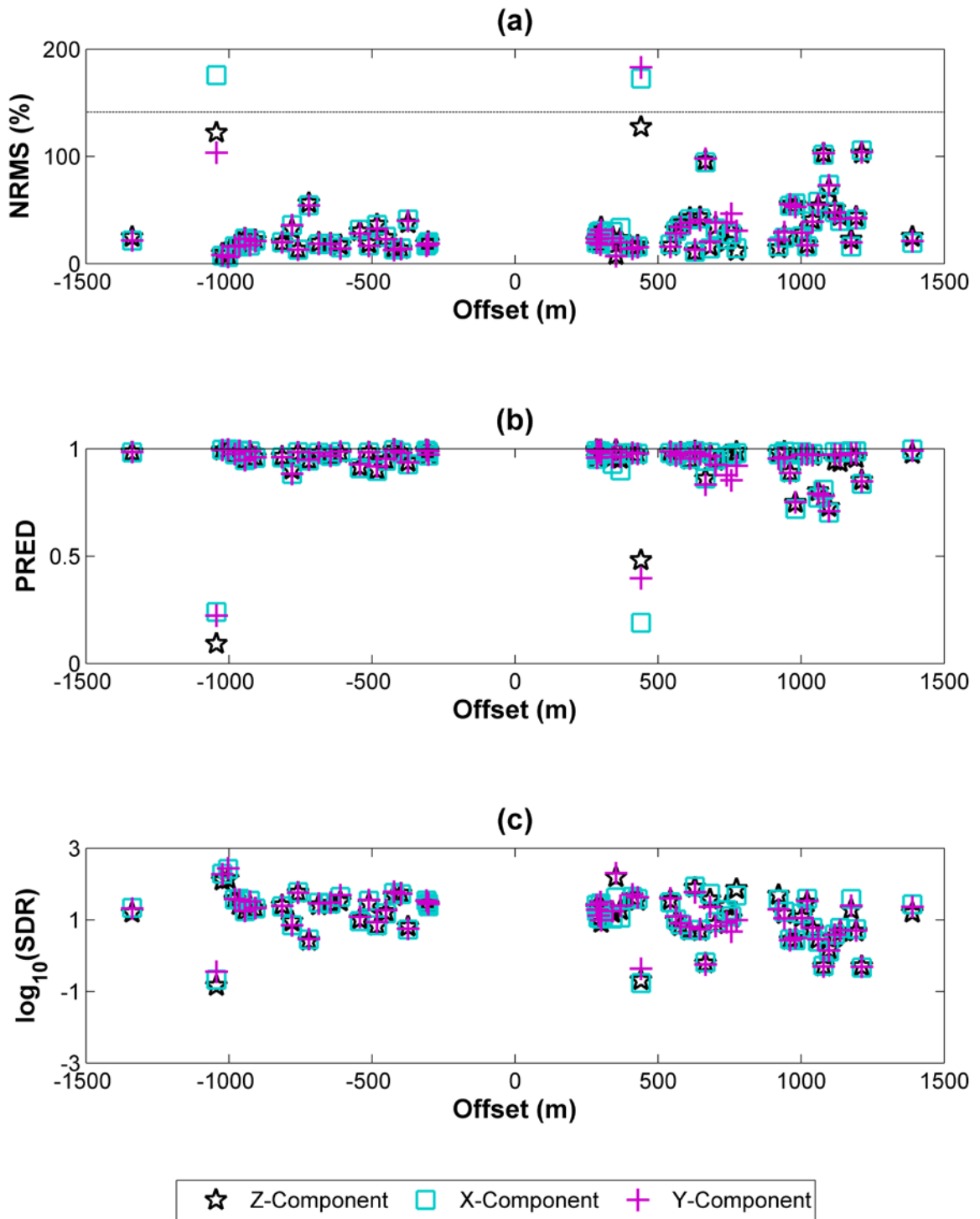


Figure 2.4: Comparison of NRMS repeatability (a), predictability (b) and \log_{10} SDR (c) of Receiver 3 for Line 1, vs. source offset. The z-component is shown in black, x-component is shown in cyan, and y-component is shown in magenta. The dashed line in the NRMS plot indicates the theoretical noise line.

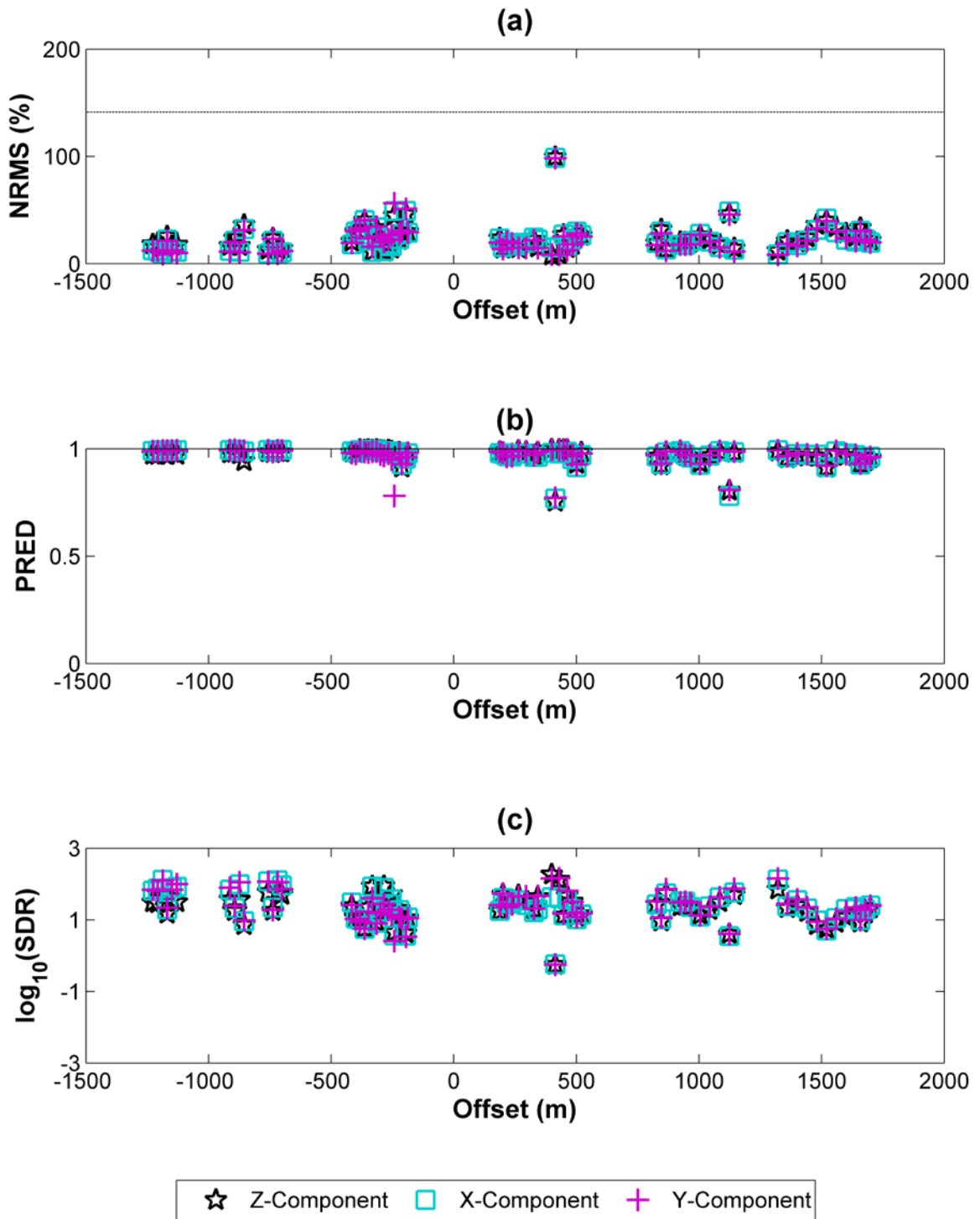


Figure 2.5: Comparison of NRMS repeatability (a), predictability (b) and \log_{10} SDR (c) of Receiver 3 for Line 2, vs. source offset. The z-component is shown in black, x-component is shown in cyan, and y-component is shown in magenta. The dashed line in the NRMS plot indicates the theoretical noise line.

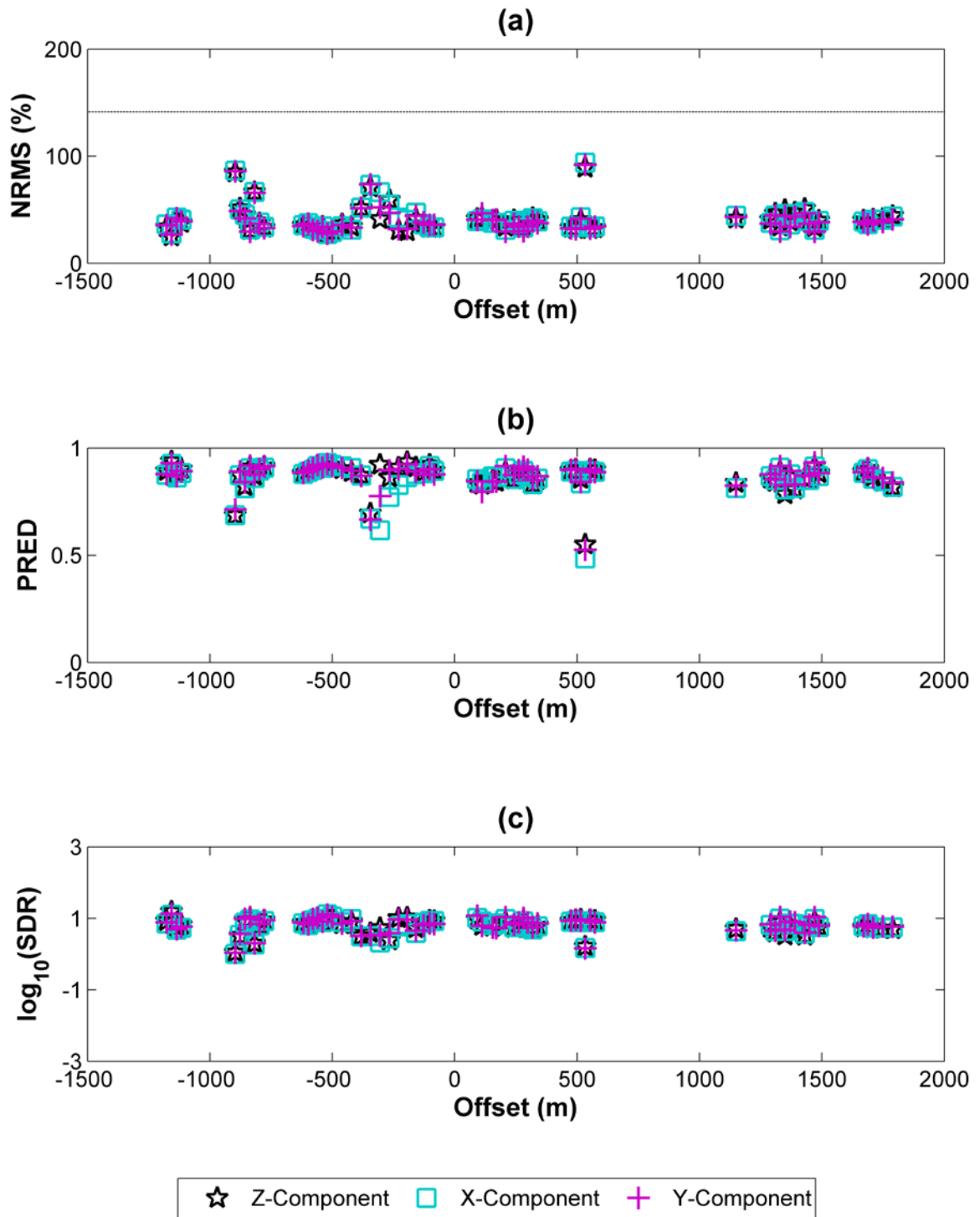


Figure 2.6: Comparison of NRMS repeatability (a), predictability (b) and \log_{10} SDR (c) of Receiver 3 for Line 3, vs. source offset. The z-component is shown in black, x-component is shown in cyan, and y-component is shown in magenta. The dashed line in the NRMS plot indicates the theoretical noise line.

**Table 2.2: Summary of repeatability metrics of Violet Grove z-component data.
Receiver 2 has been omitted.**

| Receiver | Line 1 | | | Line 2 | | | Line 3 | | |
|-----------------|---------------|--------------|-----------------|---------------|--------------|-----------------|---------------|--------------|-----------------|
| | Average NRMS | Average PRED | Average log SDR | Average NRMS | Average PRED | Average log SDR | Average NRMS | Average PRED | Average log SDR |
| 1 | 50.1 % | 0.82 | 0.60 | 49.5 % | 0.79 | 0.60 | 44.2 % | 0.86 | 0.74 |
| 3 | 33.2 % | 0.93 | 1.09 | 24.5 % | 0.96 | 1.32 | 41.2 % | 0.87 | 0.79 |
| 4 | 43.5 % | 0.85 | 0.77 | 39.9 % | 0.86 | 0.86 | 44.3 % | 0.84 | 0.75 |
| 5 | 95.9 % | 0.40 | -0.42 | 108.4 % | 0.34 | -0.68 | 42.4 % | 0.86 | 0.75 |
| 6 | 34.2 % | 0.93 | 1.05 | 25.4 % | 0.96 | 1.30 | 39.6 % | 0.88 | 0.81 |
| 7 | 36.5 % | 0.91 | 0.93 | 26.0 % | 0.95 | 1.23 | 40.8 % | 0.87 | 0.80 |
| 8 | 30.6 % | 0.93 | 1.18 | 24.5 % | 0.96 | 1.35 | 37.1 % | 0.90 | 0.89 |
| Average | 46.3 % | 0.82 | 0.74 | 42.6 % | 0.83 | 0.85 | 41.4 % | 0.87 | 0.79 |
| Std. Dev | 22.9 % | 0.19 | 0.55 | 30.6 % | 0.23 | 0.73 | 2.6 % | 0.02 | 0.05 |

**Table 2.3: Summary of repeatability metrics of Violet Grove x-component data.
Receiver 4 has been omitted.**

| Receiver | Line 1 | | | Line 2 | | | Line 3 | | |
|-----------------|---------------|--------------|-----------------|---------------|--------------|-----------------|---------------|--------------|-----------------|
| | Average NRMS | Average PRED | Average log SDR | Average NRMS | Average PRED | Average log SDR | Average NRMS | Average PRED | Average log SDR |
| 1 | 38.2 % | 0.92 | 0.97 | 26.8 % | 0.96 | 1.22 | 42.4 % | 0.86 | 0.77 |
| 2 | 43.0 % | 0.85 | 0.86 | 29.2 % | 0.94 | 1.14 | 40.1 % | 0.87 | 0.82 |
| 3 | 34.4 % | 0.93 | 1.12 | 23.7 % | 0.97 | 1.37 | 41.7 % | 0.86 | 0.78 |
| 5 | 157.6 % | 0.09 | -2.46 | 155.8 % | 0.10 | -2.29 | 50.1 % | 0.79 | 0.58 |
| 6 | 34.9 % | 0.93 | 1.09 | 24.0 % | 0.97 | 1.35 | 41.0 % | 0.86 | 0.78 |
| 7 | 51.8 % | 0.78 | 0.57 | 83.0 % | 0.55 | -0.17 | 46.5 % | 0.83 | 0.75 |
| 8 | 43.2 % | 0.86 | 0.80 | 31.6 % | 0.93 | 1.07 | 44.5 % | 0.84 | 0.72 |
| Average | 57.6 % | 0.77 | 0.42 | 53.4 % | 0.77 | 0.53 | 43.8 % | 0.84 | 0.74 |
| Std. Dev | 44.5 % | 0.30 | 1.29 | 49.8 % | 0.33 | 1.35 | 3.5 % | 0.03 | 0.08 |

Table 2.4: Summary of repeatability metrics of Violet Grove y-component data. Receiver 6 has been omitted.

| Receiver | Line 1 | | | Line 2 | | | Line 3 | | |
|-----------------|---------------|--------------|-----------------|---------------|--------------|-----------------|---------------|--------------|-----------------|
| | Average NRMS | Average PRED | Average log SDR | Average NRMS | Average PRED | Average log SDR | Average NRMS | Average PRED | Average log SDR |
| 1 | 46.5 % | 0.84 | 0.74 | 48.6 % | 0.78 | 0.67 | 48.7 % | 0.81 | 0.65 |
| 2 | 136.7 % | 0.14 | -1.43 | 167.5 % | 0.04 | -2.64 | 57.7 % | 0.73 | 0.42 |
| 3 | 34.0 % | 0.93 | 1.11 | 23.4 % | 0.96 | 1.38 | 40.2 % | 0.87 | 0.81 |
| 4 | 35.1 % | 0.93 | 1.08 | 24.8 % | 0.96 | 1.32 | 42.6 % | 0.86 | 0.76 |
| 5 | 110.9 % | 0.29 | -0.81 | 157.3 % | 0.09 | -2.43 | 54.2 % | 0.76 | 0.48 |
| 7 | 44.0 % | 0.87 | 0.78 | 29.3 % | 0.94 | 1.12 | 42.2 % | 0.85 | 0.75 |
| 8 | 37.4 % | 0.91 | 0.97 | 34.5 % | 0.91 | 0.96 | 40.7 % | 0.87 | 0.78 |
| Average | 63.5 % | 0.70 | 0.35 | 69.3 % | 0.67 | 0.05 | 46.6 % | 0.82 | 0.67 |
| Std. Dev | 42.1 % | 0.34 | 1.03 | 64.2 % | 0.42 | 1.79 | 7.0 % | 0.06 | 0.16 |

2.3.2 Orientation Azimuth

2.3.2.1 Repeatability between Surveys and Window Tests

Geophone azimuth comparisons between the Phase I and Phase III data were focused on differences for individual shots. To find differences, orientation azimuths were calculated for both surveys, only using data from repeated shots; the orientation azimuth found for Phase I was subtracted from the orientation azimuth found for the corresponding shot in Phase III, and the absolute value taken. Figures 2.7 through 2.9 show orientation azimuth differences for each geophone using window sizes of 50 ms, 100 ms and 200 ms for angle calculations. For comparison, Figure 2.10 shows the orientation azimuth differences found using hodogram analysis, using a window of 100 ms. In all cases, the window began at the first breaks. Line 1 is not included here, as the file was unreadable at the time of the analysis. Results from these figures are summarised in Table 2.5 (all receivers) and Table 2.6 (ignoring receivers 4 and 6); in general, the different window sizes produce comparable results, both numerically and visually. Finally, Table 2.7 catalogues individual receiver's differences calculated with a window of 100 ms; Line 1 has been included for these results.

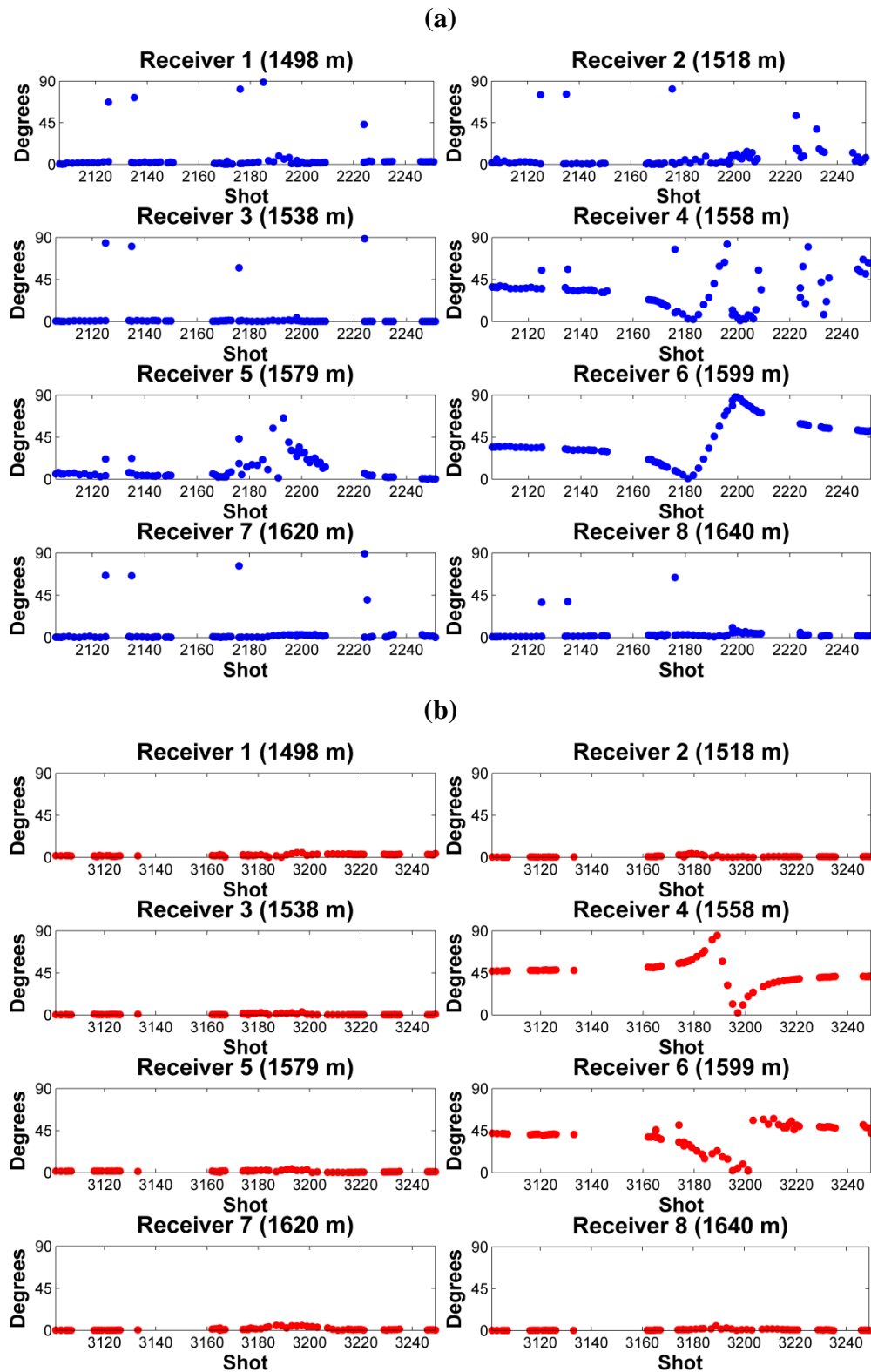


Figure 2.7: Orientation azimuth differences, calculated using a window of 50 ms, for individual geophones for (a) Line 2 and (b) Line 3.

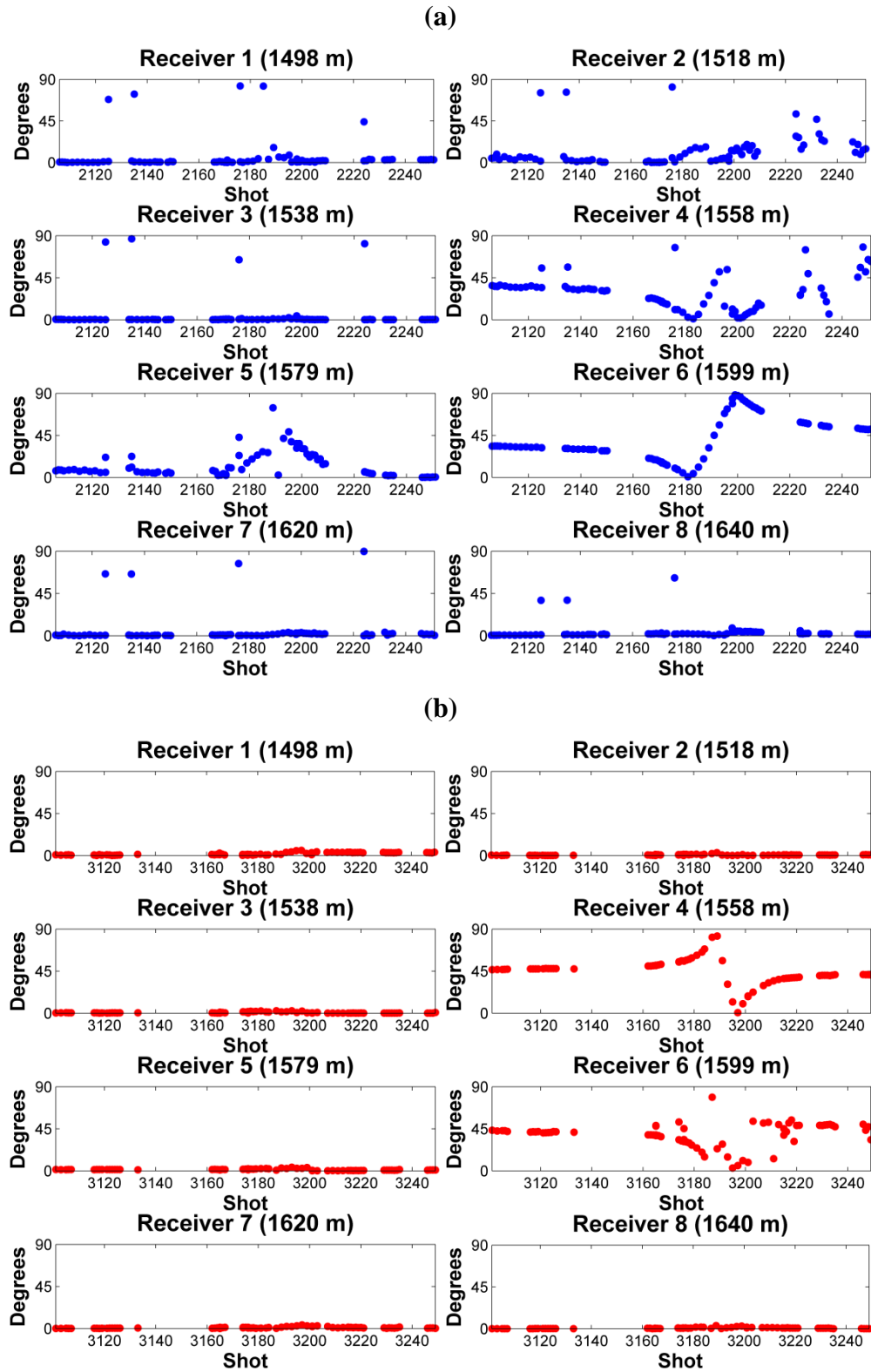


Figure 2.8: Orientation azimuth differences, calculated using a window of 100 ms, for individual geophones for (a) Line 2 and (b) Line 3.

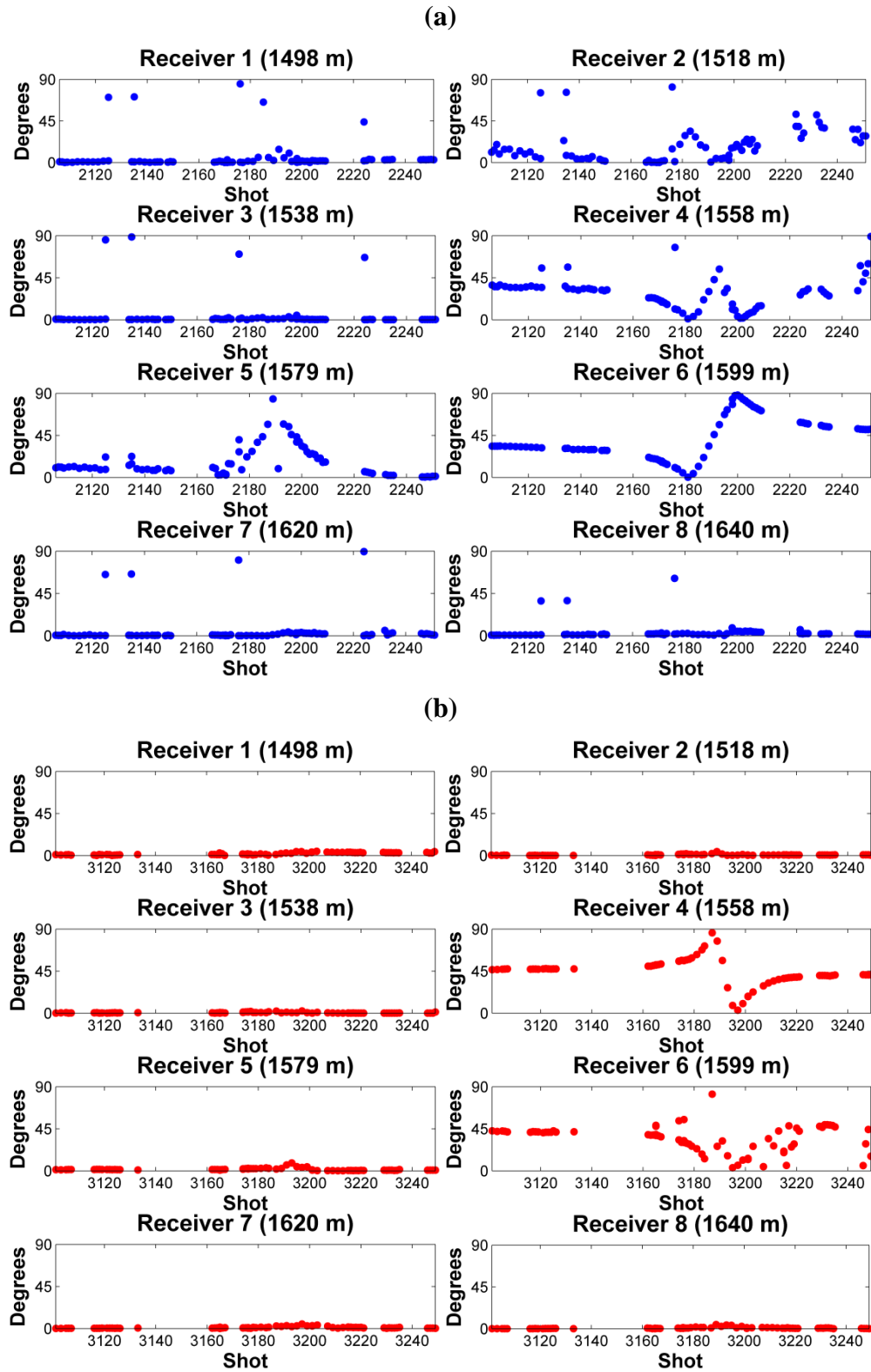


Figure 2.9: Orientation azimuth differences, calculated using a window of 200 ms, for individual geophones for (a) Line 2 and (b) Line 3.

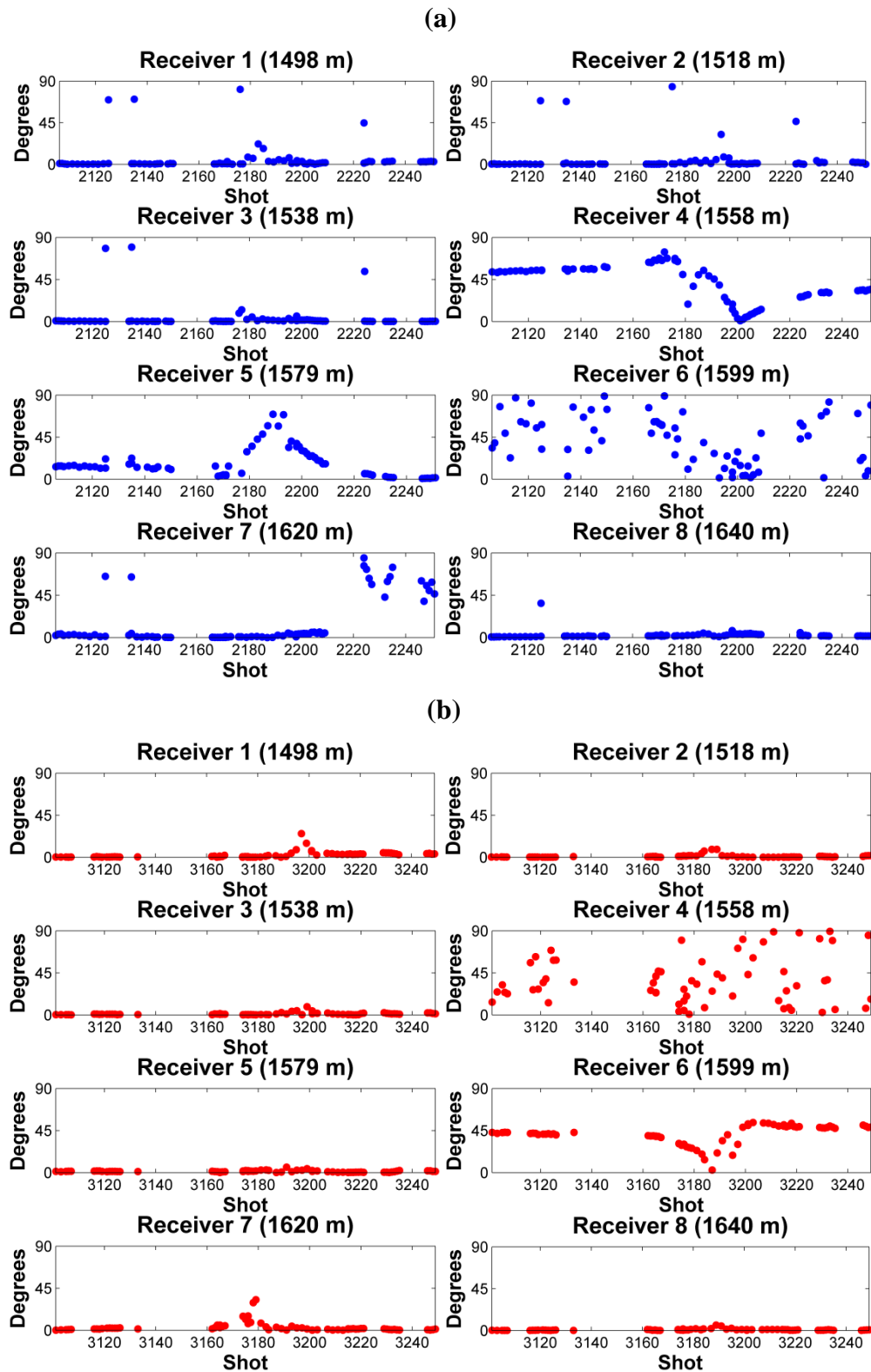


Figure 2.10: Orientation azimuth differences, calculated using hodograms with a window size of 100 ms, for individual geophones for (a) Line 2 and (b) Line 3.

Table 2.5: Percentage of orientation azimuth differences falling within 1, 2, 5 and 10 degrees, using different window sizes for angle calculations.

| Window | Line 2 | | | | Line 3 | | | |
|----------|-----------|-----------|-----------|------------|-----------|-----------|-----------|------------|
| | Within 1° | Within 2° | Within 5° | Within 10° | Within 1° | Within 2° | Within 5° | Within 10° |
| 50 ms | 29.6 % | 40.3 % | 60.9 % | 68.8 % | 48.8 % | 60.0 % | 75.5 % | 76.1 % |
| 100 ms | 27.1 % | 41.1 % | 56.6 % | 65.8 % | 42.7 % | 64.6 % | 75.0 % | 76.1 % |
| 200 ms | 26.6 % | 38.8 % | 54.3 % | 60.9 % | 46.8 % | 62.5 % | 75.2 % | 76.3 % |
| Hodogram | 30.1 % | 43.1 % | 59.2 % | 63.3 % | 41.3 % | 59.8 % | 71.8 % | 75.4 % |

Table 2.6: Percentage of orientation azimuth differences falling within 1, 2, 5 and 10 degrees, using different window sizes for angle calculations. Receivers 4 and 6 were not included.

| Window | Line 2 | | | | Line 3 | | | |
|----------|-----------|-----------|-----------|------------|-----------|-----------|-----------|------------|
| | Within 1° | Within 2° | Within 5° | Within 10° | Within 1° | Within 2° | Within 5° | Within 10° |
| 50 ms | 39.3 % | 53.3 % | 78.9 % | 87.1 % | 64.8 % | 79.8 % | 99.5 % | 100.0 % |
| 100 ms | 36.0 % | 54.2 % | 73.9 % | 83.3 % | 56.9 % | 86.0 % | 99.5 % | 100.0 % |
| 200 ms | 35.3 % | 50.9 % | 70.4 % | 77.9 % | 62.4 % | 83.3 % | 99.5 % | 100.0 % |
| Hodogram | 39.9 % | 56.4 % | 76.1 % | 80.0 % | 54.8 % | 79.5 % | 94.5 % | 97.9 % |

Table 2.7: Percentage of angle differences falling within 1, 2, and 5 degrees, for all 3 lines, calculated using a 100 ms window. Receivers 4 and 6 have been omitted.

| Receiver | Line 1 | | | Line 2 | | | Line 3 | | |
|----------------|----------------|----------------|----------------|----------------|----------------|----------------|----------------|----------------|----------------|
| | Within 1° | Within 2° | Within 5° | Within 1° | Within 2° | Within 5° | Within 1° | Within 2° | Within 5° |
| 1 | 41.5 % | 90.8 % | 96.9 % | 25.0 % | 61.8 % | 88.2 % | 8.6 % | 55.7 % | 97.1 % |
| 2 | 16.9 % | 33.8 % | 70.8 % | 27.6 % | 26.3 % | 42.1 % | 77.1 % | 97.1 % | 100.0 % |
| 3 | 93.8 % | 93.8 % | 96.9 % | 81.6 % | 92.1 % | 94.7 % | 80.0 % | 92.9 % | 100.0 % |
| 5 | 4.6 % | 9.2 % | 27.7 % | 7.9 % | 10.5 % | 30.3 % | 41.4 % | 85.7 % | 100.0 % |
| 7 | 43.1 % | 83.1 % | 92.3 % | 57.9 % | 75.0 % | 94.7 % | 61.4 % | 88.6 % | 100.0 % |
| 8 | 26.2 % | 70.8 % | 96.9 % | 15.8 % | 59.2 % | 93.4 % | 72.9 % | 95.7 % | 100.0 % |
| Average | 37.68 % | 63.58 % | 80.25 % | 35.97 % | 54.15 % | 73.90 % | 56.90 % | 85.95 % | 99.52 % |

The results of the angle differencing are encouraging, especially those for Line 3. Closer analysis reveals that for Line 3, all of the working geophones are reliable; at least 85 % of shots are within 5° between Phase I and Phase III. This is only the case for 5 of the geophones in Line 1, and 4 of the geophones in Line 2. The most consistent receiver appears to be Receiver 3, with more than 80 % of shots being within 1° for all three lines.

2.3.2.2 Consistency within Surveys

Using the x and y-coordinates of each shotpoint, and using the x and y-coordinates of the well, source-receiver azimuths (θ_s) were calculated; for this analysis, only a window of 100 ms, beginning at the first break, was considered. In order to judge the consistency of each survey, the calculated geophone rotation angles were also converted into azimuths; Figure 2.11 shows histograms of these results. Except for receivers 4 and 6, the mean geophone azimuths were generally within about $\pm 2^\circ$. When only the farther offsets, greater than 500 m, are examined (Figure 2.12) the dispersion decreases dramatically; this is an expected result, as farther offsets should contain more horizontal energy by propagating P-wave. Interestingly, while the standard deviations of the far offset angles are much lower than for all offsets, the mean values remain close to the mean values of the complete datasets (Table 2.8), given that all 3 lines (and thus the complete range of source azimuths) were analysed. Note that the choice of 500 m corresponds to approximately 1/3 of the receiver depths; it is possible to choose this value based on a desired standard deviation, but for the purposes of this study it was chosen qualitatively.

Table 2.8: Means and standard deviations of geophone orientation azimuths for Phase I and Phase III, using all data and offsets only greater than 500 m.

| | Phase I | | | | Phase III | | | |
|----------------|----------|-------|------------------------|-------------|-----------|-------|------------------------|-------------|
| | Mean (°) | | Standard Deviation (°) | | Mean (°) | | Standard Deviation (°) | |
| Offsets | All | Far | All | Far | All | Far | All | Far |
| Receiver | | | | | | | | |
| 1 | 133.7 | 133.8 | 3.72 | 1.46 | 134.5 | 134.3 | 4.78 | 2.81 |
| 2 | 246.7 | 246.8 | 2.13 | 1.32 | 245.4 | 244.9 | 8.17 | 8.44 |
| 3 | 143.7 | 143.7 | 1.48 | 0.66 | 143.9 | 143.7 | 1.73 | 0.72 |
| 4 | 134.4 | 134.2 | 4.06 | 1.81 | 126.2 | 117.5 | 59.50 | 67.64 |
| 5 | 258.3 | 258.0 | 3.09 | 1.72 | 259.7 | 258.5 | 13.66 | 11.62 |
| 6 | 315.7 | 315.6 | 2.75 | 2.33 | 305.6 | 299.0 | 47.96 | 44.16 |
| 7 | 191.3 | 191.0 | 4.57 | 3.07 | 190.7 | 190.4 | 4.07 | 2.89 |
| 8 | 90.9 | 90.6 | 3.91 | 2.16 | 91.0 | 90.6 | 3.89 | 2.28 |
| Average | | | 3.21 | 1.82 | | | 6.05 | 4.80 |

The increased reliability of the far offset data can be seen clearly when the geophone azimuths are plotted against the source-receiver offset (Figures 2.13 and 2.14). Note that for source locations nearer to the well, the data have much more scatter than for those beyond about 500 m; ignoring them results in standard deviations being reduced by as much as 50 %. Another interesting trend that can be seen is that geophone depth generally correlates to the offset required for consistent angle measurement. For example, geophones 1 and 2 appear to be approaching a stable angle at lesser offsets than geophones 7 and 8. Additionally, the trends exhibited by each line vary slightly from one another; if the geophone azimuths are plotted against the source-receiver azimuth (Figures 2.16 and 2.17), trends are noticeable that are consistent from line to line. Receiver 7 in particular shows a variation in orientation azimuth that appears to be a two-cycle sinusoid when plotted this way. The other receivers also appear to have one-cycle or two-cycle sinusoidal trends; however, these trends are less clearly defined.

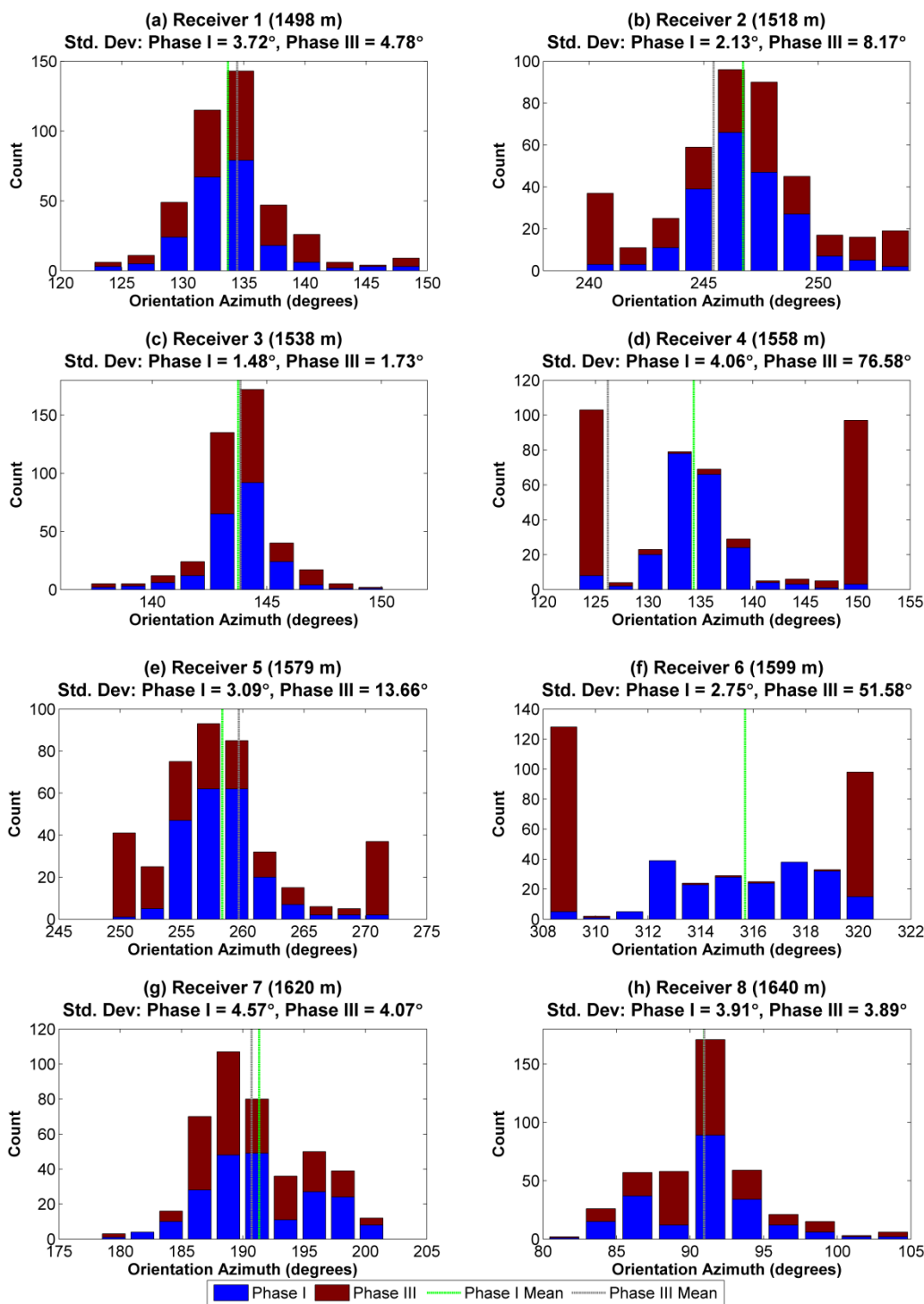


Figure 2.11: Histograms of the calculated geophone azimuths; results include both lines. Phase I is shown in blue and Phase III is shown in red. Bin sizes were based on Phase I calculations. Dashed lines indicate means; Phase I is green and Phase III is gray. Note that the Phase III means for receivers 4 and 6 are significantly different due to the high-amplitude noise on these geophones.

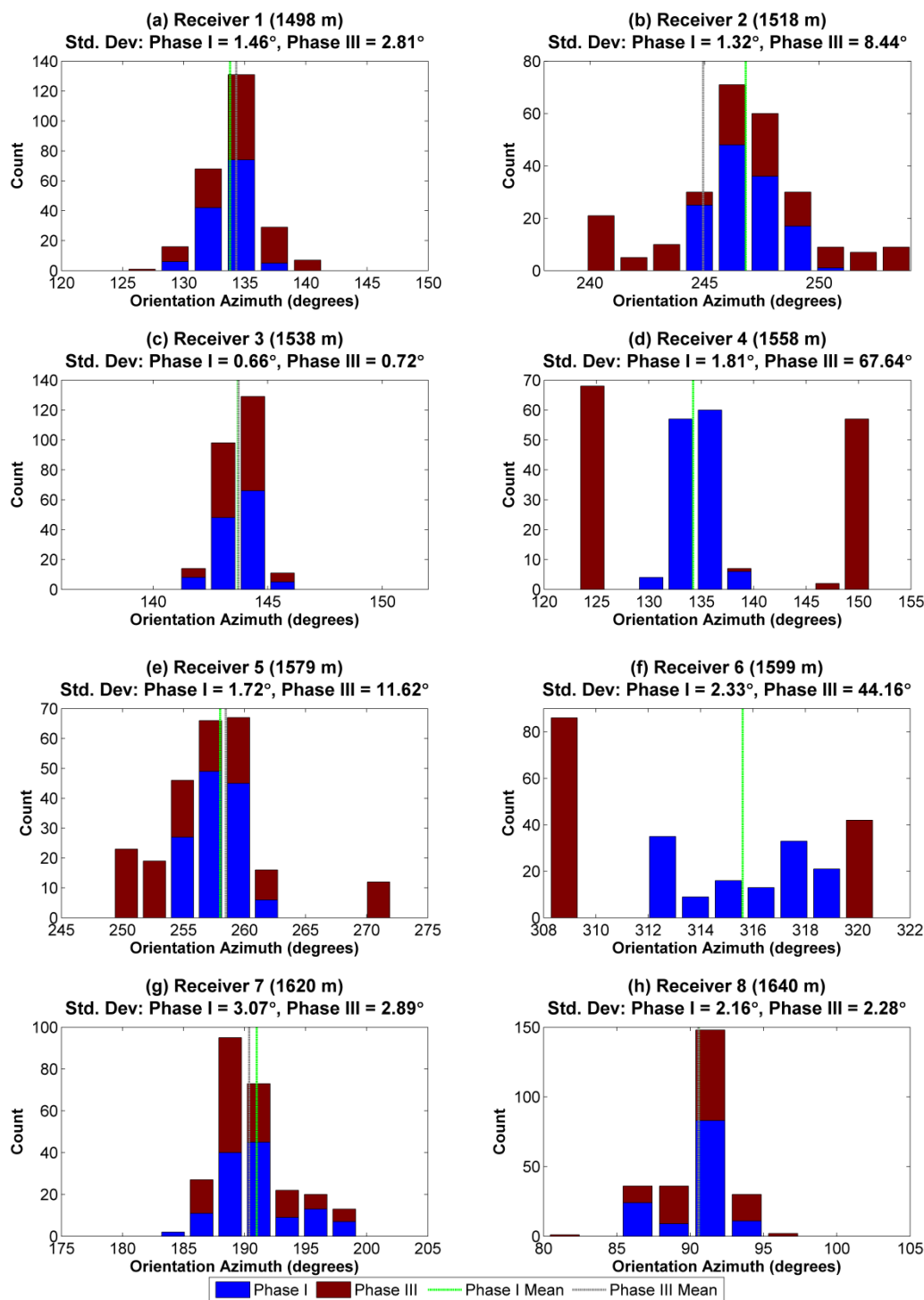


Figure 2.12: Histograms of the calculated geophone azimuths, including only the far offsets (greater than 500 m); results include both lines. Phase I is shown in blue, Phase III is shown in red. Bin sizes were based on Phase I calculations using all offsets. Dashed lines indicate means; Phase I is green and Phase III is gray.

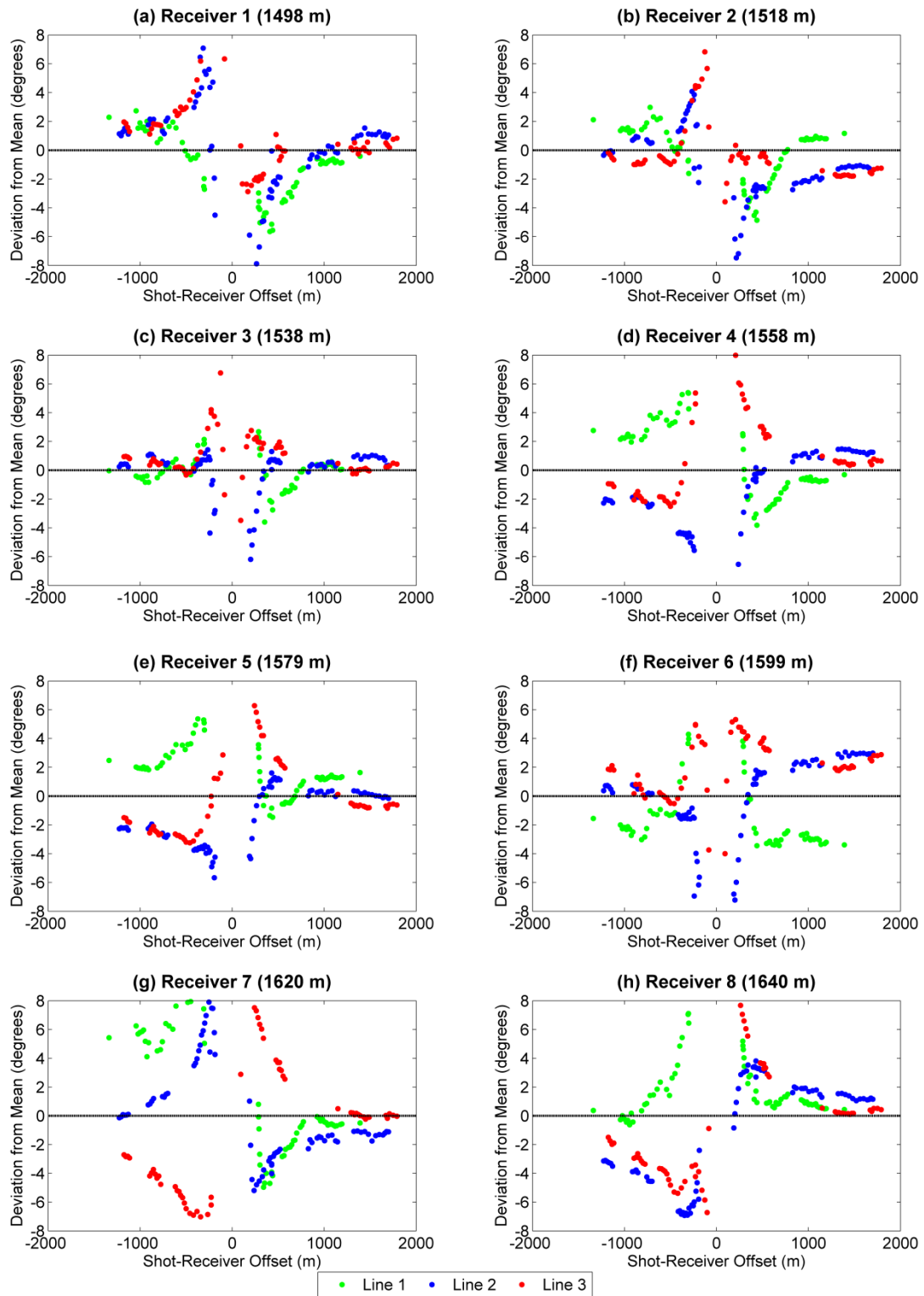


Figure 2.13: Deviation from mean geophone azimuth vs. source-receiver offset for Phase I. Line 1 is in green, Line 2 is in blue and Line 3 is in red. All plots show a window of $\pm 8^\circ$ centered on the mean.

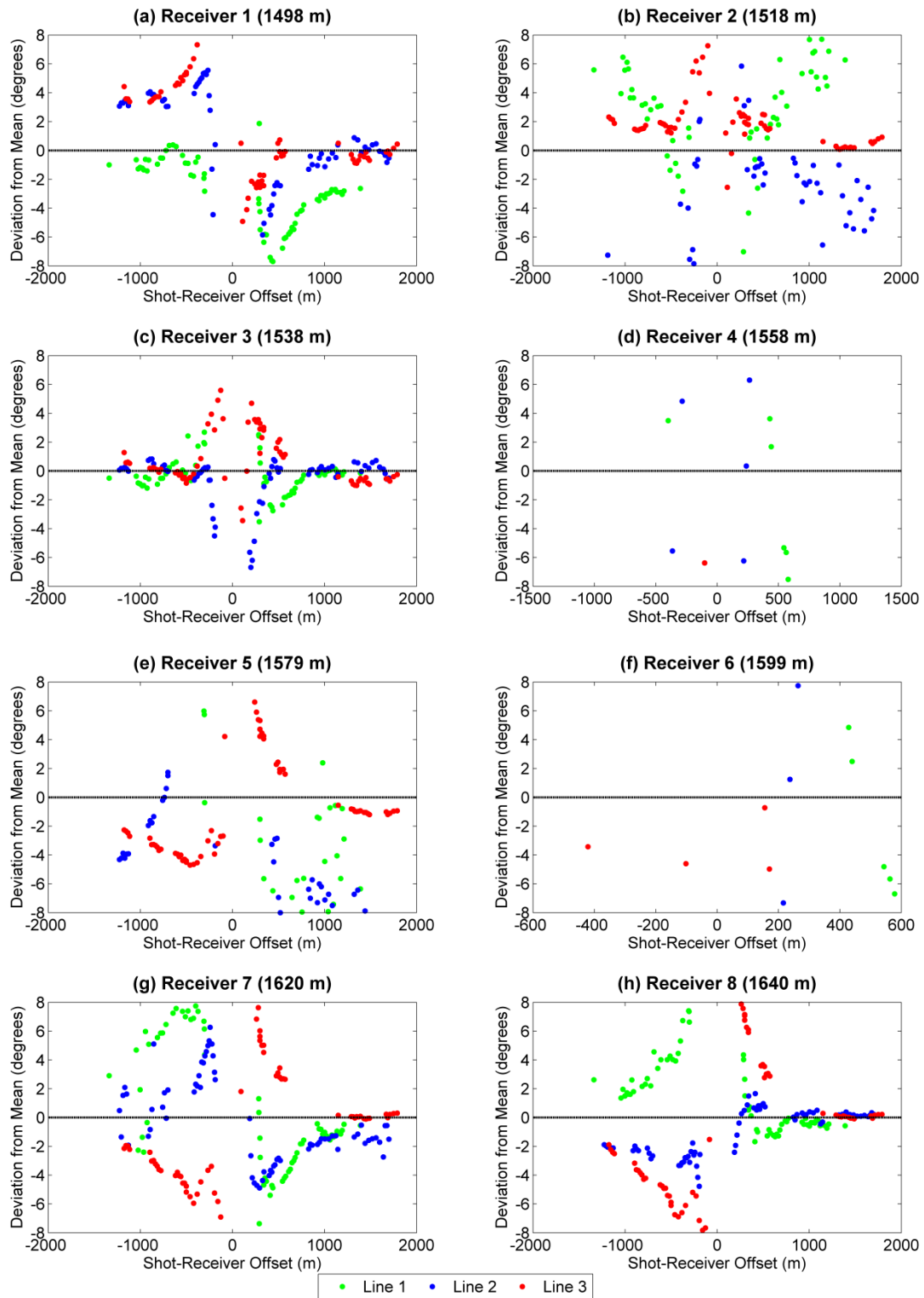


Figure 2.14: Deviation from mean geophone azimuth vs. source-receiver offset for Phase III. Line 1 is in green, Line 2 is in blue and Line 3 is in red. All plots show a window of $\pm 8^\circ$ centered on the mean.

For Phase I, results were consistent overall within each line; for Phase III, however, some problems are evident. The high-level noise on Receivers 4 and 6 causes the angle analysis to become meaningless, exhibiting essentially only the trends of the source-well azimuth; in addition, data from Lines 1 and 2 have extra scatter compared to Line 3, especially for Receivers 2 and 5. After some investigation, this large discrepancy of the results from Line 3 appears to be a result of pre-filtering of the Phase III data. Figure 2.15 shows the Phase III average frequency spectra for all three lines; Line 3 is clearly set apart from Lines 1 and 2, and has likely had a bandpass filter and a notch filter applied. Unfortunately, the supplementary data files did not suggest that these filters had already been applied, nor was I provided with the unfiltered Phase III Line 3 data.

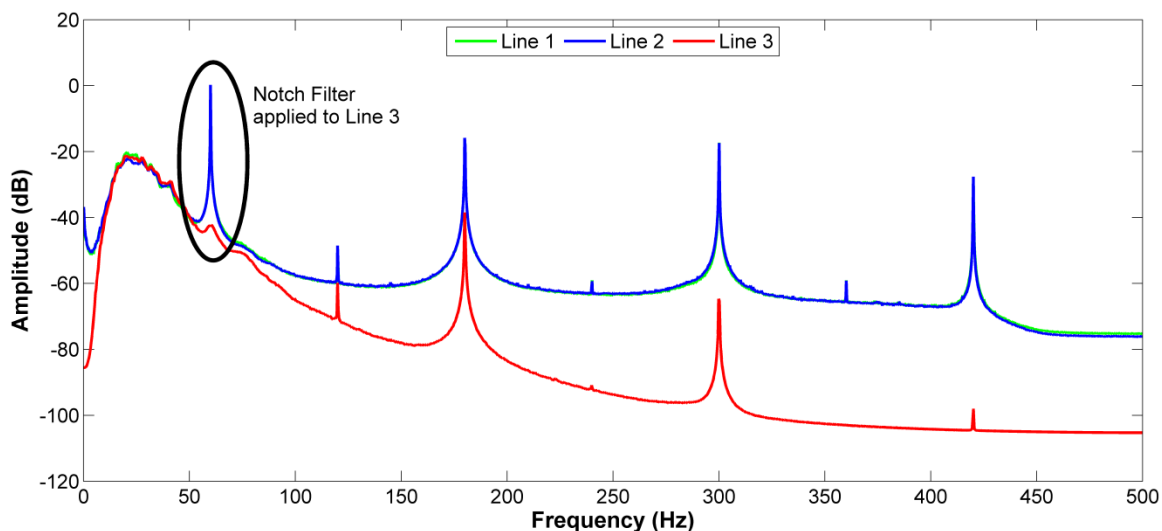


Figure 2.15: Phase III average frequency spectra for raw Line 1 (green) Line 2 (blue) and Line 3 (red) traces, measured in dB down from the maximum amplitude of Line 1.

As a final comparison, Figure 2.18 shows spider plots for Phase I and Phase III orientation angles; this provides a visual method for comparing the final orientation angles and the scatter between the two surveys; the increased scatter in Phase III compared to Phase I is especially apparent in these plots. Additionally, it is easy to compare scatter between receivers using this type of plot; for example, the superior consistency of Receiver 3 results is more easily interpreted using this display.

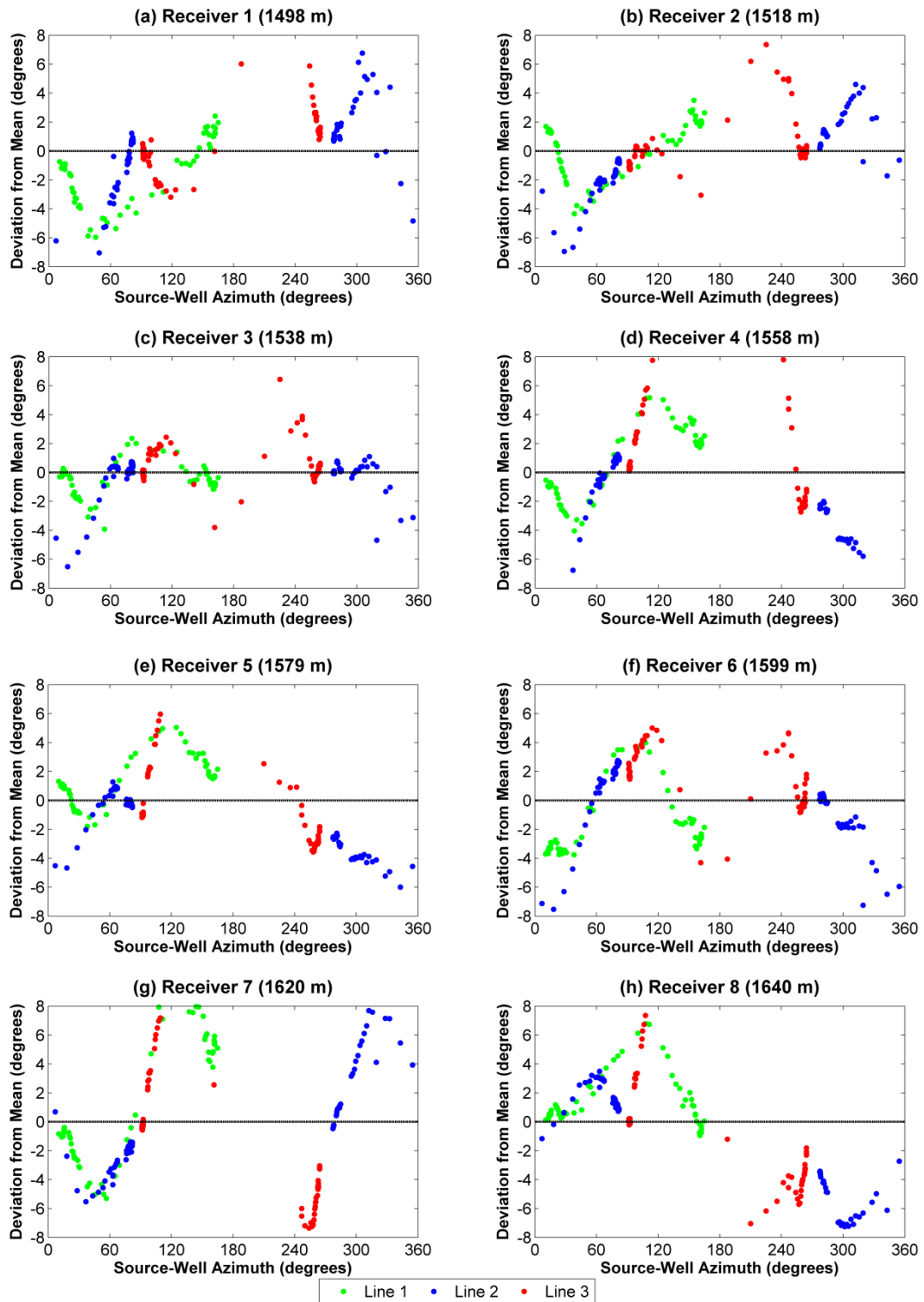


Figure 2.16: Deviation from mean geophone azimuth vs. source-receiver azimuth for Phase I. Line 1 is in green, Line 2 is in blue and Line 3 is in red. All plots show a window of $\pm 8^\circ$ centered on the mean.

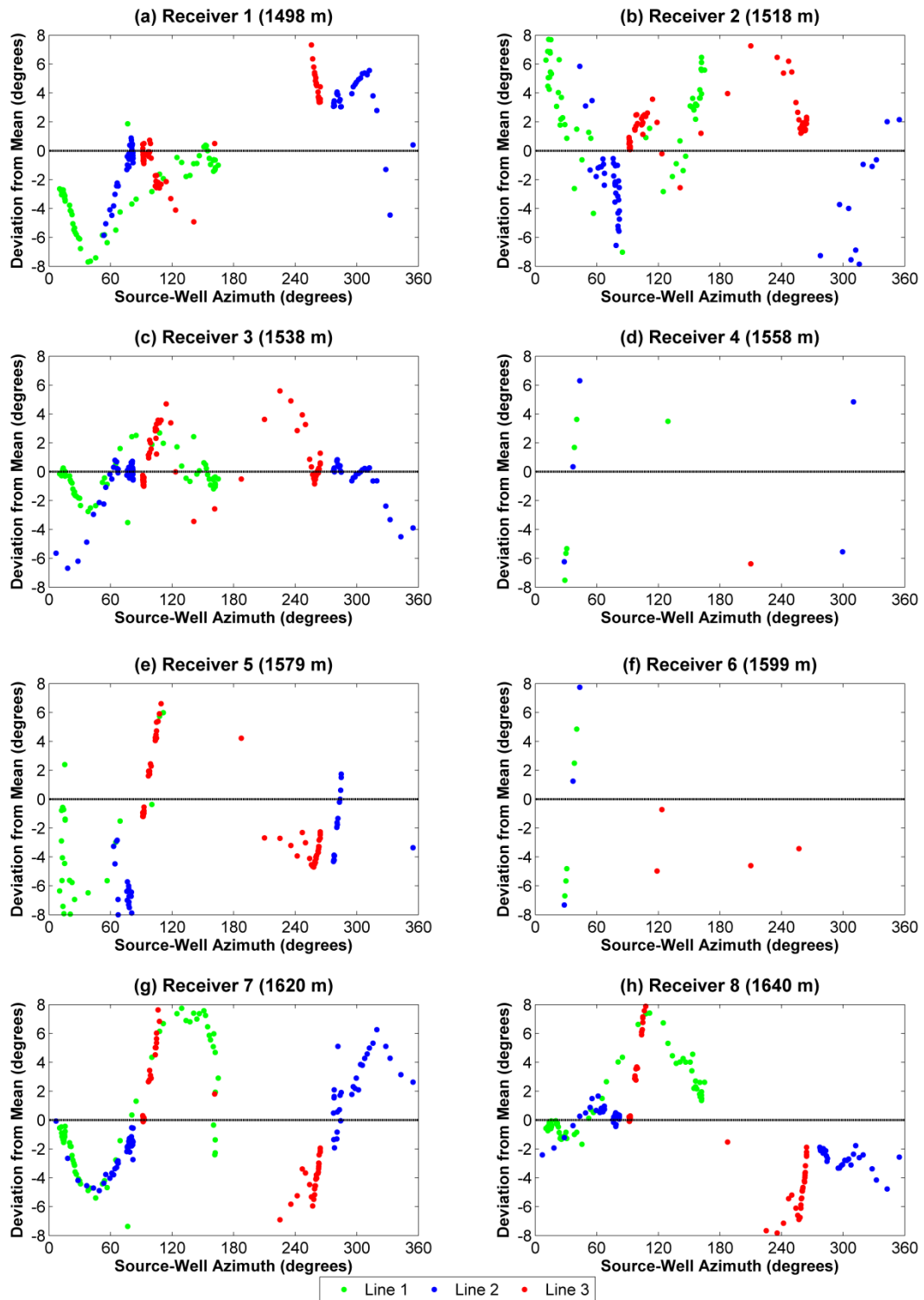


Figure 2.17: Deviation from mean geophone azimuth vs. source-receiver azimuth for Phase III. Line 1 is in green, Line 2 is in blue and Line 3 is in red. All plots show a window of $\pm 8^\circ$ centered on the mean.

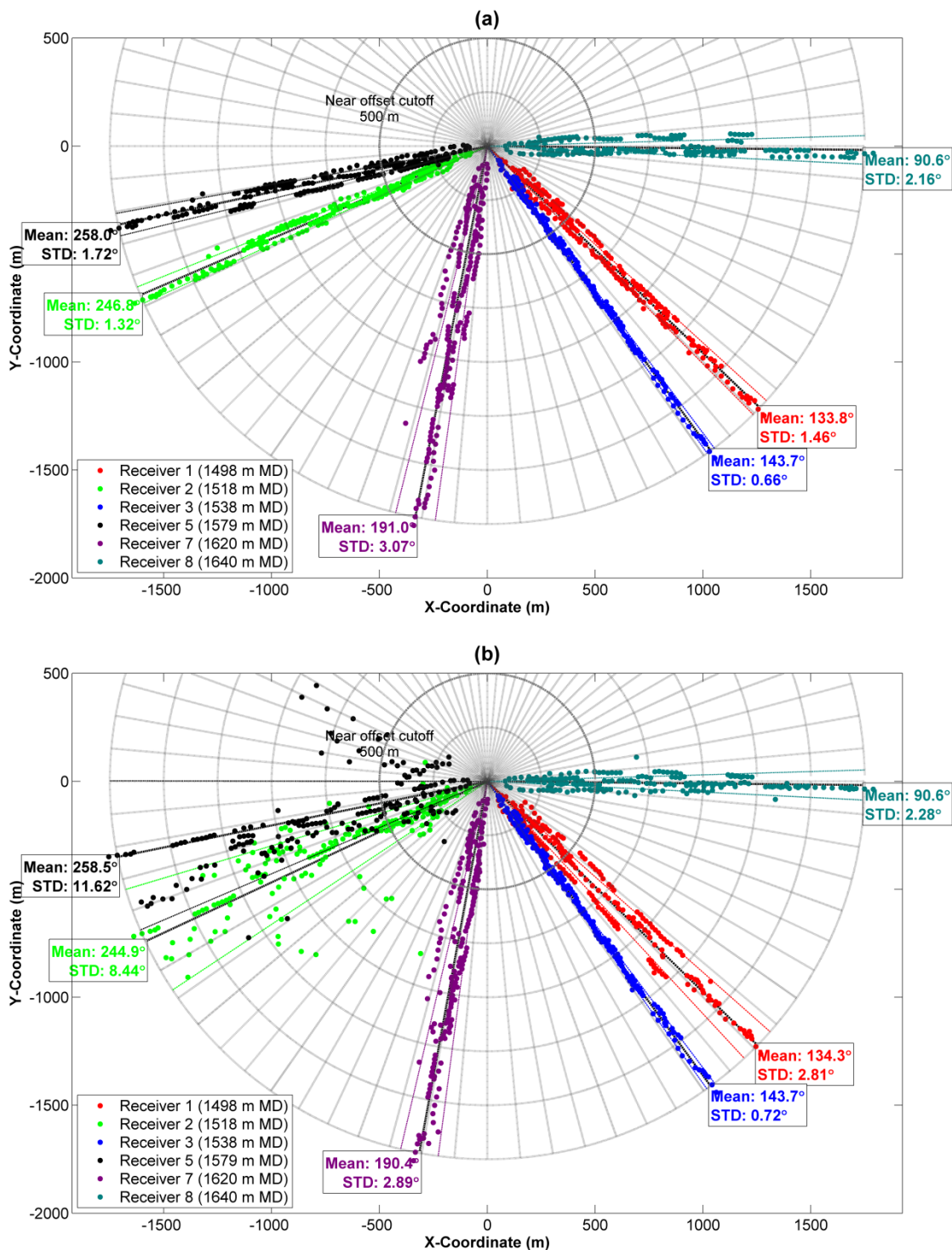


Figure 2.18: Spider plots for (a) Phase I and (b) Phase III orientation angles, using statistics calculated using far offsets. Angular grid spacing is 5° and radial grid spacing is 250 m. Receivers 4 and 6 have been omitted.

2.4 Controlled Experiment

2.4.1 Experiment Parameters

In order to test the separate effects of time-shift, amplitude difference and noise, a corresponding trace was chosen from the baseline and monitor surveys (Figure 2.19). A copy of the baseline trace was then perturbed in several ways:

- 1) The trace was time-shifted by values ranging from -5 ms to +5 ms, incrementing by 0.1 ms with and without resampling of the initial trace. The time-shift was done by phase shifting in the frequency domain, allowing for a 0.1 ms shift even when using a 1 ms sample rate.
- 2) The trace was multiplied by constants ranging from 0.5 to 1.5, incrementing by 0.01.
- 3) Noise, which was extracted from the first 500 ms of both the baseline and monitor traces, was multiplied by ratios of the maximum noise to maximum signal of the baseline trace, ranging from 0 to 0.5 in increments of 0.02. Noise taken from the baseline trace will be referred to as “Noise A”, and noise taken from the monitor trace will be referred to as “Noise B” (Figure 2.20).

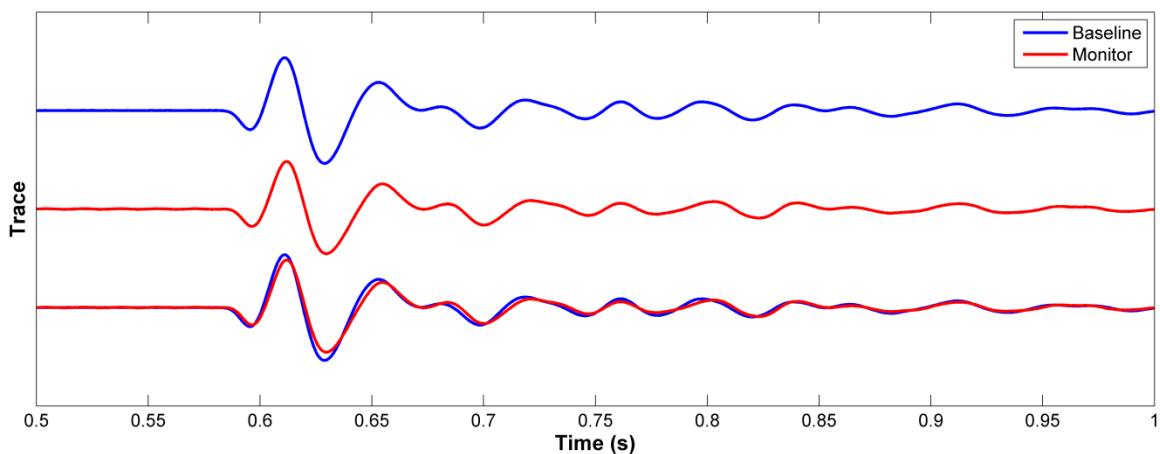


Figure 2.19: Traces used for controlled repeatability experiment; baseline is shown in blue and monitor is shown in red.

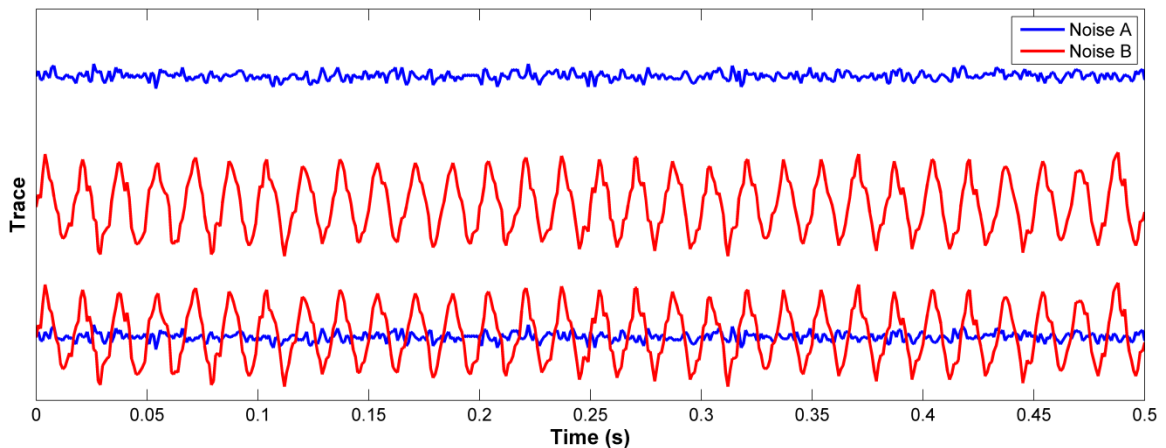


Figure 2.20: Noise used for controlled repeatability experiment; Noise A (from baseline) is shown in blue and Noise B (from monitor) is shown in red.

Finally, it should be noted that the NRMS, PRED and \log_{10} SDR values calculated between the original baseline and monitor traces were 24.9%, 0.96 and 1.49 respectively.

2.4.2 Time-Shift Tests

Figure 2.21 shows the results of the time-shift tests. First, it should be noted that the sample rate (relative to the time-shift) has a subtle effect on NRMS and PRED, and a much more noticeable effect on SDR. However, even at a 1 ms sample rate, the SDR value remains consistently above 10^4 – this suggests time-shift does not have a largely detrimental effect on this metric, which could be inferred from Equation 1.3. NRMS appears to have a linear dependence on time-shift; the result of a linear regression on these values produces a slope of approximately 15%/ms. PRED seems to have a hyperbolic trend, only changing by about 0.03 with a 1 ms time-shift. All three metrics appear to be generally symmetric between positive and negative time-shift values.

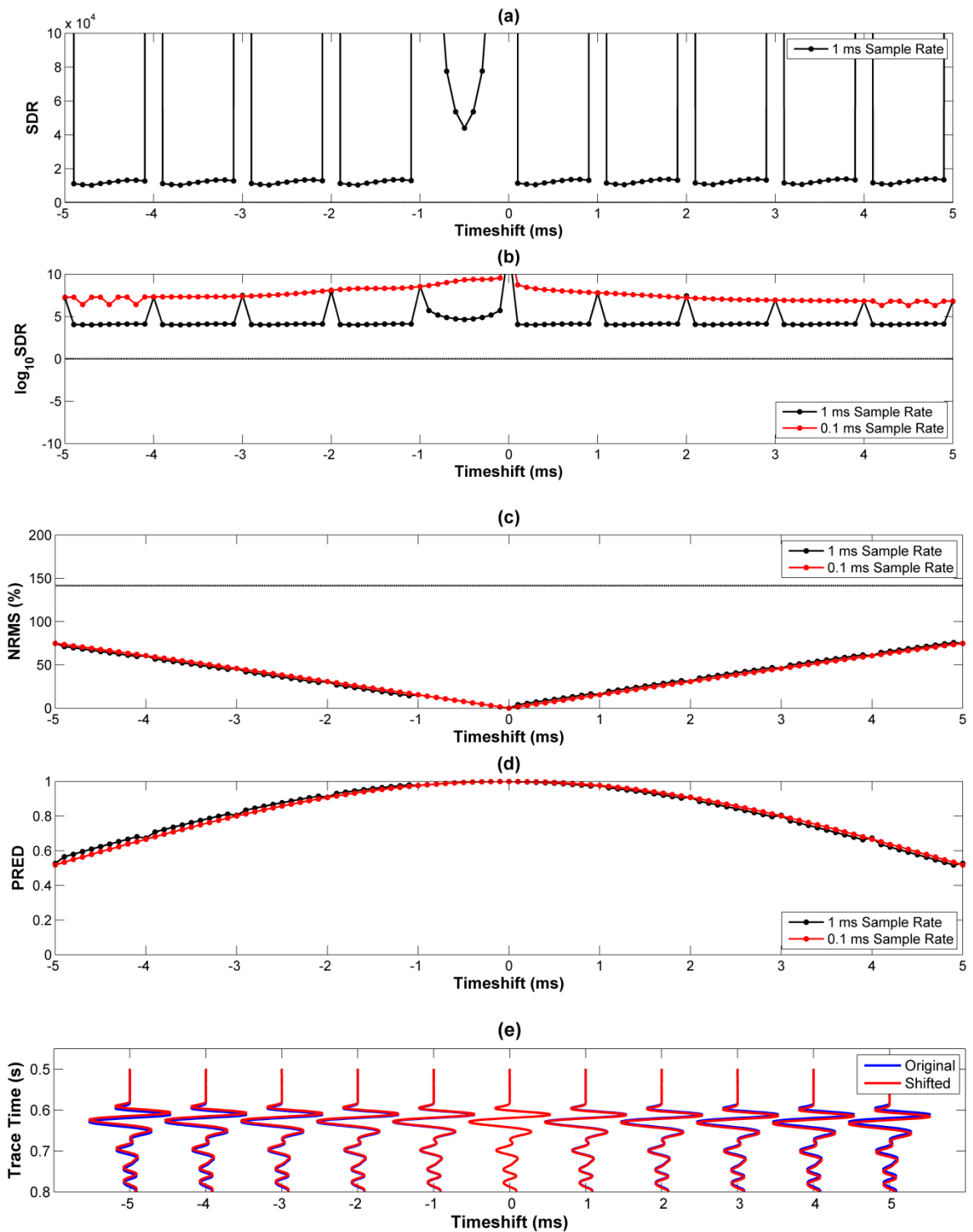


Figure 2.21: SDR (a), \log_{10} SDR (b), NRMS repeatability (c) and predictability (d) for time-shift experiment, showing traces left at the original sample rate (black) and traces resampled to 0.1 ms (red). Bottommost panel (e) is a wiggle display of the time-shifted traces (red) overlapping the original trace (blue).

2.4.3 Amplitude Tests

The results of the amplitude tests are shown in Figure 2.22. Again, the NRMS values appear to have a linear relationship to the amplitude ratio, although the graph is no longer symmetric; for example, the NRMS becomes 9.5% when the ratio of monitor to baseline amplitude is 1.1, and 10.5% when the ratio is 0.9. With the same amplitude ratios, the SDR becomes $10^{1.95}$ and $10^{2.04}$ respectively. Finally, PRED remains unchanged regardless of the amplitude ratio. The behaviour of all three of these metrics in the presence of an amplitude perturbation can be found analytically, if m is replaced with Ab , where A is a scalar; after performing this substitution in Equations 1.1 – 1.3 and simplifying, we find that

$$\begin{aligned}
 NRMS(A) &= \frac{2\sqrt{\sum_{t_1}^{t_2}(b_t - m_t)^2/N}}{\sqrt{\sum_{t_1}^{t_2}(b_t)^2/N} + \sqrt{\sum_{t_1}^{t_2}(m_t)^2/N}} \\
 &= \frac{2\sqrt{\sum_{t_1}^{t_2}(b_t - Ab_t)^2/N}}{\sqrt{\sum_{t_1}^{t_2}(b_t)^2/N} + \sqrt{\sum_{t_1}^{t_2}(Ab_t)^2/N}} \\
 &= \frac{(2\sqrt{(1-A)^2})\left(\sqrt{\sum_{t_1}^{t_2}(b_t)^2/N}\right)}{(1+\sqrt{A^2})\left(\sqrt{\sum_{t_1}^{t_2}(b_t)^2/N}\right)} = \frac{2|1-A|}{1+|A|},
 \end{aligned} \tag{2.1}$$

$$\begin{aligned}
 PRED(A) &= \frac{(\sum_{-n}^{+n} b \otimes m)^2}{(\sum_{-n}^{+n} b \otimes b)(\sum_{-n}^{+n} m \otimes m)} = \\
 &= \frac{(\sum_{-n}^{+n} b \otimes Ab)^2}{(\sum_{-n}^{+n} b \otimes b)(\sum_{-n}^{+n} Ab \otimes Ab)} \\
 &= \frac{A^2(\sum_{-n}^{+n} b \otimes b)^2}{A * A(\sum_{-n}^{+n} b \otimes b)(\sum_{-n}^{+n} b \otimes b)} = \frac{A^2}{A^2} = 1,
 \end{aligned} \tag{2.2}$$

and

$$\begin{aligned}
 SDR(A) &= \frac{\max(b \otimes m)^2}{1 - \max(b \otimes m)^2} = \frac{\max(b \otimes Ab)^2}{1 - \max(b \otimes Ab)^2} \\
 &= \frac{A^2 \max(b \otimes b)^2}{1 - A^2 \max(b \otimes b)^2} = \frac{A^2}{1 - A^2}.
 \end{aligned} \tag{2.3}$$

Note that Equation 2.3 implies that SDR approaches infinity as A approaches 1. These relationships predict the results seen in Figure 2.22.

2.4.4 Noise Tests

Finally, repeatability after the addition of additive noise is shown in Figure 2.23; the two curves represent two different types of noise: Noise A (black curve) and Noise B (red curve). Noise B, taken from the monitor trace, was dominated by a 60 Hz cable signal, and can be considered as non-random. The x-axis is calculated as the ratio of the maximum amplitudes of the noise added and the signal of the original baseline trace; that is,

$$\text{Amplitude Ratio} = \frac{\max(|A_{noise}|)}{\max(|A_b|)}. \tag{2.4}$$

As a benchmark, we may consider that the Noise B (non-random) curve crosses $SDR=1$ at a value of about 0.15; Figure 2.24 shows a detailed view of the amplitude ratio interval 0-0.15. Interestingly, $\log_{10} SDR$ is very similar for both types of noise added, whereas NRMS and PRED show a clear separation between the two noise curves; PRED is the most sensitive to the type of noise. When the ratio is at 0.1, NRMS, PRED and SDR become 37.3%, 0.92 and $10^{0.81}$ for Noise A (random) and 56.3%, 0.74 and $10^{0.39}$ for Noise B (non-random). These figures are large when considering how this appears visually, as shown in the third trace in the bottom two panels of Figure 2.23.

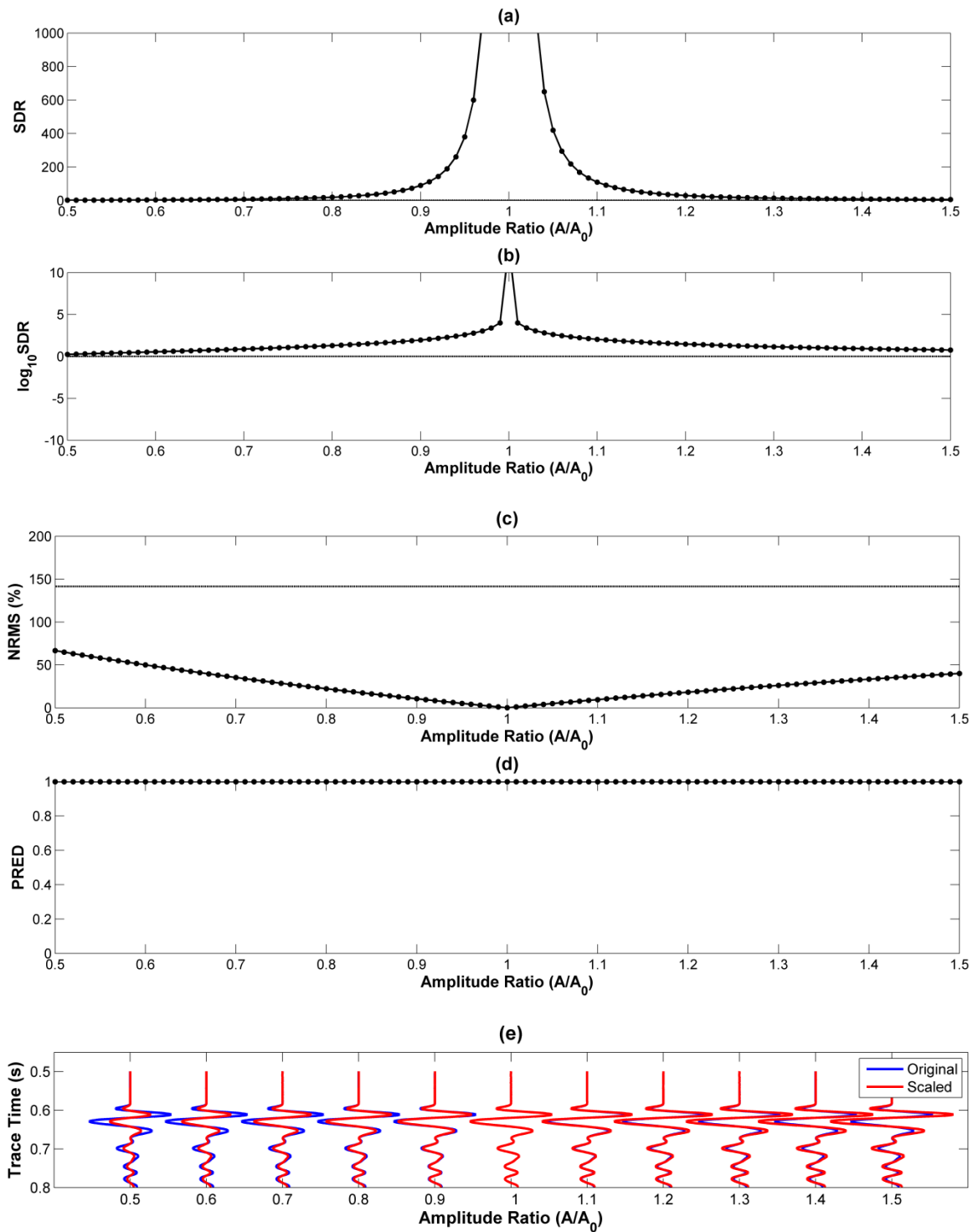


Figure 2.22: SDR (a), \log_{10} SDR (b), NRMS repeatability (c) and predictability (d) for amplitude experiment. Bottommost panel (e) is a wiggle display of the amplitude modified traces (red) overlapping the original trace (blue).

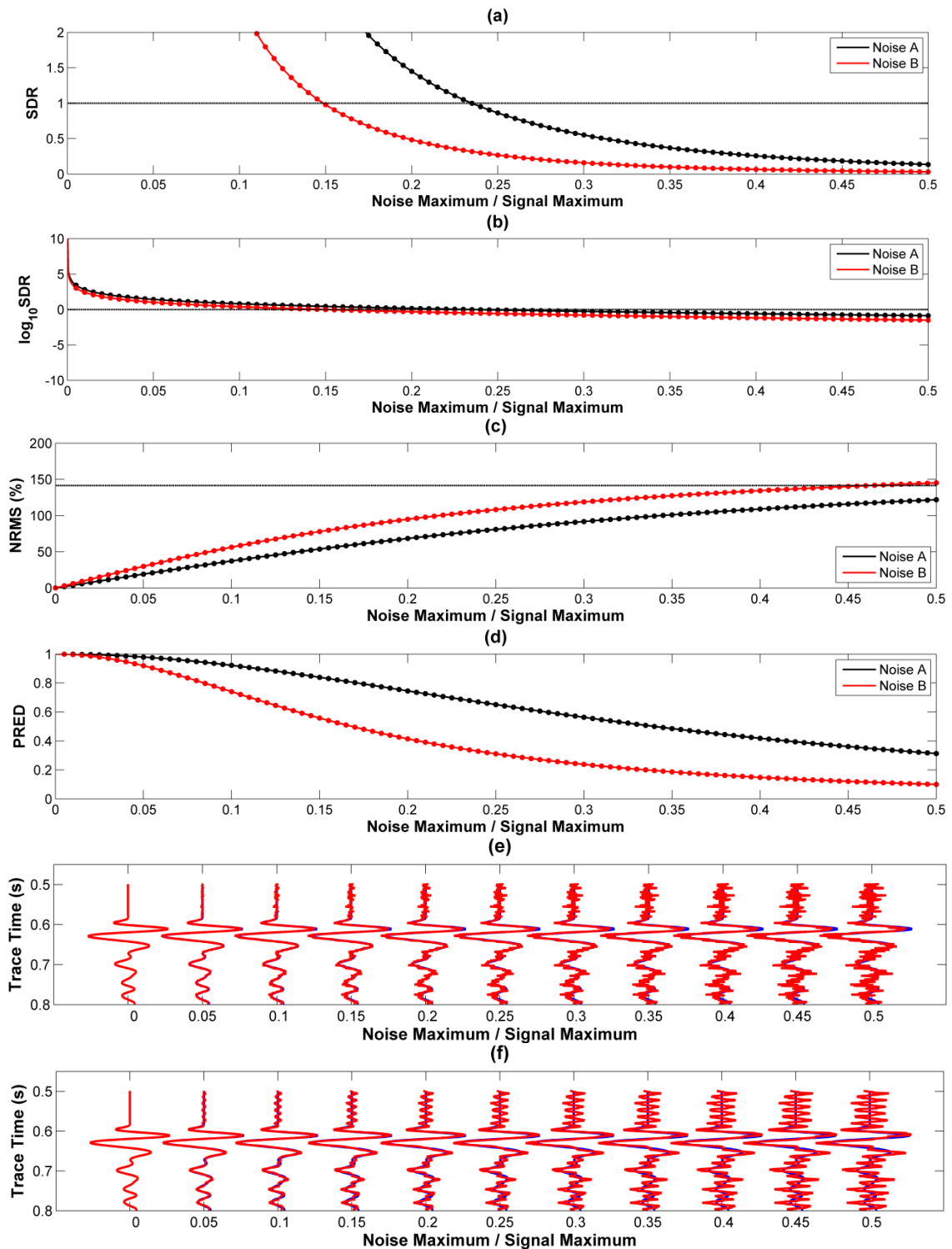


Figure 2.23: SDR (a), \log_{10} SDR (b), NRMS repeatability (c) and predictability (d) for additive noise experiment, showing addition of Noise A (black) and Noise B (red). Two bottommost panels are wiggle displays of Noise A (e) and Noise B (f), showing noisy traces (red) overlapping the original trace (blue).

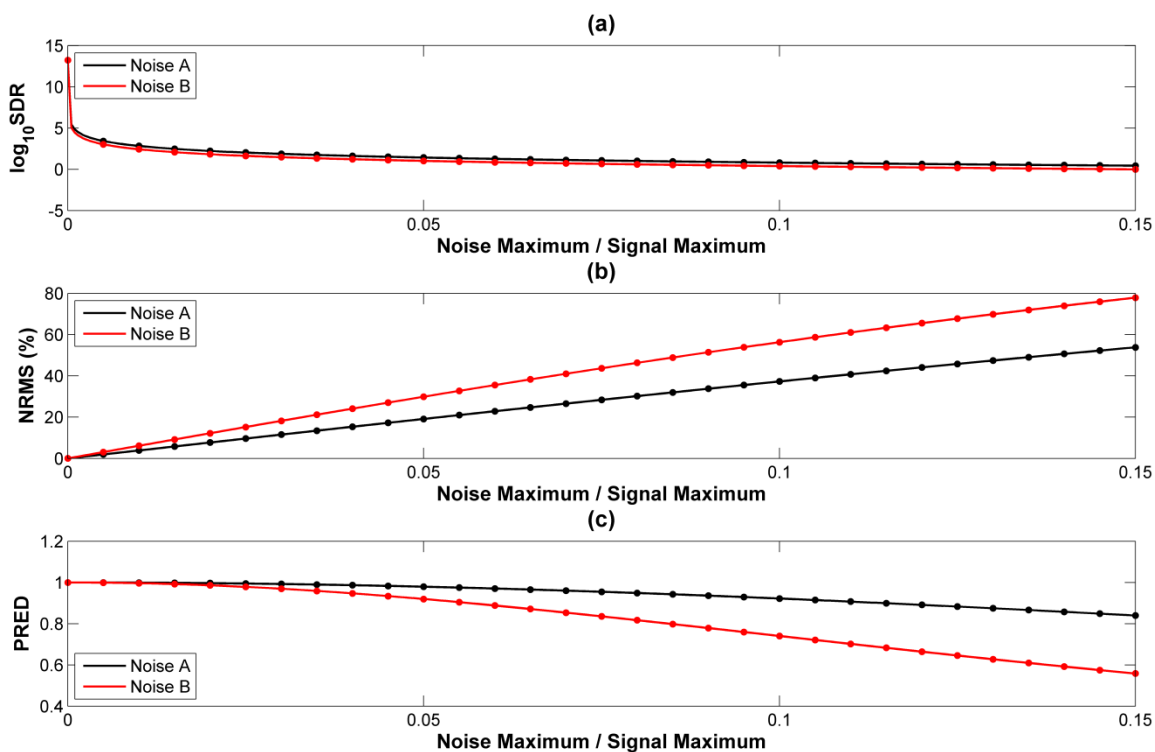


Figure 2.24: \log_{10} SDR (a), NRMS repeatability (b) and predictability (c) for additive noise experiment, detailing the interval between 0 and 0.15.

2.5 Discussion

2.5.1 Repeatability

The results presented in this study show that all three repeatability metrics can be very sensitive to effects of time-shifts, amplitude differences and random noise. Unwanted time-shifts and amplitude differences can, in general, be minimised reasonably well on a trace by trace basis, and noise can be reduced through processes such as stacking and frequency filtering. However, time-shifts and amplitude differences can also arise due to geologic changes in the subsurface. Subtle changes in these two categories will cause large changes in the repeatability calculations; in terms of time-lapse seismic monitoring, this sensitivity will help to interpret meaningful differences between surveys.

Both the controlled and field experiments show that there are differences and similarities in the way NRMS, PRED and SDR behave. NRMS appears to have a linear dependence on time-shifts and amplitude perturbations, and is easily disturbed by

strength and character of noise. PRED is insensitive to amplitude changes and is largely unaffected by small time-shifts, though it too is sensitive to noise strength and character. Noise character seems to have little influence on SDR, however, and it is also insensitive to time-shifts. In amplitude and noise tests, \log_{10} SDR changes rapidly when a slight perturbation is added, but beyond that SDR shows a linear response. Examination of the field experiment shows remarkably similar trends between NRMS and SDR and PRED and SDR. Nevertheless, it can also be seen that the three repeatability metrics do not always show the same trend; for example, the z-component shows that Line 3 has an NRMS value 1.2 % better than Line 2, while PRED is better by 0.04 and SDR is worse by $10^{0.06}$. Perhaps through further examination of these parameters, the different results they provide can be used to interpret the main contributions to 4D noise.

Overall, repeatability of the raw VSP data showed that there were issues related to noise. These problems were partially due to hardware problems with the receivers in Phase III acquisition; these issues resulted in the complete loss of data for three out of twenty-four possible components. Furthermore, strong noise was evident on two more traces that were quiet in Phase I. However, even if these five traces are omitted, it still results in somewhat poor repeatability values for this survey. Studies, such as Cantillo et al. (2010), show that the factor which most strongly affects repeatability metrics is the difference in source positioning; since the geophones were cemented into the well (and therefore receiver positions are constant) it can be inferred that the negative effects on the repeatability metrics are almost completely due to small changes in source positioning, source coupling, and changes in the subsurface. CO₂ injected into the subsurface between Phases I and III is expected to affect repeatability; therefore, repeatability values are not expected to be high even assuming minimal 4D noise.

2.5.2 Orientation Azimuths

The results from the geophone orientation calculations show good agreement between surveys, especially in Line 3. While these results are consistent with the seismic repeatability metrics in the better consistency of Line 3, they do occasionally have opposite trends – this could potentially provide information about meaningful changes in

the subsurface. For example, a shot that has a strong consistency in orientation angle would likely point to a consistent source positioning; if this shot also has poor values from repeatability metrics, it would provide evidence that a meaningful subsurface change is being measured. Additionally, it is possible that preferential changes in the stress field could induce seismic anisotropy, which could then result in differences in orientation measurements between surveys.

The relationship between orientation azimuth scatter, offset and receiver depth could have important implications regarding ideal acquisition geometry in the case of 3-component VSP surveys; these relationships will be studied more closely in Chapter 3. This study suggests that orientation analysis using nearer source-well offsets will result in higher scatter. However, there also appeared to be some error associated with source-well azimuth; these errors are likely to be related to geologic parameters, and will be studied further in this thesis. Finally, the results in this study did not clearly favour a particular window size for use in geophone azimuth calculations; this is a parameter that will most likely be primarily based on the dominant period of the wavelet. For the purposes of this thesis a window size of 100 ms is recommended.

2.6 Summary

- Residual time-shift between a noise-free baseline and monitor trace will cause NRMS to change almost linearly by 15 %/ms; the effect is much more subtle on PRED, only changing it by about 3 % for 1 ms difference. Time-shift has no effect on SDR, which is intended from its definition.
- Analytic relationships were found for the effects of amplitude perturbations between a noise-free baseline and monitor trace on NRMS, PRED and SDR; PRED remained unaffected by amplitude changes.
- When additive noise was introduced to the monitor trace, \log_{10} SDR showed results that were very similar for both Noise A (random) and Noise B (non-

random); while there was a large drop in its value when a slight amount of noise was added, further addition of noise resulted in a linear response with a gentle slope. NRMS and PRED produced curves that were easily distinguishable between the types of noise added. NRMS appeared to have a linear response while the noise strength was low; PRED changed little with low noise strength, and was more sensitive to the type of noise added.

- Repeatability analysis of the Violet Grove horizontal component data yielded NRMS values of 60.6 %, 61.4 % and 45.2 %, PRED values of 0.73, 0.72 and 0.83, and SDR values of $10^{0.38}$, $10^{0.29}$ and $10^{0.70}$ for Lines 1, 2 and 3 respectively.
- Repeatability analysis of the Violet Grove vertical component data yielded NRMS values of 46.3 %, 42.6 % and 41.4 %, PRED values of 0.82, 0.83 and 0.87, and SDR values of $10^{0.74}$, $10^{0.85}$ and $10^{0.79}$ for Lines 1, 2 and 3 respectively.
- While at a high level all three of these metrics produced similar trends in the field data example, they appear to behave differently depending on the type of 4D noise, and should thus be used together to better understand the repeatability of time-lapse seismic.
- Within surveys, angle calculations using source-well offsets greater than 500 m were shown to be much more consistent than those using near offsets. However, when the full range of source locations were considered, the mean values calculated for geophone azimuths did not significantly change when the near offsets were excluded.
- Standard deviations of geophone orientation azimuth over all working receivers were 3.21° for Phase I and 6.05° for Phase III. When offsets smaller than 500 m were rejected, these values improved to 1.82° and 4.80° .

- Plotting deviation of geophone orientation azimuth against source-well azimuth revealed a clear two-cycle sinusoidal trend in Receiver 7; additionally, other receivers showed less defined one-cycle and two-cycle sinusoidal trends. This points to systematic errors, which could be associated with azimuthally variant geologic parameters.
- Repeatability in orientation analysis, ignoring receivers 4 and 6, showed that 63.6 % of Line 1 shots, 54.2 % of Line 2 shots and 85.9 % of Line 3 shots were within 2° between surveys, and that the mean azimuth values generally had less than a 1° difference.
- Line 3 traces from Phase III were pre-filtered, likely using bandpass and notch filters. This provides a reason for the discrepancy of Line 3's repeatability results when compared to those of Lines 1 and 2.

Chapter Three: Effects of Random Noise on Orientation Analysis

3.1 Introduction

In this chapter I model the effects of random noise on geophone orientation analysis. This was done using both angle calculation methods, and the results are compared to each other in order to choose the optimal method to use for the real data examples in this thesis. The interplay of noise with source-well offset and geophone depth was also studied, in order to provide recommendations regarding survey design. The results presented in this chapter begin to characterise the dependence of scatter in orientation azimuth on source-well offset, which was seen in the case study shown in Chapter 2.

3.2 Finite Difference Modelling

In order to study the effects of random noise on geophone orientation analysis, a simple 6 layer geological model was built in TIGER; acquisition parameters are shown in Table 3.1; geologic parameters are listed in Table 3.2, and a visual representation is shown in Figure 3.1. The surface geometry consisted of a single 2D shot line running east-west, 100 m south of the well location; this offset was introduced so that there is some P-wave first arrival energy on both horizontal components of the receivers. A plan view is shown in Figure 3.2. While specification of anisotropic parameters and Q values are supported by TIGER (Hokstad et al., 2009), this work focussed on a vertical well drilled into isotropic, horizontally stratified sedimentary layers, overlain by water. Rock properties were chosen based on the default model given by TIGER. All receivers recorded 3-component data; due to limitations of the program, receiver components were all forced to be aligned perfectly with model coordinates. Finally, as an example of the modelled seismic data, Figure 3.3 shows an unprocessed common shot gather of the x-component data.

Table 3.1: Numerical parameters used for acquisition.

| TIGER Acquisition Parameters | |
|-------------------------------------|---------------------------|
| Maximum x | 3000 m |
| Maximum y | 3000 m |
| Maximum z | 2500 m |
| x interval | 10 m |
| y interval | 10 m |
| z interval | 10 m |
| Recording time | 1400 ms |
| Sample rate | 1 ms |
| Source wavelet | First Derivative Gaussian |
| Number of sources | 20 |
| Source interval | 149 m |
| Number of receivers | 64 |
| Receiver interval | 15 m |
| Receiver depth range | 800-1745 m |

Table 3.2: Numerical parameters used to create the geological model.

| Layer | Depth to top (m) | Density (kg/m³) | P-velocity (m/s) | S-velocity (m/s) | V_P/V_S |
|--------------|-----------------------------|---------------------------------------|-----------------------------|-----------------------------|------------------------------------|
| 1 | 0 | 1000 | 1480 | 0 | N/A |
| 2 | 250 | 2000 | 2000 | 1200 | 1.67 |
| 3 | 650 | 1500 | 2500 | 1500 | 1.67 |
| 4 | 950 | 2500 | 3000 | 2000 | 1.67 |
| 5 | 1450 | 2600 | 3200 | 2100 | 1.52 |
| 6 | 2000 | 2600 | 3500 | 2200 | 1.59 |

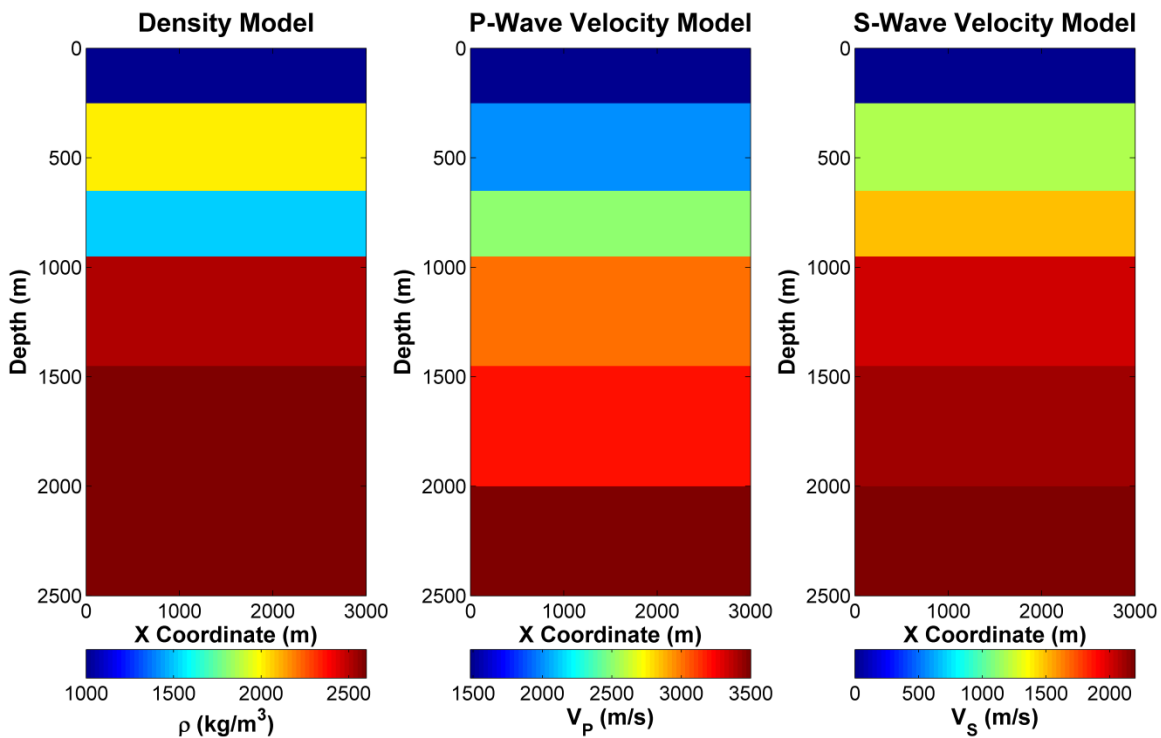


Figure 3.1: 2-D slice of the geological model used in this study. Density is shown on the left, P-velocity is shown in the middle, and S-velocity is shown on the right.

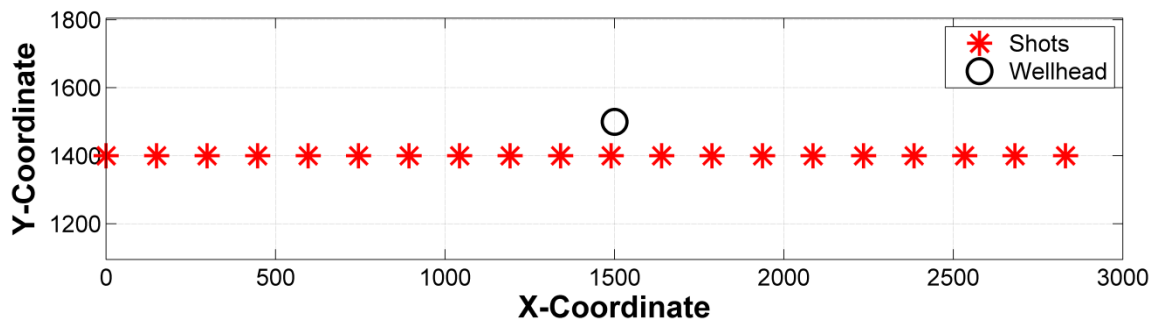


Figure 3.2: Plan view of acquisition geometry used in this experiment. Shots are numbered from left to right.

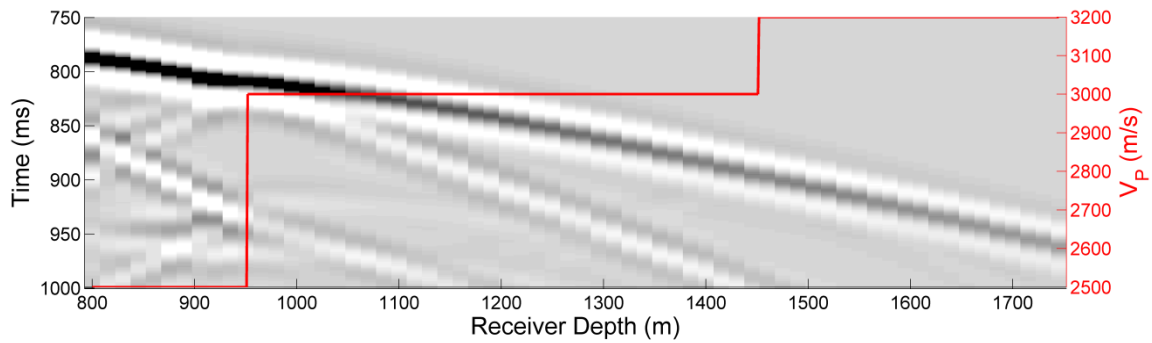


Figure 3.3: Raw x-component data from Shot 3, prior to addition of noise, overlain in red by the P-wave velocity model.

3.3 Additive Noise

3.3.1 Noise Generation

The noise used in this study was generated using the *rnoise* command in MATLAB, using trace 513 of the y-component as a reference. This command works by first creating a normal distribution, then setting its standard deviation to the RMS of the reference divided by the chosen signal to noise (S/N) ratio. S/N ratios used were 0.05, 0.1, 0.2, 0.5, 1, 2, 5, 10, and 20; noise was generated separately for each receiver component. Results shown are focussed on three of these values: a high noise level where S/N is 0.05, a moderate noise level where S/N is 1, and a low noise level where S/N is 20. The generated noise using these three values, prior to its addition to the signal, is shown in the time domain in Figure 3.4; amplitude histograms and amplitude spectra are shown in Figure 3.5. The histograms confirm that the noise follows a normal distribution, and the spectra reveal that the noise is white in nature.

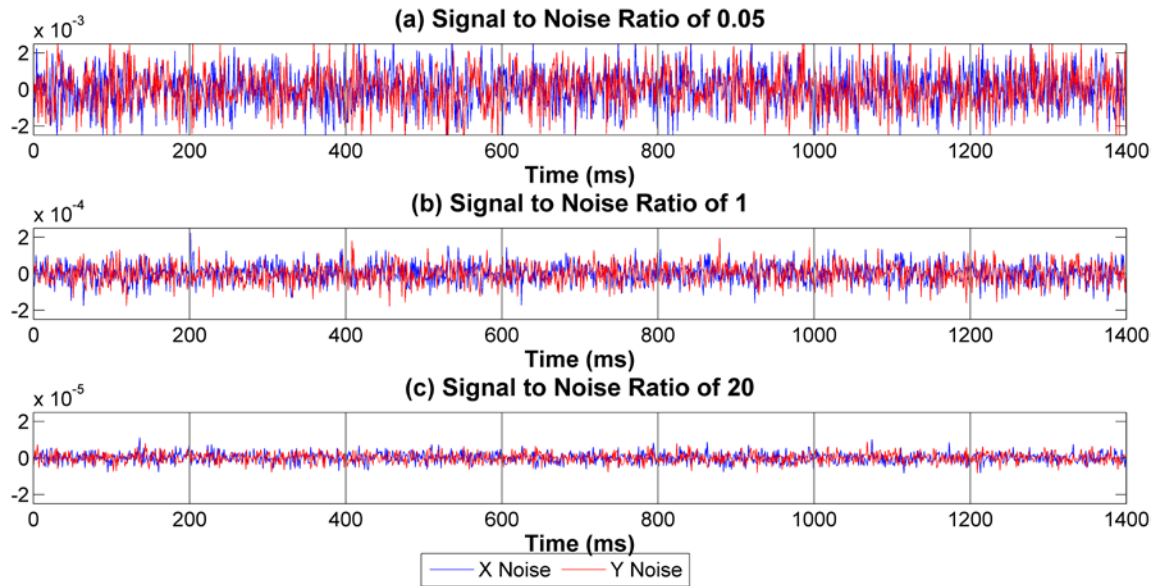


Figure 3.4: Generated random noise; noise added to the x-component is shown in blue, and noise added to the y-component is shown in red. S/N is given at the top of each panel. Note the differences in scale.

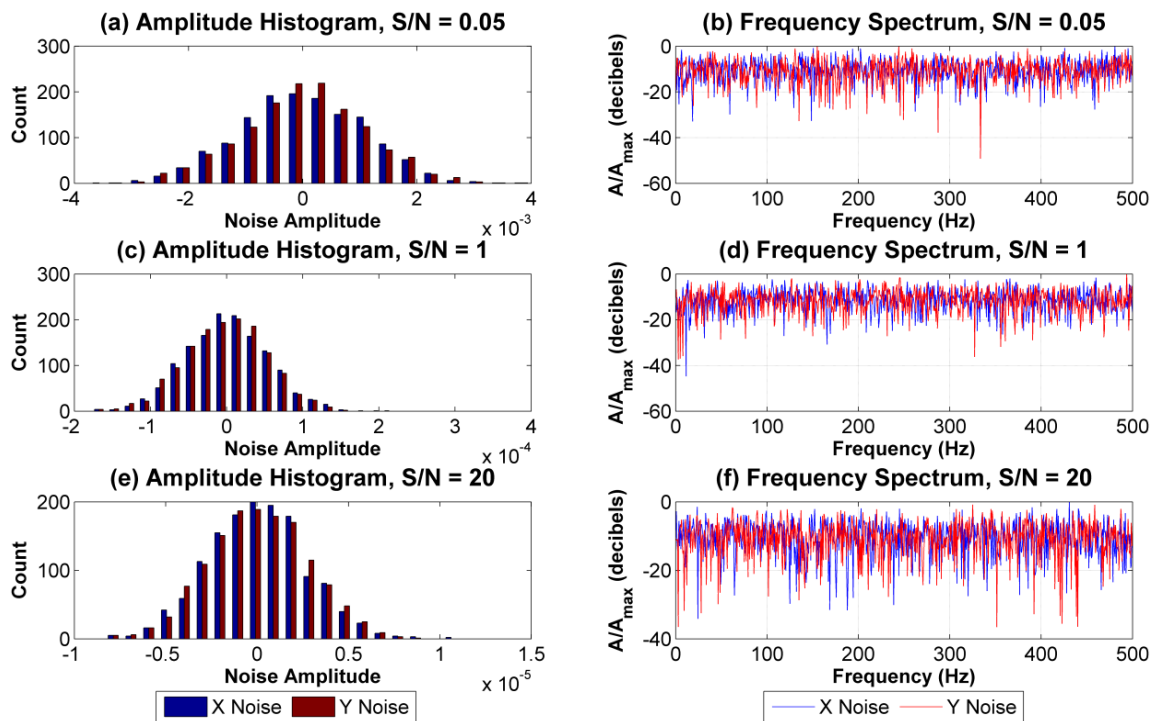


Figure 3.5: Amplitude histograms (left side) and amplitude spectra (right side) of generated noise; noise added to the x-component is shown in blue, and noise added to the y-component is shown in red. S/N is given at the top of each panel.

3.3.2 Noise Addition

After the noise traces were generated, they were added to the synthetic traces in two specific patterns. In Noise Pattern 1, receivers 1-59 were separated into groups of 10; each receiver was assigned a different S/N, in order from lowest (noisiest) to highest, with the 10th receiver in each group being left noise-free. The next 4 receivers, 60-63, had the different sine waves added to each component, again in order from lowest to highest signal to noise. Finally, geophone 64 had sine waves of differing power added to each component; the S/N ratio on the x-component was 10, that on the y-component was 1, and that on the z-component was 2. This pattern was repeated for all 20 shots; as an example, part of Shot 3 is shown after the addition of noise in Figure 3.6.

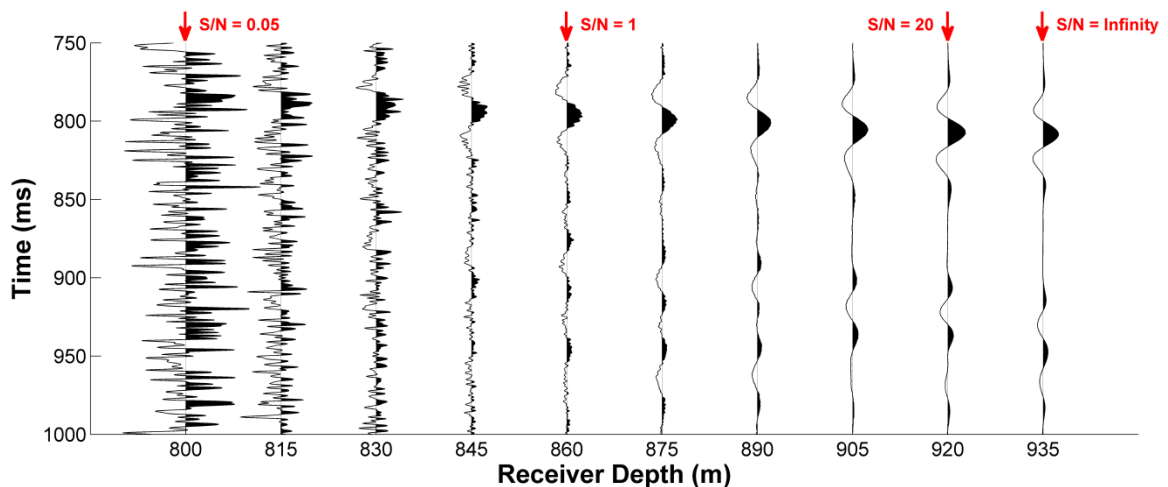


Figure 3.6: X-component traces from Shot 3, after the addition of noise, for the first 10 receivers; S/N increases to the right. Red arrows indicate traces with S/N values of 0.05, 1, 20 and infinity.

For Noise Pattern 2, 8 receivers were selected; these were at depths of 800 m, 920 m, 1040 m, 1160 m, 1280 m, 1400 m, 1520 m and 1640 m. For each of these receivers, all 9 different S/N ratios were tested, resulting in a total of 1440 traces to examine. For both noise patterns, once noise was added, geophone orientation analysis was performed on the data using the analytic and hodogram methods.

3.4 Results

3.4.1 Noise Pattern 1

Once the receiver orientation azimuth was found for every receiver, the results were plotted against source-receiver x-coordinate offset; values calculated from both methods are shown together for better comparison (Figures 3.7 - 3.8; see Appendix C for the complete set of receivers). Additionally, Figures 3.9 - 3.10 show receivers with similar noise content. There is a clear relationship between noise and angle scatter for the analytic method; once the S/N ratio reaches approximately 1, the angle seems to be much better constrained. The hodogram method seems to outperform the analytic method for low levels of signal to noise. However, while the analytic method has very little error at S/N of 1 or above, the hodogram method still shows noticeable error at near offsets. Quantitative analysis of the analytic method (Table 3.3) reveals that the standard deviation at a signal to noise ratio of 1 ranges from 1.24° - 7.69° , whereas a signal to noise ratio of 0.5 produces standard deviations as high as 22.2° . Furthermore, Table 3.3 and Figure 3.11 demonstrate that increasing receiver depth is well correlated with higher angle scatter; this is to be expected, as a deeper geophone will receive a weaker signal from the source. The tabulated results of the hodogram method are given in Appendix A.

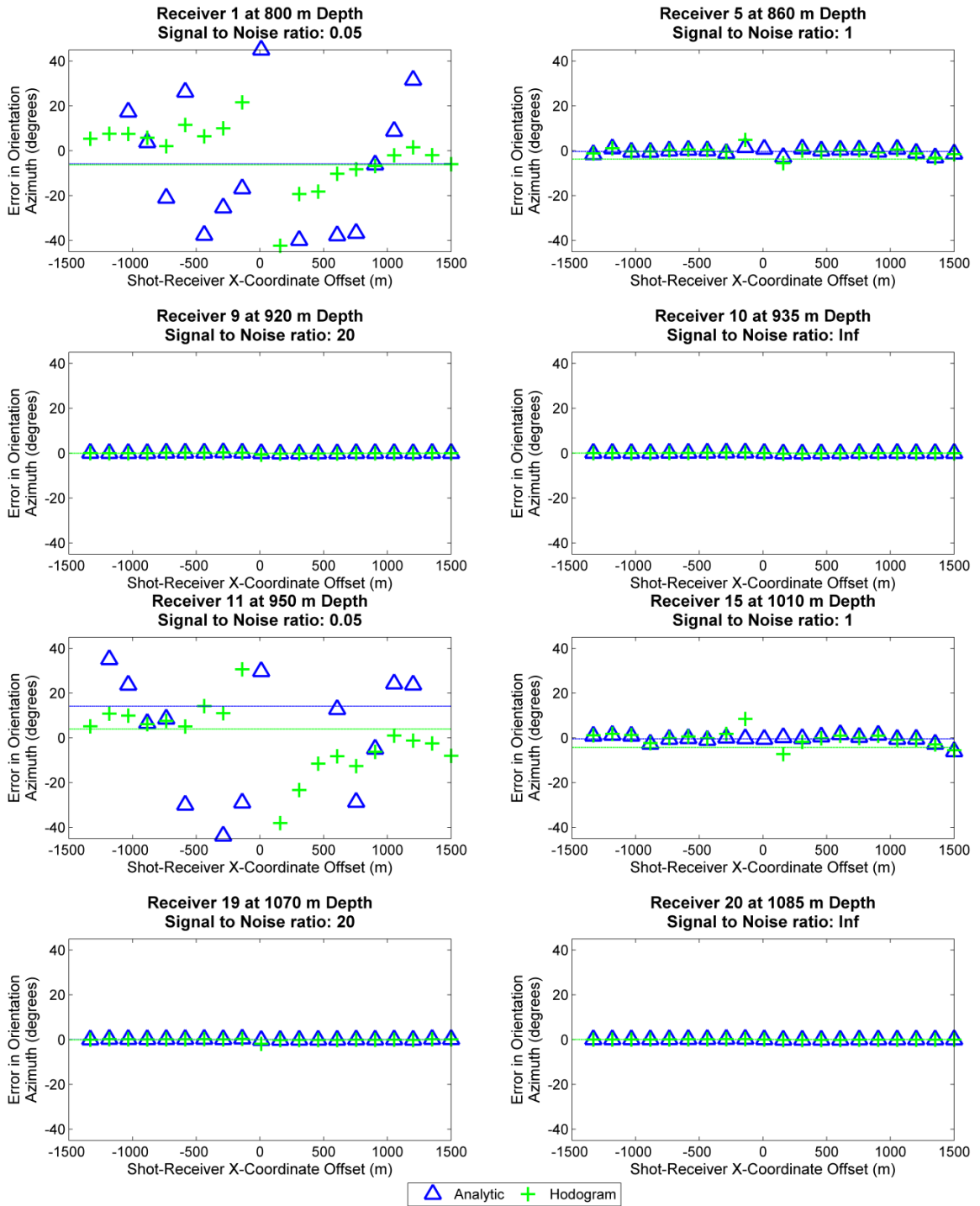


Figure 3.7: Error in orientation azimuth vs. x-coordinate offset for the first and second sets of receivers with S/N of 0.05, 1, 20 and infinity. Analytic results are shown in blue and hodogram results are shown in green.

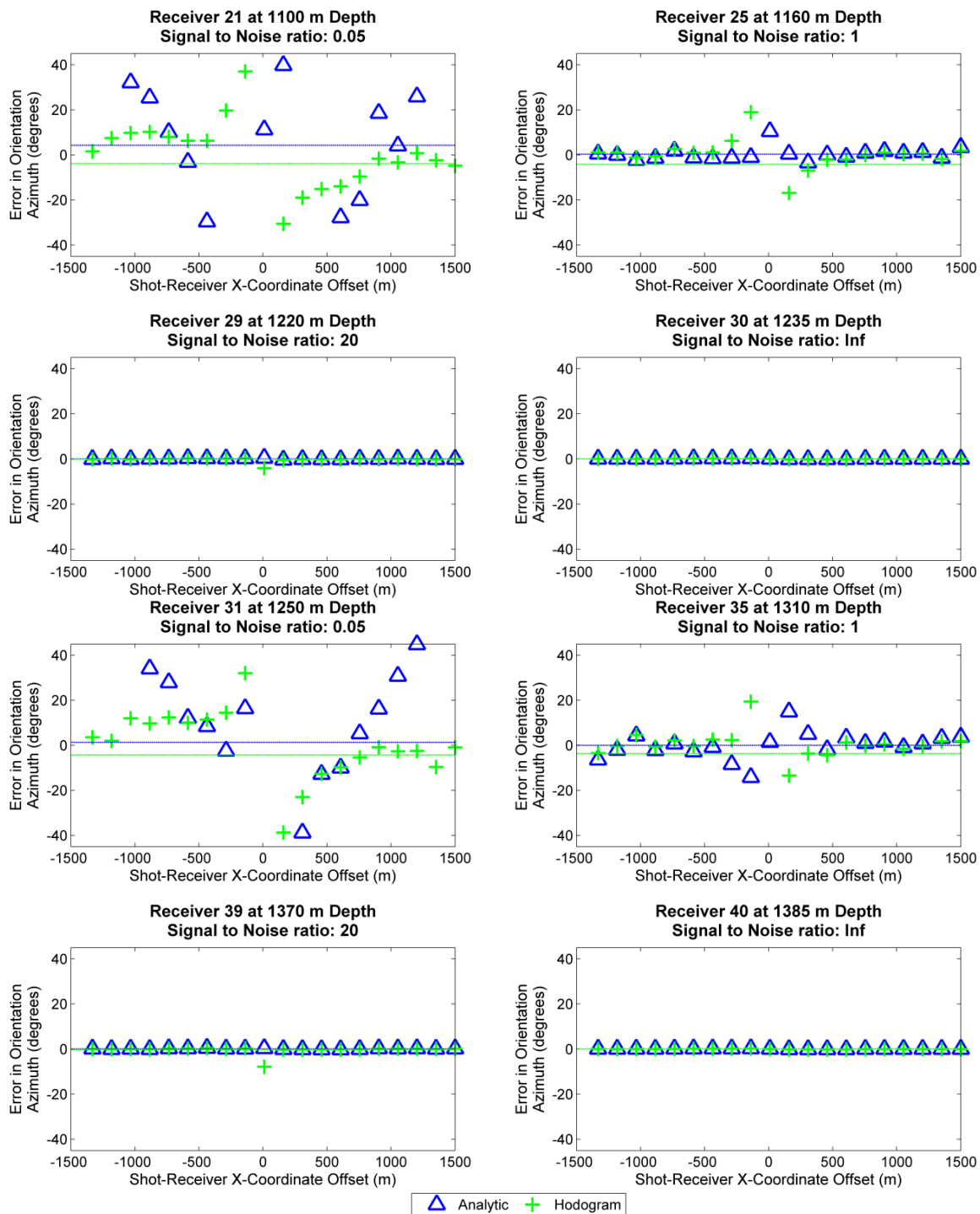


Figure 3.8: Error in orientation azimuth vs. x-coordinate offset for the third and fourth sets of receivers with S/N of 0.05, 1, 20 and infinity. Analytic results are shown in blue and hodogram results are shown in green.

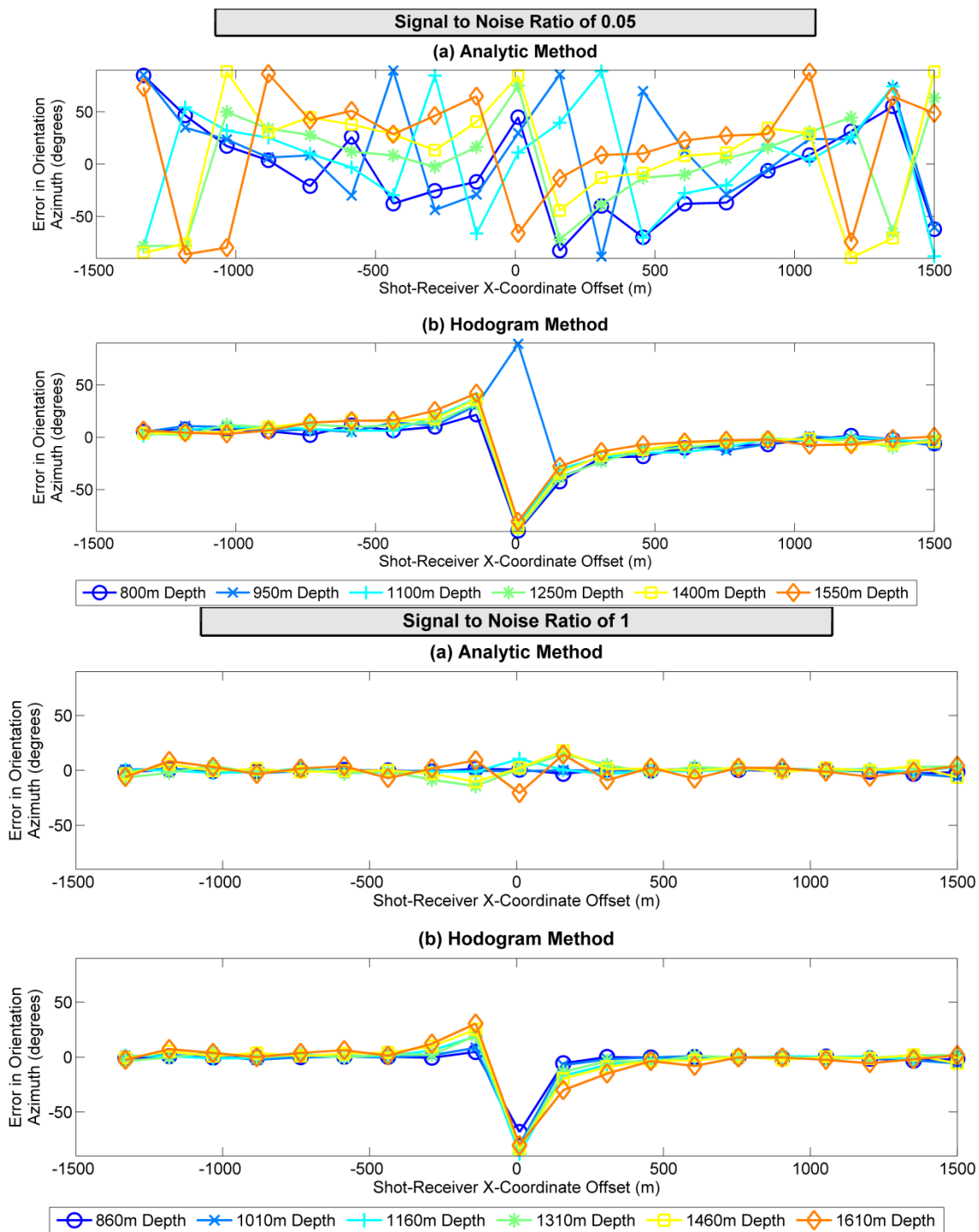


Figure 3.9: Error in orientation azimuth vs. horizontal offset for receivers with signal to noise ratios of 0.05 (top) and 1 (bottom), calculated using analytic (a) and hodogram (b) methods. Hotter colours correspond to larger depths.

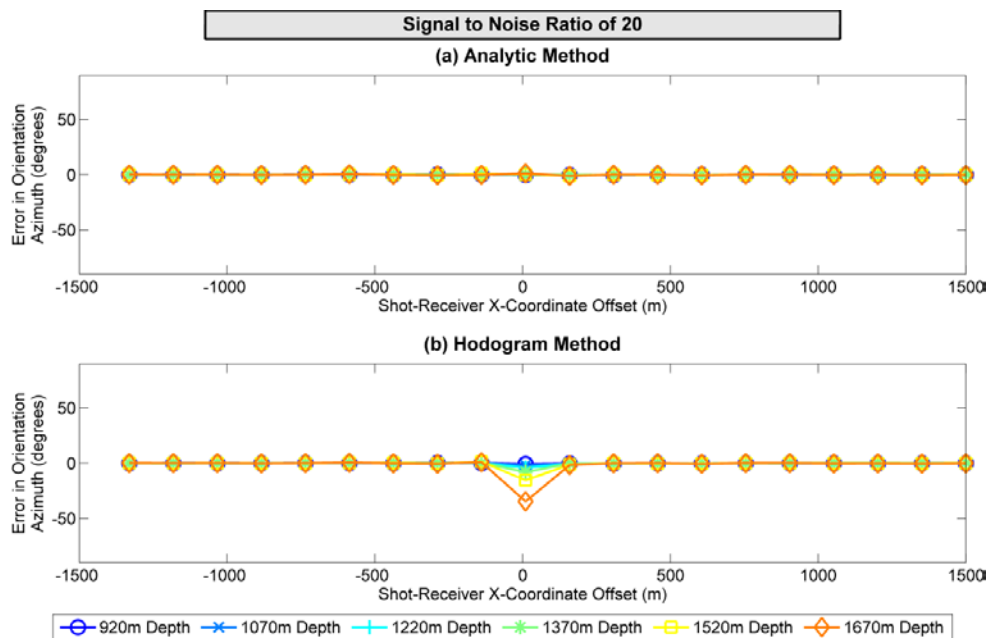


Figure 3.10: Error in orientation azimuth vs. horizontal offset for receivers with signal to noise ratio of 20, calculated using analytic (a) and hodogram (c) methods. Hotter colours correspond to larger depths.

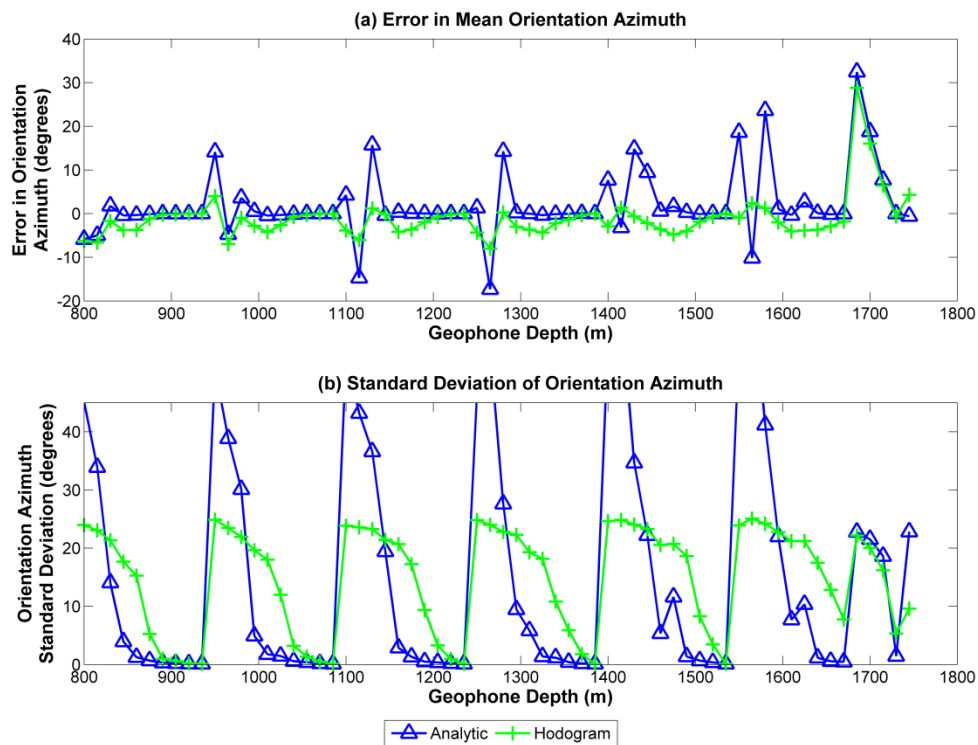


Figure 3.11: Error in mean orientation azimuth (a) and standard deviation (b) vs. receiver depth. Analytic results are shown in blue and hodogram results shown in green.

Table 3.3: Geophone orientation statistics of angles calculated analytically using Noise Pattern 1.

| | | | | | | | |
|----------------------------------|-------------|-------|--------|--------|--------|--------|--------|
| Signal to Noise: 0.05 | Depth (m) | 800 | 950 | 1100 | 1250 | 1400 | 1550 |
| | Mean (°) | 84.14 | 104.14 | 94.25 | 91.34 | 97.68 | 108.63 |
| | St. Dev (°) | 45.09 | 50.80 | 52.84 | 46.57 | 55.75 | 55.23 |
| Signal to Noise: 0.1 | Depth (m) | 815 | 965 | 1115 | 1265 | 1415 | 1565 |
| | Mean (°) | 85.04 | 85.27 | 75.29 | 72.66 | 86.81 | 79.83 |
| | St. Dev (°) | 33.92 | 38.87 | 43.20 | 54.53 | 61.37 | 65.36 |
| Signal to Noise: 0.2 | Depth (m) | 830 | 980 | 1130 | 1280 | 1430 | 1580 |
| | Mean (°) | 91.78 | 93.62 | 105.72 | 104.29 | 104.81 | 113.63 |
| | St. Dev (°) | 14.06 | 30.12 | 36.60 | 27.62 | 34.66 | 41.19 |
| Signal to Noise: 0.5 | Depth (m) | 845 | 995 | 1145 | 1295 | 1445 | 1595 |
| | Mean (°) | 89.59 | 90.54 | 89.60 | 90.20 | 99.42 | 91.07 |
| | St. Dev (°) | 3.94 | 4.93 | 19.43 | 9.47 | 22.20 | 22.00 |
| Signal to Noise: 1 | Depth (m) | 860 | 1010 | 1160 | 1310 | 1460 | 1610 |
| | Mean (°) | 89.67 | 89.55 | 90.34 | 89.99 | 90.59 | 89.67 |
| | St. Dev (°) | 1.24 | 1.75 | 2.88 | 5.82 | 5.35 | 7.69 |
| Signal to Noise: 2 | Depth (m) | 875 | 1025 | 1175 | 1325 | 1475 | 1625 |
| | Mean (°) | 89.85 | 89.70 | 90.07 | 89.65 | 91.65 | 92.68 |
| | St. Dev (°) | 0.66 | 1.47 | 1.32 | 1.37 | 11.63 | 10.36 |
| Signal to Noise: 5 | Depth (m) | 890 | 1040 | 1190 | 1340 | 1490 | 1640 |
| | Mean (°) | 90.02 | 89.88 | 90.04 | 89.89 | 90.28 | 90.09 |
| | St. Dev (°) | 0.31 | 0.56 | 0.50 | 1.17 | 1.37 | 1.15 |
| Signal to Noise: 10 | Depth (m) | 905 | 1055 | 1205 | 1355 | 1505 | 1655 |
| | Mean (°) | 89.97 | 90.03 | 89.93 | 89.99 | 89.91 | 89.84 |
| | St. Dev (°) | 0.20 | 0.39 | 0.36 | 0.39 | 0.68 | 0.55 |
| Signal to Noise: 20 | Depth (m) | 920 | 1070 | 1220 | 1370 | 1520 | 1670 |
| | Mean (°) | 90.00 | 90.02 | 90.00 | 90.06 | 90.04 | 89.97 |
| | St. Dev (°) | 0.13 | 0.18 | 0.20 | 0.18 | 0.35 | 0.45 |
| Signal to Noise: Infinity | Depth (m) | 935 | 1085 | 1235 | 1385 | 1535 | --- |
| | Mean (°) | 90.01 | 90.01 | 90.01 | 90.01 | 90.01 | --- |
| | St. Dev (°) | 0.12 | 0.11 | 0.12 | 0.11 | 0.11 | --- |

3.4.2 Noise Pattern 2

Noise Pattern 2 allowed for a more distinct separation between effects of noise and geophone depth. Figures 3.12 and 3.13 show how receiver depth affects the mean and standard deviation of calculated orientation azimuth. For each S/N value, there is an increase in scatter as receiver depth increases (Figure 3.13), though this trend is less defined when examining the orientation azimuth error (Figure 3.12). Figures 3.14 and 3.15 instead show how noise affects the mean and standard deviation. Again, an S/N value of 1 is of note; below this value, the hodogram method outperforms the analytic method, while at and above this value the analytic method is the better of the two. Additionally, Figure 3.15a shows an almost hyperbolic relationship between the natural logs of standard deviation and S/N ratio. Table 3.4 summarizes the statistics of this analysis using the analytic method; generally, angle scatter appears to increase dramatically when the signal to noise ratio is less than 1. Overall, the analysis of Noise Pattern 2 confirms what was seen in Noise Pattern 1.

When comparing the two methods using this noise pattern, a couple of interesting observations can be made. The hodogram method appears to be more robust at low levels of signal to noise, but does not show much improvement as the noise decreases. However, the analytic method performs better at high signal to noise levels, consistently improving as the S/N becomes better. Both methods show some dependence on depth, but the effect is generally less important than the effect of noise.

Table 3.4: Geophone orientation statistics of angles calculated analytically using Noise Pattern 2.

| | Depth (m) | 800 | 920 | 1040 | 1160 | 1280 | 1400 | 1520 | 1640 |
|------------------------------|-------------|-------|-------|--------|--------|--------|--------|--------|--------|
| Signal to Noise: 0.05 | Mean (°) | 92.27 | 81.17 | 89.48 | 102.56 | 92.92 | 95.52 | 94.90 | 111.50 |
| | St. Dev (°) | 46.93 | 47.42 | 47.28 | 47.14 | 52.33 | 53.37 | 58.57 | 58.19 |
| Signal to Noise: 0.1 | Mean (°) | 78.42 | 82.59 | 103.22 | 71.14 | 89.89 | 72.75 | 73.40 | 98.47 |
| | St. Dev (°) | 40.47 | 32.20 | 45.79 | 49.28 | 56.45 | 64.02 | 61.68 | 72.77 |
| Signal to Noise: 0.2 | Mean (°) | 96.16 | 93.53 | 105.65 | 108.73 | 103.55 | 114.67 | 107.70 | 94.13 |
| | St. Dev (°) | 12.16 | 14.57 | 24.86 | 35.01 | 32.72 | 35.03 | 49.00 | 45.27 |
| Signal to Noise: 0.5 | Mean (°) | 90.07 | 91.72 | 89.19 | 90.22 | 91.77 | 100.36 | 80.93 | 101.62 |
| | St. Dev (°) | 4.14 | 4.37 | 14.55 | 21.98 | 15.35 | 21.17 | 32.12 | 35.47 |
| Signal to Noise: 1 | Mean (°) | 90.20 | 90.23 | 90.43 | 89.17 | 89.48 | 87.14 | 87.31 | 90.21 |
| | St. Dev (°) | 1.05 | 1.68 | 1.65 | 4.69 | 7.45 | 9.98 | 9.11 | 19.71 |
| Signal to Noise: 2 | Mean (°) | 90.14 | 90.04 | 89.79 | 89.24 | 88.66 | 89.85 | 89.80 | 91.63 |
| | St. Dev (°) | 0.71 | 0.74 | 1.67 | 3.18 | 3.39 | 2.20 | 7.36 | 12.44 |
| Signal to Noise: 5 | Mean (°) | 90.03 | 89.95 | 89.88 | 89.80 | 90.12 | 90.26 | 90.11 | 89.45 |
| | St. Dev (°) | 0.29 | 0.38 | 0.74 | 1.02 | 0.85 | 0.83 | 2.16 | 1.43 |
| Signal to Noise: 10 | Mean (°) | 90.01 | 89.94 | 90.09 | 90.01 | 89.96 | 90.03 | 89.89 | 90.17 |
| | St. Dev (°) | 0.26 | 0.21 | 0.57 | 0.38 | 0.38 | 0.60 | 1.09 | 1.80 |
| Signal to Noise: 20 | Mean (°) | 90.00 | 90.00 | 89.99 | 90.02 | 90.02 | 89.96 | 89.95 | 90.14 |
| | St. Dev (°) | 0.14 | 0.15 | 0.18 | 0.19 | 0.23 | 0.41 | 0.46 | 0.92 |

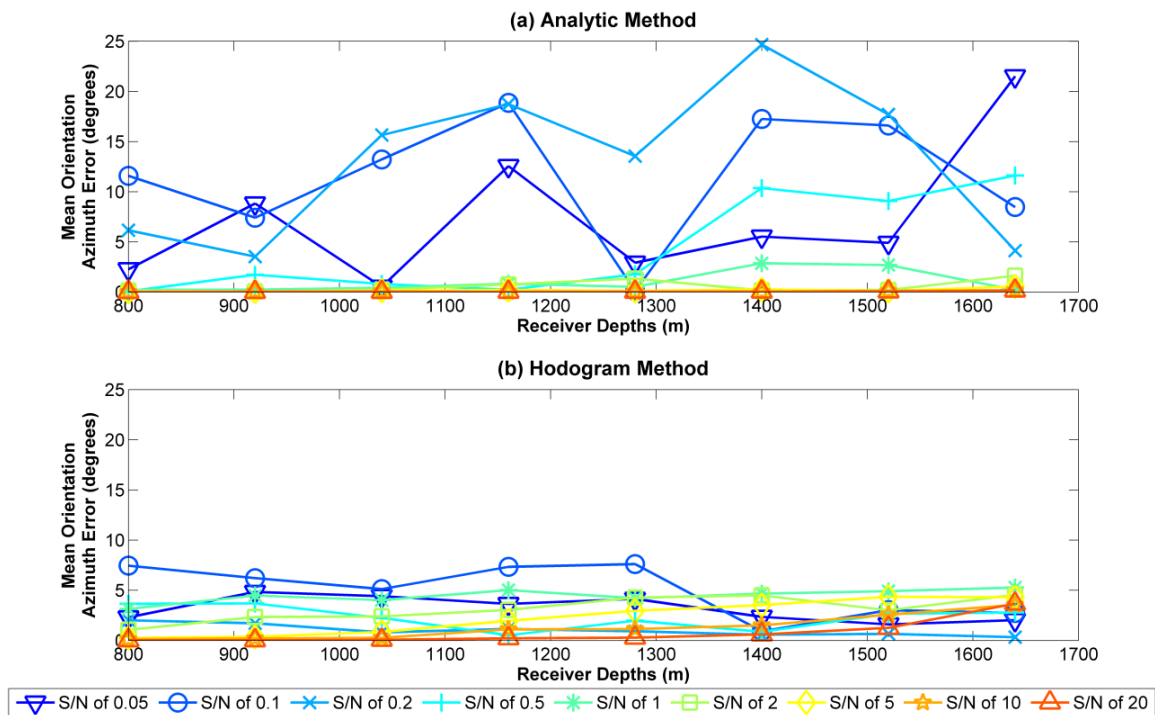


Figure 3.12: Mean orientation azimuth error vs. receiver depth for Noise Pattern 2. Cooler colours correspond to lower S/N ratios.

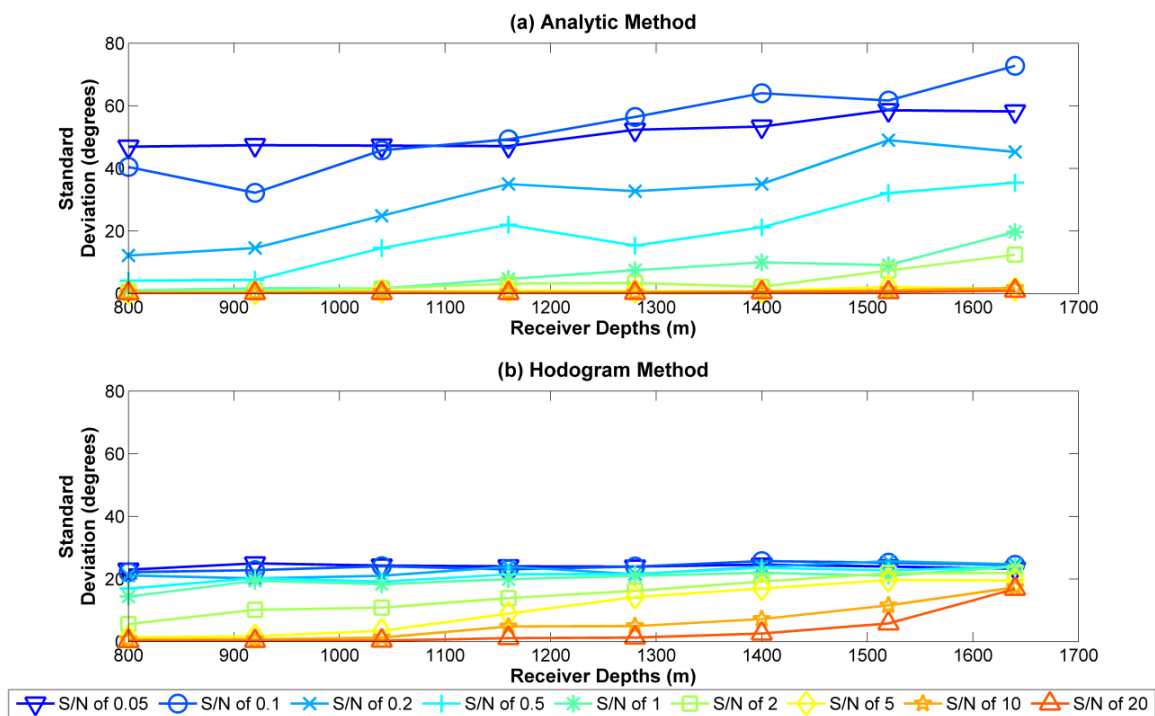


Figure 3.13: Standard deviation of orientation azimuth vs. receiver depth for Noise Pattern 2. Cooler colours correspond to lower S/N ratios.

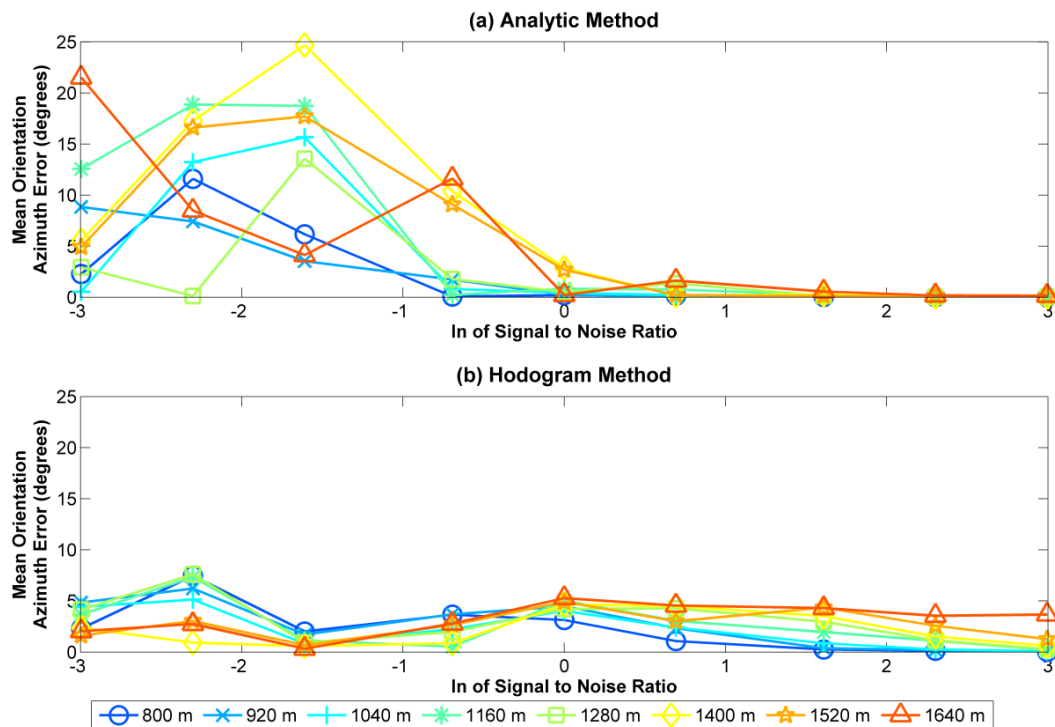


Figure 3.14: Error in mean orientation azimuth vs. natural log of S/N ratio for Noise Pattern 2. Warmer colours correspond to larger depths.

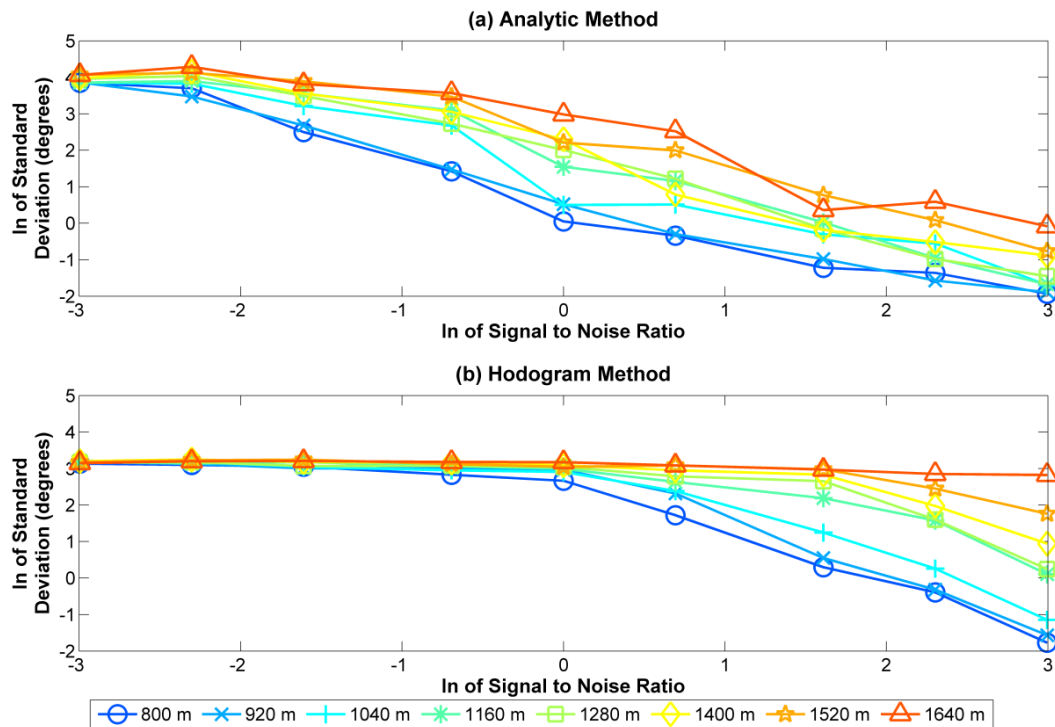


Figure 3.15: Natural log of orientation azimuth standard deviation vs. natural log of S/N ratio for Noise Pattern 2. Warmer colours correspond to larger depths.

3.5 Discussion

The results of this study show a definite dependence of geophone orientation azimuth calculations on noise content, offset and depth. In reality, the effects of these three things are most likely related to each other. For example, a nearer source offset results in less energy from P-wave first arrivals being recorded on horizontal receiver components; this would skew the signal to noise ratio to be more heavily weighted towards noise, simply due to lower signal. Similarly, deeper receivers will generally have lower signal content due to effects such as geometrical spreading and Q-related attenuation. Chapter 2 shows that field data have these same relationships to noise, offset and depth though it is harder to separate the effects in a real data example. The comparisons between the analytic and hodogram methods showed potential strengths and weaknesses of each method. The hodogram method seems to be more robust when there is high noise content, but when the noise is weaker the analytic method produces more reliable results.

3.6 Summary

The following results can be noted from this chapter:

- The calculation of geophone orientation azimuths is dependent on signal to noise ratio, source-receiver offset and receiver depth.
- Analysis of orientation azimuth became less accurate with increasing receiver depth, for both the analytic and hodogram methods.
- Analysis of orientation azimuth became more accurate with increasing source-receiver offset, for both methods.
- The analytic method was more robust at a signal to noise ratio of 1 or better; these calculations generally produced a mean within 0.5° of the receiver's true

orientation.

- The hodogram method was more robust at low levels of signal to noise; at higher levels it was outperformed by the analytic method, but still produced good statistics.

Chapter Four: Pembina Deviated Well Example

4.1 Introduction

In this chapter, I discuss the need to understand and compensate for the effects of a deviated well on geophone orientation analysis. A method is developed to determine geophone orientation azimuth in a deviated well, and it is applied to field data. In order to gauge its success, it is compared to analysis under a vertical well assumption. Additionally, effects of uncertainties in well deviation surveys are modelled, in order to quantify their impact on the robustness of geophone orientation calibrations. Finally, trends noted in this chapter are compared to the results seen in Chapter 2, in order to gain confidence in the presence of trends that are dependent on offset and azimuth.

4.2 Survey parameters

In 2007, walkaway vertical seismic profile (VSP) surveys were acquired in the Pembina field, near Violet Grove, Alberta, as part of the Pembina CO₂ enhanced oil recovery project. The well used was PennWest 102-10-11-48-9W5 (Figure 4.1), which had a maximum deviation of 17° and a total depth of 1644 m. Two coupled 8-level VSP tools were used to record the survey, placed at 3 different depth ranges in the well: 798 – 1025 m (shallow), 1038 – 1265 m (mid), and 1278 – 1505 m (deep) (Table 4.1). The shuttle spacing was 15.12 m. Shots were taken along three 2D lines over a range of source offsets, from 200 to 1700 m, using dynamite as a source (Figure 4.2). Lines 1 (trending North-South), 2 (trending East-West) and 6 (trending Northeast-Southwest) are used in this study. Some of the raw x and y-component data are shown in Figure 4.3. Visually, signal to noise of the first arrivals appears to be good, as they are easily defined.

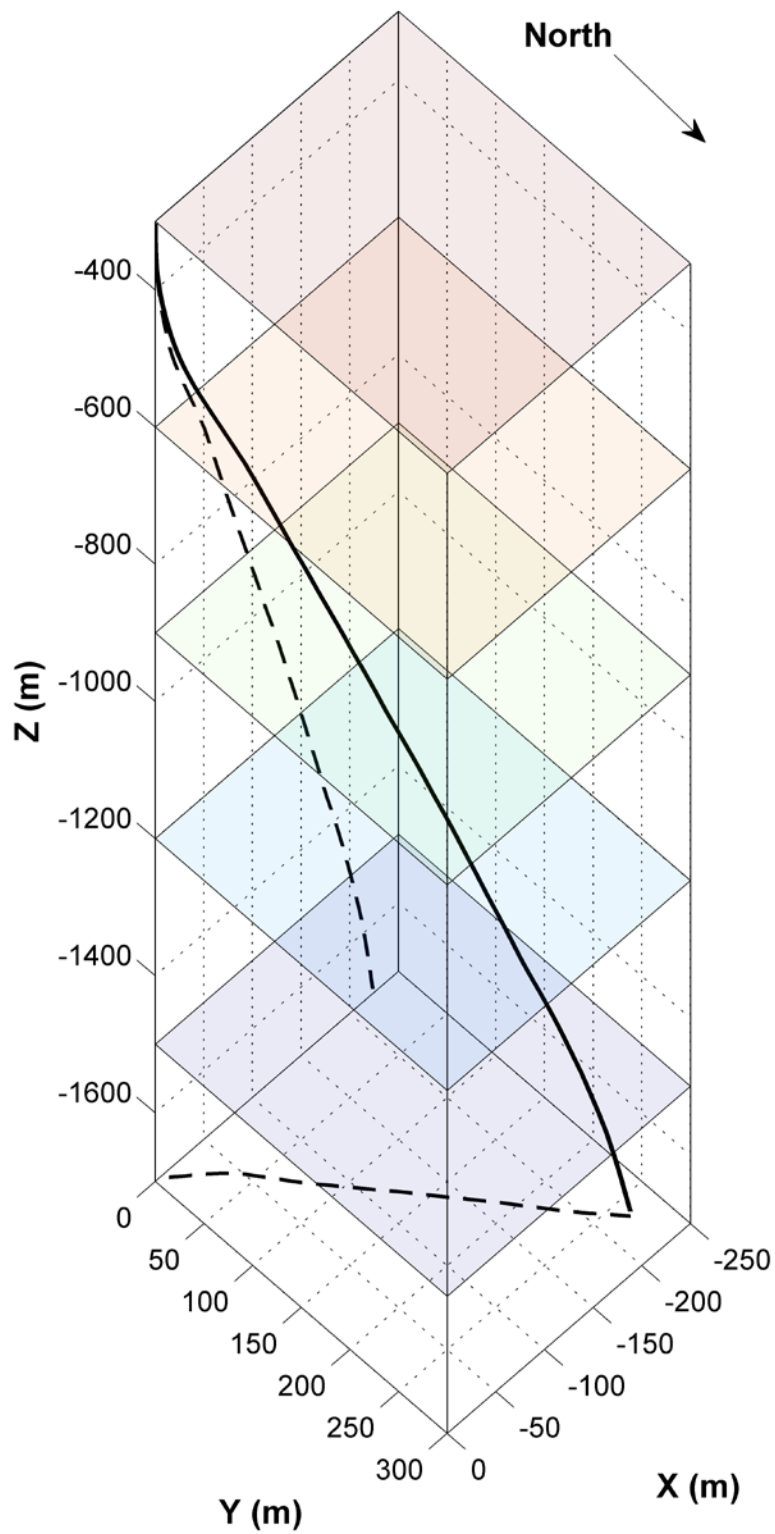


Figure 4.1: Deviation survey of the well used in this study, where the wellhead is the origin of the coordinate system. The dashed lines are projections of the well onto the $x-z$ and $x-y$ planes.

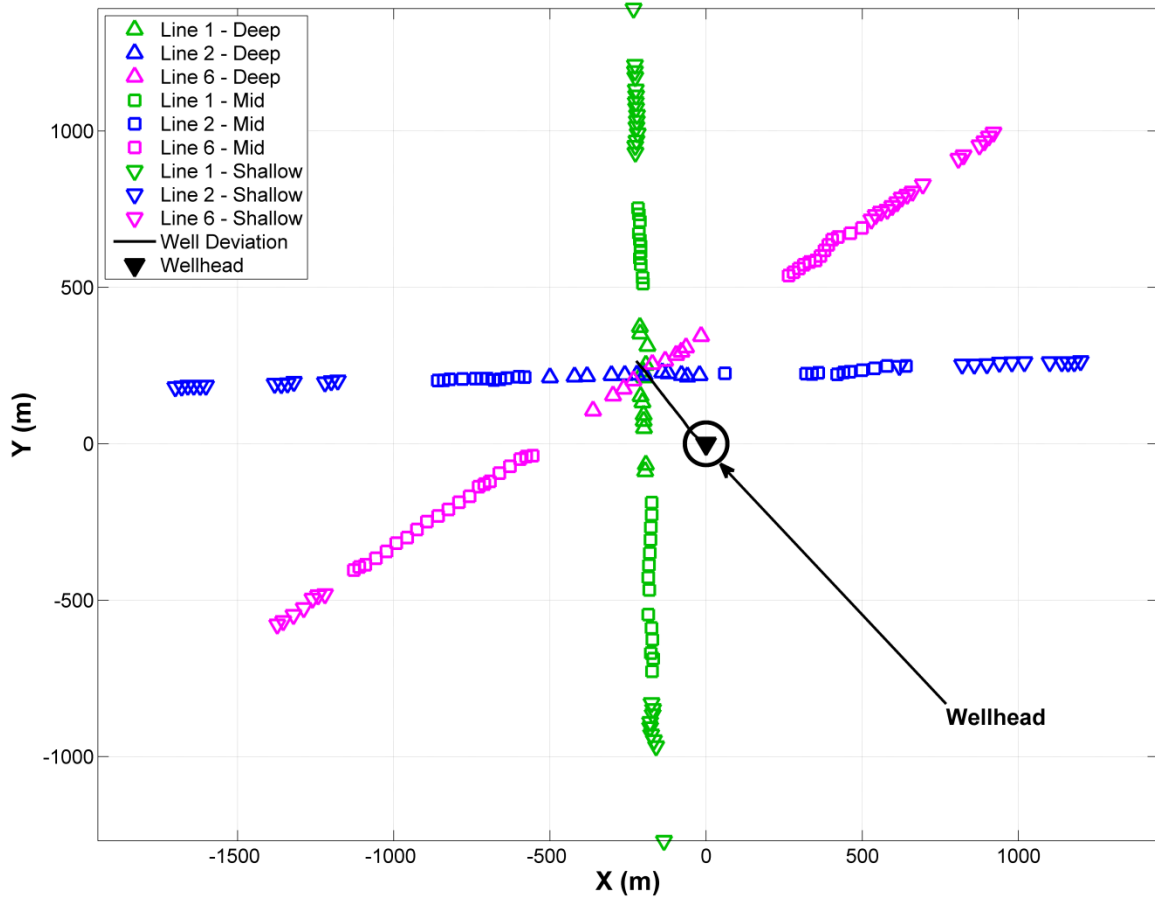


Figure 4.2: Survey geometry of shots used in 16-level VSP experiment. Line 1 is shown in green, Line 2 is shown in blue, and Line 6 is shown in magenta; different markers represent the different tool levels. The wellhead is shown in black, and represents the origin of the coordinate system.

Table 4.1: Receiver numbering of different tool levels.

| Tool Level | Receiver Numbers |
|------------|------------------|
| Shallow | 1-16 |
| Mid | 17-32 |
| Deep | 33-48 |

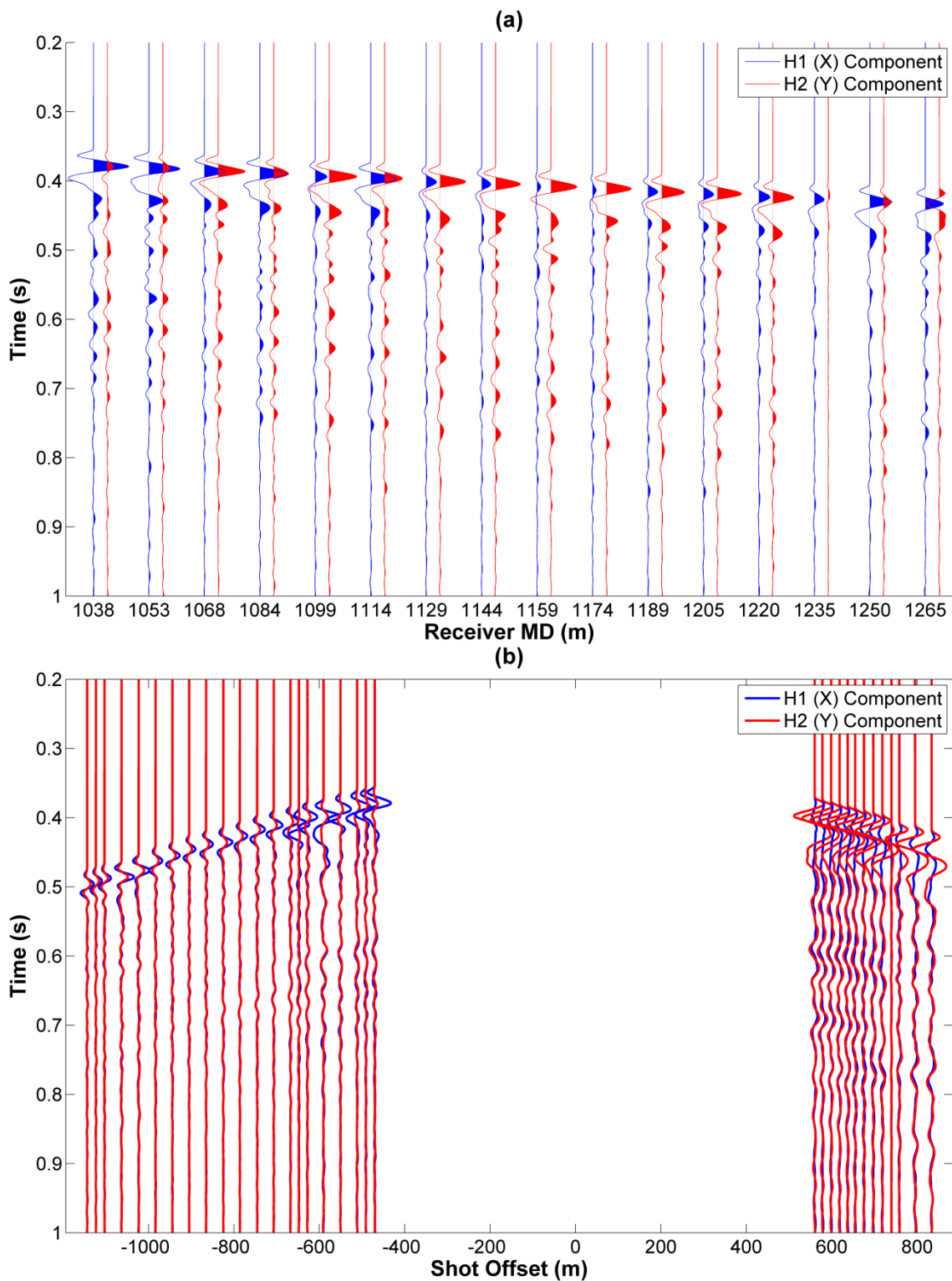


Figure 4.3: (a) Common shot gather for mid tool position, with shot coordinates $X=-555$ m and $Y=-38$ m, and (b) common receiver gather of Receiver 17 (1038 m MD), for Line 6. The x component is shown in blue, and the y component is shown in red.

4.3 Orientation in a Deviated Well

Consider an observation well that has an arbitrary deviation. At any point along the well, particularly at a receiver location, consider a line \vec{l} tangent to the deviation. This can be expressed parametrically as

$$\vec{l} = \begin{bmatrix} \sin \theta_w \cos \phi_w \\ \sin \theta_w \sin \phi_w \\ \cos \theta_w \end{bmatrix} t + \begin{bmatrix} x_r \\ y_r \\ z_r \end{bmatrix}, \quad (4.1)$$

where θ_w is the well inclination angle, ϕ_w is the horizontal direction of the well relative to the positive x-axis, x_r, y_r, z_r are the coordinates of the receiver, and t is distance away from the receiver along the well trajectory. Note that the signs of θ_w and z_r must be consistent with the coordinate system used; in the example presented here, the z-axis is defined such that it is positive upwards. Using the direction of \vec{l} , we can define the normal to a plane that is perpendicular to the well at this point; that is,

$$\hat{n} = \begin{bmatrix} \sin \theta_w \cos \phi_w \\ \sin \theta_w \sin \phi_w \\ \cos \theta_w \end{bmatrix}. \quad (4.2)$$

Finally, we must choose a useful coordinate system for this plane; for this study, the choice will be defined such that the new x-axis has zero as its vertical component, and the new y-axis is oriented along the maximum dip of the projection plane, towards the surface (Figure 4.4). The new “pseudo” x and y axes are then defined as

$$\hat{x}' = \begin{bmatrix} -\sin \phi_w \\ \cos \phi_w \\ 0 \end{bmatrix}; \quad (4.3)$$

and

$$\hat{y}' = \begin{bmatrix} -\cos \theta_w \cos \phi_w \\ -\cos \theta_w \sin \phi_w \\ \sin \theta_w \end{bmatrix}. \quad (4.4)$$

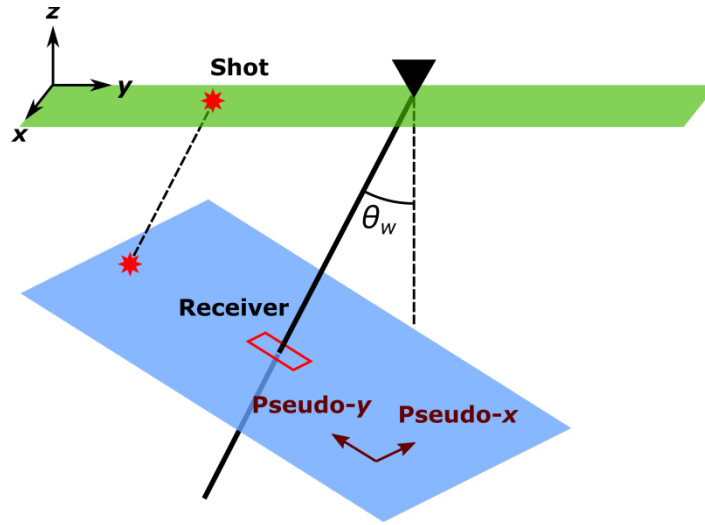


Figure 4.4: Illustration of pseudo-coordinates defined for a deviated well.

It should be noted that these two vectors, along with the normal defined in Equation 4.2, provide a suitable orthonormal vector basis for the analysis (Appendix A). In order to perform analysis of geophone orientation, we now project the source coordinates onto the plane defined above. Given source coordinates x_s , y_s and z_s , this can be done simply by:

$$x'_s = \begin{bmatrix} x_s \\ y_s \\ z_s \end{bmatrix} \cdot \hat{x}' \quad (4.5)$$

and

$$y'_s = \begin{bmatrix} x_s \\ y_s \\ z_s \end{bmatrix} \cdot \hat{y}', \quad (4.6)$$

where x'_s is the source pseudo x coordinate, and y'_s is the source pseudo y coordinate. We now define a source-receiver azimuth using the projected source coordinates such that

$$\phi'_s = \arctan\left(\frac{x'_s}{y'_s}\right). \quad (4.7)$$

Finally, substituting ϕ_s for ϕ'_s in Equation 1.7 will give us a proper receiver orientation azimuth relative to \hat{y}' , ϕ'_r ; that is,

$$\phi'_r = \phi'_s + \theta. \quad (4.8)$$

Note that Equations 4.1 through 4.7 will properly yield Equation 1.6 in the case of a vertical well (i.e. $\theta_w = 0^\circ$, ϕ_w is chosen to be -90°).

4.4 Results

The projected geometry of the Violet Grove VSP survey, using pseudo x and y coordinates, is shown in Figure 4.5. Linear interpolation was used to estimate the well inclination and azimuth at each receiver depth. It should be noted that the well deviation at each receiver was slightly different; hence, each source had multiple projections. Receiver orientation azimuths between the x-component (H1) and pseudo y-axis were calculated for Lines 1, 2 and 6. These angles were then plotted against source pseudo offset in order to judge the consistency of the analysis (Figures 4.6 to 4.8; see Appendix D for remaining receivers). Several trends are noticeable from these plots. First, as was noted in Chapters 2 and 3, increasing geophone depth results in increased scatter in the calculated angle for the same source offset and if we consider each line separately. More interestingly, however, is the clear separation of the trends of each line, especially evident in the shallow-level tool position (Figure 4.6). In order to highlight this observation, orientation azimuths were also examined with respect to source-receiver pseudo azimuth (Figures 4.9 to 4.11; see Appendix D for remaining receivers). This shows a clear relationship between source-well pseudo azimuth and variation in the orientation angle, although the limited range of azimuths makes it difficult to fully characterise this trend. If data from receivers at the same shuttle positions are combined (Figure 4.12), more definable trends are evident; each receiver shows a similar pattern when plotted this way. Finally, angle analysis was performed under a vertical well assumption (Figures 4.13 to 4.15; see Appendix D for remaining receivers) in order to gauge the importance of accounting for the well deviation. As can be seen here, the scatter is much greater, especially for the deep-level tool position.

Statistical analysis of the calculated orientation azimuths confirms the distinction between lines. Histograms of the computed angles (Figures 4.16 to 4.18; see Appendix D

for remaining receivers), along with their means and standard deviations (Tables 4.2 to 4.4) clearly show that angle analysis from Line 1 shots consistently lead to larger values than that performed from shots along both Lines 2 and 6. On average, Line 1 yielded an orientation azimuth 3.7° higher than for Line 2 and 3.0° higher than for Line 6. Figure 4.19 directly shows the variation in the mean orientation azimuths of each line. Finally, the average standard deviations for each line and tool position are shown in Table 4.5; the receiver at tool position 14 was not included in these calculations, as there were data quality problems with this receiver.

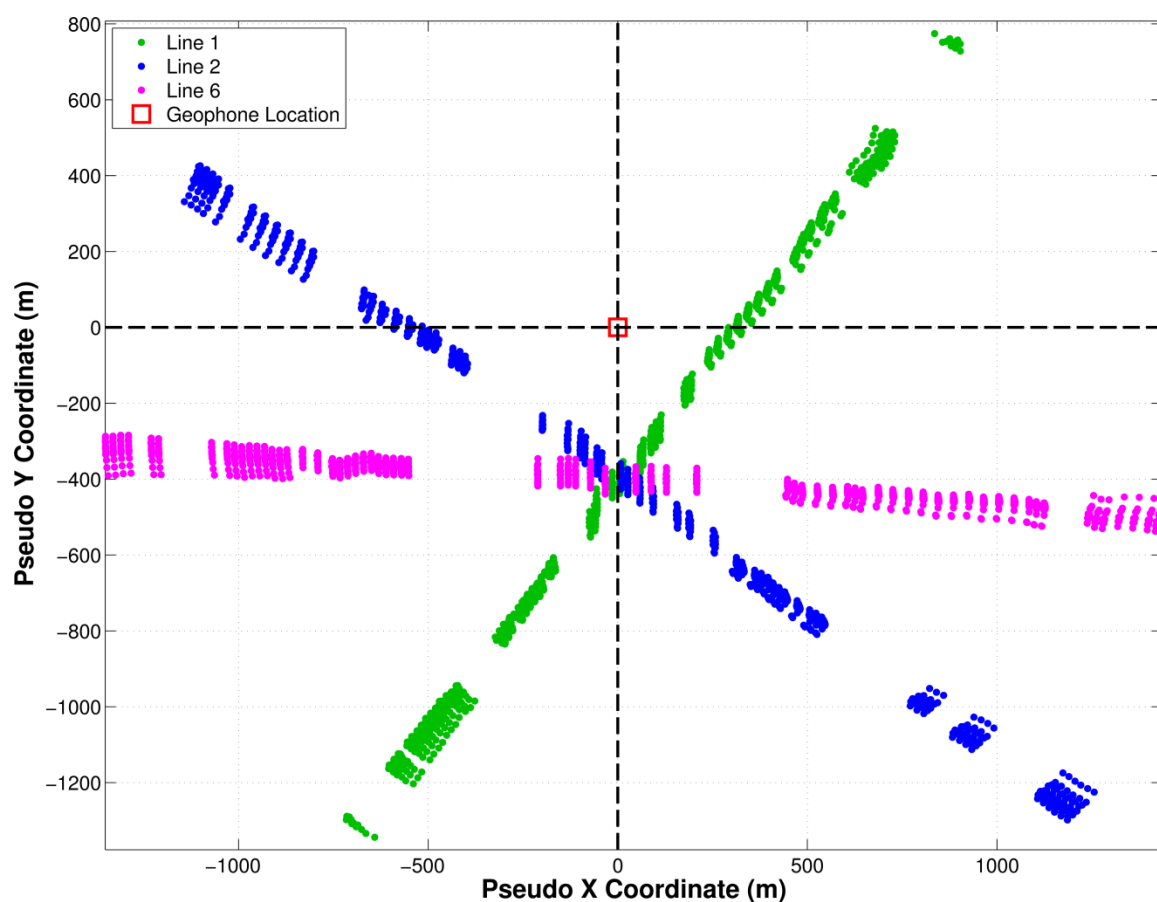


Figure 4.5: Survey geometry of shots used in 16-level VSP experiment, after being projected using Equations 4.5 and 4.6. Shots are shown relative to the geophone location, displayed as a red square at the origin. Line 1 is shown in green, Line 2 is shown in blue and Line 6 is shown in magenta.

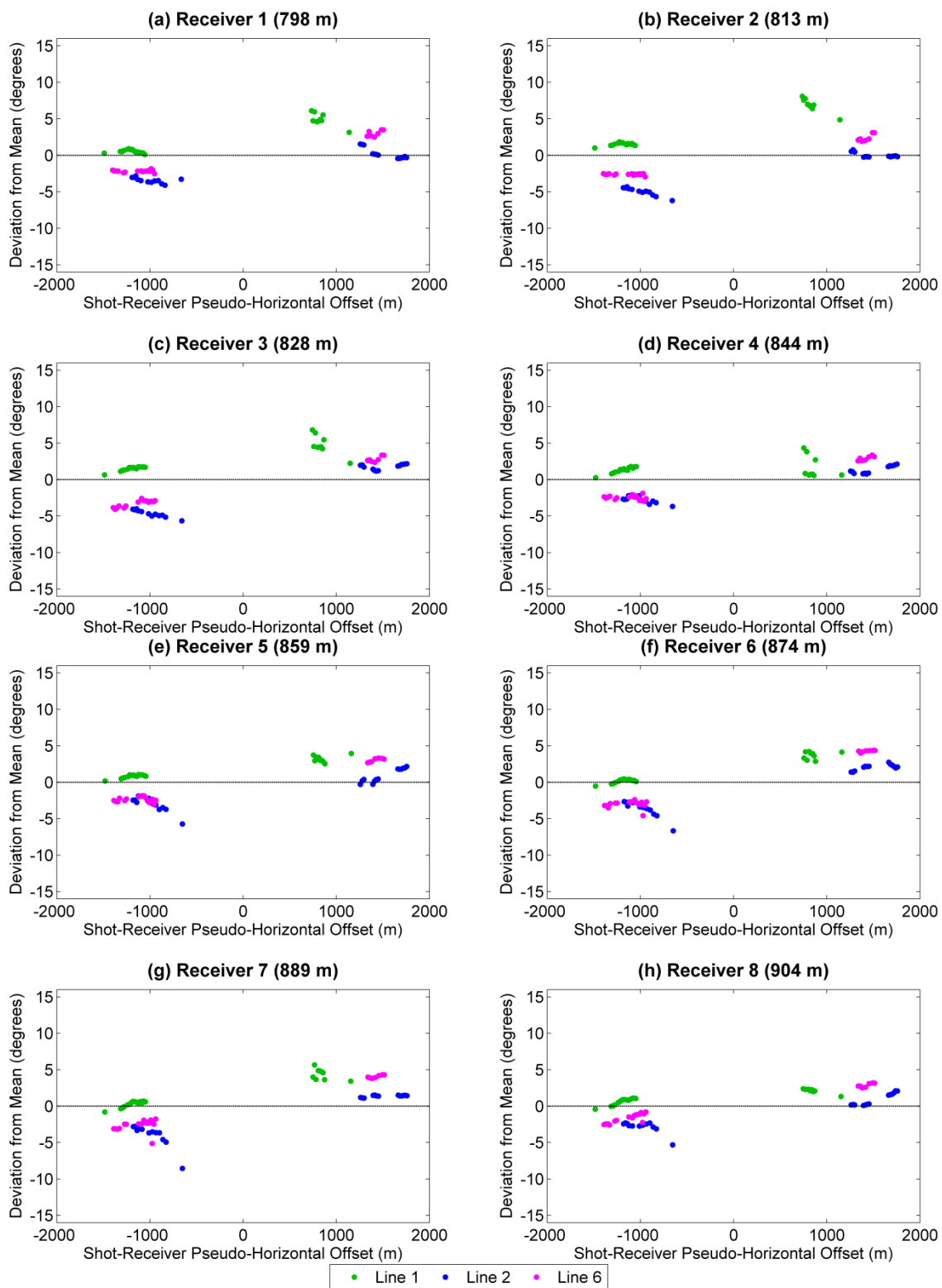


Figure 4.6: Deviation from mean orientation azimuth vs. pseudo offset for Receivers 1-8 (shallow-level). Line 1 is shown in green, Line 2 in blue, and Line 6 in magenta.

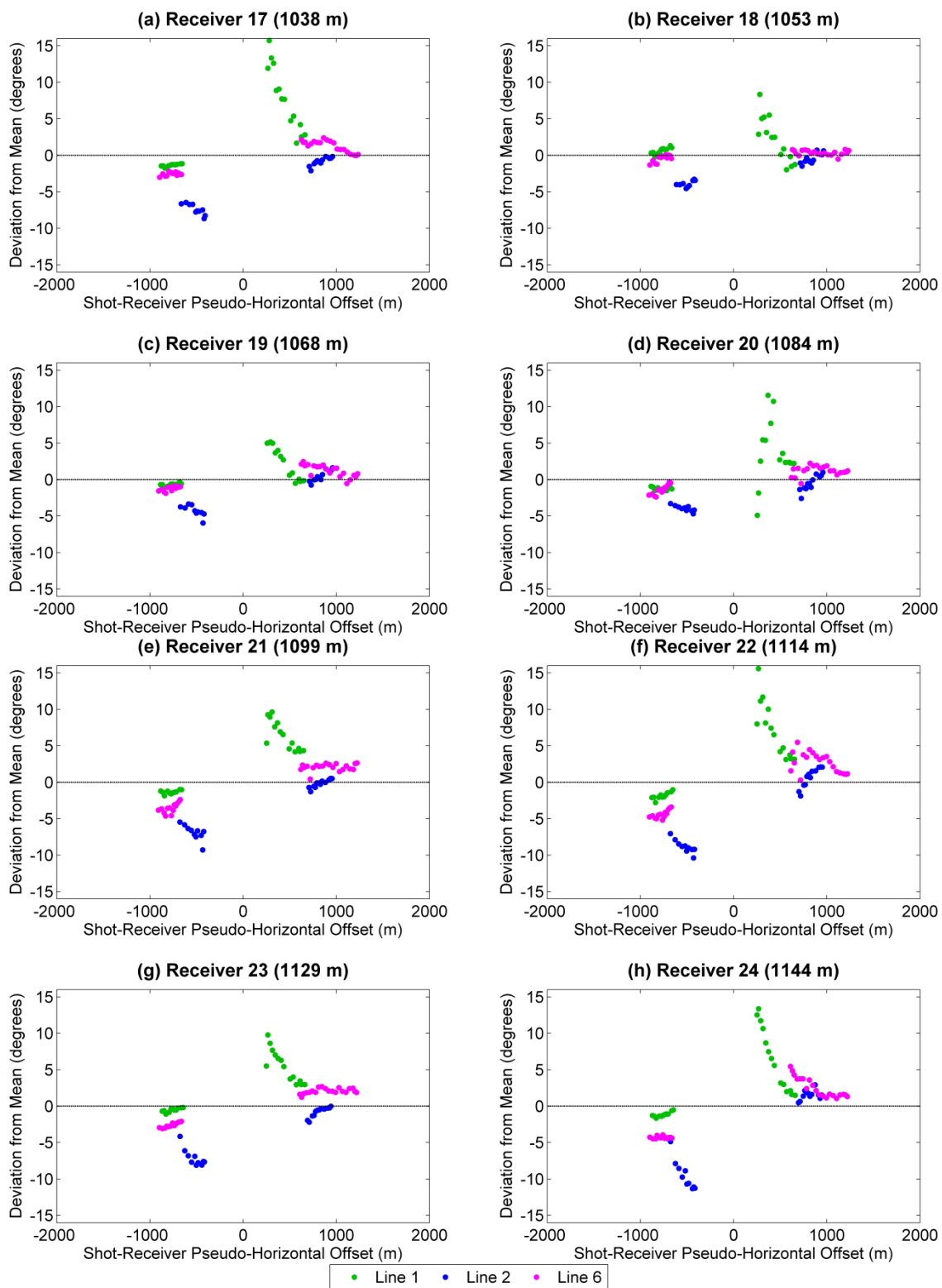


Figure 4.7: Deviation from mean orientation azimuth vs. pseudo offset for Receivers 17-24 (mid-level). Line 1 is shown in green, Line 2 in blue, and Line 6 in magenta.

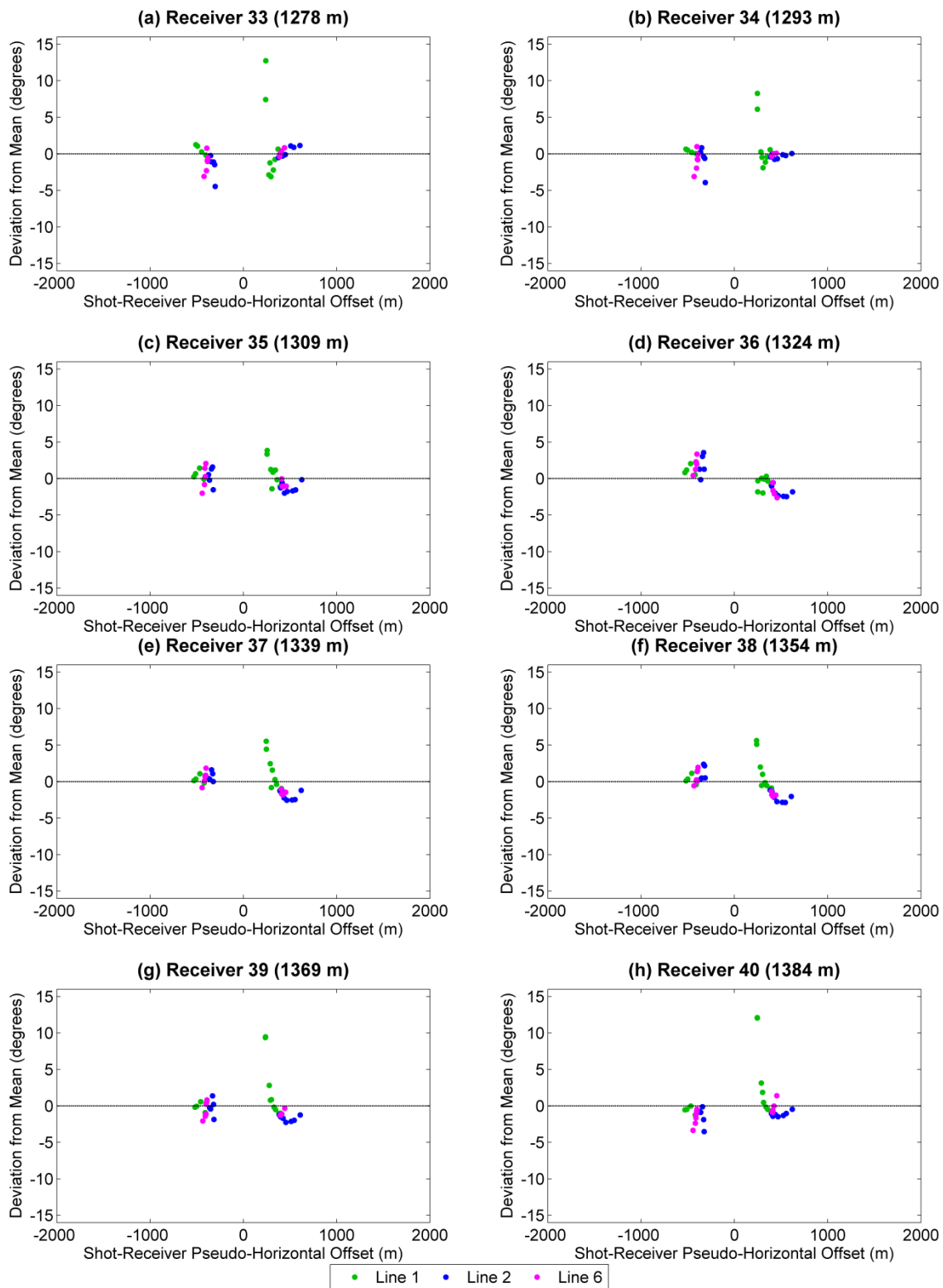


Figure 4.8: Deviation from mean orientation azimuth vs. pseudo offset for Receivers 33-40 (deep-level). Line 1 is shown in green, Line 2 in blue, and Line 6 in magenta.

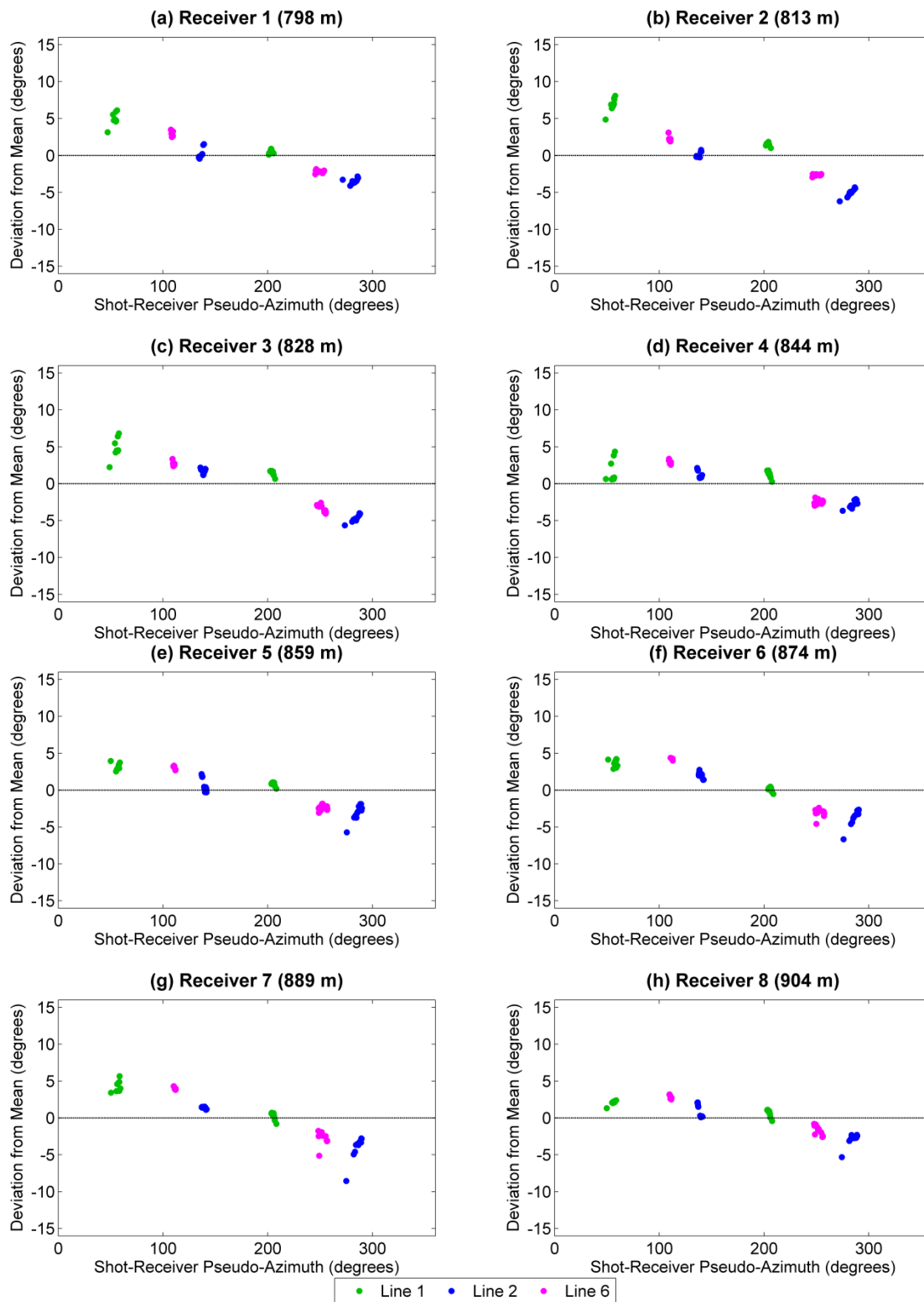


Figure 4.9: Deviation from mean orientation azimuth vs. pseudo azimuth for Receivers 1-8 (shallow-level). Line 1 is shown in green, Line 2 in blue, and Line 6 in magenta.

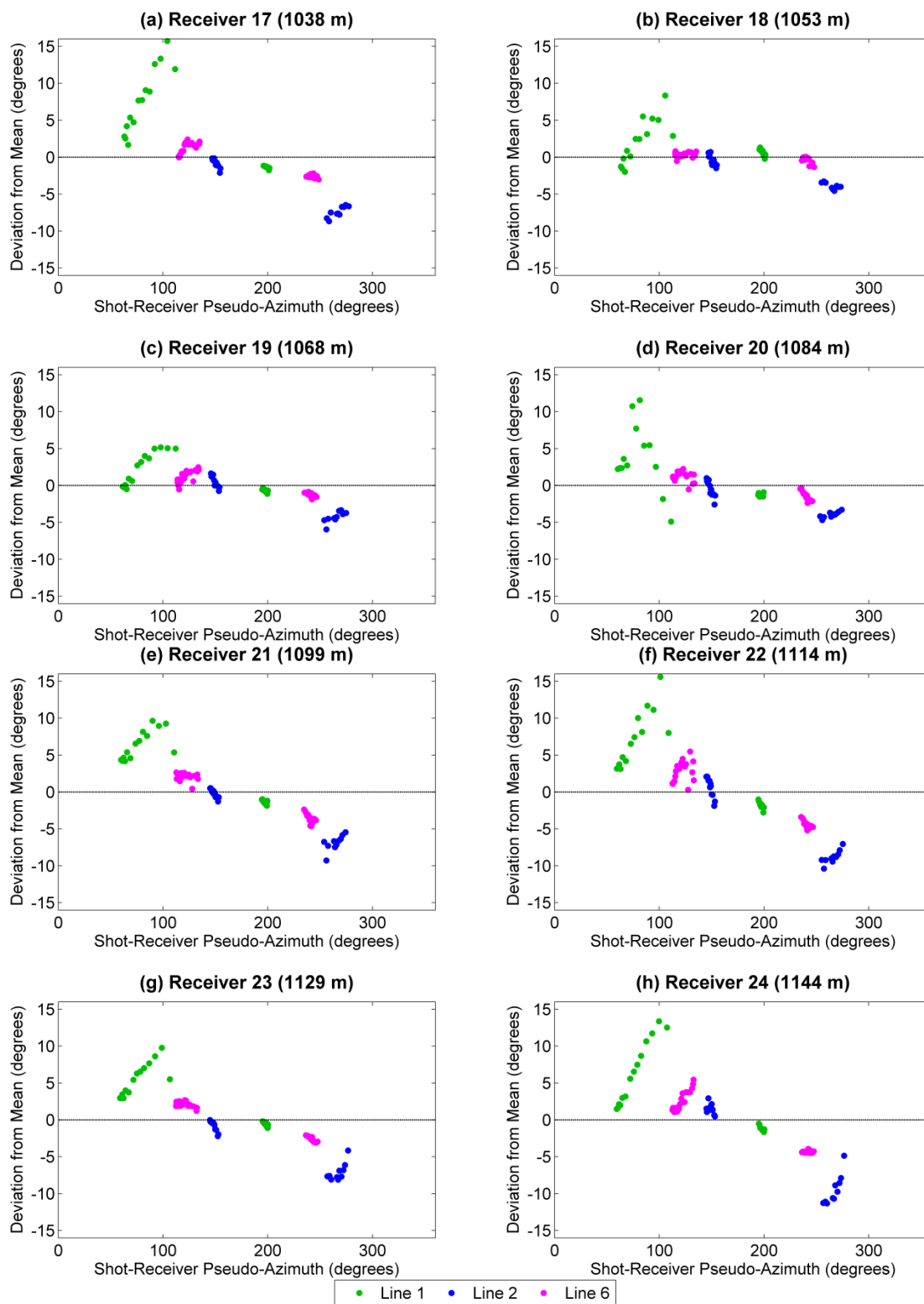


Figure 4.10: Deviation from mean orientation azimuth vs. pseudo azimuth for Receivers 17-24 (mid-level). Line 1 is shown in green, Line 2 in blue, and Line 6 in magenta.

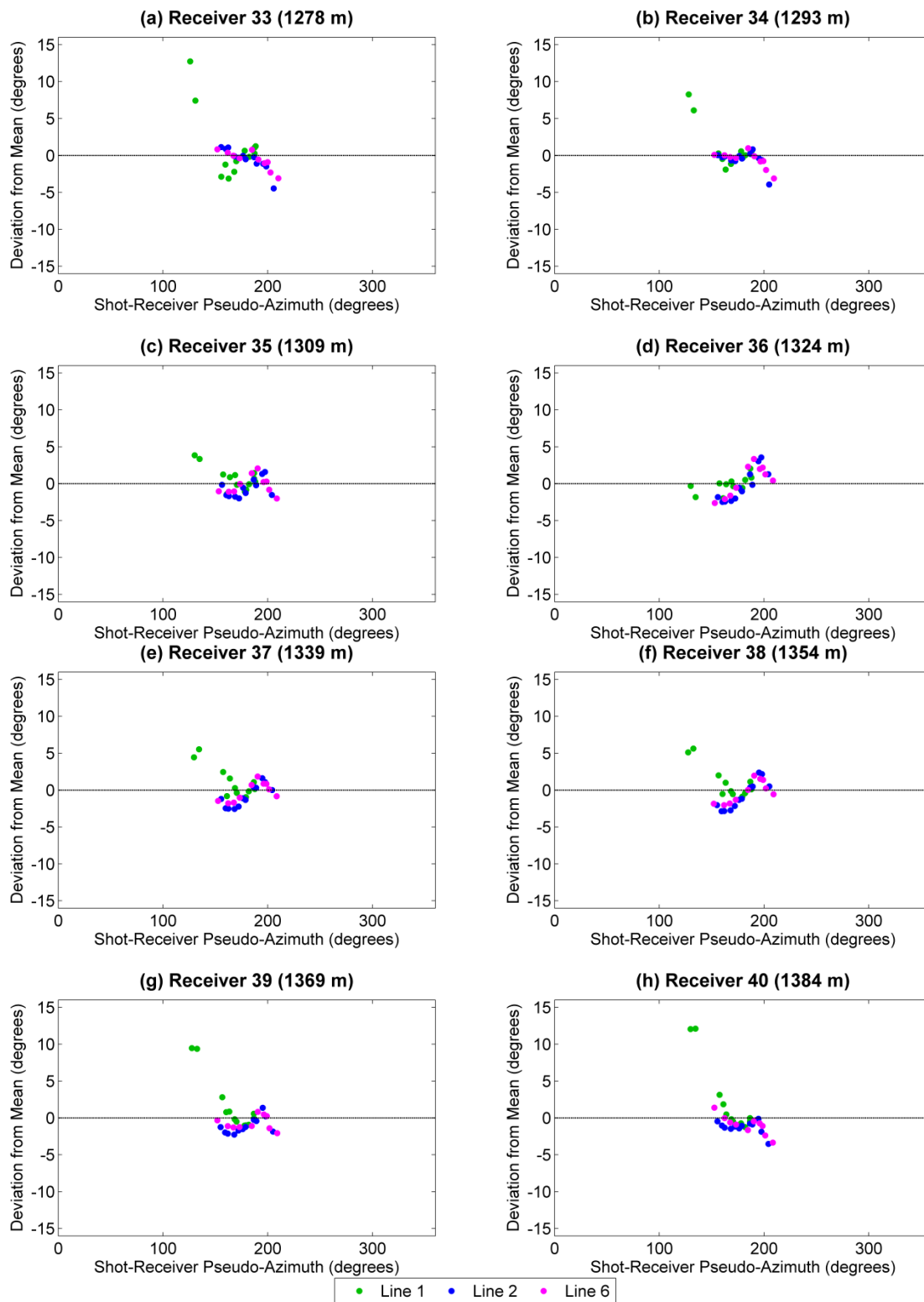


Figure 4.11: Deviation from mean orientation azimuth vs. pseudo azimuth for Receivers 33-40 (deep-level). Line 1 is shown in green, Line 2 in blue, and Line 6 in magenta.

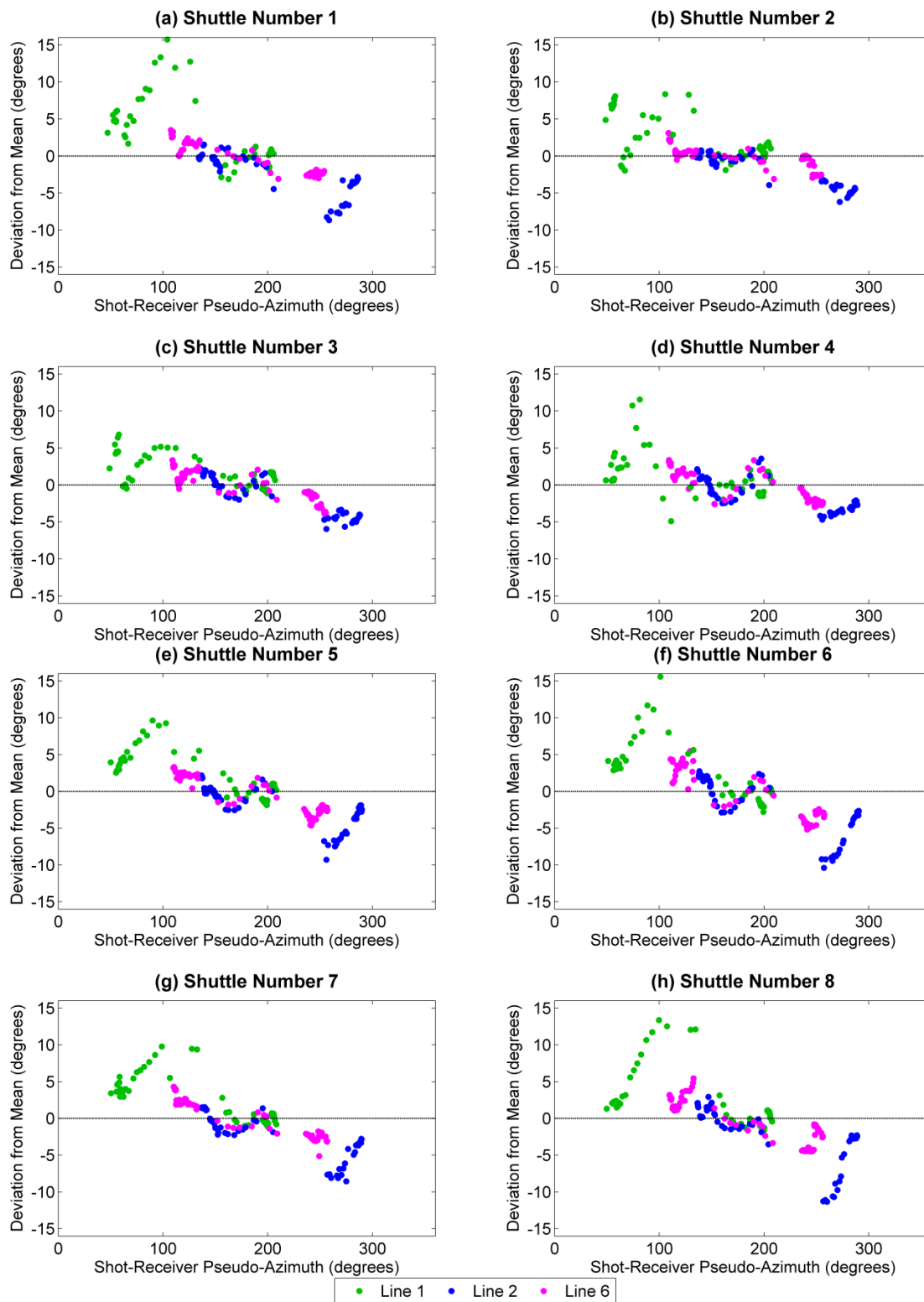


Figure 4.12: Deviation from mean orientation azimuth vs. pseudo azimuth for shuttle positions 1-8, combining data from all tool levels. Line 1 is shown in green, Line 2 in blue, and Line 6 in magenta.

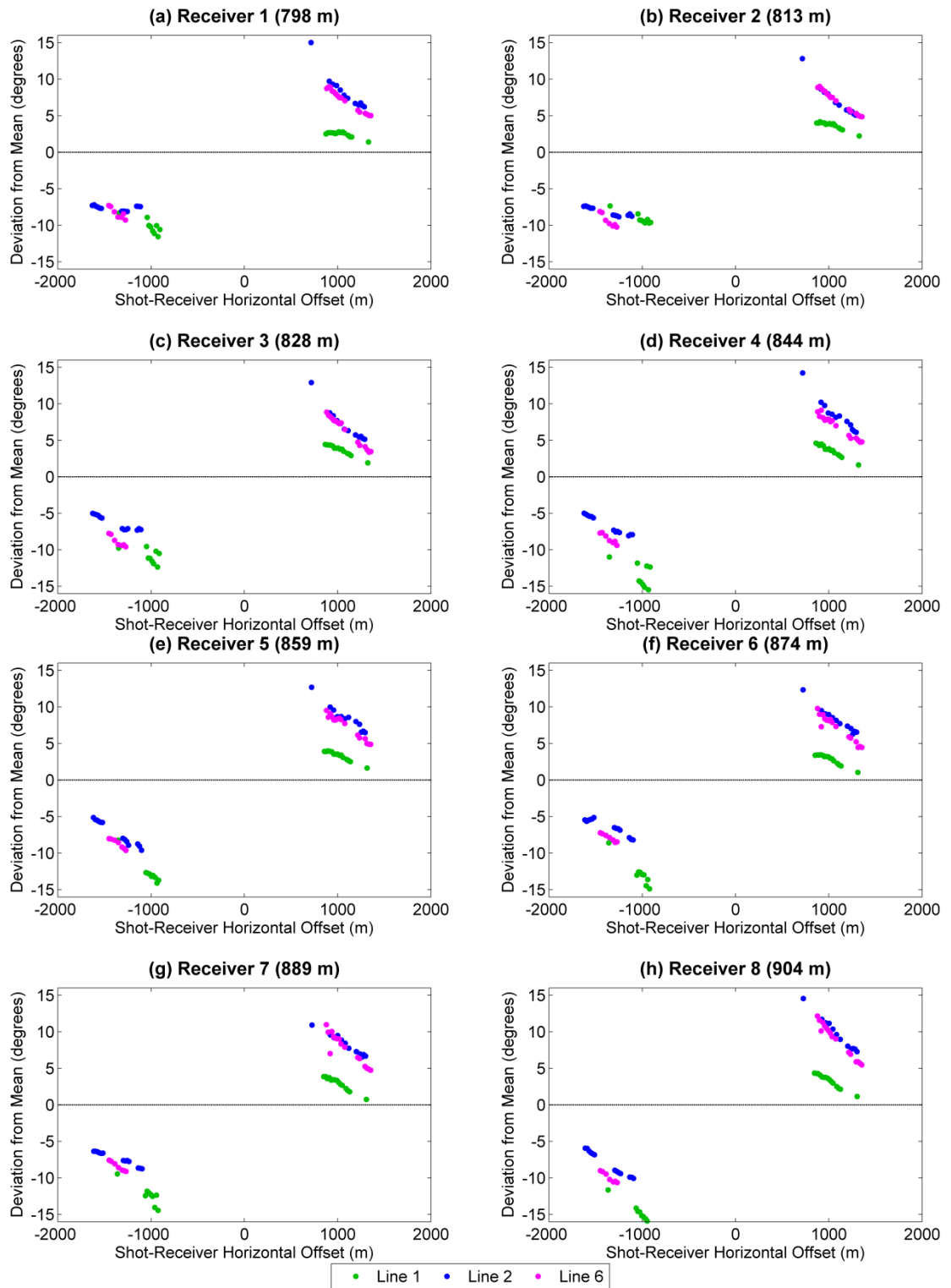


Figure 4.13: Deviation from mean orientation azimuth vs. offset for Receivers 1-8 (shallow-level), calculated under a vertical well assumption. Line 1 is shown in green, Line 2 in blue, and Line 6 in magenta.

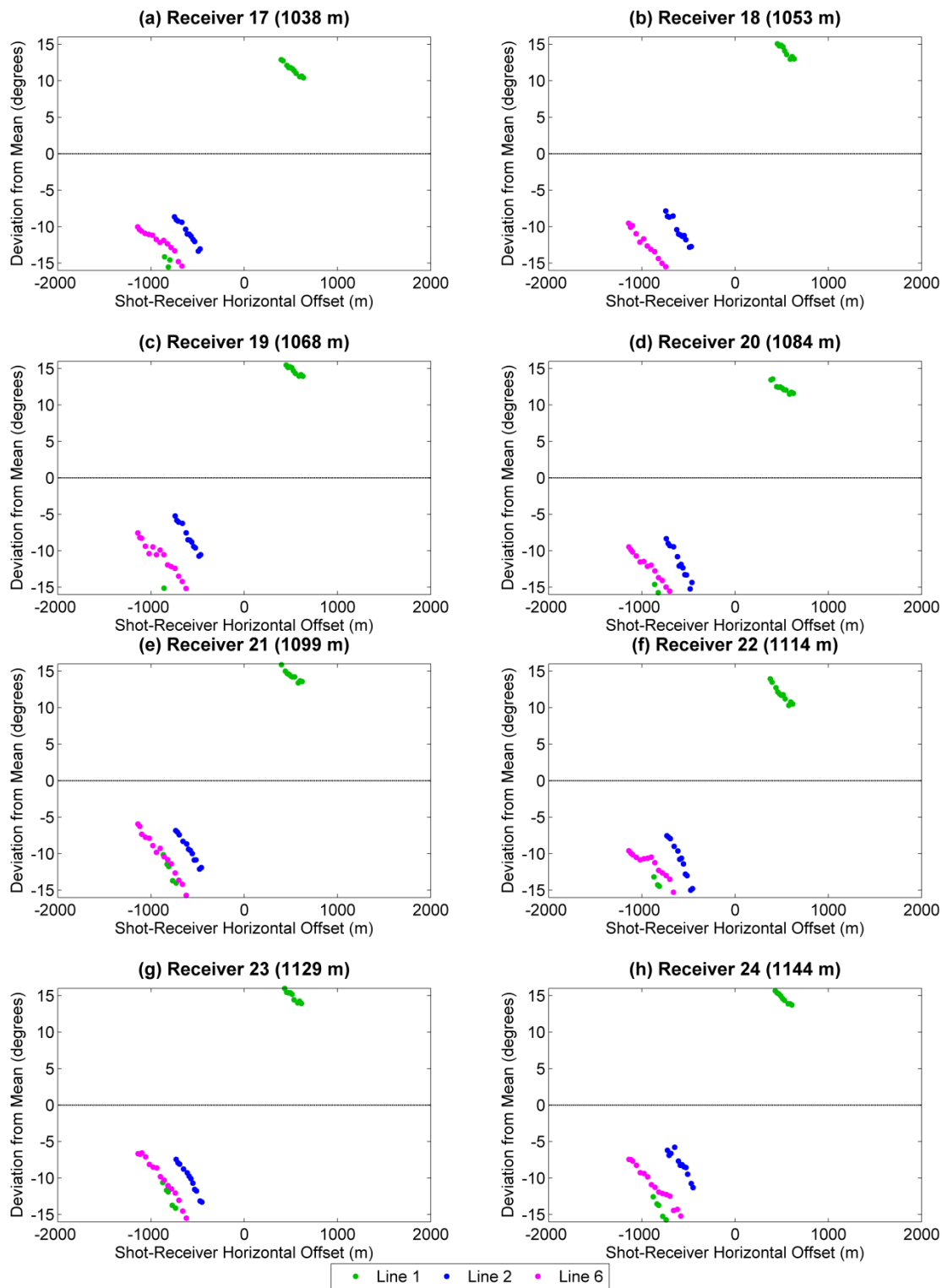


Figure 4.14: Deviation from mean orientation azimuth vs. offset for Receivers 17-24 (mid-level), calculated under a vertical well assumption. Line 1 is shown in green, Line 2 in blue, and Line 6 in magenta.

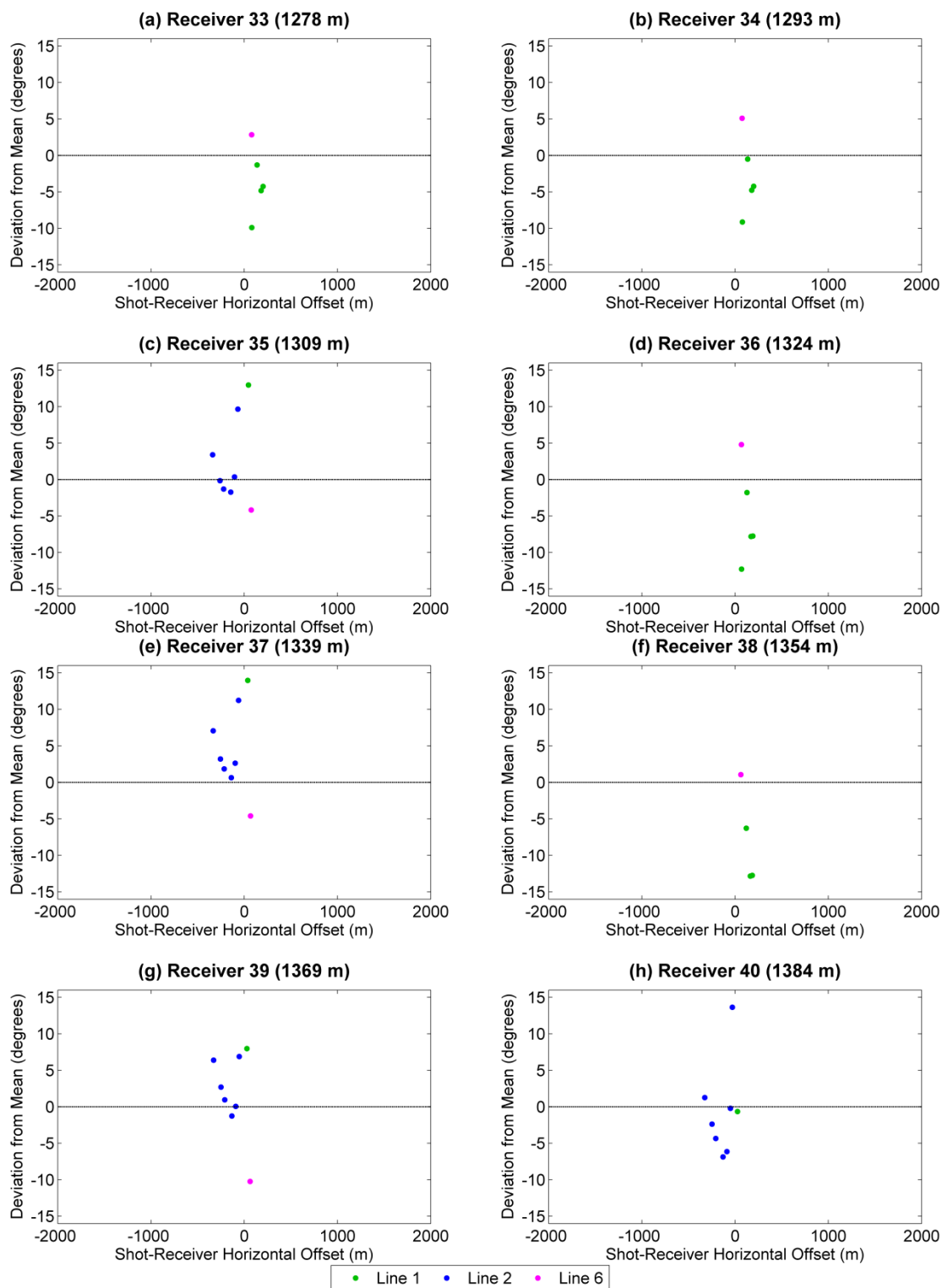


Figure 4.15: Deviation from mean orientation azimuth vs. offset for Receivers 33-40 (deep-level), calculated under a vertical well assumption. Line 1 is shown in green, Line 2 in blue, and Line 6 in magenta.

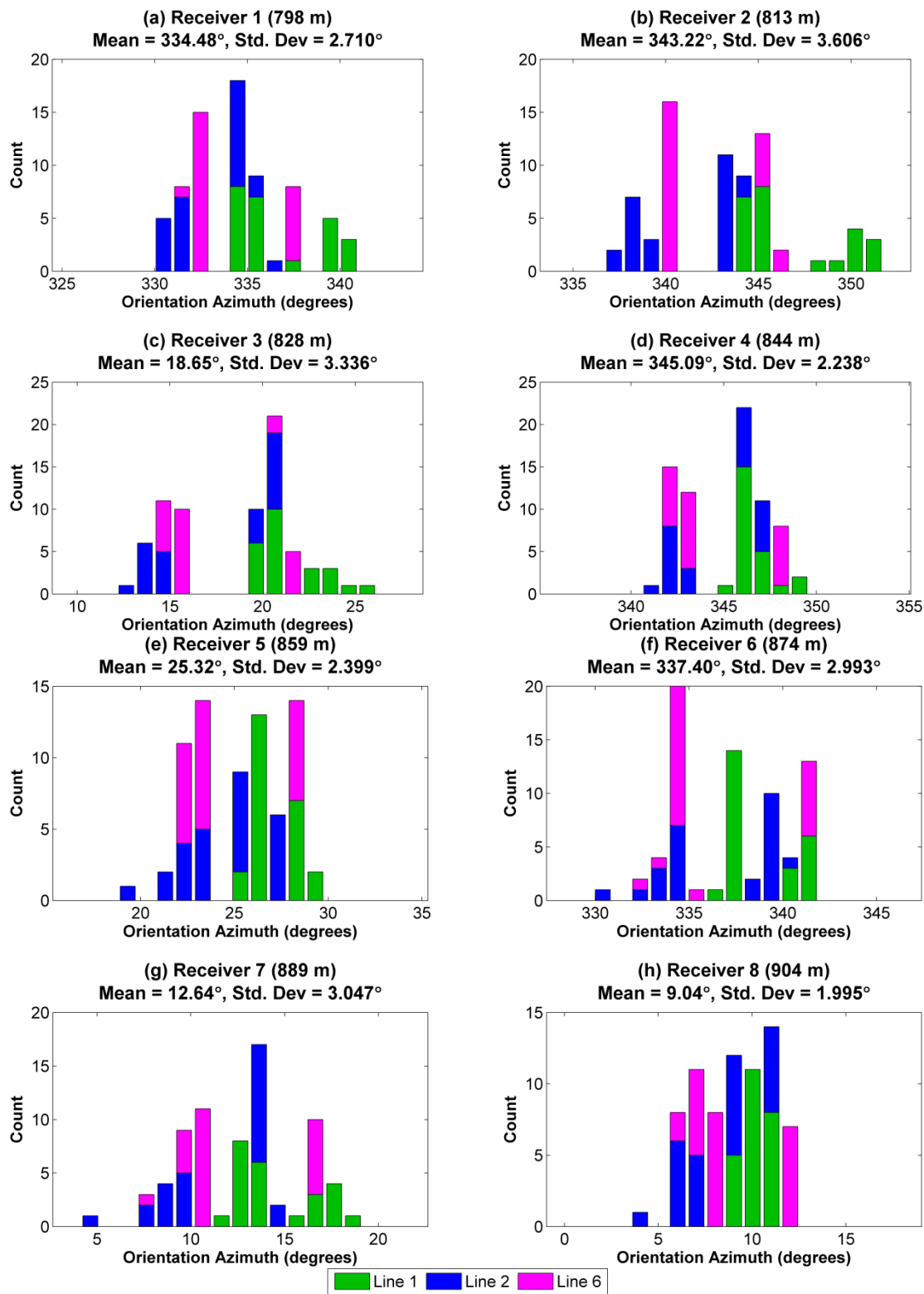


Figure 4.16: Orientation azimuth histograms for Receivers 1-8 (shallow-level). Line 1 is shown in green, Line 2 in blue, and Line 6 in magenta.

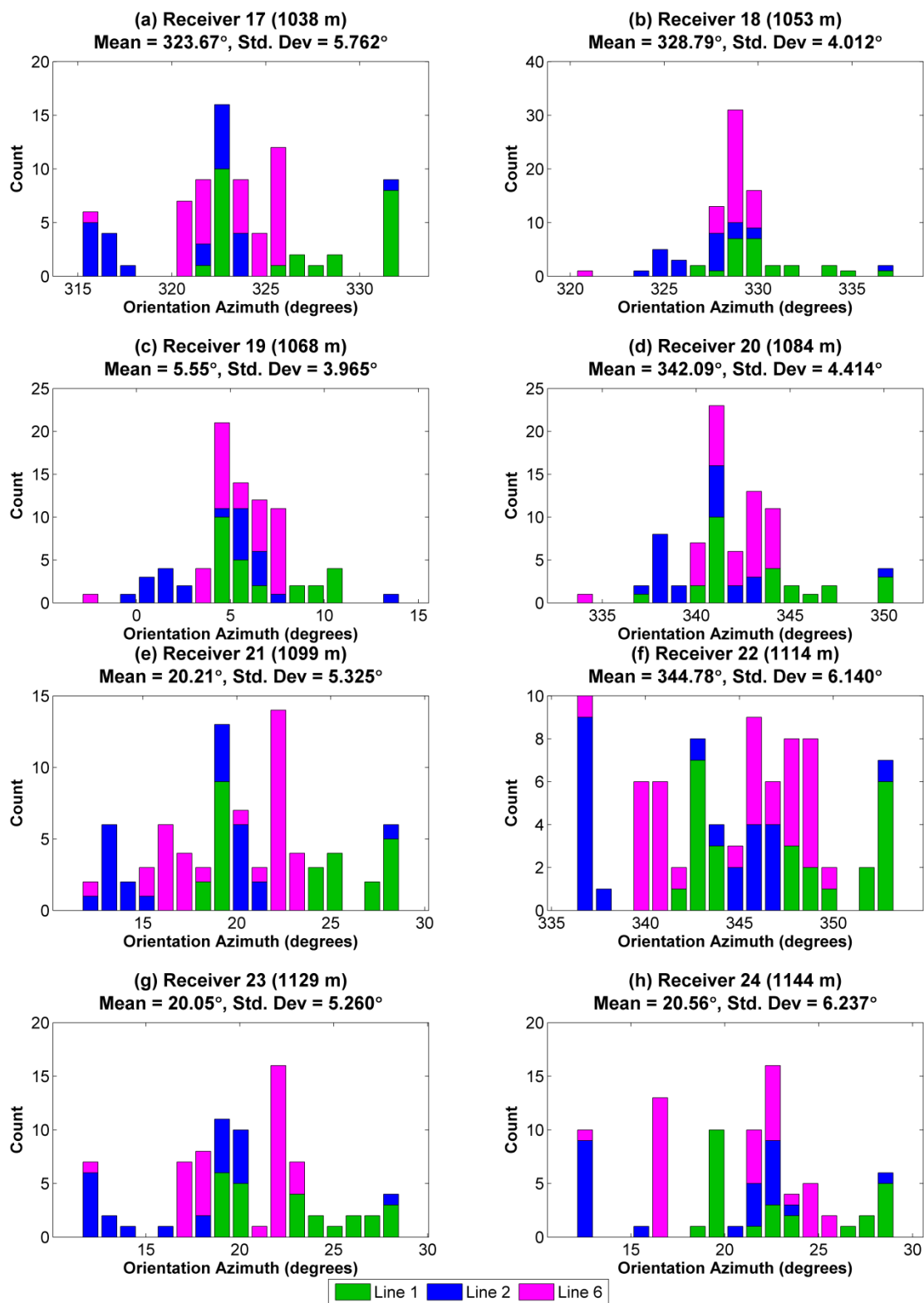


Figure 4.17: Orientation azimuth histograms for Receivers 17-24 (mid-level). Line 1 is shown in green, Line 2 in blue, and Line 6 in magenta.

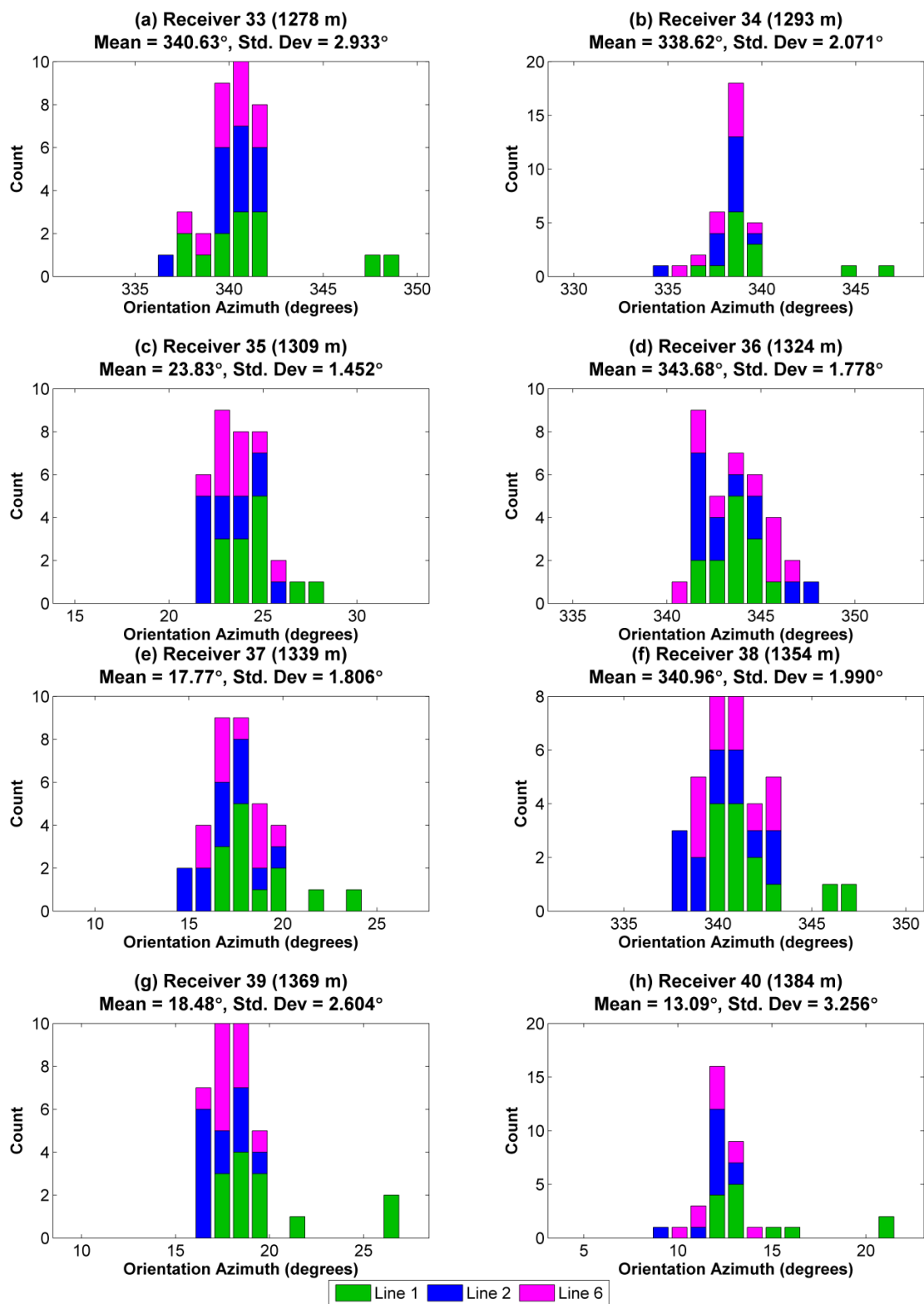


Figure 4.18: Orientation azimuth histograms for Receivers 30-40 (deep-level). Line 1 is shown in green, Line 2 in blue, and Line 6 in magenta.

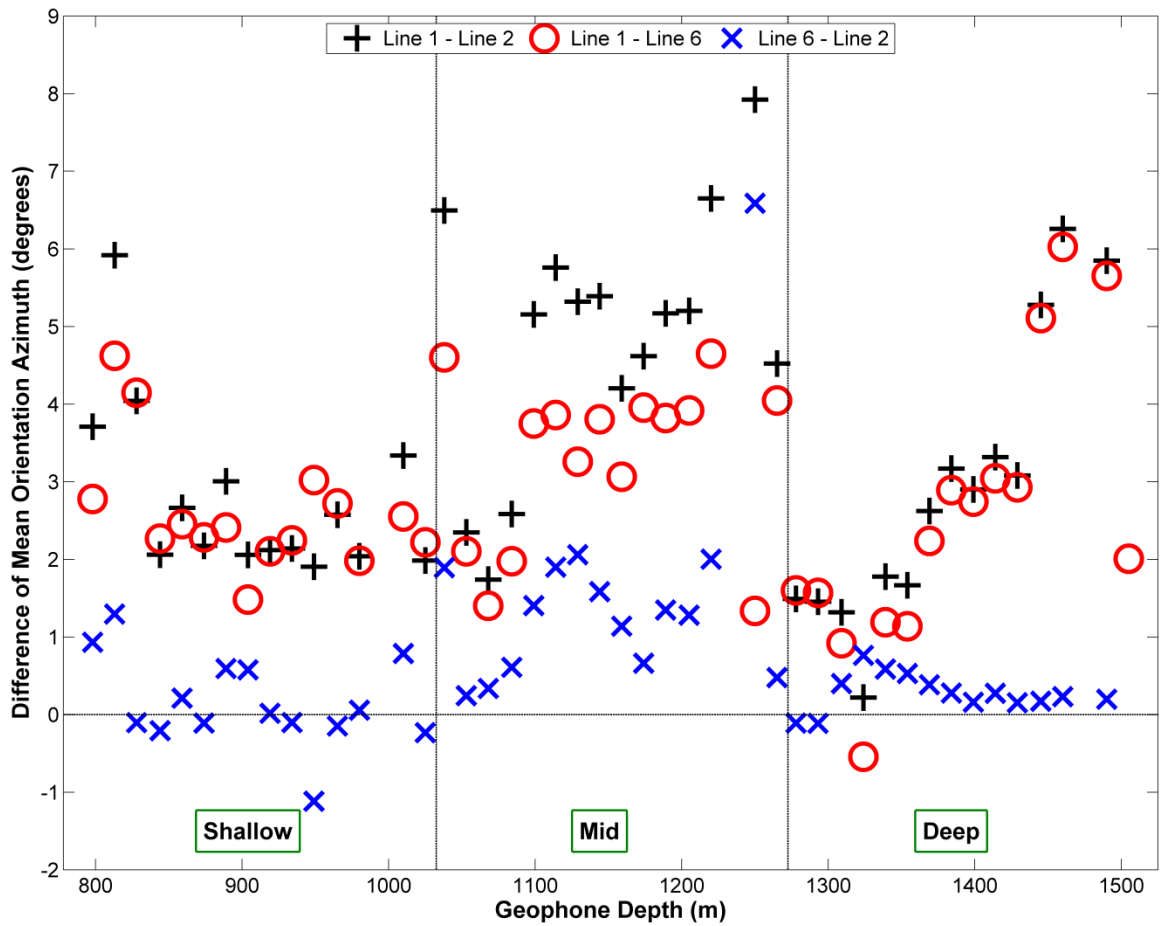


Figure 4.19: Differences in mean orientation azimuth for each geophone depth. Differences between Line 1 and 2 are shown in black; differences between Line 1 and 6 are shown in red; and differences between Line 6 and 2 are shown in blue.

Table 4.2: Geophone orientation statistics for shallow-level receivers.

| Receiver Number | Geophone Depth (m) | Line 1 Mean(°) | Line 1 St Dev (°) | Line 2 Mean(°) | Line 2 St Dev (°) | Line 6 Mean(°) | Line 6 St Dev (°) | Overall Mean (°) | Overall St Dev (°) |
|-----------------|--------------------|----------------|-------------------|----------------|-------------------|----------------|-------------------|------------------|--------------------|
| 1 | 798 | 336.5 | 2.18 | 333.1 | 1.90 | 333.9 | 2.42 | 334.5 | 2.60 |
| 2 | 813 | 346.6 | 2.64 | 341.0 | 2.50 | 342.2 | 2.33 | 343.3 | 3.47 |
| 3 | 828 | 21.3 | 1.80 | 17.5 | 3.27 | 17.3 | 2.86 | 18.7 | 3.26 |
| 4 | 844 | 346.4 | 0.98 | 344.6 | 2.15 | 344.3 | 2.55 | 345.1 | 2.19 |
| 5 | 859 | 26.9 | 1.18 | 24.5 | 2.24 | 24.6 | 2.59 | 25.3 | 2.34 |
| 6 | 874 | 338.8 | 1.74 | 336.9 | 2.99 | 336.6 | 3.44 | 337.4 | 2.93 |
| 7 | 889 | 14.3 | 2.11 | 11.6 | 2.92 | 12.0 | 3.23 | 12.7 | 3.00 |
| 8 | 904 | 10.1 | 0.85 | 8.3 | 2.05 | 8.7 | 2.21 | 9.0 | 1.94 |
| 9 | 919 | 22.8 | 0.94 | 21.0 | 2.84 | 20.8 | 2.55 | 21.5 | 2.42 |
| 10 | 934 | 27.4 | 2.58 | 25.5 | 4.24 | 25.2 | 3.98 | 26.0 | 3.75 |
| 11 | 949 | 373.0 | 2.58 | 371.3 | 4.58 | 370.0 | 4.06 | 371.4 | 3.98 |
| 12 | 965 | 371.7 | 2.96 | 369.3 | 3.12 | 369.0 | 2.52 | 370.0 | 3.09 |
| 13 | 980 | 366.5 | 2.35 | 364.7 | 2.23 | 364.6 | 2.19 | 365.3 | 2.40 |
| 14 | 995 | 216.9 | 15.05 | NaN | NaN | 264.0 | 18.24 | 239.9 | 28.97 |
| 15 | 1010 | 151.0 | 1.59 | 147.9 | 1.80 | 148.5 | 1.26 | 149.1 | 2.07 |
| 16 | 1025 | 106.8 | 1.47 | 105.0 | 1.45 | 104.6 | 0.94 | 105.5 | 1.60 |

Table 4.3: Geophone orientation statistics for mid-level receivers.

| Receiver Number | Geophone Depth (m) | Line 1 Mean(°) | Line 1 St Dev (°) | Line 2 Mean(°) | Line 2 St Dev (°) | Line 6 Mean(°) | Line 6 St Dev (°) | Overall Mean (°) | Overall St Dev (°) |
|-----------------|--------------------|----------------|-------------------|----------------|-------------------|----------------|-------------------|------------------|--------------------|
| 17 | 1038 | 327.6 | 6.02 | 320.9 | 6.15 | 322.9 | 4.24 | 323.8 | 5.97 |
| 18 | 1053 | 330.6 | 2.74 | 328.0 | 5.53 | 328.3 | 3.58 | 328.9 | 4.10 |
| 19 | 1068 | 6.9 | 2.76 | 4.9 | 5.55 | 5.3 | 3.77 | 5.7 | 4.14 |
| 20 | 1084 | 343.9 | 4.29 | 341.1 | 5.27 | 341.8 | 3.91 | 342.2 | 4.54 |
| 21 | 1099 | 23.5 | 4.67 | 18.0 | 6.31 | 19.5 | 4.71 | 20.3 | 5.59 |
| 22 | 1114 | 348.3 | 5.87 | 342.2 | 7.37 | 344.2 | 5.17 | 344.9 | 6.46 |
| 23 | 1129 | 23.2 | 4.01 | 17.5 | 6.70 | 19.7 | 4.56 | 20.2 | 5.52 |
| 24 | 1144 | 24.0 | 5.51 | 18.2 | 8.18 | 19.9 | 5.09 | 20.7 | 6.55 |
| 25 | 1159 | 37.4 | 4.30 | 32.8 | 7.94 | 34.1 | 4.79 | 34.7 | 5.94 |
| 26 | 1174 | 37.1 | 4.38 | 32.1 | 7.46 | 32.9 | 4.35 | 33.9 | 5.74 |
| 27 | 1189 | 382.7 | 3.39 | 377.1 | 8.53 | 378.6 | 5.15 | 379.5 | 6.25 |
| 28 | 1205 | 380.4 | 4.85 | 374.7 | 8.61 | 376.2 | 5.18 | 377.1 | 6.58 |
| 29 | 1220 | 376.2 | 6.44 | 369.1 | 9.62 | 371.2 | 6.09 | 372.1 | 7.78 |
| 30 | 1235 | 230.6 | 31.35 | NaN | NaN | 279.3 | 30.69 | 258.7 | 39.14 |
| 31 | 1250 | 155.3 | 7.54 | 146.9 | 8.55 | 153.7 | 28.22 | 152.3 | 19.31 |
| 32 | 1265 | 99.5 | 4.38 | 94.5 | 7.84 | 95.2 | 4.87 | 96.3 | 6.05 |

Table 4.4: Geophone orientation statistics for deep-level receivers.

| Receiver Number | Geophone Depth (m) | Line 1 Mean(°) | Line 1 St Dev (°) | Line 2 Mean(°) | Line 2 St Dev (°) | Line 6 Mean(°) | Line 6 St Dev (°) | Overall Mean (°) | Overall St Dev (°) |
|-----------------|--------------------|----------------|-------------------|----------------|-------------------|----------------|-------------------|------------------|--------------------|
| 33 | 1278 | 342.0 | 4.75 | 340.2 | 1.79 | 340.0 | 1.66 | 340.8 | 3.26 |
| 34 | 1293 | 340.0 | 3.31 | 338.1 | 1.36 | 338.0 | 1.48 | 338.8 | 2.43 |
| 35 | 1309 | 25.0 | 1.99 | 23.3 | 1.10 | 23.6 | 1.26 | 24.0 | 1.68 |
| 36 | 1324 | 344.0 | 0.90 | 343.4 | 1.84 | 344.1 | 1.75 | 343.8 | 1.52 |
| 37 | 1339 | 19.2 | 2.56 | 17.0 | 1.21 | 17.5 | 1.02 | 18.0 | 2.01 |
| 38 | 1354 | 342.3 | 2.72 | 340.2 | 1.57 | 340.8 | 1.18 | 341.2 | 2.16 |
| 39 | 1369 | 20.5 | 4.18 | 17.5 | 0.94 | 17.7 | 1.02 | 18.7 | 2.96 |
| 40 | 1384 | 15.5 | 5.22 | 11.9 | 1.07 | 12.2 | 1.68 | 13.3 | 3.69 |
| 41 | 1399 | 33.9 | 5.25 | 30.6 | 1.15 | 30.7 | 1.90 | 31.9 | 3.70 |
| 42 | 1414 | 30.4 | 5.55 | 26.7 | 1.78 | 27.0 | 2.45 | 28.1 | 4.07 |
| 43 | 1429 | 371.1 | 6.06 | 367.6 | 2.20 | 367.8 | 2.97 | 368.9 | 4.43 |
| 44 | 1445 | 359.3 | 8.38 | 353.6 | 3.59 | 353.6 | 4.36 | 355.7 | 6.46 |
| 45 | 1460 | 338.9 | 10.09 | 332.3 | 4.40 | 332.6 | 4.68 | 334.8 | 7.64 |
| 46 | 1475 | 181.2 | 41.42 | NaN | NaN | 179.2 | 14.49 | 180.3 | 31.98 |
| 47 | 1490 | 210.8 | 10.33 | 204.4 | 2.60 | 204.6 | 3.17 | 206.8 | 7.22 |
| 48 | 1505 | 93.3 | 3.82 | 90.6 | 0.97 | 90.6 | 1.47 | 91.6 | 2.77 |

Table 4.5: Average standard deviations for each tool position, excluding the receiver at shuttle position 14.

| Tool Position | Line 1 Average St Dev (°) | Line 2 Average St Dev (°) | Line 6 Average St Dev (°) | Overall Average St Dev (°) |
|----------------|---------------------------|---------------------------|---------------------------|----------------------------|
| Shallow | 1.86 | 2.69 | 2.61 | 2.74 |
| Mid | 4.74 | 7.31 | 6.25 | 6.70 |
| Deep | 5.01 | 1.84 | 2.14 | 3.73 |
| Overall | 3.87 | 3.95 | 3.67 | 4.39 |

A spider plot for the receivers at shuttle positions 1 and 3 is shown in Figure 4.20. Each of the three tool positions is shown for these receivers; the differences in orientation at each level appear similar, which is expected since they are on the same tool. Overall, the change in mean orientation azimuth for each shuttle position appears to be most consistent between the shallow and mid tool levels, and Tool Number 1 shows more consistent rotation than Tool Number 2 (Figure 4.21). However, it should be noted that the differences in pseudo-coordinates at each tool level will cause some expected

inconsistencies that will become more influential where the well has stronger changes in its deviation; for this study, in the deeper part of the well.

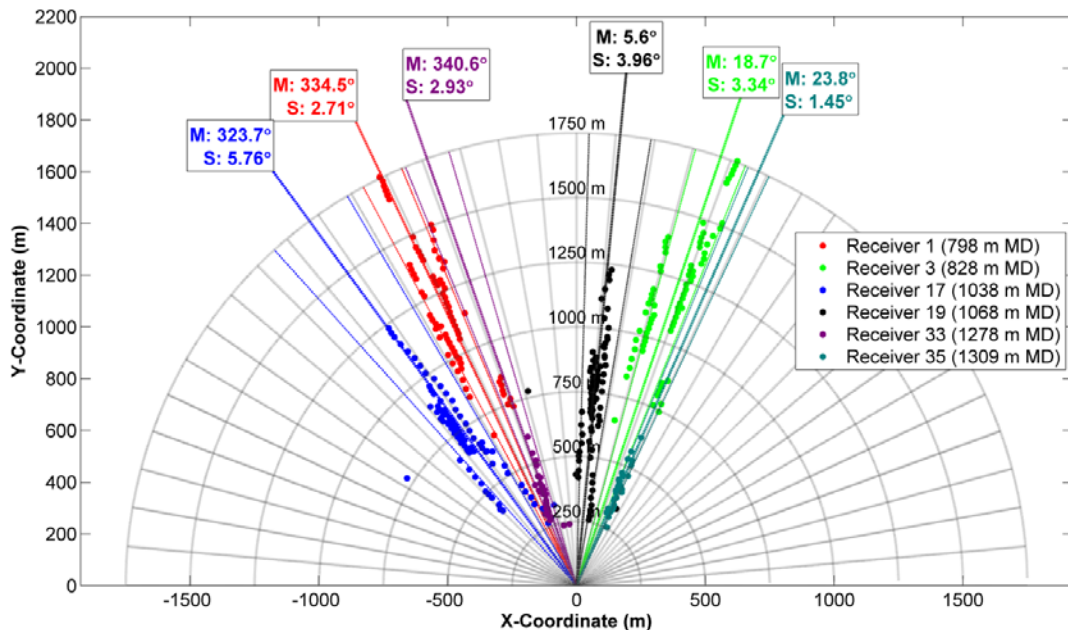


Figure 4.20: Spider plot showing the first and third receivers at each level; angular grid spacing is 5° and radial grid spacing is 250 m.

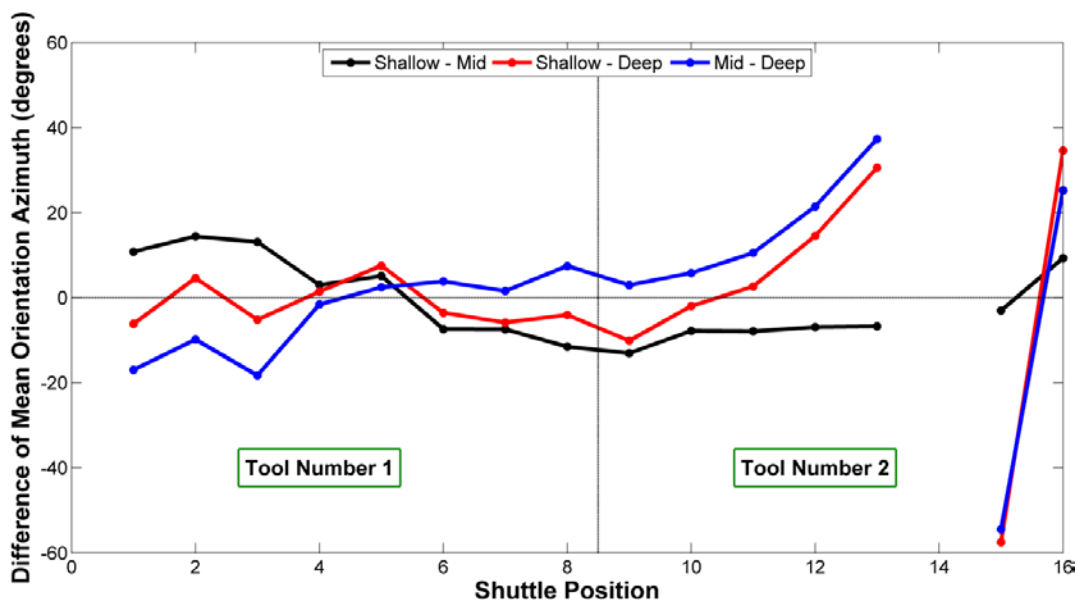


Figure 4.21: Difference of mean orientation azimuth for each shuttle position; differences from shallow-mid tool level are shown in black, shallow-deep tool level in red and mid-deep tool level in blue.

4.5 Modelling Deviation Error

In order to examine the effect of errors in the well deviation survey, a simple numerical experiment was performed. The azimuth and inclination angles were randomly varied by $\pm 2^\circ$, using a Gaussian distribution (Figure 4.22). The cumulative effects of these errors are shown in Figure 4.23, given as total 3-D positioning errors. Overall positioning errors remain below 3 m, and in this case are primarily affected by errors in the inclination angle.

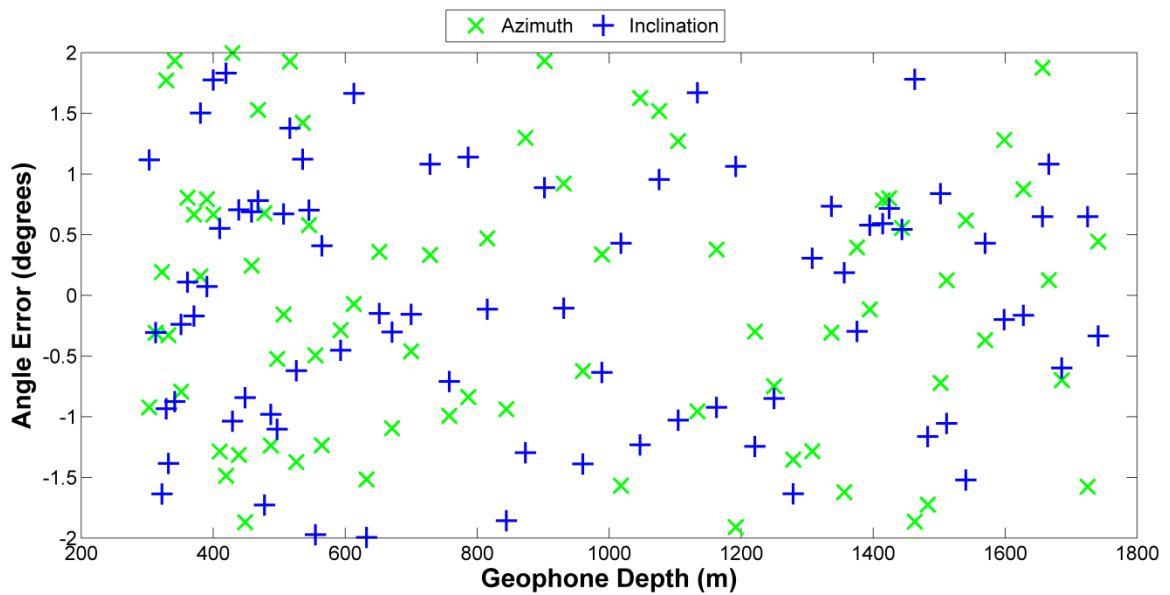


Figure 4.22: Randomly generated error in deviation azimuth angle (green) and inclination angle (blue).

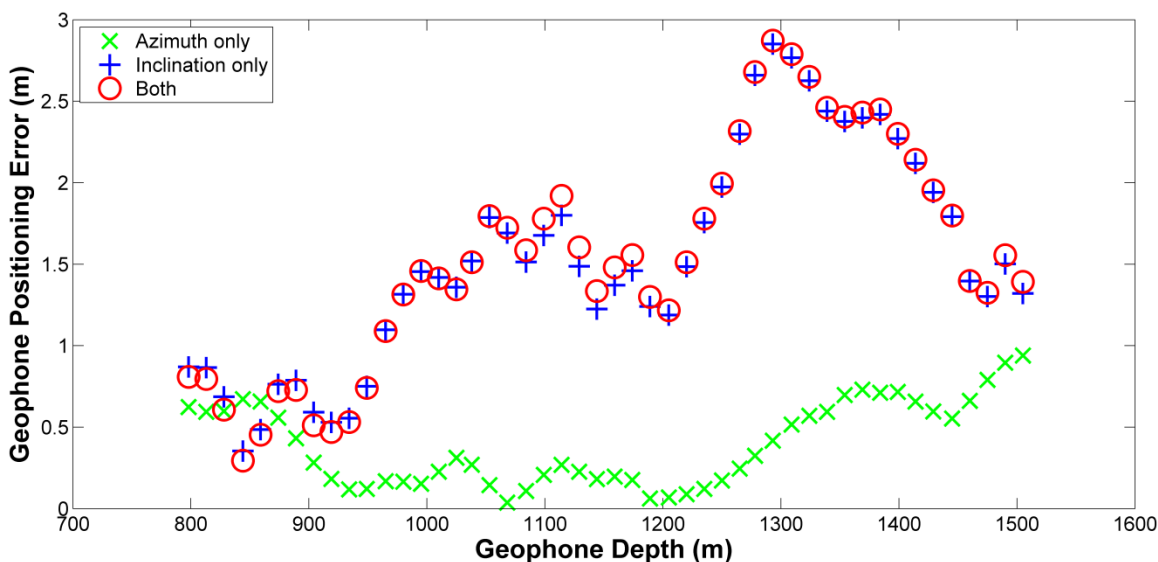


Figure 4.23: Cumulative geophone positioning error resulting from modelled deviation survey error. Isolated effects of azimuth and inclination are shown in green and blue respectively, and overall effects are shown in red.

The theoretical orientations were then calculated for 48 receivers at measured depths matching those of the original Violet Grove tool positions. This was done for four cases:

- 1) The deviation survey contained no error.
- 2) The deviation survey had error only in the azimuth angle.
- 3) The deviation survey had error only in the inclination angle.
- 4) The deviation survey had error in both the azimuth and inclination angles.

Pseudo x and y axes were found using Equations 4.3 and 4.4, and the horizontal components of the geophones were oriented parallel to these axes. Source locations were chosen to match those of the Violet Grove survey, and the incoming angles at each geophone were calculated; the amplitude that would be recorded by each component was then found. It should be noted that raybending was not taken into consideration for this process. Finally, for all four cases, orientation analysis was performed assuming the original deviation survey, and error from the known orientation was found. Figures 4.24 to 4.26 show the results of this analysis for Receivers 1, 15 and 48 (MDs of 798 m, 1159 m and 1505 m), and Table 4.6 summarises the statistics for odd-numbered receivers.

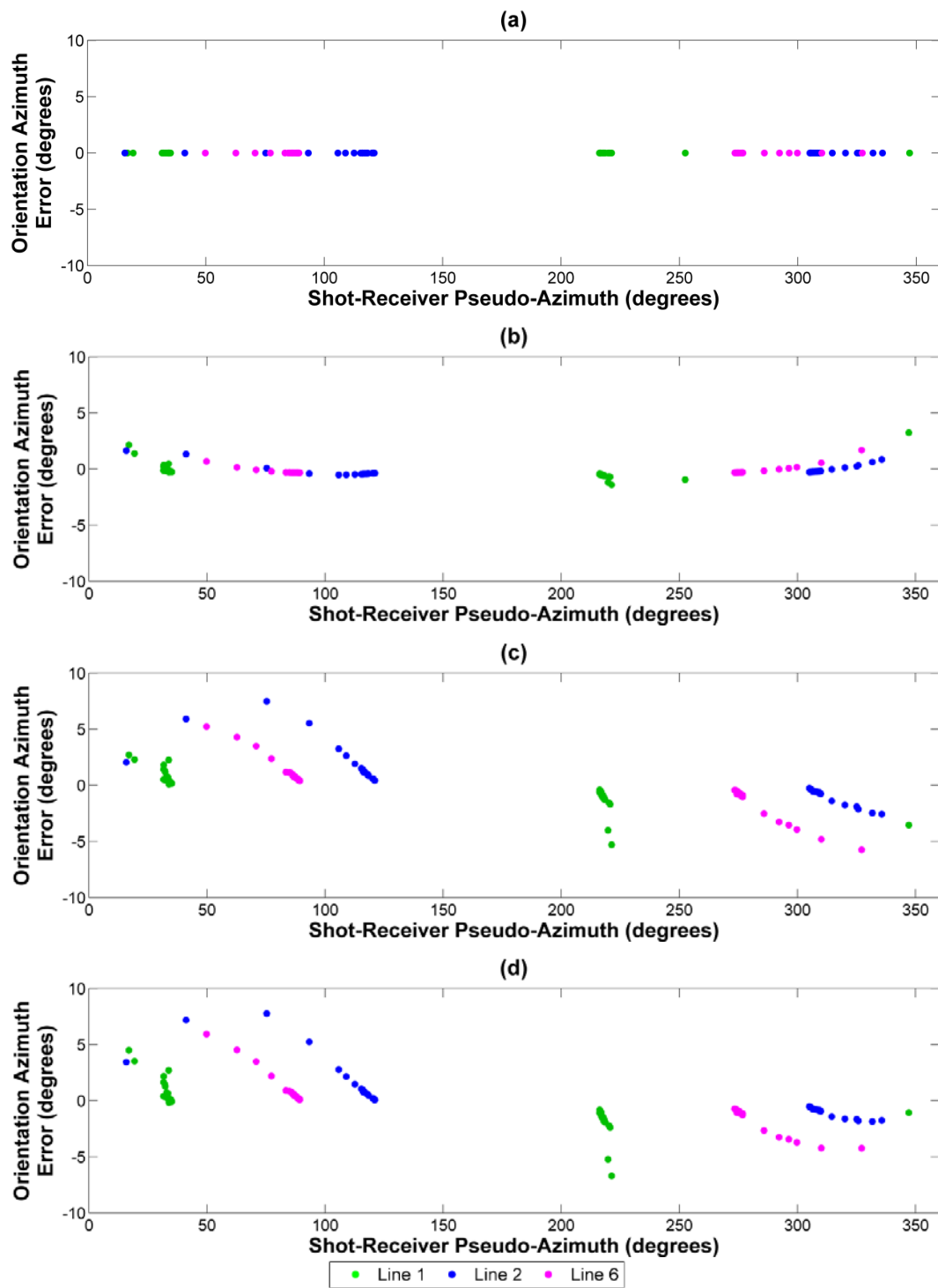


Figure 4.24: Modelled errors in orientation angle for Receiver 1 (798 m), resulting from (a) correct deviation survey, (b) errors in azimuth angle, (c) inclination angle, and (d) errors in both angles.

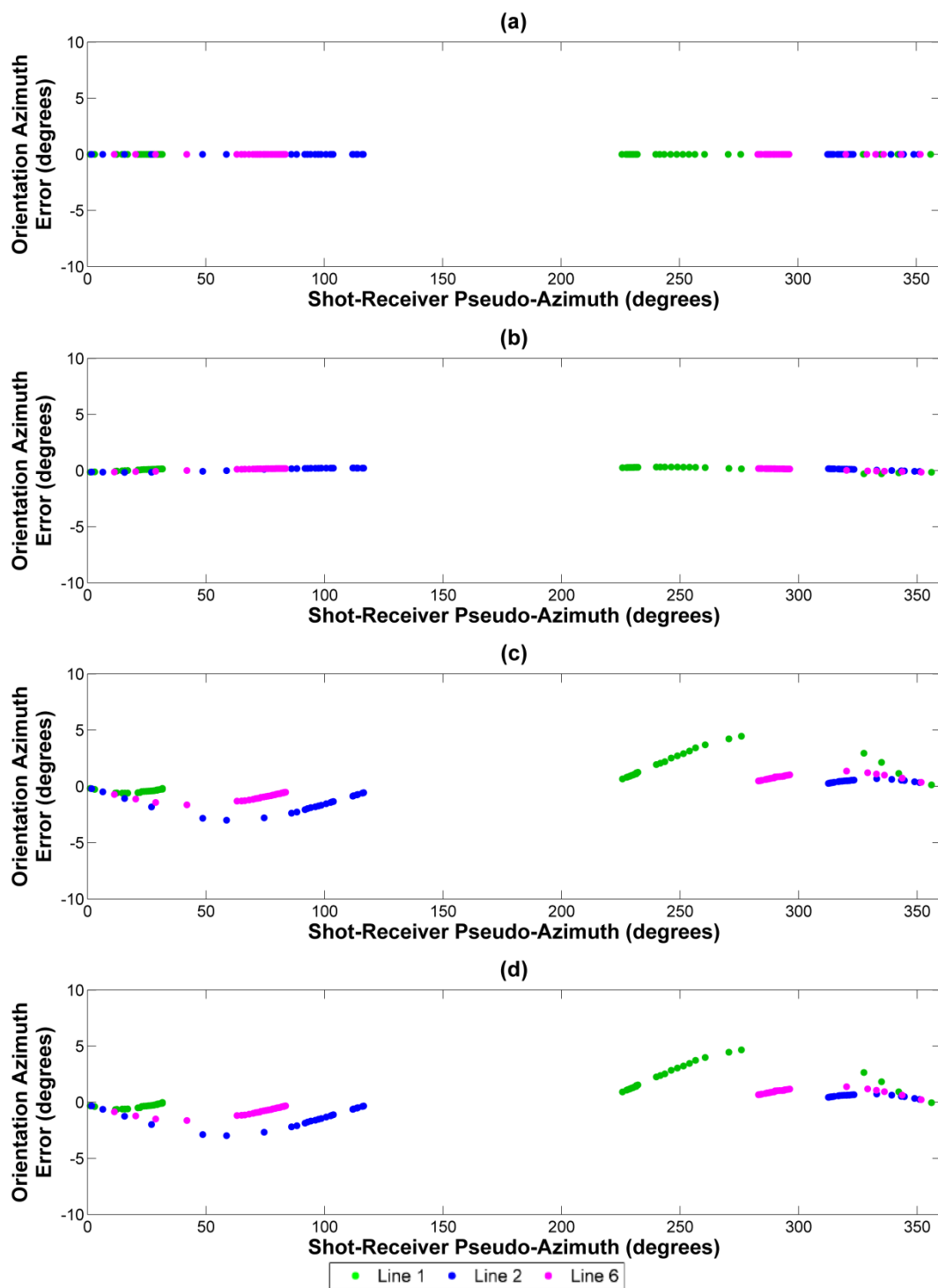


Figure 4.25: Modelled errors in orientation angle for Receiver 25 (1159 m), resulting from (a) correct deviation survey, (b) errors in azimuth angle, (c) inclination angle, and (d) errors in both angles.

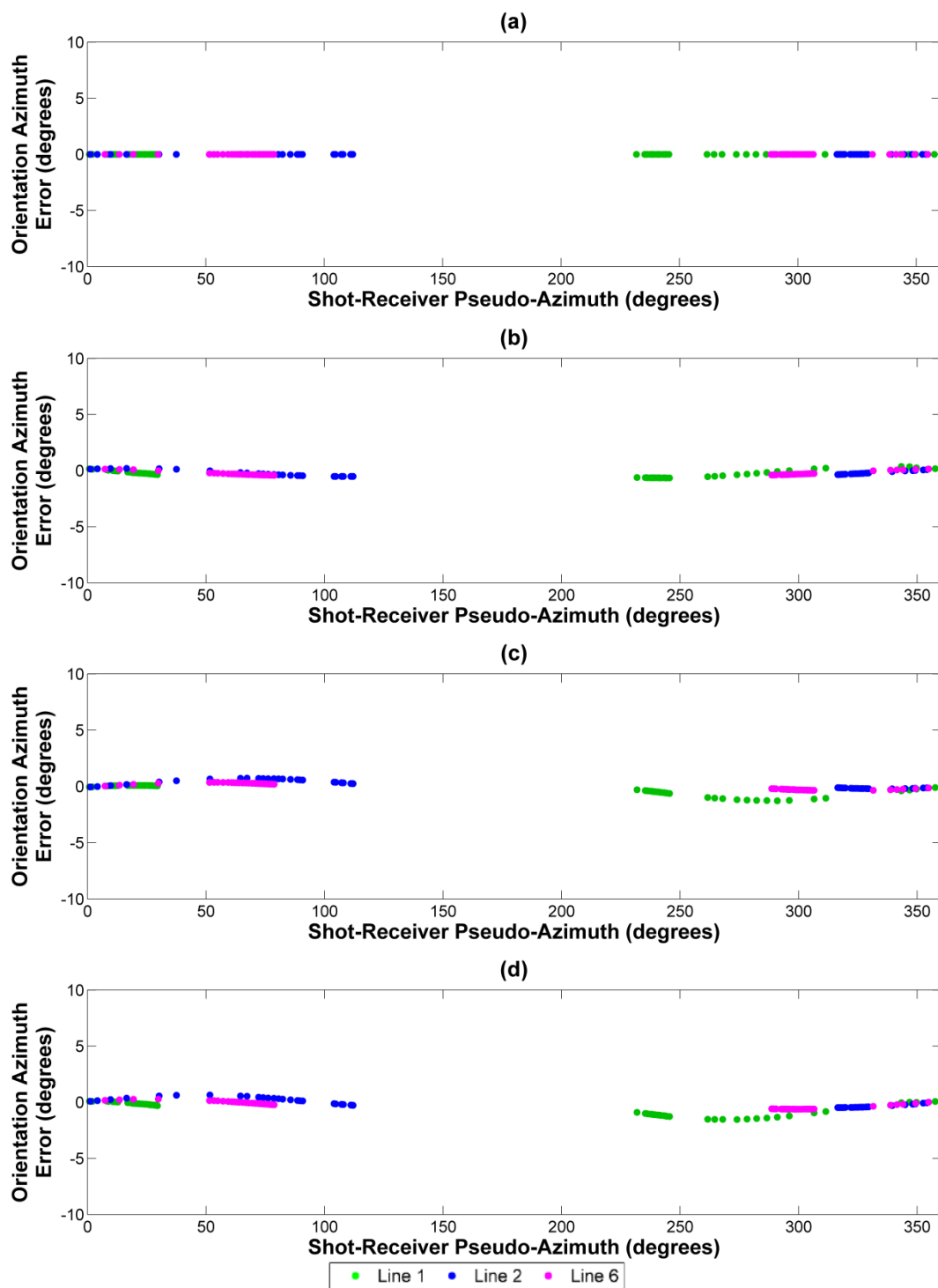


Figure 4.26: Modelled errors in orientation angle for Receiver 48 (1505 m), resulting from (a) correct deviation survey, (b) errors in azimuth angle, (c) inclination angle, and (d) errors in both angles.

Table 4.6: Geophone orientation statistics for modelled deviation surveys. Averages are calculated using all receivers.

| Receiver Depth (m) | No Error | | Azimuth | | Inclination | | Both | |
|-----------------------|-------------|--------------|-------------|--------------|-------------|--------------|-------------|--------------|
| | Mean (°) | St. Dev. (°) |
| 798 | 0.00 | 0.00 | -0.20 | 0.47 | -0.02 | 1.83 | -0.23 | 1.92 |
| 828 | 0.00 | 0.00 | -0.08 | 0.25 | 0.00 | 2.29 | -0.08 | 2.28 |
| 859 | 0.00 | 0.00 | 0.19 | 0.04 | 0.03 | 4.33 | 0.22 | 4.34 |
| 889 | 0.00 | 0.00 | 1.26 | 1.09 | -0.01 | 0.34 | 1.25 | 1.23 |
| 919 | 0.00 | 0.00 | 1.02 | 0.87 | -0.05 | 0.68 | 0.97 | 1.10 |
| 949 | 0.00 | 0.00 | -0.02 | 0.03 | 0.08 | 2.15 | 0.06 | 2.15 |
| 980 | 0.00 | 0.00 | 0.03 | 0.00 | 0.08 | 2.08 | 0.12 | 2.08 |
| 1010 | 0.00 | 0.00 | -1.73 | 12.96 | -0.02 | 0.16 | -1.75 | 12.97 |
| 1038 | 0.00 | 0.00 | 1.44 | 13.03 | 0.05 | 1.57 | 1.50 | 13.11 |
| 1068 | 0.00 | 0.00 | 1.13 | 0.86 | -0.05 | 0.55 | 1.07 | 1.02 |
| 1099 | 0.00 | 0.00 | 0.96 | 0.73 | 0.06 | 1.34 | 1.03 | 1.60 |
| 1129 | 0.00 | 0.00 | -0.45 | 0.29 | -0.15 | 2.18 | -0.59 | 2.22 |
| 1159 | 0.00 | 0.00 | 0.14 | 0.12 | 0.06 | 1.21 | 0.20 | 1.23 |
| 1189 | 0.00 | 0.00 | -1.23 | 0.79 | -0.12 | 1.54 | -1.32 | 1.78 |
| 1220 | 0.00 | 0.00 | -0.25 | 0.17 | 0.13 | 2.44 | -0.13 | 2.43 |
| 1250 | 0.00 | 0.00 | -0.54 | 0.35 | 0.10 | 1.81 | -0.45 | 1.80 |
| 1278 | 0.00 | 0.00 | -0.97 | 0.61 | 0.21 | 3.45 | -0.79 | 3.44 |
| 1309 | 0.00 | 0.00 | -0.86 | 0.56 | -0.05 | 0.43 | -0.90 | 0.71 |
| 1339 | 0.00 | 0.00 | -0.29 | 0.23 | -0.14 | 1.15 | -0.42 | 1.18 |
| 1369 | 0.00 | 0.00 | -0.17 | 0.16 | 0.02 | 0.45 | -0.15 | 0.45 |
| 1399 | 0.00 | 0.00 | 0.08 | 0.01 | -0.12 | 0.96 | -0.04 | 0.96 |
| 1429 | 0.00 | 0.00 | 0.51 | 0.26 | -0.13 | 1.13 | 0.36 | 1.15 |
| 1460 | 0.00 | 0.00 | -0.94 | 0.60 | -0.35 | 2.87 | -1.24 | 2.93 |
| 1490 | 0.00 | 0.00 | -0.89 | 0.55 | 0.07 | 0.95 | -0.83 | 1.06 |
| Average | 0.00 | 0.00 | 0.68 | 1.47 | 0.09 | 1.63 | 0.67 | 2.53 |

Overall, the scatter in orientation angle appears to be about the same as the error in the deviation survey – approximately 2° in this case. The error in the mean angle, however, was only about a third of this. When considering error in both the azimuth and inclination of the deviation survey, scatter in orientation angle ranged from 0.06° to 13.19°; a total of 5 receivers showed a scatter less than 0.5°, while 4 receivers showed scatter greater than 10°. While the errors in inclination angle increased scatter of the calculated orientation, the errors in the azimuth angle of the well deviation provided a much greater contribution

to the error in the mean orientation angle of the receiver. Thus, the effects due to error in the deviation survey varied greatly.

4.6 Discussion

The results of this study show that the orientation azimuths had good consistency in the shallow and deep-level tool positions, and slightly worse consistency in the mid-level tool position. The reason that this tool position had significantly more scatter in orientation azimuths than the other two is currently unknown; perhaps there was a coupling problem with the borehole in this depth range that led to poorer data quality. Results from Chapters 2 and 3 indicate that the precision of the orientation azimuth analysis is strongly dependent on noise, source-receiver offset and receiver depth, which appears to be the case for this field example. Finally, changes in the mean orientation angles at each tool position appeared visually consistent in the transition between shallow and mid tool positions, but began to deviate substantially for Tool 2 in the transition to the deep tool position. At about 1400 MD, the well deviation begins to change, which could provide a reason for this difference.

The deviation of the well adds another level of uncertainty to this analysis; any errors in the deviation survey will affect the analysis done for this study, although a vertical well suffers from this problem as well. Specifically, the magnitude of these uncertainties is proportional to an increased scatter in values of geophone orientation. In this case, errors of $\pm 2^\circ$ in the inclination and azimuth of the deviation survey generally increased the scatter in orientation azimuth by about 2.5° .

Perhaps the most interesting result seen in this study is the distinction in trends between the different source lines, particularly regarding Line 1, where the average separation of 3.7° from Line 2 and 3.0° from Line 6 could be a lithological indication rather than a statistical one; examination of the orientation azimuth vs. pseudo-offset plots provides even more compelling evidence that there are lithologic influences, such as lateral velocity heterogeneity, to this difference. Analysis of other field examples and synthetic models would provide some further insight; in fact, the orientation analysis performed in Chapter 2 produced azimuthally dependent trends similar to those found in

this study. Azimuthal anisotropy is a possible explanation of these trends, since there is a different directionality associated with each of the lines. Lateral raybending is another factor that must be considered, since the well is deviated. Even if the bedding is near-horizontal, the deviation of the well will cause the plane defined by the horizontal components of the receiver to be at an angle to the bedding. These effects will be modelled in the following two chapters.

4.7 Summary

- A method for examining borehole geophone orientation azimuths for the case of a deviated well was successfully developed. Ignoring the well deviation resulted in scatter in orientation azimuth increasing by at least a factor of 2; scatter of the deepest receivers increased by more than a factor of 10.
- Orientation azimuths, using all three lines, had an average standard deviation of 4.39° over all receivers, for all shots.
- Orientation azimuth consistency was best for the shallow-level tool position (2.74°); this was judged to be due to the shallower depth of receivers and farther source-well offsets. Orientation azimuth consistency was poorest for the mid-level tool position (6.70°).
- Rotation of each shuttle as the tools were brought up the well appeared consistent between the shallow- and mid-levels; it showed some deviation in the lower positions of the deep-level, where the deviation of the well began to change.
- A simple model was created that introduced errors within $\pm 2^\circ$ to the inclination and azimuth angles of the deviation survey; this translated to standard deviation in orientation angle of 2.53° across all 48 receiver depths, ranging from 0.06° to

13.19° for individual receivers.

- Orientation azimuth values calculated using sources from Line 1 were, on average, 3.7° higher than Line 2 and 3.0° higher than Line 6. This could be related to geological properties of the area, such as azimuthal anisotropy and lateral velocity heterogeneity, resulting in lateral raybending.

Chapter Five: Dipping Beds

5.1 Introduction

In this chapter I report on the modelling of the effects of dipping interfaces on geophone orientation analysis. These effects are modelled using raytracing code I developed in MATLAB and compared to results output by TIGER. The characteristics of these effects are studied to determine their signature and expected impact on real data. Results shown in this chapter are compared to the results of all three field studies in Chapter 8.

5.2 Raytracing

5.2.1 Algorithm

5.2.1.1 Overview

In order to examine the effects of dipping beds on geophone orientation azimuth, code was developed in MATLAB to perform 3D raytracing across a single planar velocity interface. Since it was important to have a fixed receiver location, the rays were traced from the receiver to a source location on the surface; under seismic reciprocity, this is equivalent to tracing the ray from the same source to the receiver. Additionally, in order to simplify calculations, the recording surface was made horizontal.

The final raytracing algorithm is outlined in Figure 5.1. This algorithm was iterated over many values of the ray launch angle and direction, providing a large population of source locations at the surface. The computed source-well azimuth was then compared to the launch direction; the difference between these angles was used as the modelled deviation in geophone orientation angle. Figure 5.2 shows a cross-sectional, schematic view of the geologic model used.

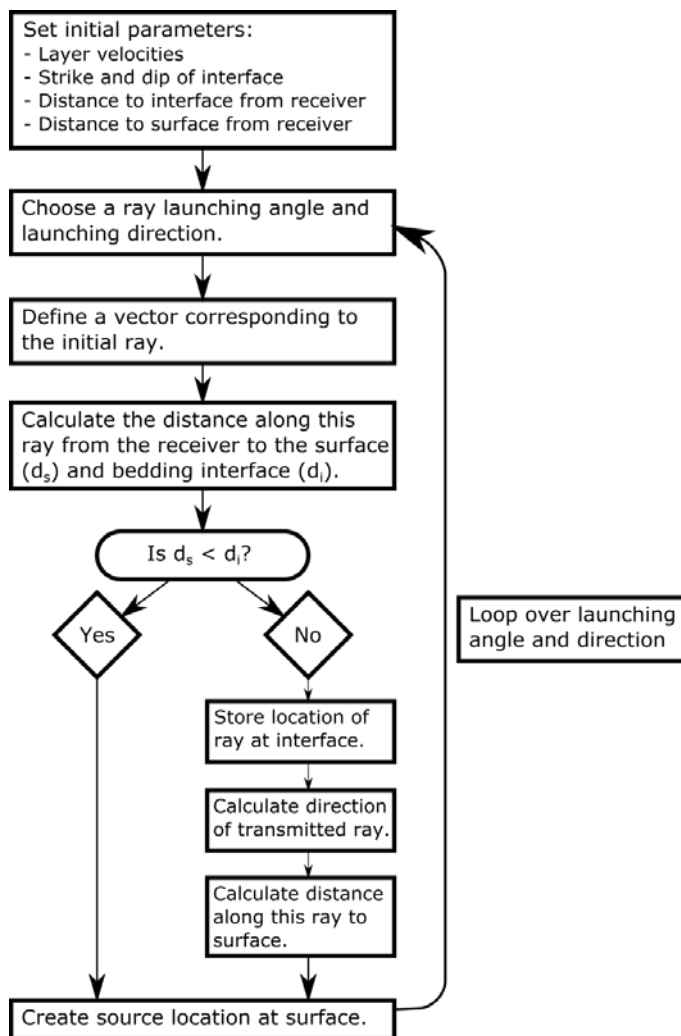


Figure 5.1: Flowchart of the algorithm used for raytracing.

Several steps in this algorithm warrant further explanation:

- 1) definitions of interface plane and initial ray,
- 2) calculation of transmitted ray direction using a vector form of Snell's Law,
and
- 3) calculation of initial and transmitted raypath distances.

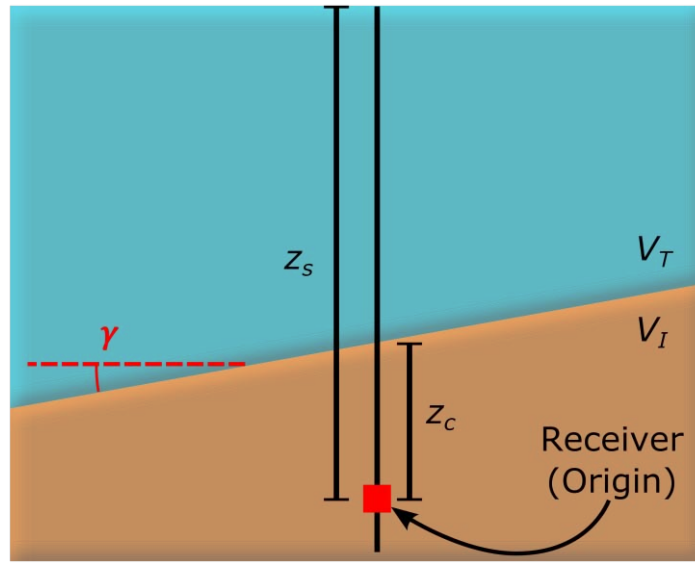


Figure 5.2: Schematic diagram of the general setup of raytracing experiment. V_I and V_T are the velocities of the lower and upper layer, z_c is the vertical distance from the receiver to the interface, z_s is the depth of the receiver, and γ is the dip of the interface.

5.2.1.2 Definitions of Interface Plane and Initial Ray

An interface between two geologic units is best described using strike and dip, expressed here as ϕ_B and γ respectively. An expression of the normal to this interface can be given, using spherical coordinates, as:

$$\hat{n} = \begin{bmatrix} \sin \gamma \cos(90^\circ - \phi_B) \\ \sin \gamma \sin(90^\circ - \phi_B) \\ \cos \gamma \end{bmatrix} = \begin{bmatrix} -\sin \gamma \sin \phi_B \\ -\sin \gamma \cos \phi_B \\ \cos \gamma \end{bmatrix}. \quad (5.1)$$

Given the vertical distance from the receiver to the interface, z_c , the plane of the interface can be expressed as

$$\hat{n} \cdot (\vec{x} - \vec{x}_0) = -x \sin \gamma \sin \phi_B - y \sin \gamma \cos \phi_B + (z - z_c) \cos \gamma = 0. \quad (5.2)$$

The direction of the initial ray, again using spherical coordinates, is defined as

$$\begin{bmatrix} -\sin \theta_G \sin \phi_G \\ -\sin \theta_G \cos \phi_G \\ \cos \theta_G \end{bmatrix}, \quad (5.3)$$

where θ_G is the angle of the ray, measured from positive z , and ϕ_G is the azimuth of the ray, measured clockwise from North. Thus the initial ray, beginning at the origin and ending at the interface, is defined as

$$\vec{I} = \hat{I}d_I = \begin{bmatrix} -\sin \theta_G \sin \phi_G \\ -\sin \theta_G \cos \phi_G \\ \cos \theta_G \end{bmatrix} d_I, \quad (5.4)$$

where d_I is the distance the ray has to travel.

5.2.1.3 Vector Form of Snell's Law

The direction of the transmitted ray was found using Snell's Law; however, for optimal use in the raytracing algorithm it was converted into a vector form. Snell's Law can be expressed simply as

$$\frac{\sin \theta_I}{V_I} = \frac{\sin \theta_T}{V_T}, \quad (5.5)$$

where V_I and V_T are the velocities of the incident and transmitted media, and θ_I and θ_T are the angles of incidence and transmission relative to the normal of the interface. Figure 5.3 shows the variables involved in this relationship.

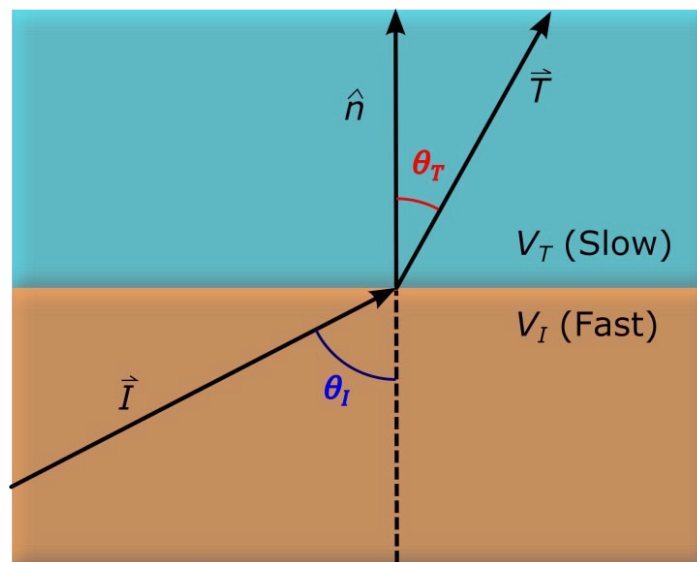


Figure 5.3: Snell's Law, with $V_I > V_T$.

Since the ray bends perpendicular to the interface, an expression for the direction of the transmitted ray will have the form

$$\hat{T} = a\hat{I} + b\hat{n}, \quad (5.6)$$

where \hat{T} , \hat{I} and \hat{n} are all unit vectors, and a and b are constants. These constants can be found using the following two relationships:

$$\hat{T} \cdot \hat{n} = \cos \theta_T, \text{ and} \quad (5.7)$$

$$\hat{T} \cdot \hat{T} = 1. \quad (5.8)$$

Using Equations 5.5, 5.7 and 5.8, Equation 5.6 becomes

$$\hat{T} = \frac{V_T}{V_I} \hat{I} + \left(\sqrt{1 - \left(\frac{V_T}{V_I}\right)^2 [1 - (\hat{I} \cdot \hat{n})^2]} - \frac{V_T}{V_I} (\hat{I} \cdot \hat{n}) \right) \hat{n}; \quad (5.9)$$

for a more detailed derivation, see Appendix A.

5.2.1.4 Raypath Distances and Source-Well Azimuth

The final location of a given ray, with respect to the receiver, can be expressed as a linear combination of the initial and transmitted rays, that is,

$$\vec{T} = \hat{T}d_T + \hat{I}d_I. \quad (5.10)$$

First, the distance travelled by the initial ray can be found by substituting Equation 5.4 into Equation 5.2, resulting in

$$d_I = \frac{z_c \cos \gamma}{\hat{I} \cdot \hat{n}}. \quad (5.11)$$

Next, to find the distance travelled by the transmitted ray, we can exploit that the surface is horizontal; specifically, it is defined at $z = z_s$. Thus, Equation 5.10 can be rewritten as

$$\vec{T}_z = z_s = \hat{T}_z d_T + \hat{I}_z d_I, \quad (5.12)$$

which can be rearranged to give

$$d_T = \frac{z_s - \hat{I}_z d_I}{\hat{T}_z}, \quad (5.13)$$

where \hat{T}_z can be found using Equation 5.9.

Finally, the resulting source-well azimuth is found to be

$$\begin{aligned} \phi_s &= 90^\circ - \arctan\left(\frac{\vec{T}_y}{\vec{T}_x}\right) \\ &= 90^\circ - \arctan\left(\frac{\hat{T}_y d_T + \hat{I}_y d_I}{\hat{T}_x d_T + \hat{I}_x d_I}\right). \end{aligned} \quad (5.14)$$

5.2.2 Tests Using Constant Dip and Constant Velocity

The raytracing code was used to simulate a variety of geologic scenarios using different velocity contrasts and dip angles. Firstly, the dip of the interface was held constant while the velocity of the deeper layer varied. Secondly, the velocity of the deeper layer was held constant while the dip of the interface varied. For both of these experiments, the velocity of the upper layer, receiver depth and distance to the bedding interface were held constant. The different parameters are summarised in Table 5.1.

Table 5.1: Parameters used for raytracing tests.

| Parameter | Constant Dip Test | Constant Velocity Test |
|---|----------------------------|-------------------------------|
| Velocity of upper layer (V_T) | 2000 m/s | 2000 m/s |
| Velocity of lower layer (V_I) | 2600, 2900, 3200, 3500 m/s | 2900 m/s |
| Velocity ratio (V_I / V_T) | 1.30, 1.45, 1.60, 1.75 | 1.45 |
| Dip of interface (γ) | 10° | 5°, 10°, 15°, 20° |
| Strike of interface (ϕ_B) | 180° | 180° |
| Receiver depth (z_s) | 300 m | 300 m |
| Distance from receiver to bedding plane (z_c) | 150 m | 150 m |

Results of the constant dip test are shown in Figure 5.4, and the results from the constant velocity test are shown in Figure 5.5. Figure 5.4b and Figure 5.5b are identical, providing a common reference for the two tests. In both cases, the x and y axes are ray launching azimuth and inclination, and the azimuth deviation scale is -20° to $+20^\circ$; contours are shown at intervals of 5° . Finally, red and blue triangles mark the largest negative and positive deviation along a line of constant inclination.

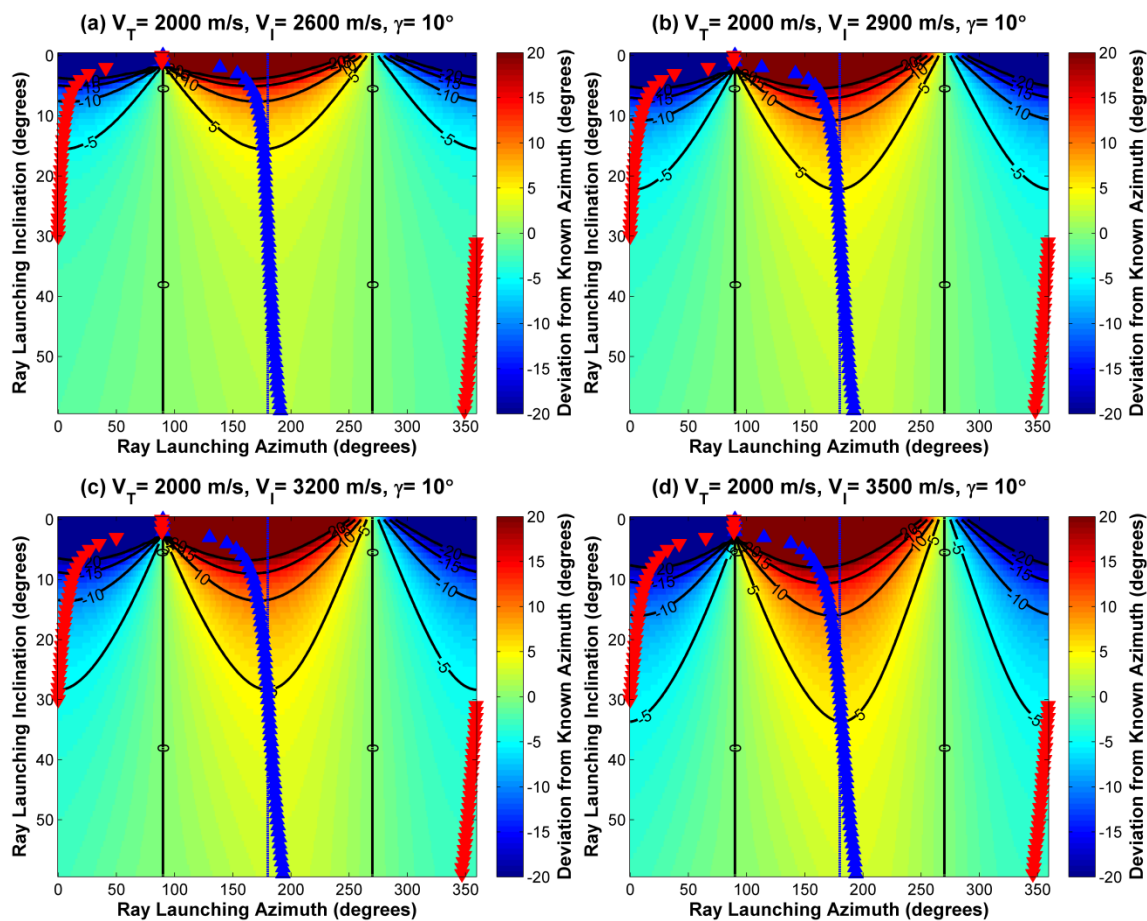


Figure 5.4: Deviation in azimuth resulting from constant dip test, plotted against ray launching azimuth and inclination. Hotter colours represent positive deviation, cooler colours represent negative deviation. Red and blue triangles represent largest negative and positive deviation for constant inclination angles.

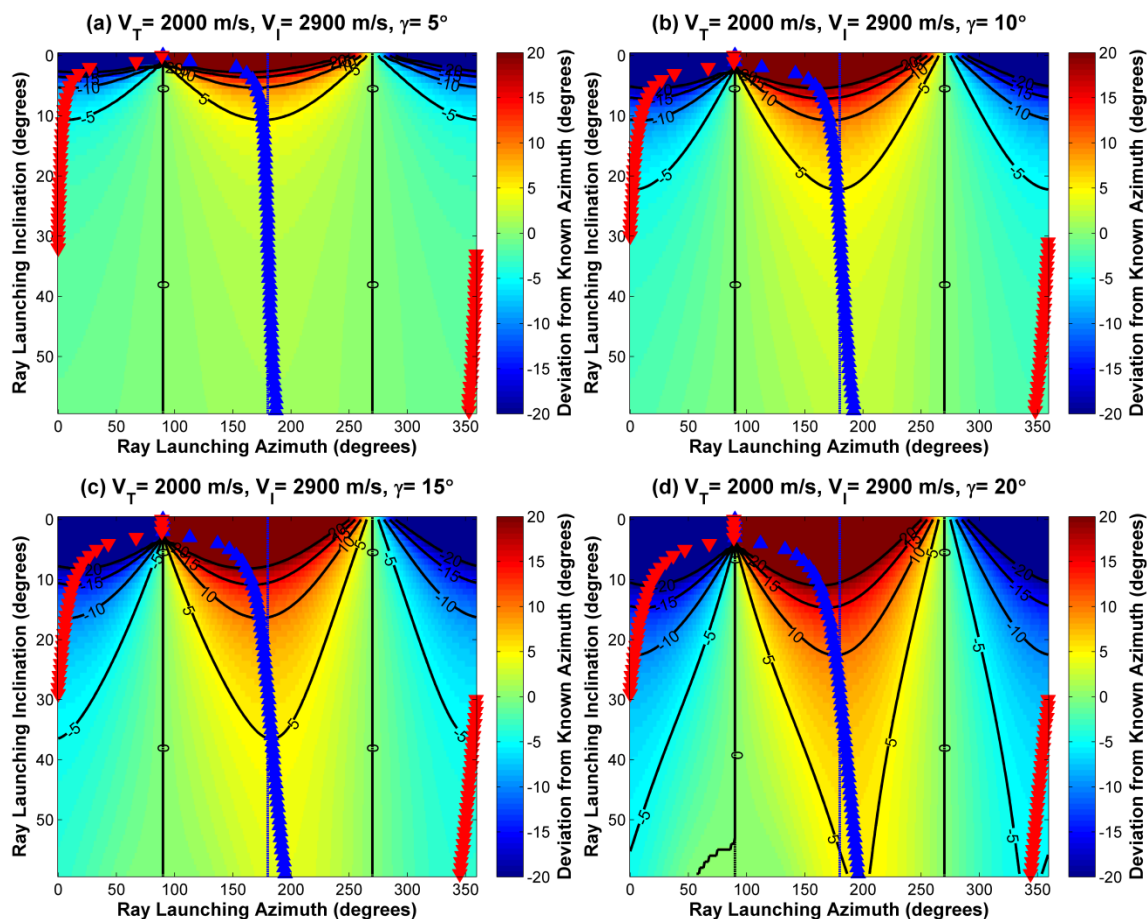


Figure 5.5: Deviation in azimuth resulting from constant velocity test, plotted against ray launching azimuth and inclination. Hotter colours represent positive deviation, cooler colours represent negative deviation. Red and blue triangles represent largest negative and positive deviation for constant inclination angles.

There are several important trends discernible from these tests. First, the deviation becomes 0° as the ray launch azimuth approaches both the pure updip and downdip directions, which in this case are 90° and 270° respectively. However, the azimuths that produce the most positive and negative deviation are variable; they converge to the updip direction as inclination angle decreases, and converge to the downdip direction as inclination angle increases. Also, the magnitude of the deviation decreases as the inclination angle increases; note that an increase in inclination angle is related to an increase in source-well offset, suggesting that orientation azimuths determined from shots farther from the well will be less prone to deviation in azimuth due to dipping velocity interfaces. In one example (Figure 5.5d) the 0° deviation contour associated with the

updip direction deviates from a straight line at high inclination angles; this is range of inclination and azimuth angles where the ray travels directly to the surface. Finally, it is apparent that the deviation in orientation azimuth becomes more significant as either dip or velocity contrast increases. Figure 5.4d, which represents a 30 % increase in velocity contrast from the reference, and Figure 5.5c, which represents a 33 % increase in dip from the reference, appear to be identical. Thus, in this case, relative changes in velocity contrast and dip affect the deviation in orientation azimuth in a similar fashion.

5.3 Finite Difference Modelling

5.3.1 Model Parameters

The effects of a dipping layer boundary was also studied using TIGER. A simple 2 layer geologic model was created using the parameters shown in Table 5.2; surface geometry is shown in Figure 5.6. Three shot lines were recorded, each trending East-West with 10 m shot spacing; Line 1 was 100 m south of the well location, Line 2 went directly over the well location, and Line 3 was 100 m north of the well location. Figure 5.6 shows a plan view of the surface geometry. Receivers were defined from 10 – 300 m depth, at 10 m intervals. Finally, examples of a common shot gather and common receiver gather are shown in Figures 5.7 and 5.8. Note how the character of the first arrival changes noticeably for the deeper receivers, especially on the y-component; this is likely due to converted wave arrivals that are generated at the velocity interface.

Table 5.2: Numerical parameters used for acquisition.

| TIGER Acquisition Parameters | |
|---------------------------------------|---------------------------|
| Dimensions | 490 x 490 x 490 m |
| Grid size | 10 m |
| Recording time | 700 ms |
| Sample rate | 1 ms |
| Source wavelet | First Derivative Gaussian |
| Number of source lines | 3 |
| Number of sources per line | 30 |
| Source interval | 10 m |
| Number of receivers | 30 |
| Receiver interval | 10 m |
| Receiver depth range | 10-300 m |
| Upper layer velocities (V_P, V_S) | 2000 m/s, 1000 m/s |
| Lower layer velocities (V_P, V_S) | 2900 m/s, 1740 m/s |
| Strike and dip of velocity interface | $180^\circ / 30^\circ$ |
| Depth of interface at well | 175 m |

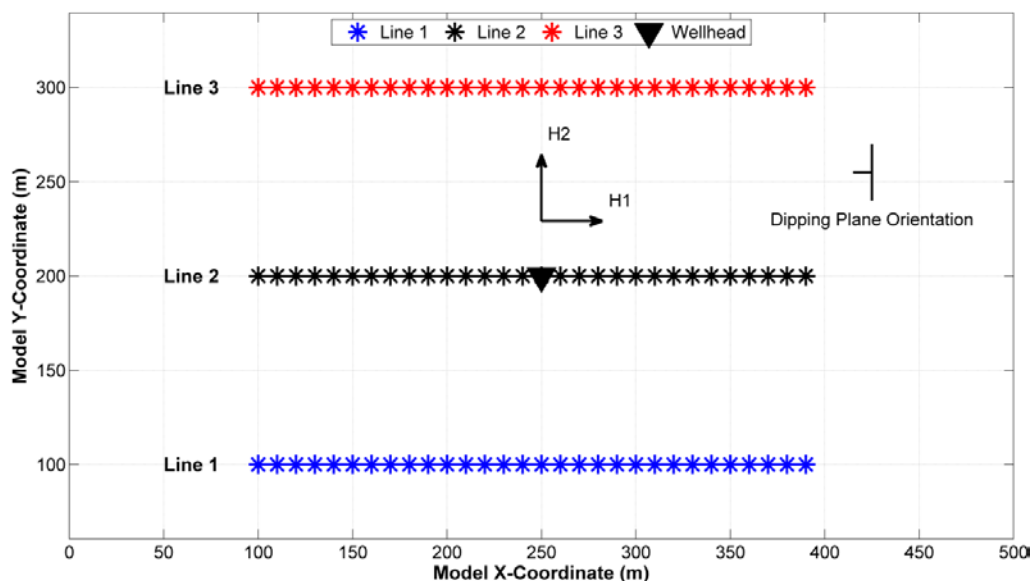


Figure 5.6: Plan view of surface geometry used in TIGER. Line 1 is shown in blue, Line 2 is shown in black and Line 3 is shown in red. Additionally, the strike and dip of the layer interface are indicated, and the orientations of the H1 and H2 components are shown.

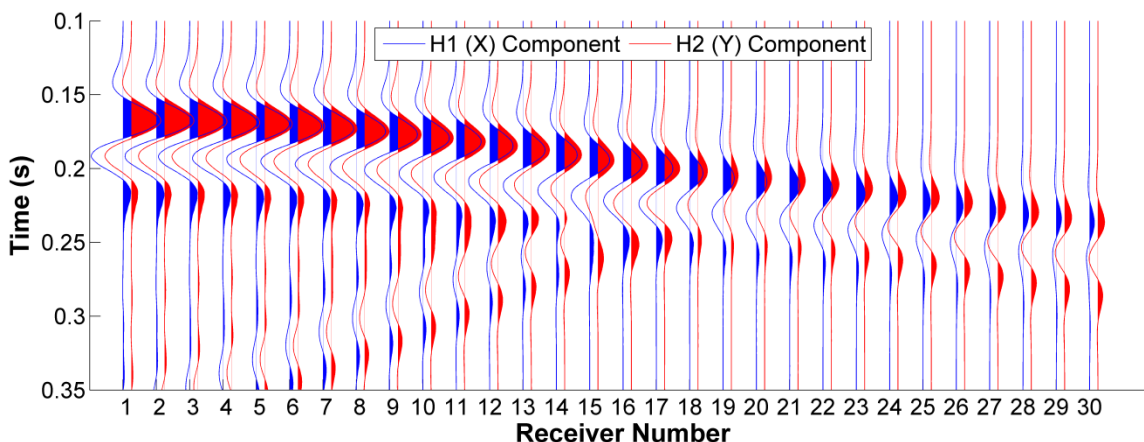


Figure 5.7: Example of raw TIGER output from the shot at $x = 130$ m and $y = 100$ m. H1-component output is shown in blue and H2-component output is shown in red.

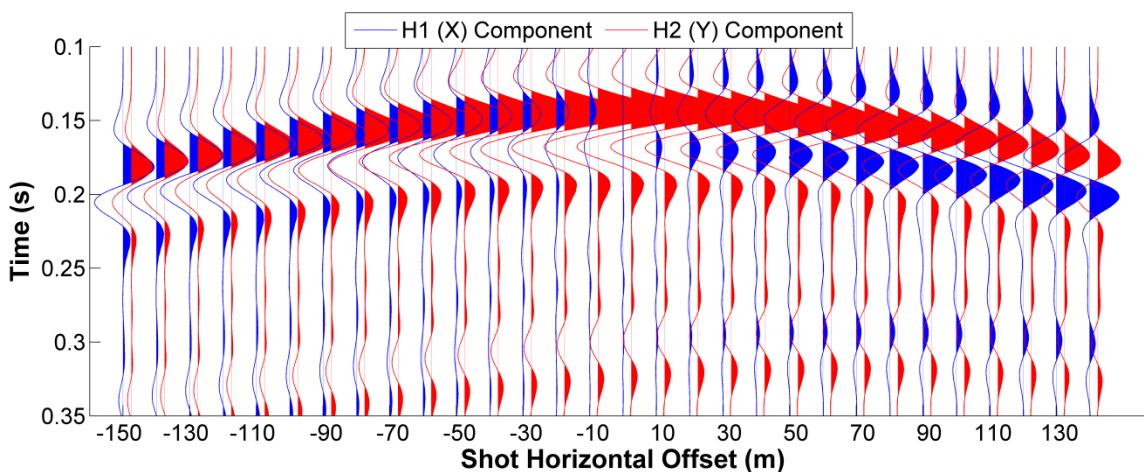


Figure 5.8: Example of raw TIGER output from Receiver 5 at 50 m. H1-component output is shown in blue and H2-component output is shown in red.

5.3.2 Results

Results shown here will focus on four receivers: Receiver 5 (at 50 m depth), above the interface; Receiver 15 (at 150 m depth), just above the interface; Receiver 20 (at 200 m depth), just below the interface; and Receiver 30 (at 300 m depth), well below the interface. For further results from Receivers 12 through 25, refer to Appendix E. First, Figures 5.9 – 5.12 show the deviation in orientation azimuth calculated using the analytic method, using a 100 ms analysis window beginning at the first breaks. Receiver 5 shows no deviation; this is expected, as the energy from the first arrivals will not yet have encountered any velocity contrast. Receiver 15 shows a small amount of deviation, which

is likely due to interference of the reflection from the velocity interface. Receivers 20 and 30 both show pronounced deviation; however, the shape and strength of the deviation is quite different between the two. For example, the deviation shown by Receiver 20 appears to be a two-cycle sinusoid over the full range of source-well azimuths, whereas that of Receiver 30 is a one-cycle sinusoid. Additionally, the maximum deviation for Receiver 30 is high, reaching a maximum of approximately 40° , which is larger than the dip of the velocity interface. Both of these effects can likely be explained by the presence of transmitted converted waves generated at the layer boundary; in order to test this assertion, the analysis was done again for Receivers 20 and 30 using a window size of 50 ms (Figures 5.13 and 5.14). The change in window size results in much smaller deviation for both of these receivers, suggesting that converted waves are a significant source of deviation in geophone orientation analysis. The standard deviations of orientation azimuth are shown in Table 5.3 for every 5 receivers, found using both window sizes. This information is shown graphically, for all receivers, in Figure 5.15. The curve representing the 50 ms window size reaches a maximum at about 270 m, and the curve representing the 100 ms window size appears to be nearing a maximum at 300 m. Finally, curves representing both window sizes show a generally smooth variation throughout the range of receivers, with the exception of a minor anomaly between the receivers at 180 and 190 m depth.

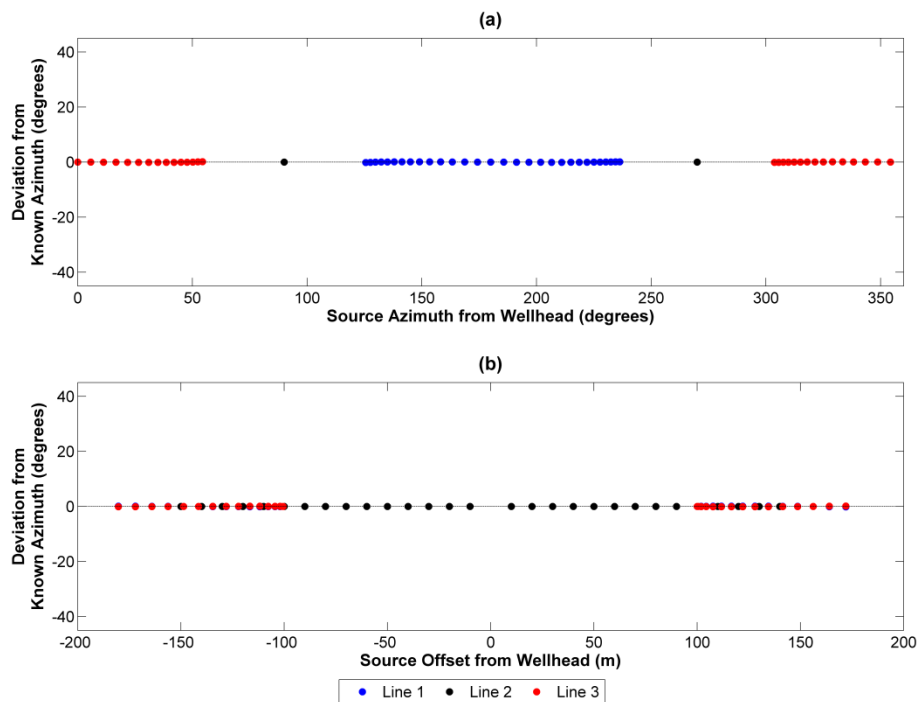


Figure 5.9: Deviation of orientation angle for Receiver 5 (50 m depth) plotted as a function of source-well azimuth (a) and source-well offset (b). Line 1 is shown in blue, Line 2 in black and Line 3 in red.

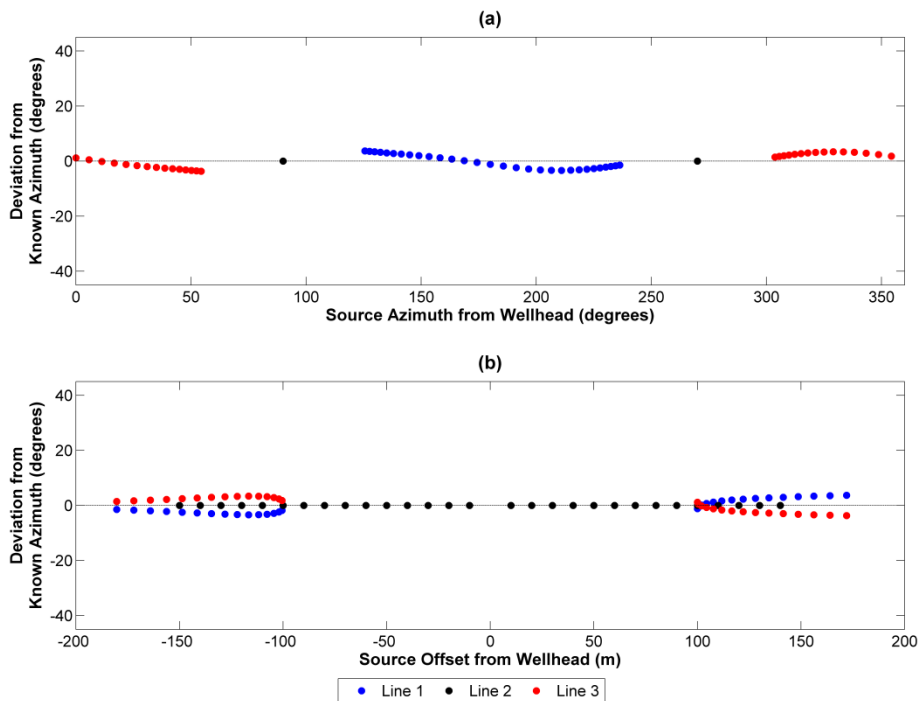


Figure 5.10: Deviation of orientation angle for Receiver 15 (150 m depth) plotted as a function of source-well azimuth (a) and source-well offset (b). Line 1 is shown in blue, Line 2 in black and Line 3 in red.

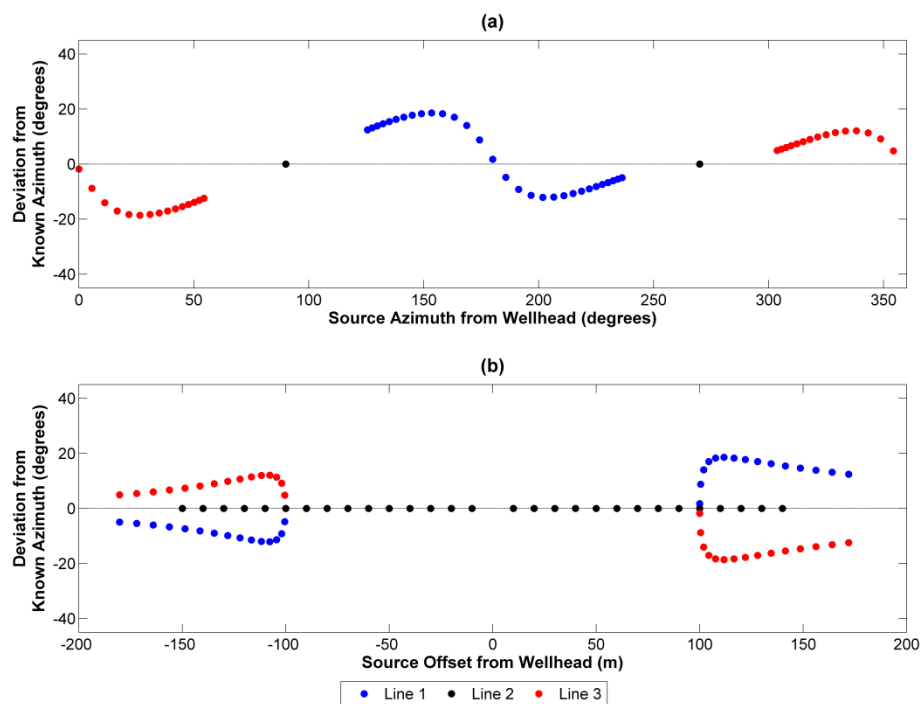


Figure 5.11: Deviation of orientation angle for Receiver 20 (200 m depth) plotted as a function of source-well azimuth (a) and source-well offset (b). Line 1 is shown in blue, Line 2 in black and Line 3 in red.

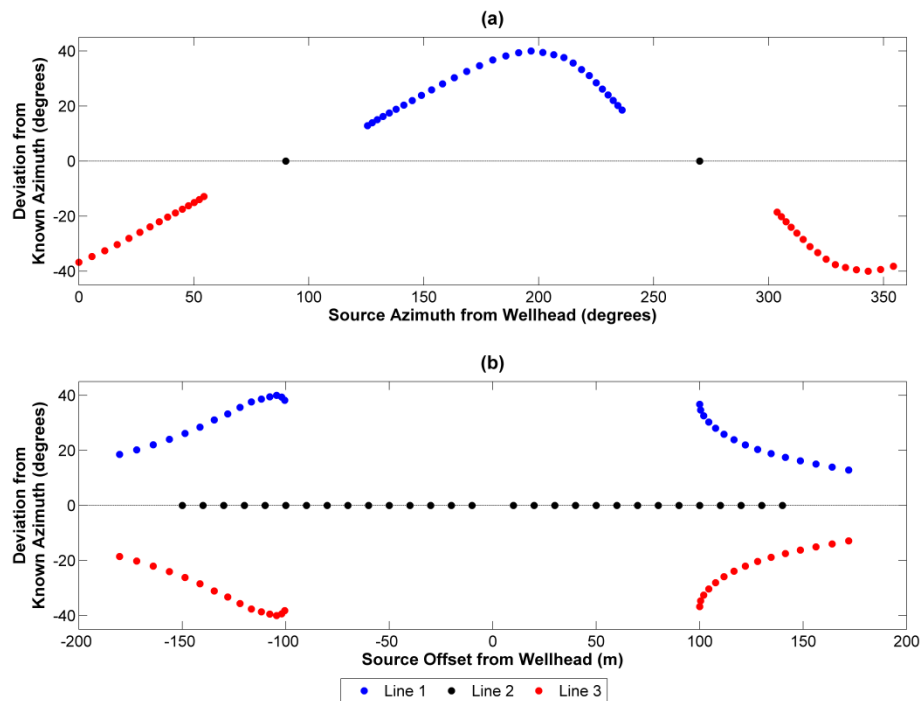


Figure 5.12: Deviation of orientation angle for Receiver 30 (300 m depth) plotted as a function of source-well azimuth (a) and source-well offset (b). Line 1 is shown in blue, Line 2 in black and Line 3 in red.

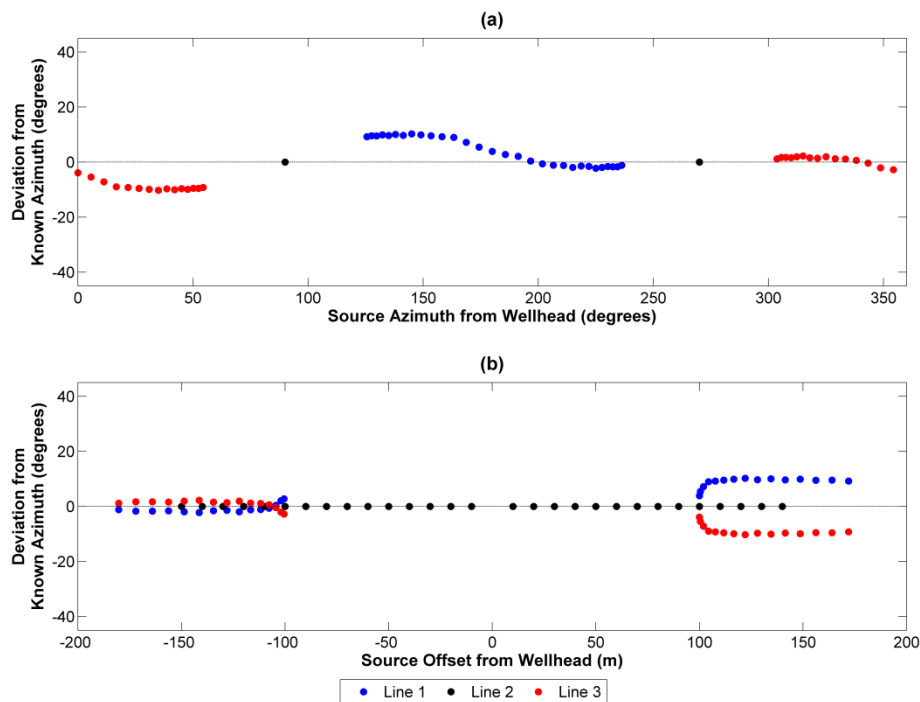


Figure 5.13: Deviation of orientation angle for Receiver 20 (200 m depth), using a 50 ms analysis window, plotted as a function of source-well azimuth (a) and source-well offset (b). Line 1 is shown in blue, Line 2 in black and Line 3 in red.

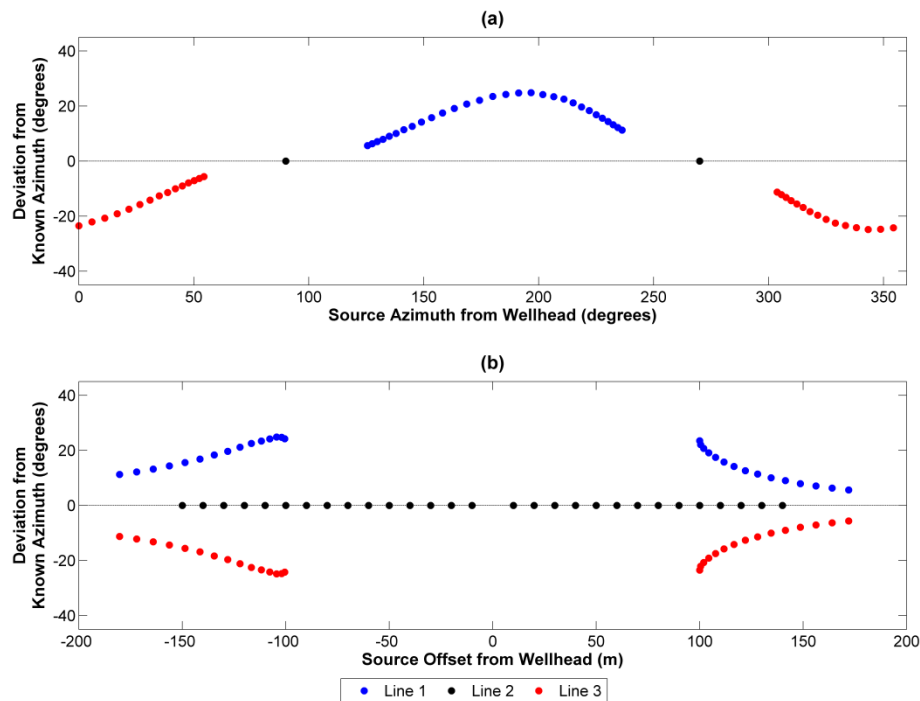


Figure 5.14: Deviation of orientation angle for Receiver 30 (300 m depth), using a 50 ms analysis window, plotted as a function of source-well azimuth (a) and source-well offset (b). Line 1 is shown in blue, Line 2 in black and Line 3 in red.

Table 5.3: Standard deviation of receiver orientation azimuth.

| Receiver | Depth (m) | 100 ms Window St. Dev. (°) | 50 ms Window St. Dev. (°) |
|----------|-----------|-------------------------------|------------------------------|
| 5 | 50 | 0.06 | 0.03 |
| 10 | 100 | 0.27 | 0.02 |
| 15 | 150 | 2.09 | 1.12 |
| 20 | 200 | 10.25 | 5.34 |
| 25 | 250 | 20.47 | 15.14 |
| 30 | 300 | 23.68 | 14.34 |

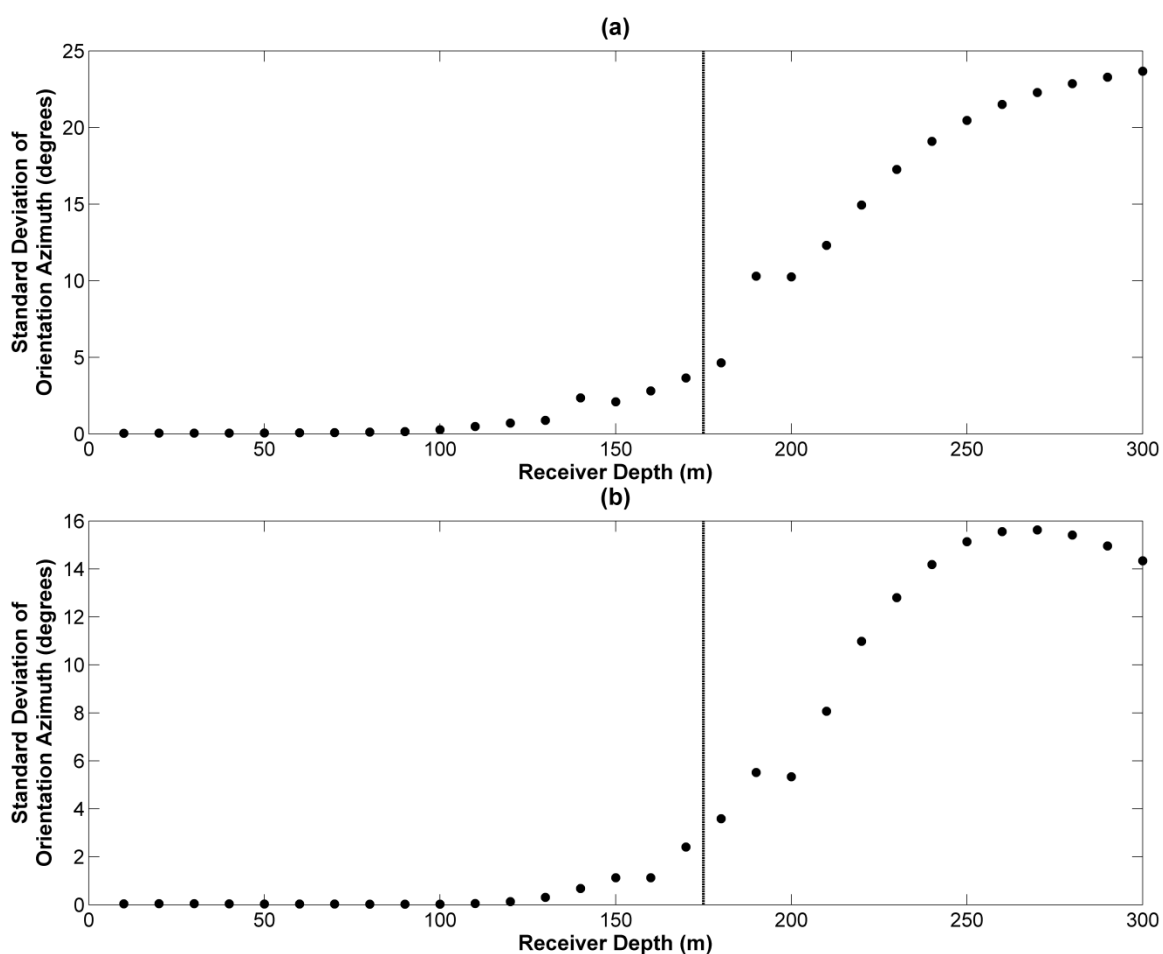


Figure 5.15: Standard deviation of orientation azimuth found using 100 ms window (a) and 50 ms window (b). The depth of the velocity interface at the well is indicated with a black line.

5.3.3 Comparison to Raytracing Method

In order to directly compare results from the raytracing code to results using TIGER, the raytracing code was run using the same velocity model, for a receiver depth of 300 m; deviations in azimuth were chosen from the source locations best matching the surface geometry of TIGER. In order to minimise the error present from converted wave arrivals, the comparison was made using results from TIGER calculated from a 50 ms window. Figure 5.16 shows the results of this comparison; the two methods produce very similar output, though the results using raytracing show less deviation when compared to the results from TIGER. Since the raytracing code only models P-waves, it is likely that the difference between the two methods is primarily due to transmitted converted waves modelled by TIGER. Additionally, there may be some discretisation error present in TIGER; for example, the layer boundary at the well is between grid points.

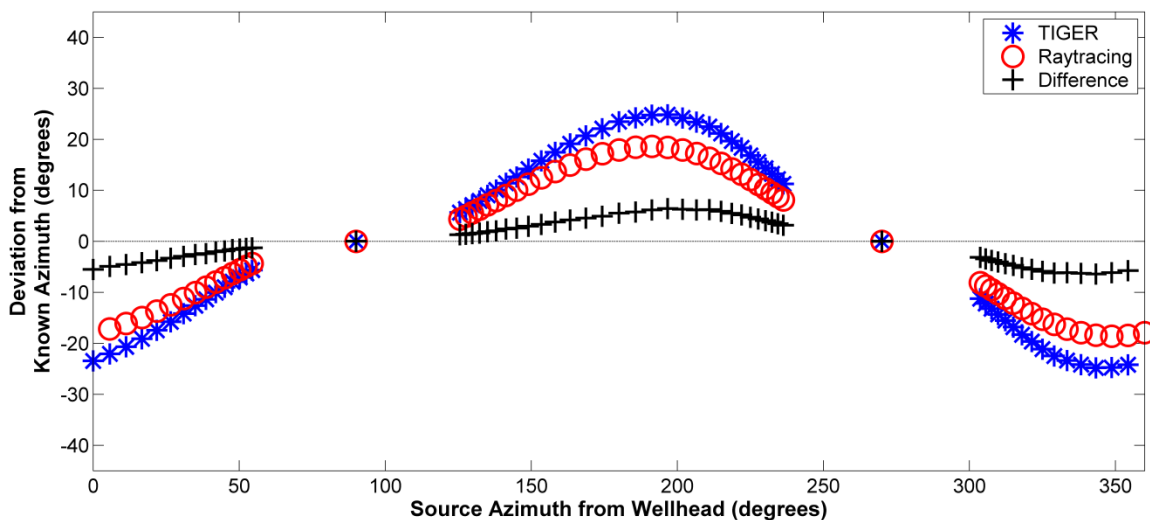


Figure 5.16: Comparison of deviation in geophone orientation angle using TIGER (blue) and raytracing (red) methods. The difference between the two methods is shown in black.

5.4 Discussion

There are several important trends regarding deviation in geophone orientation azimuth to note from the results of the raytracing experiments. First, the deviation should be zero along the dip direction of interface; this suggests that, where possible, sources for

geophone calibration experiments should be placed such that the source-receiver azimuth is in the updip or downdip direction. Second, rays which arrive at the receiver at an angle closer to vertical will have more deviation associated with them. Thus, error can be reduced if sources are placed farther from the receiver, since this angle is increased with increasing offset. Additionally, the results of this experiment show that increasing dip or velocity contrast will result in higher deviation, and that their effects are similar.

The experiments done using TIGER provide some additional insight in the deviations encountered. The predicted anomaly, when examining deviation as a function of source-receiver azimuth, is sinusoidal in nature, which provides a pattern that could potentially be recognised in field data. Interestingly, there were also recognisable trends when comparing the deviation to source-well offset. The choice of window size is shown to have an appreciable effect on the final results of this analysis; this is related to contamination from turning, reflected and converted waves. Examination of the standard deviation across receiver depths shows a definite trend. The error is near zero well above the interface, then begins to increase at depths just above the interface, and reaches a maximum somewhere below the interface; this maximum was at 95 m below the interface for the 50 ms window, and deeper than 125 m below the interface for the 100 ms window. This is likely due to the presence of converted waves in the analysis window. Finally, the comparison to the raytracing method, when using a 50 ms window, showed a good match in terms of character, though the magnitude of the deviation found using the raytracing method was slightly less.

5.5 Summary

The following results can be noted from this chapter:

- A method was successfully developed to model the deviation in observed geophone orientation azimuth due to a single dipping velocity interface, using raytracing.

- Observed deviation in geophone orientation increases with increasing dip and velocity contrast; these two factors affect the deviation in a similar fashion.
- There is zero error if the source-receiver azimuth is along the maximum dip direction of the interface.
- The maximum and minimum deviations occur at a range of azimuths depending on source-receiver offset. Generally, as offset increases they tend towards the downdip direction, and as offset decreases they tend towards the updip direction.
- The choice of window size was shown to be important when using finite difference modelling. Decreasing the window size from 100 ms to 50 ms resulted in a decrease in deviation of geophone orientation of almost 50 %. This is at least partially due to effects from transmitted converted waves.
- The receivers 30 – 40 m above the velocity interface showed slight deviation, which is likely due to headwaves and reflected waves. Further, the deviation pattern as a function of source-receiver azimuth did not match that of the receivers below the interface, nor did it match the deviation predicted by raytracing.
- Deviation for receivers below the interface continued to increase with depth, reaching a maximum at 95 m below the interface when using the 50 ms window and approaching a maximum at 125 m below the interface when using the 100 ms window.
- Deviation for the receiver at 300 m found from finite difference modelling, using a 50 ms window, matched the deviation predicted by the raytracing method well.

Chapter Six: HTI Medium

6.1 Introduction

In this chapter I model the effects of a horizontal transversely isotropic (HTI) geological medium on geophone orientation analysis. The effects are modelled analytically and compared to results output by TIGER; their characteristics are studied to determine the expected impact on field data. Results shown in this chapter are compared to the results of all three field studies in Chapter 8.

6.2 Background

6.2.1 Weak Anisotropy

A medium is said to be seismically anisotropic if the speed of propagation of elastic waves in the medium varies with the direction of travel (Vestrum, 1994). In the case of transverse isotropy, also called hexagonal symmetry, two orthogonal directions of travel produce equivalent velocities, while the third produces a different velocity. This is a simple case of anisotropy which is applicable to seismic studies (Thomsen, 1986). Three values commonly used to describe this type of anisotropy are ε , γ and δ (Thomsen, 1986). The parameters ε and γ provide a measure of the relative change in P and S-waves; δ is more difficult to understand, but relates to the shape of the wavefront. Weak anisotropy is the case where these three values are much less than one (Thomsen, 1986); it will be the case considered for this analysis.

6.2.2 Group and Phase Angle

In the case of weak anisotropy, the phase velocity of a P-wave is given by (Thomsen, 1986)

$$v(\theta) = v_0 \{1 + \delta \sin^2 \theta \cos^2 \theta + \varepsilon \sin^4 \theta\}, \quad (6.1)$$

where v_0 is the velocity parallel to the axis of symmetry (slow velocity direction), θ is the phase angle, and δ and ε are weak anisotropic parameters, defined in Thomsen (1986); see Figure 1.6 in Chapter 1 for a reminder of the definitions of phase and group angle. It

should be noted that the case of $\delta = \varepsilon$ will result in a special case called elliptical anisotropy (Thomsen, 1986). The group angle can be calculated using (Vestrum et al., 1999):

$$\phi = \theta + \arctan\left(\frac{\partial v}{\partial \theta}/v\right), \quad (6.2)$$

where

$$\frac{\partial v}{\partial \theta} = v_0\{2\delta(\cos^3 \theta \sin \theta - \cos \theta \sin^3 \theta) + 4\varepsilon \cos \theta \sin^3 \theta\}. \quad (6.3)$$

Note that, in a homogeneous, purely HTI medium with a vertical well, ϕ will be the source azimuth with respect to the well, while θ will relate to the direction of polarisation measured by the receiver in the well. Using Equation 6.2 we can write that the difference between group and phase angle is given by

$$\phi - \theta = \varphi = \arctan\left(\frac{\partial v}{\partial \theta}/v\right); \quad (6.4)$$

this will contribute to deviation in geophone orientation calibration.

6.2.3 Measurement at Receiver

For analytic modelling, it was assumed that the polarisation measurement at the receiver is in the direction of the phase (wavefront) angle, since this angle is parallel to the propagation vector and thus normal to the wavefront. However, Musgrave (1970) states that, in a general anisotropic medium, none of the three particle displacement vectors are parallel to the wave normal, and at least one study (Li et al., 1987) shows a field example where the particle motion at a receiver in an anisotropic medium is described by neither the wavefront propagation vector nor the ray vector. Additionally, much work has been done in order to determine which velocity (i.e. phase or group) is measured when performing experiments on rock samples (Dellinger and Vernik, 1994; Vestrum, 1994). Li et al. (1987) are able to calculate a vector that theoretically describes P-wave particle motion, which explains observed particle motion better than either the

propagation or ray vectors. This vector generally lies between the other two; thus, it is possible that the difference between the phase and group angle is an overestimate of the deviations in geophone orientation azimuth in a weakly anisotropic medium.

6.3 Analytic Modelling

6.3.1 Maximum Angle Difference Dependent on δ and ε

Using Equation 6.4, the maximum angle difference between group and phase angle was computed for a range of values of δ and ε . Figure 6.1 shows a contour plot of these values, given on a range of $-0.15 \leq \delta \leq 0.15$, $0 \leq \varepsilon \leq 0.35$. Values range from 0° , in the isotropic case, to 22° and higher. In Figure 6.2 I hold ε constant at 0.15, while letting δ vary; note that the range here is about 6° . In Figure 6.3, by contrast, I hold δ constant at 0.05, while varying ε ; the range here is almost 20° . Figures 6.1 – 6.3 all indicate that ε has a more noticeable effect on the maximum deviation between group and phase angle than does δ , and that this deviation can reach values that are large.

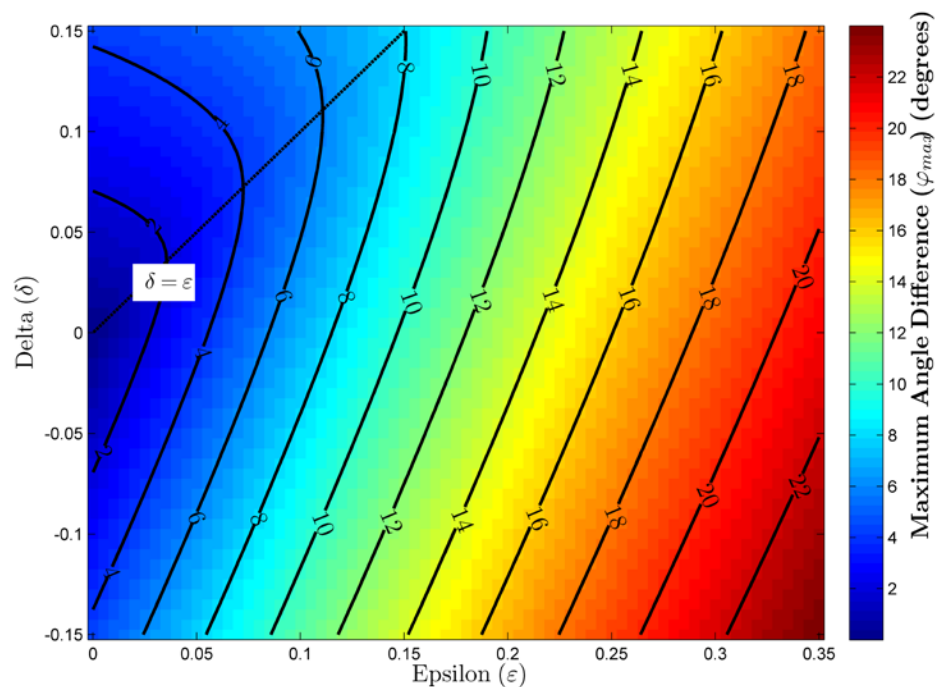


Figure 6.1: Maximum difference between group and phase angle, in degrees, as a function of epsilon and delta; the line $\delta = \varepsilon$ is drawn in for convenience. Hotter colours represent larger values.

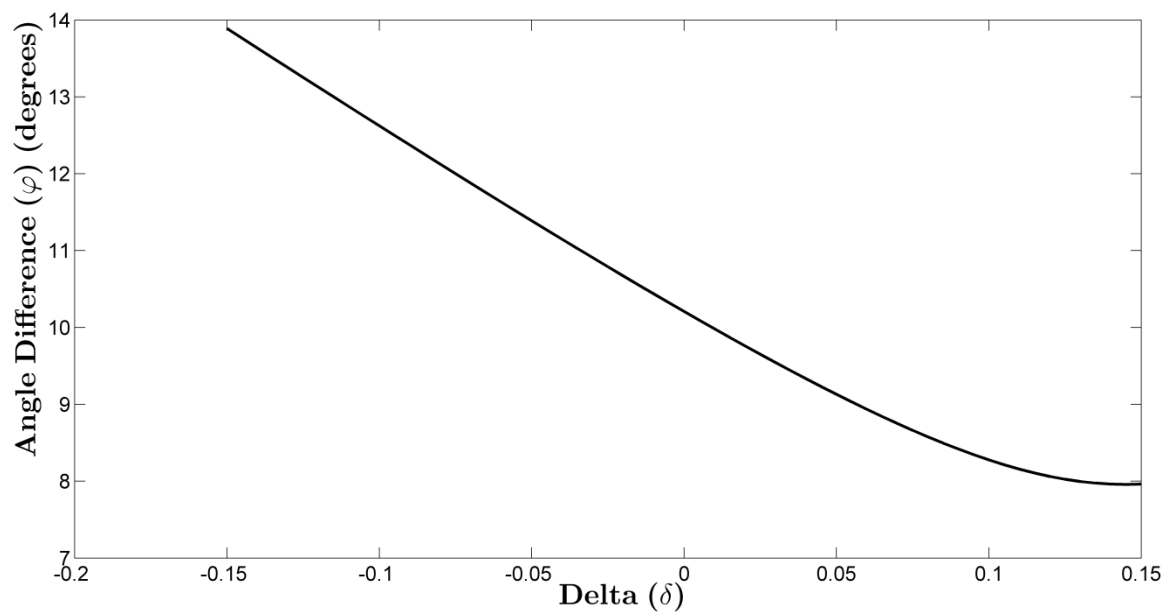


Figure 6.2: Maximum difference between group and phase angle, in degrees, using a constant epsilon of 0.15.

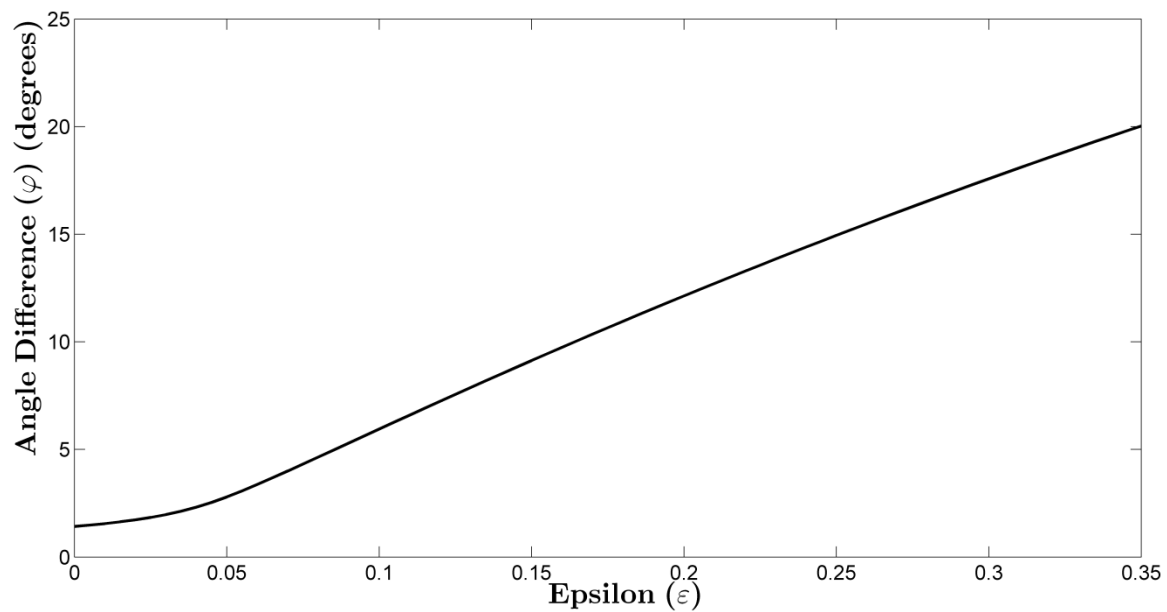


Figure 6.3: Maximum difference between group and phase angle, in degrees, using a constant delta of 0.05.

6.3.2 Modelled Calibration Survey

In order to better understand the effects of anisotropy in the context of a geophone orientation study, a simple synthetic experiment was devised. The parameters used, taken from results of a Foothills imaging study done by Vestrum et al. (1999), were $\varepsilon = 0.1$ and $\delta = 0.025$. v_0 was chosen to be 3000 m/s, though this choice will not affect the magnitude of angle differences in the case of a single layer; finally, an east-west axis of symmetry was chosen. Figure 6.4 shows the shape of this wavefront as a function of both phase angle and group angle; the differences between them are most noticeable at angles near 90° and 270° . Figure 6.5 plots the difference between these two angles as a function of phase angle. In this example, the maximum angle difference is 6.45° , which occurs at azimuths of 57.4° , 122.6° , 237.4° and 302.6° . Note that the angles shown in Figures 6.4 and 6.5 are all measured counter clockwise from the positive x-axis (East).

Once the parameters of the medium were chosen, a surface acquisition geometry was created, designed to mimic that of the field study analysed in Chapter 4. Three lines were used in this synthetic experiment: Line 1, trending East-West 200 m north of the well; Line 2, trending north-south 200 m east of the well; and Line 3, intersecting the well at an angle 30° east of north. All three lines had a shot spacing of 100 m, and had a shot spread of 3000 m (Figure 6.6). Finally, the anisotropic axis of symmetry for the HTI medium was chosen to be at an azimuth 60° west of north, perpendicular to the azimuth of Line 3. Using these model parameters, the differences between phase and group angles at each of the shot locations were found; in order to do this, the group angle was first calculated by finding source-receiver azimuth of each location. Next, a table relating group and phase angle was created, to a phase angle precision of 0.1° ; this was necessary due to the difficulty of solving Equation 6.2 directly for phase angle. The table was searched for the closest matching group angle for each shot location, and the corresponding phase angle recorded.

Figure 6.7a shows the difference between the phase and group angles calculated using the modelled survey, as a function of source-receiver offset. In the context of this study, this is effectively the predicted deviation that will be produced for a noise-free geophone orientation calibration. Note that each line follows a distinctly different trend; Line 1

shows predominantly positive deviation, while Line 2 shows predominantly negative deviation. Additionally, the curve produced by Line 2 shows a concave up character for both positive and negative offsets, whereas Line 1 is concave up for negative offsets and concave down for positive offsets. Line 3 shows no deviation; this is an expected result, since the azimuth of this line is perpendicular to the symmetry axis and contains the well. On the other hand, if we examine the orientation angle deviation as a function of source-receiver azimuth, the pattern seen is more consistent between lines (Figure 6.7b). In fact, the relationship appears very similar to that seen in Figure 6.5, though it is reversed and phase-shifted due to the use of different angle conventions. Finally, statistical analysis of these values produces a mean deviation of -0.46° , and a standard deviation of 3.52° .

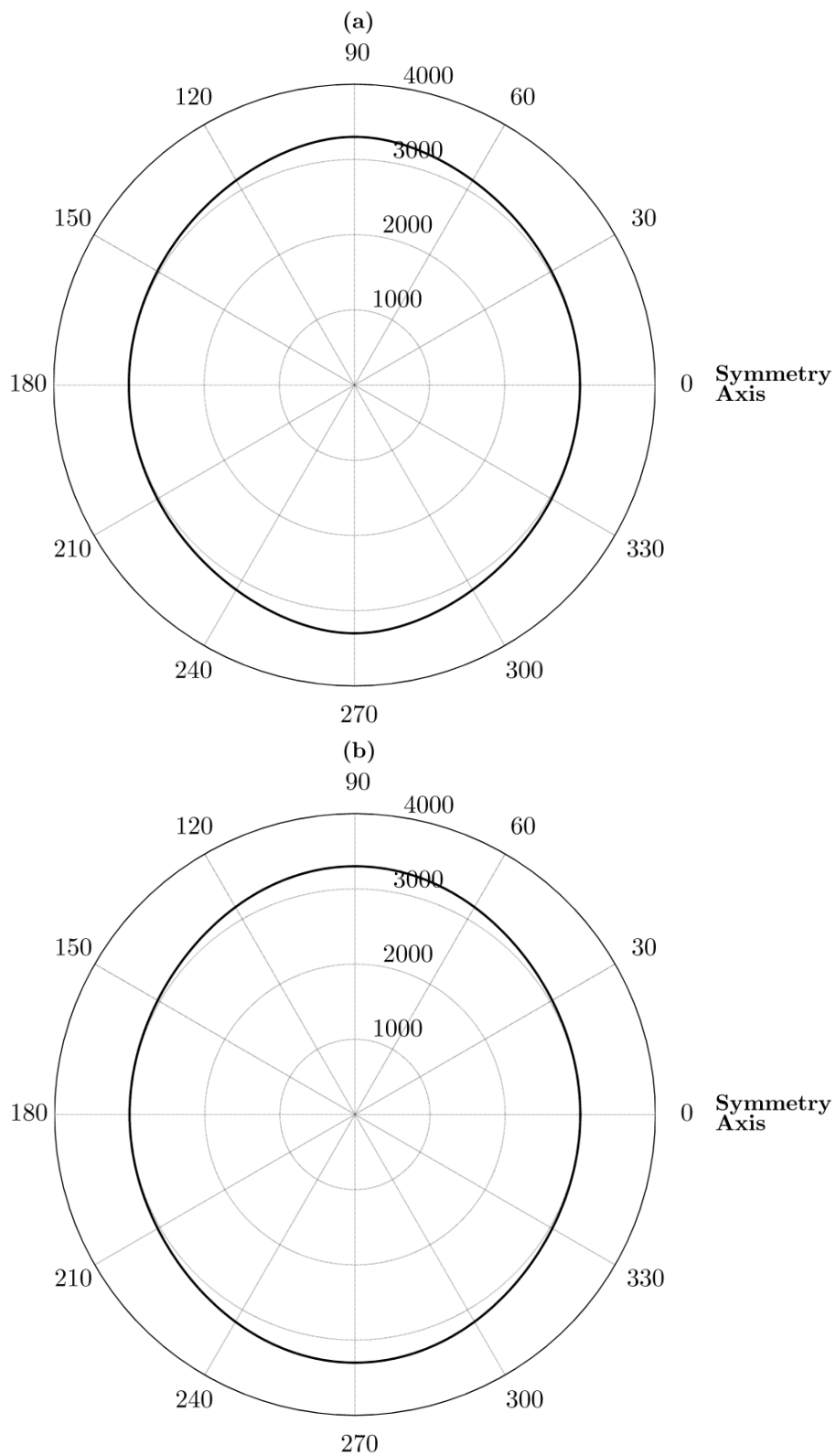


Figure 6.4: Anisotropic wavefront as a function of group angle (a) and phase angle (b), using parameters $v_0 = 3000$ m/s, $\delta = 0.025$ and $\varepsilon = 0.1$.

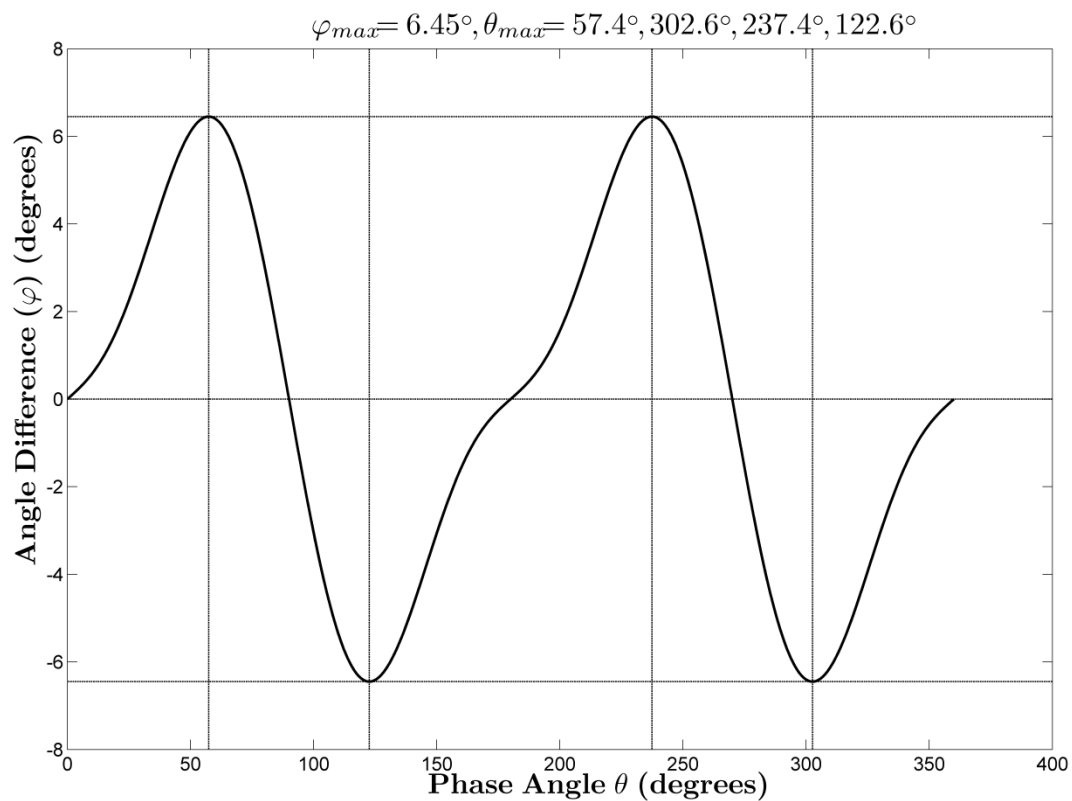


Figure 6.5: Difference between group and phase angle, in degrees, using parameters $v_\theta = 3000$ m/s, $\delta = 0.025$ and $\varepsilon = 0.1$.

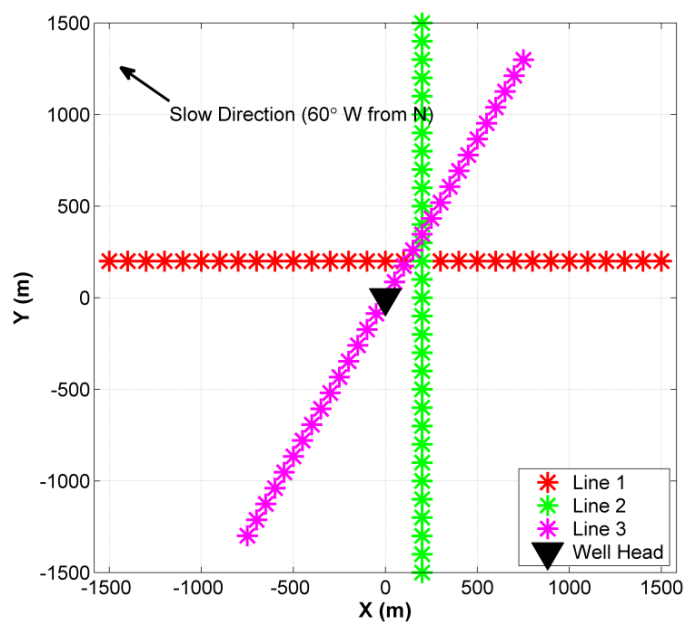


Figure 6.6: Surface geometry used in modelled calibration survey. Coordinates are relative to the well location.

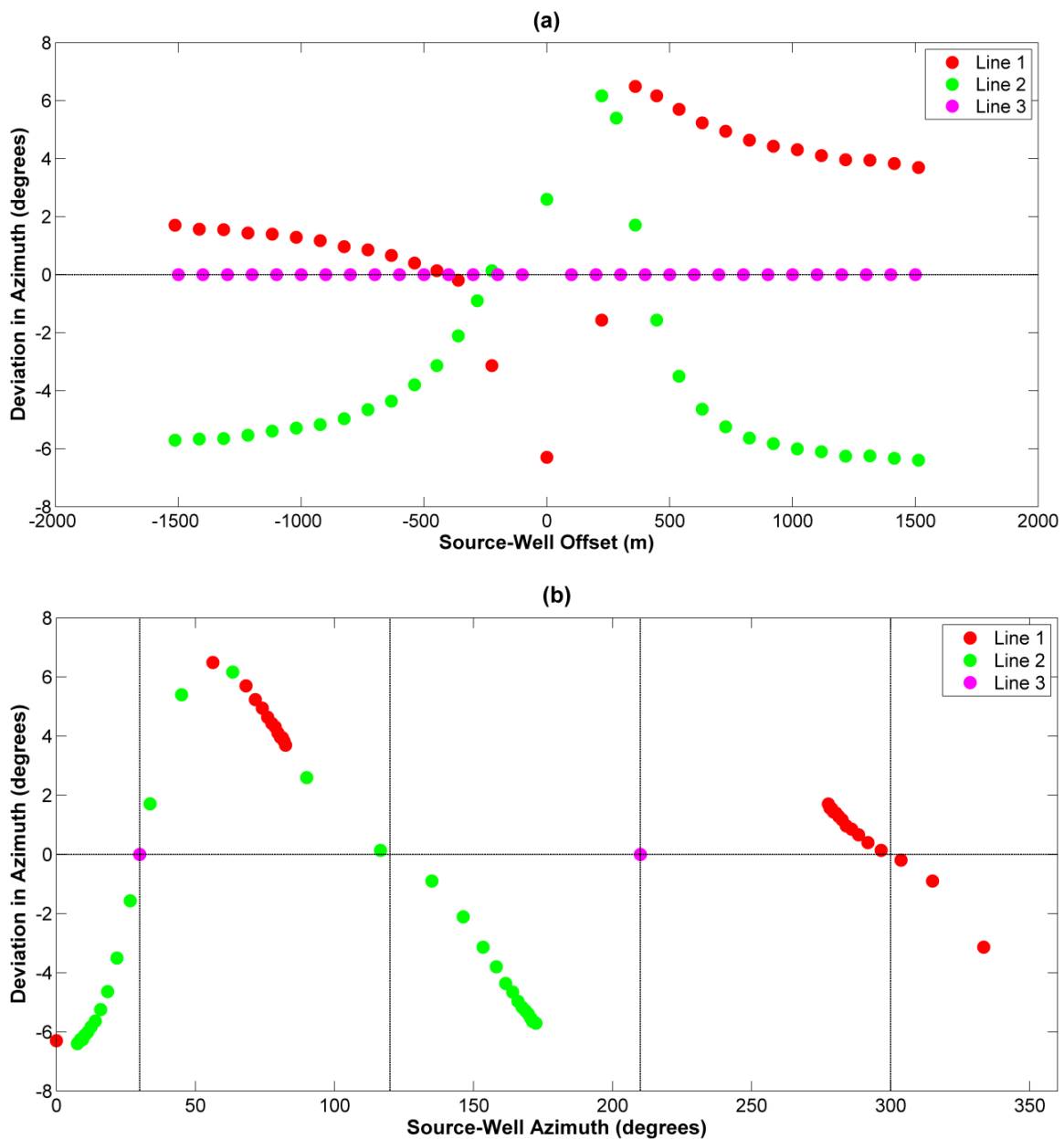


Figure 6.7: Calculated deviation in orientation angle due to anisotropy vs. source-well offset (a) and azimuth (b). Deviation for Line 1 is shown in red, deviation for Line 2 is shown in green, and deviation for Line 3 is shown in magenta. Azimuths where zero deviation is expected are shown as vertical lines.

6.4 Finite Difference Modelling

6.4.1 Model Parameters

Effects of HTI on geophone orientation azimuth analysis were also modelled using TIGER. A simple 2 layer geologic model was constructed using the parameters shown in Table 6.1; note that the interface has no dip. There were three shot lines recorded, each trending East-West with 10 m shot spacing; Lines 1 and 3 were 100 m south and north of the well location respectively, and Line 2 went directly over the well location (Figure 6.8). Receivers were placed at 10 m intervals from 10-300 m below the surface. The parameters were purposefully chosen to be similar to the finite difference model constructed in Chapter 5, in order to simplify comparison. An example of a common shot gather is shown in Figure 6.9, and an example of a common receiver gather is shown in Figure 6.10. Direct shear waves are visible in the shot gather, as evidenced by the second set of downgoing arrivals visible in receivers 9 – 17, which are above the layer interface.

Table 6.1: Numerical parameters used for acquisition.

| TIGER Acquisition Parameters | |
|---------------------------------------|--|
| Dimensions | 490 x 490 x 490 m |
| Grid size | 10 m |
| Recording time | 700 ms |
| Sample rate | 1 ms |
| Source wavelet | First Derivative Gaussian |
| Number of source lines | 3 |
| Number of sources per line | 30 |
| Source interval | 10 m |
| Number of receivers | 30 |
| Receiver interval | 10 m |
| Receiver depth range | 10-300 m |
| Upper layer velocities (V_P, V_S) | 2000 m/s, 1000 m/s |
| Lower layer velocities (V_P, V_S) | 2900 m/s, 1740 m/s |
| Thomsen parameters of upper medium | $\epsilon = 0.1, \delta = 0.025, \gamma = 0.1$ |
| Thomsen parameters of lower medium | $\epsilon = 0, \delta = 0, \gamma = 0$ |
| Depth of interface | 180 m |

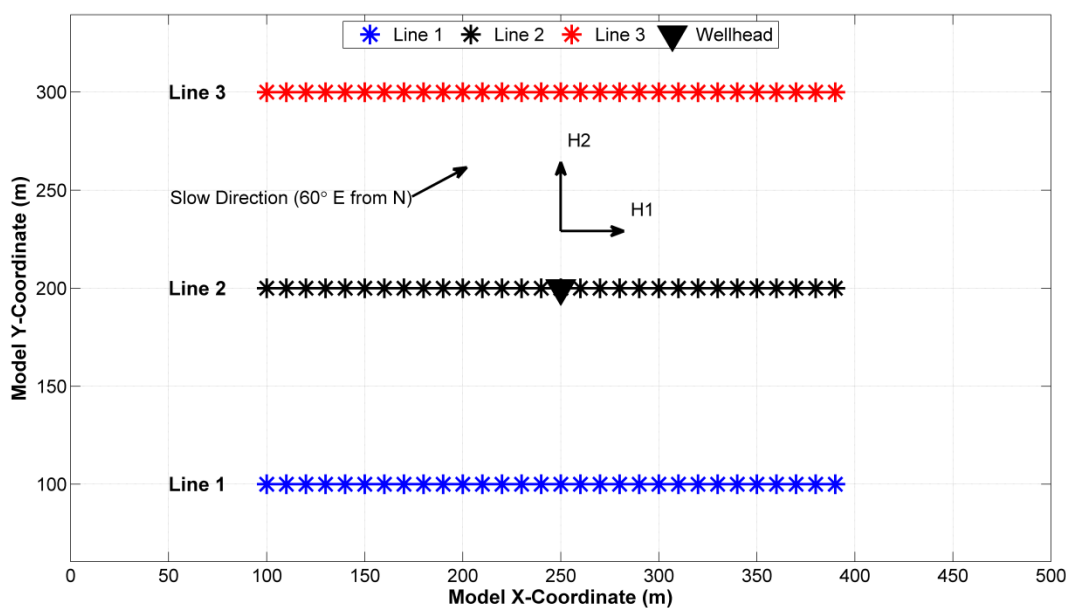


Figure 6.8: Plan view of surface geometry used in TIGER. Line 1 is shown in blue, Line 2 is shown in black and Line 3 is shown in red.

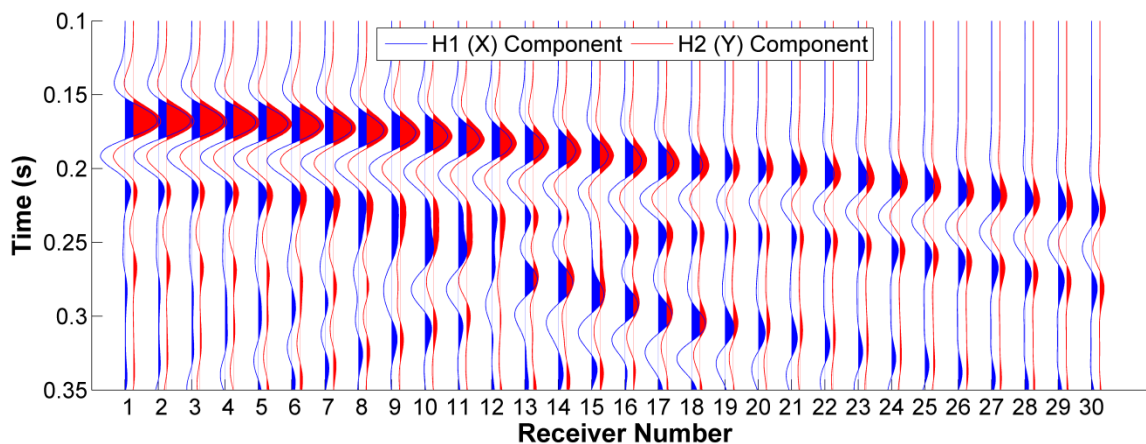


Figure 6.9: Example of raw TIGER output from the shot at $x = 130$ m and $y = 100$ m. H1-component output is shown in blue and H2-component output is shown in red.

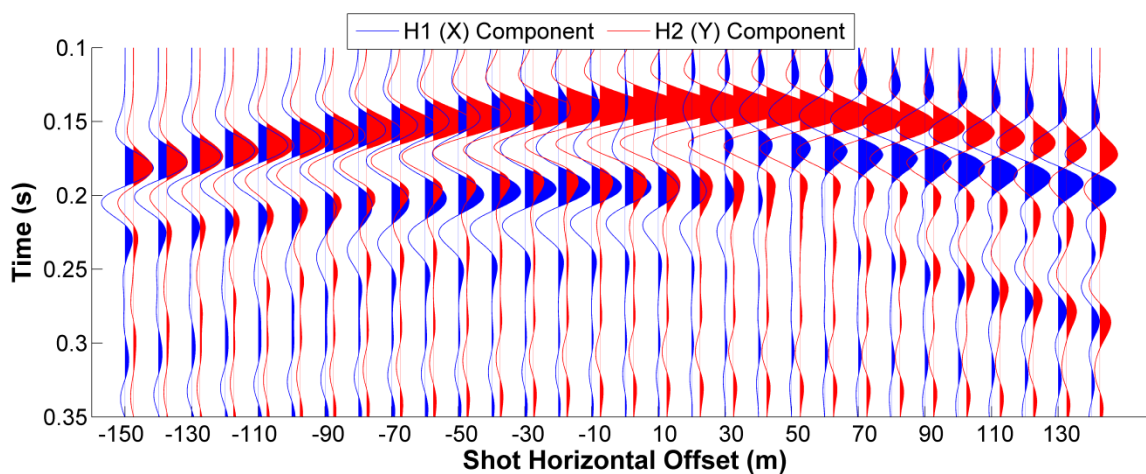


Figure 6.10: Example of raw TIGER output from the receiver at 50 m depth. H1-component output is shown in blue and H2-component output is shown in red.

6.4.2 Results

Results shown here will focus on four receivers, which are the same as those chosen in Chapter 5: Receiver 5 (at 50 m depth), well above the interface; Receiver 15 (at 150 m depth), just above the interface; Receiver 20 (at 200 m depth), just below the interface; and Receiver 30 (at 300 m depth), well below the interface. For further results using Receivers 8 through 23, see Appendix E. Figures 6.11 – 6.14 show the deviation in orientation azimuth calculated using the analytic method, when using a 100 ms analysis window beginning at the first breaks. The deviation has a sinusoidal trend with respect to azimuth, though its shape is different than that predicted by the direct subtraction of the phase and group angles. Interestingly, the magnitude of the deviation is largest at Receiver 5; it decreases towards the interface, and increases again for receivers deeper than the interface.

Additionally, these plots, especially that of Receiver 5, show that the deviation has a dependence on offset; this is clear when examining the data from Line 2. A likely source of this trend is the direct S-wave arrivals, created from the source due to birefringence; as offset increases, the gap between the P and S-wave direct arrivals will increase, which should decrease deviation in orientation analysis. Decreasing the analysis window should therefore provide some mitigation of this effect; Figures 6.15 and 6.16 show the results of this analysis when using a 50 ms window for Receivers 5 and 30. Indeed, the magnitude of the deviation is reduced for both of these cases, and the dependence on offset is drastically reduced for Receiver 5.

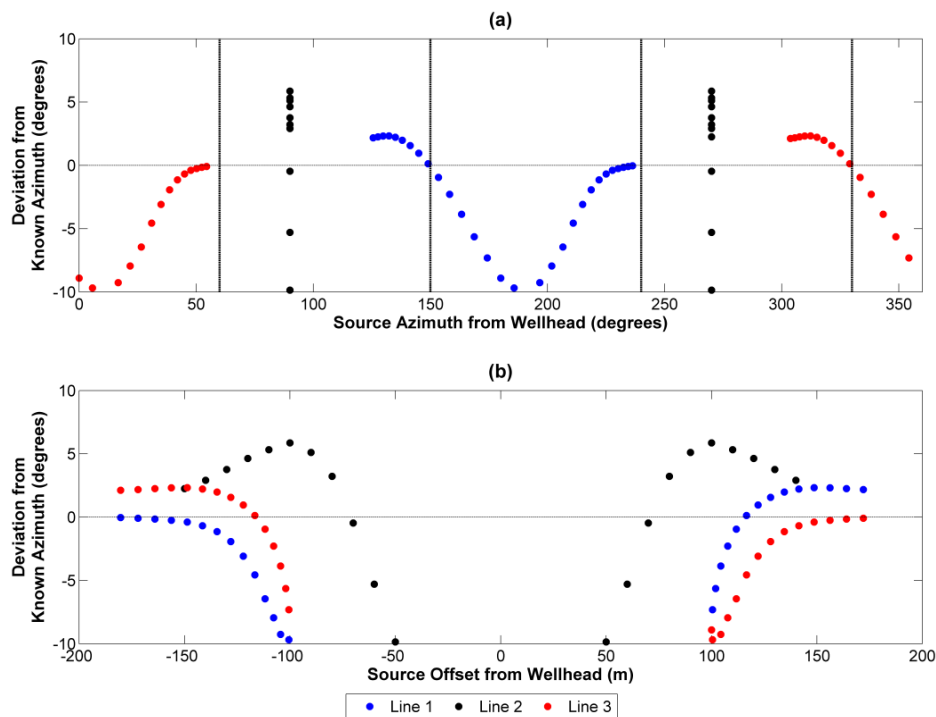


Figure 6.11: Deviation in orientation angle for Receiver 5 (50 m depth) plotted as a function of source-well azimuth (a) and source-well offset (b). Line 1 is shown in blue, Line 2 in black and Line 3 in red.

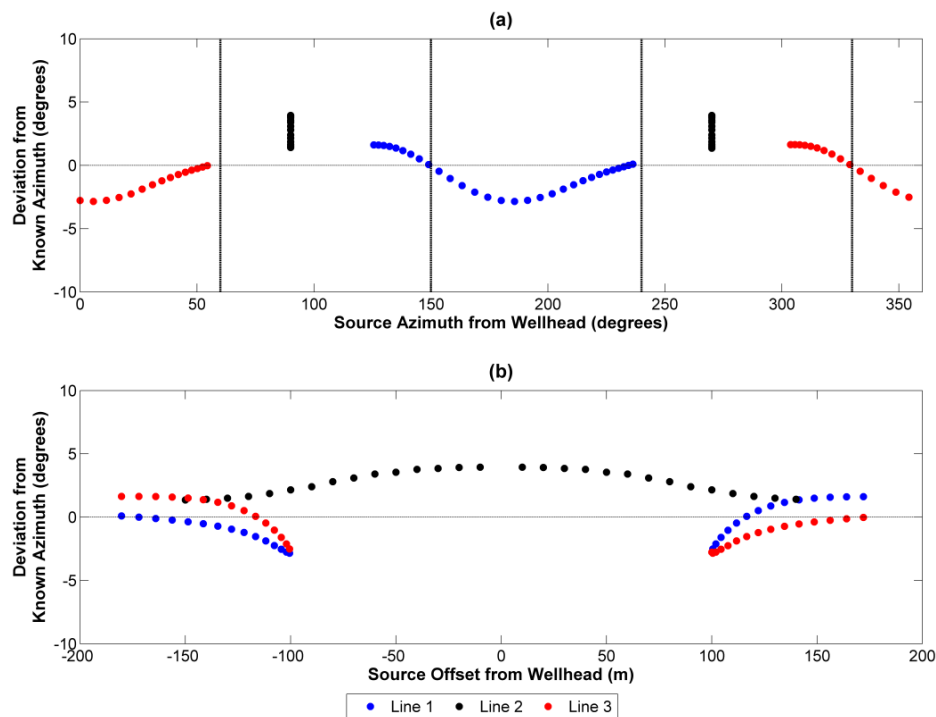


Figure 6.12: Deviation in orientation angle for Receiver 15 (150 m depth) plotted as a function of source-well azimuth (a) and source-well offset (b). Line 1 is shown in blue, Line 2 in black and Line 3 in red.

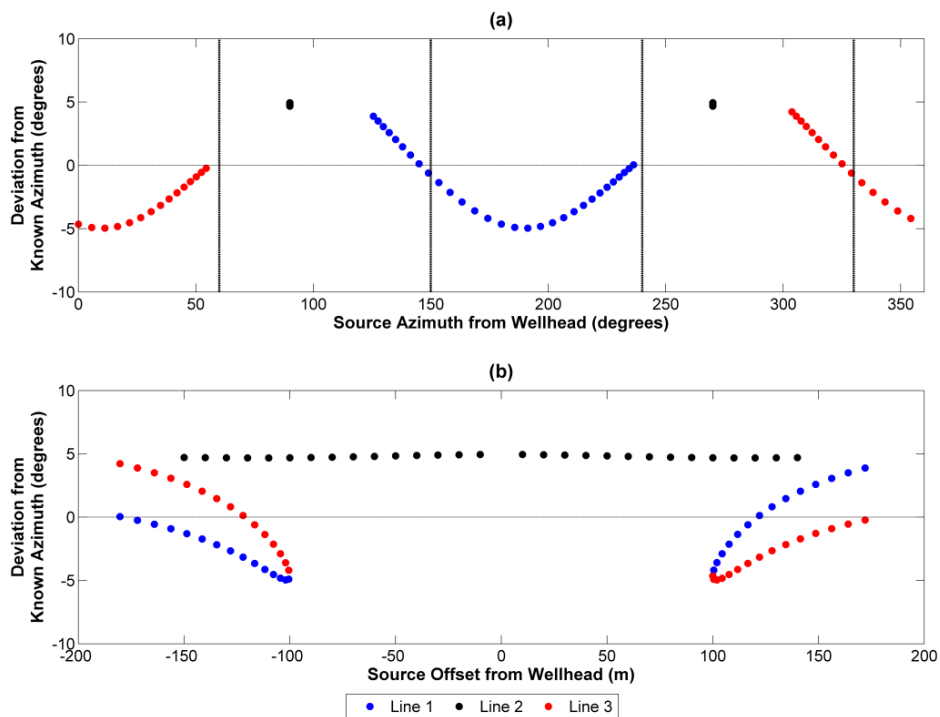


Figure 6.13: Deviation in orientation angle for Receiver 20 (200 m depth) plotted as a function of source-well azimuth (a) and source-well offset (b). Line 1 is shown in blue, Line 2 in black and Line 3 in red.

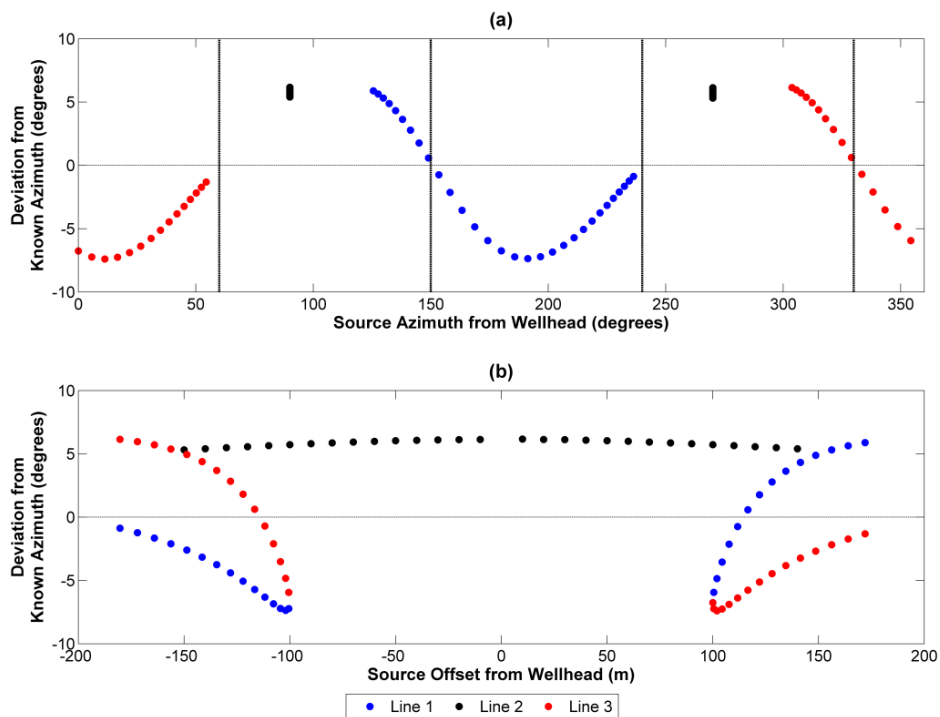


Figure 6.14: Deviation in orientation angle for Receiver 30 (300 m depth) plotted as a function of source-well azimuth (a) and source-well offset (b). Line 1 is shown in blue, Line 2 in black and Line 3 in red.

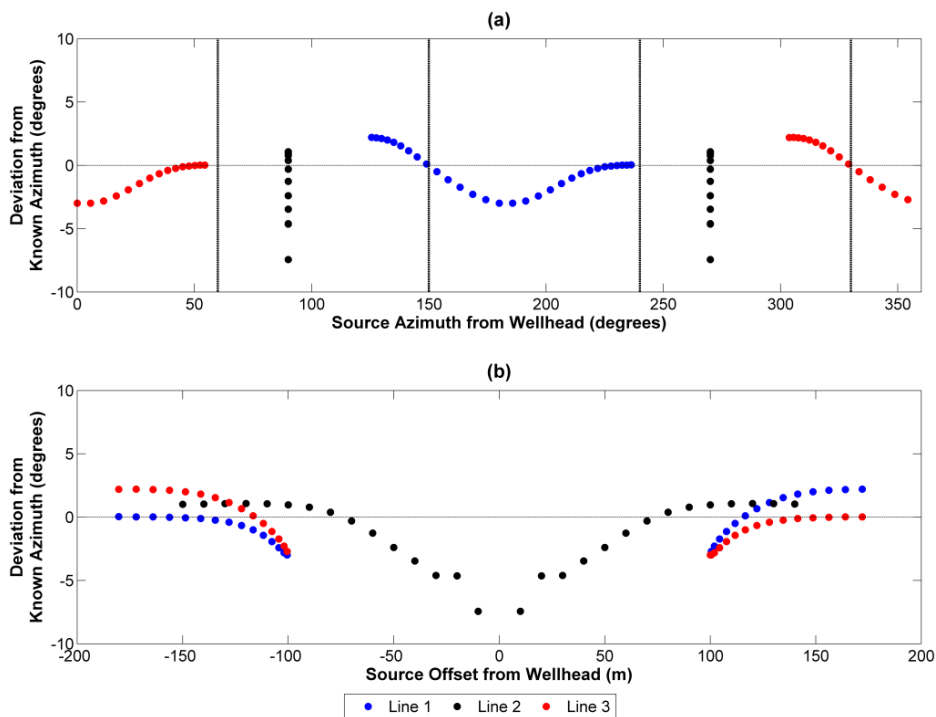


Figure 6.15: Deviation in orientation angle for Receiver 5 (50 m depth), using a 50 ms analysis window, plotted as a function of source-well azimuth (a) and source-well offset (b). Line 1 is shown in blue, Line 2 in black and Line 3 in red.

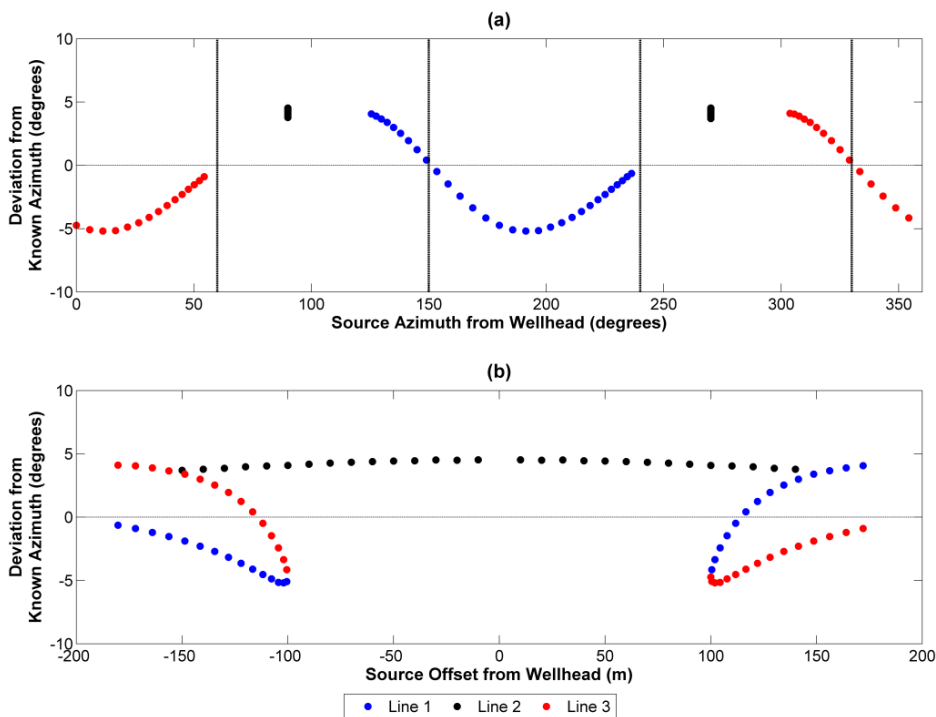


Figure 6.16: Deviation in orientation angle for Receiver 30 (300 m depth), using a 50 ms analysis window, plotted as a function of source-well azimuth (a) and source-well offset (b). Line 1 is shown in blue, Line 2 in black and Line 3 in red.

Table 6.2 shows the standard deviation of every 5th receiver, found using both window sizes. It is also shown graphically in Figure 6.17 for all receivers. For receivers in the top 140 m, analysis performed using a 50 ms window shows much less scatter, again suggesting that direct S-wave arrivals have a considerable impact on this analysis. For both window sizes, there is a slight increase in scatter in the 2-3 receivers directly above the interface, which most likely arises due to contamination from reflected waves; scatter drops for the receiver located on the interface. For receivers below the interface, scatter increases with depth up to a maximum value at about 50 m below the interface, and then begins to decrease again. Note that the maximum scatter occurs at the same receiver regardless of window size.

Table 6.2: Standard deviation of receiver orientation azimuth.

| Receiver | Depth (m) | 100 ms Window St. Dev. (°) | 50 ms Window St. Dev. (°) |
|-----------------|------------------|---------------------------------------|--------------------------------------|
| 5 | 50 | 5.68 | 2.08 |
| 10 | 100 | 4.47 | 2.05 |
| 15 | 150 | 2.06 | 1.98 |
| 20 | 200 | 3.66 | 3.81 |
| 25 | 250 | 6.06 | 4.97 |
| 30 | 300 | 5.09 | 3.62 |

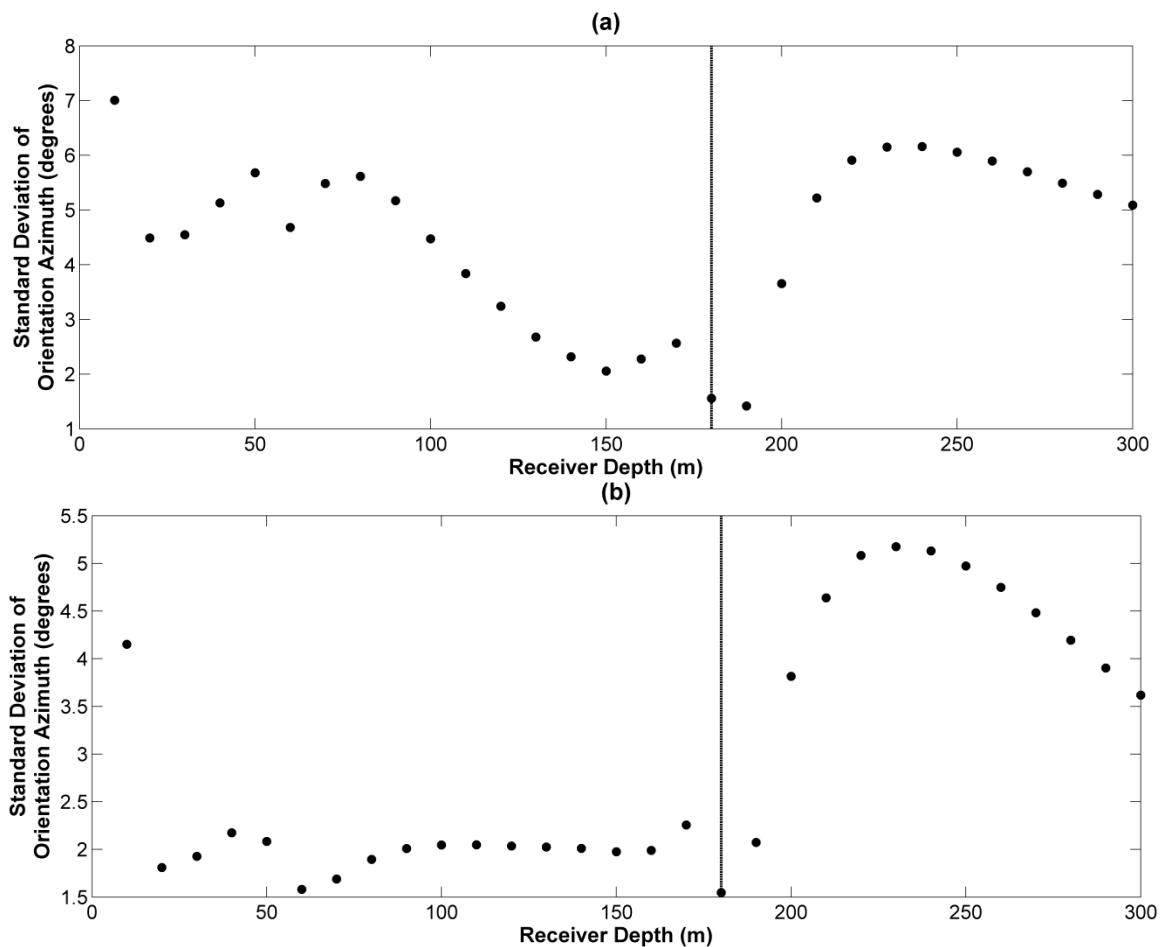


Figure 6.17: Standard deviation of orientation azimuth found using 100 ms window (a) and 50 ms window (b). The depth of the layer interface is indicated with a black line.

6.4.3 Comparison to Analytic Method

Based on the plots shown above, simply differencing the group and phase angles does not match the results given by finite difference, in terms of geophone orientation azimuth deviation. To more explicitly note this difference, the survey geometry and anisotropic parameters modelled using TIGER were replicated using analytic modelling. Figure 6.18 shows a direct comparison of the results given by both methods. Here, results from TIGER are from Receiver 15, using a 50 ms analysis window; these parameters were chosen in order to minimise contamination due to the direct S-wave arrivals. This comparison reveals that the difference in phase and group angles overestimates the deviation when compared to results from TIGER, most notably at the maximum and

minimum values. Zero-crossings for both methods appear to coincide well, however, matching azimuths parallel to the fast and slow directions where deviation is expected to be zero.

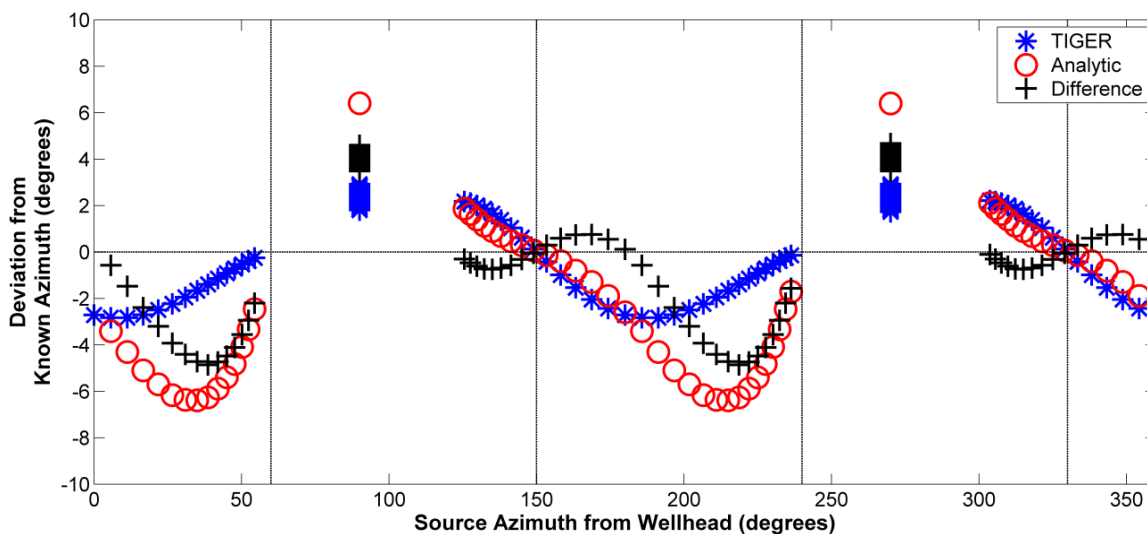


Figure 6.18: Comparison of deviation in geophone orientation angle using TIGER (blue) and analytic (red) methods. The difference between the two methods is shown in black. Azimuths with an expected error of zero are labelled with vertical lines.

6.5 Discussion

In the first example presented above, the maximum deviation in angle is more sensitive to ε than it does to δ . At modest values of these parameters, the maximum difference of group and phase angle can exceed 10° ; additionally, it was shown to become larger than 5° even with relatively small values for δ and ε . To give a sense of what this means, an error of 5° at 1000 m offset would cause a lateral mispositioning of about 87 m. In a study by Van Dok et al. (2011), the danger of ignoring anisotropy is illustrated by comparing the locations of microseismic events calculated with and without incorporation of anisotropy in the velocity model; the result is lateral mispositioning of these events by hundreds of feet.

The modelled calibration study also shows some interesting results. First, when plotting the calculated orientation angle deviation against offset, each line shows a distinct, seemingly unrelated trend, making it difficult to interpret the meaning of the

results; this is with the exception of Line 3, which was strategically chosen to be parallel to the symmetry axis of the HTI medium, and shows no deviation. The scatter observed in the angles calculated from Lines 1 and 2 may, in fact, be mistakenly attributed to the effects of random noise. At the farther offsets, these lines appear to have an asymptotic behaviour; the reason for this is that the source-receiver azimuth is being less affected as the offset increases. This can be seen when examining the plot of orientation angle against source-receiver azimuth – shot locations for Line 1 are approaching azimuths of 90° and 270° , while those for Line 2 are approaching 0° and 180° . However, unlike results found from modelling of random noise and dipping velocity interfaces, the deviation approached with increasing offset is non-zero.

Finally, results from finite difference modelling deviated moderately from the analytic modelling. Part of this difference was due to the presence of direct S-wave arrivals in this method; this added a noticeable offset dependence to the deviation in geophone orientation azimuth. However, the finite difference model generally showed less deviation than the analytic model, implying that there is still something unaccounted for in either the analytic code or the finite-difference approach. Most likely, the main reason for this overestimation lies in the polarisation vector being measured by the geophone. The analytic model assumes that the geophone is measuring energy polarised in the direction of the phase angle; if the actual polarisation direction lies somewhere between the phase and group angles, as was shown in Li et al. (1987), this model would lead to an overestimation of deviation.

6.6 Summary

The following results can be noted from this chapter:

- The maximum deviation in geophone orientation angle due to anisotropy is more sensitive to the parameter ε than it is to δ . Even given δ within ± 0.05 , differences between group and phase angle can exceed 5° for values of ε as small as 0.05.

- An analytic model created using $\varepsilon = 0.1$ and $\delta = 0.025$ showed a maximum difference in phase and group angle of 6.45° .
- The effect of anisotropy on geophone orientation angle is difficult to interpret when examined as a function of source-receiver offset; however, it produces a much more consistent trend when examined as a function of source-receiver azimuth.
- The choice of window size was shown to be important when using finite difference modelling. Decreasing the window size from 100 ms to 50 ms resulted in a decrease in geophone orientation deviation of over 50 % for receivers above the interface. This is primarily due to effects from the direct S-wave arrivals.
- Deviation for receivers above the interface was consistent when using a 50 ms window, resulting in a standard deviation of approximately 2° .
- For both window sizes, deviation for receivers below the interface increased with depth, reaching a maximum at 50 m below the interface before decreasing.
- Deviation found using finite difference modelling was less than that found using analytic modelling. One possible explanation for this discrepancy is that the polarisation angle of first arrival energy is not equal to the phase angle, as was assumed by the analytic modelling code; rather, it lies between the phase and group angles.
- For both methods, deviation was at zero for source-receiver azimuths parallel to the fast and slow directions.

Chapter Seven: Lousana 3D Field Example

7.1 Introduction

In this chapter, I determine the orientation azimuths of 3-component receivers in a downhole tool, placed in a vertical well, from first arrival analysis of the horizontal components. Results were examined for consistency, for a large range of surface source offsets and azimuths. The methods that were used to find geophone orientation were an analytic method developed by DiSiena et al. (1984), as well as hodogram analysis, both windowed on the direct P-wave arrivals. The relationship between source-well offset and scatter in orientation azimuth is examined in further detail, which build on the results found in previous chapters.

7.2 Survey Geometry

In July 2007, several vertical seismic profile (VSP) surveys were acquired for EnCana Corporation, using a vertical well near Lousana, Alberta; these surveys were comprised of a zero offset VSP, three 2D walkaway VSP's and a 3D VSP. The walkaway survey consisted of three lines, trending south, southeast and east; each line had 10 source locations with a maximum source-well offset of 1391 m (Figure 7.1). The 3D survey consisted of 249 source locations with a maximum offset of 3255 m (Figure 7.2). Both surveys used two coupled geophone tools, each with eight 3-component geophones, and 2 kg of dynamite at a depth of 15 m was used as a source. All source locations in the walkaway dataset were repeated 4 times using different tool levels, resulting in a total of 64 receiver locations. The 3D VSP was performed separately after the walkaway, using a single tool position. The receiver depth range for the walkaway survey was 468 m to 1420 m, and the depth range of the 3D survey was 717 m to 944 m. An example of a common shot gather from a near-offset shot from the east-trending line is shown in Figure 7.3; an example of a common shot gather from the 3D VSP survey, again from a near-offset shot, is shown in Figure 7.4. It should be noted that data from the receiver at position 2 of each level were not used in the analysis, as there was a problem with one of its horizontal components. The VSP surveys were undertaken primarily for imaging deep coal seams, but in this study I focus on a statistical analysis of the geophone orientations

in the well. Both angle analysis methods were used for the 2D walkaway dataset; Figure 7.5 shows sample hodograms for a near and far offset shot, along with the lines of best fit.

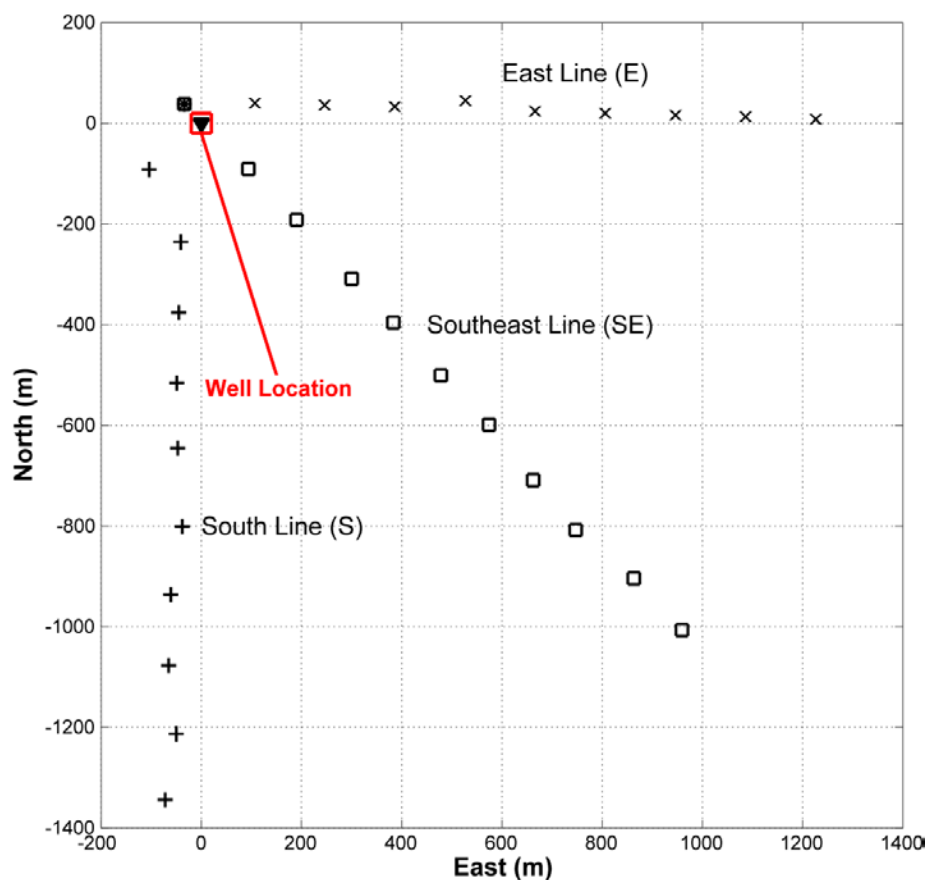


Figure 7.1: Surface geometry for the 2D walkaway VSP surveys. Coordinate origin is at the well. Lines are identified as E, SE and S.

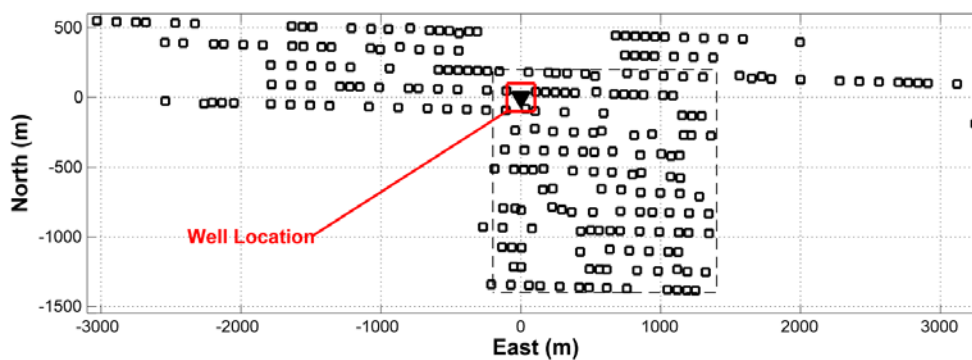


Figure 7.2: Surface geometry for the 3D VSP survey, showing an outline of the 2D walkaway VSP area. Coordinate origin is at the well.

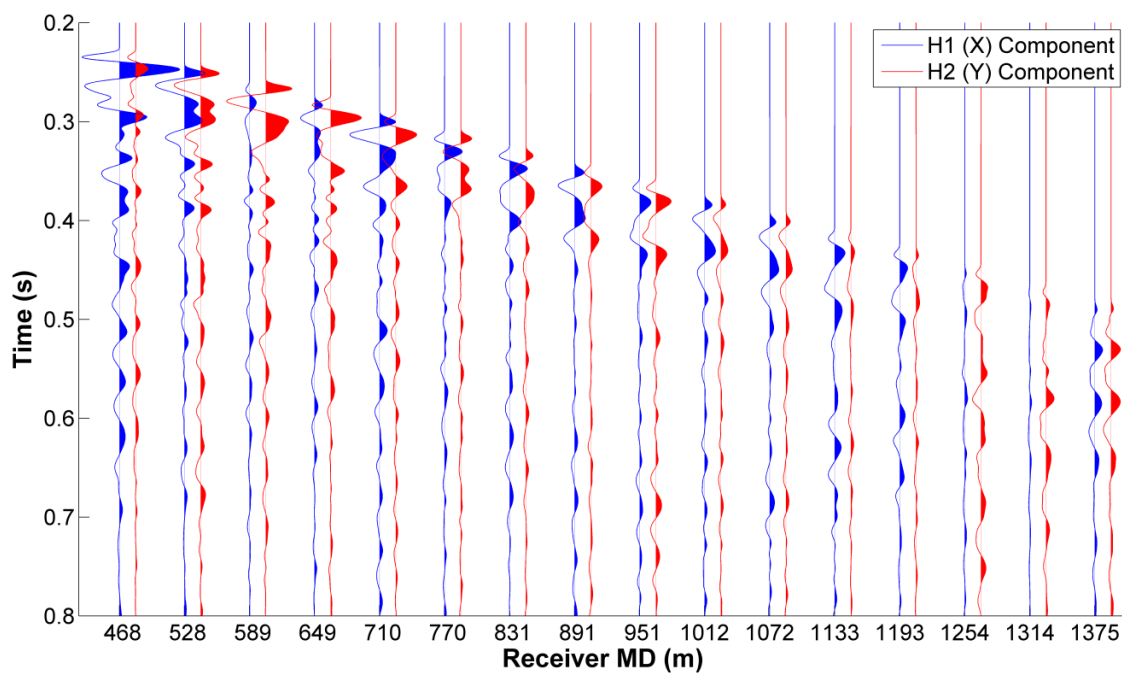


Figure 7.3: Raw shot gather from a near offset shot of the East line of the 2D walkaway VSP survey; coordinates are 33 m north and 386 m east of the well. H1-component is shown in blue and H2-component is shown in red. No gain has been applied.

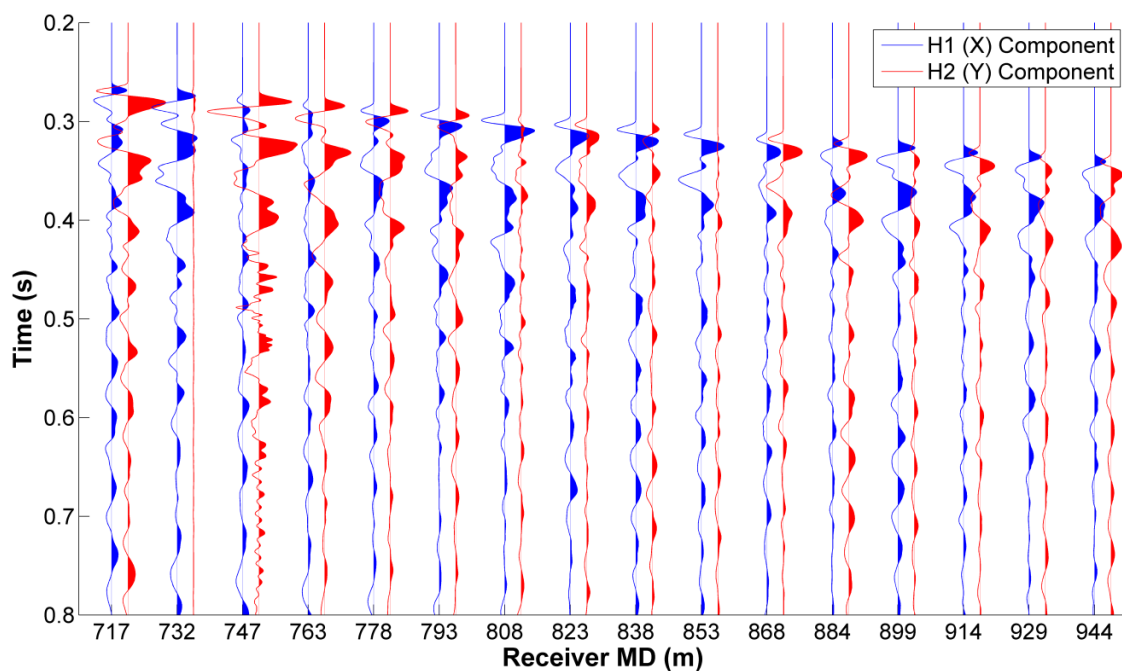


Figure 7.4: Raw shot gather from a near offset shot of the 3D VSP survey; coordinates are 81 m south and 33 m east of the well. H1-component is shown in blue and H2-component is shown in red. No gain has been applied.

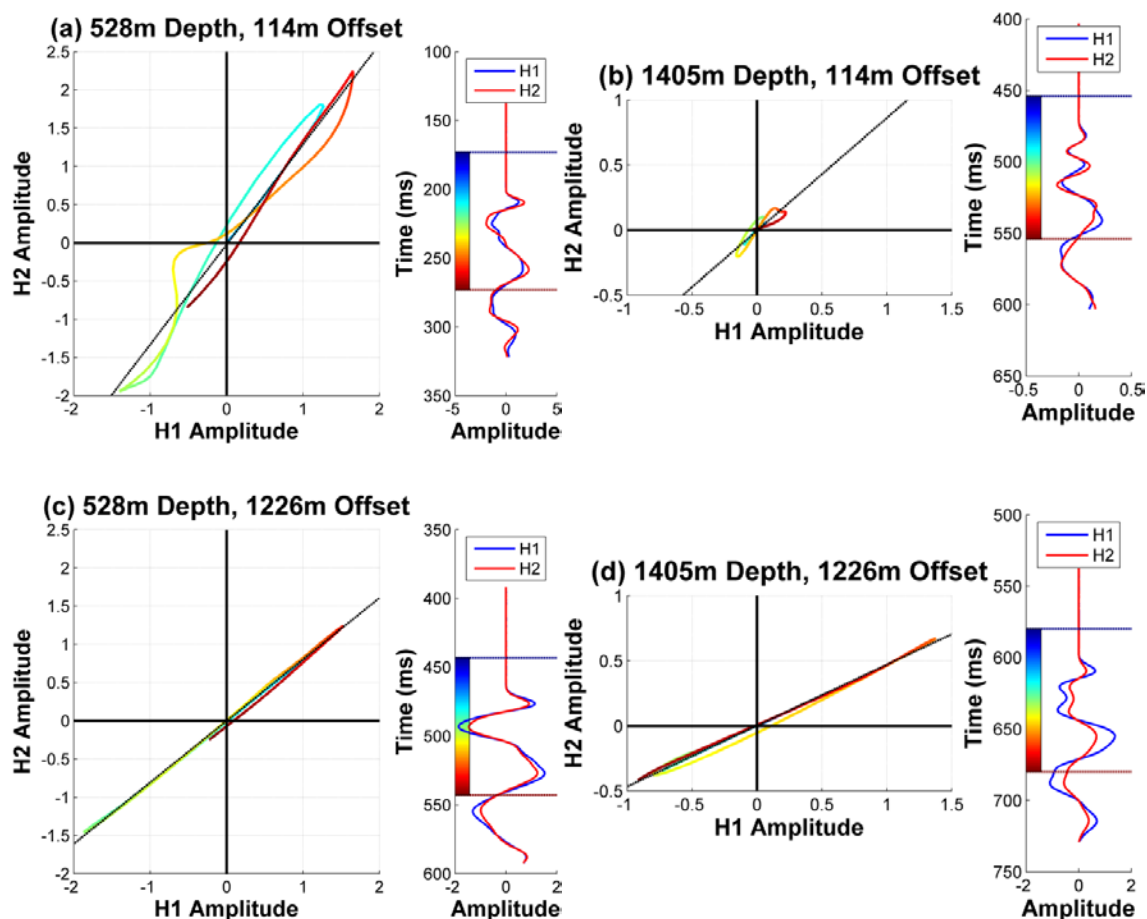


Figure 7.5: Examples of hodograms from the East line of the 2D walkaway VSP data.

7.3 2D walkaway results

Figure 7.6 shows the results of geophone orientation azimuths calculated using the analytic method, for a subset of receivers. Each of the three walkaway datasets is shown in a different colour; there were an equal number of data points for all three lines, and they each had a similar offset distribution. Figure 7.6 shows that the orientation azimuths have no clear dependence on the orientation of the line chosen, and agreement is good between each of the lines. More scatter can be seen in the nearer source offsets, and the deeper receiver positions retain this scatter for larger source-well offsets. These effects are related to the incoming angle of the direct P-wave energy at the receiver: small receiver depths and large source-well offsets result in incident angles at the receiver close

to 90°, resulting in horizontal components recording a greater proportion of the direct energy, thereby reducing scatter in analysis of geophone orientation azimuth.

Table 7.1 summarises the statistical analysis of a subset of receivers in the 2D walkaway dataset, using 3σ , 2σ and 1σ cutoff values for outlier removal, as well as removal of data points from source-well offsets smaller than 500 m. There is a significant decrease in scatter of orientation azimuth when reducing the outlier cutoff from 3σ to 2σ , whereas reducing the cutoff from 2σ to 1σ only slightly decreases scatter. Removal of data points from near offsets shows the least scatter, quantitatively confirming the trend noticed in Figure 7.6. Table 7.2 provides a comparison of orientation statistics of far offset data using the analytic and hodogram methods for the same subset of receivers. Direct comparison of standard deviation values is shown in Figure 7.7a, and the differences between means calculated using the two methods are shown in Figure 7.7b. Mean values calculated using the two methods are generally within $\pm 0.5^\circ$ of each other, and scatter is slightly better when using the analytic method. Finally, Figure 7.8 shows the standard deviation for each receiver, calculated using both methods. Overall, the two methods produced similar results; thus, results using the hodogram method will be omitted for the 3D VSP.

Table 7.1: Geophone orientation statistics for a subset of the 2D dataset made using the analytic method, for different outlier conditions. Means and standard deviations are in degrees.

| Receiver Number | Depth (m) | 3σ | | 2σ | | 1σ | | Far Offsets | |
|-----------------|-----------|-----------|--------|-----------|--------|-----------|--------|-------------|--------|
| | | Mean | S. Dev | Mean | S. Dev | Mean | S. Dev | Mean | S. Dev |
| 1 | 468 | 275.1 | 4.65 | 276.5 | 1.63 | 276.3 | 1.35 | 276.6 | 0.48 |
| 13 | 649 | 195.8 | 5.64 | 197.5 | 1.82 | 197.3 | 1.38 | 197.5 | 1.00 |
| 25 | 831 | 229.1 | 1.20 | 228.8 | 0.84 | 228.8 | 0.51 | 228.9 | 0.47 |
| 37 | 1012 | 119.5 | 6.41 | 117.6 | 1.71 | 117.8 | 0.95 | 118.0 | 0.71 |
| 49 | 1193 | 242.7 | 7.23 | 240.5 | 1.91 | 240.5 | 1.91 | 240.8 | 0.59 |
| 61 | 1375 | 317.1 | 6.93 | 315.0 | 2.21 | 315.3 | 1.79 | 315.4 | 0.82 |
| Average | | | 5.22 | | 1.63 | | 1.26 | | 0.67 |

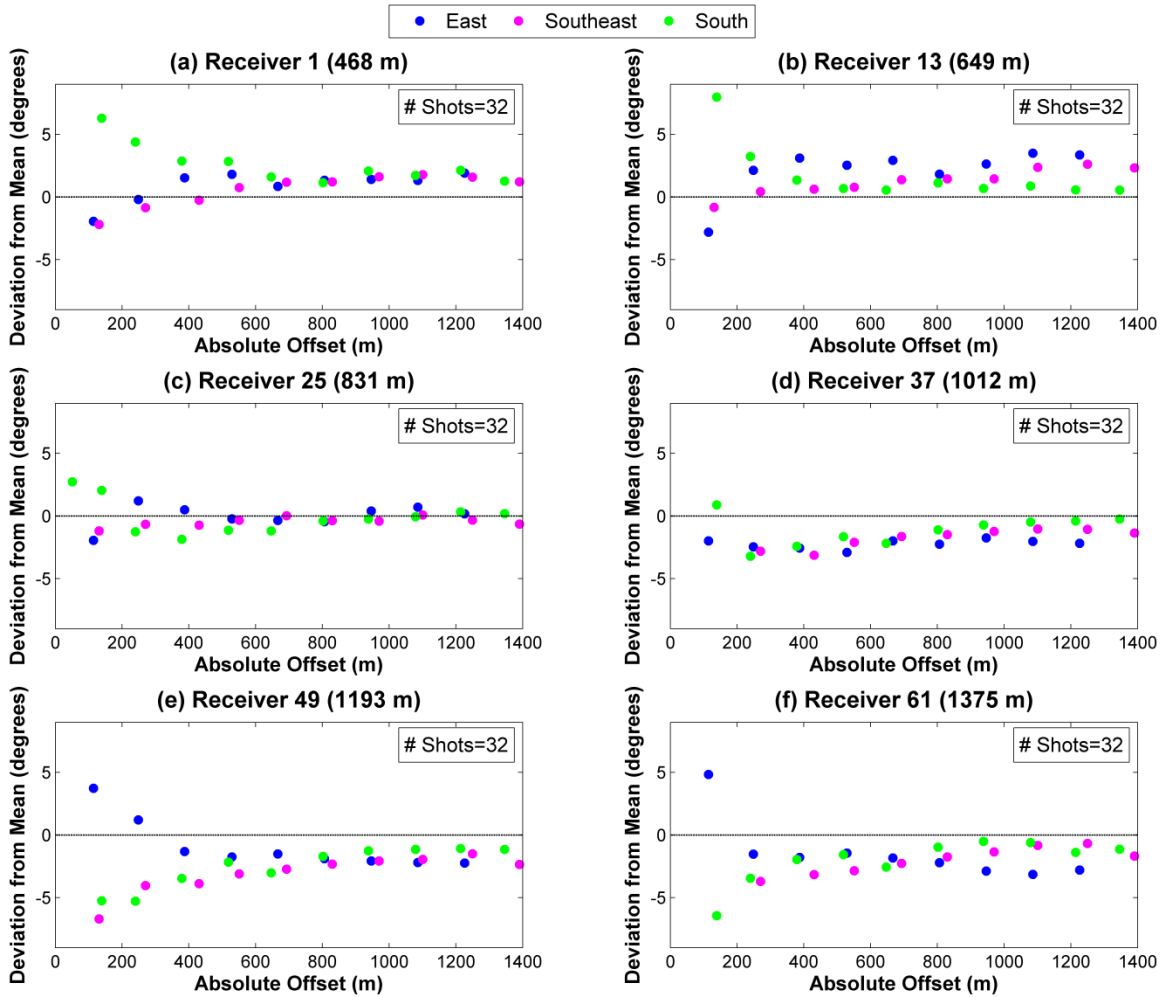


Figure 7.6: Variation in geophone orientation azimuths for several receiver positions, calculated using the analytic method, for the 2D walkaway dataset coloured by line; E is shown in blue, SE is shown in magenta and S is shown in green.

Table 7.2: Comparison of geophone orientation statistics for a subset of the 2D dataset for different analysis methods. Means and standard deviations are in degrees.

| Receiver Number | Depth (m) | Analytic | | Hodogram | | Difference | |
|-----------------|-----------|----------|----------|----------|----------|------------|----------|
| | | Mean | Std. Dev | Mean | Std. Dev | Mean | Std. Dev |
| 1 | 468 | 276.6 | 0.48 | 277.3 | 1.27 | -0.69 | -0.79 |
| 13 | 649 | 197.5 | 1.00 | 197.5 | 1.06 | 0.01 | -0.06 |
| 25 | 831 | 228.9 | 0.47 | 229.1 | 0.51 | -0.17 | -0.04 |
| 37 | 1012 | 118.0 | 0.71 | 118.1 | 0.72 | -0.02 | -0.01 |
| 49 | 1193 | 240.8 | 0.59 | 240.8 | 0.58 | -0.04 | 0.01 |
| 61 | 1375 | 315.4 | 0.82 | 315.4 | 0.86 | 0.01 | -0.03 |
| Average | | | 0.67 | | 0.90 | | -0.23 |

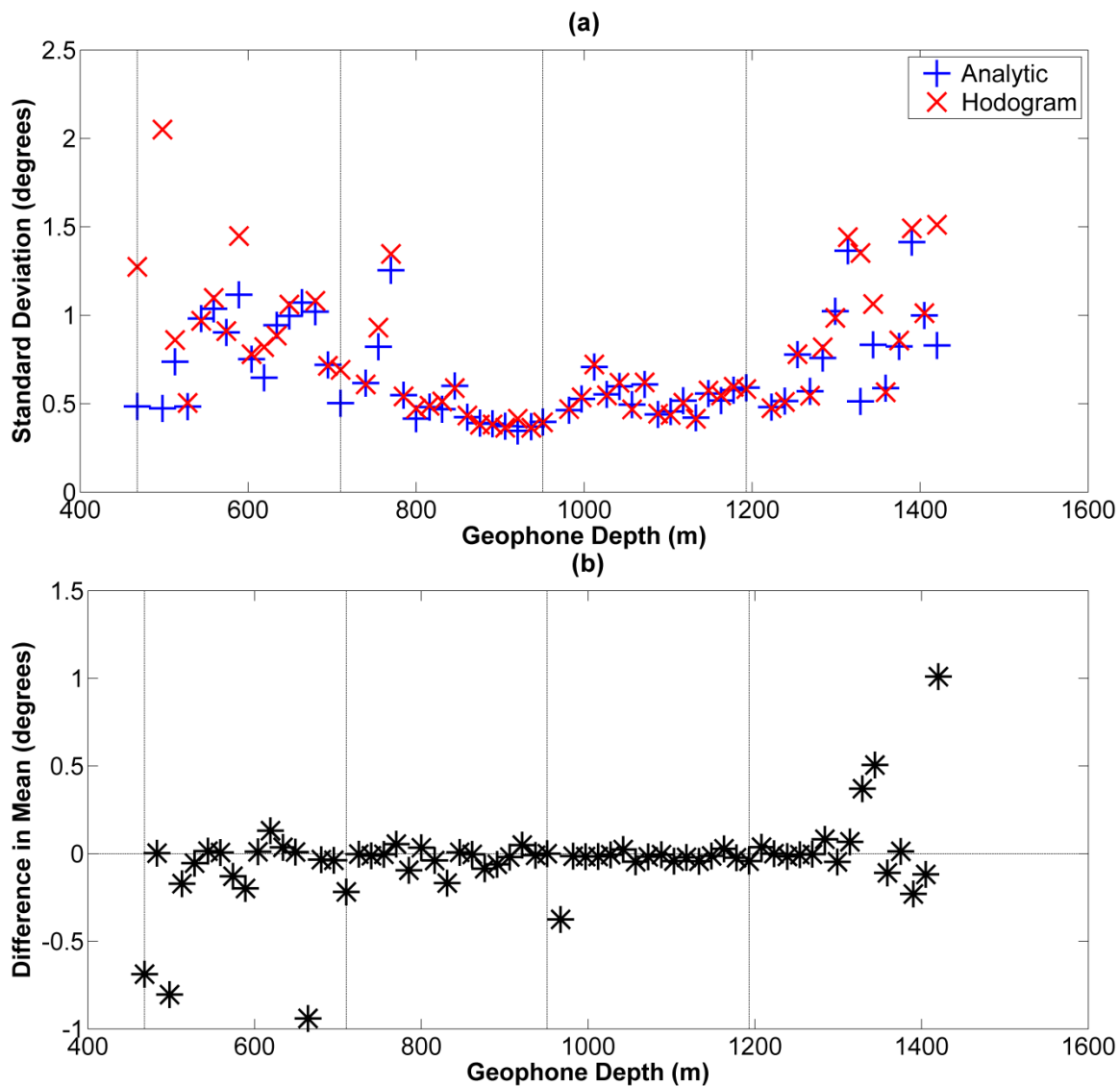


Figure 7.7: (a) Standard deviations for each receiver using the analytic (blue) and hodogram (red) methods. (b) Differences in mean orientation for each receiver; value is calculated by subtracting the hodogram mean from the analytic mean. Vertical lines are represent the top of each tool level.

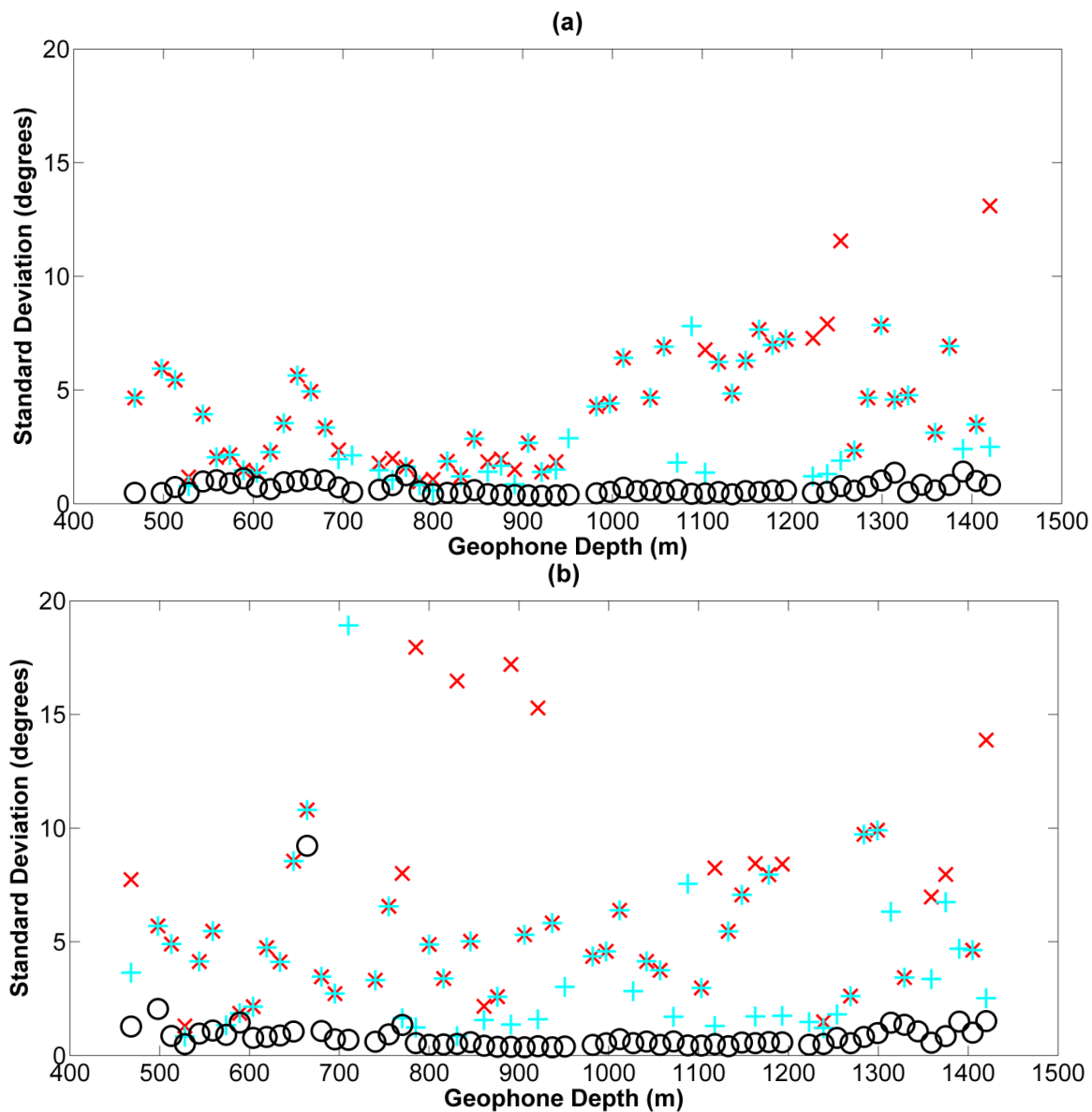


Figure 7.8: Orientation standard deviations for each receiver calculated using the (a) analytic and (b) hodogram methods. Red is calculated using all data points, cyan after removal of outliers and black after removal of outliers and near offsets less than 500 m.

7.4 3D walkaway Results

7.4.1 Sector analysis

In order to examine consistency of the relationship of geophone orientation and source-well azimuth, the 3D dataset was divided into 4 sectors based on the source-well azimuth (Figure 7.9). Sector centers were lines trending at 0° - 180° (Sector 1), 45° - 225° (Sector 2), 90° - 270° (Sector 3) and 135° - 315° (Sector 4) azimuths. As shown in Figure 7.9, due to the acquisition geometry, there was a large variation in the number of source locations between each sector. Figure 7.10 shows orientation azimuths calculated using the analytic method, plotted against offset. For all receivers, the calculated azimuths become much less scattered beyond about 500 m source-well offset, or about 1/2 of the geophone depth. It is not possible to discern any noticeable difference between angles calculated in each of the sectors; however, the lower number of source locations and more restricted offsets in Sectors 1, 2 and 4 is noticeable.

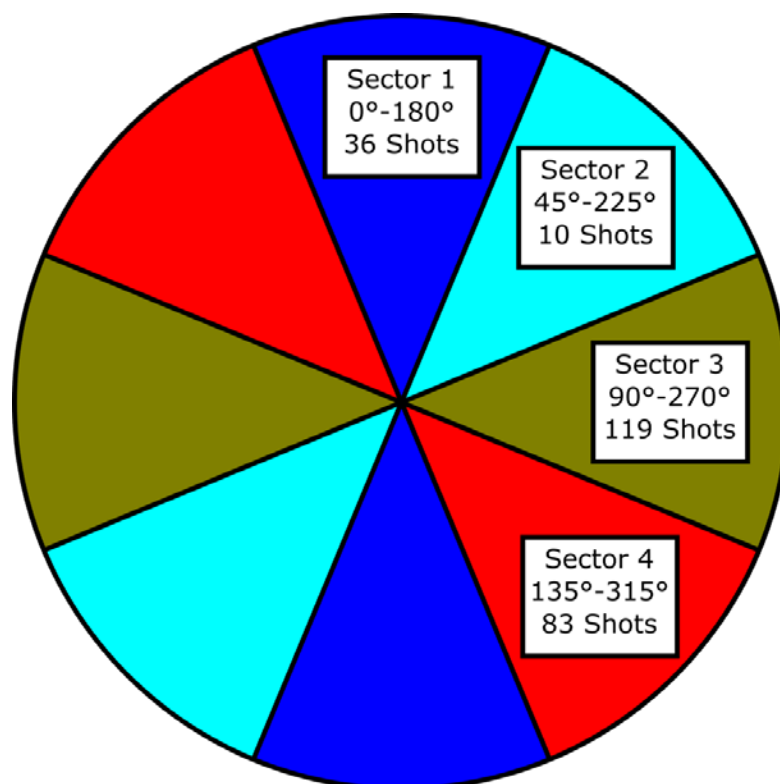


Figure 7.9: Azimuthal sectoring for the 3D walkaway VSP survey.

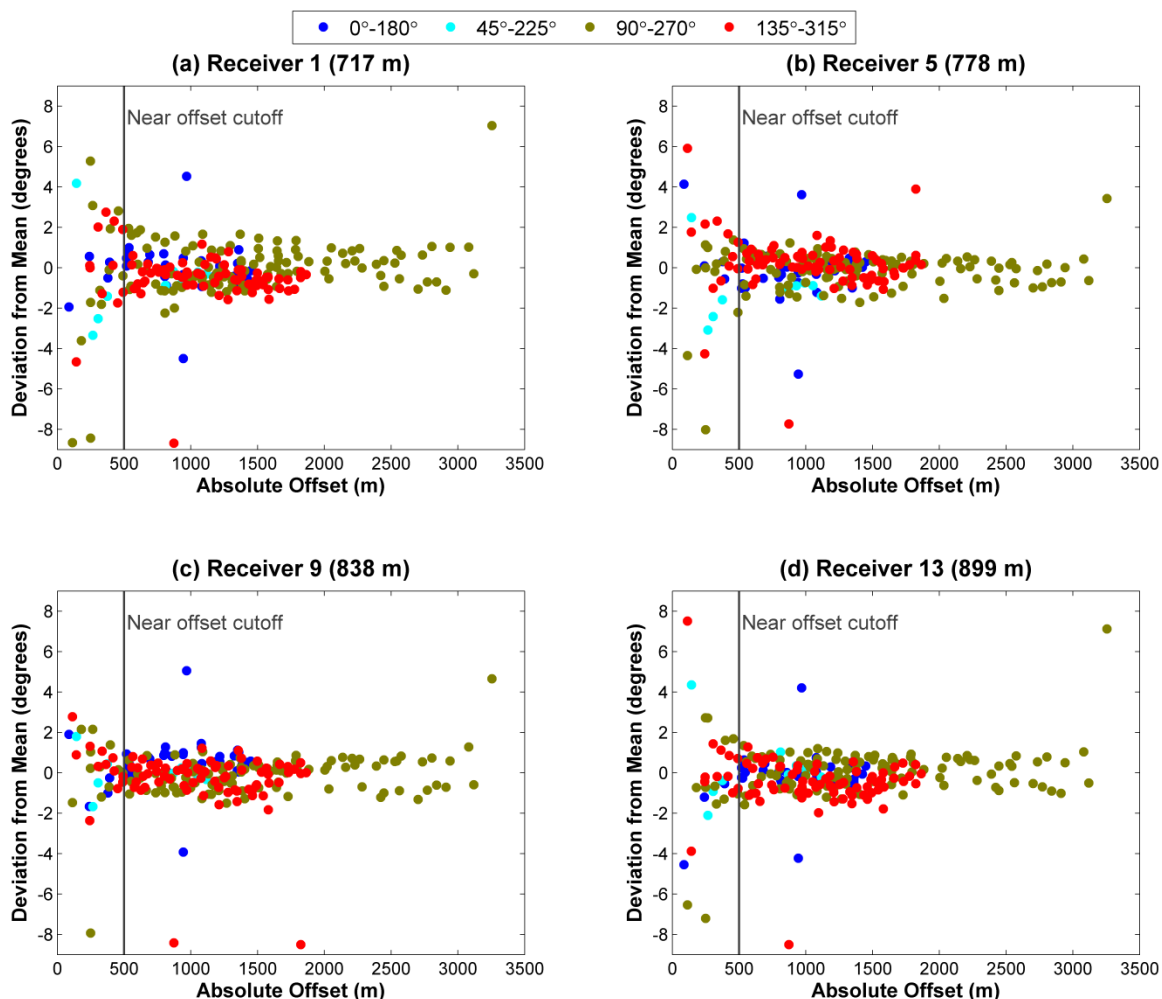


Figure 7.10: Deviation in geophone orientation azimuths, versus source-well offset, for several receivers in the 3D dataset calculated using analytic method, coloured by bin; 0°-180° is shown in blue, 45°-225° is shown in cyan, 90°-270° is shown in yellow and 135°-315° is shown in red.

Figure 7.11 shows orientation azimuths plotted against source-well azimuth. When viewed this way, there appears to be a subtle increase of calculated orientation angle at larger source-well azimuths. Histograms of orientation azimuth are shown in Figure 7.12 (all offsets) and Figure 7.13 (offsets greater than 500 m). Finally, Figure 7.14 shows a radial plot of results for a subset of the geophones; data points are plotted in plan view, showing the calculated azimuth as a function of source-well offset. This display provides a clear picture of the relationship between offset, orientation angle error and overall deviation for of each shot.

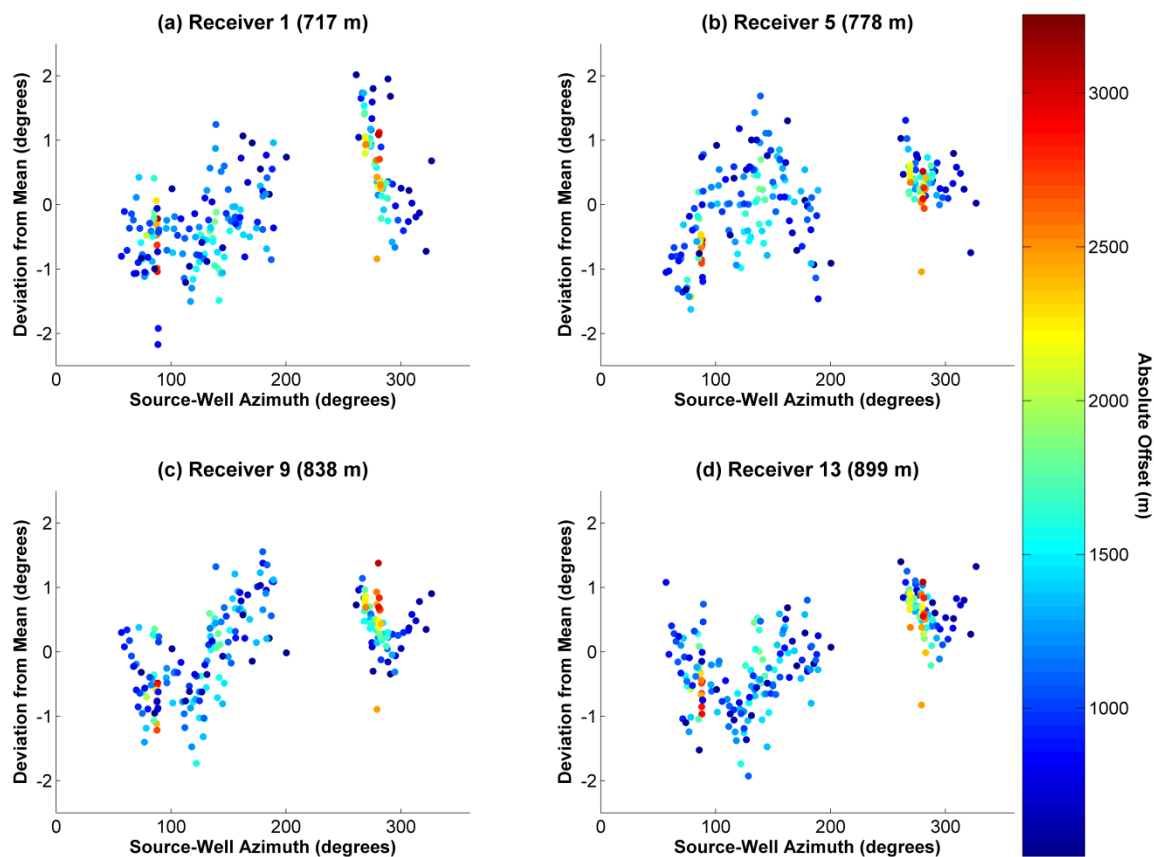


Figure 7.11: Deviation in geophone orientation azimuths, versus source-well azimuth, for several receivers in the 3D dataset calculated using analytic method, for 3D walkaway coloured by offset. Hotter colours represent far offsets, cooler colours represent near offsets.

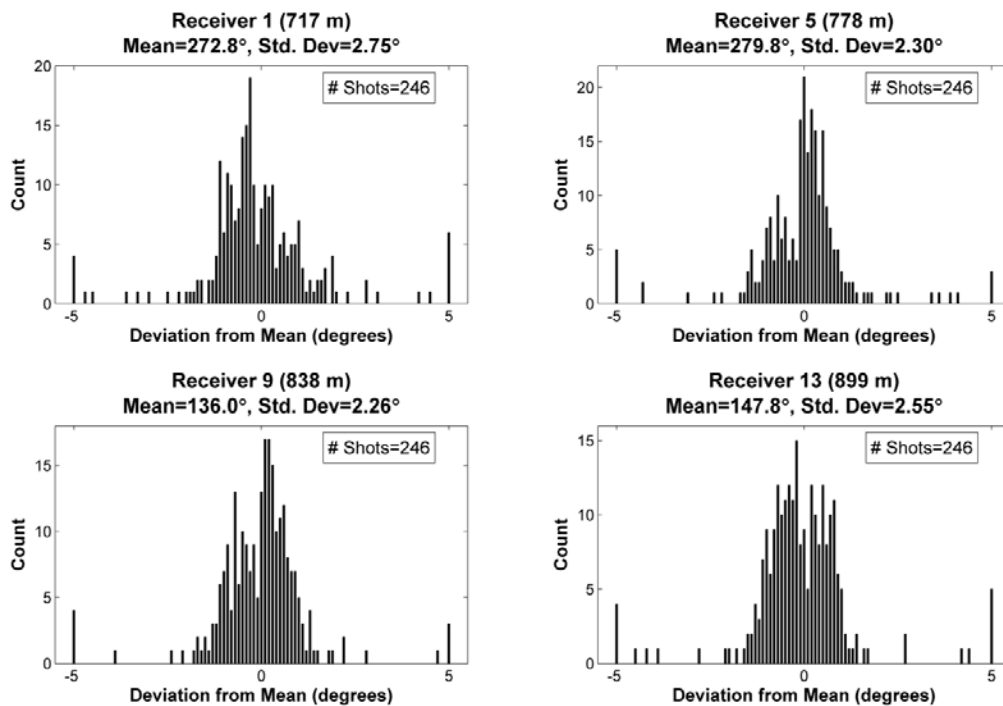


Figure 7.12: Histograms of orientation azimuth for several receivers in the 3D dataset calculated using analytic method.

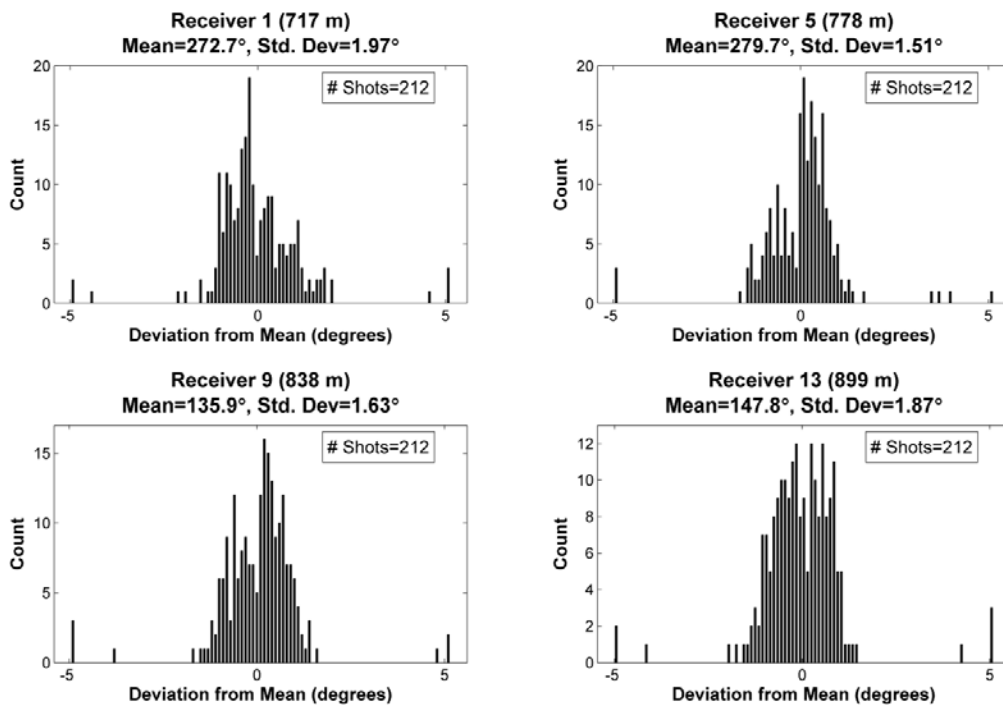


Figure 7.13: Histograms of orientation azimuth for several receivers in the 3D dataset calculated using analytic method, after rejection of near offset shots (less than 500 m).

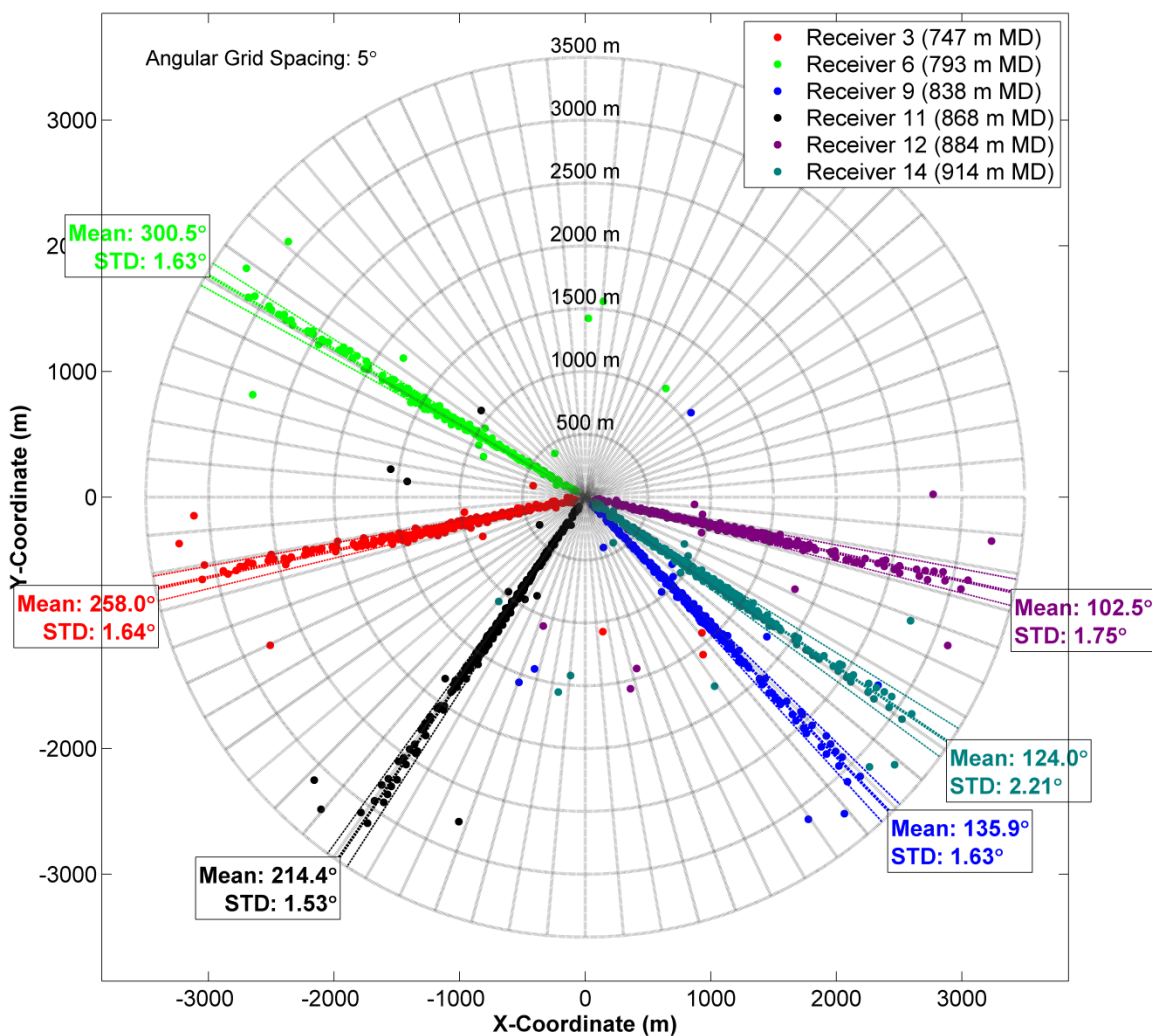


Figure 7.14: Radial plot of geophone orientation azimuths for a subset of receivers. All shots are shown, but statistics are found from far offset data only. Envelope lines represent one standard deviation. Radial spacing is 500m, angular spacing is 5°.

7.4.2 Geophone orientation statistics

Table 7.3 shows orientation azimuth means and standard deviations, for the complete 3D dataset, using the analytic method. Table 7.4 shows the binned orientation azimuth means and standard deviations, after the removal of outliers and source-well offsets less than 500 m from the well. The removal of outliers was done separately for the binned and unbinned calculations; this is apparent through the different standard deviations. Examining the mean orientation angle for each receiver across bins, slight differences can be seen, but none of the differences is greater than 2° and there does not

appear to be any consistent trend in the differences. The maximum mean angle difference is less than 1° for most receivers, despite the large variety in bin sizes. Figure 7.15 shows the standard deviation for each bin, using the analytic method, as a function of receiver depth.

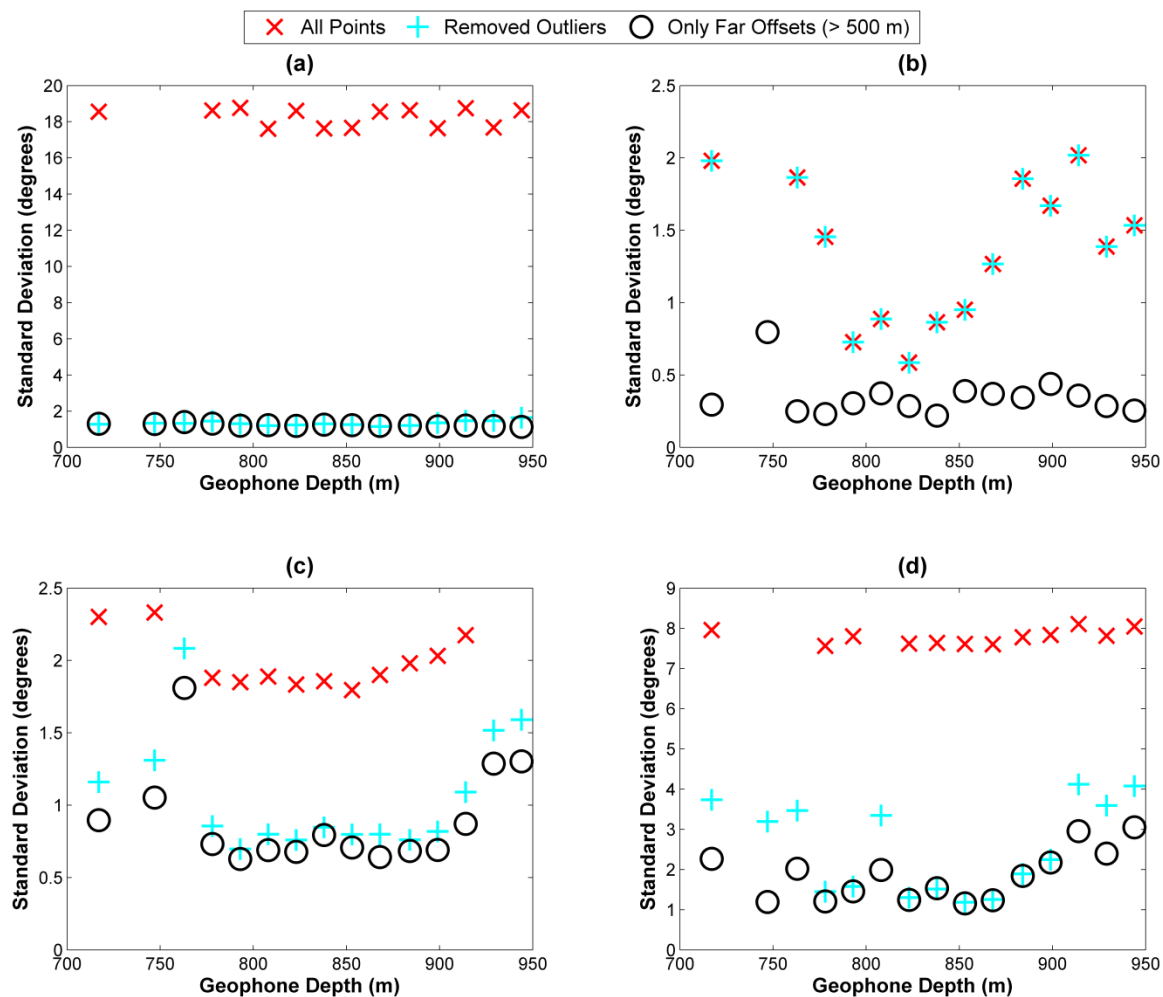


Figure 7.15: Orientation azimuth standard deviations for each receiver calculated using the analytic method, using azimuthal sectoring. Red is calculated using all data points, cyan after removal of outliers and black after removal of outliers and near offsets less than 500 m.

Table 7.3: Geophone orientation statistics for 3D dataset made using the analytic method. Means and standard deviations are in degrees.

| Receiver Number | Depth (m) | All | | Removed Outliers | | Far | |
|-----------------|-----------|-------|----------|------------------|----------|-------|----------|
| | | Mean | Std. Dev | Mean | Std. Dev | Mean | Std. Dev |
| 1 | 717 | 273.6 | 8.63 | 272.8 | 2.75 | 272.7 | 1.97 |
| 2 | 732 | 56.0 | 56.93 | 56.0 | 56.93 | 55.8 | 57.51 |
| 3 | 747 | 256.8 | 12.04 | 258.1 | 2.62 | 258.0 | 1.64 |
| 4 | 763 | 261.5 | 13.33 | 263.1 | 2.60 | 263.1 | 1.82 |
| 5 | 778 | 280.7 | 8.49 | 279.8 | 2.30 | 279.7 | 1.51 |
| 6 | 793 | 301.5 | 8.56 | 300.6 | 2.32 | 300.5 | 1.63 |
| 7 | 808 | 163.1 | 10.15 | 163.7 | 2.40 | 163.6 | 1.79 |
| 8 | 823 | 195.5 | 8.49 | 194.6 | 2.19 | 194.5 | 1.50 |
| 9 | 838 | 136.2 | 8.06 | 136.0 | 2.26 | 135.9 | 1.63 |
| 10 | 853 | 158.6 | 8.07 | 158.3 | 1.52 | 158.3 | 1.47 |
| 11 | 868 | 215.3 | 8.48 | 214.4 | 2.23 | 214.4 | 1.53 |
| 12 | 884 | 103.5 | 8.56 | 102.6 | 2.43 | 102.5 | 1.75 |
| 13 | 899 | 148.0 | 8.16 | 147.8 | 2.55 | 147.8 | 1.87 |
| 14 | 914 | 124.9 | 8.70 | 124.0 | 2.89 | 124.0 | 2.21 |
| 15 | 929 | 136.1 | 9.81 | 135.5 | 2.41 | 135.4 | 1.71 |
| 16 | 944 | 118.7 | 10.58 | 117.4 | 2.69 | 117.3 | 2.02 |
| Average | | | 9.34 | | 2.41 | | 1.74 |

Table 7.4: Geophone orientation statistics for binned 3D dataset made using the analytic method. Means and standard deviations are in degrees.

| Receiver Number | Depth (m) | 0-180 | | 45-225 | | 90-270 | | 135-315 | |
|-----------------|-----------|-------|--------|--------|--------|--------|--------|---------|--------|
| | | Mean | S. Dev | Mean | S. Dev | Mean | S. Dev | Mean | S. Dev |
| 1 | 717 | 272.8 | 1.30 | 272.3 | 0.30 | 272.8 | 0.90 | 272.4 | 2.26 |
| 2 | 732 | -3.8 | 11.75 | 61.7 | 3.73 | 87.2 | 9.87 | 37.2 | 80.74 |
| 3 | 747 | 258.5 | 1.29 | 258.6 | 0.80 | 258.3 | 1.05 | 257.4 | 1.19 |
| 4 | 763 | 262.5 | 1.40 | 262.3 | 0.25 | 263.1 | 1.81 | 263.3 | 2.02 |
| 5 | 778 | 279.5 | 1.32 | 278.8 | 0.23 | 279.7 | 0.73 | 279.9 | 1.20 |
| 6 | 793 | 300.3 | 1.19 | 300.8 | 0.30 | 300.9 | 0.63 | 299.9 | 1.46 |
| 7 | 808 | 164.5 | 1.22 | 163.8 | 0.37 | 163.6 | 0.69 | 163.3 | 1.99 |
| 8 | 823 | 194.9 | 1.19 | 194.7 | 0.29 | 194.6 | 0.68 | 194.3 | 1.25 |
| 9 | 838 | 136.7 | 1.25 | 136.0 | 0.22 | 135.9 | 0.79 | 135.6 | 1.53 |
| 10 | 853 | 158.3 | 1.22 | 158.7 | 0.39 | 158.5 | 0.71 | 158.0 | 1.16 |
| 11 | 868 | 214.8 | 1.19 | 214.5 | 0.37 | 214.5 | 0.64 | 214.1 | 1.23 |
| 12 | 884 | 102.6 | 1.21 | 102.8 | 0.34 | 102.8 | 0.68 | 102.1 | 1.84 |
| 13 | 899 | 147.8 | 1.16 | 148.0 | 0.44 | 147.9 | 0.69 | 147.5 | 2.18 |
| 14 | 914 | 124.0 | 1.20 | 123.9 | 0.36 | 124.1 | 0.87 | 123.7 | 2.96 |
| 15 | 929 | 135.7 | 1.17 | 135.5 | 0.29 | 135.5 | 1.29 | 135.3 | 2.40 |
| 16 | 944 | 117.6 | 1.13 | 117.5 | 0.25 | 117.4 | 1.30 | 117.1 | 3.05 |
| Average | | | 1.23 | | 0.35 | | 0.90 | | 1.85 |

7.4.3 Offset analysis

In order to more closely examine the relationship between offset and scatter in orientation angle, data were binned at different offset panels: 0-600 m, 600-950 m, 950-1300 m, 1300-1650 m and greater than 1650 m. Bins were chosen to have a consistent number of shots, encompassing 45, 47, 56, 46 and 47 source locations respectively. Figure 7.16 shows the standard deviation as a function of offset bin and geophone depth. Though there is no consistent relationship between standard deviation and geophone depth, there is a strong relationship between the standard deviation and offset bin. Each receiver reaches a minimum scatter in the 1300-1650 m offset range; reasons for this are discussed later in this section. This is more closely examined in Figure 7.17, which shows curves representing the 600-950 m, 950-1300 m and 1300-1650 m bins, and Figure 7.18, which shows the overall standard deviation of all receivers for each bin. It is interesting to note that the two latter bins have markedly less scatter in orientation angle than results involving all offsets.

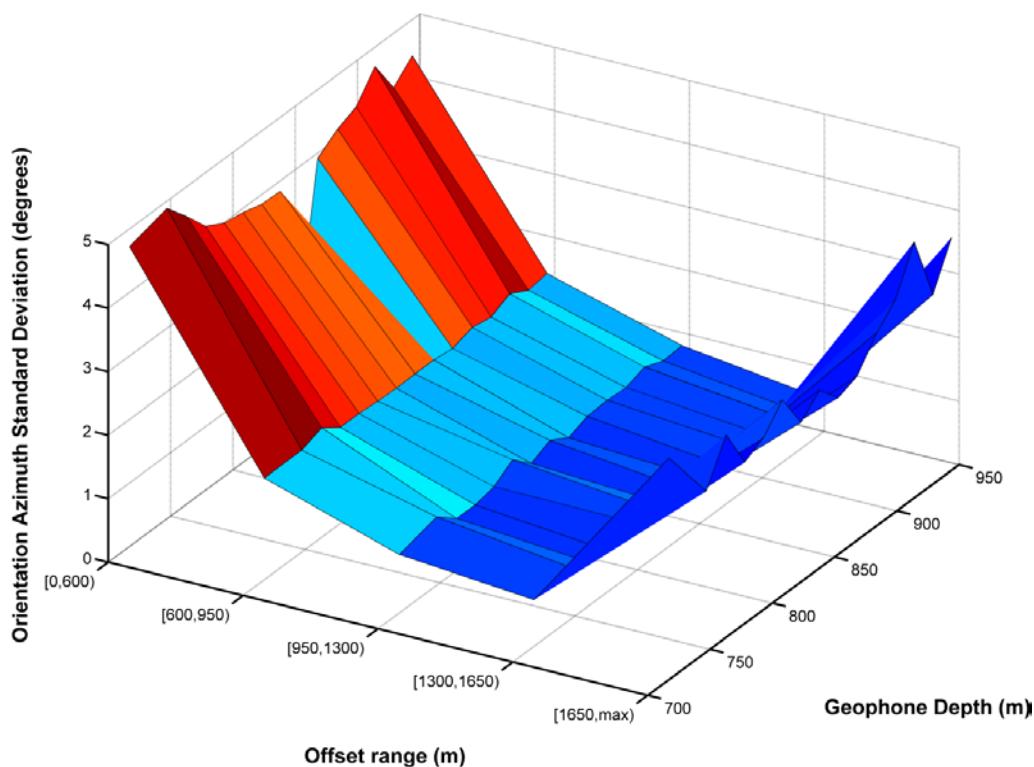


Figure 7.16: Standard deviation of geophone orientation azimuth versus geophone depth and sectorized offset range.

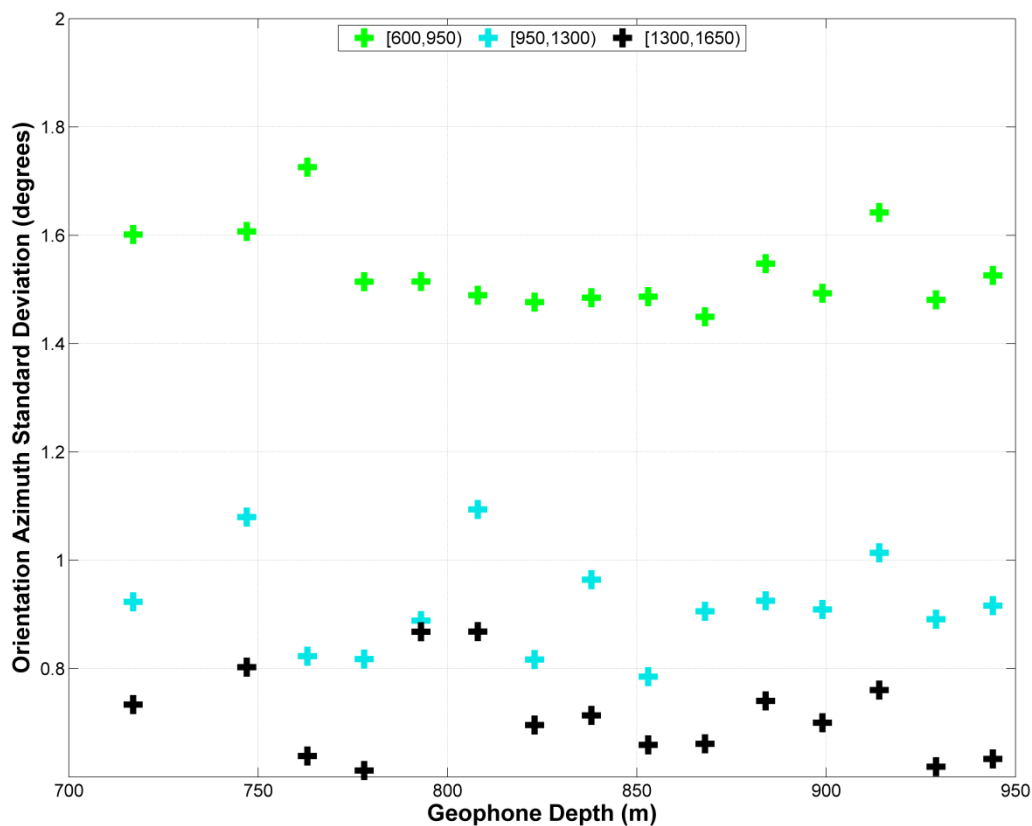


Figure 7.17: Constant offset slices from Figure 7.16, showing 600-950 m bin in green, 950-1300 m bin in cyan, and 1300-1650 m bin in black.

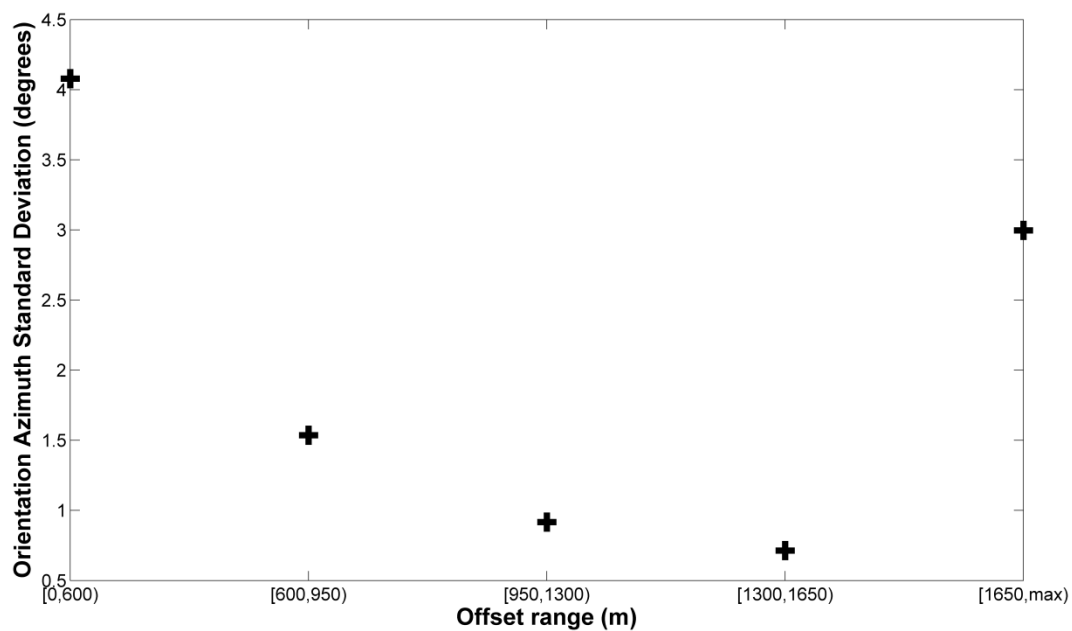


Figure 7.18: Average standard deviation for all receivers (except receiver 2) at each offset bin.

Finally, in order to better understand the effects of source-well offset on the analysis of geophone orientation azimuth, a simple analytic model was devised. For a vertical well in a homogeneous, isotropic medium with a very high quality factor (Figure 7.19), the amplitude of the direct P-wave arrival measured by the horizontal components will depend on two factors. Geometric spreading must be taken into account, which is given simply by:

$$\frac{A}{A_0} = \frac{1}{r} = \frac{1}{\sqrt{x^2+z^2}}, \quad (7.1)$$

where A is the amplitude at the receiver, and A_0 is the original amplitude. However, the amplitude measured by the horizontal components of the geophone will be a function of the angle θ , such that:

$$\frac{A_H}{A_0} = \frac{A}{A_0} \sin \theta = \frac{A}{A_0} \frac{x}{\sqrt{x^2+z^2}}, \quad (7.2)$$

where A_H is the horizontal amplitude at the receiver. Combining equations (7.1) and (7.2), the overall amplitude measured by the horizontal components of the geophones can be written as:

$$\frac{A_H}{A_0} = \frac{x}{x^2+z^2}. \quad (7.3)$$

Using Equation 7.3, the relationship between the relative horizontal amplitude and the offset/depth ratio was examined (Figure 7.20). The peak amplitude is predicted to occur at an offset/depth ratio of 1, supporting the results of the 3D walkaway; offset/depth ratios with amplitudes of at least -2 dB from the peak occur between 0.5 and 2, again supporting results of the 3D walkaway. Estimates of signal to noise ratio were found for each trace of the rotated horizontal (H_{\max}) components, and the values were plotted against source-well offset (Figure 7.21). The estimate was made by calculating the RMS amplitude of the first break window of a trace, which was 100 ms long, and dividing it by the RMS amplitude of the first 100 ms of that trace, which was considered noise. The results here provide a good match to what was modelled; however, the peak amplitude occurs at a source-well offset that is smaller than the geophone depth. This is likely due to the effects of raybending, which will cause the incoming ray at the receiver to be closer to horizontal than expected for a homogeneous medium (Figure 7.22).

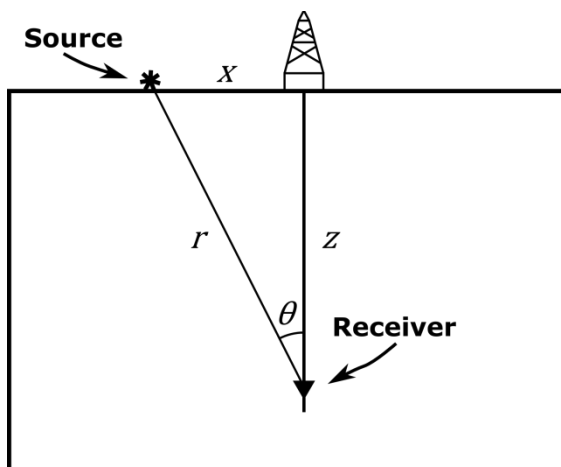


Figure 7.19: Diagram illustrating geometry of a surface source and a borehole geophone embedded in a homogeneous, isotropic medium.

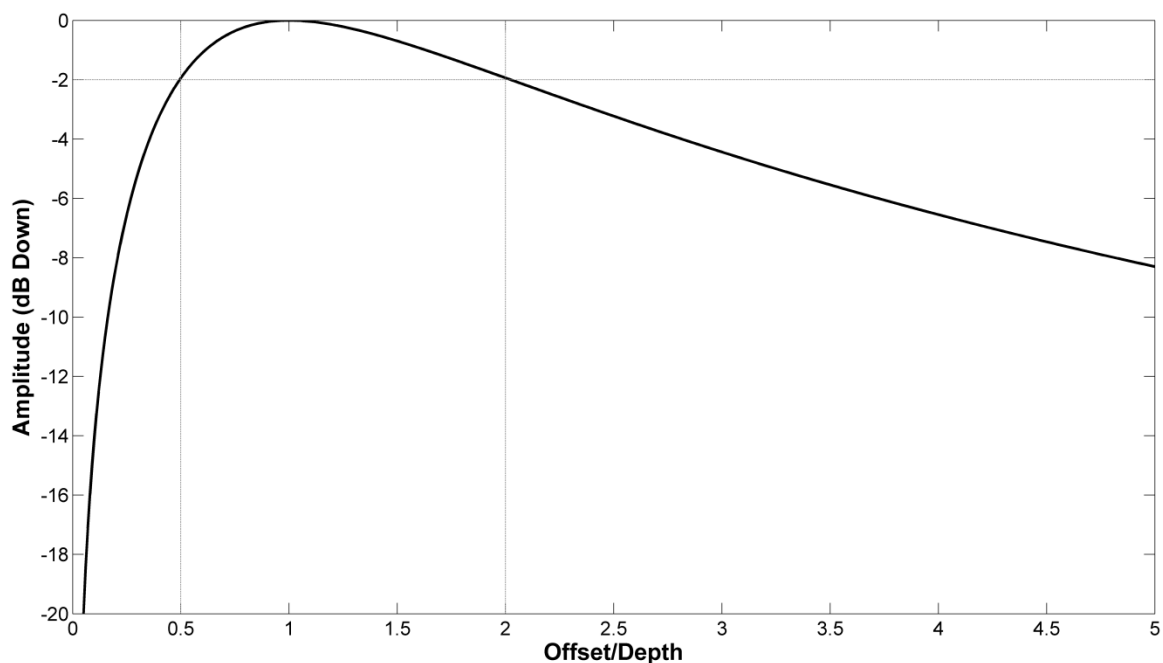


Figure 7.20: Modelled relative amplitude change of the horizontal components of a borehole geophone, as a function of the source-well offset/receiver depth ratio. Horizontal line is drawn in at -2 dB, which intersects the curve at offset/depth ratios of approximately 0.5 and 2.

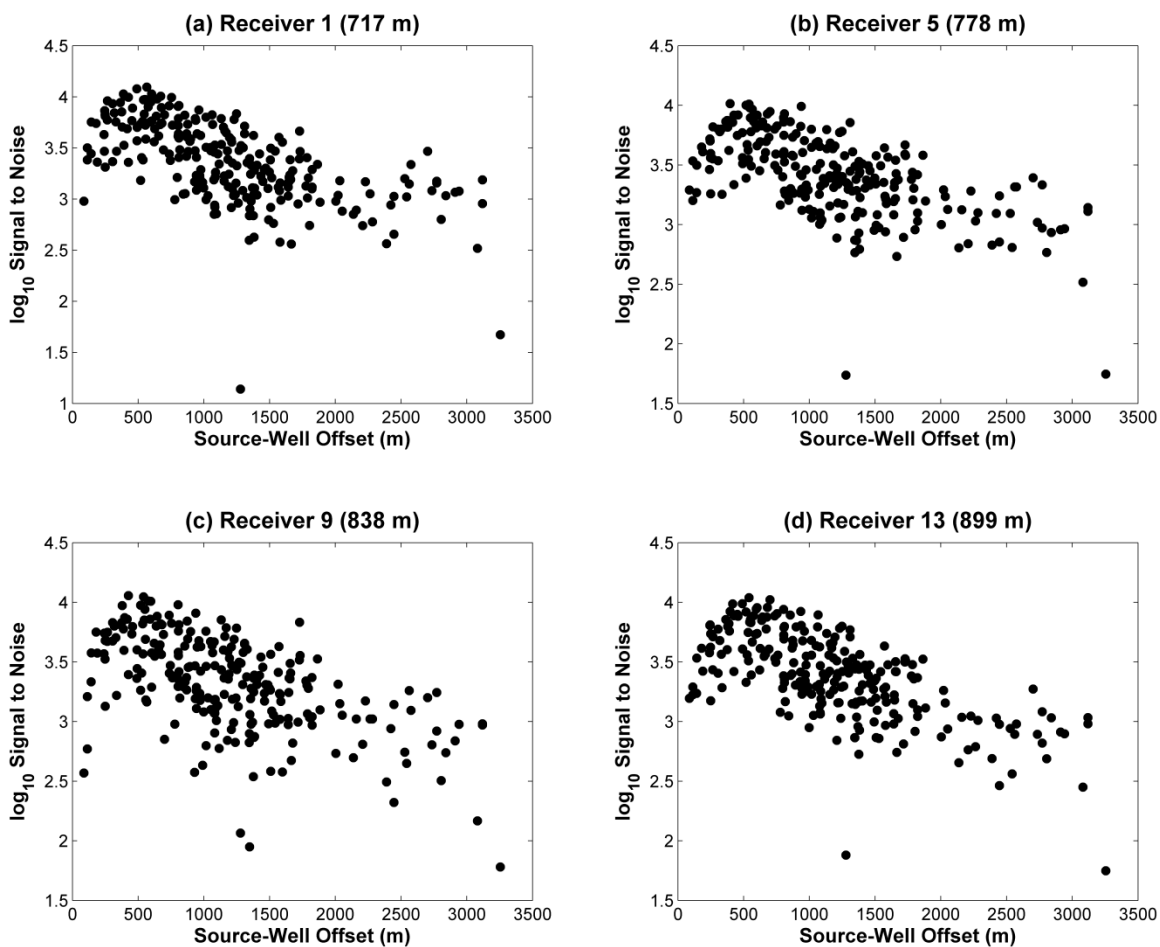


Figure 7.21: Estimated signal to noise of first break window, versus offset, for the H_{\max} component of a subset of receivers in the 3D dataset. Data were rotated using angle estimates from the analytic method.

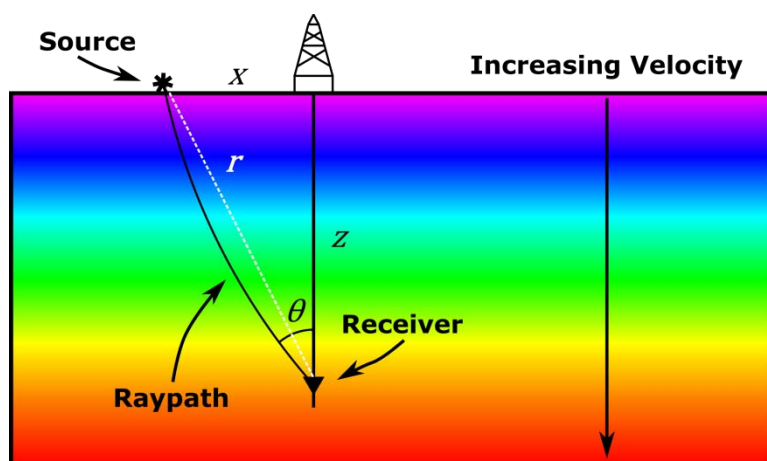


Figure 7.22: Illustration of raybending that would occur due to a linear velocity gradient where velocity increases downwards.

7.5 Discussion

The geophone orientation azimuths calculated in this study, for both the 3D and 2D walkaway surveys, resulted in robust outcomes. The 2D walkaway data showed similar scatter in orientation azimuth when for all 3 walkaway shot lines, but the scatter in the 3D walkaway data changed significantly when the data were split into separate bins, although mean angles were very similar. Additionally, the removal of shots from source-well offsets less than about 1/3 of the geophone depth had a large effect on the 2D walkaway orientation statistics, while having less effect on the 3D dataset. This is probably due to the low proportion of near offset source locations in the 3D walkaway survey.

The geophone orientation azimuths calculated in this study, for both the 3D and 2D walkaway surveys, resulted in robust outcomes. The 2D walkaway data showed similar scatter in orientation azimuth when for all 3 walkaway shot lines, but the scatter in the 3D walkaway data changed significantly when the data were split into separate bins, although mean angles were very similar. Additionally, the removal of shots from source-well offsets less than about 1/2 of the geophone depth had a large effect on the 2D walkaway orientation statistics, while having less effect on the 3D dataset. This is probably due to the low proportion of near offset source locations in the 3D walkaway survey.

The results found using the azimuthally binned (3D walkaway) and line by line (2D walkaway) analysis do not show any clear indication that, in this area, there is significant source-well azimuthal dependence on computed borehole geophone orientations. Mean angles were very consistent regardless of the bin or line chosen; differences are generally no greater than the standard deviations involved, nor are there any consistent trends for a particular bin or line. Direct examination of the orientation angle versus source-well azimuth in the 3D walkaway shows only a subtle trend. The consistency of the orientation azimuths can be interpreted to mean that the local geology is likely azimuthally consistent, which is expected from flat, isotropic layers.

The offset binning of the 3D dataset showed a strong dependence of geophone orientation scatter to source-well offset. For all 15 working receivers, scatter was reduced

in the 600-1650 m offset range, reaching a minimum in the 1300-1650 m bin. Scatter in the bins containing offsets less than 600 m and greater than 1650 m was significantly higher, which is due to a combination of effects. First, the signal to noise of the first arrival on the horizontal components is reduced in these two offset ranges; the near offsets will have a near-vertical angle of incidence, and the far offsets will be more affected by geometric spreading. Second, analysis of orientation angle is more sensitive to source positioning errors at near offsets. Thus, for the 3D dataset, the optimal offset range to perform orientation analysis was between 1 and 2 times the receiver depth. Modelling of the amplitude change in a homogeneous, isotropic medium with high quality factor confirms this, predicting an optimal source-well offset equal to the receiver depth.

Finally, comparison of the analytic and hodogram methods revealed that the two are very similar, though the analytic method gave slightly less scatter in computed azimuths. The mean of the two methods rarely differed by greater than 1° and on average differed by less than 0.5° . The similarity of results through both of these methods gives confidence that each of them can estimate reliable information about geophone orientation.

7.6 Summary

The following results can be noted from this chapter:

- Geophone orientations for the 2D dataset were determined using the DiSiena et al. (1984) analytic method. The standard deviation was 0.67° for all lines, 0.45° for the east line, 0.41° for the southeast line and 0.55° for the south line.
- Geophone orientation angles for the 2D dataset were also found using a linear regression, or hodogram, method. The standard deviation was 0.90° for all lines, and 0.77° for the east line, 0.42° for the southeast line and 0.62° for the south line.

- Absolute difference in mean angles between the two methods averaged 0.12° for all lines, and 0.14° , 0.12° and 0.17° for separate lines.
- Geophone orientation angles for the 3D dataset were found using the analytic method. The standard deviation was 1.74° using all azimuths, and became 1.23° , 0.35° , 0.90° and 1.85° when the data were binned into centers of 0° - 180° , 45° - 225° , 90° - 270° and 135° - 315° respectively.
- Signal to noise in the rotated horizontal component reached a maximum where the source-well offset was approximately equal to geophone depth.
- Scatter in orientation angle for the 3D dataset reduced noticeably as source locations became more than 600 m from the well. The scatter minimised in the offsets between 1300 and 1650 m.
- The optimal offset range for geophone orientation calibration was found to be in the range of 1-2 times the receiver depth.
- Removal of data points nearer than $1/2$ of the receiver depth reduced the scatter of orientation angles in the unbinned 3D walkaway, from 2.41° to 1.74° . It significantly improved the scatter in the 2D walkaway surveys, decreasing the standard deviation from 5.22° to 0.67° overall.
- For both the 3D and the 2D walkaways, the geophone orientations were not found to have any consistent dependence on source-well azimuth. This is expected for flat, isotropic geology near the well.
- The analytic and linear regression methods of calculating geophone orientations produced comparable results overall; however, the analytic method was found to consistently give slightly less scatter.

Chapter Eight: Discussion, Conclusions and Recommendations

8.1 Discussion

The modelling described in Chapter 3 and all three of the case studies examined in this thesis show that precision of geophone orientation azimuth is highly dependent on source-well offset. In particular, the case studies presented in Chapters 2 and 7 show strong improvements in the standard deviation of these measurements when data from near offsets, closer than approximately $1/3$ to $1/2$ of receiver depth, are rejected. When this relationship was examined in further detail in Chapter 7, it was found that an offset range of 1 to 2 times the receiver depth produced the best precision in measurements of geophone orientation azimuth. This range is likely optimal due to a good balance between the incident angle of direct P-wave arrivals at the receiver, which will be closer to horizontal as offset increases, and the overall amplitude of these arrivals, which will approach 90° as source offset decreases. Theoretical modelling of these two effects (Chapter 7) supports this idea, producing a peak in predicted amplitude at an offset equal to the receiver depth. Thus, there appears to be a “sweet-spot” in terms of source-well offsets chosen for a calibration survey, which will be dependent on receiver depth.

However, calibration survey design and analysis must also be guided by knowledge of the geology in the area. The modelling discussed in Chapters 5 and 6 shows that HTI anisotropy and dipping layer interfaces will produce distinct, systematic deviations in measured geophone orientation azimuth. When examining these deviations as a function of source-well azimuth, interpretable patterns may be recognised. Dipping layer interfaces will produce deviations that appear as a one-cycle sine wave that is somewhat asymmetric; deviations due to HTI anisotropy approximately match a two-cycle sine wave. For dipping layers, the strength of these deviations is proportional to the velocity contrast and dip angle; for anisotropy, it is proportional to the Thomsen parameters of the medium. It is fairly straightforward to predict source-well azimuths that minimise these deviations: those due to dipping layer interfaces can be minimised if sources are placed along the dip direction of bedding, and those due to HTI anisotropy can be minimised if sources are placed along the slow or fast directions of geologic units.

The general observations made from the modelling of these two effects can be used to better understand the results obtained in the field examples. When examining the deviation in geophone orientation azimuth as a function of source-well offset for the field study in Chapter 2, there appear to be trends in the data similar to those found in Chapters 5 and 6 (Figure 8.1). In particular, Receivers 5 through 8 exhibit these patterns: deviations in orientation azimuth for Receivers 5 and 8 are consistent with trends modelled in the case of a dipping interface; those for Receivers 6 and 7 are consistent with trends modelled in the case of a layer with HTI anisotropy. In fact, the trends shown by Receivers 7 and 8 appear to be repeatable between Phase I and Phase III data, while Receivers 5 and 6 were unreliable for Phase III due to cable degradation. Evidence of these trends is much more subtle for the field study in Chapter 7, however (Figure 8.2). This may be due to the large gaps in source-well azimuth coverage between 0° to 50° , 200° to 260° and 330° to 360° , which account for more than a third of possible azimuth ranges. Finally, there also appears to be an azimuthal control on the deviation of orientation azimuth for the field study in Chapter 4 (Figure 8.3). Since the well is deviated, the layer interfaces will no longer appear horizontal with respect to the horizontal components of the geophones. Thus, it is likely that the trends shown in this study are a combination of the effects of lateral raybending and anisotropy with an axis of symmetry that is at an angle to the vertical component of the geophones.

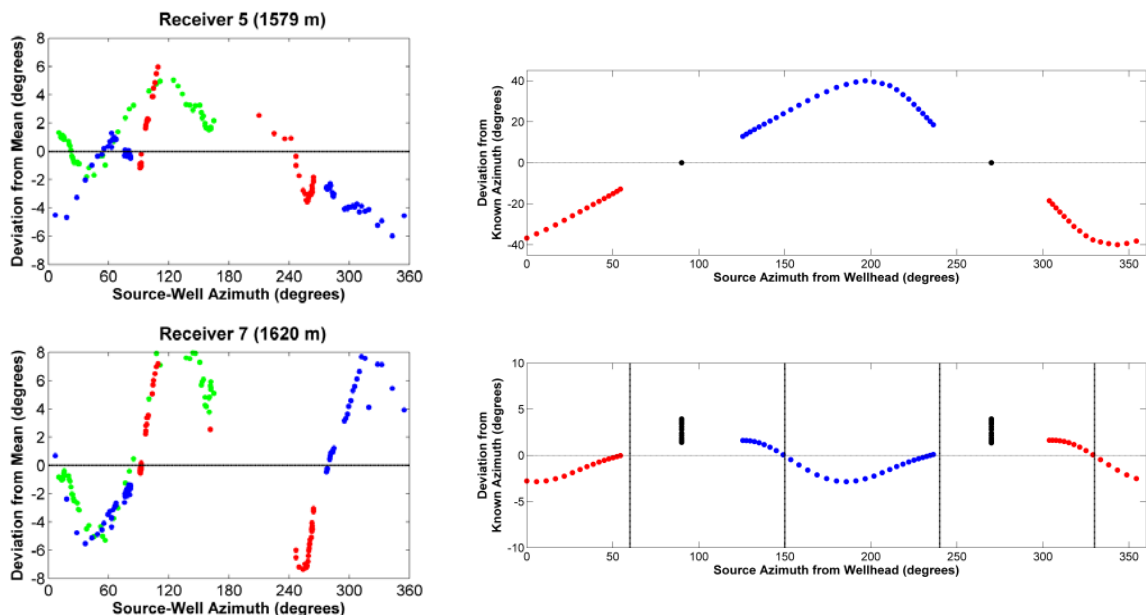


Figure 8.1: Comparison of Violet Grove time-lapse dataset deviations (Chapter 2) as a function of source-well azimuth (left) with modelled deviations due to a dipping interface (upper right) and anisotropy (lower right).

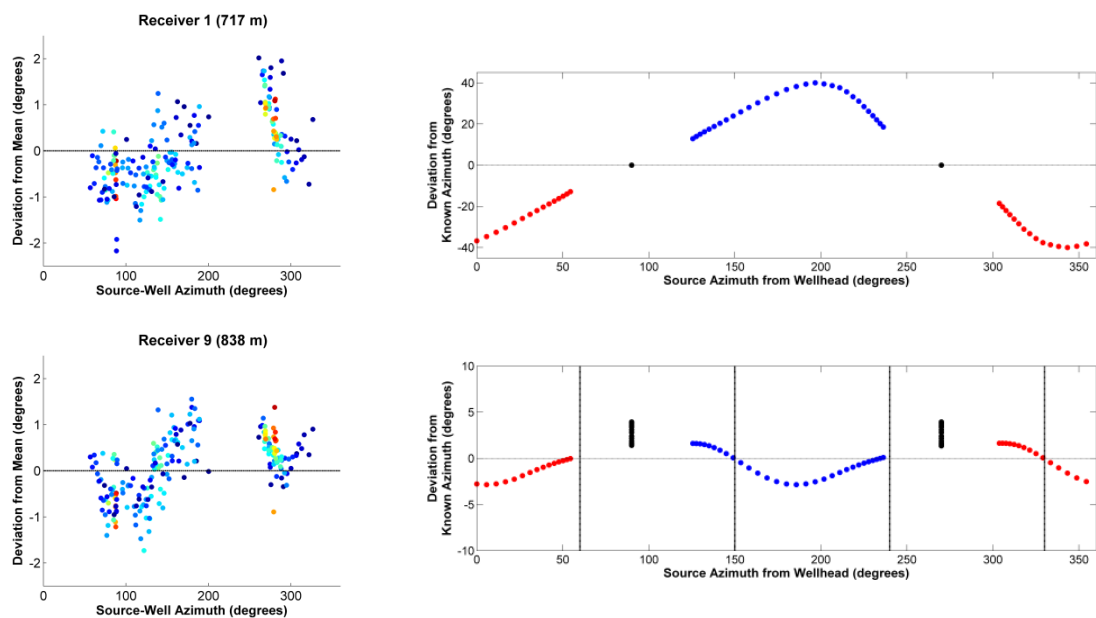


Figure 8.2: Comparison of Lousana 3D dataset (Chapter 7) deviations as a function of source-well azimuth (left) with modelled deviations due to a dipping interface (upper right) and anisotropy (lower right).

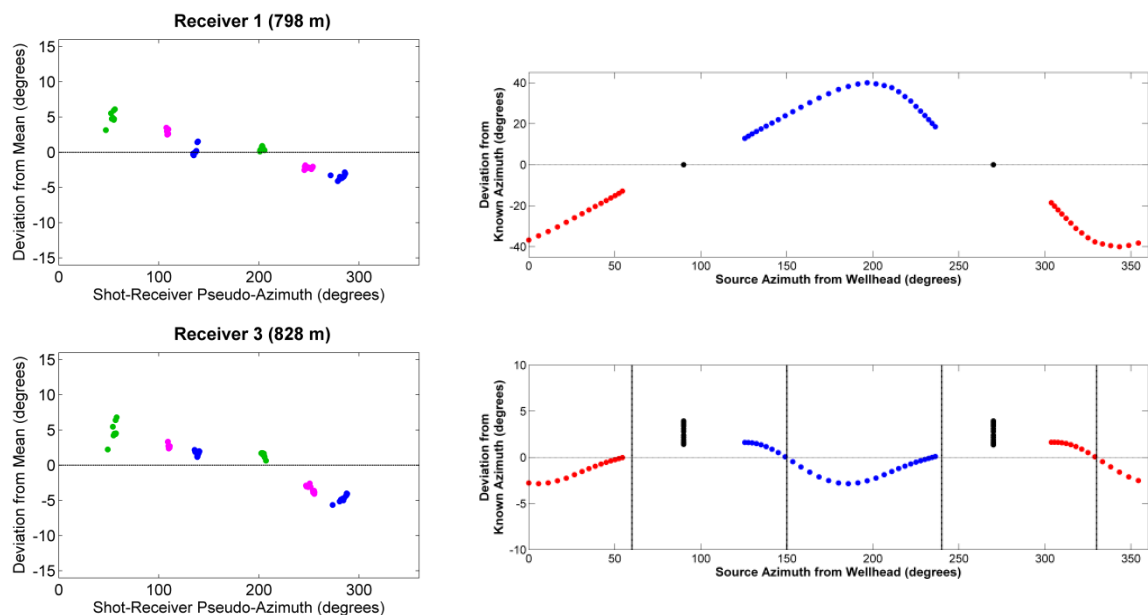


Figure 8.3: Comparison of Violet Grove deviated well dataset (Chapter 4) deviations as a function of source-well azimuth (left) with modelled deviations due to a dipping interface (upper right) and anisotropy (lower right).

The Violet Grove time-lapse dataset (Chapter 2), which used a geophone array that was cemented in place, showed slightly better consistency than the deviated well dataset (Chapter 4); Lines 1 and 2 were common to both of these studies. Standard deviation in geophone orientation azimuths for Phase I of the time-lapse dataset was 3.21° overall, and 1.82° when only using source-well offsets greater than 500 m, whereas those of the deviated well dataset had an overall standard deviation of 4.39° . However, as there were three different tool positions in the latter, each receiver depth had fewer data points contributing to geophone orientation statistics, which provides a bias towards the time-lapse results.

The scatter of orientation azimuths for the Lousana case study (Chapter 7) when considering source-well offsets greater than 500 m was reduced compared to either of the Violet Grove case studies, showing a standard deviation of 0.67° for the 2D walkaway and 1.74° for the 3D walkaway. The 2D walkaway had a limited range of source-well azimuths, which likely contributed to its smaller scatter.

8.2 Conclusions

8.2.1 Objective 1: Effects of Noise, Deviation, Raybending and Anisotropy

The first objective of this thesis was to characterise and quantify the effects of noise, well deviation, lateral raybending and seismic anisotropy on geophone orientation azimuth calibration surveys, and to develop a method to determine geophone orientation in a deviated well.

These conclusions can be summarised as follows:

- 1) In the presence of noise, a signal to noise ratio of 1 or better was able to produce a mean within 0.5° of the receiver's true orientation.
- 2) A method was developed to determine geophone orientation in a deviated well. It was then successfully applied to a field dataset; scatter in orientation azimuth was up to 10 times larger if the well was assumed to be vertical.
- 3) A simple model was created to examine the effects of random error of up to $\pm 2^\circ$ in the inclination and azimuth angles for a well deviation survey on analysis of geophone orientation. Scatter varied greatly for individual receivers, ranging from 0.06° to 13.19° ; it was 2.53° over all receivers, which is similar to the maximum inclination and azimuth errors in the deviation survey.
- 4) Lateral raybending, where the interface plane is at an angle to the plane made by the horizontal components of a receiver, was found to produce significant deviations in the calibrated orientation of borehole geophones. The deviation pattern is approximately a one-cycle sinusoid when viewed as a function of source-well azimuth; zero-crossings are along the dip direction, and the amplitude is proportional to the velocity contrast and dip angle.
- 5) Anisotropy where the axis of symmetry is not normal to the plane made by the horizontal components of a receiver was also found to produce deviations in

orientation analysis of borehole geophones. The deviation pattern is approximately a two-cycle sinusoid when viewed as a function of source-well azimuth; zero crossings are approximately along the fast and slow directions, and the amplitude is proportional to the value of the Thomsen parameters.

- 6) Transmitted converted waves produce further deviations where lateral raybending is present, and shear wave splitting produces further deviations where anisotropy is present. The size of the analysis window can be shortened, in both cases, in order to reduce these effects.

8.2.2 Objective 2: Analysis Method and Survey Design

The second objective of this thesis was to determine the optimal method and survey design for geophone orientation calibration surveys and understand their repeatability.

These conclusions can be summarised as follows:

- 1) The analytic and hodogram methods of determining geophone orientation azimuth are comparable. In field examples, the analytic method was shown to produce marginally more consistent results than the hodogram method.
- 2) The size of the analysis window used in geophone orientation azimuth studies should be determined on a case-by-case basis, primarily from the wavelength of the direct P-wave arrival. However, secondary effects, such as those from transmitted converted waves, can lead to a smaller window size providing more robust results.
- 3) Shallower receivers generally provide better orientation statistics than deeper receivers. This was shown through field examples and finite difference modelling of random noise.

- 4) Source locations with offsets nearer than 1/2 of the receiver depth significantly increase scatter in geophone orientation analysis; the optimal source offset range is between 1 and 2 times the receiver depth.

8.2.3 Objective 3: Analysis of Field Data

The third objective of this thesis was to look for signatures of well deviation, lateral raybending and seismic anisotropy in a field example where their effects are initially assumed to be minimal.

These conclusions can be summarised as follows:

- 1) For the Violet Grove time-lapse case study, standard deviations of geophone orientation azimuth over all working receivers were 3.21° for Phase I and 6.05° for Phase III. When offsets smaller than 500 m were rejected, these values improved to 1.82° and 4.80° . Repeatability in orientation analysis showed that 63.6 % of Line 1 shots, 54.2 % of Line 2 shots and 85.9 % of Line 3 shots were within 2° between surveys; mean azimuth values generally had less than a 1° difference.
- 2) For the Violet Grove deviated well case study, standard deviation of geophone orientation azimuth over all working receivers was 4.39° . It was best for the shallow-level tool position (2.74°); this was judged to be due to the large source-well offset to geophone depth ratio.
- 3) For the Lousana case study, standard deviations of geophone orientation azimuth over all working receivers were 5.22° for the 2D walkaway and 2.41° for the 3D walkaway. When offsets smaller than 500 m were rejected, these values improved to 0.67° and 1.74° .
- 4) Plots of deviation in geophone orientation azimuth vs. source-well azimuth revealed interesting patterns for all three case studies. In particular, those of the

Violet Grove time-lapse case study agree well with the patterns predicted by modelling of dipping layer interfaces and HTI anisotropy; these patterns were repeatable between Phase I and Phase III surveys. Plots for the Violet Grove deviated well case study and the Lousana case study were more difficult to characterise, but still showed systematic deviations greater than the standard deviations calculated for orientation azimuth.

8.2.4 Other Conclusions

Finally, there were several conclusions made in this thesis that did not directly relate to the three main objectives.

These conclusions can be summarised as follows:

- 1) Repeatability analysis of the Violet Grove horizontal component data yielded NRMS values of 60.6 %, 61.4 % and 45.2 %, PRED values of 0.73, 0.72 and 0.83, and SDR values of $10^{0.38}$, $10^{0.29}$ and $10^{0.70}$ for Lines 1, 2 and 3 respectively.
- 2) Repeatability analysis of the Violet Grove vertical component data yielded NRMS values of 46.3 %, 42.6 % and 41.4 %, PRED values of 0.82, 0.83 and 0.87, and SDR values of $10^{0.74}$, $10^{0.85}$ and $10^{0.79}$ for Lines 1, 2 and 3 respectively.
- 3) Analytic relationships were found for the effects of amplitude perturbations between a noise-free baseline and monitor trace on NRMS, PRED and SDR
- 4) Effects of time-shifts, trace amplitude differences and random and non-random additive noise on NRMS, PRED and SDR were modelled separately using controlled perturbations of a control trace taken from the Violet Grove dataset. Time-shifts had no effect on SDR and amplitude perturbations had no effect on PRED. SDR was effected little by the type of noise added, whereas the responses of NRMS and PRED were noticeably different for the two types of noise.

8.3 Recommendations

Based on the findings of this thesis, the following recommendations can be made with regard to geophone orientation azimuth calibration:

- 1) All three of the seismic repeatability metrics outlined in this thesis (NRMS, PRED and SDR) are useful in examining time-lapse data, and should be used together where possible.
- 2) The analytic and hodogram methods for determining geophone orientation azimuth should both be considered in analyses of real data; the variable nature of noise makes it difficult to predict which one will perform better in any particular field study.
- 3) An analysis window with a length approximately equal to the wavelength of the direct P-wave arrivals is a good value for initial attempts at determining orientation azimuth. However, due to interference from turning and converted waves, time should be taken on any given calibration experiment to test different window lengths.
- 4) If a well deviation survey is known, it should be considered in geophone orientation azimuth analysis. The method described in this thesis is able to successfully account for this.
- 5) Uncertainties in inclination and azimuth angle of the deviation survey will be reflected in the scatter in geophone orientation analysis, and should be minimised where possible.
- 6) In geologic settings which involve dipping beds and a vertical well, survey geometry for geophone orientation calibration can be optimised by aligning

source-receiver azimuths to be along the dip direction.

- 7) In geologic settings which involve HTI anisotropy, survey geometry can be optimised by aligning source-receiver azimuths parallel (slow direction) or perpendicular (fast direction) to the axis of symmetry.
- 8) If a one-cycle sinusoid is recognised when plotting variation in geophone orientation azimuth against source-receiver azimuth, lateral raybending with respect to the H1 and H2 components should be considered as affecting measurements at the receiver.
- 9) If a two-cycle sinusoid is recognised when plotting variation in geophone orientation azimuth against source-receiver azimuth, seismic anisotropy (HTI) should be considered as potentially affecting measurements at the receiver.
- 10) The robustness of geophone orientation azimuth estimates can be significantly improved by rejecting data from source-well offsets nearer than half the depth of the geophone. For optimal results, sources should be placed at offsets 1-2 times the receiver depth.

References

- Bulant, P., Eisner, L., Pšenčík, I. and Le Calvez, J., 2007, Importance of borehole deviation surveys for monitoring of hydraulic fracturing treatments: *Geophysical Prospecting*, **55**, 891-899.
- Calvert, R., 2005, 4D technology: where are we, and where are we going? *Geophysical Prospecting*, **53**, 161-171.
- Cantillo, J., 2011, A quantitative discussion on time-lapse repeatability and its metrics: *SEG Expanded Abstracts*, **30**, 4160-4164.
- Cantillo, J., Boelle, J., Lafram, P. A. and Lecerf, D., 2010, Ocean Bottom Nodes (OBN) repeatability and 4D: *SEG Expanded Abstracts*, **29**, 61-65.
- Cassell, B. R., 1984, Vertical seismic profiles - an introduction: *First Break*, **2**, 9-19.
- Dashtgard, S. E., Buschkuehle, M. B. E., Berhane, M. and Fairgrieve, B., 2006, Local-Scale Baseline Geological Report for the Pembina-Cardium CO₂-Enhanced Oil Recovery Site: Alberta Geological Survey.
- Dellinger, J. and Vernik, L., 1994, Do traveltimes in pulse-transmission experiments yield anisotropic group or phase velocities? *Geophysics*, **59**, 1774-1779.
- DiSiena, J. P., Gaiser, J. E. and Corrigan, D., 1984, Three-component vertical seismic profiles; orientation of horizontal components for shear wave analysis, in Toksoz, M. N. and Stewart, R. R., eds., *Vertical seismic profiling, Part B Advanced concepts*, 189-204.
- Eisner, L., Duncan, P. M., Heigl, W. M. and Keller, W. R., 2009, Uncertainties in passive seismic monitoring: *The Leading Edge*, **28**, 648-655.

- Hinds, R. C., Anderson, N. L. and Kuzmiski, R. D., 1996, VSP Interpretive Processing: Society of Exploration Geophysicists.
- Hitchon, B., 2009, Pembina Cardium CO₂ Monitoring Pilot: A CO₂-EOR Project, Alberta, Canada: Final Report: Geoscience Publishing, Limited.
- Hokstad, K., Maaø, F., Nguyen, A. K. and Streich, R., 2009, 3D Anisotropic Elastic Finite-Difference Modeling in Transversely Isotropic Media: 1-45.
- Kragh, E. and Christie, P., 2002, Seismic repeatability, normalized rms, and predictability: The Leading Edge, **21**, 640-647.
- Le Calvez, J. H., Bennett, L., Tanner, K. V., Grant, W. D., Nutt, L., Jochen, V., Underhill, W. and Drew, J., 2005, Monitoring microseismic fracture development to optimize stimulation and production in aging fields: The Leading Edge, **24**, 72-75.
- Li, X. and Yuan, J., 1999, Geophone orientation and coupling in three-component sea-floor data: a case study: Geophysical Prospecting, **47**, 995-1013.
- Li, Y.-G., Leary, P. C. and Aki, K., 1987, Observation and modelling of fault-zone fracture seismic anisotropy – II. P-wave polarization anomalies: Geophys. J. R. astr. Soc. **91**, 485-492.
- Lines, L. R. and Newrick, R. T., 2004, Vertical Seismic Profiles, in Fitterman, D. V. and Ellefsen, K., eds., Fundamentals of Geophysical Interpretation: Society of Exploration Geophysicists, 219-230.
- Lumley, D., 2010, 4D seismic monitoring of CO₂ sequestration: The Leading Edge, **29**, 150-155.

- Lumley, D. E., 2001, Time-lapse seismic reservoir monitoring: *Geophysics*, **66**, 50-53.
- Maxwell, S. C., Rutledge, J., Jones, R. and Fehler, M., 2010, Petroleum reservoir characterization using downhole microseismic monitoring: *Geophysics*, **75**, 75A129-75A137.
- Müller, K. W., Soroka, W. L., Paulsson, B. N. P., Marmash, S., Al Baloushi, M. and Al Jeelani, O., 2010, 3D VSP technology now a standard high-resolution reservoir-imaging technique: *The Leading Edge*, **29**, 686-697.
- Musgrave, M. J. P., 1970, Propagation of Elastic Waves in a General Anisotropic Continuum, *Crystal Acoustics: Acoustical Society of America*, 83-93.
- Oye, V. and Ellsworth, W. L., 2005, Orientation of Three-Component Geophones in the San Andreas Fault Observatory at Depth Pilot Hole, Parkfield, California: *Bulletin of the Seismological Society of America*, **95**, 751-758.
- Refunjol, X. E., Keranen, K. M., Le Calvez, J. H. and Marfurt, K. J., 2012, Integration of hydraulically induced microseismic event locations with active seismic attributes: A North Texas Barnett Shale case study: *Geophysics*, **77**, KS1-KS12.
- Thomsen, L., 1986, Weak elastic anisotropy: *Geophysics*, **51**, 1954-1966.
- Van Dok, R., Fuller, B., Engelbrecht, L. and Sterling, M., 2011, Seismic anisotropy in microseismic event location analysis: *The Leading Edge*, **30**, 766-770.
- Vestrum, R. W., 1994, Group- and Phase-Velocity Inversions for the General Anisotropic Stiffness Tensor: M. Sc. thesis, University of Calgary.
- Vestrum, R. W., Lawton, D. C. and Schmid, R., 1999, Imaging structures below dipping TI media: *Geophysics*, **64**, 1239-1246.

APPENDIX A: MATHEMATICAL PROOFS

A.1. Orthonormal Vector Basis of Pseudo-Coordinates

In order to form an orthonormal vector basis in 3D, three vectors, \hat{x}' , \hat{y}' and \hat{z}' , must be defined such that the following conditions are satisfied:

$$\hat{x}' \cdot \hat{y}' = 0; \quad (\text{A.1.1})$$

$$\hat{x}' \times \hat{y}' = \hat{z}'; \quad (\text{A.1.2})$$

and

$$\|\hat{x}'\| = \|\hat{y}'\| = \|\hat{z}'\| = 1; \quad (\text{A.1.3})$$

Additionally, \hat{x}' and \hat{y}' need to be defined on the plane defined by the normal \hat{n} , which implies

$$\hat{x}' \cdot \hat{n} = \hat{y}' \cdot \hat{n} = 0. \quad (\text{A.1.4})$$

Using \hat{x}' and \hat{y}' defined in Equations 4.3 and 4.4, we can check condition A.1.1:

$$\hat{x}' \cdot \hat{y}' = \begin{bmatrix} -\sin \phi_w \\ \cos \phi_w \\ 0 \end{bmatrix} \cdot \begin{bmatrix} -\cos \theta_w \cos \phi_w \\ -\cos \theta_w \sin \phi_w \\ \sin \theta_w \end{bmatrix}.$$

Calculating the dot product gives

$$\begin{aligned} \hat{x}' \cdot \hat{y}' &= ((-\sin \phi_w)(-\cos \theta_w) \cos \phi_w) + (\cos \phi_w (-\cos \theta_w) \sin \phi_w) + (0(\sin \theta_w)) \\ &= \sin \phi_w \cos \phi_w \cos \theta_w - \sin \phi_w \cos \phi_w \cos \theta_w + 0 \\ &= 0. \end{aligned}$$

We can now use \hat{x}' and \hat{y}' to define \hat{z}' using condition A.1.2:

$$\hat{z}' = \hat{x}' \times \hat{y}' = \begin{bmatrix} -\sin \phi_w \\ \cos \phi_w \\ 0 \end{bmatrix} \times \begin{bmatrix} -\cos \theta_w \cos \phi_w \\ -\cos \theta_w \sin \phi_w \\ \sin \theta_w \end{bmatrix}.$$

Calculating the cross product gives

$$\begin{aligned} \hat{x}' \times \hat{y}' &= \begin{vmatrix} \hat{i} & \hat{j} & \hat{k} \\ -\sin \phi_w & \cos \phi_w & 0 \\ -\cos \theta_w \cos \phi_w & -\cos \theta_w \sin \phi_w & \sin \theta_w \end{vmatrix} \\ &= - \begin{bmatrix} \begin{vmatrix} \cos \phi_w & -\cos \theta_w \sin \phi_w \\ 0 & \sin \theta_w \end{vmatrix} \\ \begin{vmatrix} -\sin \phi_w & -\cos \theta_w \cos \phi_w \\ 0 & \sin \theta_w \end{vmatrix} \\ \begin{vmatrix} \cos \phi_w & -\cos \theta_w \sin \phi_w \\ -\sin \phi_w & -\cos \theta_w \cos \phi_w \end{vmatrix} \end{bmatrix}; \end{aligned}$$

taking the determinants gives

$$\begin{aligned} \hat{x}' \times \hat{y}' &= \begin{bmatrix} \cos \phi_w \sin \theta_w - 0 \\ -1(-\sin \phi_w) \sin \theta_w \\ (\cos \phi_w (-\cos \theta_w) \cos \phi_w) - \sin \phi_w (-\cos \theta_w) \sin \phi_w \end{bmatrix} \\ &= \begin{bmatrix} \sin \theta_w \cos \phi_w \\ \sin \theta_w \sin \phi_w \\ \cos \theta_w \cos^2 \phi_w + \cos \theta_w \sin^2 \phi_w \end{bmatrix} \\ &= \begin{bmatrix} \sin \theta_w \cos \phi_w \\ \sin \theta_w \sin \phi_w \\ \cos \theta_w (\cos^2 \phi_w + \sin^2 \phi_w) \end{bmatrix} \\ &= \begin{bmatrix} \sin \theta_w \cos \phi_w \\ \sin \theta_w \sin \phi_w \\ \cos \theta_w \end{bmatrix} \\ &= \hat{n}. \end{aligned}$$

In order for these three orthogonal vectors to be unit vectors, condition A.1.3 must be satisfied:

For \hat{x}' ,

$$\begin{aligned} \|\hat{x}'\| &= \begin{bmatrix} -\sin \phi_w \\ \cos \phi_w \\ 0 \end{bmatrix} \cdot \begin{bmatrix} -\sin \phi_w \\ \cos \phi_w \\ 0 \end{bmatrix} \\ &= \sin^2 \phi_w + \cos^2 \phi_w + 0 \end{aligned}$$

$$= 1;$$

For \hat{y}' ,

$$\begin{aligned} \|\hat{y}'\| &= \begin{bmatrix} -\cos \theta_w \cos \phi_w \\ -\cos \theta_w \sin \phi_w \\ \sin \theta_w \end{bmatrix} \cdot \begin{bmatrix} -\cos \theta_w \cos \phi_w \\ -\cos \theta_w \sin \phi_w \\ \sin \theta_w \end{bmatrix} \\ &= \cos^2 \theta_w \cos^2 \phi_w + \cos^2 \theta_w \sin^2 \phi_w + \sin^2 \theta_w \\ &= \cos^2 \theta_w (\cos^2 \phi_w + \sin^2 \phi_w) + \sin^2 \theta_w \\ &= \cos^2 \theta_w + \sin^2 \theta_w \\ &= 1; \end{aligned}$$

For \hat{z}' ,

$$\begin{aligned} \|\hat{z}'\| &= \begin{bmatrix} \sin \theta_w \cos \phi_w \\ \sin \theta_w \sin \phi_w \\ \cos \theta_w \end{bmatrix} \cdot \begin{bmatrix} \sin \theta_w \cos \phi_w \\ \sin \theta_w \sin \phi_w \\ \cos \theta_w \end{bmatrix} \\ &= \sin^2 \theta_w \cos^2 \phi_w + \sin^2 \theta_w \sin^2 \phi_w + \cos^2 \theta_w \\ &= \sin^2 \theta_w (\cos^2 \phi_w + \sin^2 \phi_w) + \cos^2 \theta_w \\ &= \sin^2 \theta_w + \cos^2 \theta_w \\ &= 1. \end{aligned}$$

Finally, since we have $\hat{n} = \hat{z}'$, the cross product of condition A.1.2 forces condition A.1.4 to become true. Therefore, the definitions of \hat{x}' , \hat{y}' and \hat{n} form a suitable orthonormal vector basis for a three-component geophone in a deviated well.

A.2. Snell's Law in Vector Form

Snell's Law is generally given in the form

$$\frac{\sin \theta_I}{V_I} = \frac{\sin \theta_T}{V_T}, \quad (\text{A.2.1})$$

where V_I and V_T are the velocities of the incident and transmitted media, and θ_I and θ_T are the angles of incidence and transmission relative to the normal of the interface. An expression which gives the general vector form of the transmitted ray direction \hat{T} , given an incoming ray direction \hat{I} and the normal to a velocity interface \hat{n} , is given by:

$$\hat{T} = a\hat{I} + b\hat{n}, \quad (\text{A.2.2})$$

where a and b are constants that can be found using

$$\hat{T} \cdot \hat{n} = \cos \theta_T, \text{ and} \quad (\text{A.2.3})$$

$$\hat{T} \cdot \hat{T} = 1. \quad (\text{A.2.4})$$

Note that Equation A.2.3 is a direct result of Snell's Law, and Equation A.2.4 implies that \hat{T} is a unit vector; in fact, \hat{I} and \hat{n} are also defined as unit vectors in this case.

Expanding Equation A.2.3, we get:

$$\begin{aligned} \hat{T} \cdot \hat{n} &= \cos \theta_T = (a\hat{I} + b\hat{n}) \cdot \hat{n} \\ &= a(\hat{I} \cdot \hat{n}) + b(\hat{n} \cdot \hat{n}) \\ &= a \cos \theta_I + b. \end{aligned}$$

This can be rearranged to give

$$b = \cos \theta_T - a \cos \theta_I. \quad (\text{A.2.5})$$

Next, expanding Equation A.2.4 results in:

$$\begin{aligned} \hat{T} \cdot \hat{T} &= 1 = (a\hat{I} + b\hat{n}) \cdot (a\hat{I} + b\hat{n}) \\ &= a^2(\hat{I} \cdot \hat{I}) + 2ab(\hat{I} \cdot \hat{n}) + b^2(\hat{n} \cdot \hat{n}) \\ &= a^2 + 2ab \cos \theta_I + b^2 \end{aligned} \quad (\text{A.2.6})$$

Substituting Equation A.2.5 into Equation A.2.6 gives:

$$\begin{aligned} 1 &= a^2 + 2a(\cos \theta_T - a \cos \theta_I) \cos \theta_I + (\cos \theta_T - a \cos \theta_I)^2 \\ &= a^2 + 2a \cos \theta_T \cos \theta_I - 2a^2 \cos^2 \theta_I + \cos^2 \theta_T - 2a \cos \theta_T \cos \theta_I + a^2 \cos^2 \theta_I \\ &= a^2 - a^2 \cos^2 \theta_I + \cos^2 \theta_T \end{aligned}$$

$$\begin{aligned}
&= a^2(1 - \cos^2 \theta_I) + \cos^2 \theta_T \\
&= a^2 \sin^2 \theta_I + \cos^2 \theta_T.
\end{aligned}$$

This can be rearranged to give

$$\begin{aligned}
a^2 &= \frac{1 - \cos^2 \theta_T}{\sin^2 \theta_I} \\
&= \frac{\sin^2 \theta_T}{\sin^2 \theta_I} \\
a &= \frac{\sin \theta_T}{\sin \theta_I}
\end{aligned}$$

Finally, applying Snell's Law gives us:

$$a = \frac{V_T}{V_I}. \quad (\text{A.2.7})$$

Applying Snell's Law and Equation A.2.7 to Equation A.2.5, and rewriting in terms of V_I , V_T , \hat{I} and \hat{n} , we get:

$$\begin{aligned}
b &= \cos \theta_T - a \cos \theta_I \\
&= \cos \theta_T - \frac{V_T}{V_I} \cos \theta_I \\
&= \sqrt{1 - \sin^2 \theta_T} - \frac{V_T}{V_I} (\hat{I} \cdot \hat{n}) \\
&= \sqrt{1 - \left(\frac{V_T}{V_I}\right)^2 \sin^2 \theta_I} - \frac{V_T}{V_I} (\hat{I} \cdot \hat{n}) \\
&= \sqrt{1 - \left(\frac{V_T}{V_I}\right)^2 [1 - \cos^2 \theta_I]} - \frac{V_T}{V_I} (\hat{I} \cdot \hat{n}) \\
&= \sqrt{1 - \left(\frac{V_T}{V_I}\right)^2 [1 - (\hat{I} \cdot \hat{n})^2]} - \frac{V_T}{V_I} (\hat{I} \cdot \hat{n})
\end{aligned} \quad (\text{A.2.8})$$

Finally, substituting Equations A.2.7 and A.2.8 into Equation A.2.2 provides a useable vector form of Snell's Law:

$$\hat{\mathbf{T}} = \frac{V_T}{V_I} \hat{\mathbf{I}} + \left(\sqrt{1 - \left(\frac{V_T}{V_I}\right)^2 [1 - (\hat{\mathbf{I}} \cdot \hat{\mathbf{n}})^2]} - \frac{V_T}{V_I} (\hat{\mathbf{I}} \cdot \hat{\mathbf{n}}) \right) \hat{\mathbf{n}}.$$

APPENDIX B: EXPANDED RESULTS FOR PEMBINA TIME-LAPSE STUDY

This appendix provides a more complete suite of repeatability results for the Pembina time-lapse study performed in Chapter 2.

- 1) Figure B.1 to Figure 2.6 show seismic repeatability for Receiver 1 (1498 m).
- 2) Figure B.4 to Figure B.6 show seismic repeatability for Receiver 2 (1518 m).
- 3) Figure B.7 to Figure B.9 show seismic repeatability for Receiver 3 (1538 m).
- 4) Figure B.10 to Figure B.12 show seismic repeatability for Receiver 4 (1558 m).
- 5) Figure B.13 to Figure B.15 show seismic repeatability for Receiver 5 (1579 m).
- 6) Figure B.16 to Figure B.18 show seismic repeatability for Receiver 6 (1599 m).
- 7) Figure B.19 to Figure B.21 show seismic repeatability for Receiver 7 (1620 m).
- 8) Figure B.22 to Figure B.24 show seismic repeatability for Receiver 8 (1640 m).

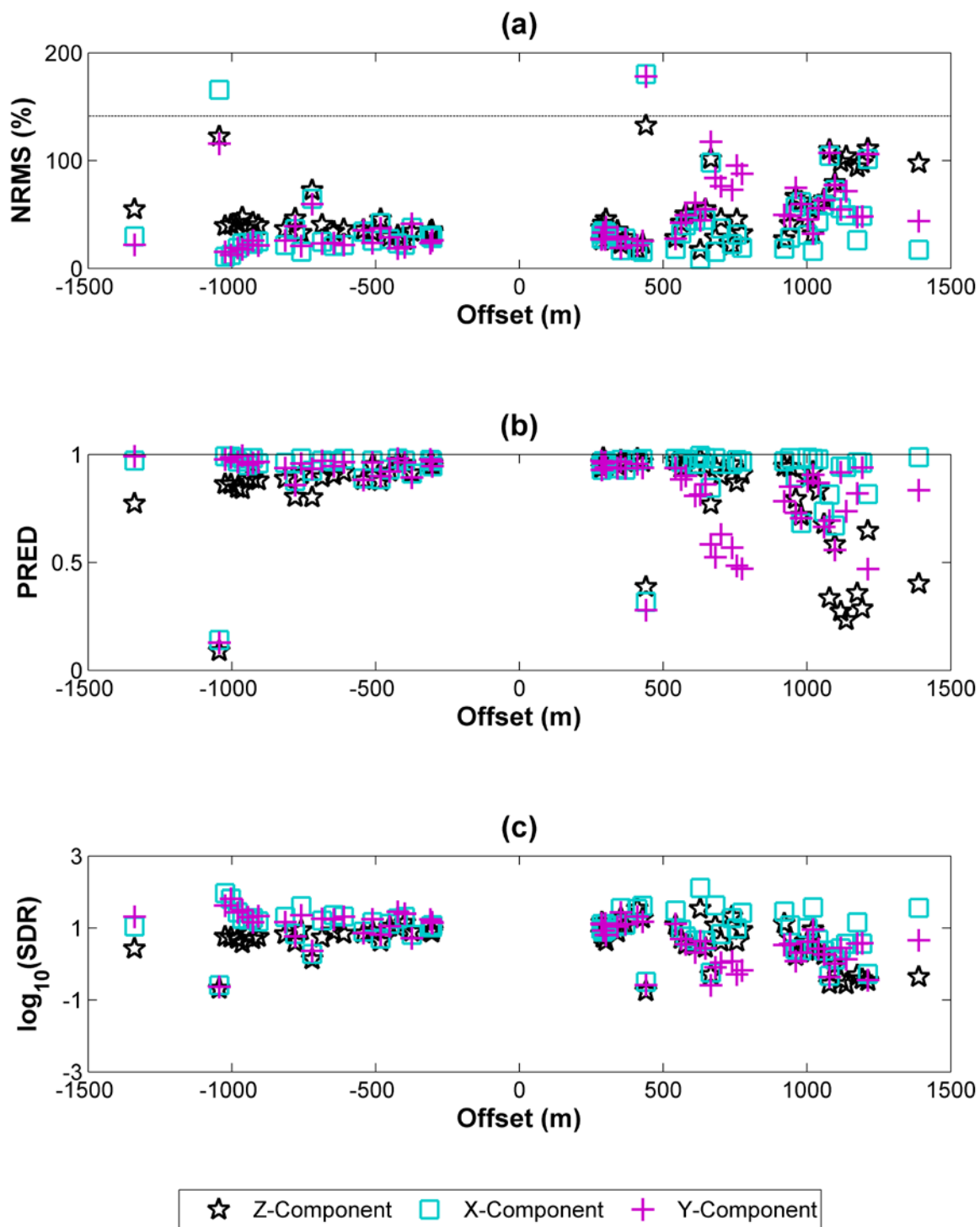


Figure B.1: Comparison of NRMS repeatability (a), predictability (b) and \log_{10} SDR (c) of Receiver 1 for Line 1, vs. source offset. The z-component is shown in black, x-component is shown in cyan, and y-component is shown in magenta. The dashed line in the NRMS plot indicates the theoretical noise line.

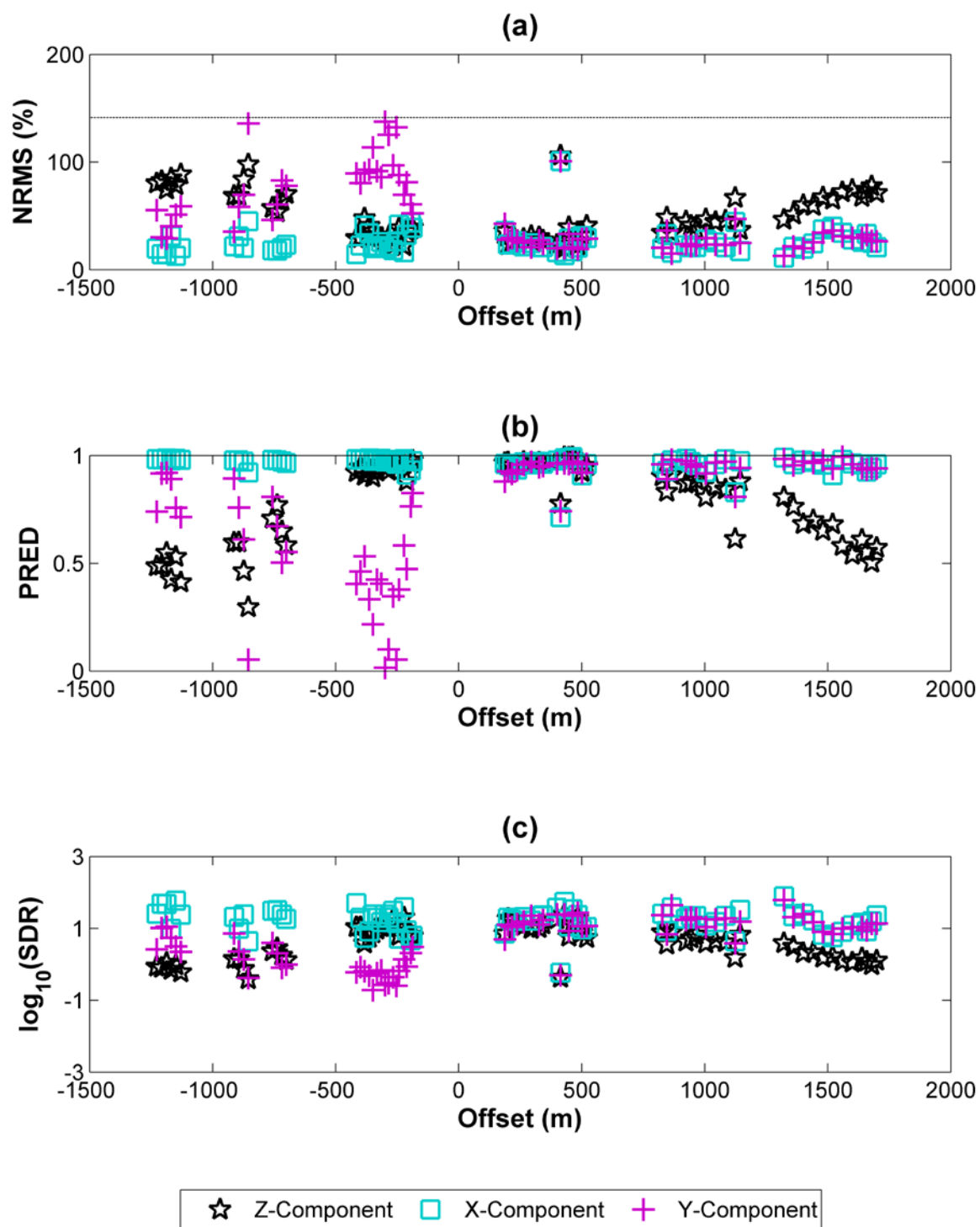


Figure B.2: Comparison of NRMS repeatability (a), predictability (b) and \log_{10} SDR (c) of Receiver 1 for Line 2, vs. source offset. The z-component is shown in black, x-component is shown in cyan, and y-component is shown in magenta. The dashed line in the NRMS plot indicates the theoretical noise line.

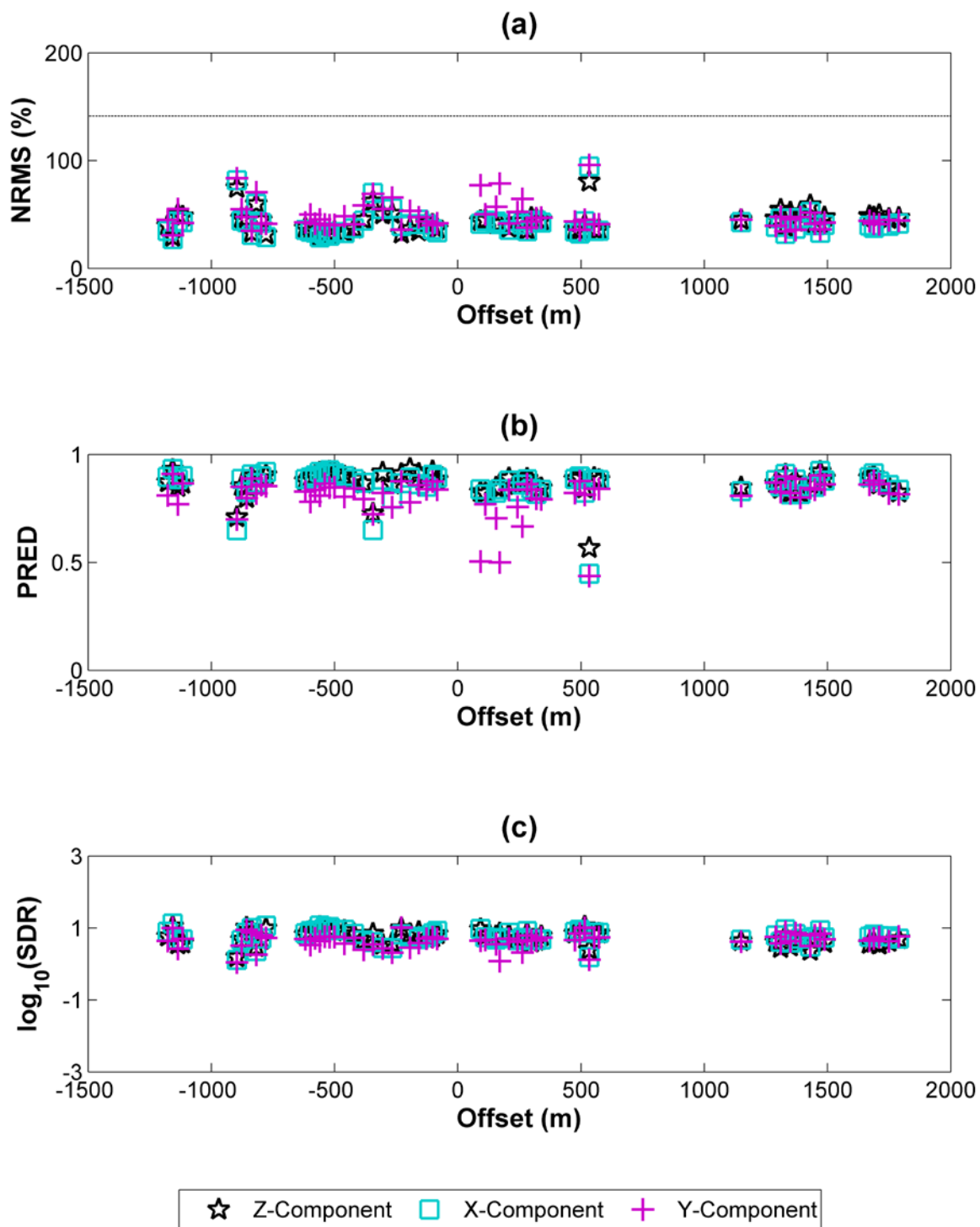


Figure B.3: Comparison of NRMS repeatability (a), predictability (b) and \log_{10} SDR (c) of Receiver 1 for Line 3, vs. source offset. The z-component is shown in black, x-component is shown in cyan, and y-component is shown in magenta. The dashed line in the NRMS plot indicates the theoretical noise line.

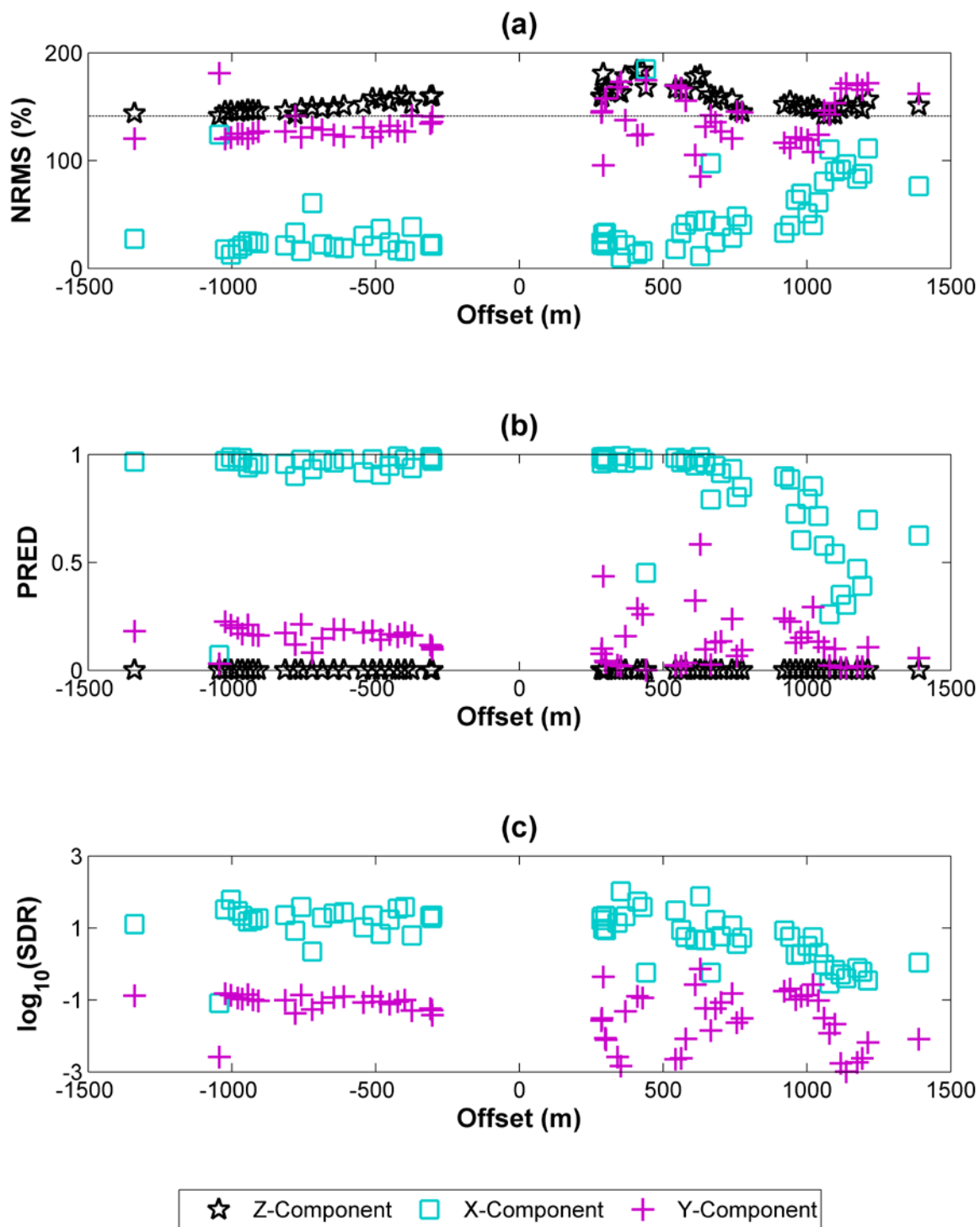


Figure B.4: Comparison of NRMS repeatability (a), predictability (b) and \log_{10} SDR (c) of Receiver 2 for Line 1, vs. source offset. The z-component is shown in black, x-component is shown in cyan, and y-component is shown in magenta. The dashed line in the NRMS plot indicates the theoretical noise line.

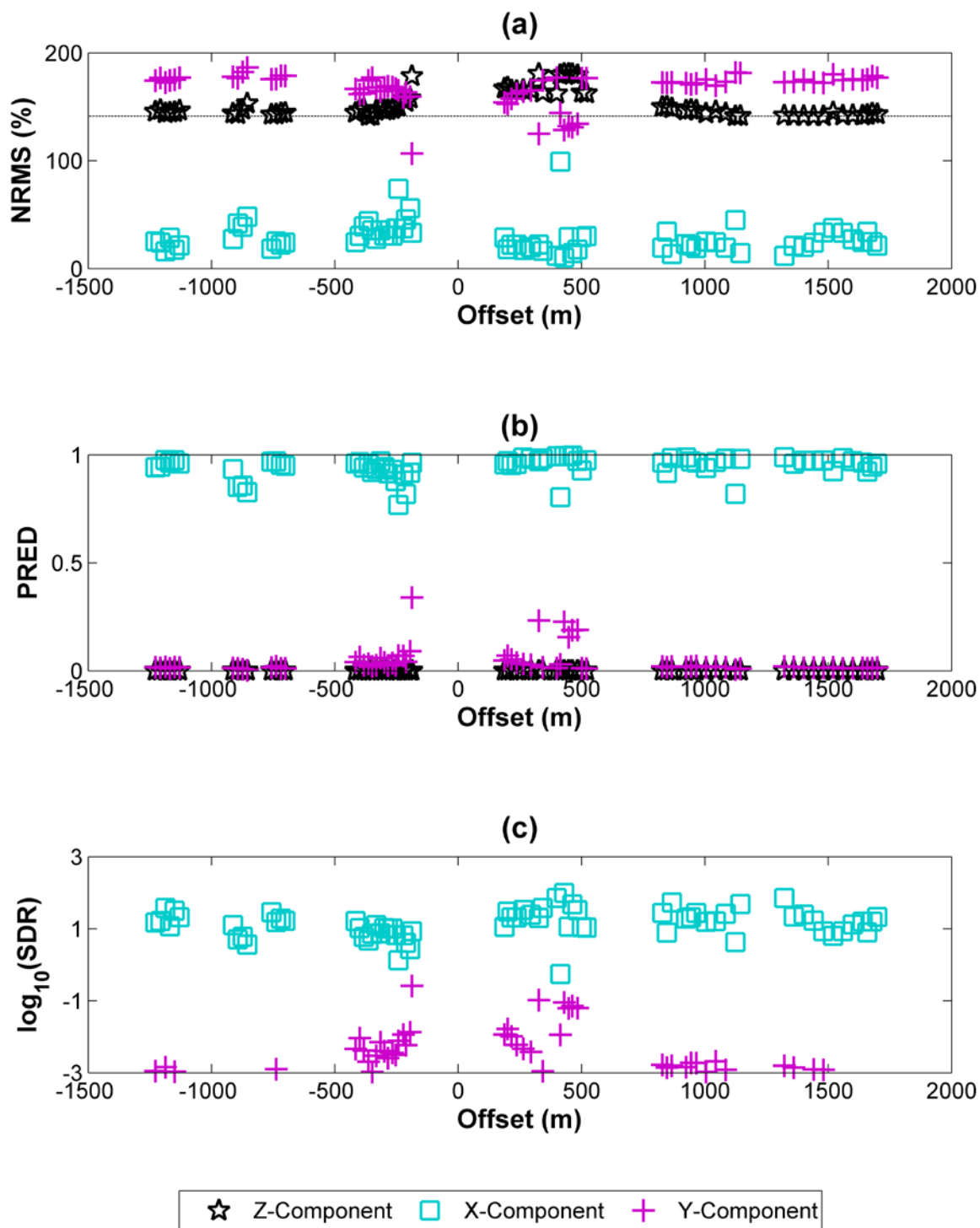


Figure B.5: Comparison of NRMS repeatability (a), predictability (b) and \log_{10} SDR (c) of Receiver 2 for Line 2, vs. source offset. The z-component is shown in black, x-component is shown in cyan, and y-component is shown in magenta. The dashed line in the NRMS plot indicates the theoretical noise line.

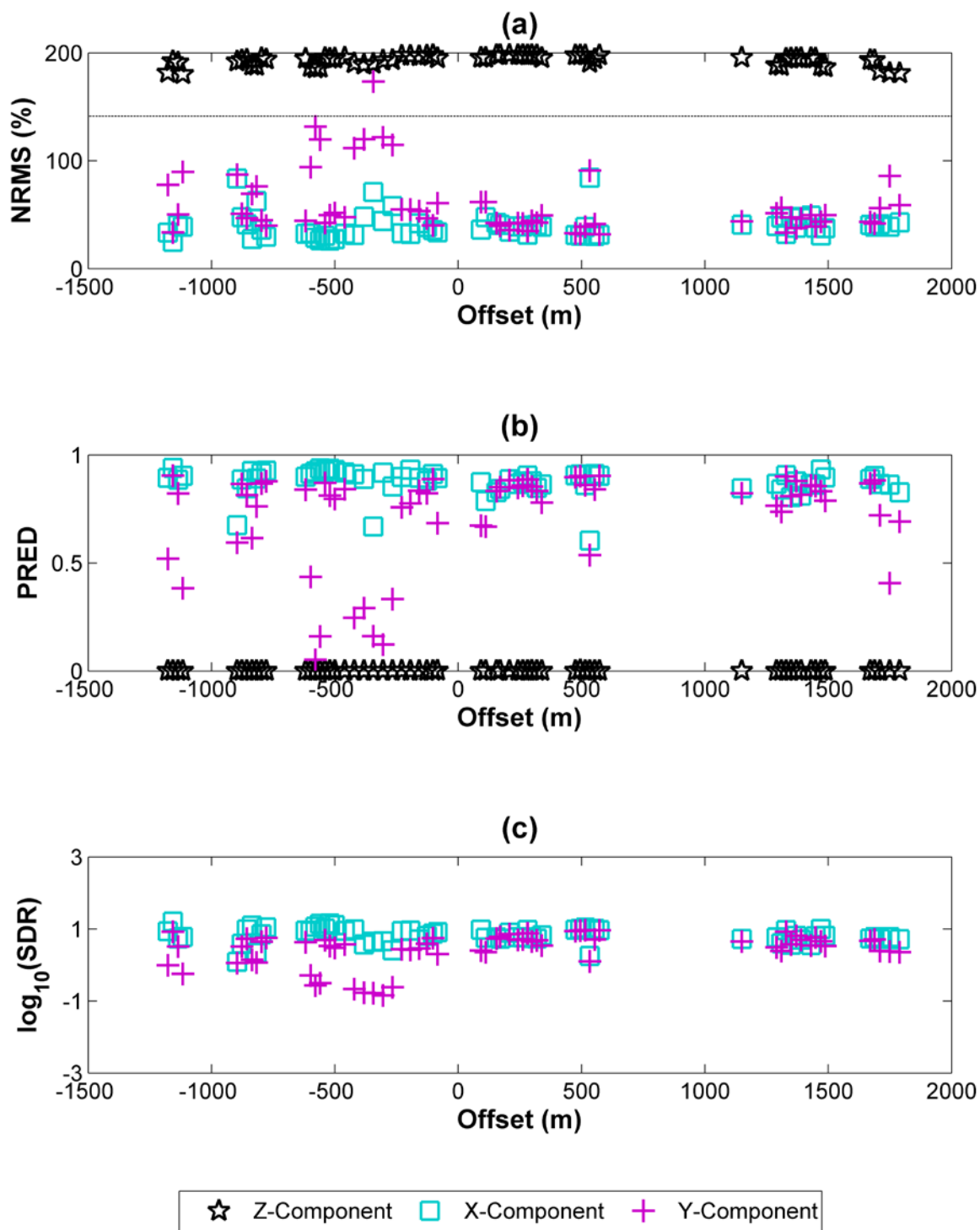


Figure B.6: Comparison of NRMS repeatability (a), predictability (b) and \log_{10} SDR (c) of Receiver 2 for Line 3, vs. source offset. The z-component is shown in black, x-component is shown in cyan, and y-component is shown in magenta. The dashed line in the NRMS plot indicates the theoretical noise line.

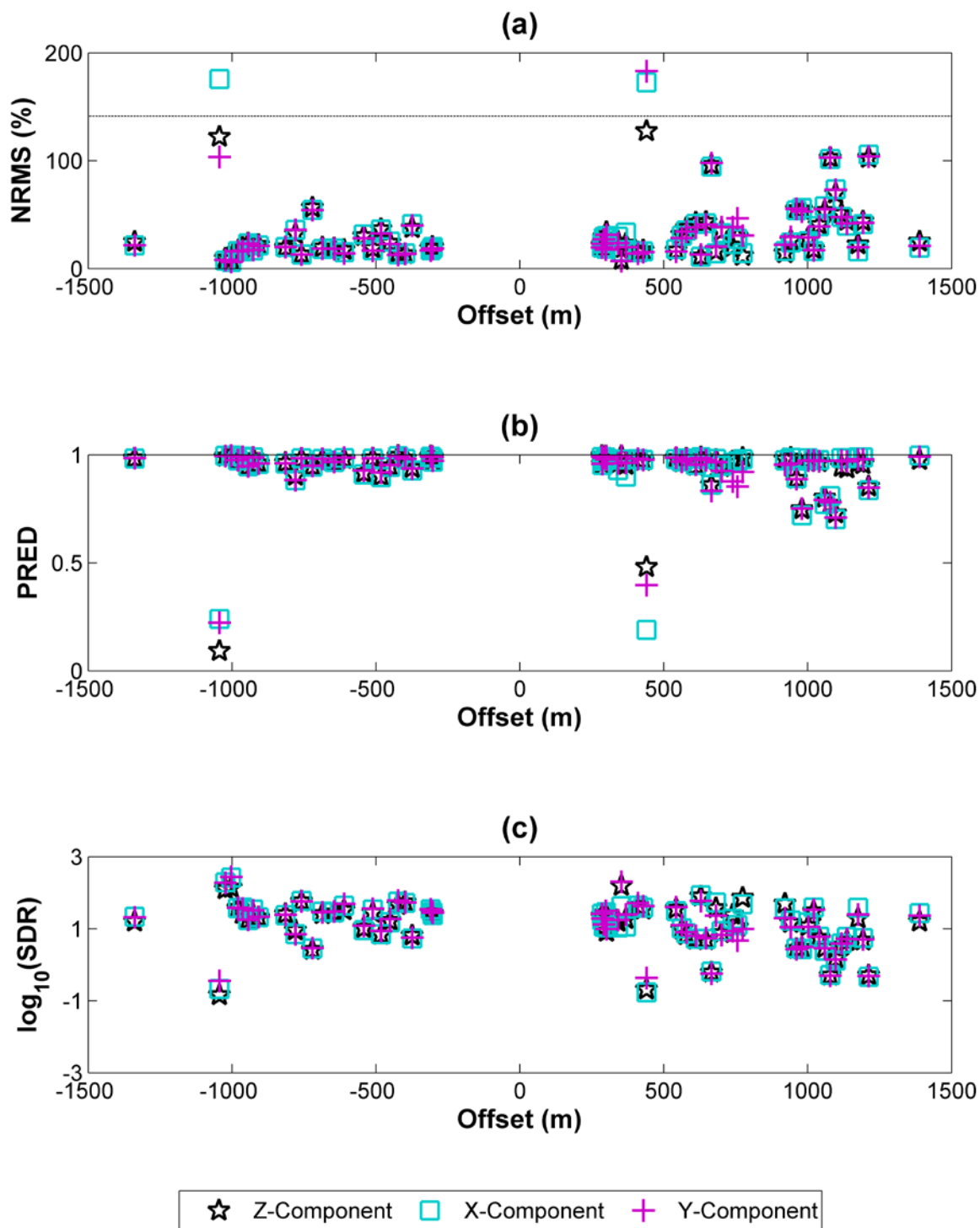


Figure B.7: Comparison of NRMS repeatability (a), predictability (b) and \log_{10} SDR (c) of Receiver 3 for Line 1, vs. source offset. The z-component is shown in black, x-component is shown in cyan, and y-component is shown in magenta. The dashed line in the NRMS plot indicates the theoretical noise line.

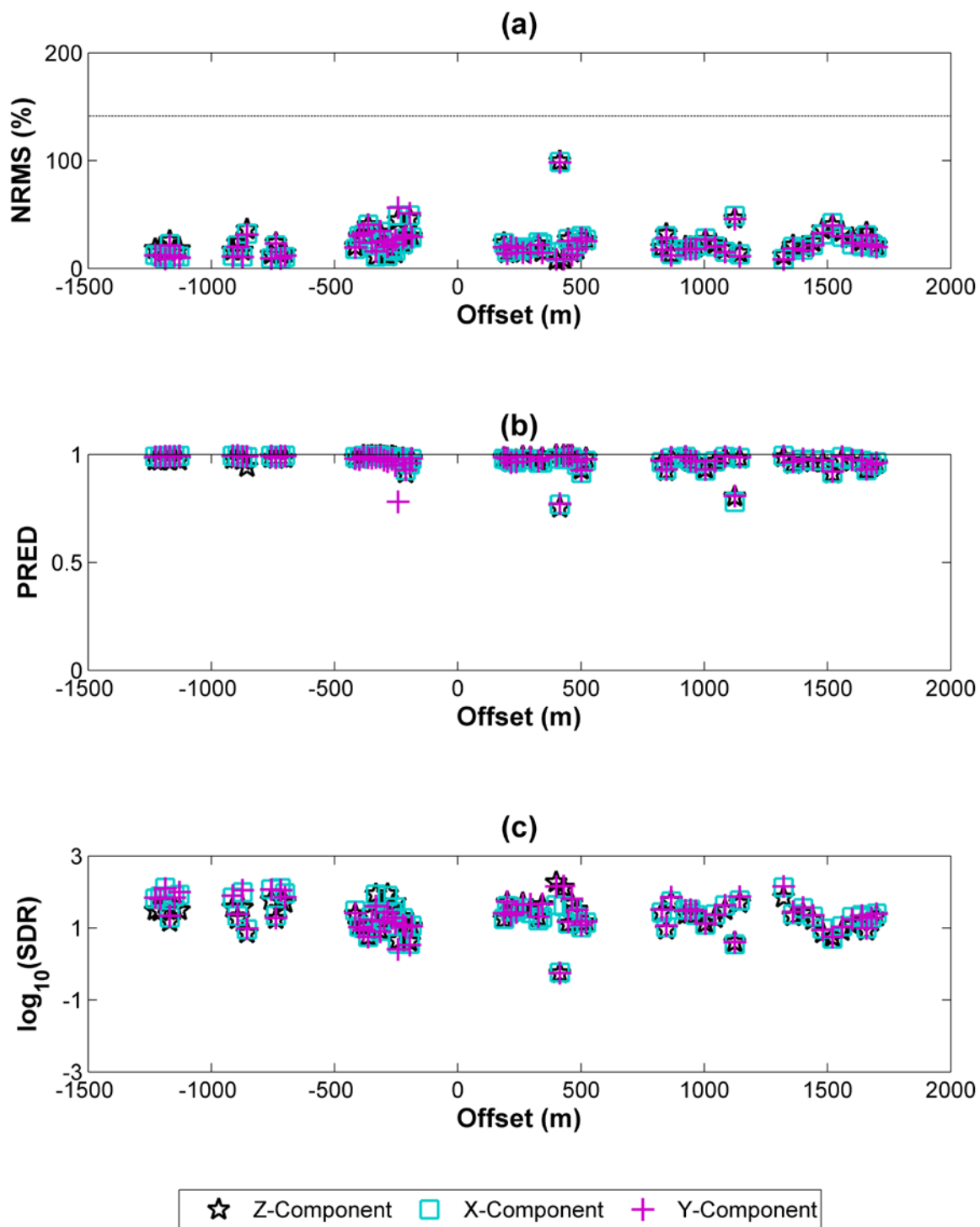


Figure B.8: Comparison of NRMS repeatability (a), predictability (b) and \log_{10} SDR (c) of Receiver 3 for Line 2, vs. source offset. The z-component is shown in black, x-component is shown in cyan, and y-component is shown in magenta. The dashed line in the NRMS plot indicates the theoretical noise line.

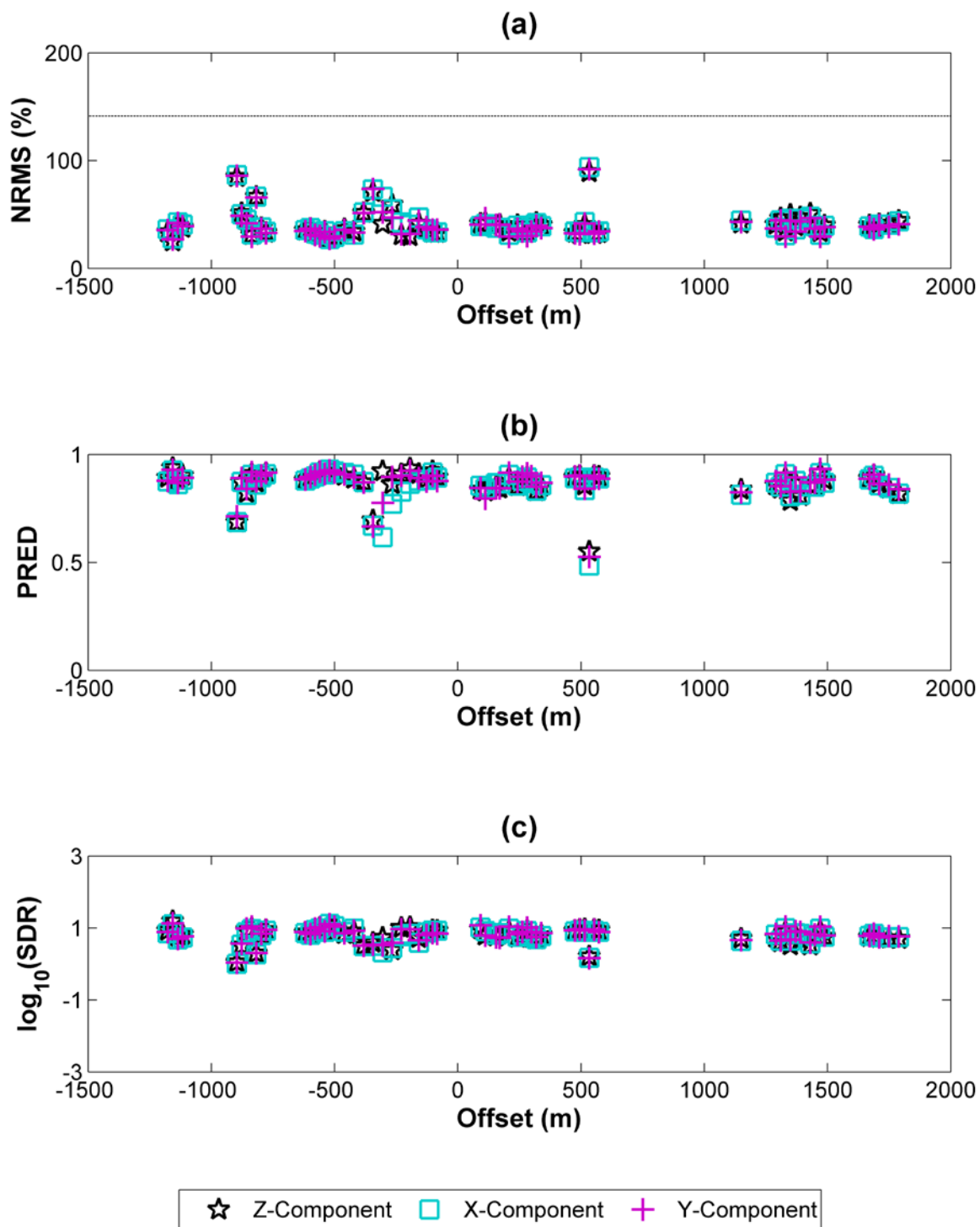


Figure B.9: Comparison of NRMS repeatability (a), predictability (b) and \log_{10} SDR (c) of Receiver 3 for Line 3, vs. source offset. The z-component is shown in black, x-component is shown in cyan, and y-component is shown in magenta. The dashed line in the NRMS plot indicates the theoretical noise line.

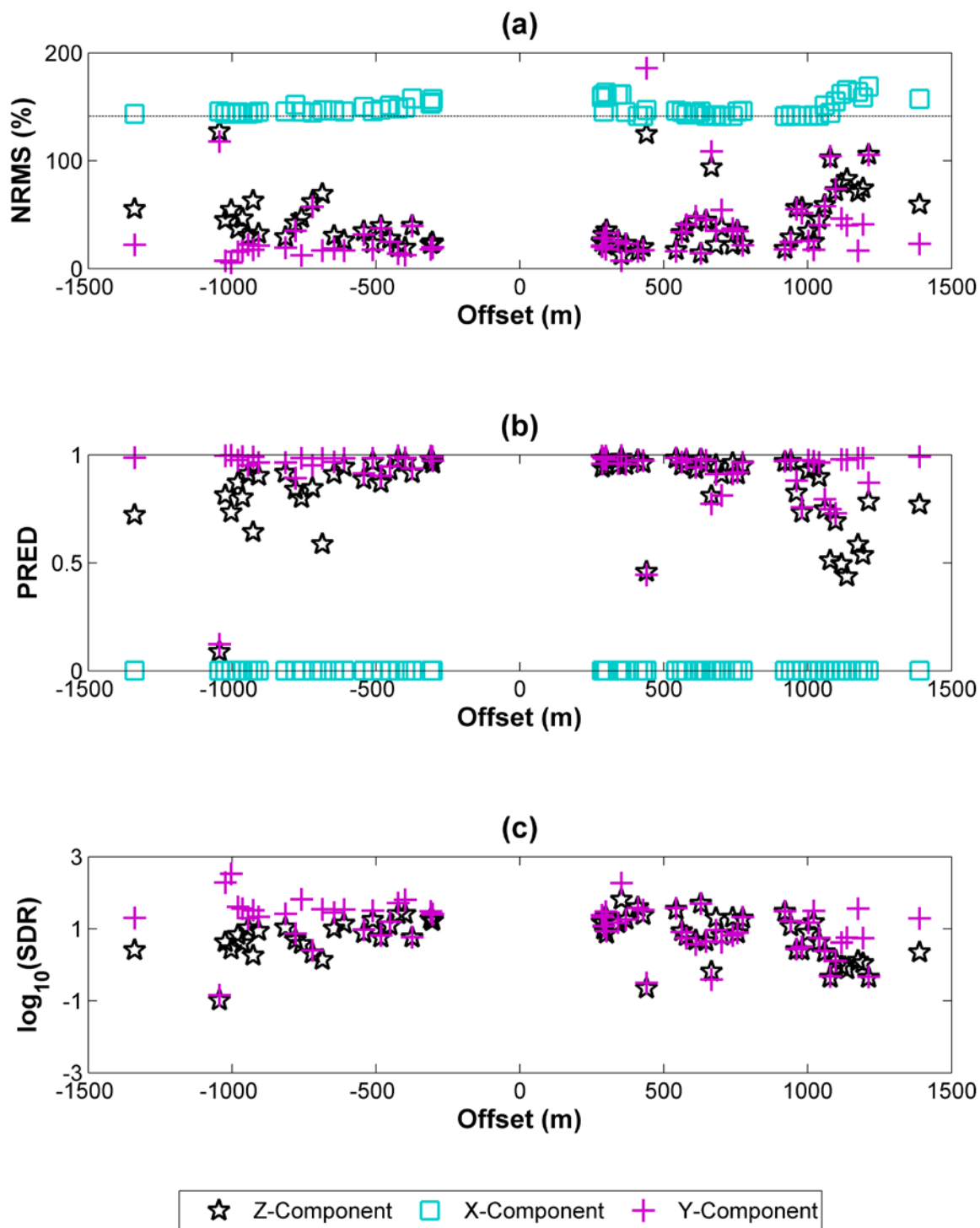


Figure B.10: Comparison of NRMS repeatability (a), predictability (b) and \log_{10} SDR (c) of Receiver 4 for Line 1, vs. source offset. The z-component is shown in black, x-component is shown in cyan, and y-component is shown in magenta. The dashed line in the NRMS plot indicates the theoretical noise line.

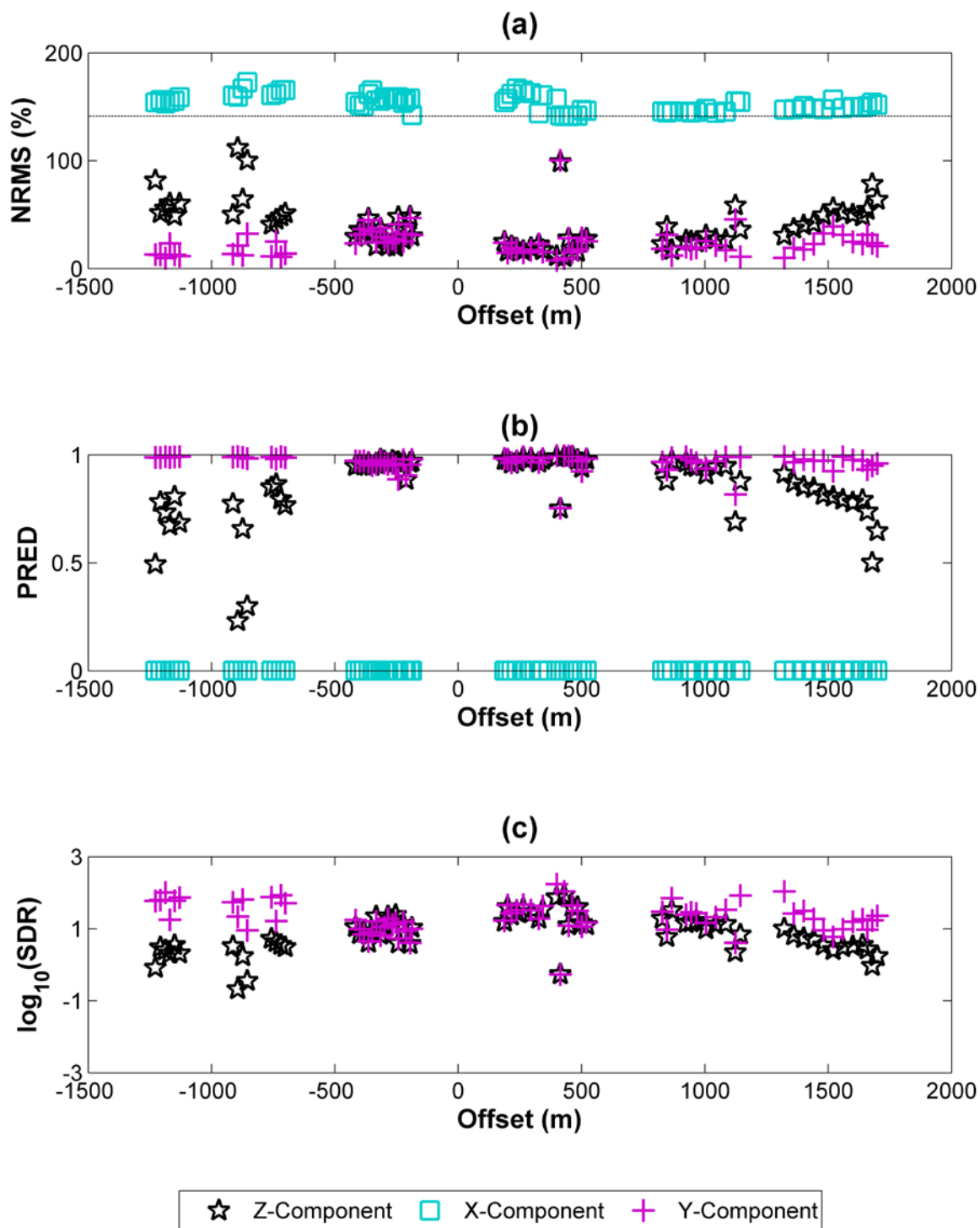


Figure B.11: Comparison of NRMS repeatability (a), predictability (b) and \log_{10} SDR (c) of Receiver 4 for Line 2, vs. source offset. The z-component is shown in black, x-component is shown in cyan, and y-component is shown in magenta. The dashed line in the NRMS plot indicates the theoretical noise line.

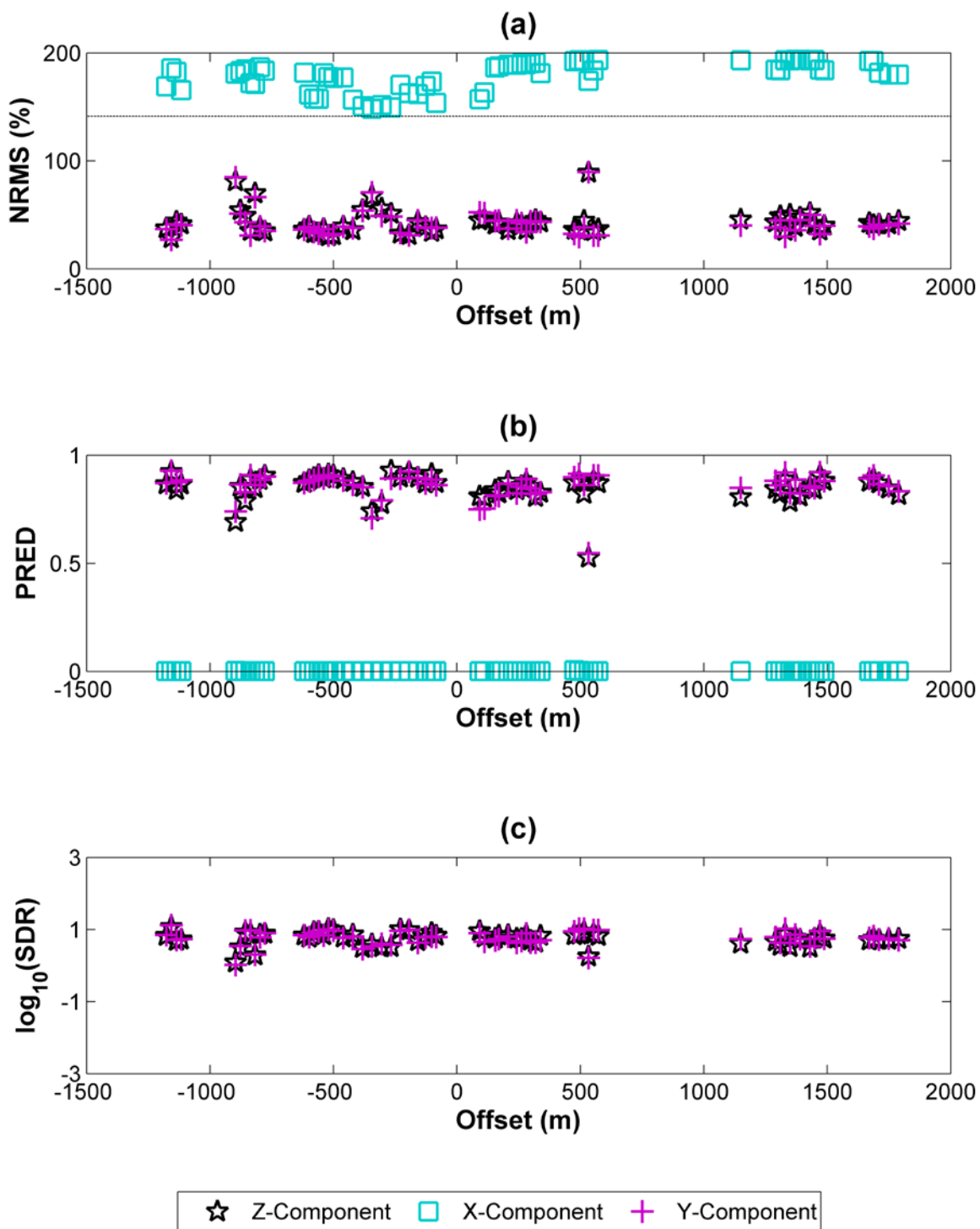


Figure B.12: Comparison of NRMS repeatability (a), predictability (b) and \log_{10} SDR (c) of Receiver 4 for Line 3, vs. source offset. The z-component is shown in black, x-component is shown in cyan, and y-component is shown in magenta. The dashed line in the NRMS plot indicates the theoretical noise line.

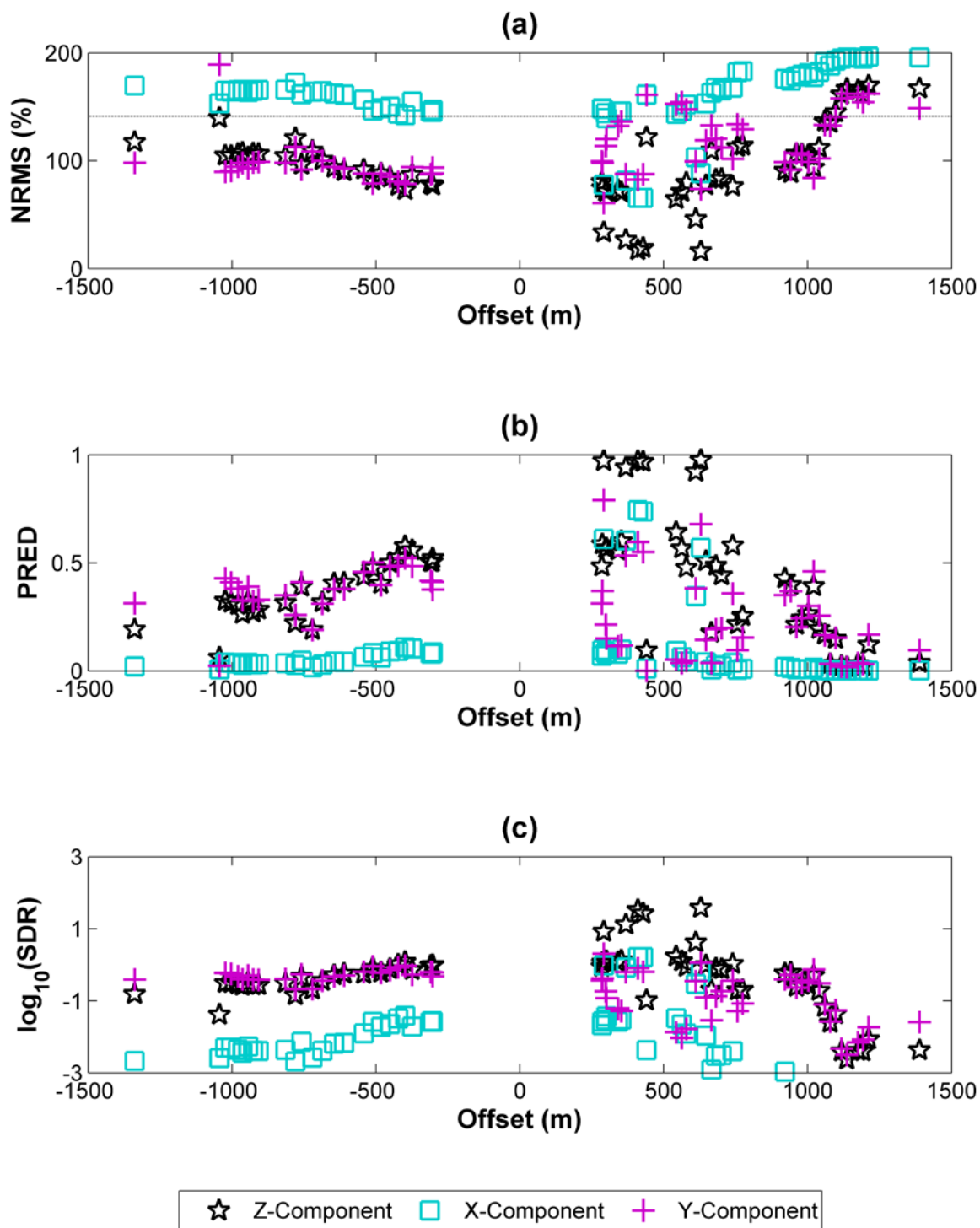


Figure B.13: Comparison of NRMS repeatability (a), predictability (b) and \log_{10} SDR (c) of Receiver 5 for Line 1, vs. source offset. The z-component is shown in black, x-component is shown in cyan, and y-component is shown in magenta. The dashed line in the NRMS plot indicates the theoretical noise line.

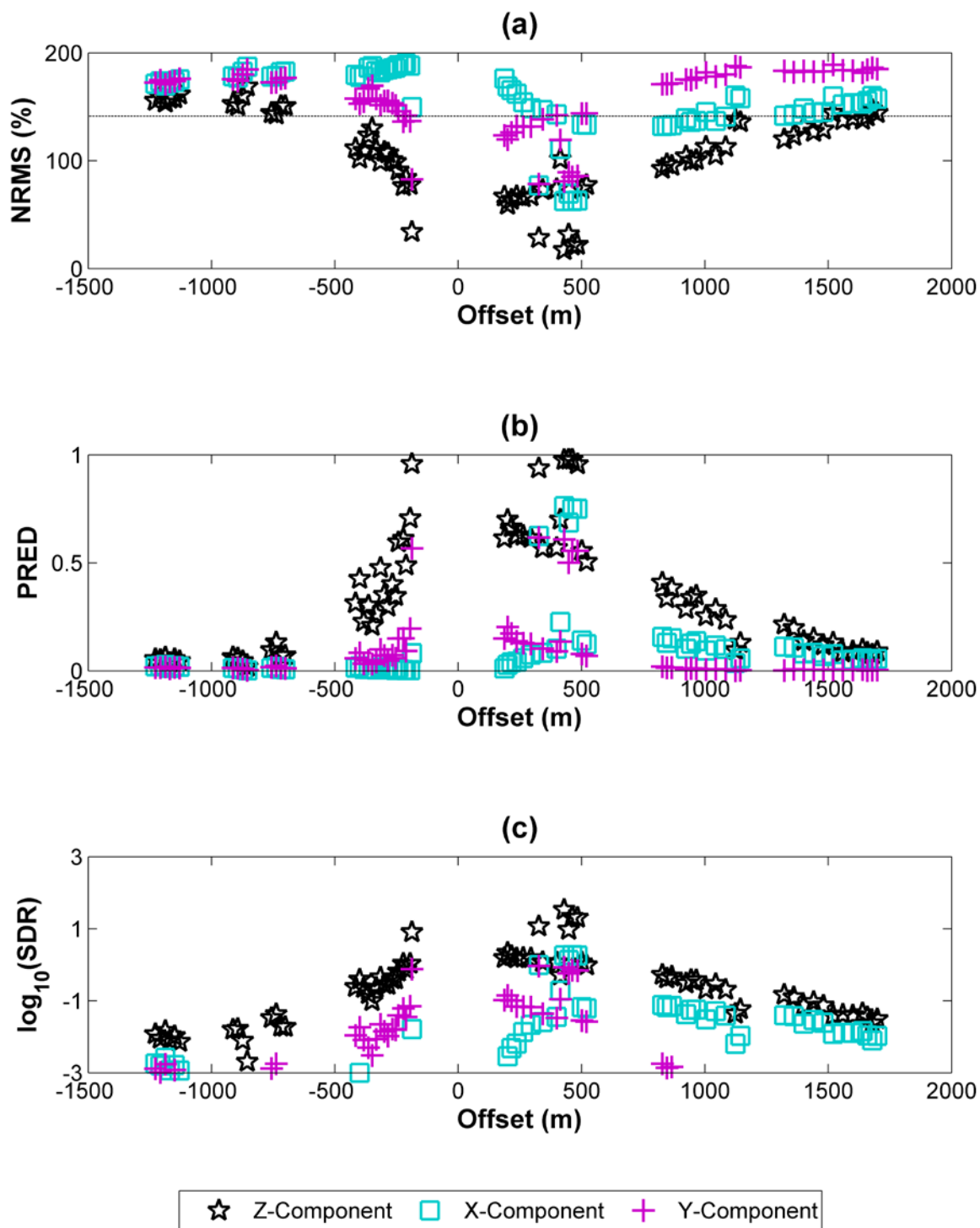


Figure B.14: Comparison of NRMS repeatability (a), predictability (b) and \log_{10} SDR (c) of Receiver 5 for Line 2, vs. source offset. The z-component is shown in black, x-component is shown in cyan, and y-component is shown in magenta. The dashed line in the NRMS plot indicates the theoretical noise line.

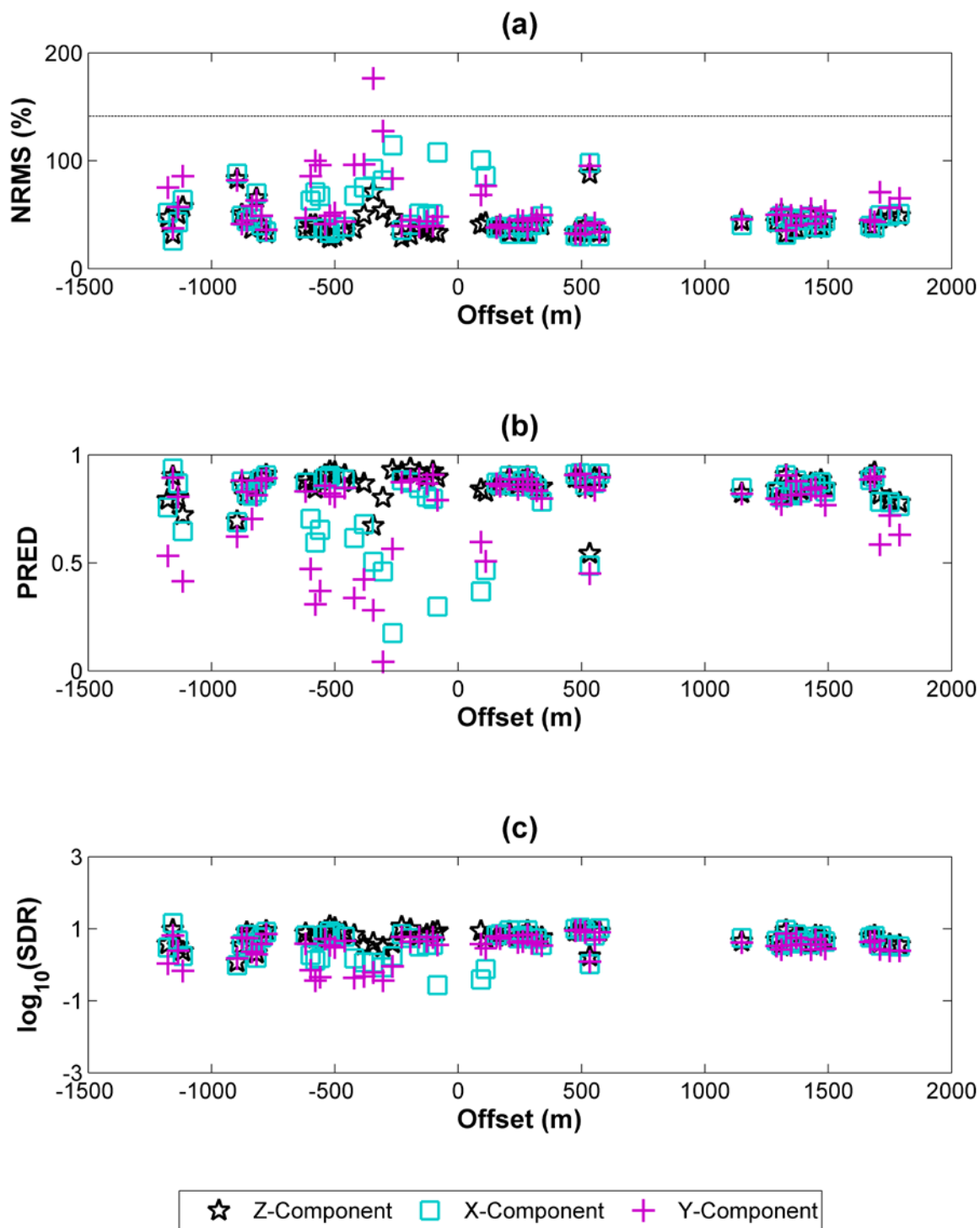


Figure B.15: Comparison of NRMS repeatability (a), predictability (b) and \log_{10} SDR (c) of Receiver 5 for Line 3, vs. source offset. The z-component is shown in black, x-component is shown in cyan, and y-component is shown in magenta. The dashed line in the NRMS plot indicates the theoretical noise line.

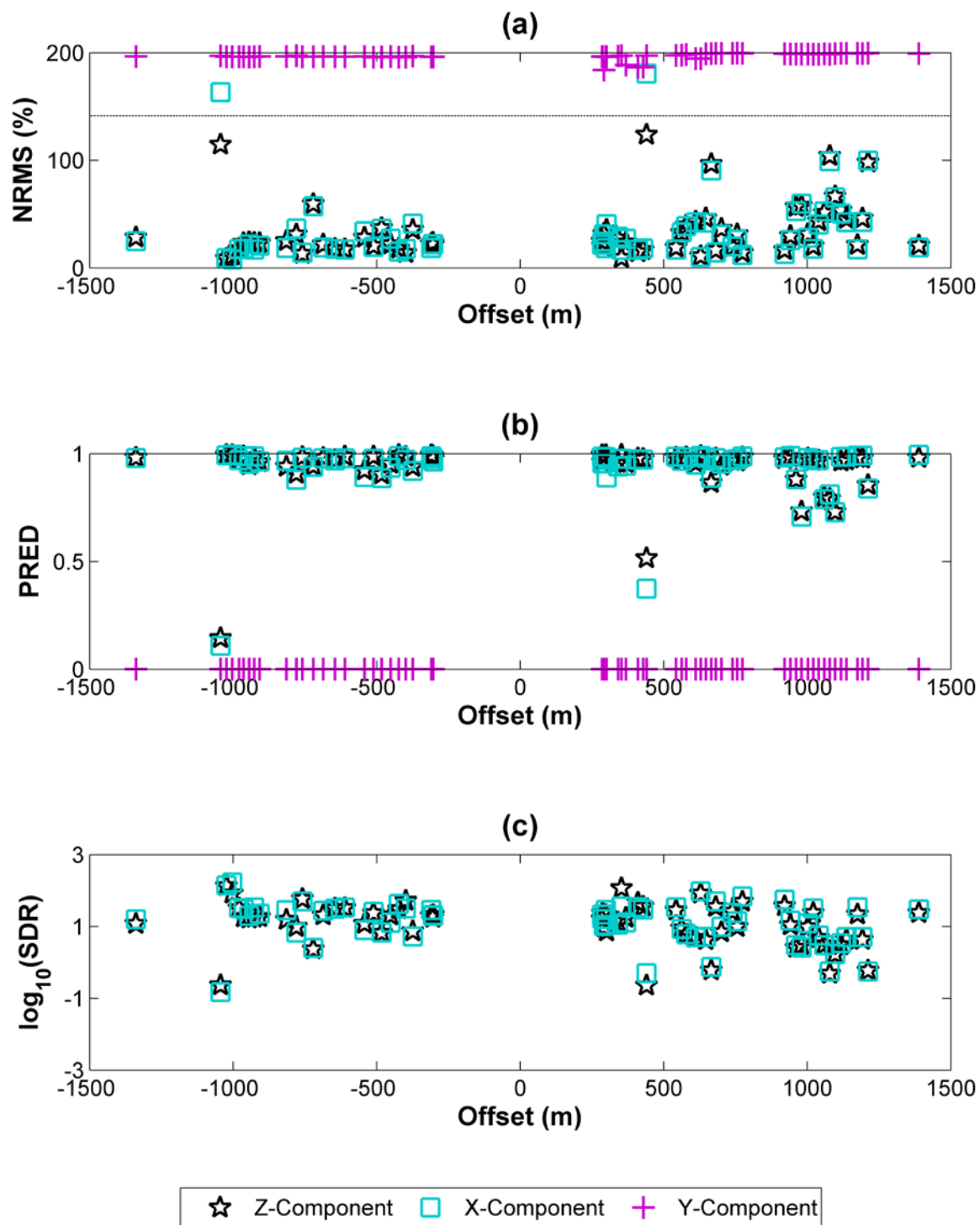


Figure B.16: Comparison of NRMS repeatability (a), predictability (b) and \log_{10} SDR (c) of Receiver 6 for Line 1, vs. source offset. The z-component is shown in black, x-component is shown in cyan, and y-component is shown in magenta. The dashed line in the NRMS plot indicates the theoretical noise line.

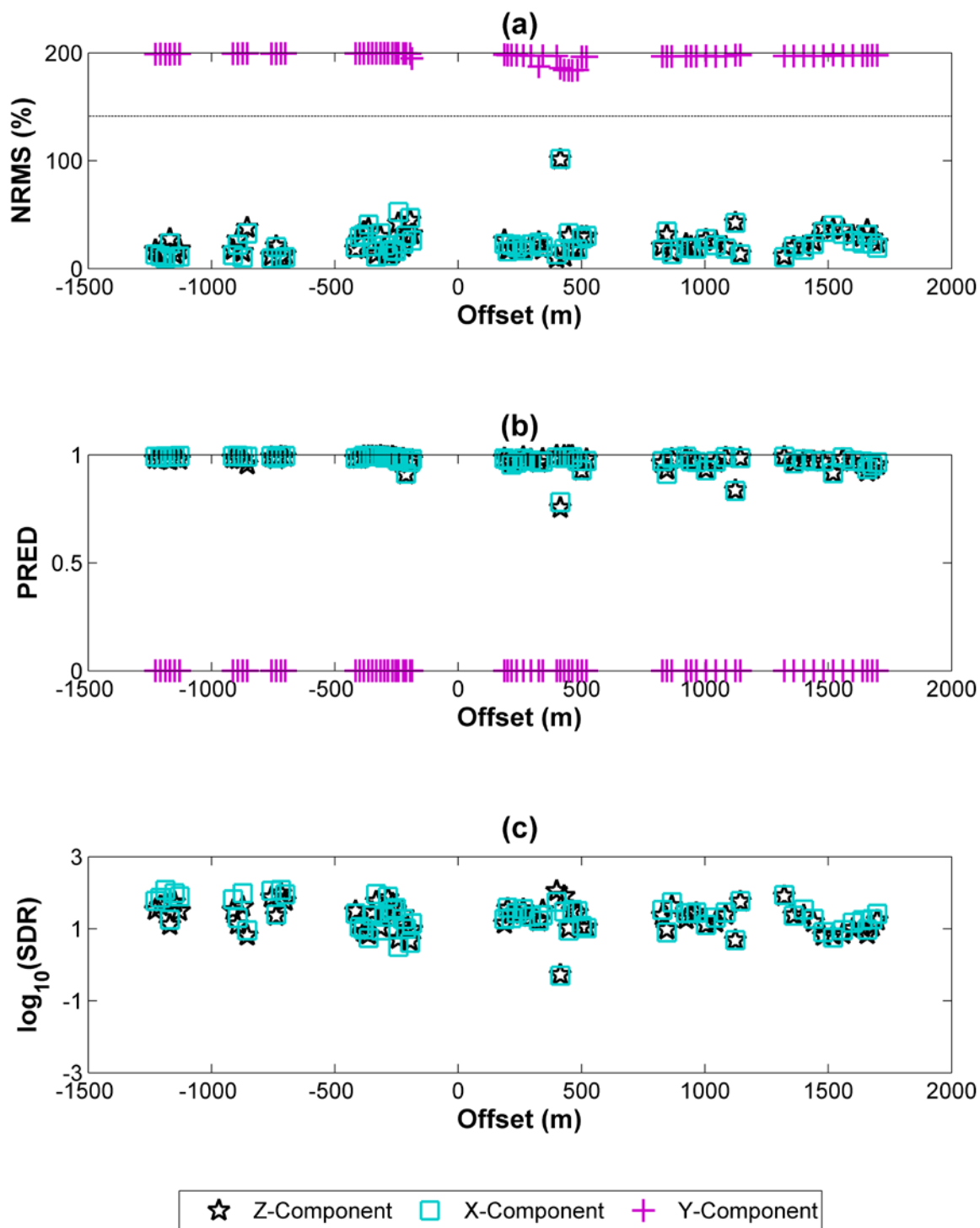


Figure B.17: Comparison of NRMS repeatability (a), predictability (b) and \log_{10} SDR (c) of Receiver 6 for Line 2, vs. source offset. The z-component is shown in black, x-component is shown in cyan, and y-component is shown in magenta. The dashed line in the NRMS plot indicates the theoretical noise line.

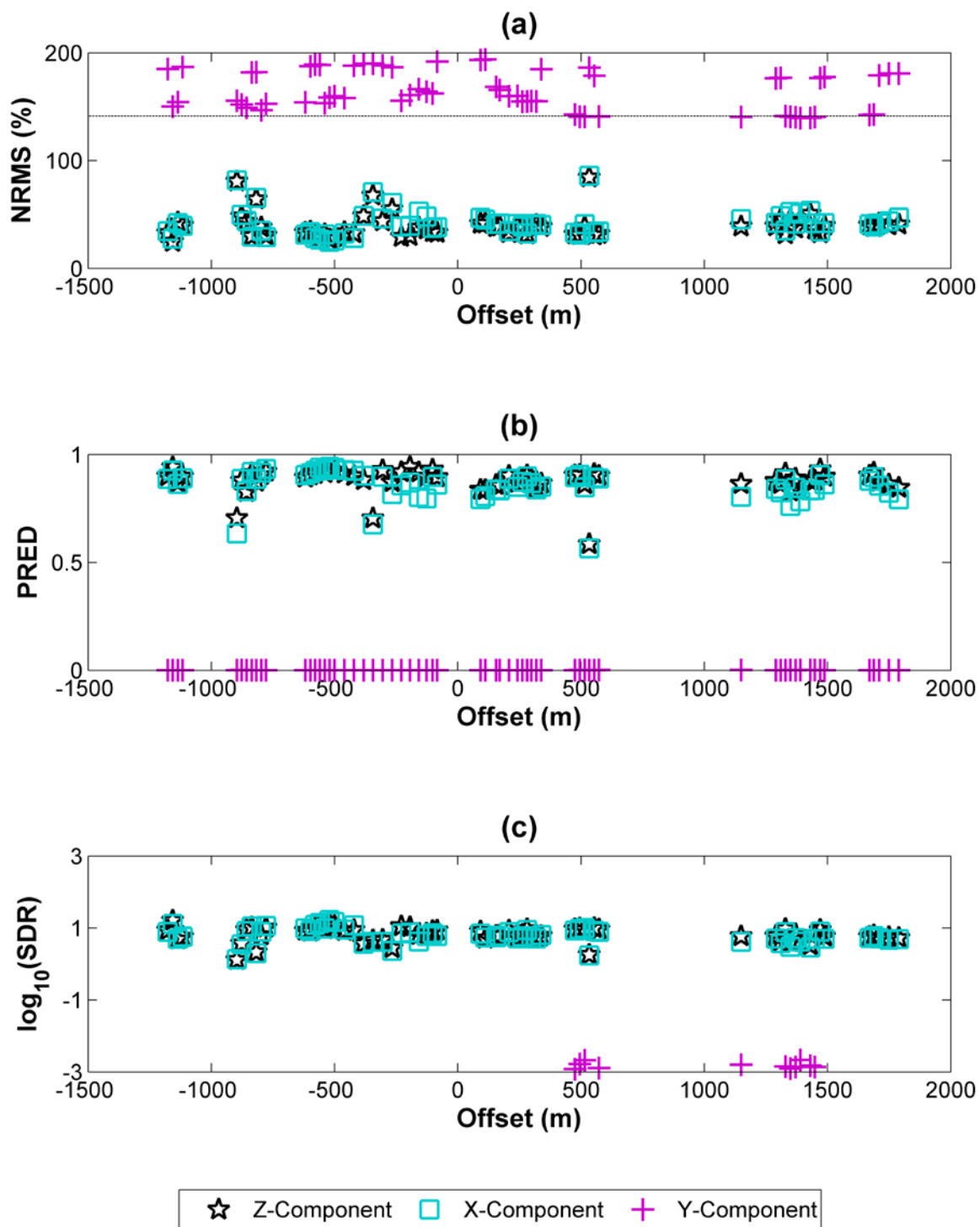


Figure B.18: Comparison of NRMS repeatability (a), predictability (b) and \log_{10} SDR (c) of Receiver 6 for Line 3, vs. source offset. The z-component is shown in black, x-component is shown in cyan, and y-component is shown in magenta. The dashed line in the NRMS plot indicates the theoretical noise line.

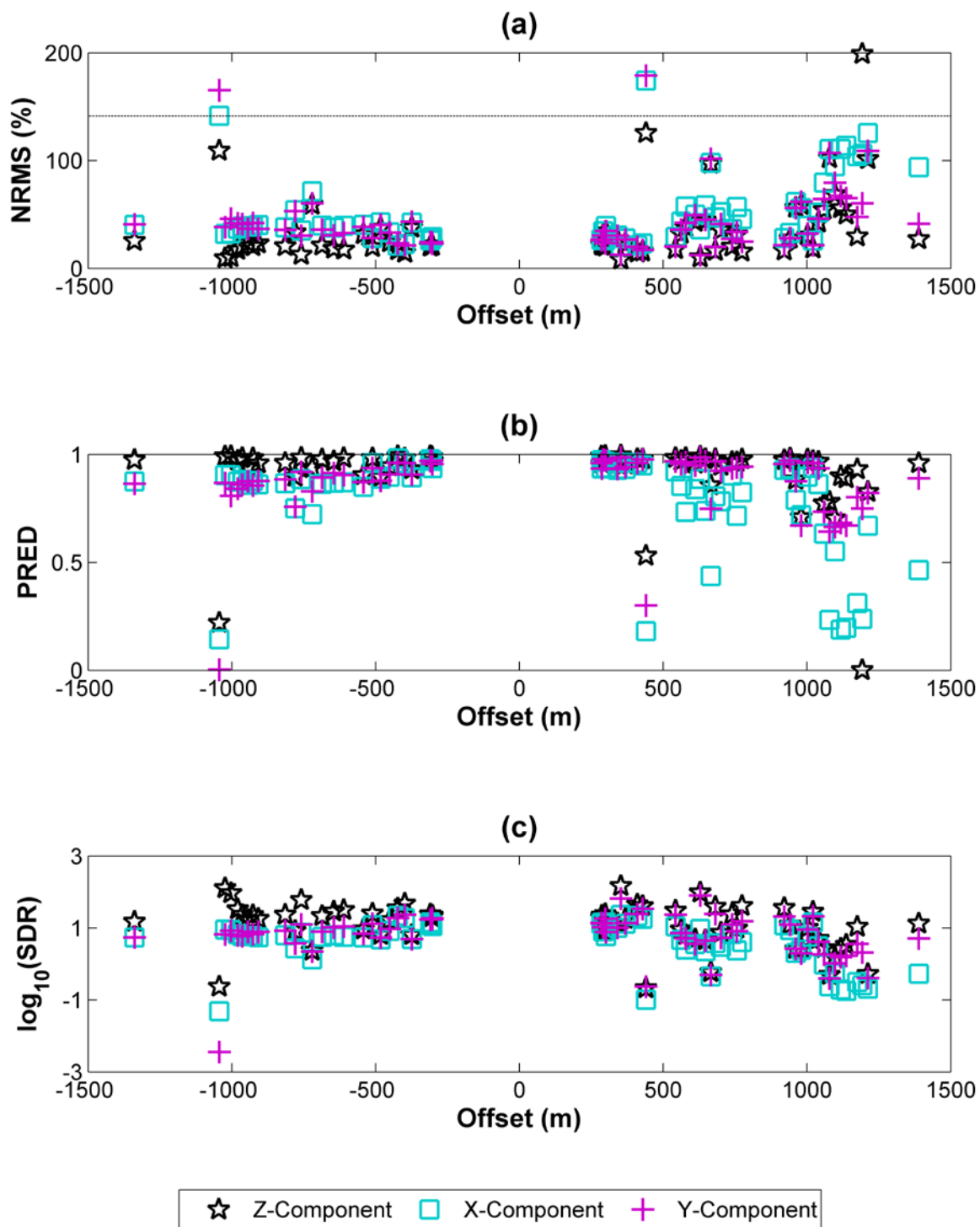


Figure B.19: Comparison of NRMS repeatability (a), predictability (b) and \log_{10} SDR (c) of Receiver 7 for Line 1, vs. source offset. The z-component is shown in black, x-component is shown in cyan, and y-component is shown in magenta. The dashed line in the NRMS plot indicates the theoretical noise line.

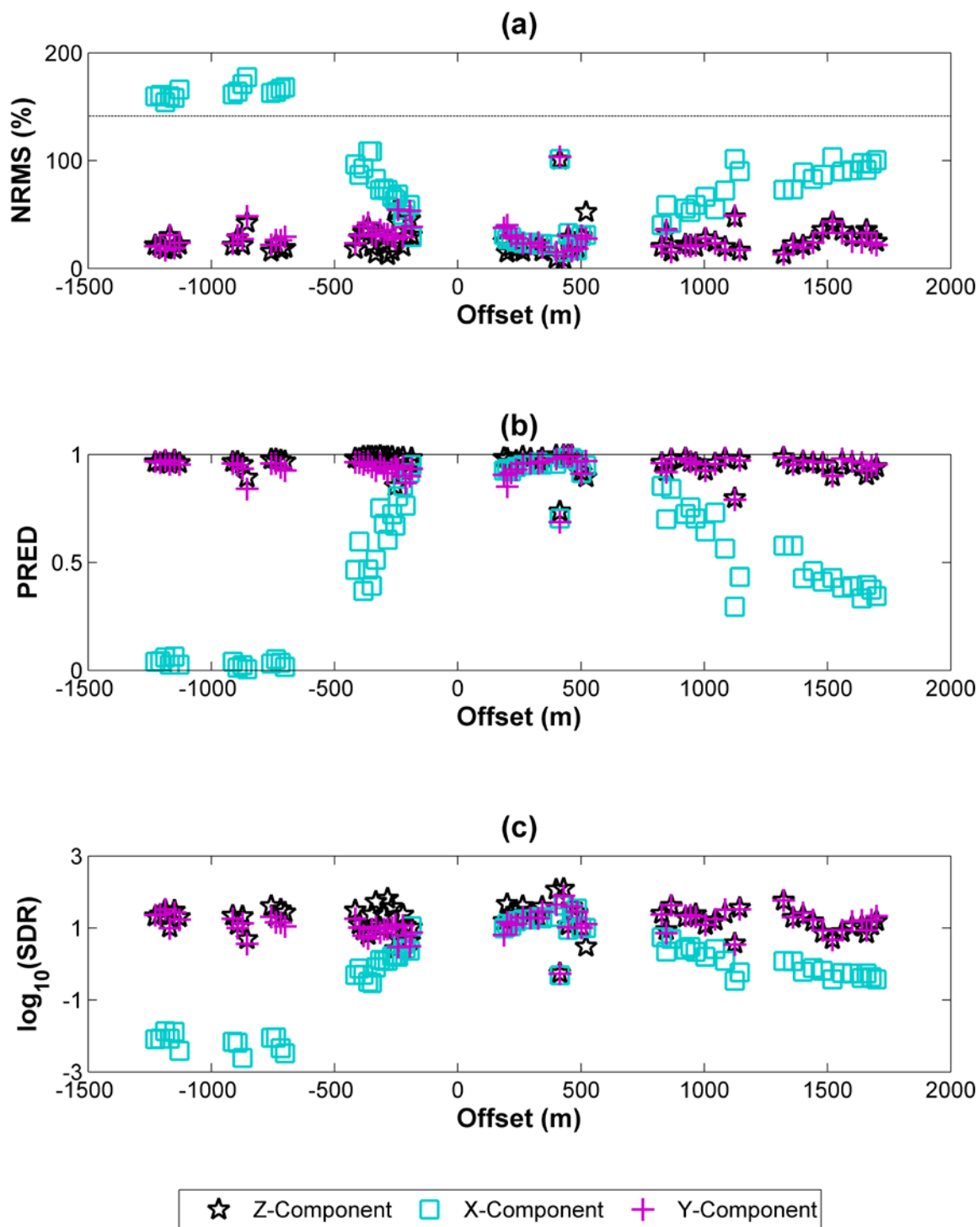


Figure B.20: Comparison of NRMS repeatability (a), predictability (b) and \log_{10} SDR (c) of Receiver 7 for Line 2, vs. source offset. The z-component is shown in black, x-component is shown in cyan, and y-component is shown in magenta. The dashed line in the NRMS plot indicates the theoretical noise line.

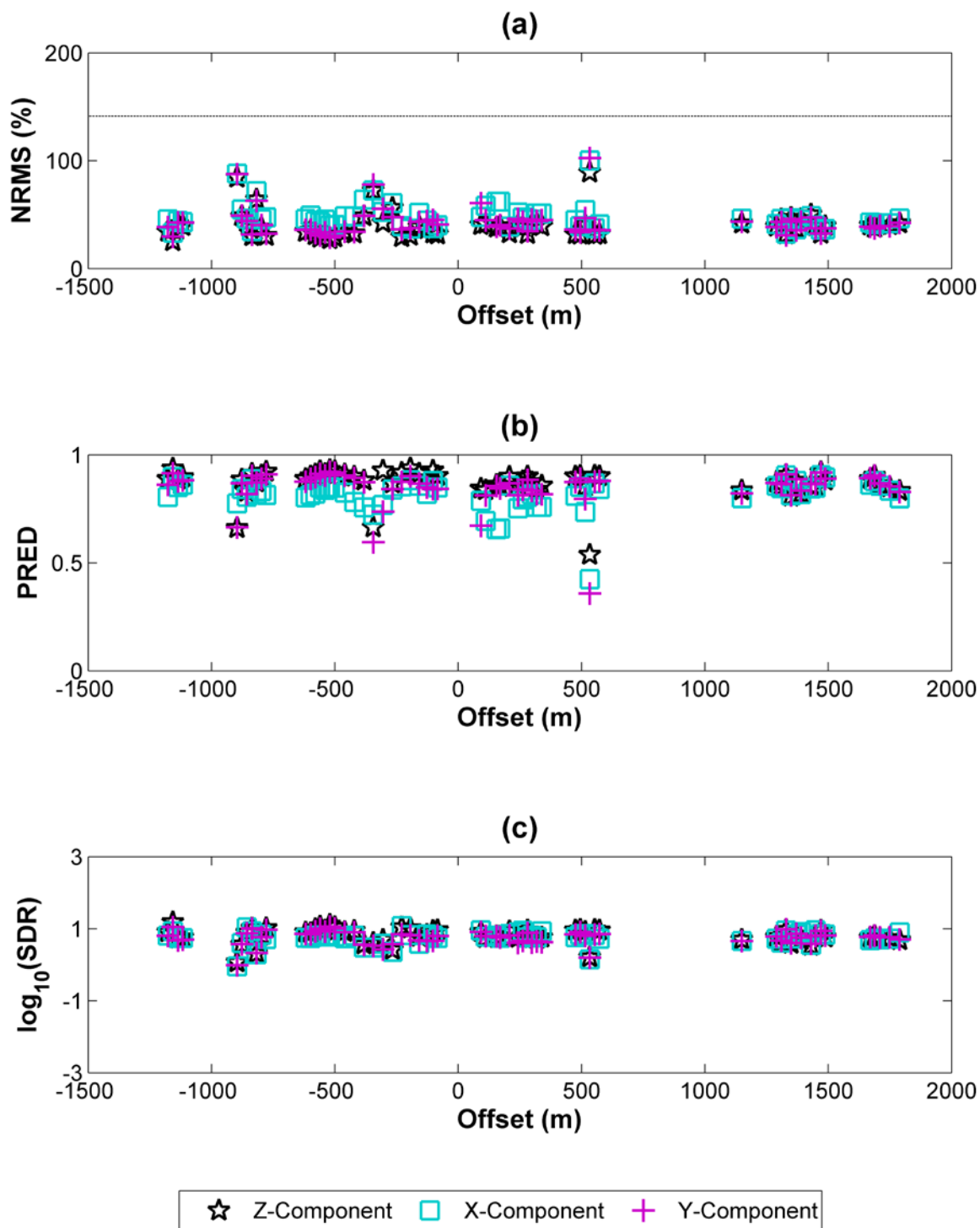


Figure B.21: Comparison of NRMS repeatability (a), predictability (b) and \log_{10} SDR (c) of Receiver 7 for Line 3, vs. source offset. The z-component is shown in black, x-component is shown in cyan, and y-component is shown in magenta. The dashed line in the NRMS plot indicates the theoretical noise line.

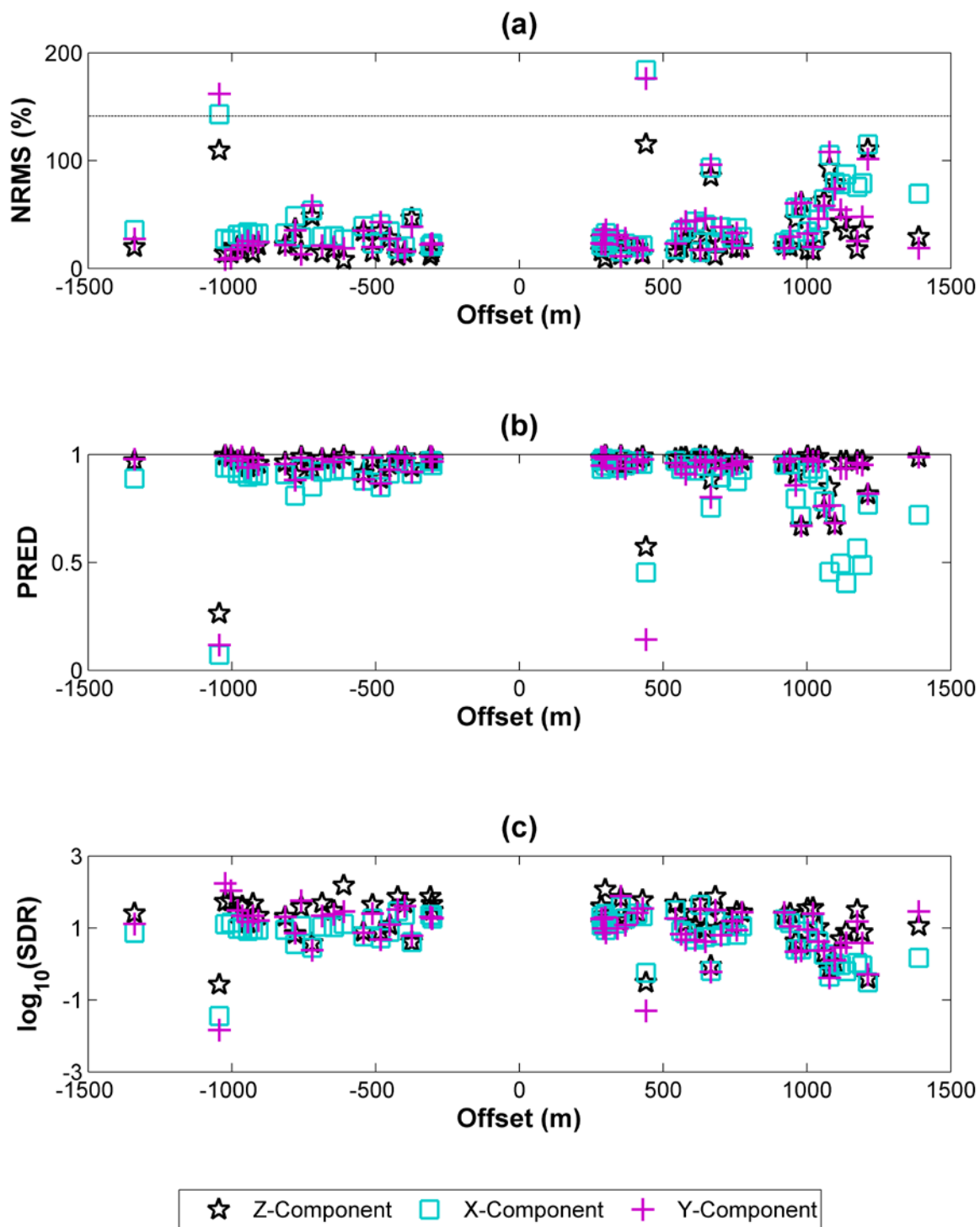


Figure B.22: Comparison of NRMS repeatability (a), predictability (b) and \log_{10} SDR (c) of Receiver 8 for Line 1, vs. source offset. The z-component is shown in black, x-component is shown in cyan, and y-component is shown in magenta. The dashed line in the NRMS plot indicates the theoretical noise line.

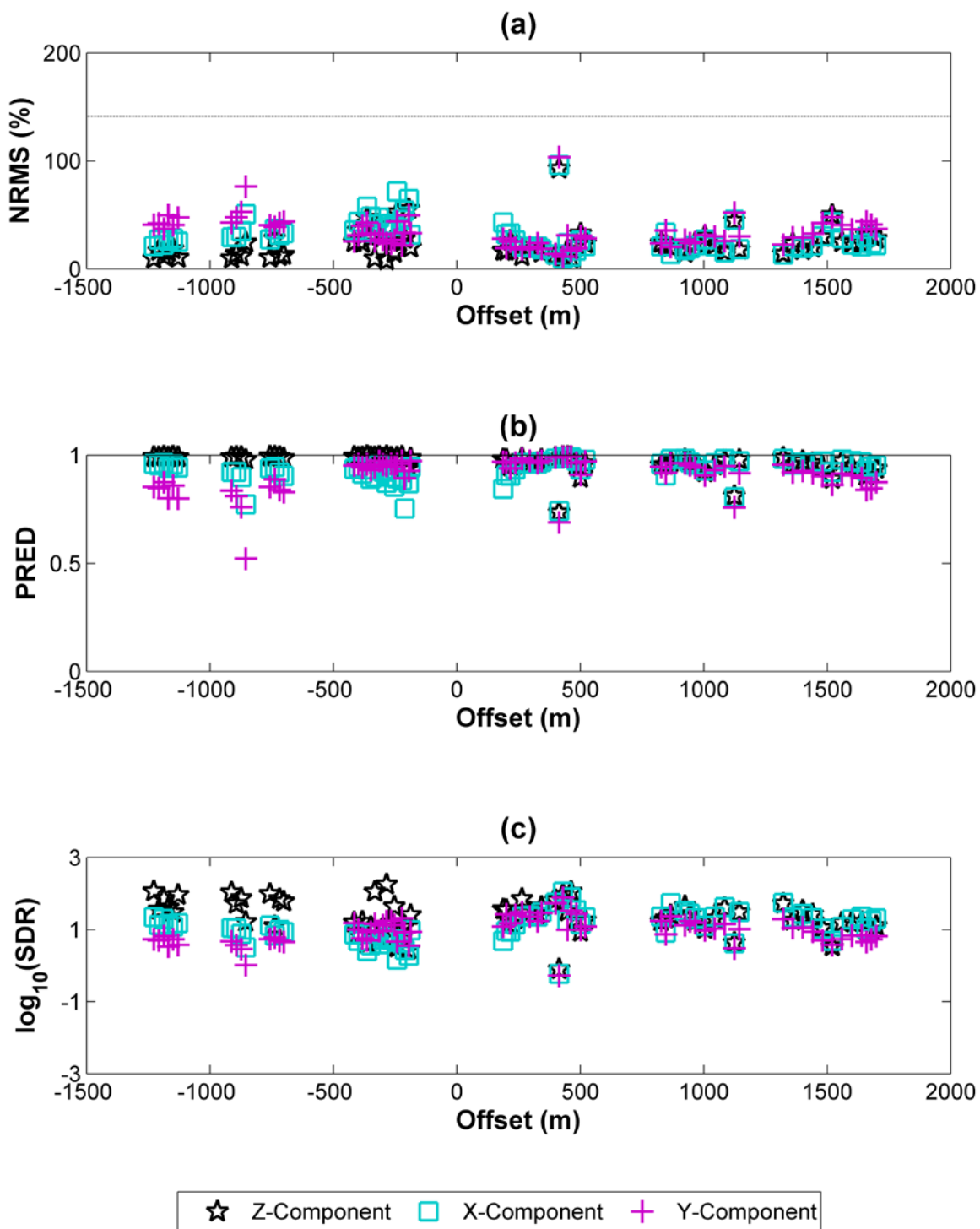


Figure B.23: Comparison of NRMS repeatability (a), predictability (b) and \log_{10} SDR (c) of Receiver 8 for Line 2, vs. source offset. The z-component is shown in black, x-component is shown in cyan, and y-component is shown in magenta. The dashed line in the NRMS plot indicates the theoretical noise line.

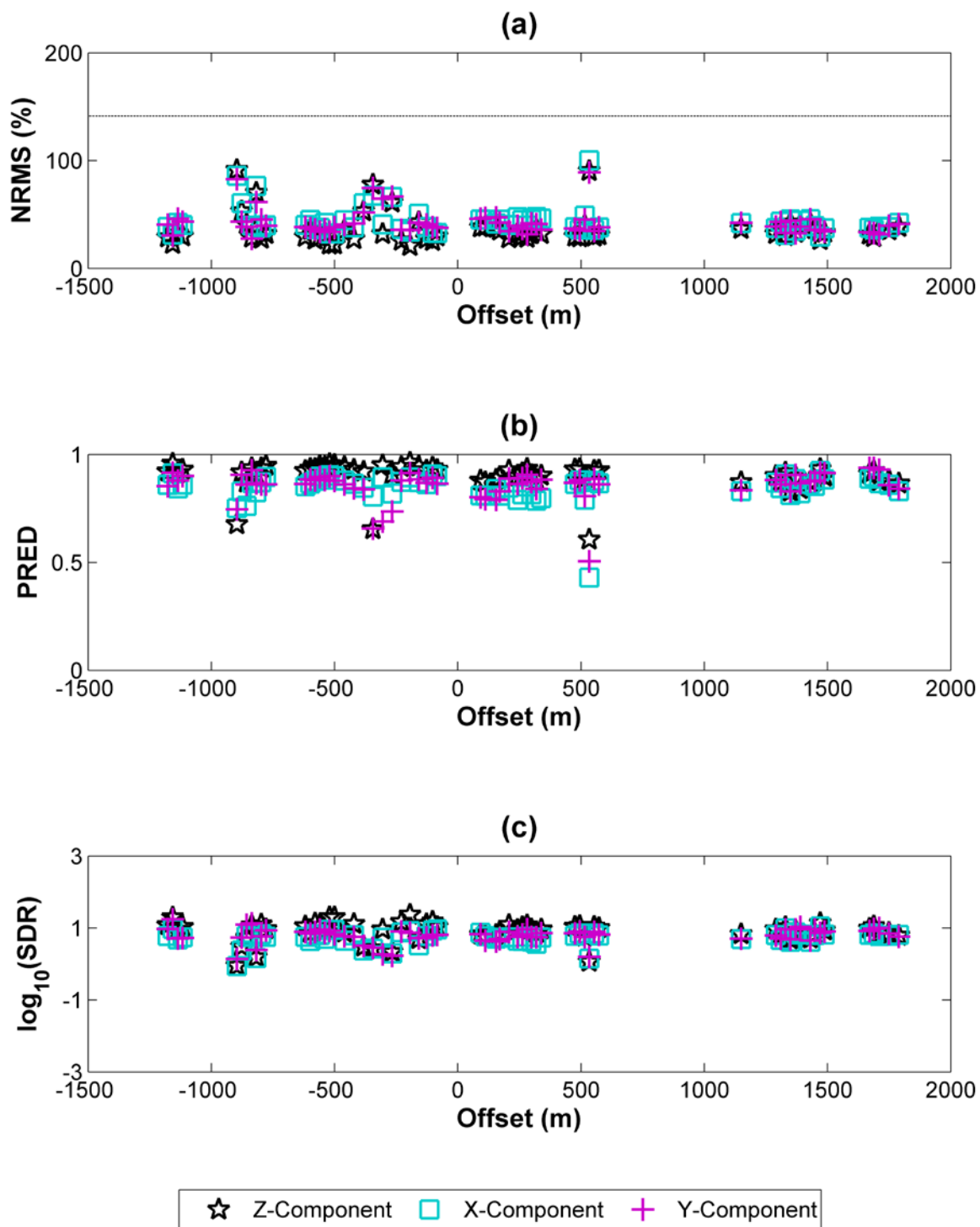


Figure B.24: Comparison of NRMS repeatability (a), predictability (b) and \log_{10} SDR (c) of Receiver 8 for Line 3, vs. source offset. The z-component is shown in black, x-component is shown in cyan, and y-component is shown in magenta. The dashed line in the NRMS plot indicates the theoretical noise line.

APPENDIX C: EXPANDED RESULTS FOR RANDOM NOISE MODELLING

This appendix provides a more complete suite of receiver orientation results for the modelling of effects of random noise on orientation analysis performed in Chapter 3.

- 1) Figure C.1 through Figure C.8 show error in calculated receiver orientations as a function of source-receiver x-coordinate offset for all 64 receivers. Values calculated using analytic and hodogram methods are shown together.
- 2) Figure C.9 through Figure C.13 show receivers with similar noise content, for all 9 noise levels.

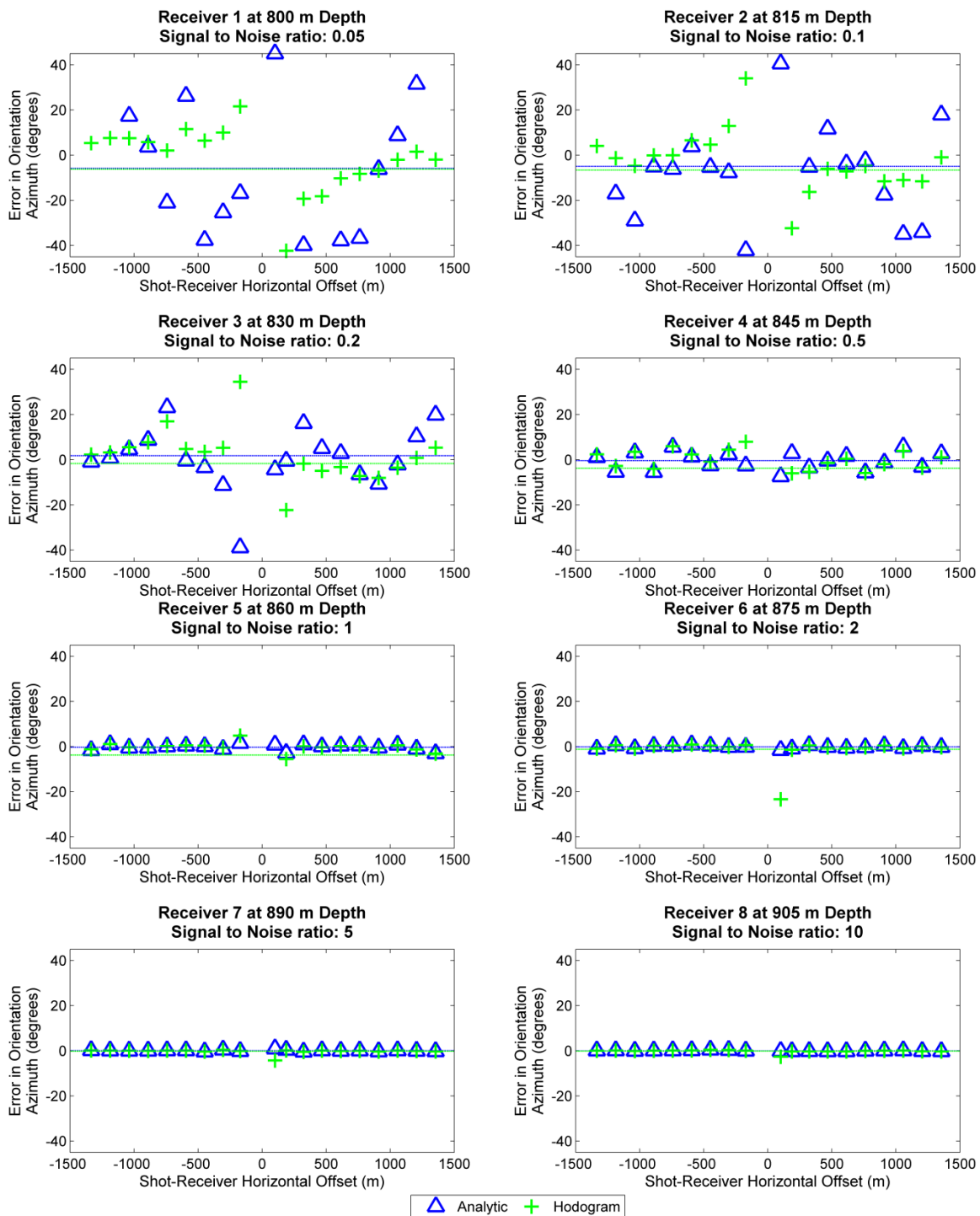


Figure C.1: Error in orientation azimuth vs. x-coordinate offset for Receivers 1 to 8. Analytic results are shown in blue and hodogram results are shown in green.

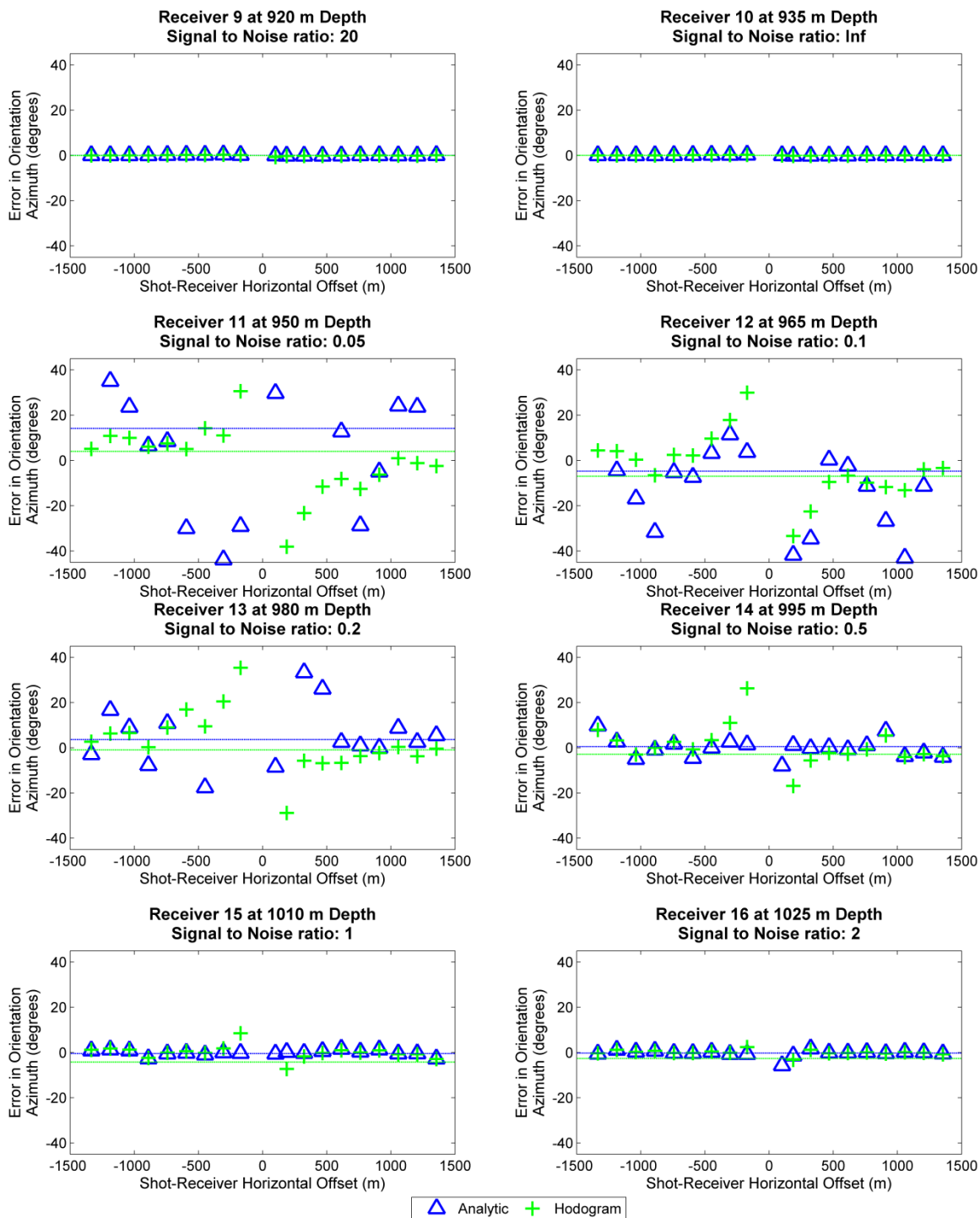


Figure C.2: Error in orientation azimuth vs. x-coordinate offset for Receivers 1 to 8. Analytic results are shown in blue and hodogram results are shown in green.

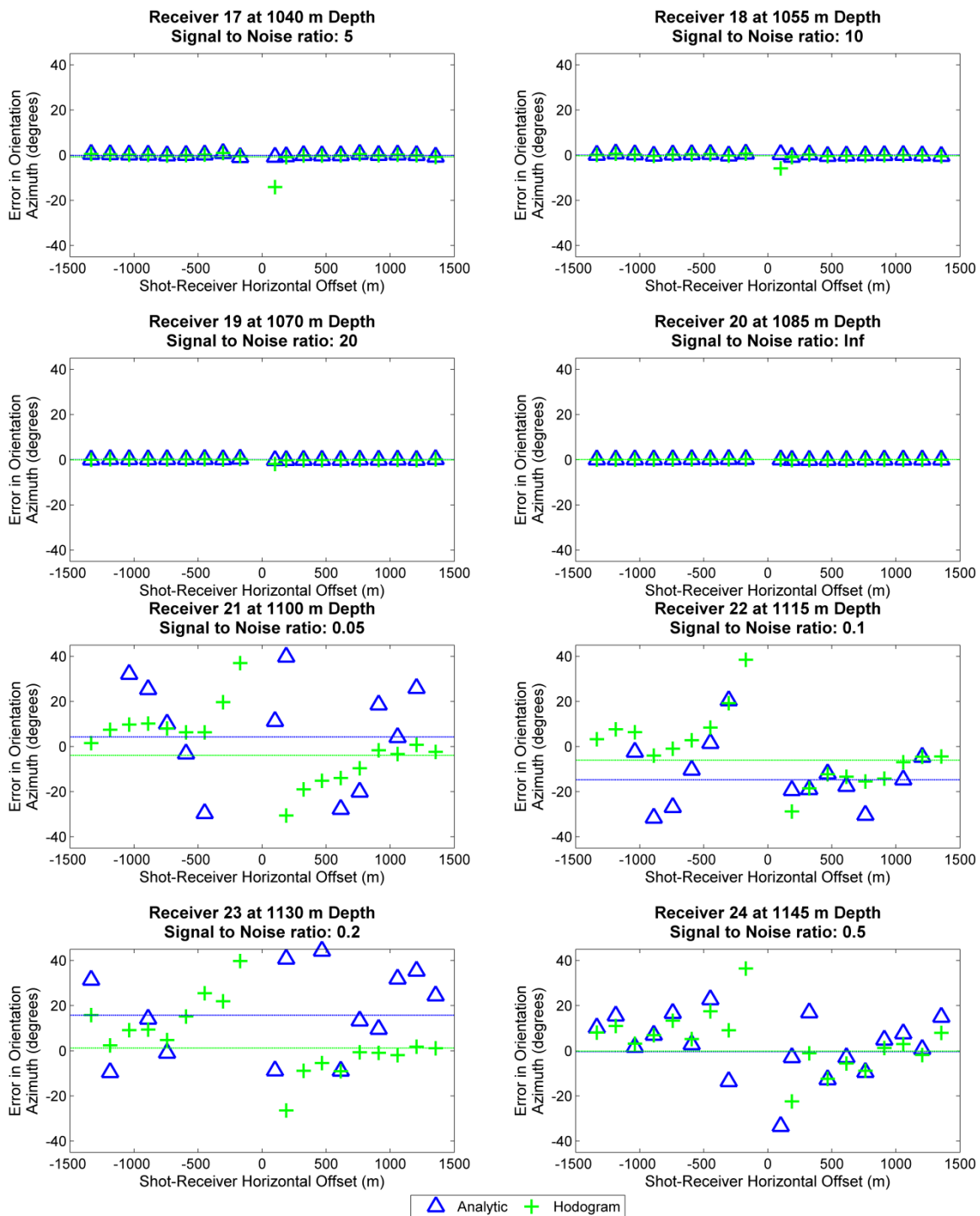


Figure C.3: Error in orientation azimuth vs. x-coordinate offset for Receivers 1 to 8. Analytic results are shown in blue and hodogram results are shown in green.

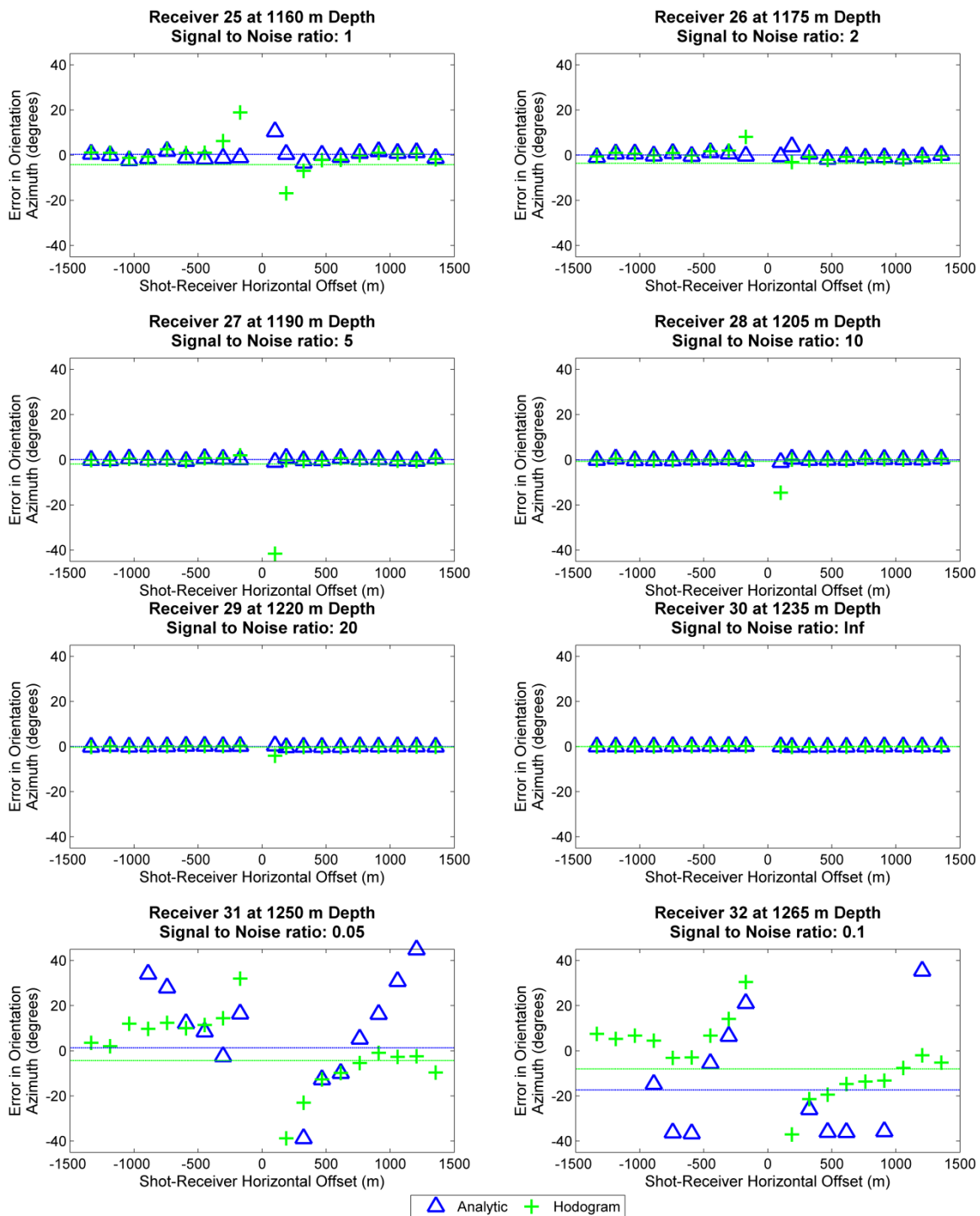


Figure C.4: Error in orientation azimuth vs. x-coordinate offset for Receivers 1 to 8. Analytic results are shown in blue and hodogram results are shown in green.

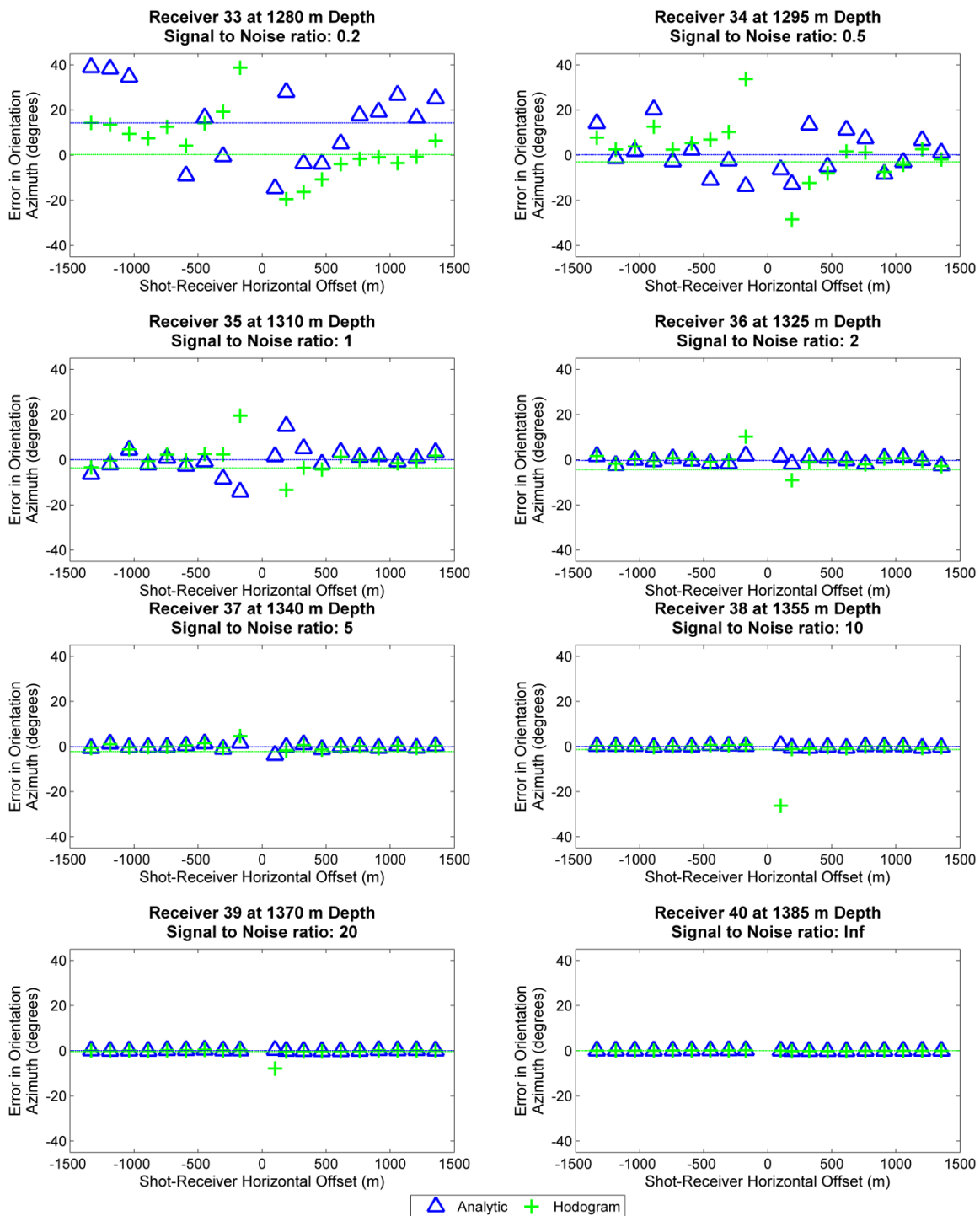


Figure C.5: Error in orientation azimuth vs. x-coordinate offset for Receivers 1 to 8. Analytic results are shown in blue and hodogram results are shown in green.

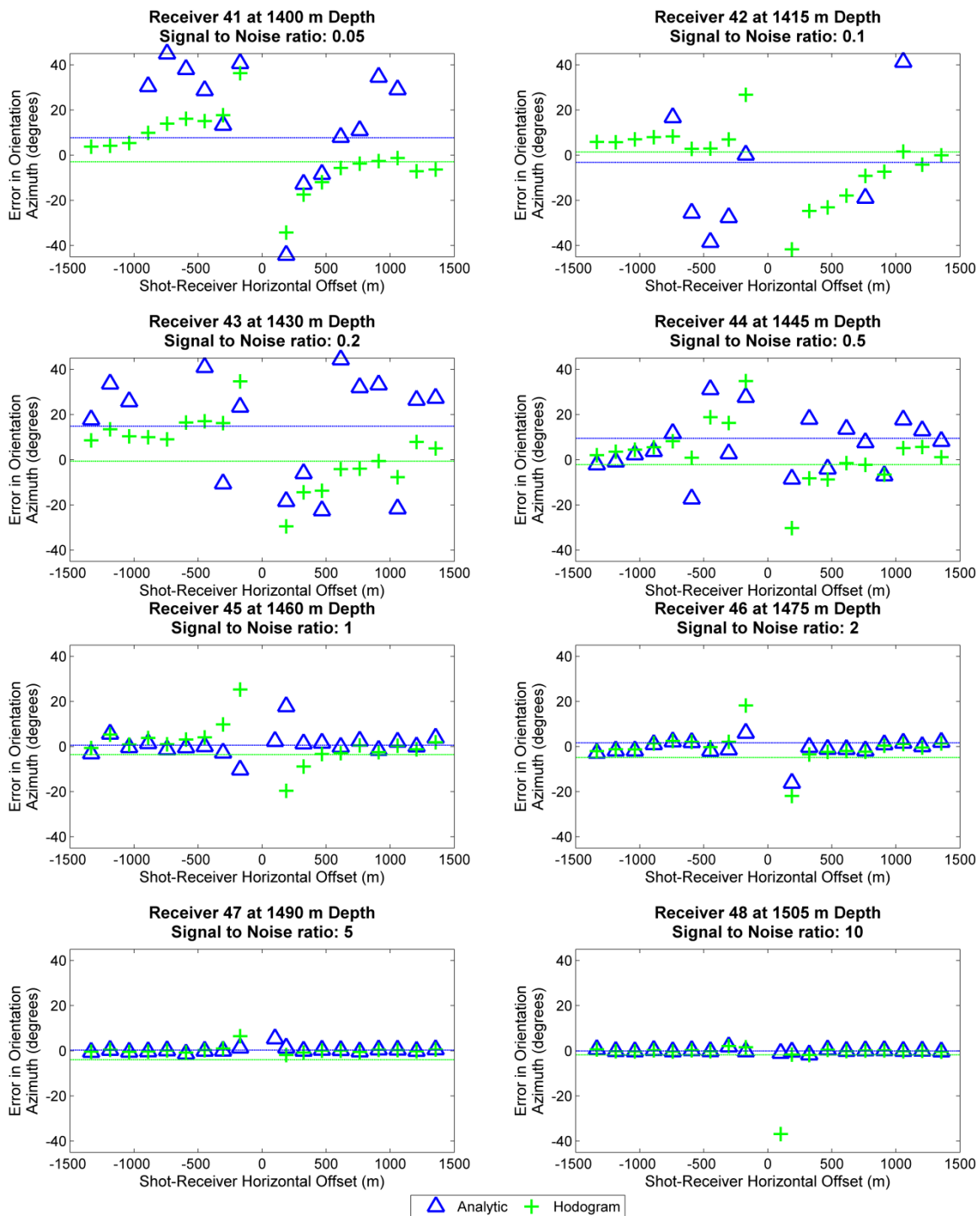


Figure C.6: Error in orientation azimuth vs. x-coordinate offset for Receivers 1 to 8. Analytic results are shown in blue and hodogram results are shown in green.

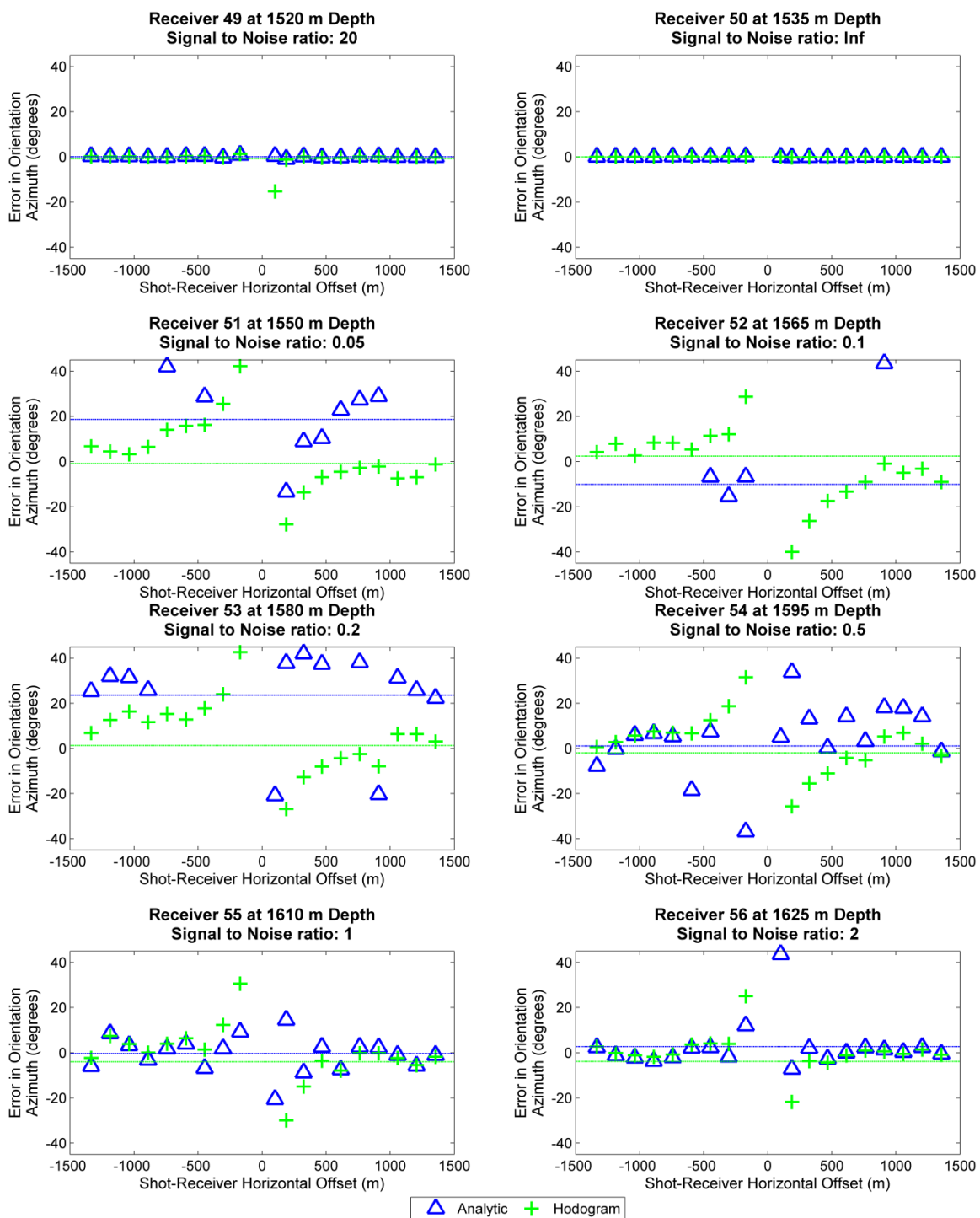


Figure C.7: Error in orientation azimuth vs. x-coordinate offset for Receivers 1 to 8. Analytic results are shown in blue and hodogram results are shown in green.

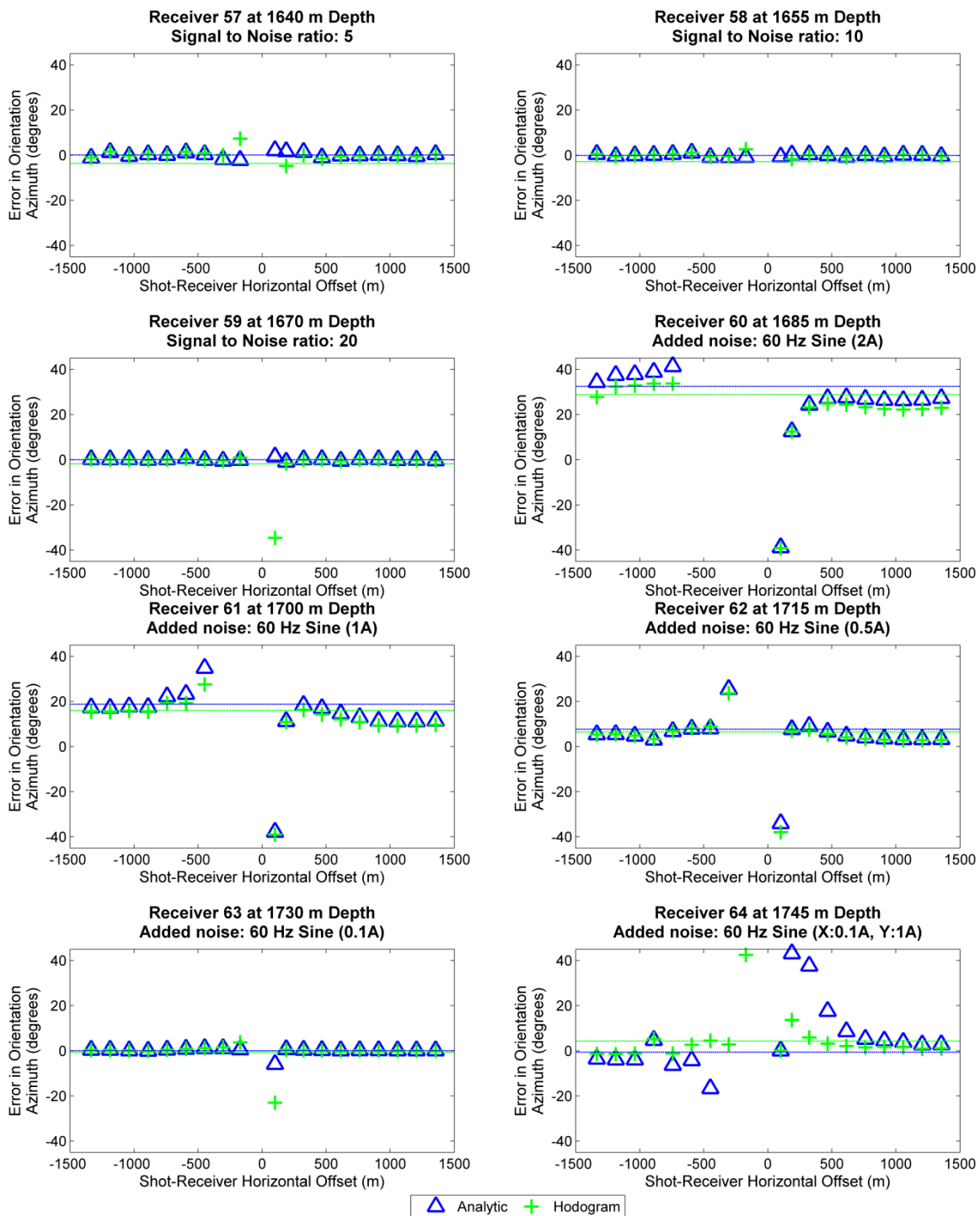


Figure C.8: Error in orientation azimuth vs. x-coordinate offset for Receivers 1 to 8. Analytic results are shown in blue and hodogram results are shown in green.

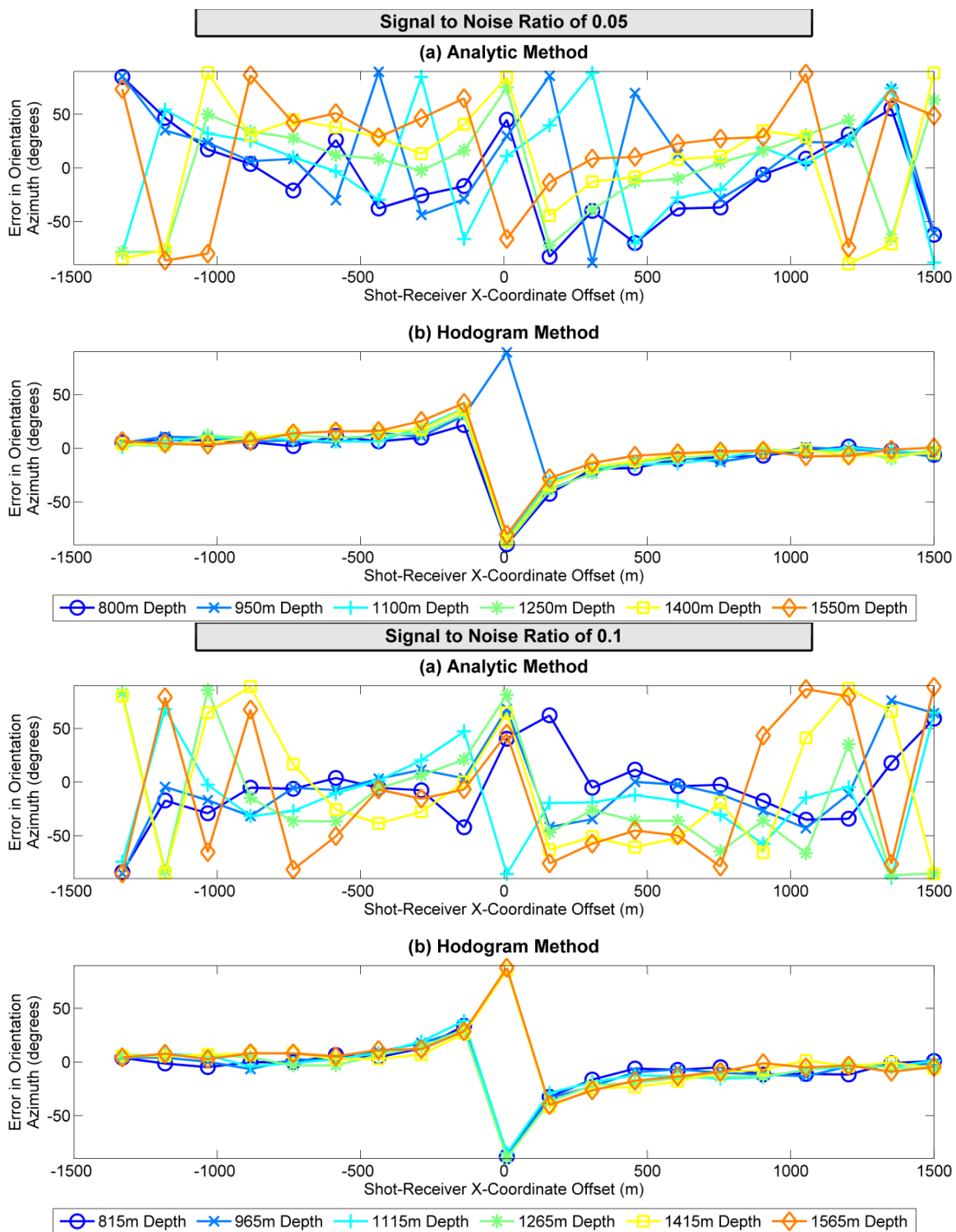


Figure C.9: Error in orientation azimuth vs. horizontal offset for receivers with signal to noise ratios of 0.05 (top) and 0.1 (bottom), calculated using analytic (a) and hodogram (b) methods. Hotter colours correspond to larger depths.

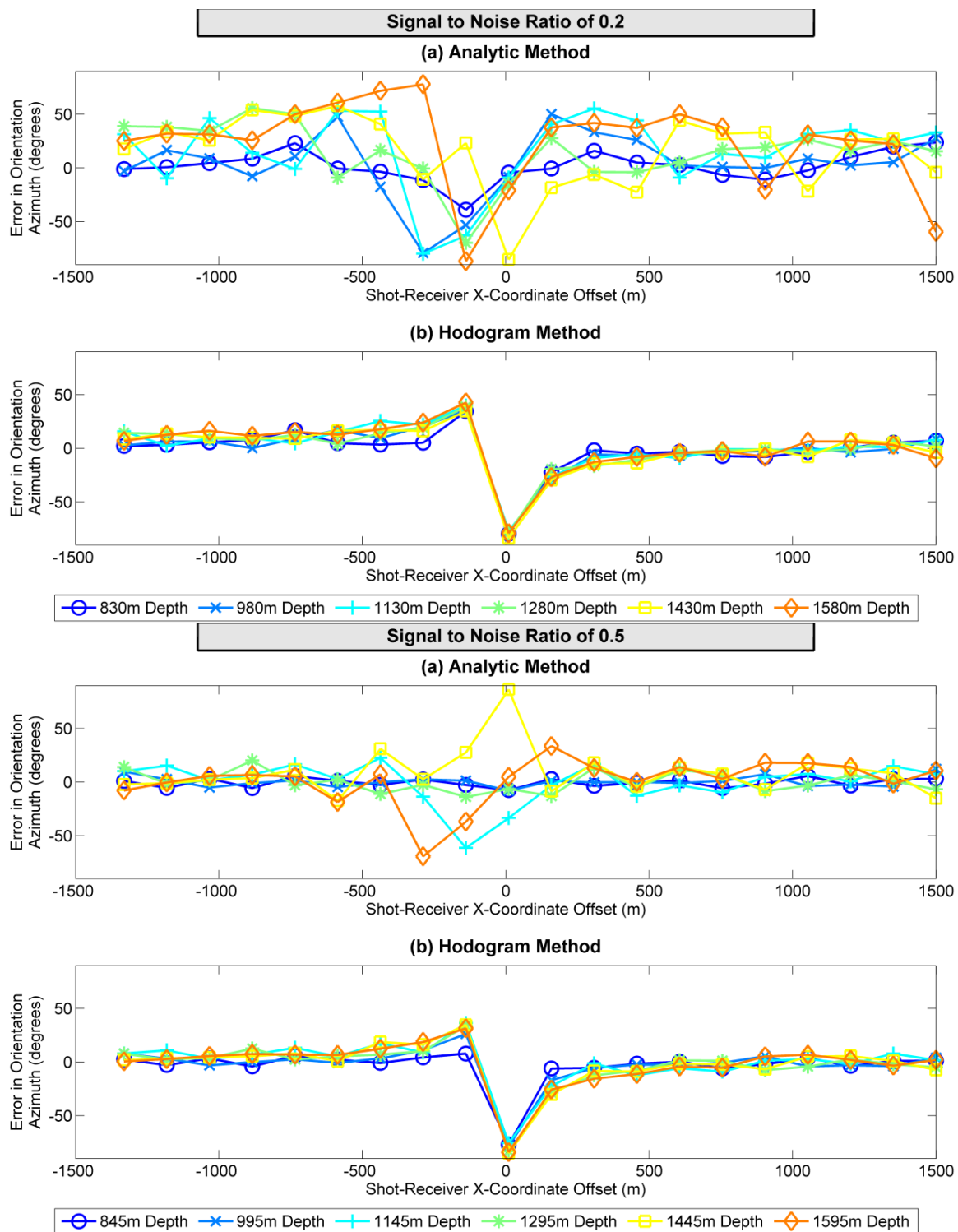


Figure C.10: Error in orientation azimuth vs. horizontal offset for receivers with signal to noise ratios of 0.05 (top) and 0.1 (bottom), calculated using analytic (a) and hodogram (b) methods. Hotter colours correspond to larger depths.

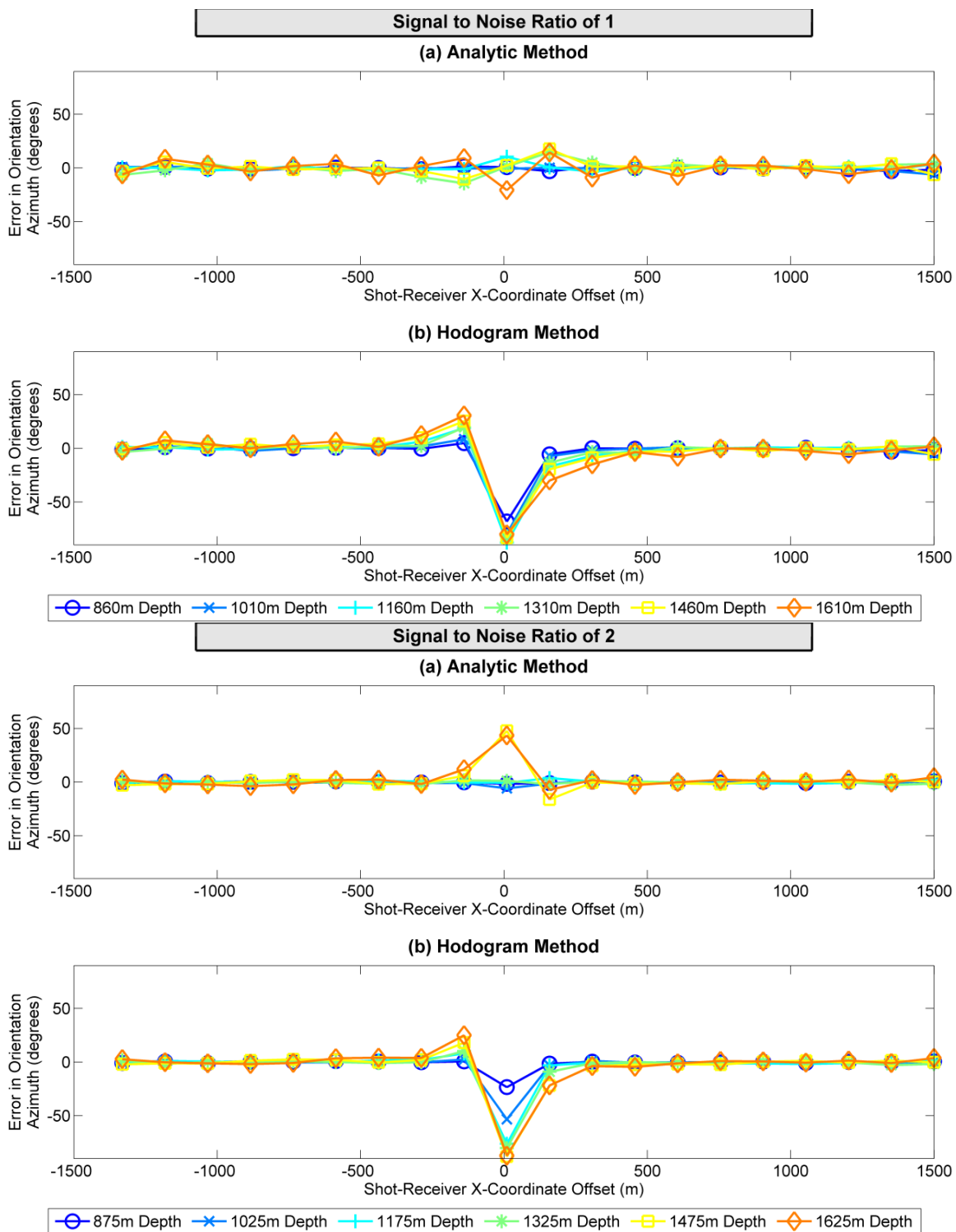


Figure C.11: Error in orientation azimuth vs. horizontal offset for receivers with signal to noise ratios of 0.05 (top) and 0.1 (bottom), calculated using analytic (a) and hodogram (b) methods. Hotter colours correspond to larger depths.

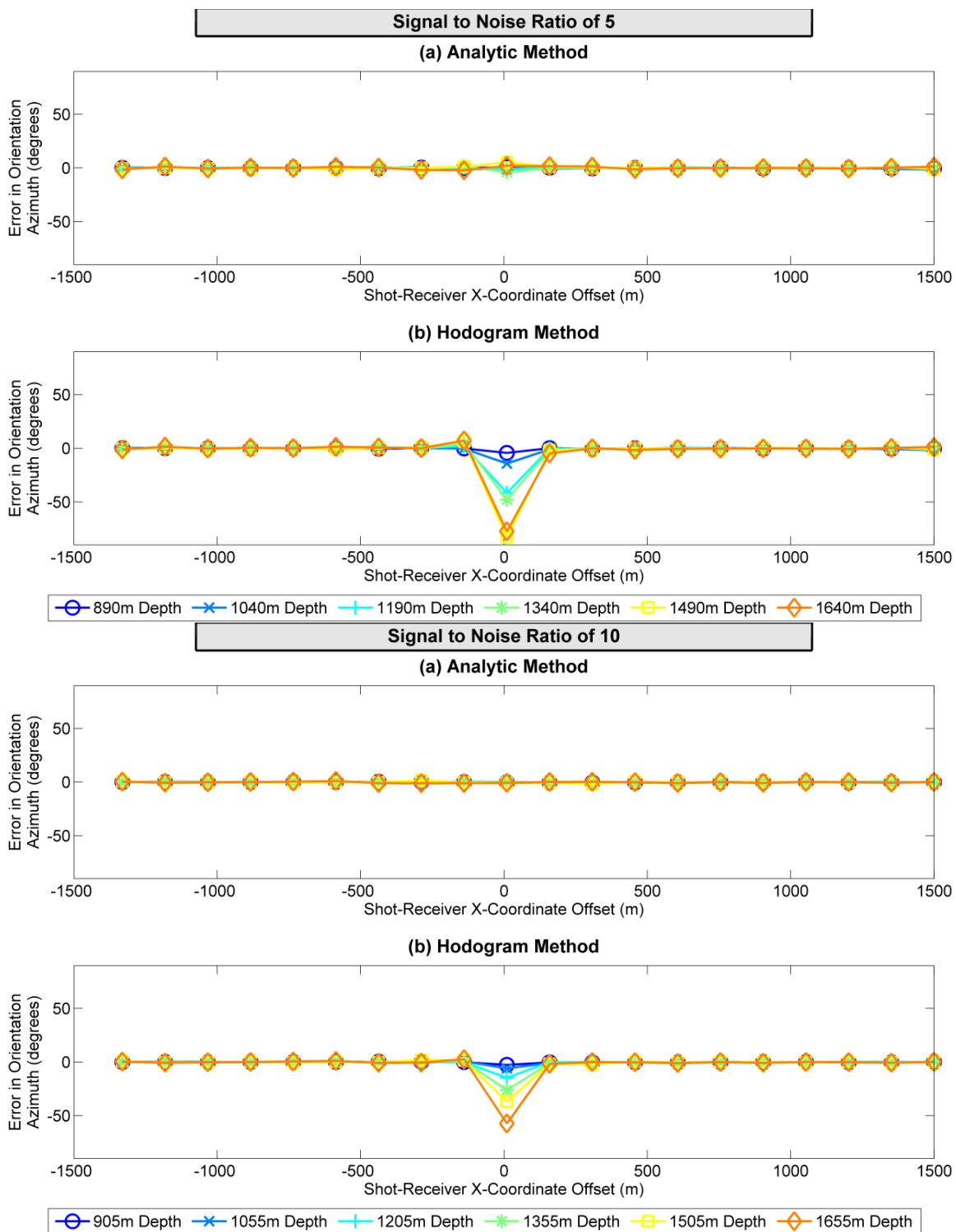


Figure C.12: Error in orientation azimuth vs. horizontal offset for receivers with signal to noise ratios of 0.05 (top) and 0.1 (bottom), calculated using analytic (a) and hodogram (b) methods. Hotter colours correspond to larger depths.

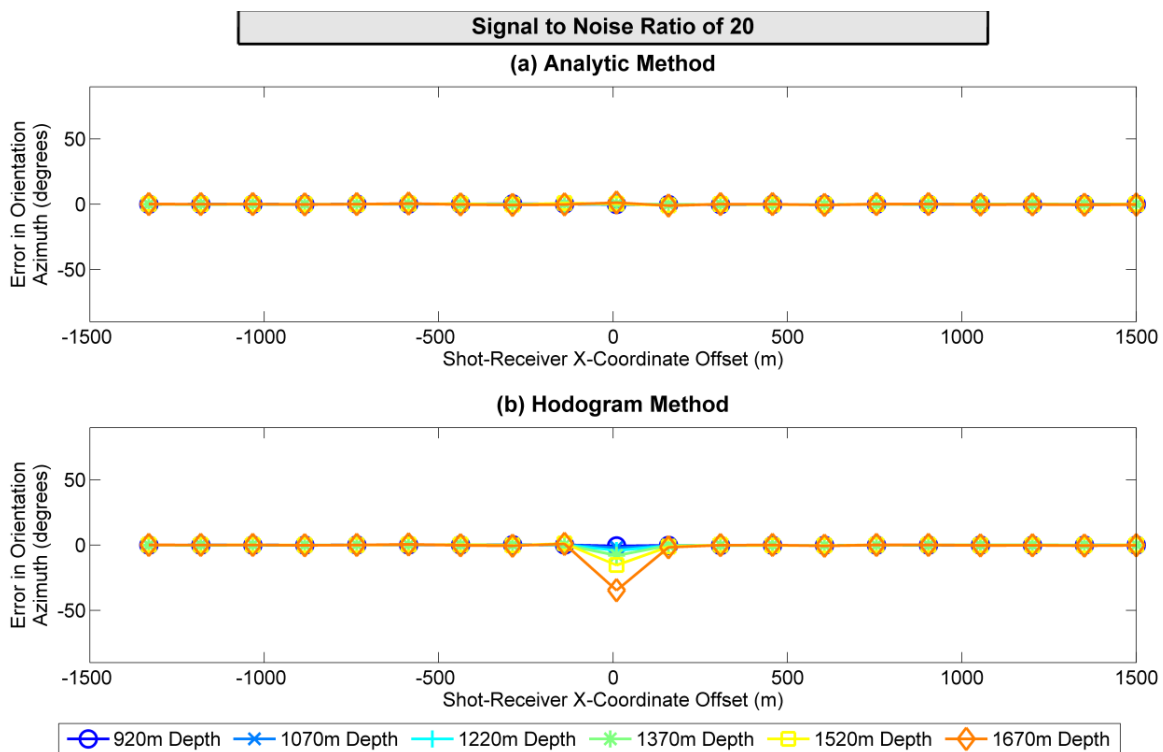


Figure C.13: Error in orientation azimuth vs. horizontal offset for receivers with signal to noise ratios of 0.05 (top) and 0.1 (bottom), calculated using analytic (a) and hodogram (b) methods. Hotter colours correspond to larger depths.

APPENDIX D: EXPANDED RESULTS FOR DEVIATED WELL STUDY

This appendix provides results for shuttle positions 9-16 for the Pembina deviated well study performed in Chapter 4. These correspond to Receivers 9-16 (shallow-level), 25-32 (mid-level) and 41-48 (deep level).

- 1) Figure D.1 through Figure D.3 show variation in orientation azimuth vs. pseudo offset.
- 2) Figure D.4 through Figure D.6 show variation in orientation azimuth vs. pseudo azimuth.
- 3) Figure D.7 shows variation in orientation azimuth vs. pseudo azimuth, combining receivers in the same shuttle position.
- 4) Figure D.8 through Figure D.10 show variation in orientation azimuth vs. pseudo offset under a vertical well assumption.
- 5) Figure D.11 through Figure D.13 show histograms of orientation azimuth.

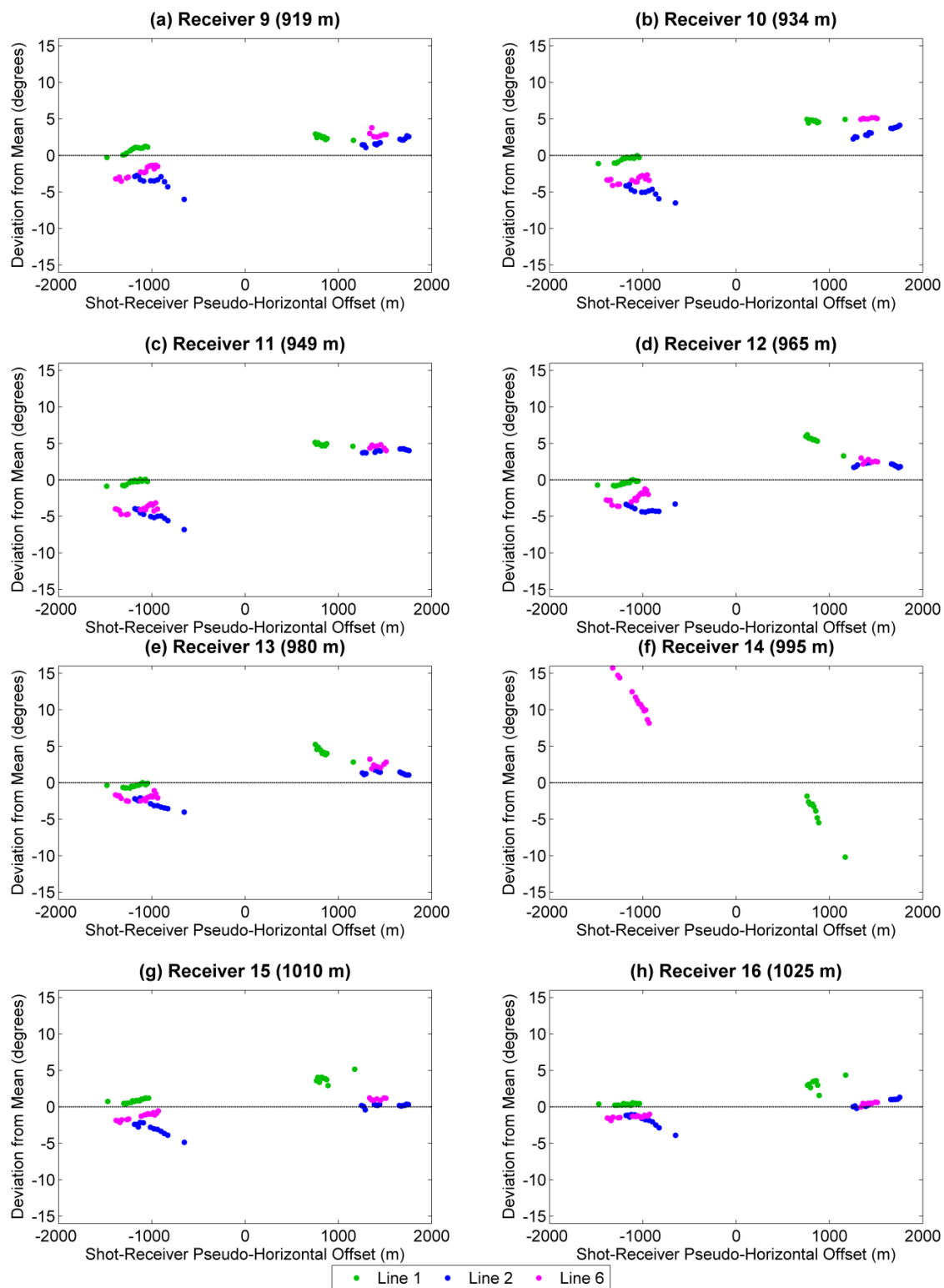


Figure D.1: Deviation from mean orientation azimuth vs. pseudo offset for Receivers 9-16 (shallow-level). Line 1 is shown in green, Line 2 in blue, and Line 6 in magenta.

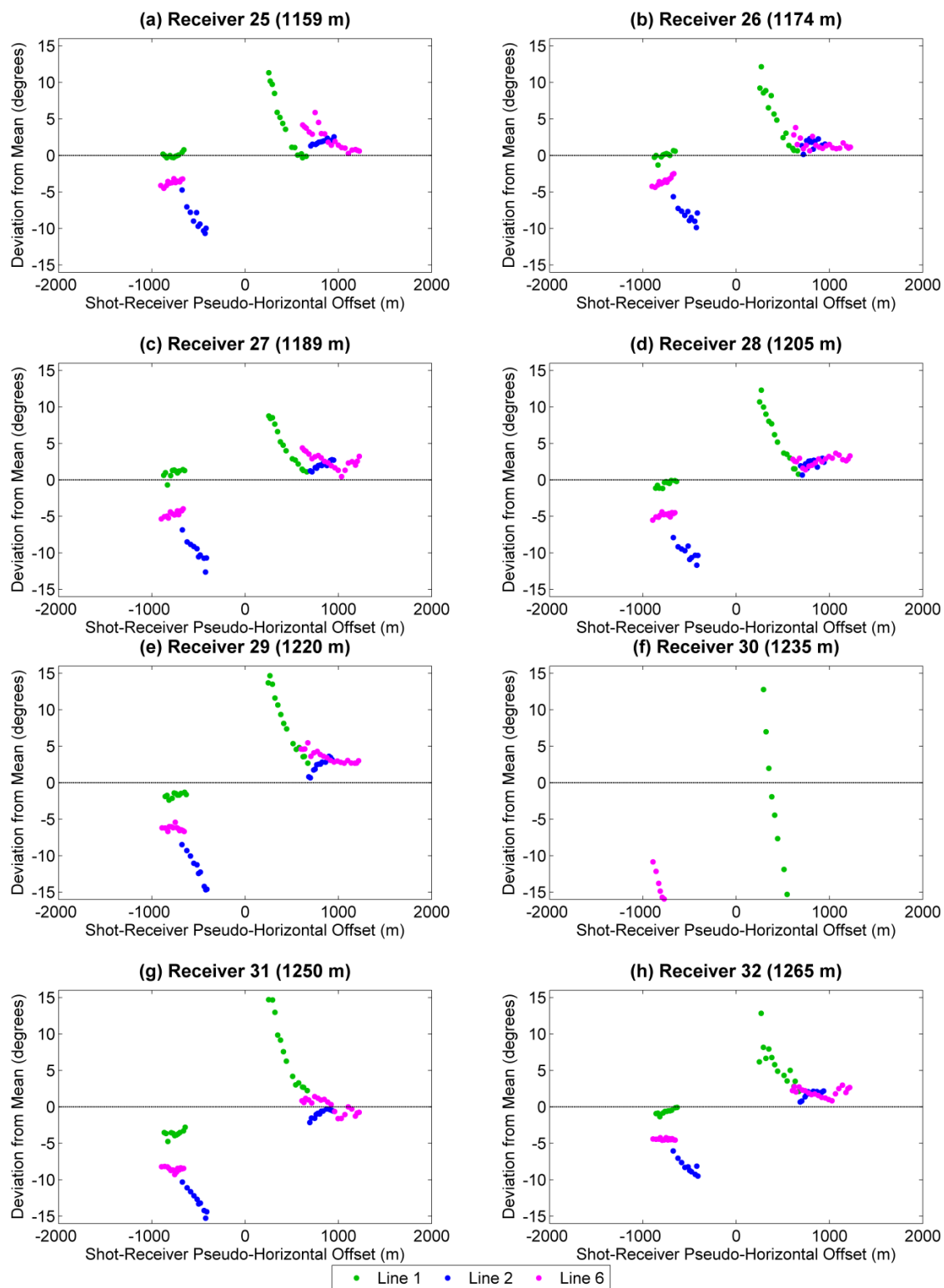


Figure D.2: Deviation from mean orientation azimuth vs. pseudo offset for Receivers 25-32 (mid-level). Line 1 is shown in green, Line 2 in blue, and Line 6 in magenta.

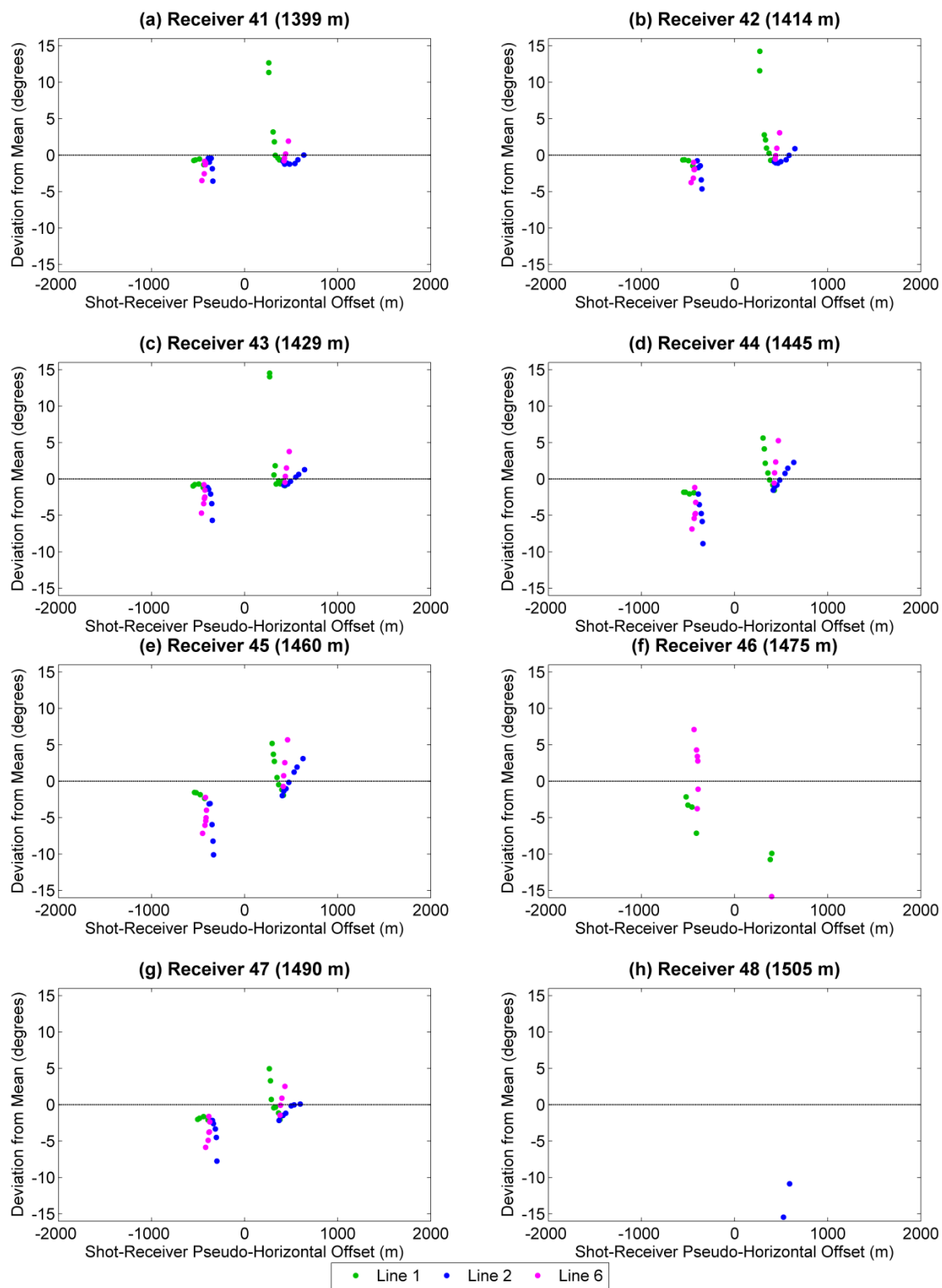


Figure D.3: Deviation from mean orientation azimuth vs. pseudo offset for Receivers 41-48 (deep-level). Line 1 is shown in green, Line 2 in blue, and Line 6 in magenta.

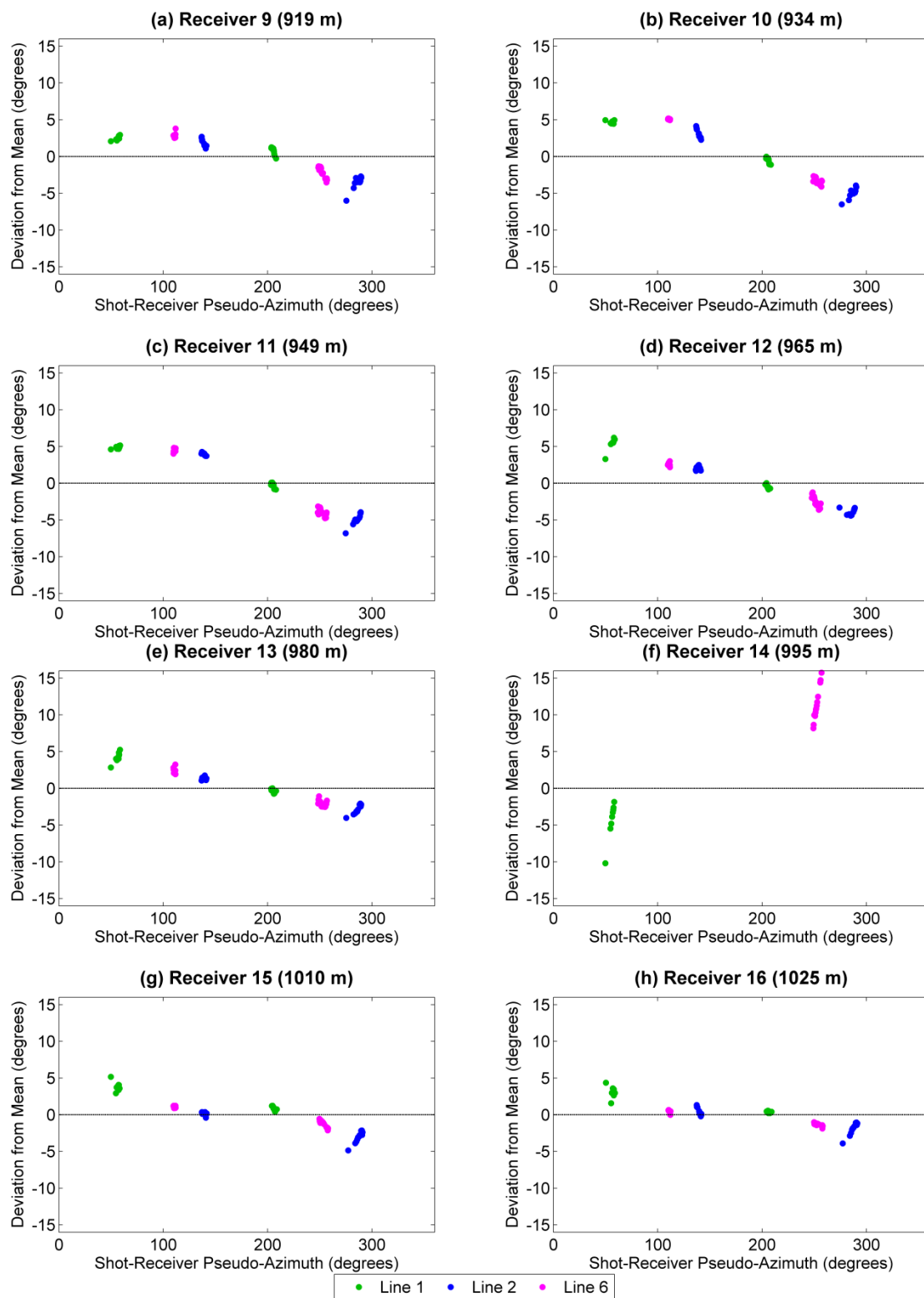


Figure D.4: Deviation from mean orientation azimuth vs. pseudo azimuth for Receivers 9-16 (shallow-level). Line 1 is shown in green, Line 2 in blue, and Line 6 in magenta.

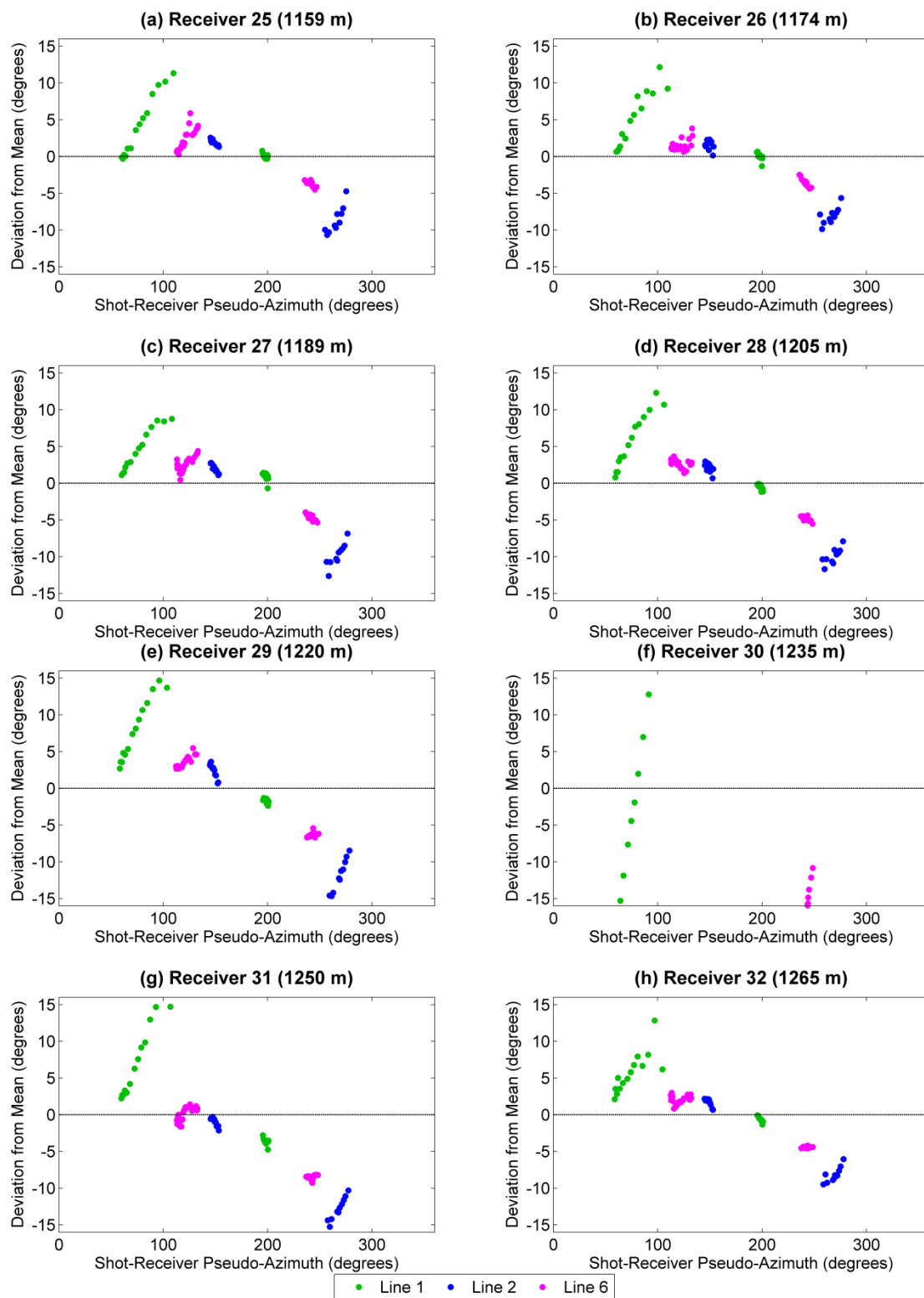


Figure D.5: Deviation from mean orientation azimuth vs. pseudo azimuth for Receivers 25-32 (mid-level). Line 1 is shown in green, Line 2 in blue, and Line 6 in magenta.

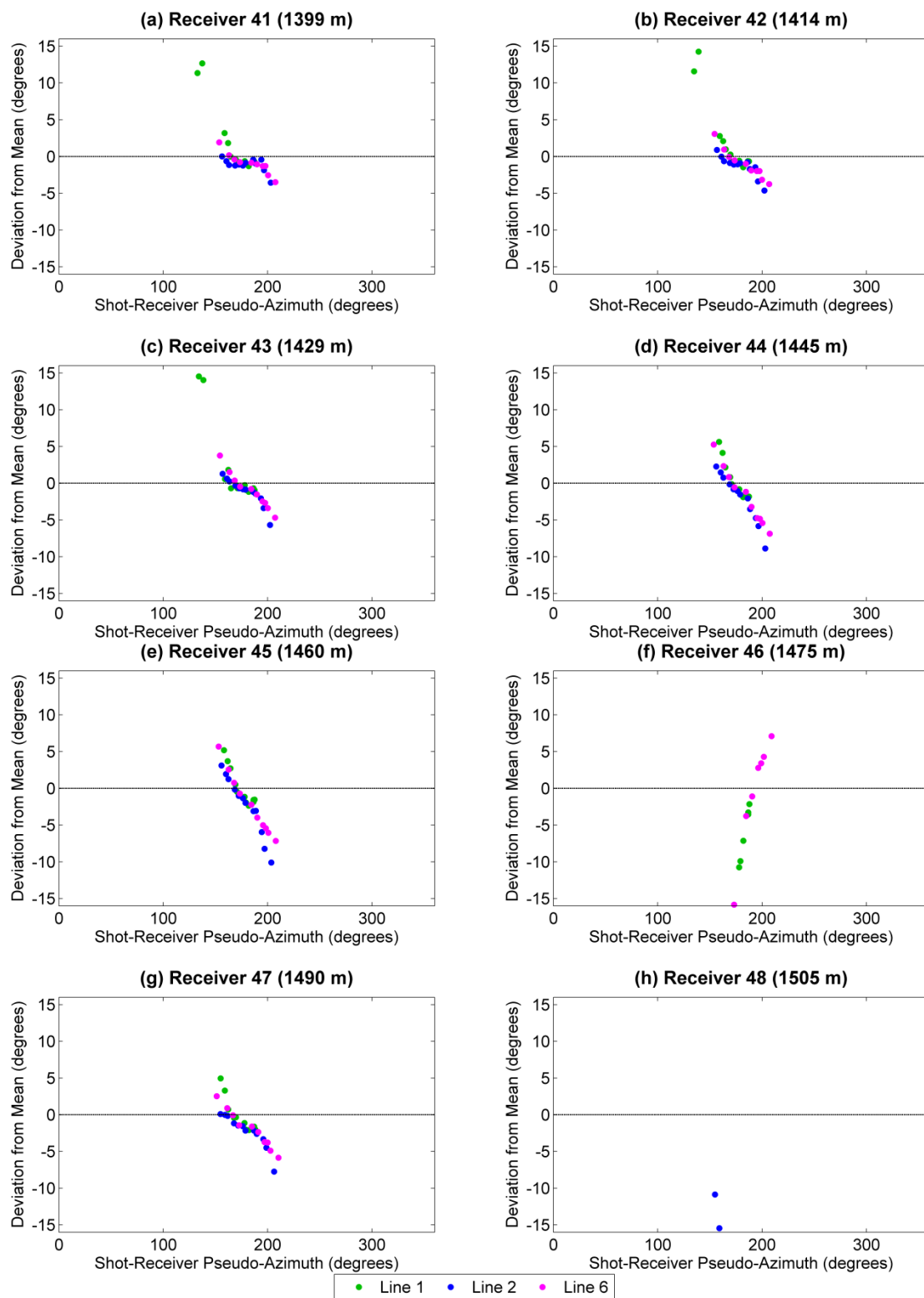


Figure D.6: Deviation from mean orientation azimuth vs. pseudo azimuth for Receivers 41-48 (deep-level). Line 1 is shown in green, Line 2 in blue, and Line 6 in magenta.

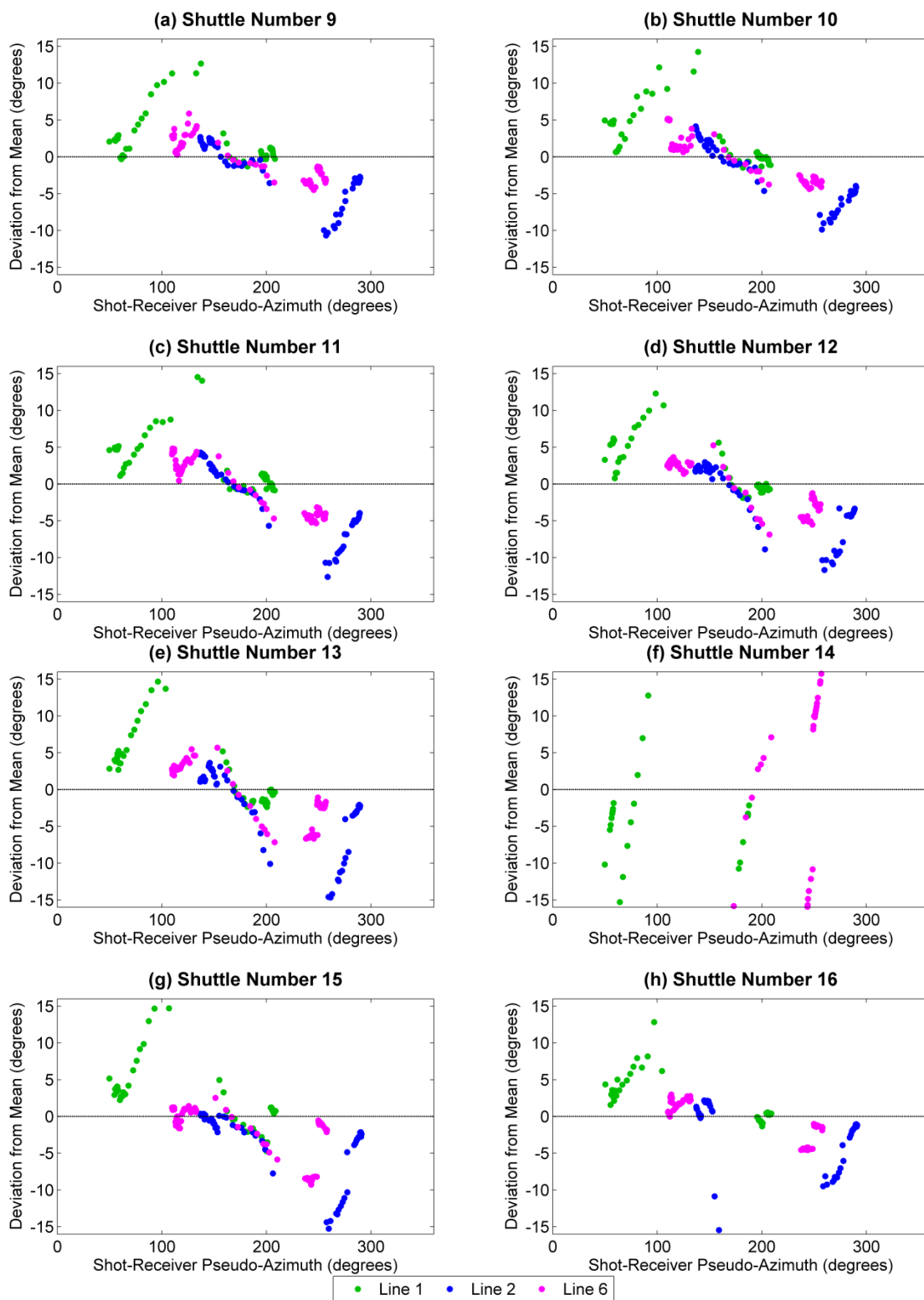


Figure D.7: Deviation from mean orientation azimuth vs. pseudo azimuth for shuttle positions 9-16, combining data from all tool levels. Line 1 is shown in green, Line 2 in blue, and Line 6 in magenta.

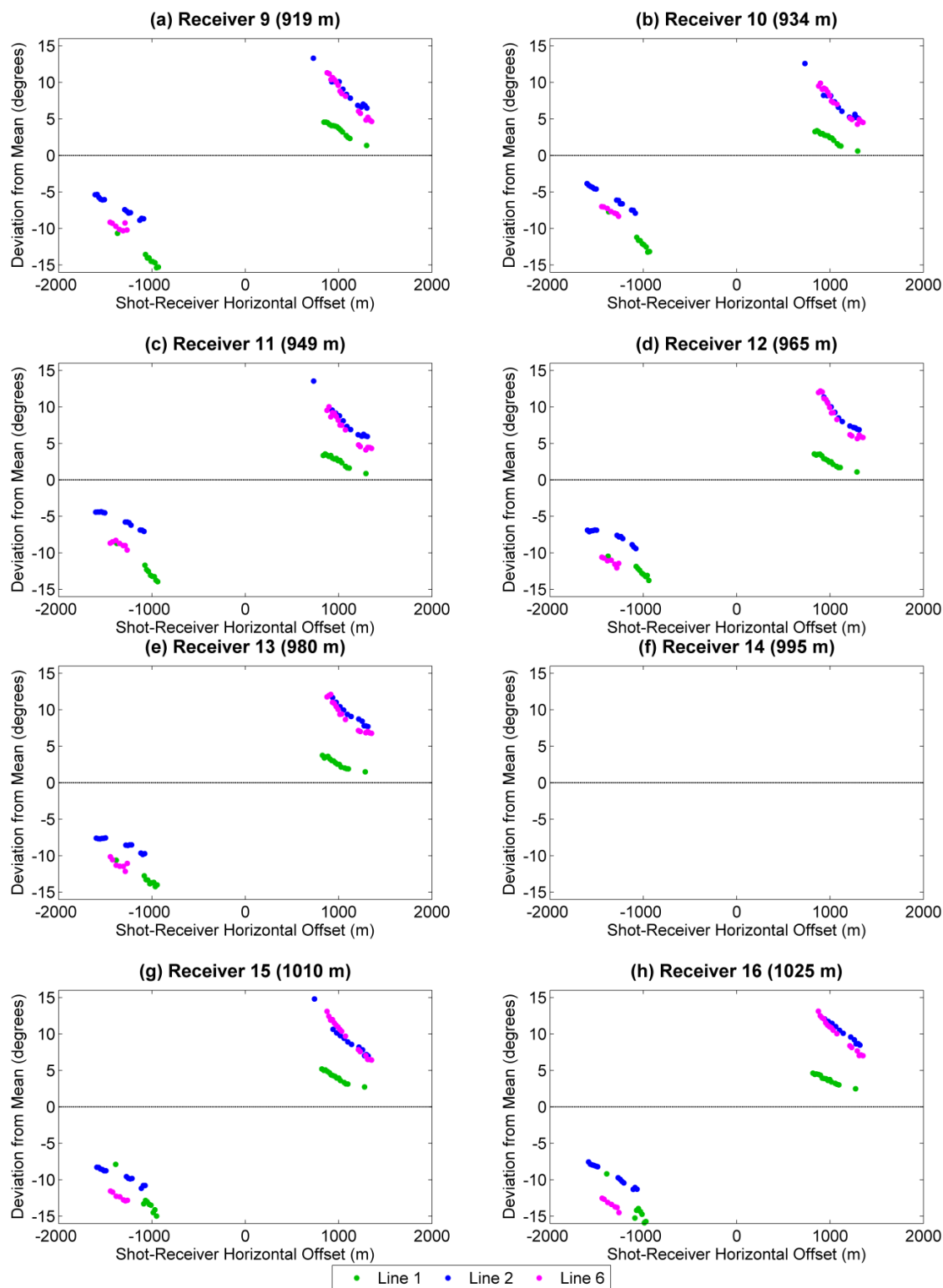


Figure D.8: Deviation from mean orientation azimuth vs. offset for Receivers 9-16 (shallow-level), calculated under a vertical well assumption. Line 1 is shown in green, Line 2 in blue, and Line 6 in magenta.

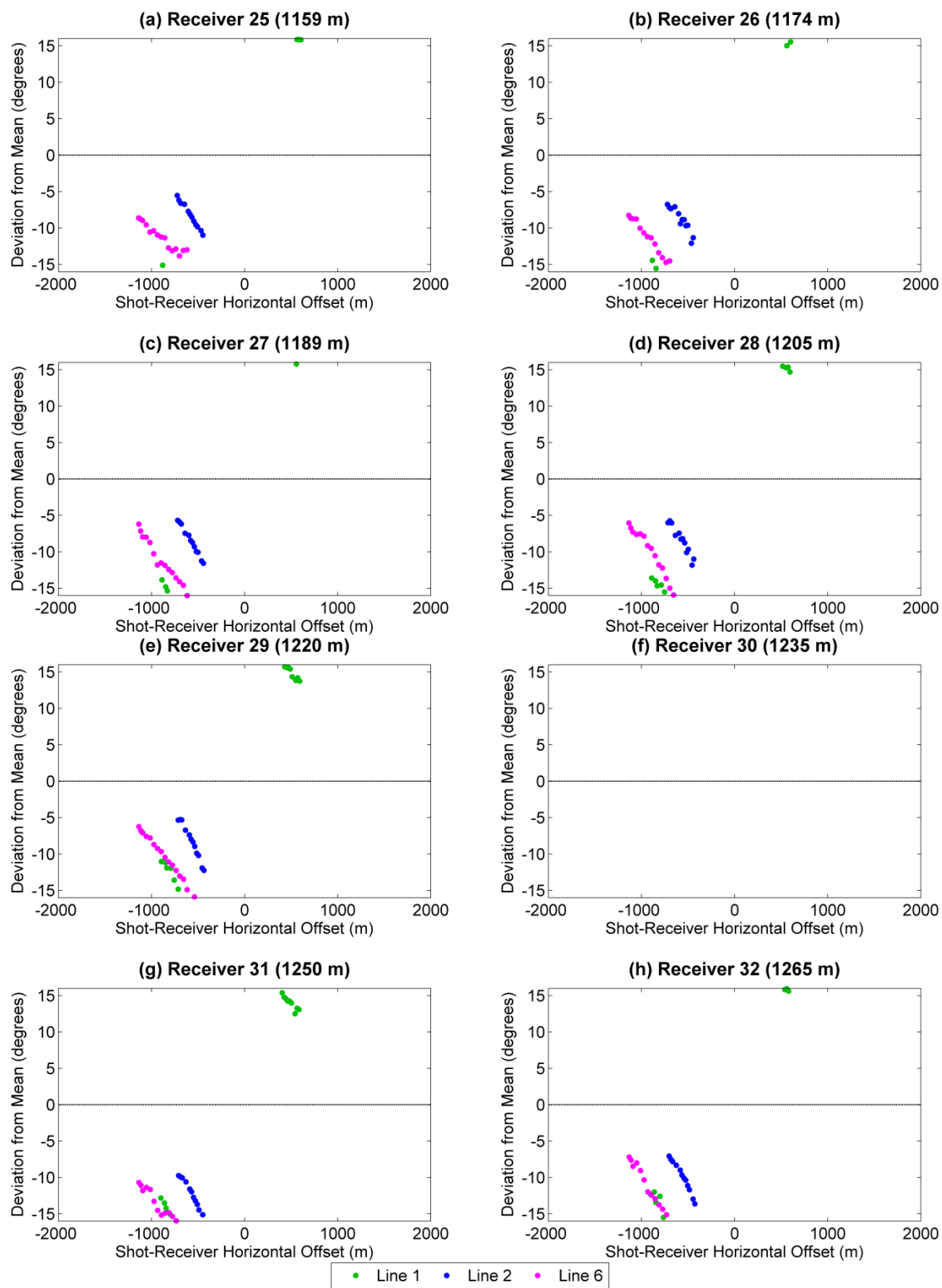


Figure D.9: Deviation from mean orientation azimuth vs. offset for Receivers 25-32 (mid-level), calculated under a vertical well assumption. Line 1 is shown in green, Line 2 in blue, and Line 6 in magenta.

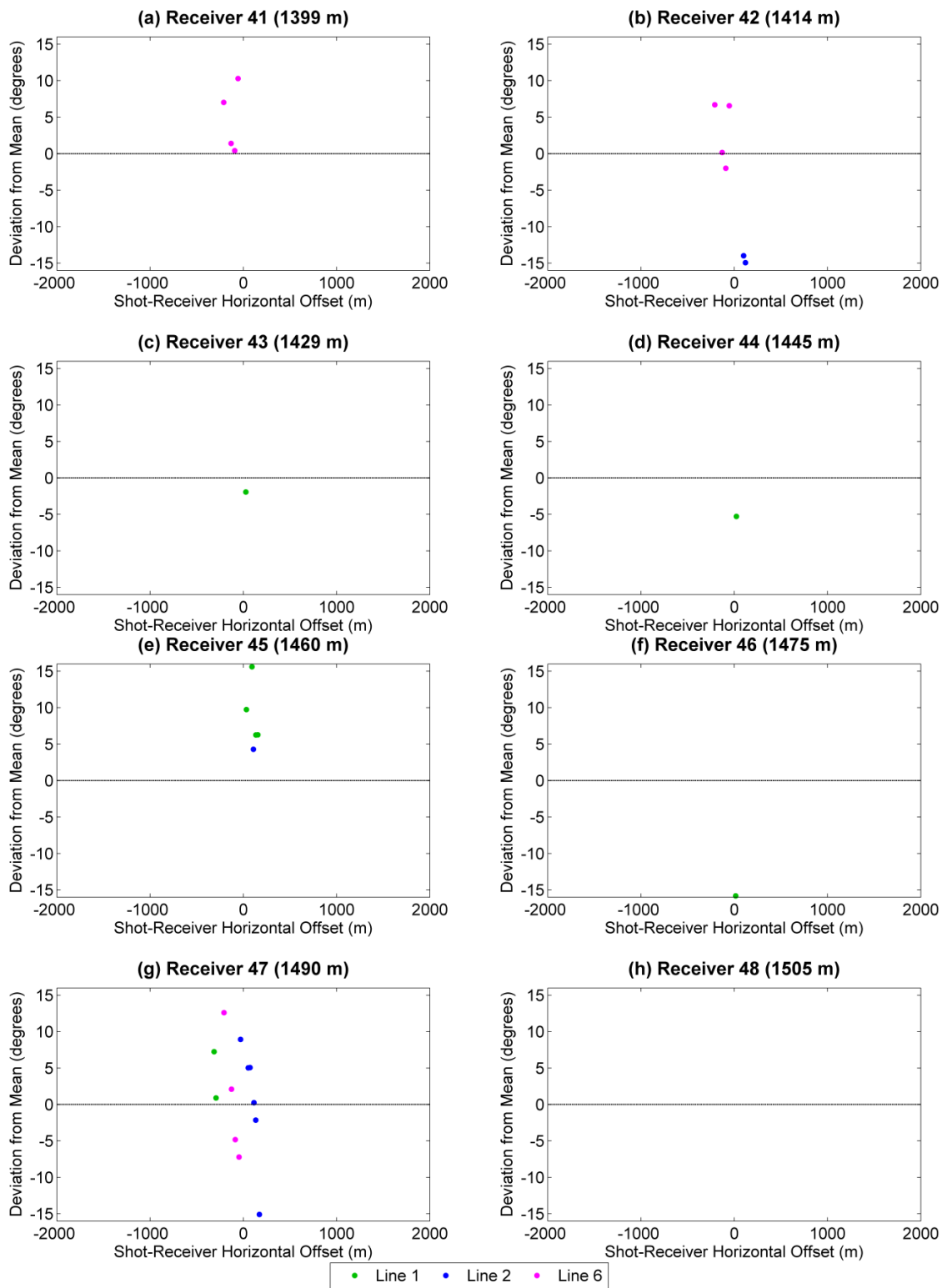


Figure D.10: Deviation from mean orientation azimuth vs. offset for Receivers 41-48 (deep-level), calculated under a vertical well assumption. Line 1 is shown in green, Line 2 in blue, and Line 6 in magenta.

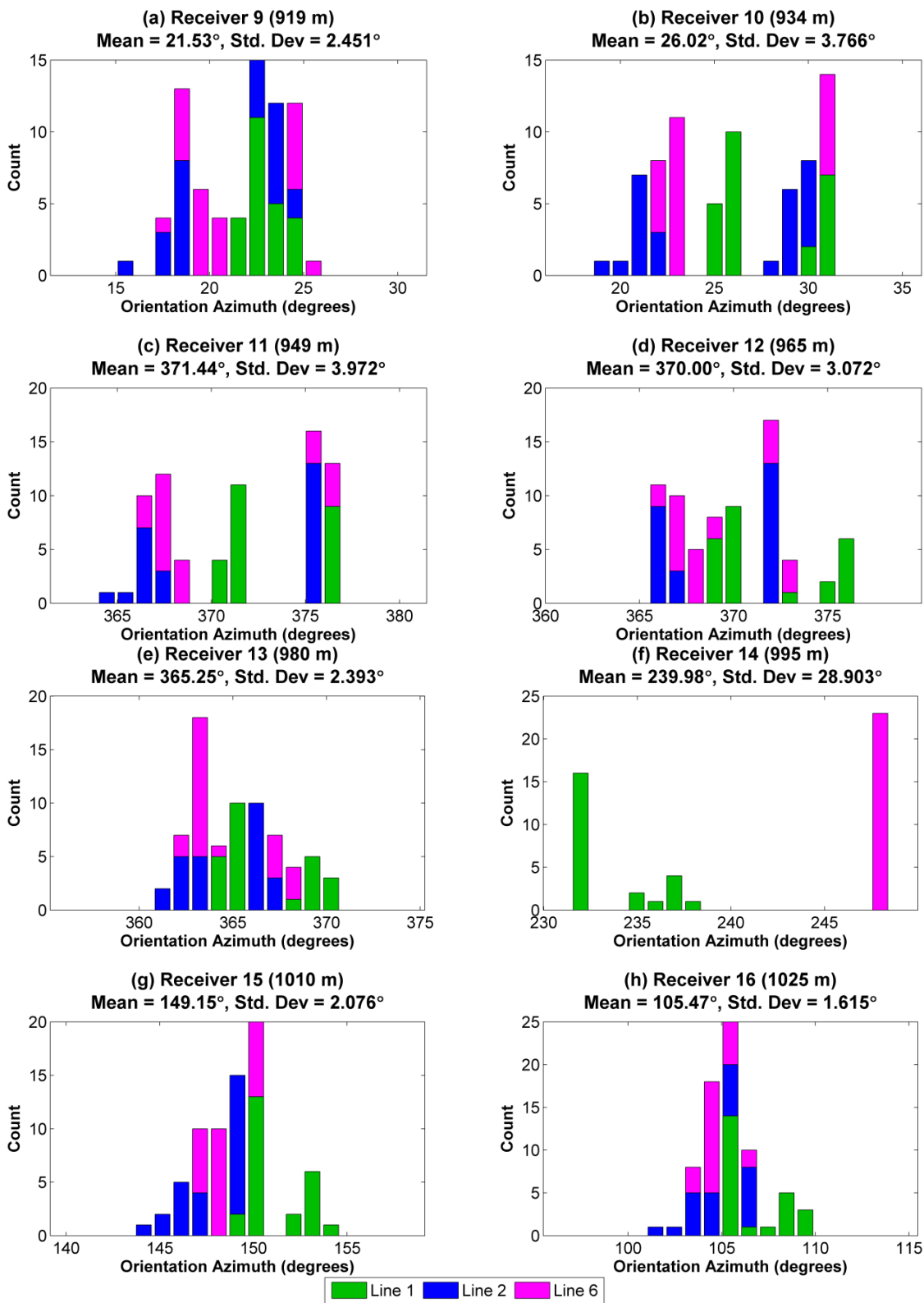


Figure D.11: Orientation azimuth histograms for Receivers 9-16 (shallow-level). Line 1 is shown in green, Line 2 in blue, and Line 6 in magenta.

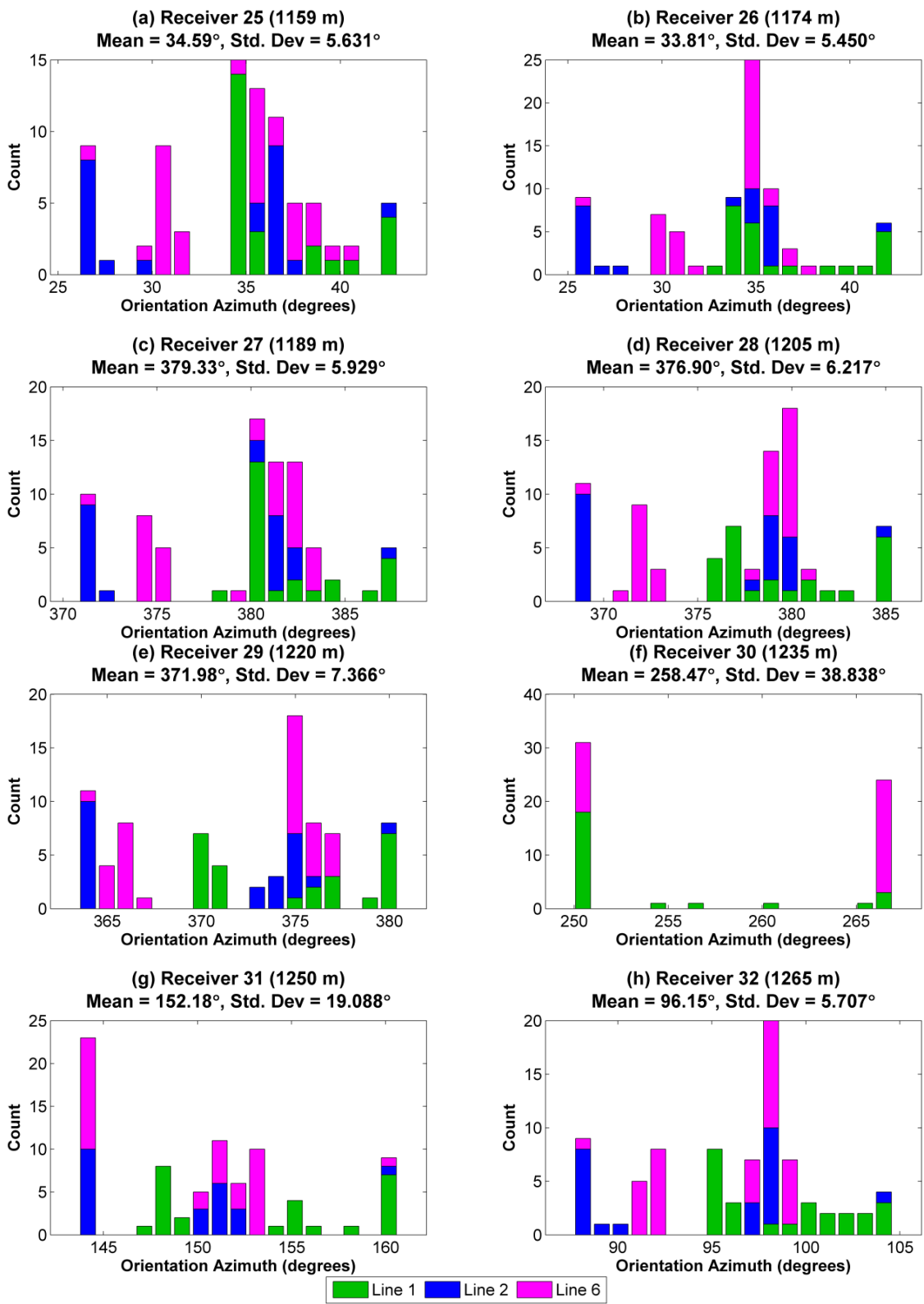


Figure D.12: Orientation azimuth histograms for Receivers 25-32 (mid-level). Line 1 is shown in green, Line 2 in blue, and Line 6 in magenta.

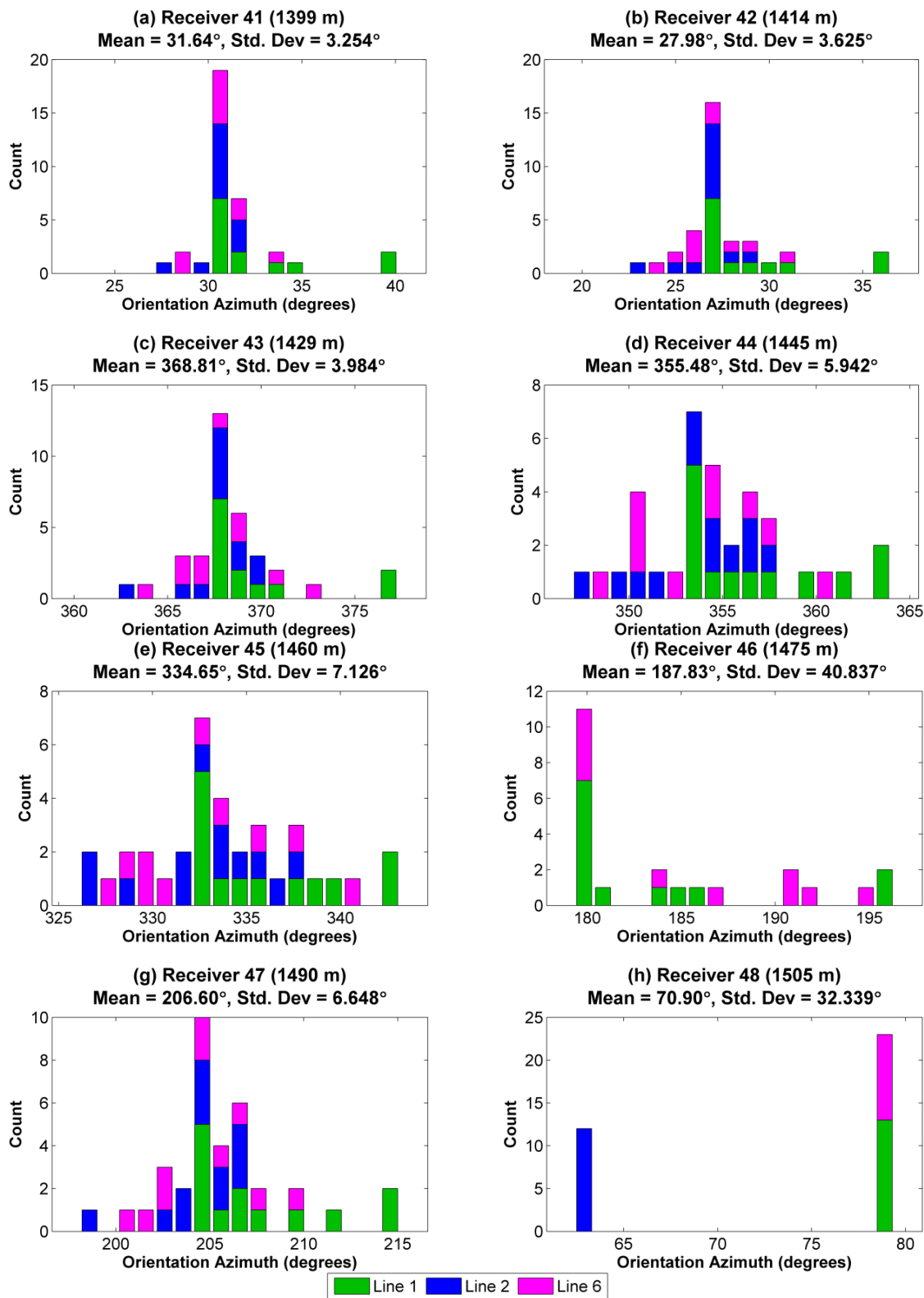


Figure D.13: Orientation azimuth histograms for Receivers 41-48 (deep-level). Line 1 is shown in green, Line 2 in blue, and Line 6 in magenta.

APPENDIX E: EXPANDED RESULTS FOR FINITE-DIFFERENCE MODELS

E.1. Dipping Interface

Figure E.1 through Figure E.14 show the deviation in orientation azimuth for Receivers 12 (120 m) through 25 (250 m), using a 100 ms analysis window. These expand upon the results of finite-difference modelling of a dipping interface examined in Chapter 5.

E.2. HTI Medium

Figure E.15 through Figure E.30 show the deviation in orientation azimuth for Receivers 8 (80 m) through 23 (230 m), using a 100 ms analysis window. These expand upon the results of finite-difference modelling of an HTI medium examined in Chapter 6. Vertical dashed lines indicate directions parallel to the fast and slow directions.

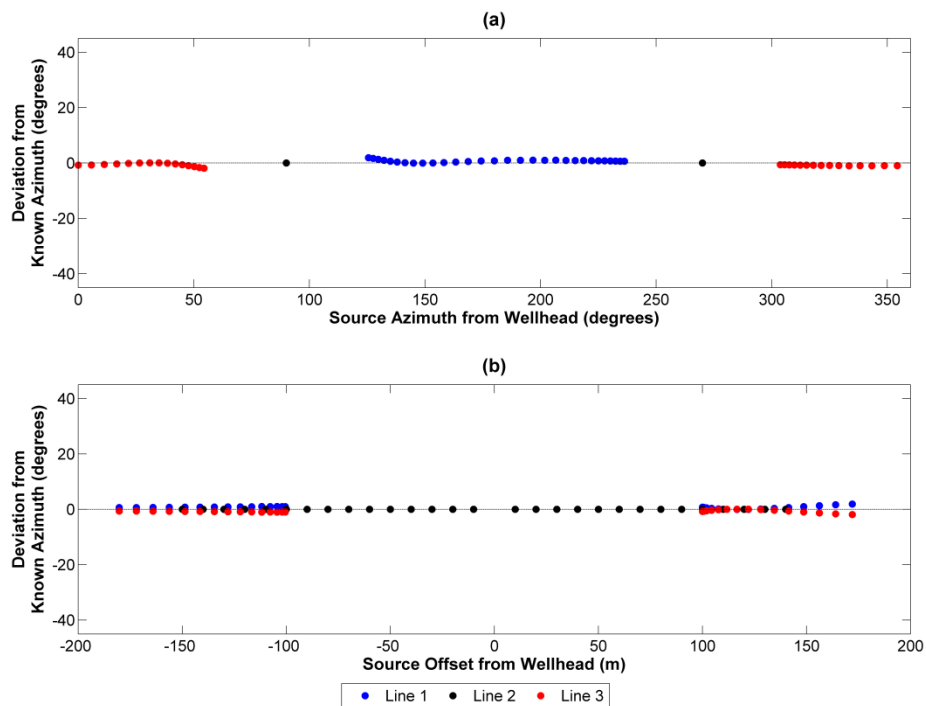


Figure E.1: Deviation of orientation angle for Receiver 12 (120 m depth) plotted as a function of source-well azimuth (a) and source-well offset (b), using a dipping interface model.

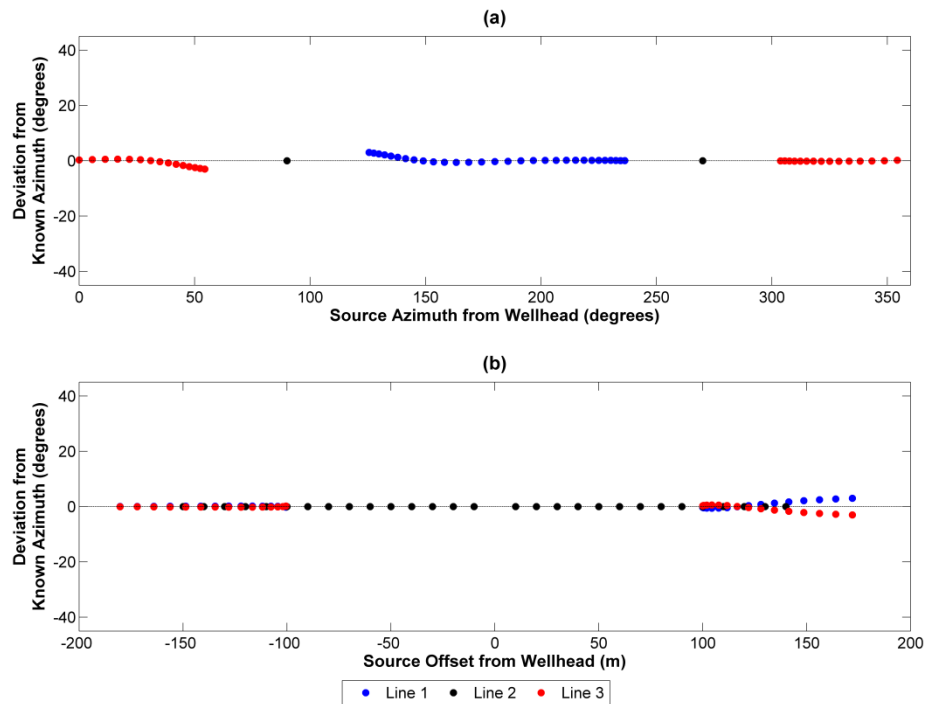


Figure E.2: Deviation of orientation angle for Receiver 13 (130 m depth) plotted as a function of source-well azimuth (a) and source-well offset (b), using a dipping interface model.

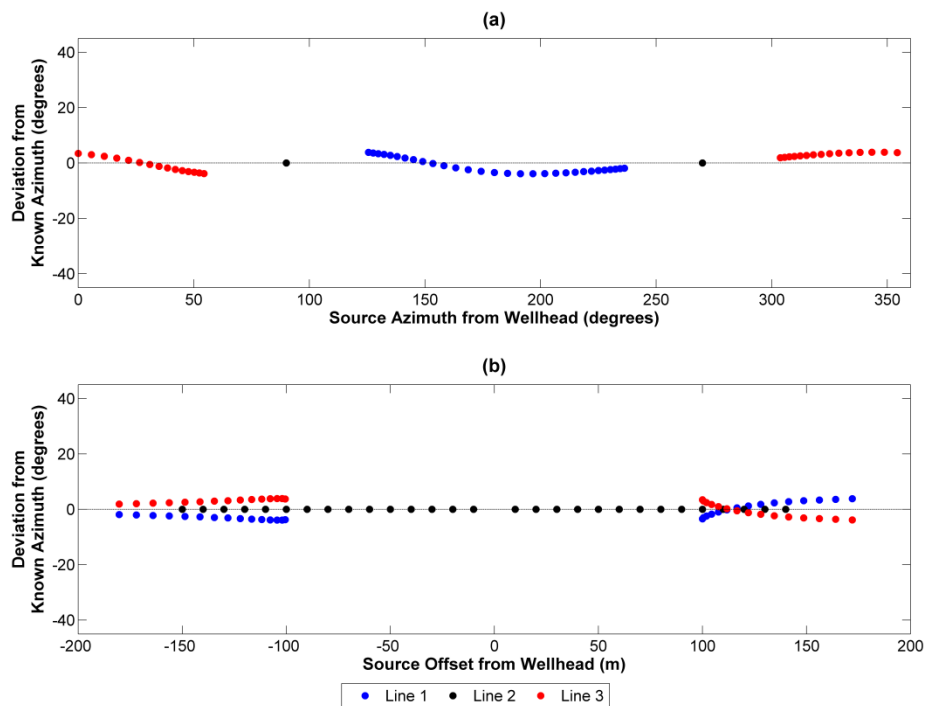


Figure E.3: Deviation of orientation angle for Receiver 14 (140 m depth) plotted as a function of source-well azimuth (a) and source-well offset (b), using a dipping interface model.

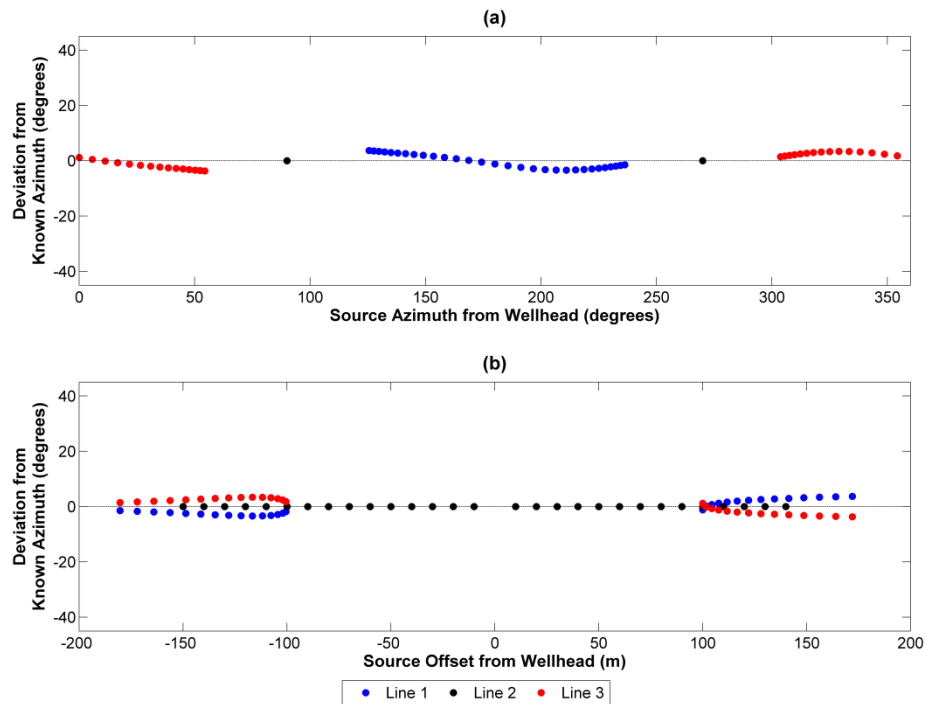


Figure E.4: Deviation of orientation angle for Receiver 15 (150 m depth) plotted as a function of source-well azimuth (a) and source-well offset (b), using a dipping interface model.

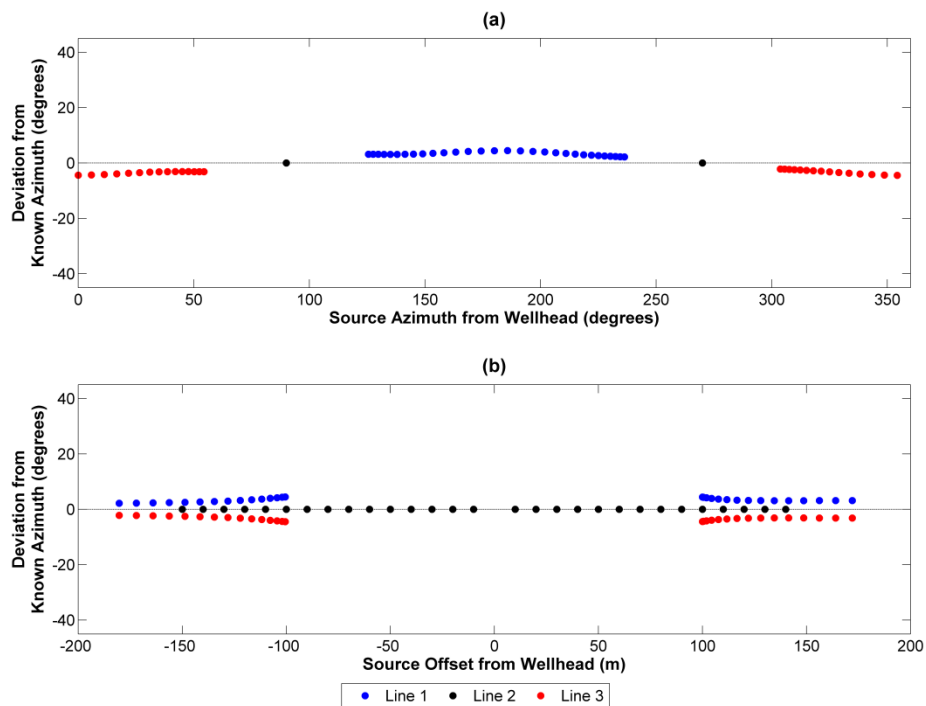


Figure E.5: Deviation of orientation angle for Receiver 16 (160 m depth) plotted as a function of source-well azimuth (a) and source-well offset (b), using a dipping interface model.

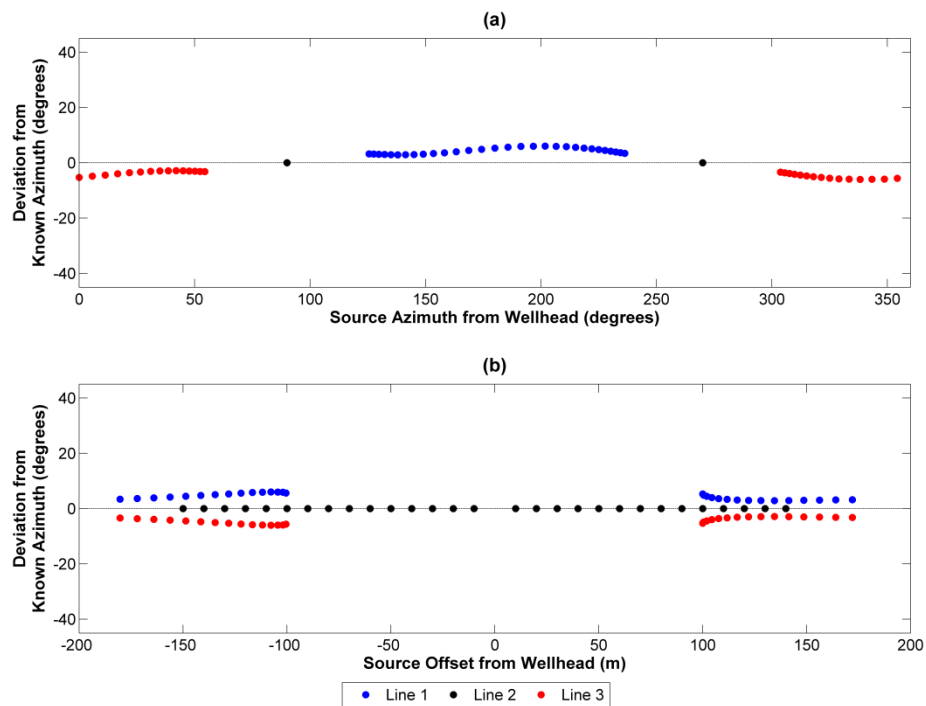


Figure E.6: Deviation of orientation angle for Receiver 17 (170 m depth) plotted as a function of source-well azimuth (a) and source-well offset (b), using a dipping interface model.

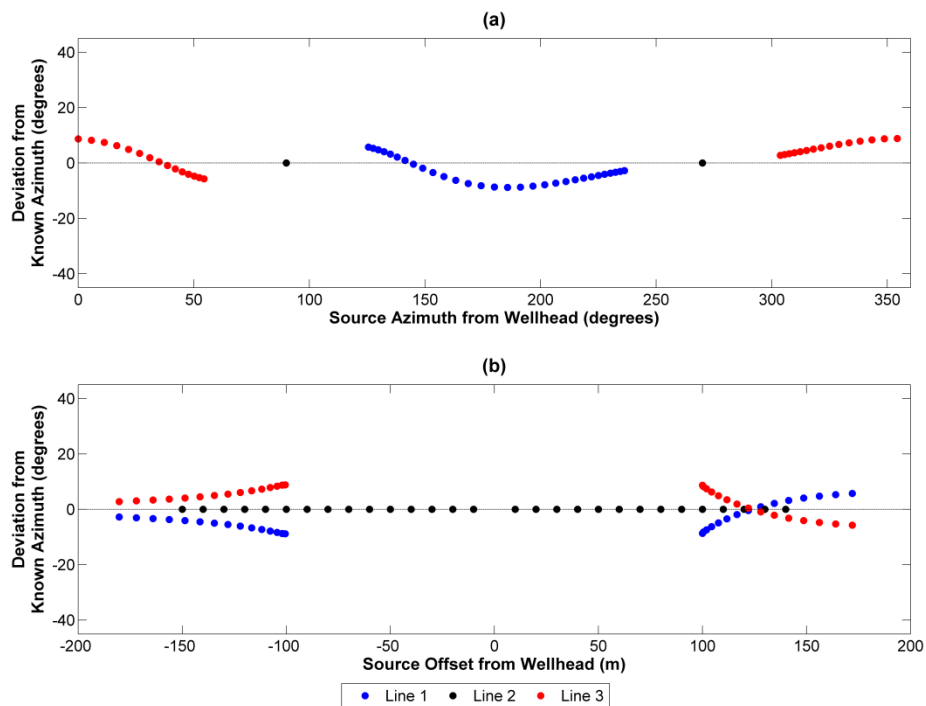


Figure E.7: Deviation of orientation angle for Receiver 18 (180 m depth) plotted as a function of source-well azimuth (a) and source-well offset (b), using a dipping interface model.

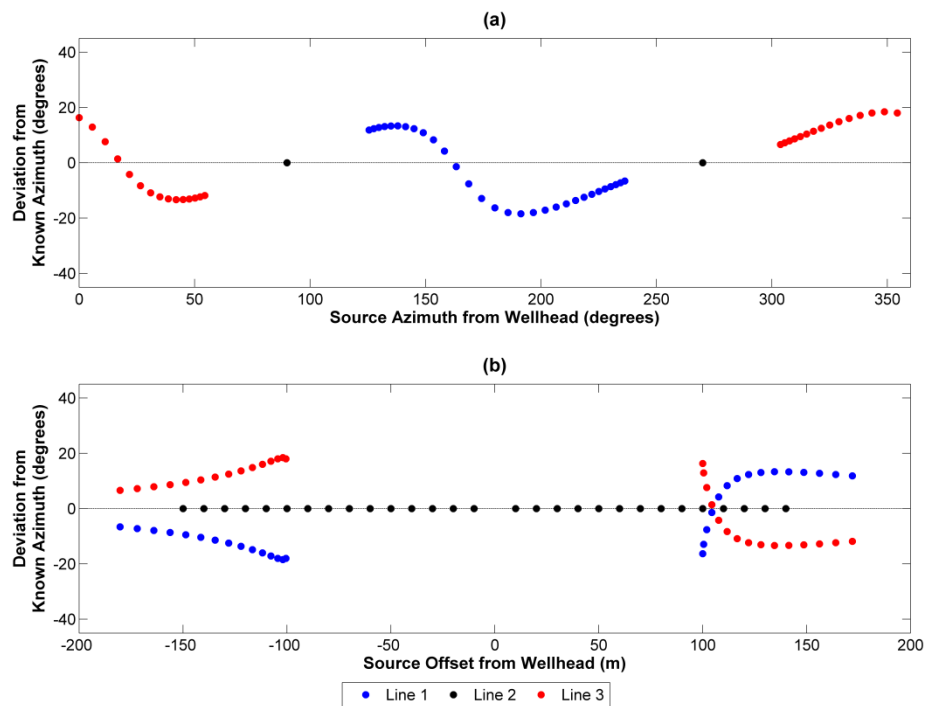


Figure E.8: Deviation of orientation angle for Receiver 19 (190 m depth) plotted as a function of source-well azimuth (a) and source-well offset (b), using a dipping interface model.

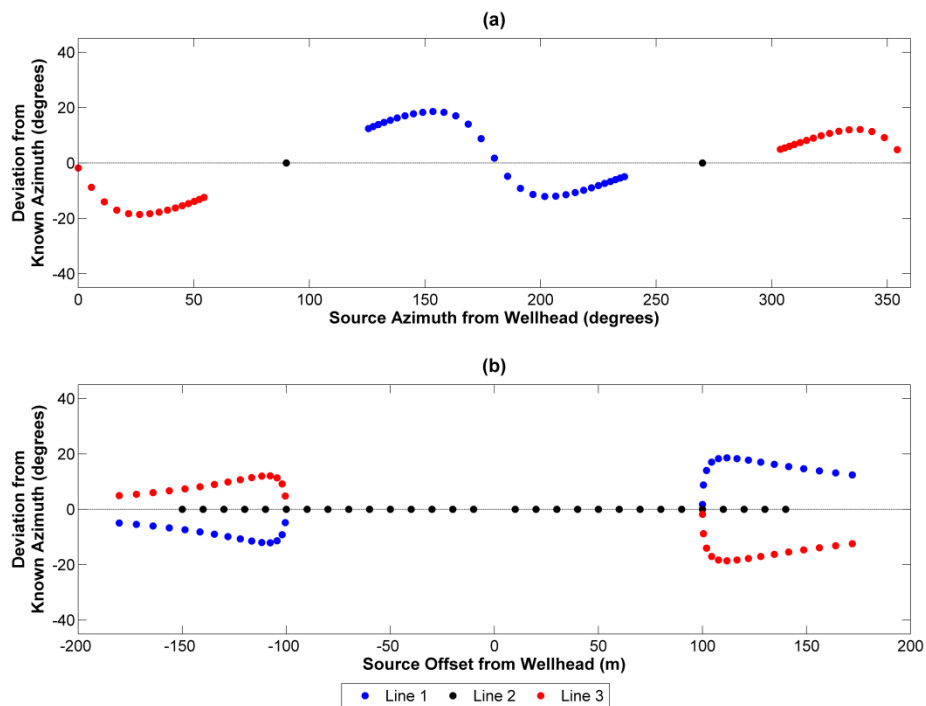


Figure E.9: Deviation of orientation angle for Receiver 20 (200 m depth) plotted as a function of source-well azimuth (a) and source-well offset (b), using a dipping interface model.

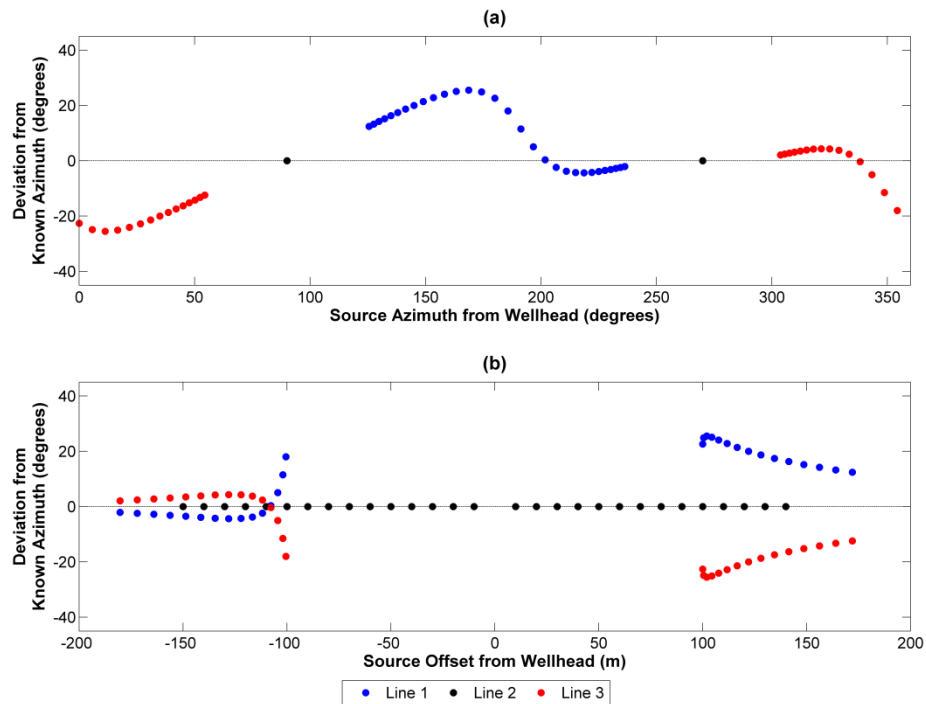


Figure E.10: Deviation of orientation angle for Receiver 21 (210 m depth) plotted as a function of source-well azimuth (a) and source-well offset (b), using a dipping interface model.

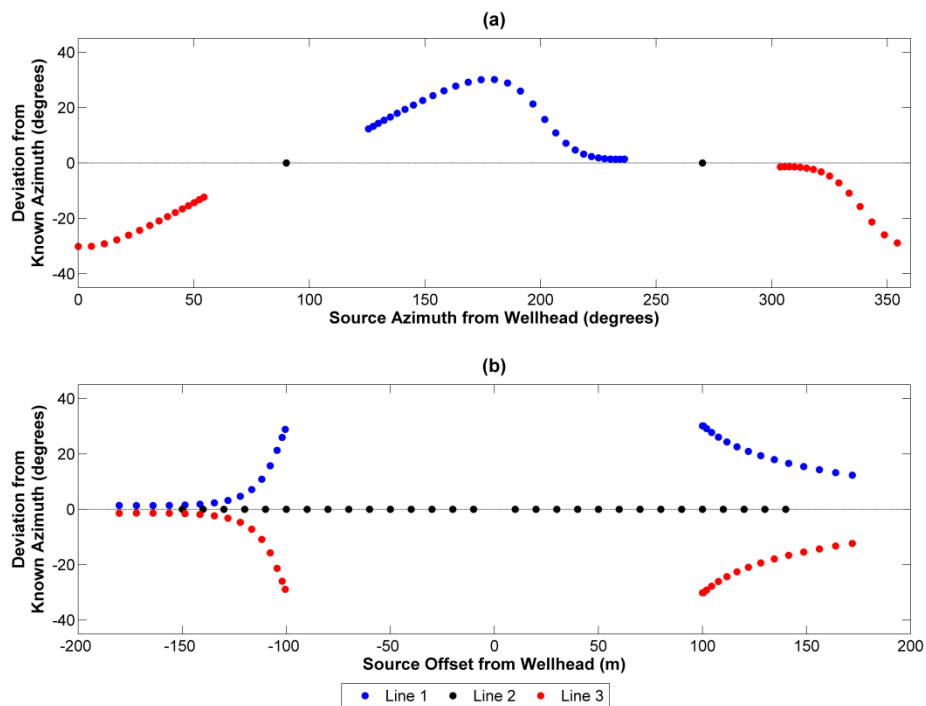


Figure E.11: Deviation of orientation angle for Receiver 22 (220 m depth) plotted as a function of source-well azimuth (a) and source-well offset (b), using a dipping interface model.

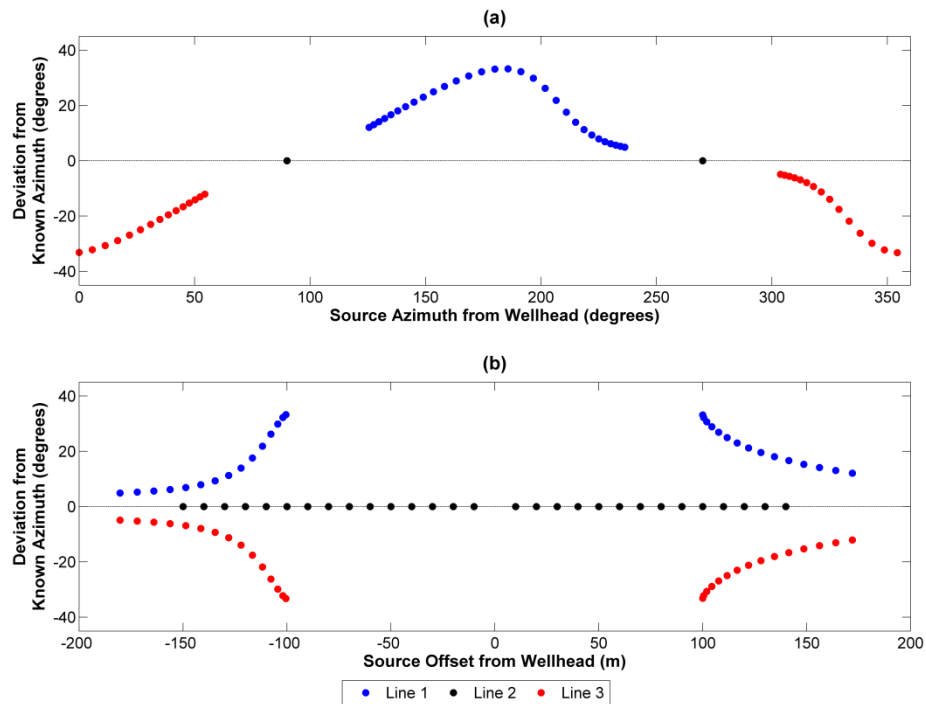


Figure E.12: Deviation of orientation angle for Receiver 23 (230 m depth) plotted as a function of source-well azimuth (a) and source-well offset (b), using a dipping interface model.

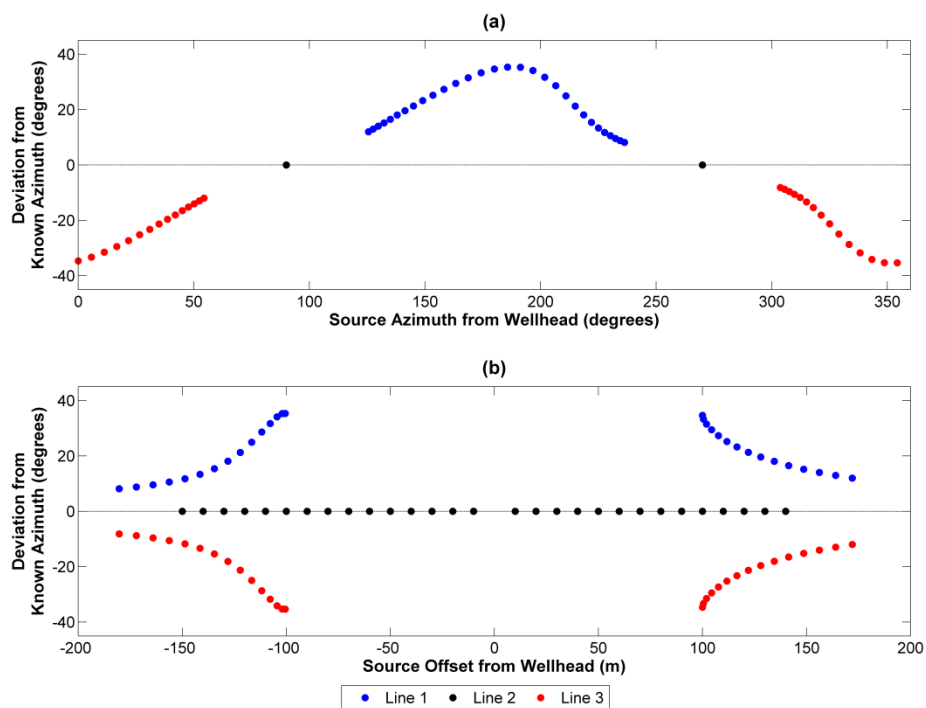


Figure E.13: Deviation of orientation angle for Receiver 24 (240 m depth) plotted as a function of source-well azimuth (a) and source-well offset (b), using a dipping interface model.

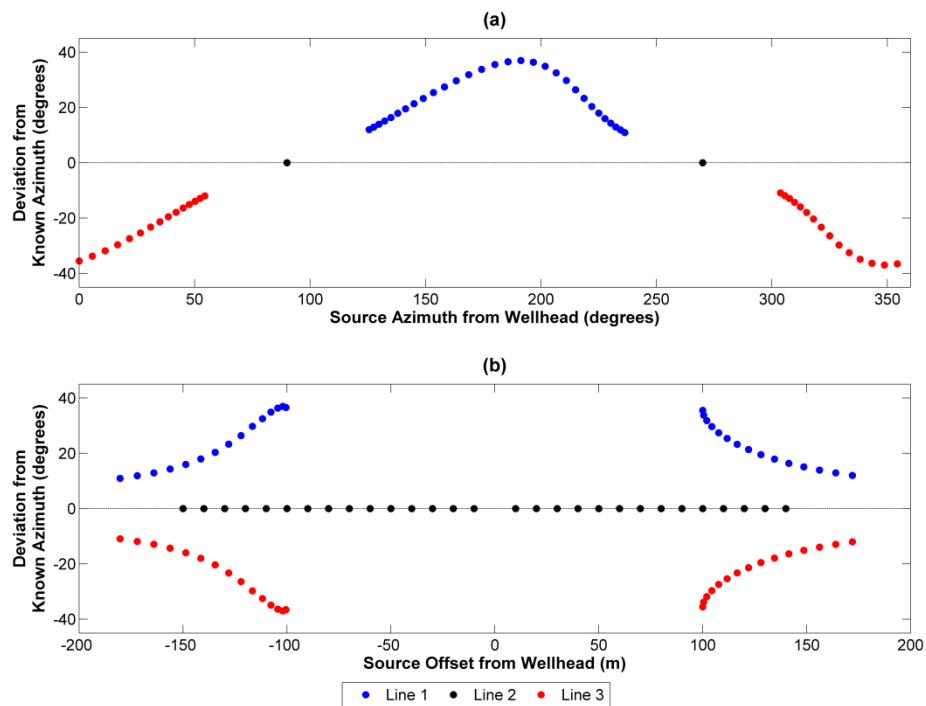


Figure E.14: Deviation of orientation angle for Receiver 25 (250 m depth) plotted as a function of source-well azimuth (a) and source-well offset (b), using a dipping interface model.

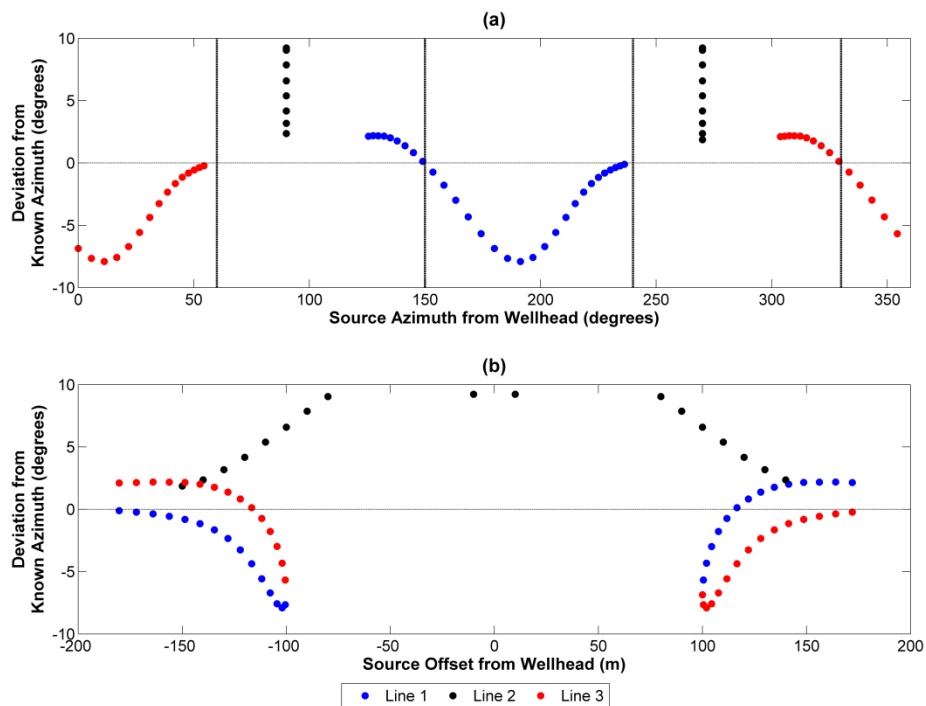


Figure E.15: Deviation of orientation angle for Receiver 8 (80 m depth) plotted as a function of source-well azimuth (a) and source-well offset (b), using a model of an HTI medium.

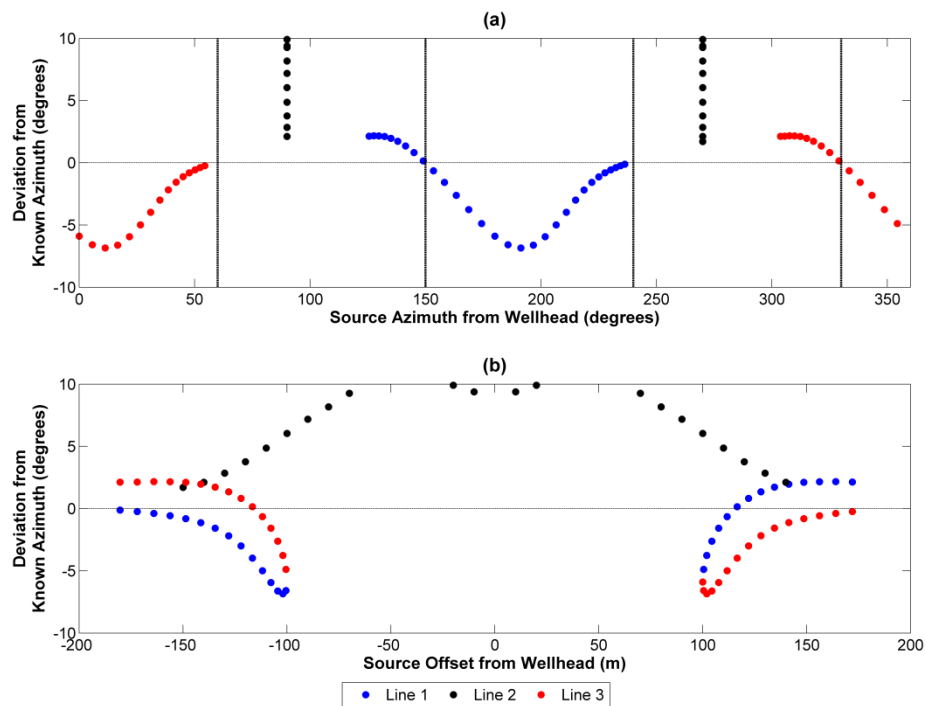


Figure E.16: Deviation of orientation angle for Receiver 9 (90 m depth) plotted as a function of source-well azimuth (a) and source-well offset (b), using a model of an HTI medium.

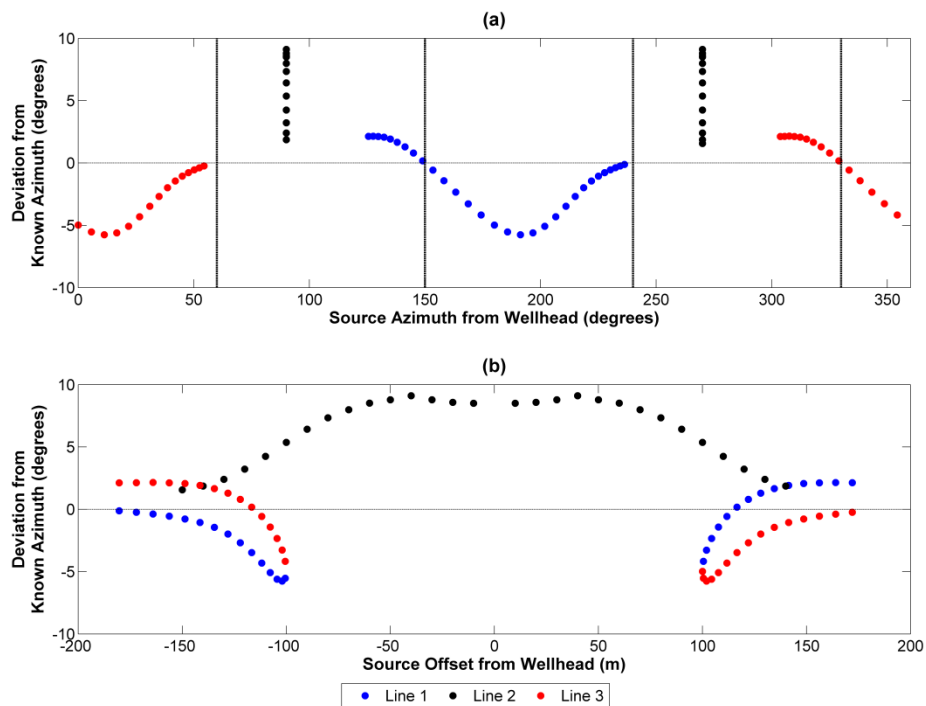


Figure E.17: Deviation of orientation angle for Receiver 10 (100 m depth) plotted as a function of source-well azimuth (a) and source-well offset (b), using a model of an HTI medium.

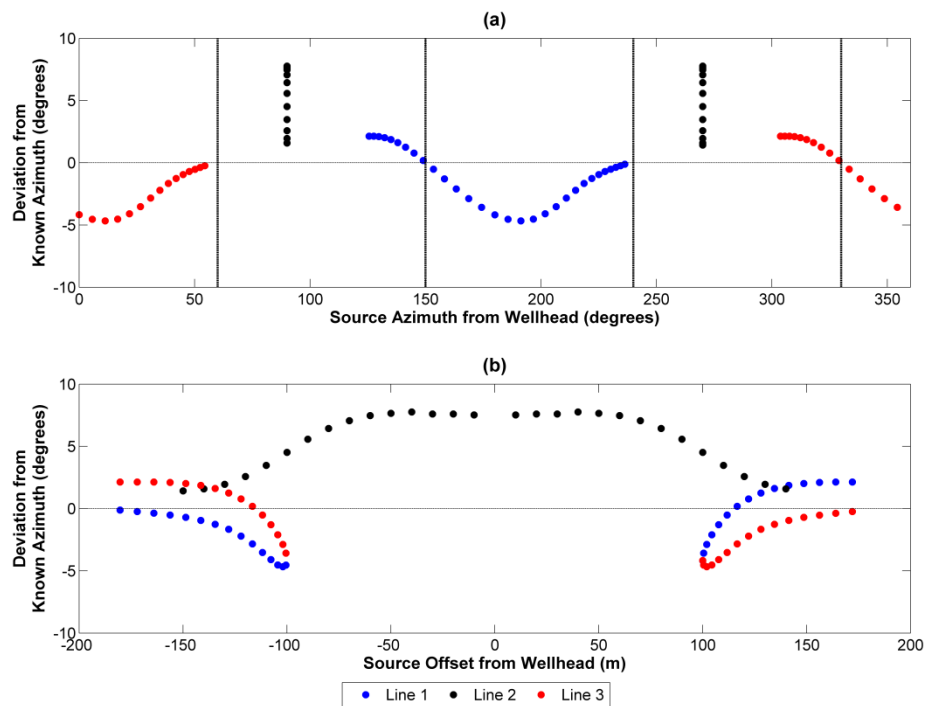


Figure E.18: Deviation of orientation angle for Receiver 11 (110 m depth) plotted as a function of source-well azimuth (a) and source-well offset (b), using a model of an HTI medium.

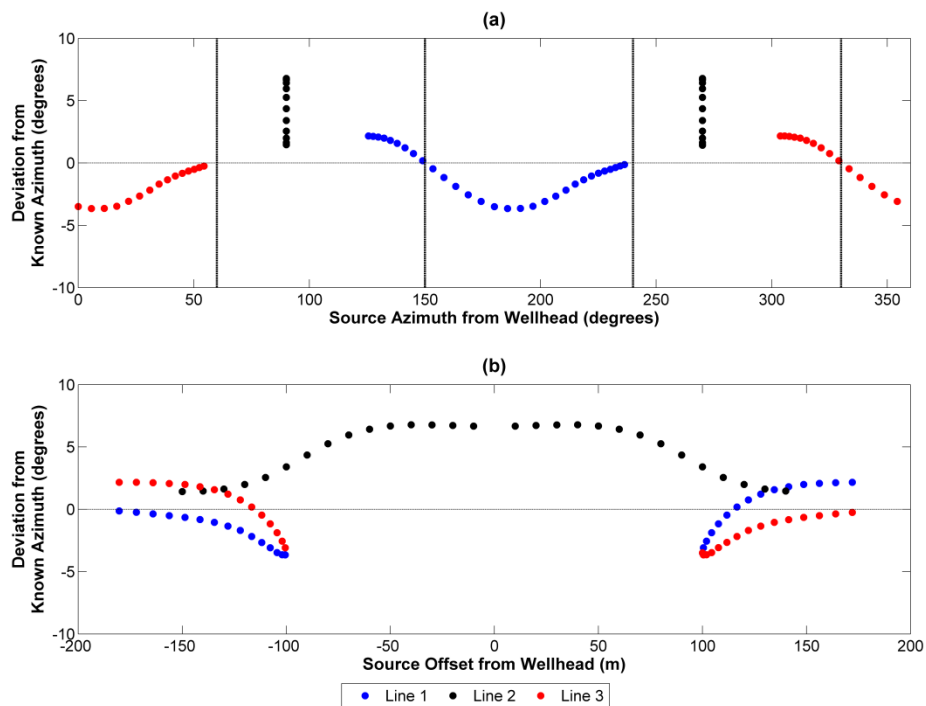


Figure E.19: Deviation of orientation angle for Receiver 12 (120 m depth) plotted as a function of source-well azimuth (a) and source-well offset (b), using a model of an HTI medium.

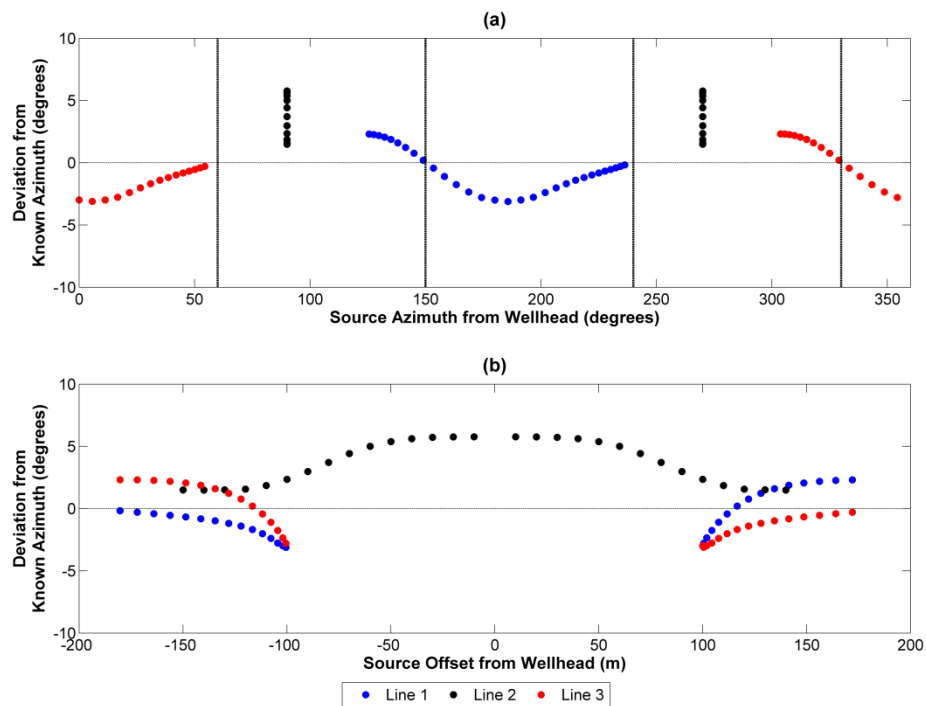


Figure E.20: Deviation of orientation angle for Receiver 13 (130 m depth) plotted as a function of source-well azimuth (a) and source-well offset (b), using a model of an HTI medium.

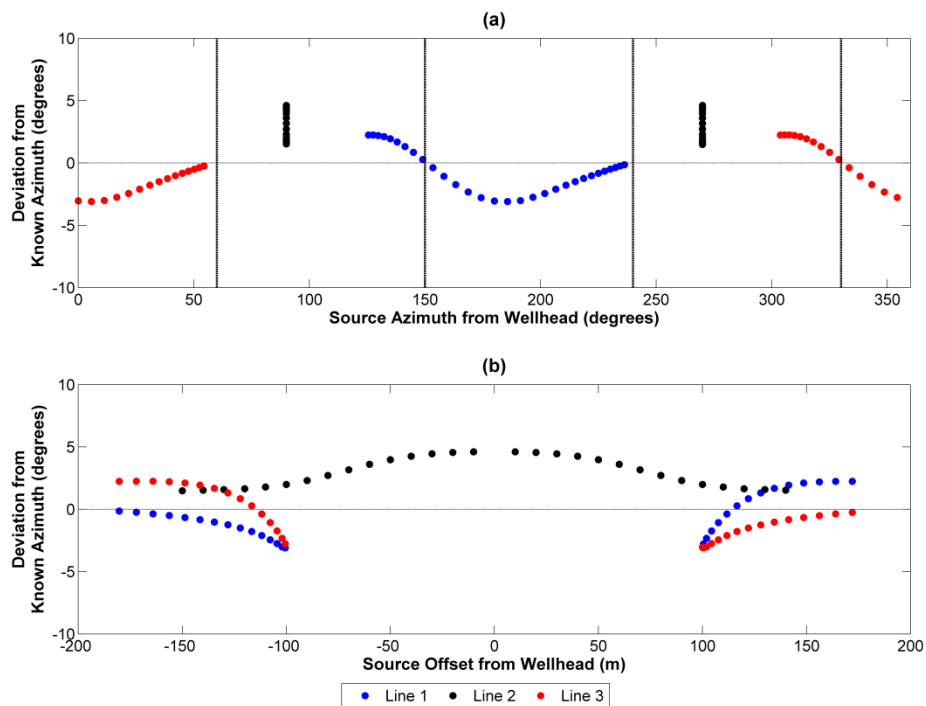


Figure E.21: Deviation of orientation angle for Receiver 14 (140 m depth) plotted as a function of source-well azimuth (a) and source-well offset (b), using a model of an HTI medium.

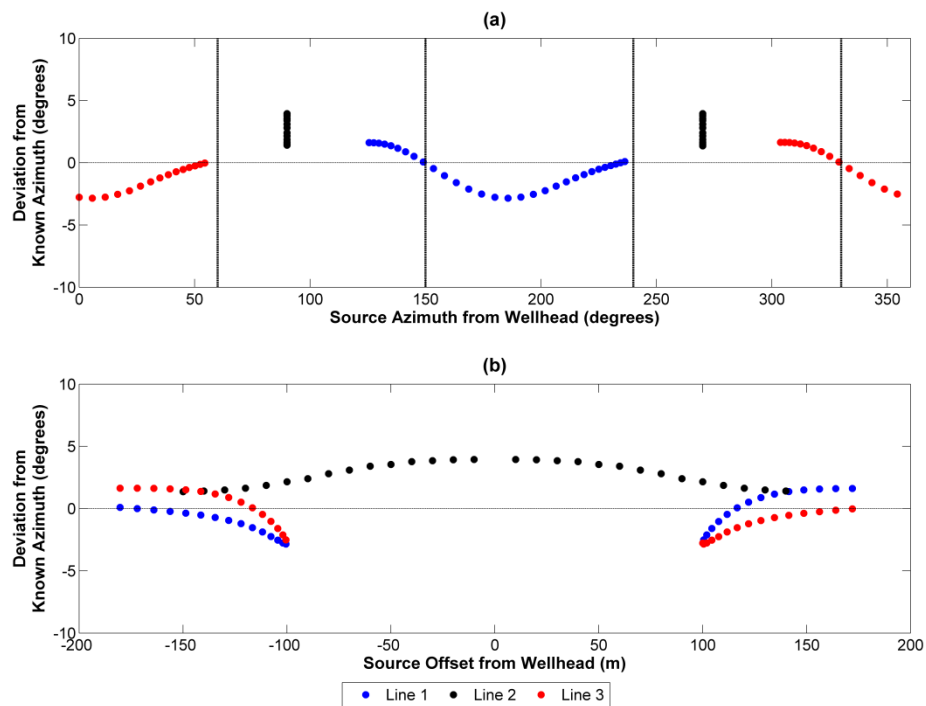


Figure E.22: Deviation of orientation angle for Receiver 15 (150 m depth) plotted as a function of source-well azimuth (a) and source-well offset (b), using a model of an HTI medium.

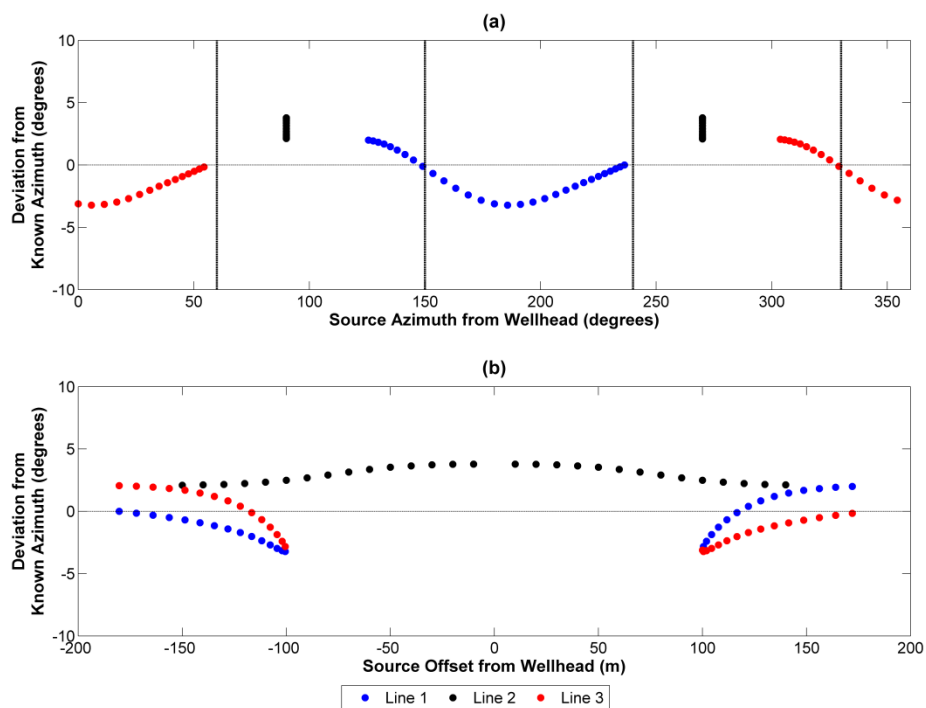


Figure E.23: Deviation of orientation angle for Receiver 16 (160 m depth) plotted as a function of source-well azimuth (a) and source-well offset (b), using a model of an HTI medium.

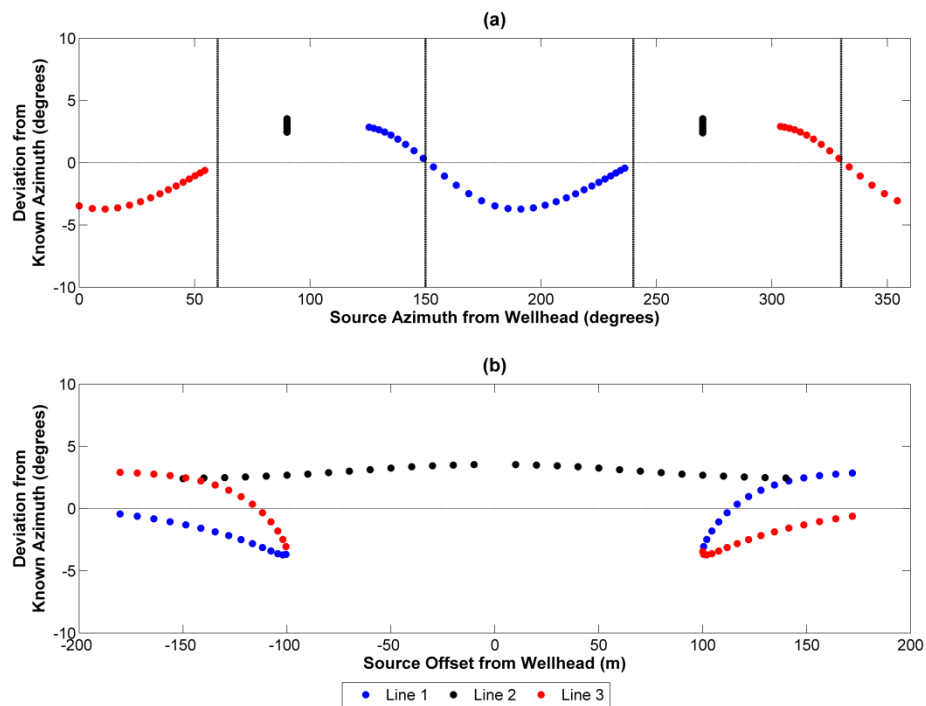


Figure E.24: Deviation of orientation angle for Receiver 17 (170 m depth) plotted as a function of source-well azimuth (a) and source-well offset (b), using a model of an HTI medium.

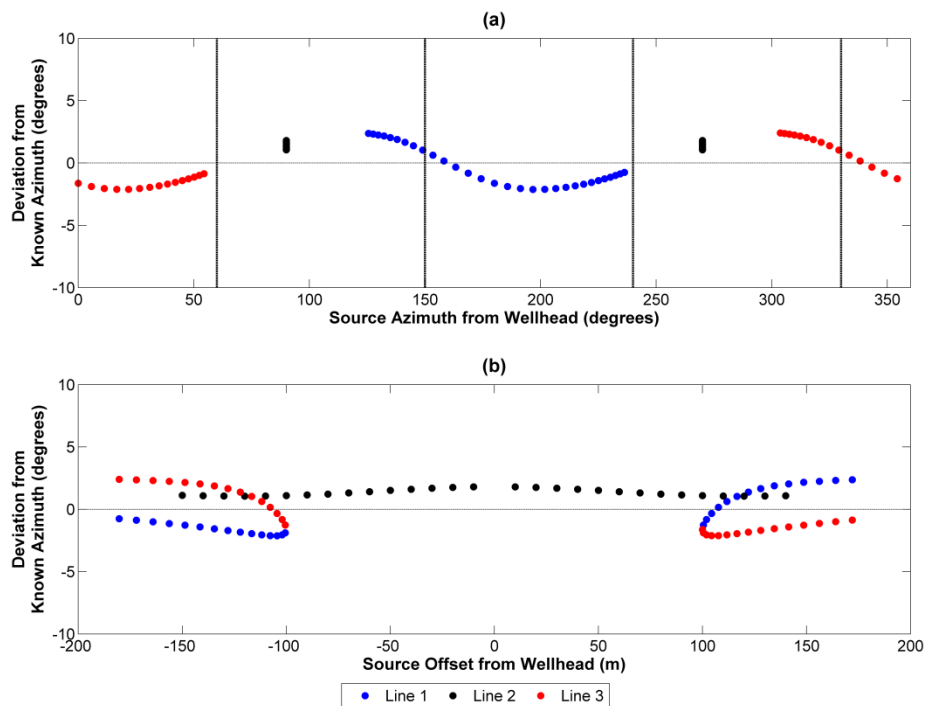


Figure E.25: Deviation of orientation angle for Receiver 18 (180 m depth) plotted as a function of source-well azimuth (a) and source-well offset (b), using a model of an HTI medium.

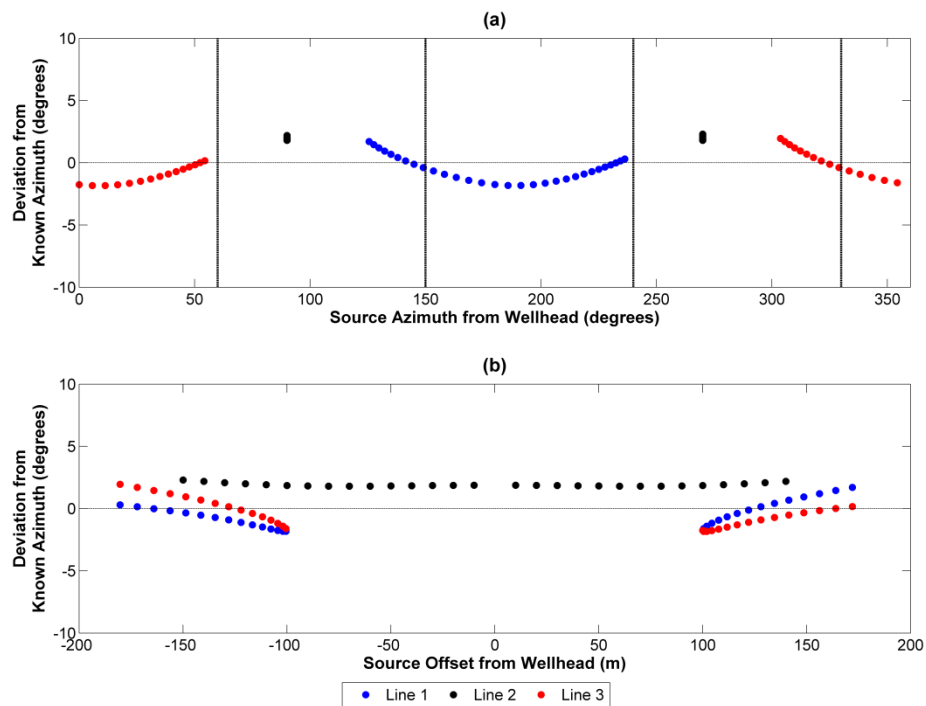


Figure E.26: Deviation of orientation angle for Receiver 19 (190 m depth) plotted as a function of source-well azimuth (a) and source-well offset (b), using a model of an HTI medium.

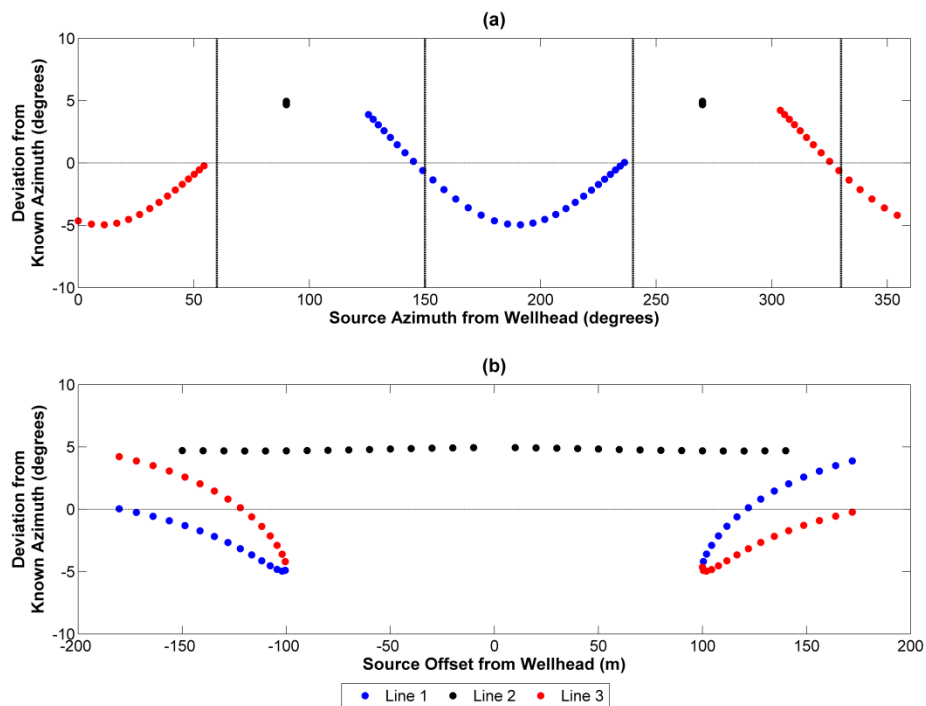


Figure E.27: Deviation of orientation angle for Receiver 20 (200 m depth) plotted as a function of source-well azimuth (a) and source-well offset (b), using a model of an HTI medium.

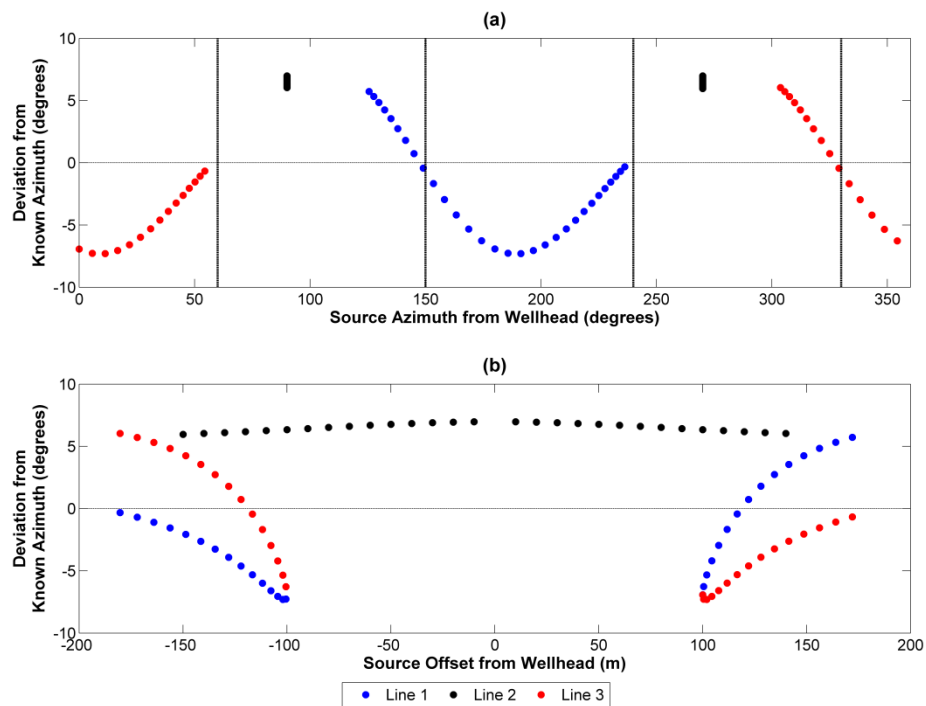


Figure E.28: Deviation of orientation angle for Receiver 21 (210 m depth) plotted as a function of source-well azimuth (a) and source-well offset (b), using a model of an HTI medium.

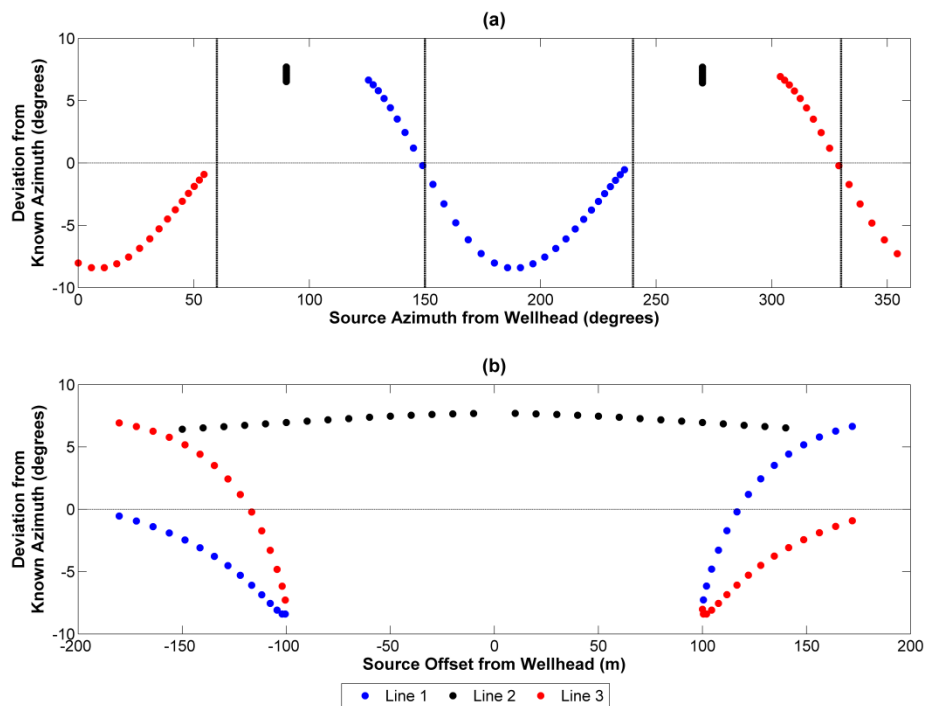


Figure E.29: Deviation of orientation angle for Receiver 22 (220 m depth) plotted as a function of source-well azimuth (a) and source-well offset (b), using a model of an HTI medium.

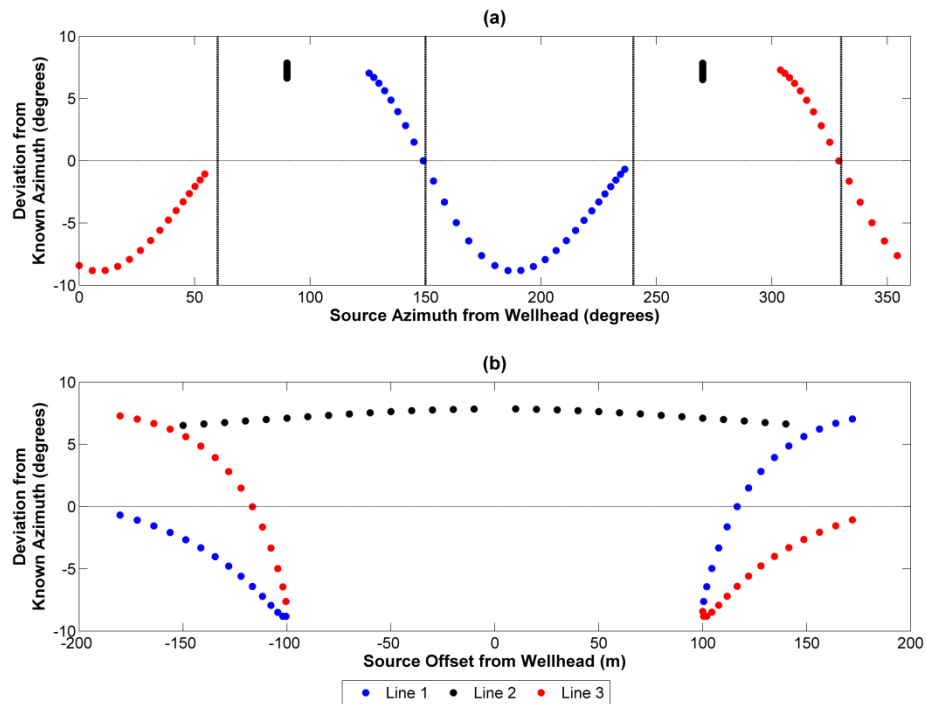


Figure E.30: Deviation of orientation angle for Receiver 23 (230 m depth) plotted as a function of source-well azimuth (a) and source-well offset (b), using a model of an HTI medium.

APPENDIX F: EXPANDED RESULTS FOR LOUSANA STUDY

This appendix provides a more complete suite of results for the Lousana study performed in Chapter 7.

- 6) Figure F.1 through Figure F.8 show variation in orientation azimuth vs. absolute offset for the 2D walkaway, using the analytic method.
- 7) Figure F.9 and Figure F.10 show variation in orientation azimuth vs. absolute offset for the 3D walkaway.
- 8) Figure F.11 and Figure F.12 show variation in orientation azimuth vs. source-well azimuth for the 3D walkaway.
- 9) Figure F.13 and Figure F.14 show histograms of orientation azimuth which use data from all source-well offsets, for the 3D walkaway.
- 10) Figure F.15 and Figure F.16 show histograms of orientation azimuth which only use data from source-well offsets greater than 500 m, for the 3D walkaway.

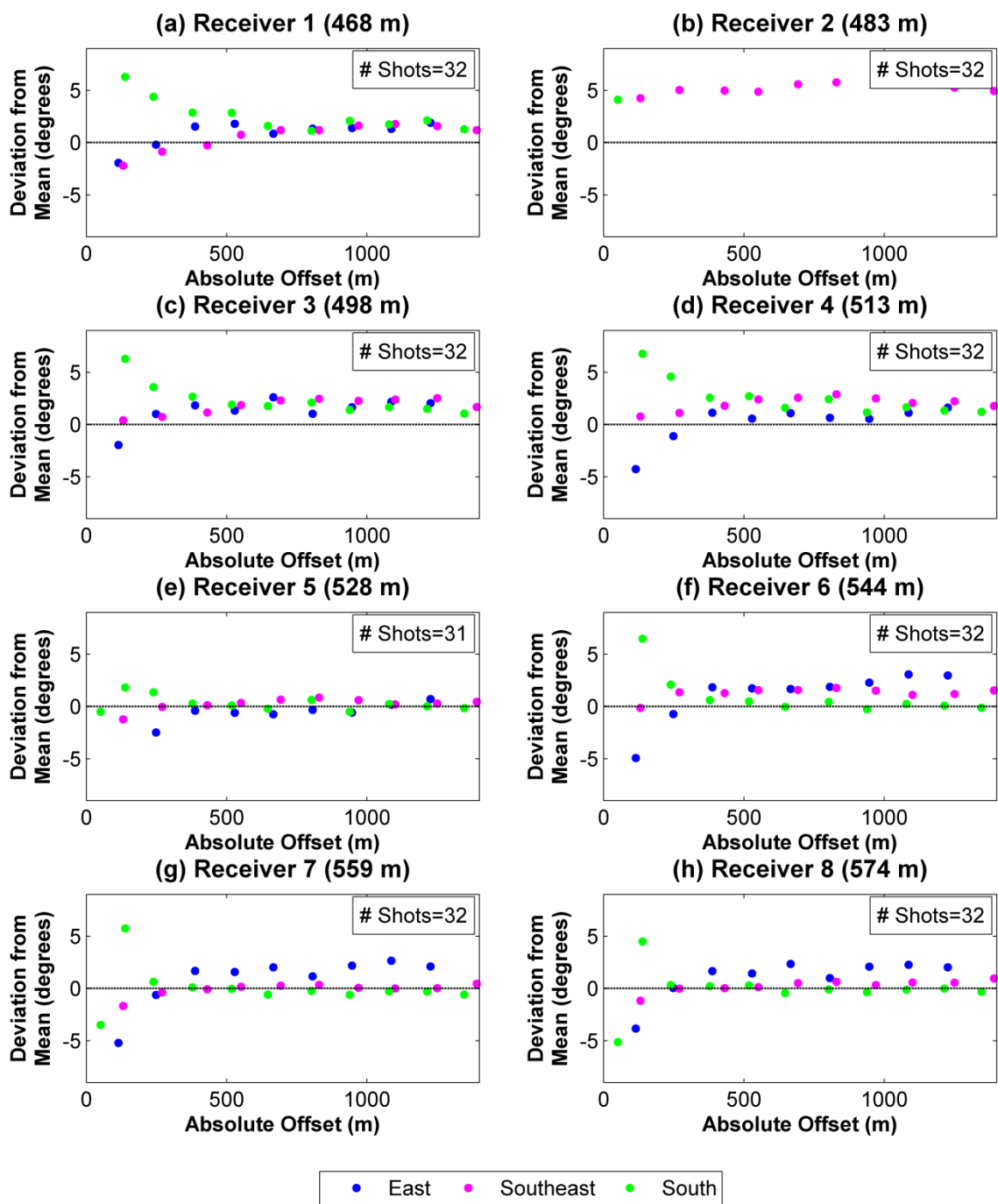


Figure F.1: Deviation in geophone orientation azimuths, versus source-well offset, for Receivers 1-8 in the 2D dataset calculated using analytic method, coloured by line; E is shown in blue, SE is shown in magenta and S is shown in green.

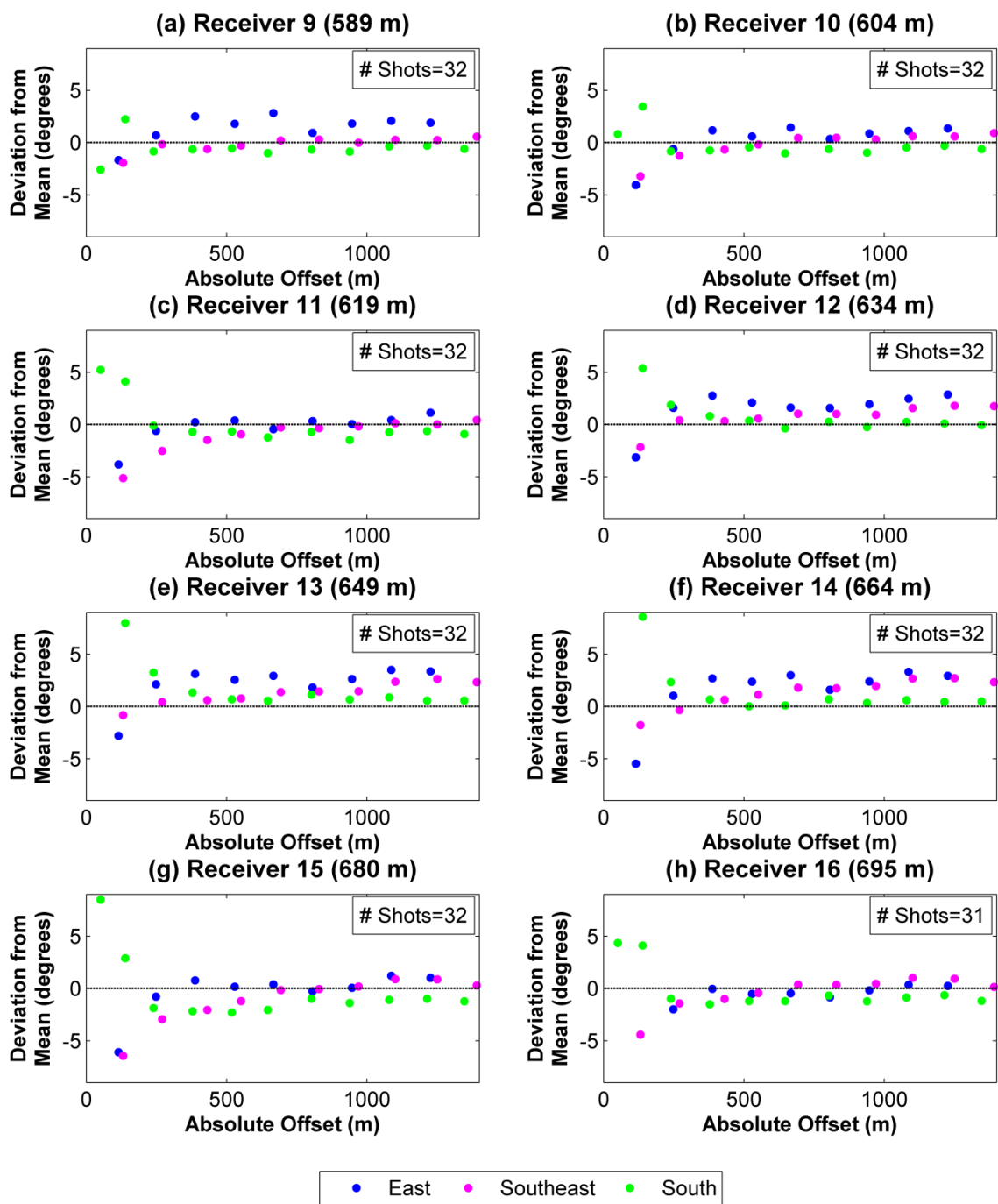


Figure F.2: Deviation in geophone orientation azimuths, versus source-well offset, for Receivers 9-16 in the 2D dataset calculated using analytic method, coloured by line; E is shown in blue, SE is shown in magenta and S is shown in green.

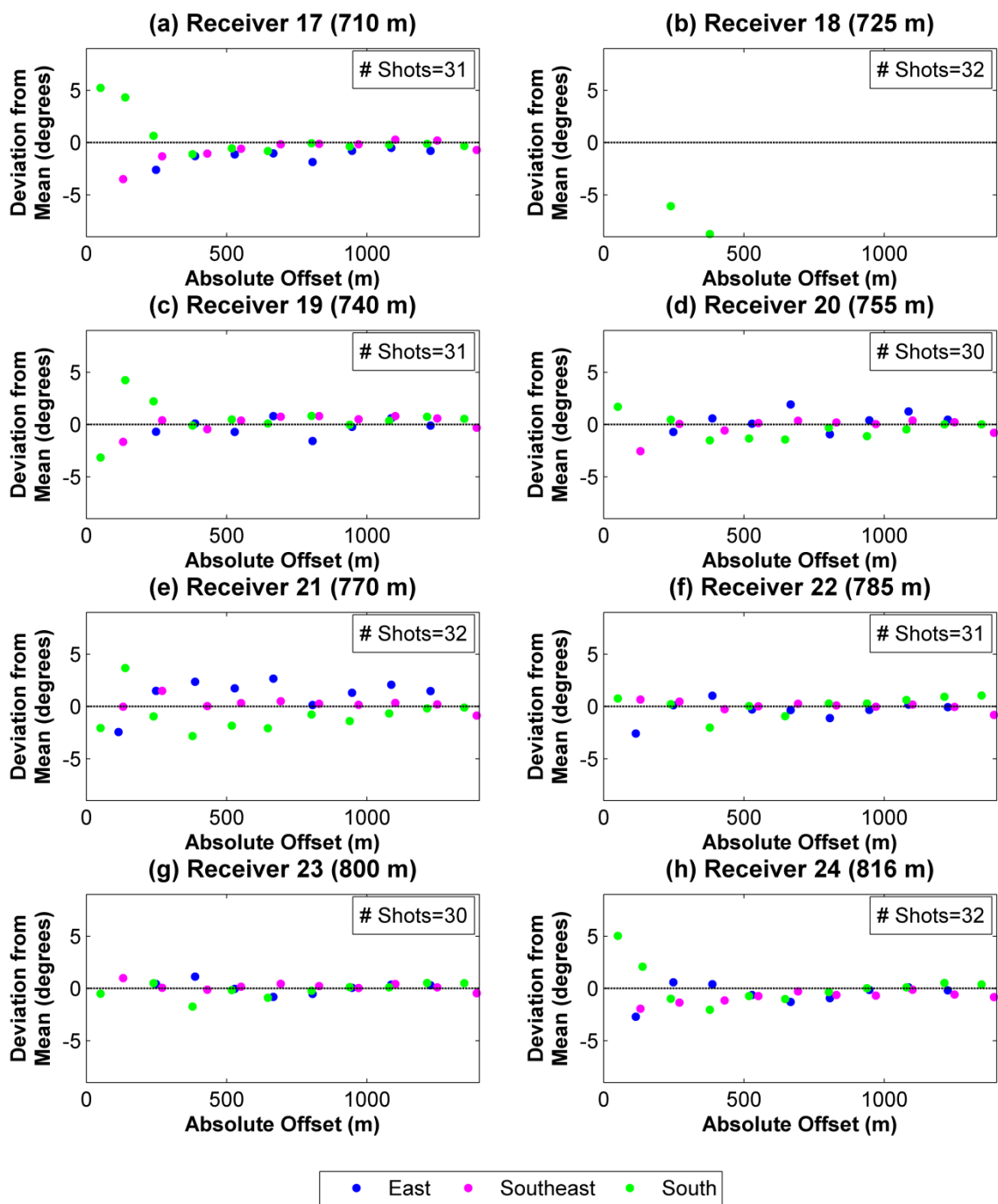


Figure F.3: Deviation in geophone orientation azimuths, versus source-well offset, for Receivers 17-24 in the 2D dataset calculated using analytic method, coloured by line; E is shown in blue, SE is shown in magenta and S is shown in green.

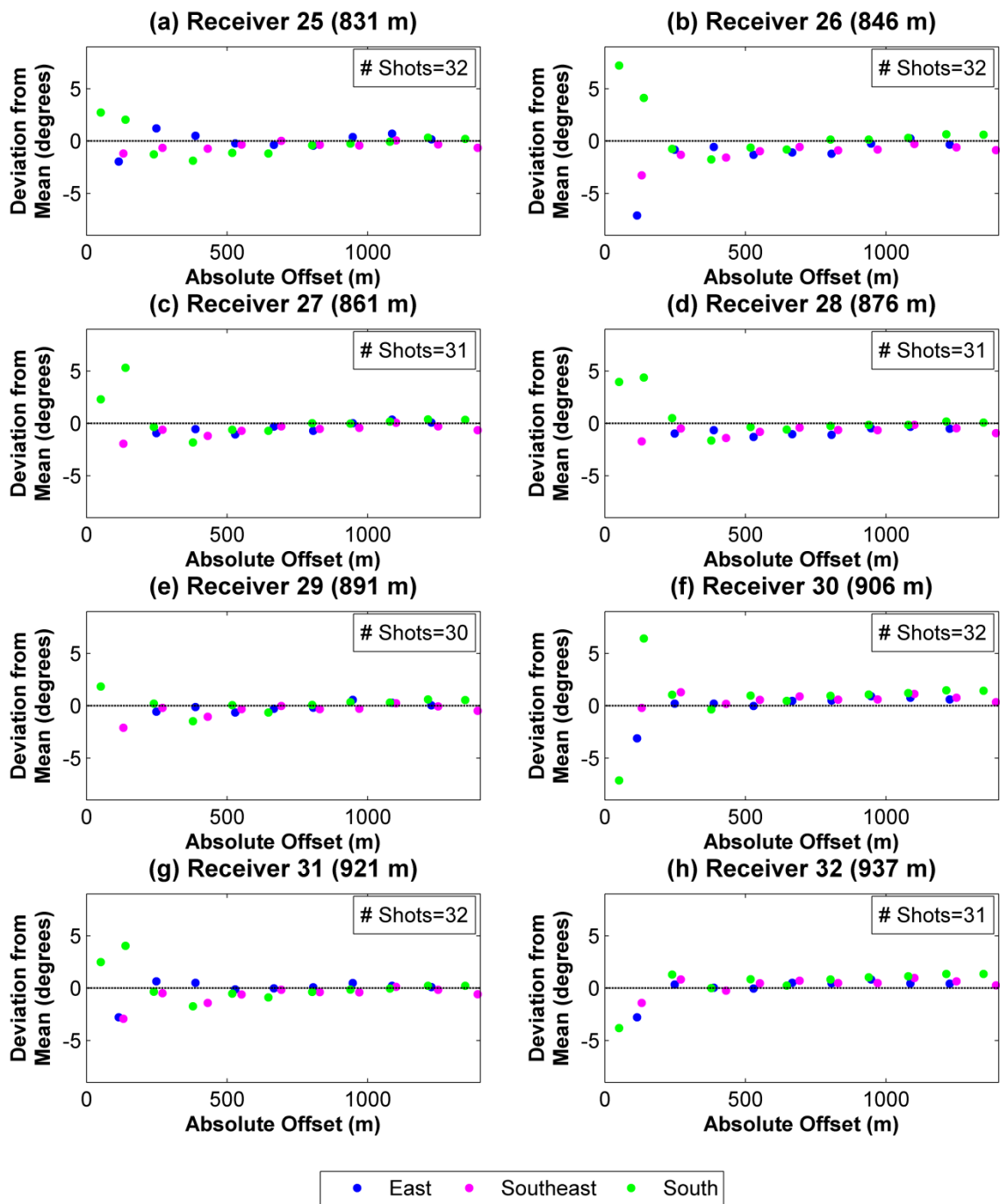


Figure F.4: Deviation in geophone orientation azimuths, versus source-well offset, for Receivers 25-32 in the 2D dataset calculated using analytic method, coloured by line; E is shown in blue, SE is shown in magenta and S is shown in green.

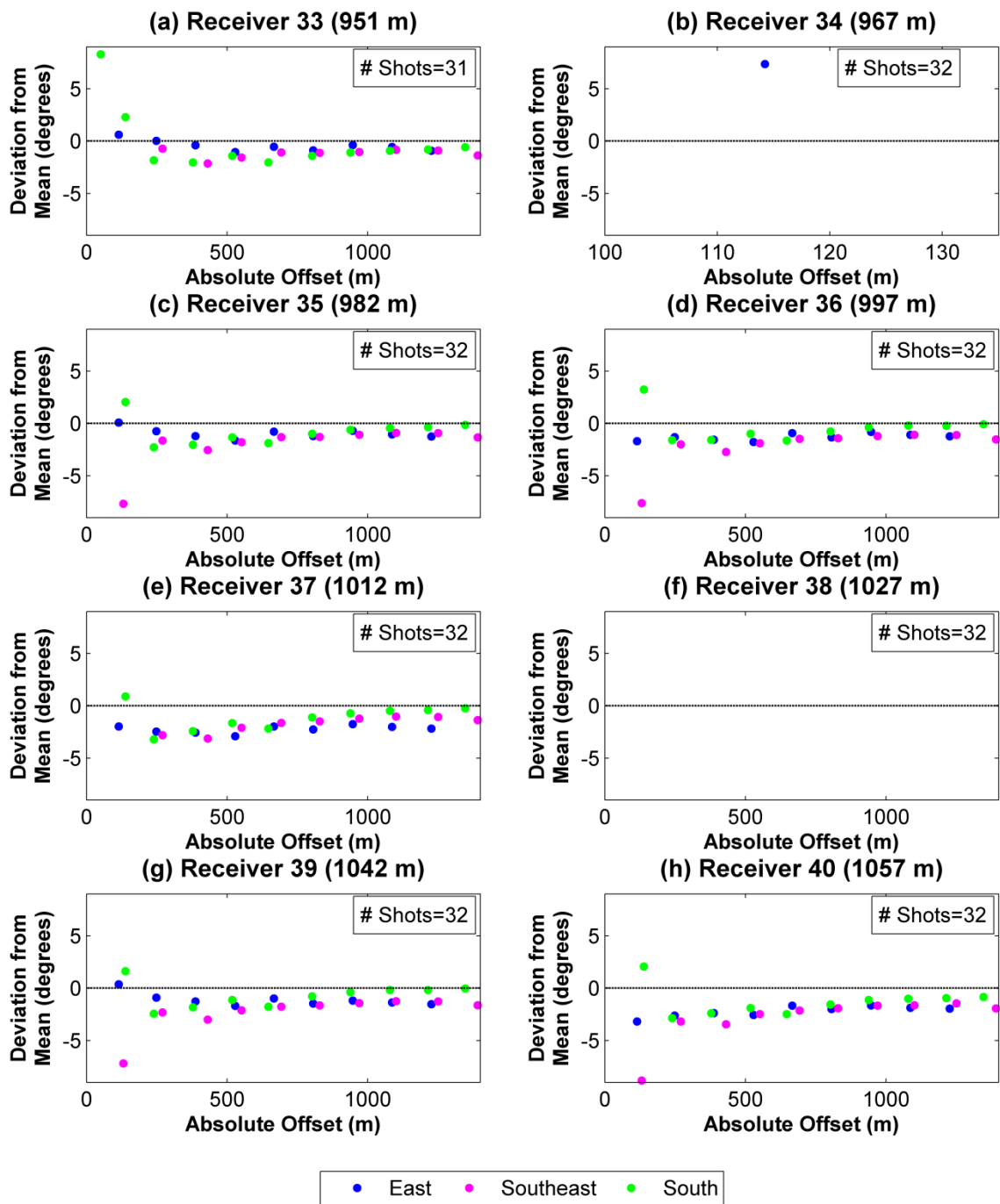


Figure F.5: Deviation in geophone orientation azimuths, versus source-well offset, for Receivers 33-40 in the 2D dataset calculated using analytic method, coloured by line; E is shown in blue, SE is shown in magenta and S is shown in green.

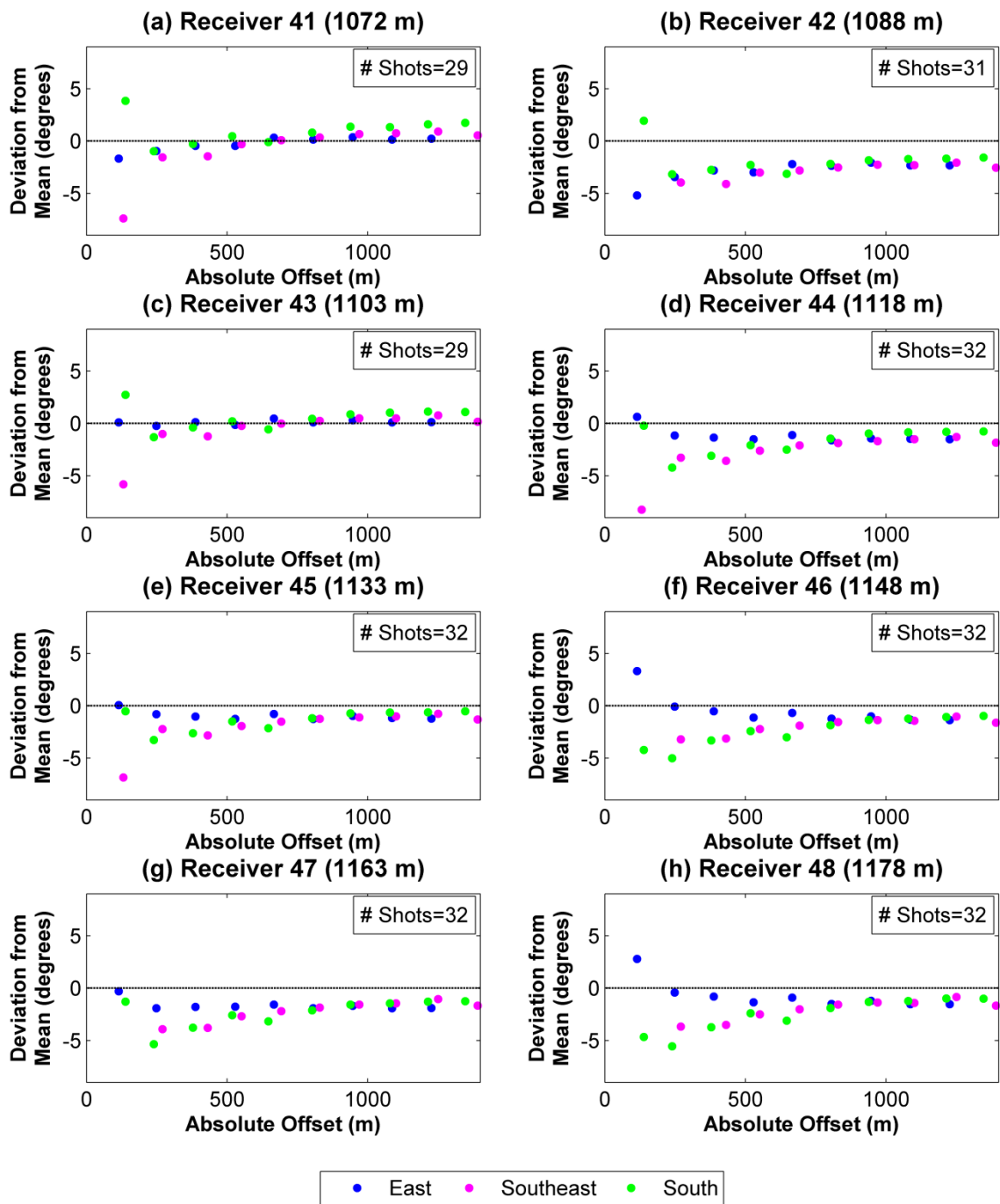


Figure F.6: Deviation in geophone orientation azimuths, versus source-well offset, for Receivers 41-48 in the 2D dataset calculated using analytic method, coloured by line; E is shown in blue, SE is shown in magenta and S is shown in green.

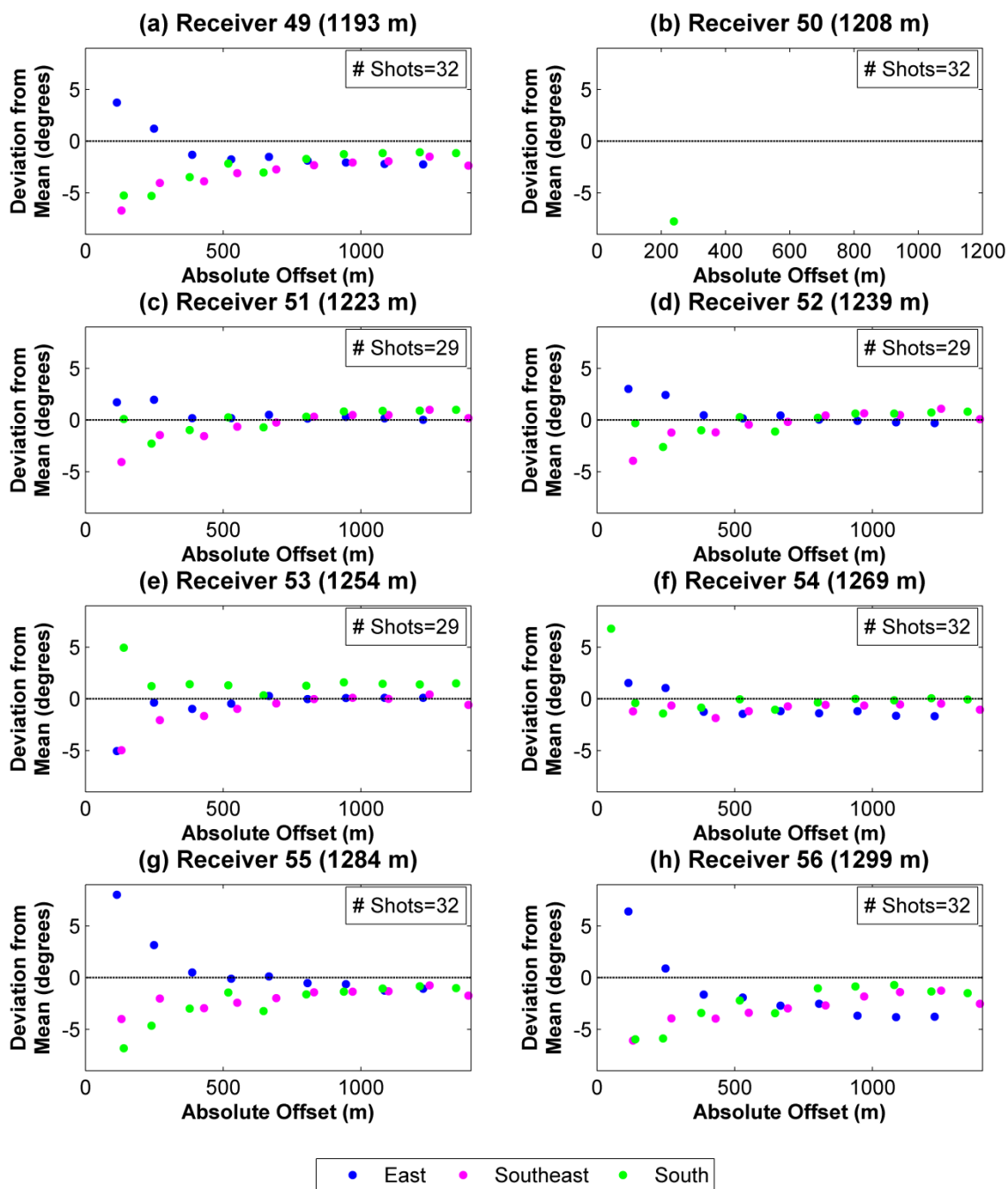


Figure F.7: Deviation in geophone orientation azimuths, versus source-well offset, for Receivers 49-56 in the 2D dataset calculated using analytic method, coloured by line; E is shown in blue, SE is shown in magenta and S is shown in green.

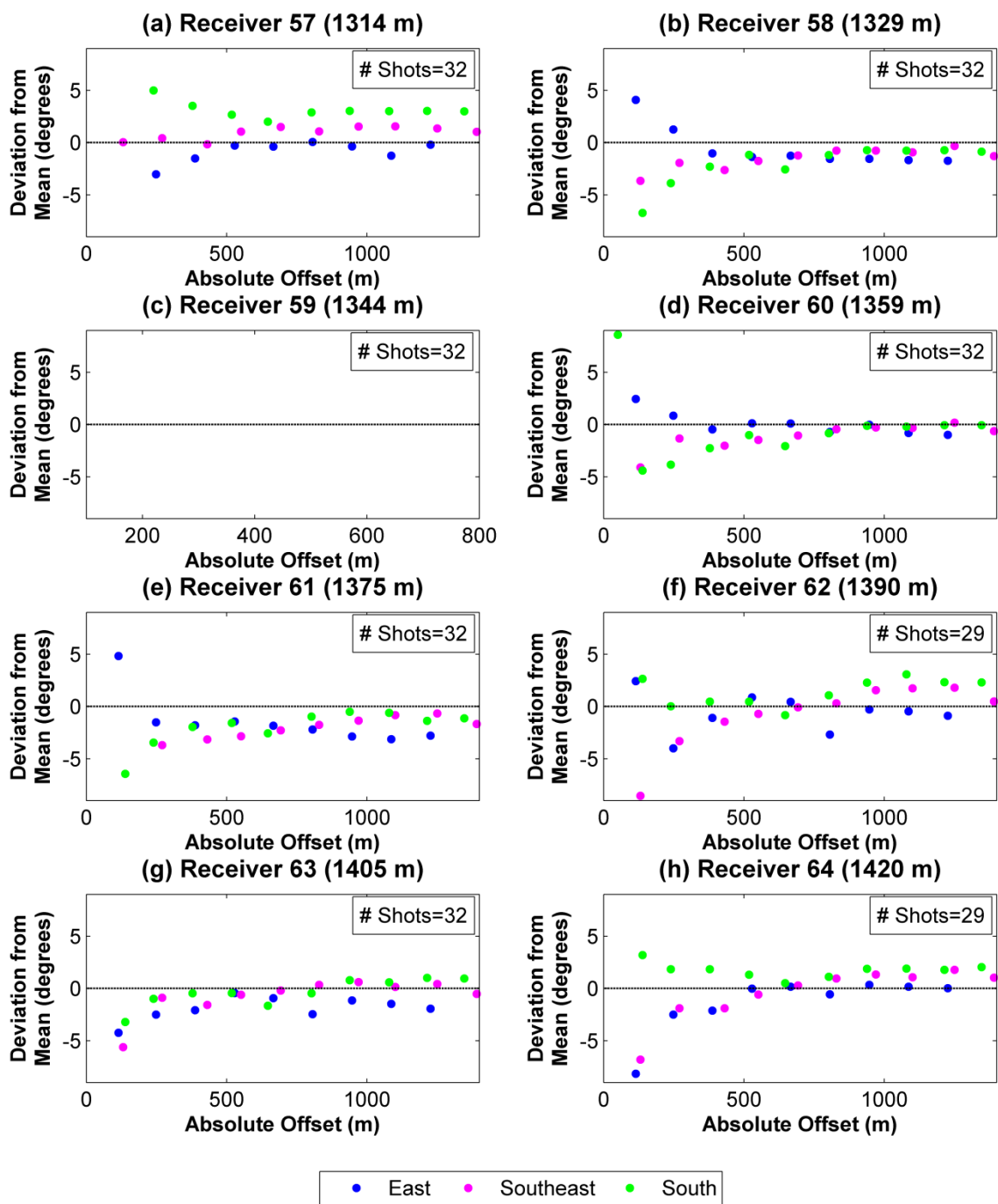


Figure F.8: Deviation in geophone orientation azimuths, versus source-well offset, for Receivers 57-64 in the 2D dataset calculated using analytic method, coloured by line; E is shown in blue, SE is shown in magenta and S is shown in green.

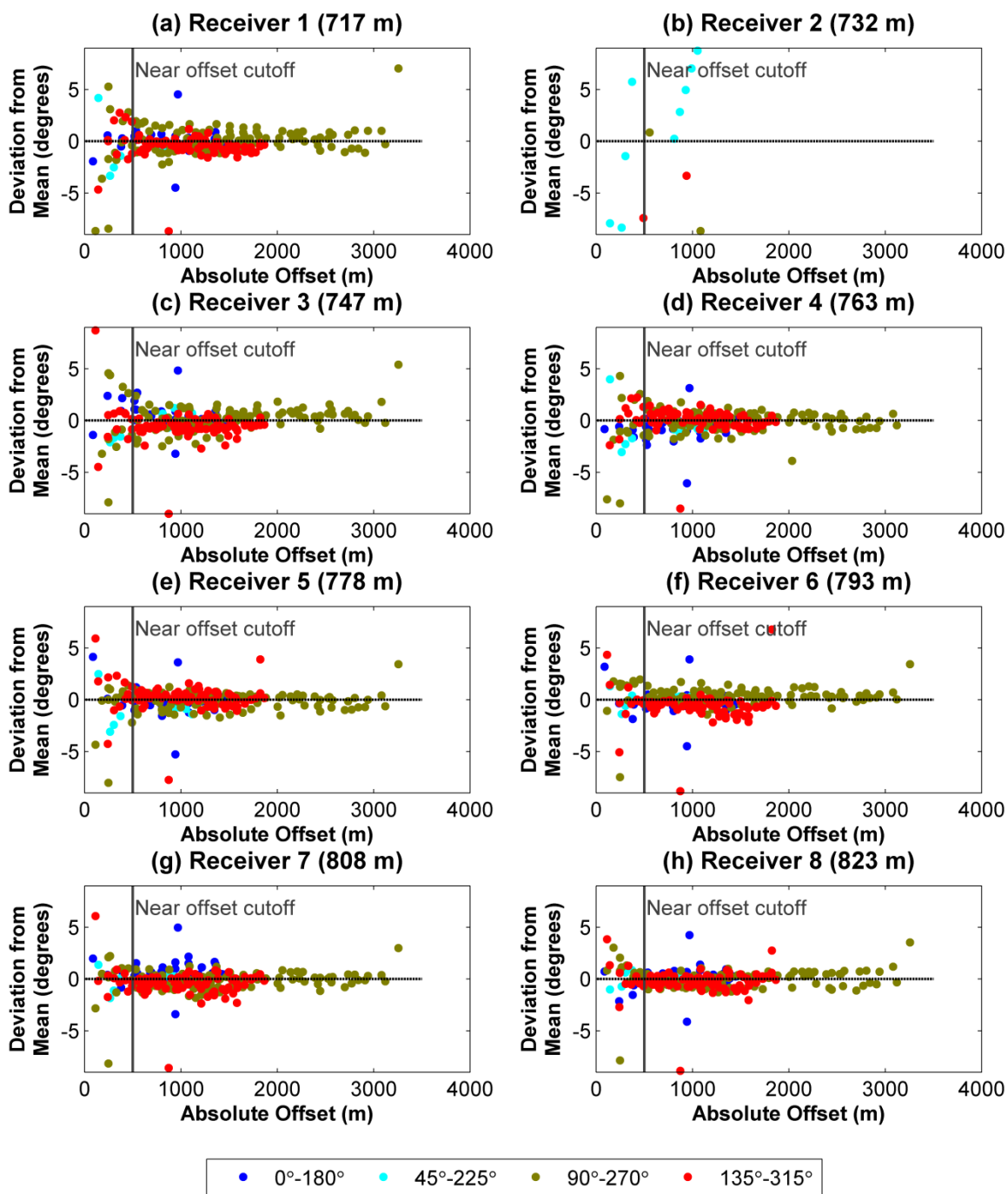


Figure F.9: Deviation in geophone orientation azimuths, versus source-well offset, for Receivers 1-8 in the 3D dataset calculated using analytic method, coloured by bin; 0°-180° is shown in blue, 45°-225° is shown in cyan, 90°-270° is shown in yellow and 135°-315° is shown in red.

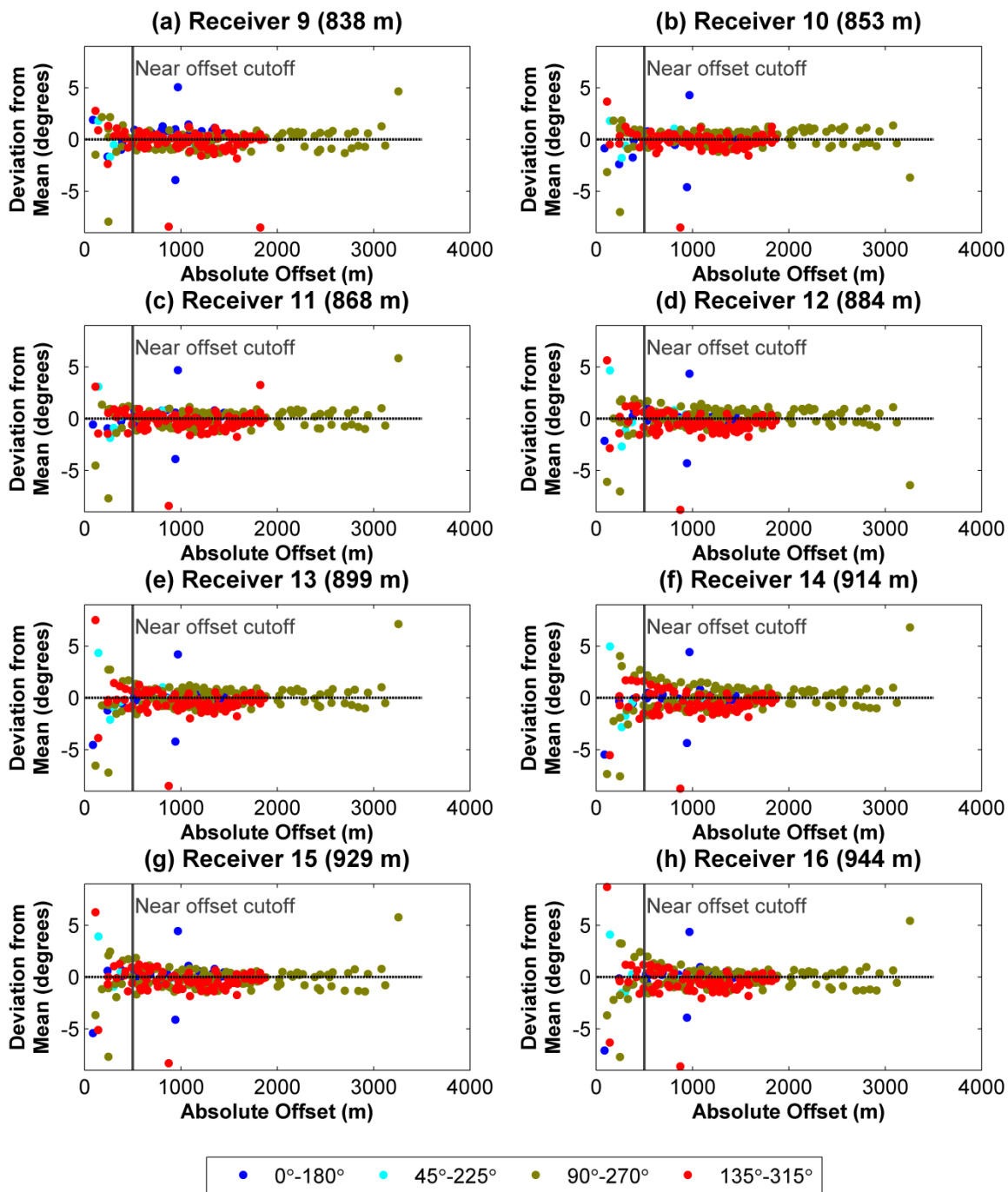


Figure F.10: Deviation in geophone orientation azimuths, versus source-well offset, for Receivers 9-16 in the 3D dataset calculated using analytic method, coloured by bin; 0°-180° is shown in blue, 45°-225° is shown in cyan, 90°-270° is shown in yellow and 135°-315° is shown in red.

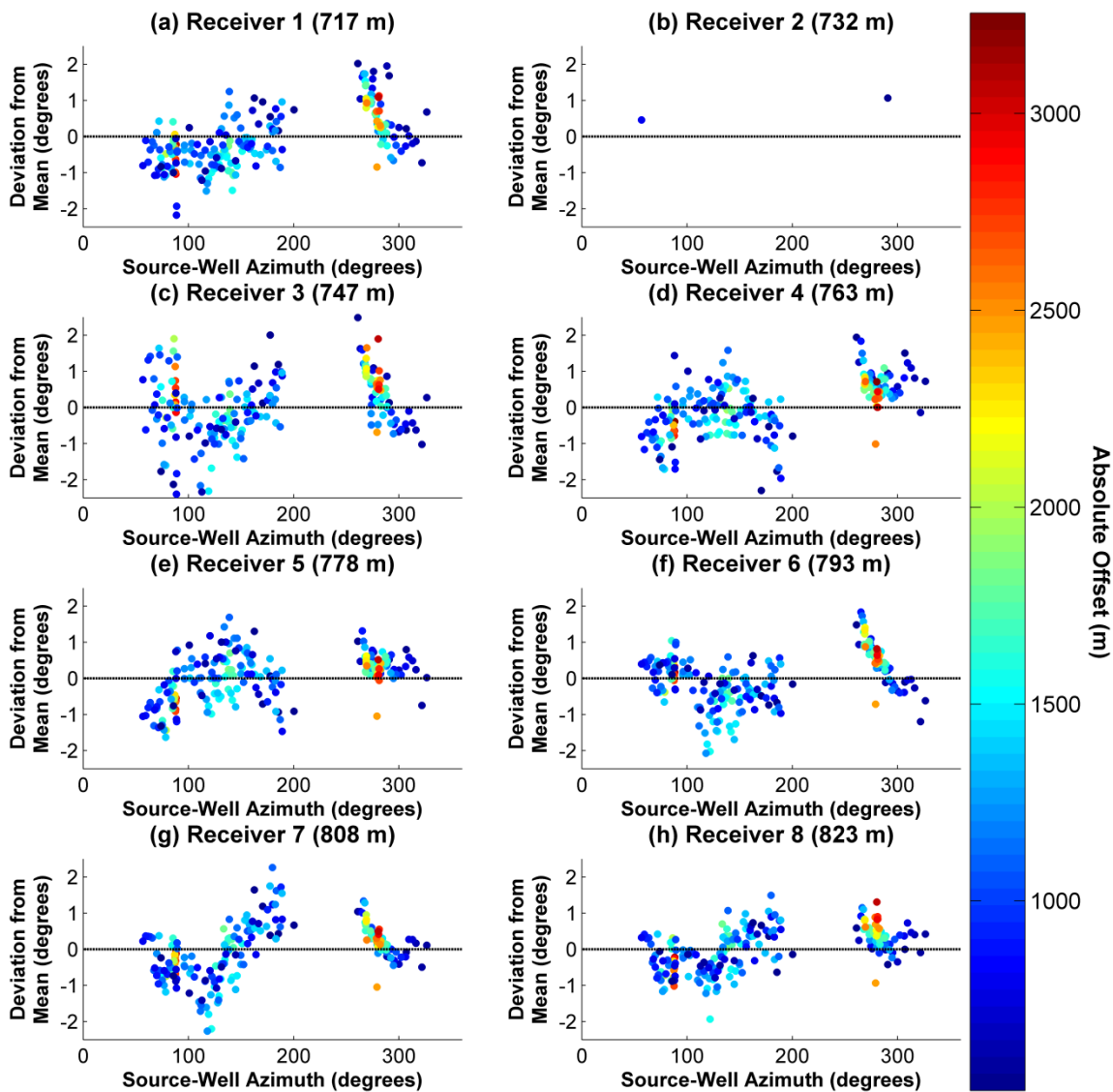


Figure F.11: Deviation in geophone orientation azimuths, versus source-well azimuth, for Receivers 1-8 in the 3D dataset calculated using analytic method, for 3D walkaway coloured by offset. Hotter colours represent far offsets, cooler colours represent near offsets.

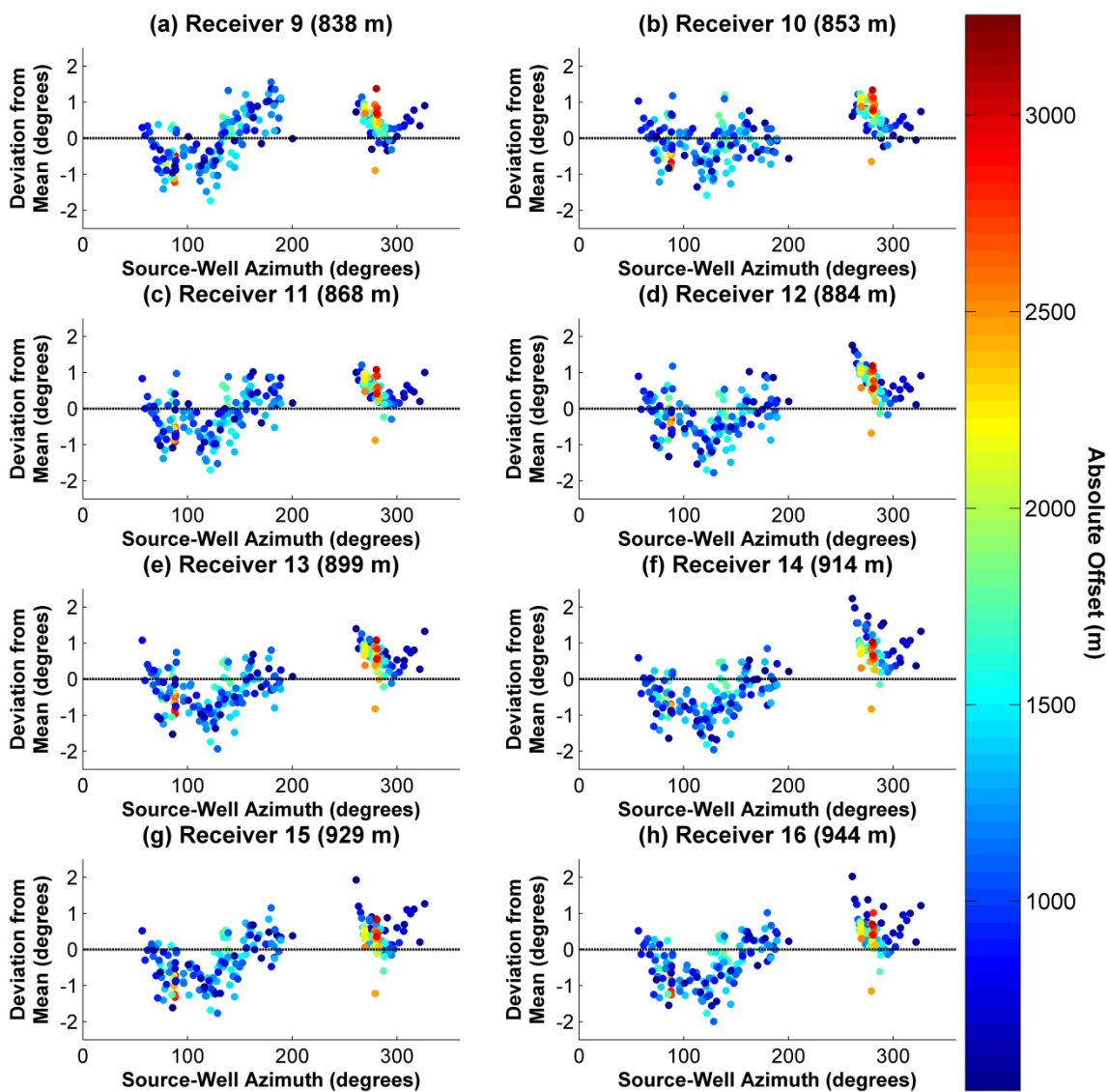


Figure F.12: Deviation in geophone orientation azimuths, versus source-well azimuth, for Receivers 9-16 in the 3D dataset calculated using analytic method, for 3D walkaway coloured by offset. Hotter colours represent far offsets, cooler colours represent near offsets.

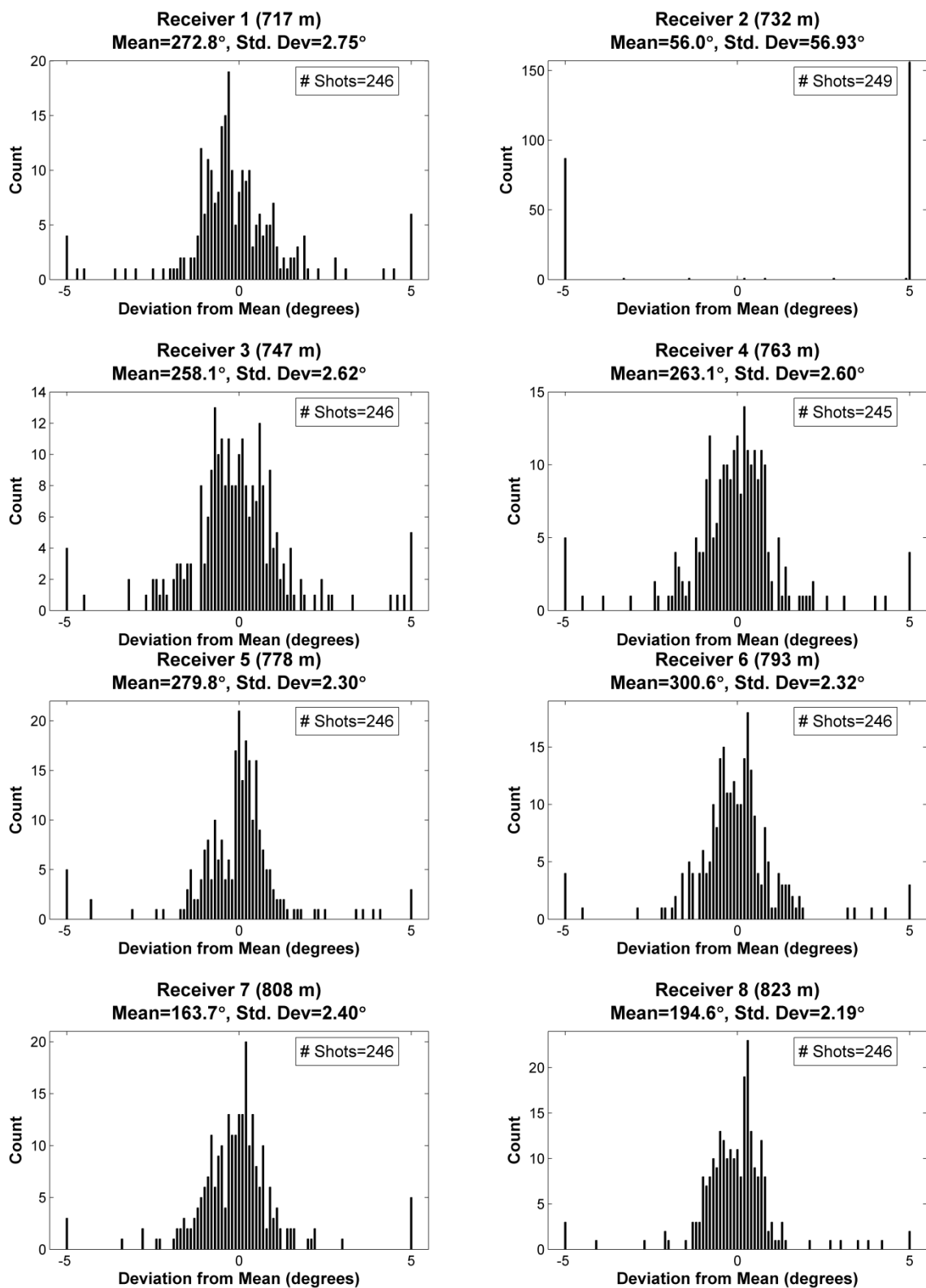


Figure F.13: Histograms of orientation azimuth for Receivers 1-8 in the 3D dataset calculated using analytic method.

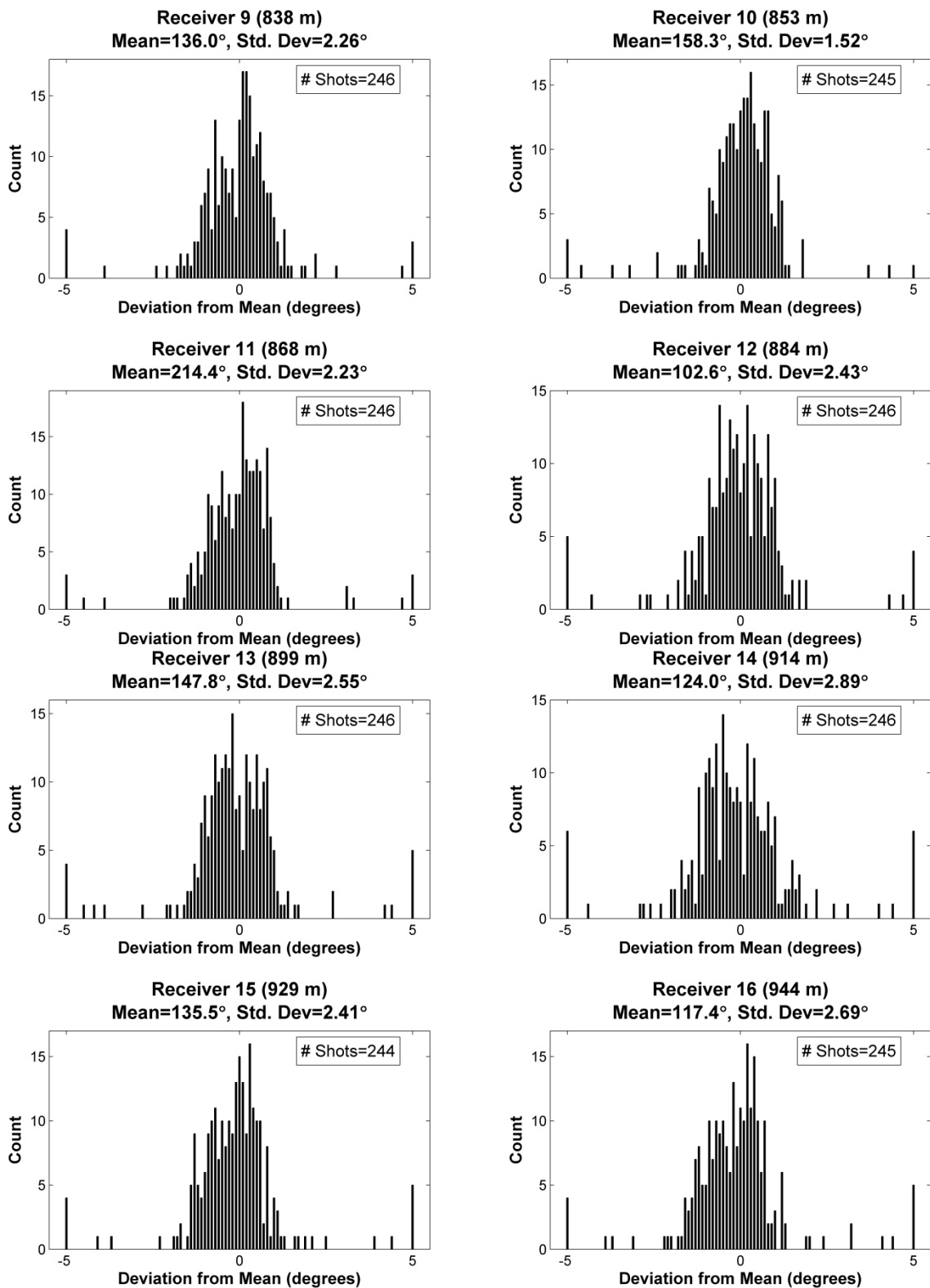


Figure F.14: Histograms of orientation azimuth for Receivers 9-16 in the 3D dataset calculated using analytic method.

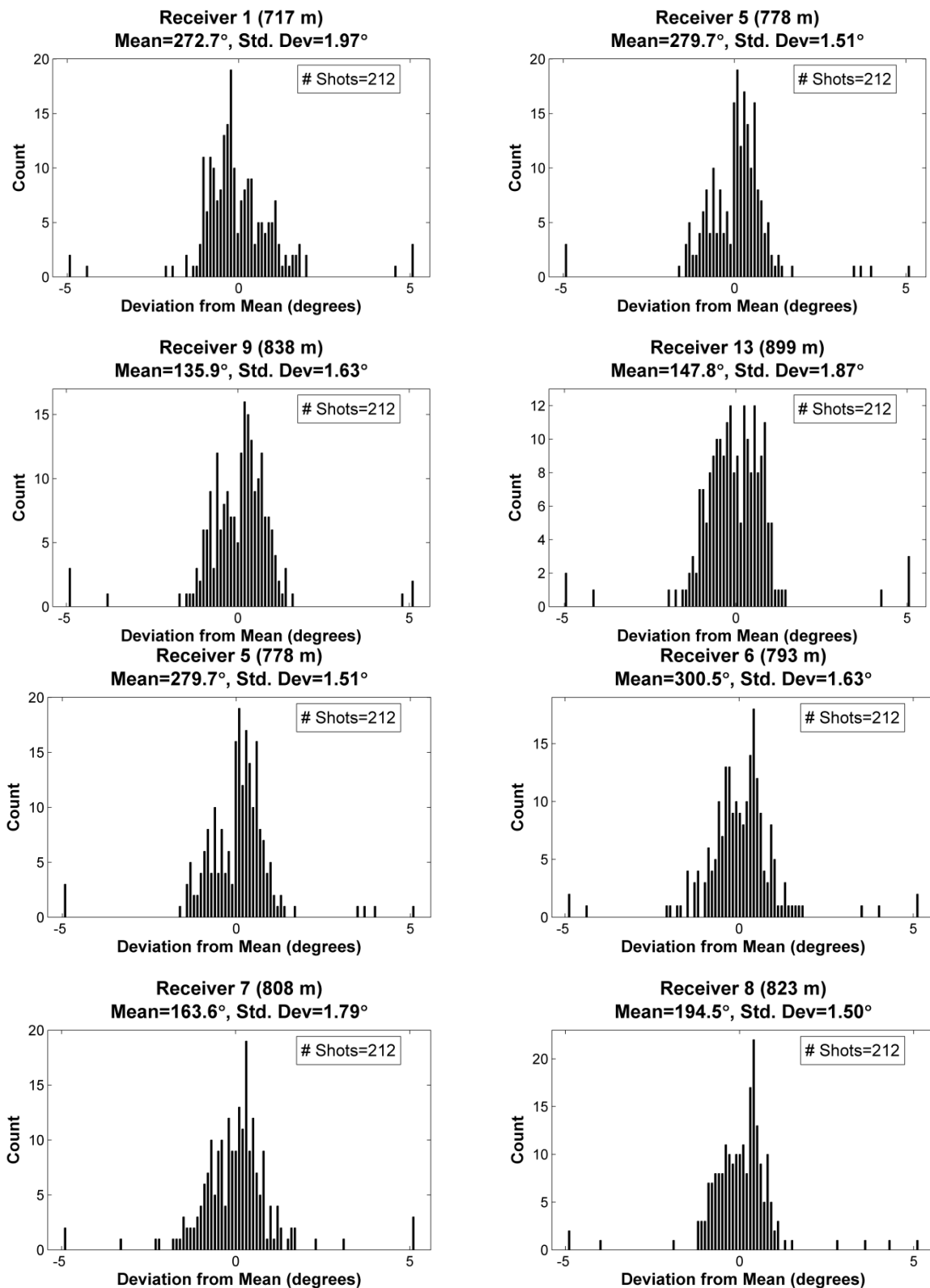


Figure F.15: Histograms of orientation azimuth for Receivers 1-8 in the 3D dataset calculated using analytic method, after rejection of near offset shots.

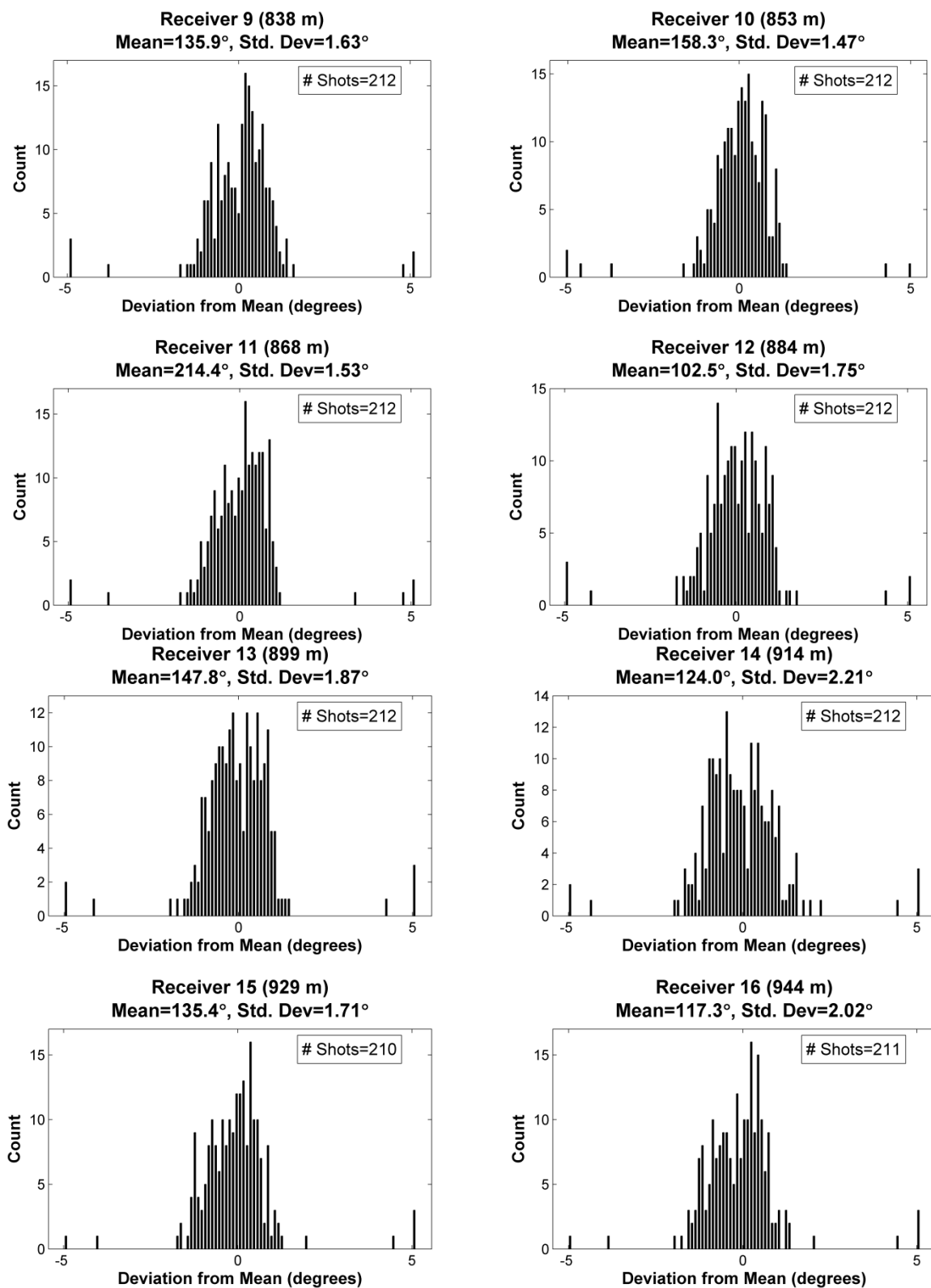


Figure F.16: Histograms of orientation azimuth for Receivers 9-16 in the 3D dataset calculated using analytic method, after rejection of near offset shots.